ARCHIVES OF MECHANICS **Appears since 1949**

Aims and Scope

ARCHIVES OF MECHANICS provides a forum for original research on mechanics of solids, fluids and discrete systems, including the development of mathematical methods for solving mechanical problems. The journal encompasses all aspects of the field, with the emphasis placed on:

- mechanics of materials: elasticity, plasticity, time-dependent phenomena, phase transformation, damage, fracture; physical and experimental foundations, micromechanics, thermodynamics, instabilities
- methods and problems in continuum mechanics: general theory and novel applications, thermomechanics, structural analysis, porous media, contact problems
- dynamics of material systems
- fluid flows and interactions with solids

Address of the Editorial Office:
Institute of Fundamental Technological Research
Świętokrzyska 21
PL 00-049 Warsaw, Poland

Tel.: (48-22) 826 60 22, Fax: (48-22) 826 98 15, E-mail: publikac@ippt.gov.pl

Abstracted/indexed in:

Applied Mechanics Reviews, Current Mathematical Publications, Mathematical Reviews, MathSci, Zentralblatt für Mathematik, UnCover.

Polish Academy of Sciences

Institute of Fundamental Technological Research

Archives of Mechanics

Archiwum Mechaniki Stosowanej

volume 52 issue 4-5

Agencja Reklamowo-Wydawnicza A. Grzegorczyk
Warszawa 2000

SUBSCRIPTIONS

Address of the Editorial Office: Archives of Mechanics
Institute of Fundamental Technological Research, Świętokrzyska 21
PL 00-049 Warsaw, Poland
Tel.: (48-22) 826 60 22, Fax: (48-22) 826 98 15, E-mail: publikac@ippt.gov.pl

Subscription orders for all journals edited by IFTR may be sent directly to the Editorial Office of the Institute of Fundamental Technological Research

Subscription rates

Annual subscription rate (2000) including postage is US $ 192.
Please transfer the subscription fee to our bank account: Payee: IPPT PAN,
Bank: PKO SA. IV O/Warszawa,
Account no. 12401053-40054492-3000-401112-001.

All journals edited by IFTR are available also through:

- Foreign Trade Enterprise ARS POLONA Krakowskie Przedmieście 7, 00-068 Warszawa, Poland fax: (48-22) 826 86 73
- RUCH S.A. ul. Towarowa 28, 00-958 Warszawa, Poland fax:(48-22) 620 17 62
- Agencja Reklamowo-Wydawnicza A. Grzegorczyk, Bitwy Warszawskiej 1920r. 3, 00-973 Warszawa, Poland tel./fax: (48-22) 822 49 36

Warunki prenumeraty

Redakcja przyjmuje prenumeratę na wszystkie czasopisma wydawane przez IPPT PAN. Bieżące numery można nabyć a także zaprenumerować roczne wydanie Archiwum Mechaniki Stosowanej bezpośrednio w Dziale Wydawnictw IPPT PAN, Świętokrzyska 21, 00-049 Warszawa, Tel.: (48-22) 826 60 22; Fax: (48-22) 826 98 15.
Cena rocznej prenumeraty z bonifikatą (na rok 2000) dla krajowego odbiorcy wynosi 150 zł

Również można je nabyć, a także zamówić (przesyłka za zaliczeniem pocztowym) we Wzorcowni Ośrodka Rozpowszechniania Wydawnictw Naukowych PAN,
00-818 Warszawa, ul. Twarda 51/55, tel. (48-22) 697 88 35.
Wpłaty na prenumeratę przyjmują także jednostki kolportażowe RUCH S.A. Oddział Krajowej Dystrybucji Prasy, 00-958 Warszawa, ul. Towarowa 28. Konto: PBK.S.A. XIII Oddział Warszawa nr 11101053-16551-2700-1-67. Dostawa odbywa się pocztą zwykłą w ramach opłaconej prenumeraty z wyjątkiem zlecenia dostawy pocztą lotniczą, której koszt w pełni pokrywa zleceniodawca. Tel.: (48-22) 620 10 39, fax: (48-22) 620 17 62

Arkuszy wydawniczych 32 Arkuszy drukarskich 34.25/A5.
Papier offset. kl III 70 g. B1.
Oddano do składania w lipcu 2000 r. Druk ukończono w październiku 2000 r.
Skład i łamanie: G. Wasilewska. Druk i oprawa: Drukarnia OMIKRON, Stare Babice ul. Kutrzeby 15.

Professor ZENON MRÓZ

Arch. Mech., **52**, 4–5, pp. 487–488, Warszawa 2000

Preface

This special issue of *Archives of Mechanics* is dedicated to Professor Zenon Mróz on the occasion of his 70th birthday.

Zenon Mróz was born at Suchowola in Poland on November 2, 1930. He completed his university education in 1952 at the Department of Mechanical Engineering of the Warsaw University of Technology. In the period 1952-1955 he worked as a designer in the Central Design Office for Internal Combustion Engines. Next, he attended doctoral studies at the Institute of Fundamental Technological Research (known under the Polish abbreviation as IPPT) of the Polish Academy of Sciences in Warsaw. He completed a Ph.D. thesis entitled "Limit load-carrying capacity of plates and shells" under the supervision of Professor Wacław Olszak in 1959. His scientific career was significantly influenced by a postdoctoral fellowship in 1960-1961 at Brown University, Providence, where he worked on the theory of plasticity and structural optimization with Professor William Prager. A few years later, in 1965, he defended at IPPT his D.Sc. (habilitation) thesis on "Constitutive modelling of elastic-plastic materials". He was conferred the title of full professor in 1978, and in 1986 he was elected a corresponding member of the Polish Academy of Sciences. In 1961 Zenon Mróz was married to Barbara, and they have one son and one daughter.

The permanent position of Zenon Mróz, till today, has been at the IPPT in Warsaw, where he is the head of the Division of Inelastic Analysis of Structures and Materials. However, his scientific activity has always had international character. He was invited as visiting professor to a number of foreign universities, including Virginia Polytechnic Institute and State University (1985, 1987, 1990) and University of Minnesota (1996, 2000) in the United States, Ecole Polytechnique (1980) and Université Paris Nord (1992) in France, University of Wales (1979) and Cambridge University (1983) in the United Kingdom, University of Waterloo, Canada (1972), University of Kyoto, Japan (1984). Also, many foreign and Polish researchers stayed at IPPT in Warsaw for longer or shorter periods to take the advantage of co-operating and exchanging ideas with Professor Mróz. His broad spectrum of interests, readiness for deeper discussions and inspiring criticism have been widely appreciated.

Zenon Mróz has made significant scientific contributions to several branches of applied mechanics. One of the main subjects of his work has been the constitutive modelling of inelastic materials. His basic paper "On the description of anisotropic workhardening" (*J. Mech. Phys. Solids*, 15, 163-175, 1967), where an original model of multi-surface plasticity was proposed, has been exceptionally frequently cited and followed in the literature world-wide. In his related papers,

the concepts of discrete memory and damage accumulation under cyclic loading were developed both for metals and geomaterials. The Mróz model of multi-surface plasticity, in different versions, has been implemented in many numerical codes for analysis of inelastic materials and structures. Zenon Mróz is also known as one of the pioneers of non-associative plasticity.

Another important area of his activity encompasses limit states, sensitivity analysis and optimal design of structures. In a series of papers, he developed a unified variational approach to the sensitivity analysis of structures with respect to variable design parameters, shape and topology in pre- and post-critical states. Numerous applications have been presented to optimal design of various structures composed of beams and plates.

The work of Zenon Mróz has also been directed at contact mechanics and the modelling of effects of sliding, friction and wear. Recently, he has developed two-scale models for interaction of surface asperities, as well as phenomenological models for friction and wear in metal forming processes.

Zenon Mróz is the author of over 240 publications, most of them in recognized international journals, and several monographs written jointly with his collaborators. He is currently a member of editorial boards of 17 scientific journals: *Acta Mechanica, Acta Mechanica Sinica, Archives of Computational Methods in Engineering, Archives of Machine Design, Archives of Mechanics, Engineering Computations, European J. Mechanics A/Solids, Int. J. Analytical Methods in Geomechanics, Int. J. Cohesive and Frictional Materials, Int. J. Engineering Analysis and Design, Int. J. Numerical Methods in Engineering, Int. J. Solids and Structures, J. Theoretical and Applied Mechanics, J. Structures and Machines, J. Thermal Stresses, Mechanics of Materials, Mechanics Research Communications.* Impressive is also the list of his invited lectures and memberships in scientific committees of international conferences, including the IUTAM Congress Committee in 1988-1996. Among many distinctions and awards, he received an honorary doctor's degree from 4 universities: Miskolc University, Hungary (1995), Polytechnique de Mons, Belgium (1997), Cracow University of Technology, Poland (1997), University of Waterloo, Canada (1999).

Many friends and colleagues around the world have contributed to this Anniversary Issue to honour Professor Zenon Mróz for his inspiring work and scientific achievements. The journal *Archives of Mechanics*, edited at his home institute and supported by his activity as a member of the International Advisory Board, seemed to be a natural place for publishing the articles dedicated to him.

Henryk Petryk

Arch. Mech., **52**, 4–5, pp. 489–509, Warszawa 2000

Hencky's elasticity model with the logarithmic strain measure: a study on Poynting effect and stress response in torsion of tubes and rods

Dedicated to Professor Zenon Mróz on the occasion of his 70th birthday

O. T. BRUHNS, H. XIAO and A. MEYERS

Institute of Mechanics, Ruhr-University Bochum
D-44780 Bochum, Germany

HENCKY'S ELASTICITY MODEL is a finite strain elastic constitutive equation derived by replacing the infinitesimal strain measure in the classical strain-energy function of infinitesimal isotropic elasticity with Hencky's logarithmic strain measure. ANAND [1, 2] has demonstrated that, with only the two classical Lamé elastic constants measurable at infinitesimal strains, predictions of the just-mentioned simple model for a wide class of materials for moderately large deformations may be in better agreement with experimental data than other known finite elasticity models. The deformation modes considered in Anand's work are simple tension and compression, simple shear, and simple torsion and combined extension-torsion of solid cylinders, etc. Here, we indicate some remarkable properties of this Hencky model and, mainly, we investigate the large deformation responses of this model in torsion of cylindrical tubes and rods with free ends. It is pointed out that if in inelastic modeling, especially in modeling of metal plasticity, the widely-used hypoelastic formulation for the elastic rate of deformation is required to be exactly integrable to an elastic relation, as it should be, then the resulting elastic relation is just the Hencky model, and, further, this model is hyperelastic and the only possible one. In the main aspect, i.e. for the torsion of cylindrical tubes and rods with free ends, we derive explicit analytical solutions for the case of compressible small deformations and for the case of incompressible large deformations. The results derived show, in a clear and direct manner, the second order effects, including the well-known Poynting effect regarding the length change in the axial direction. It is noticeable that, with only the material properties measurable at infinitesimal strains, the Hencky model can predict the just-mentioned second order effects, in particular the Poynting effect, and its predictions are in good accord with experiments reported in the literature.

1. Introduction

LET $\tilde{\mathbf{e}}$ BE THE INFINITESIMAL strain measure. Then the classical strain-energy function of infinitesimal isotropic elasticity is of the form

$$W = \frac{1}{2}\Lambda(\mathrm{tr}\tilde{\mathbf{e}})^2 + G\mathrm{tr}\tilde{\mathbf{e}}^2 . \tag{1.1}$$

Here and henceforth, Λ and G are the Lamé elastic constants, and $\mathrm{tr}\mathbf{S}$ is used to denote the trace of a second order tensor $\mathbf{S}$, i.e. $\mathrm{tr}\mathbf{S} := S_{ii}$ in a Cartesian frame.

Hencky's logarithmic strain measure $\mathbf{h}$ (cf. HENCKY [14 – 16])[1] is defined by

$$\mathbf{h} = \frac{1}{2}\ln\mathbf{B} = \frac{1}{2}\sum_{i=1}^{3}(\ln b_i)\mathbf{n}_i \otimes \mathbf{n}_i , \tag{1.2}$$

where $\mathbf{B}$ is the left Cauchy-Green tensor and b_i and $\mathbf{n}_i$ are the three eigenvalues (possibly repeated) and the three corresponding orthonormal eigenvectors of $\mathbf{B}$. Considering possible multiple eigenvalues and the uniqueness problems that may occur when the triplet $\mathbf{n}_i \otimes \mathbf{n}_i$ in Eq. (1.2) is used, it has been proved more convenient to use the following alternate formulation

$$\mathbf{h} = \frac{1}{2}\sum_{\sigma=1}^{m}(\ln b_\sigma)\mathbf{B}_\sigma , \tag{1.3}$$

where m is the number of distinct eigenvalues and the $\mathbf{B}_\sigma$ are the corresponding eigenprojections. (For detail see e.g. XIAO, BRUHNS and MEYERS [31].)

Replacing now the infinitesimal strain measure $\tilde{\mathbf{e}}$ in Eq. (1.1) with Hencky's strain measure $\mathbf{h}$ given by Eq. (1.2), an isotropic scalar function is obtained:

$$W = \frac{1}{2}\Lambda(\mathrm{tr}\mathbf{h})^2 + G\mathrm{tr}\mathbf{h}^2 . \tag{1.4}$$

Let $\boldsymbol{\sigma}$ be the Cauchy stress tensor and $\mathbf{I}$ the identity tensor. Then we derive a finite strain isotropic elastic constitutive equation as follows:

$$\boldsymbol{\tau} = J\boldsymbol{\sigma} = \frac{\partial W}{\partial \mathbf{h}} = \Lambda(\mathrm{tr}\mathbf{h})\mathbf{I} + 2G\mathbf{h} , \tag{1.5}$$

where $\boldsymbol{\tau}$ $(:=J\boldsymbol{\sigma})$ with $J = \sqrt{b_1 b_2 b_3}$ is the Kirchhoff stress tensor. Evidently, the constitutive equation (1.5), which establishes a linear relation between the Kirchhoff stress and the Hencky strain measure, is a direct generalization of the classical Hooke's law.

ANAND [1, 2] has demonstrated that, with only the two classical Lamé elastic constants Λ and G measurable at infinitesimal strains, predictions of the simple

[1] Although it seems that Hencky independently introduced the logarithmic strain measure in 1928 and was the first to make an extensive use of this strain measure in studying finite elastic deformations of rubbers etc. in a series of works, it had been introduced earlier by several other researchers, including Imbert in 1880 and Ludwik in 1909, *et al.* For detail, refer to a survey by CURNIER and RAKOTOMANANA [7].

elastic equation (1.5) for a wide class of materials for moderately large[2] deformations, where the principal stretch falls within the range $(0.7; 1.3)$, may be in better agreement with experimental data than other known finite elasticity models. In Anand's work a number of basic deformation modes are considered, including simple tension and compression, simple shear, and simple torsion and combined extension-torsion of incompressible solid cylinders, etc.

The finite elasticity equation (1.5) will be called *Hencky's elasticity model.* In Sec. 2, we shall indicate some remarkable properties of this model, and, mainly, in the other sections, besides the basic deformation modes considered by ANAND [1, 2], we further study stress and deformation response of this model, in particular the Poynting effect, in torsion of cylindrical tubes and rods with free ends.

2. Some remarkable properties of the Hencky model

First, we show that the Hencky model (1.5) is a finite elasticity model in Green's sense, i.e. a finite hyperelasticity model, and that its strain-energy function is just given by Eq. (1.4). This fact has been pointed out in XIAO, BRUHNS and MEYERS [29] by virtue of the integrability conditions for the hypoelasticity model with the logarithmic stress rate. In what follows we supply a short alternative proof.

In fact, for the elastic material defined by the Hencky model (1.5), the specific stress power per unit reference volume is given by

$$\operatorname{tr}(\boldsymbol{\tau}\mathbf{D}) = \operatorname{tr}\left(\frac{\partial W}{\partial \mathbf{h}}\mathbf{D}\right), \tag{2.1}$$

where $\mathbf{D}$ is the stretching tensor, or the tensor of rate of deformation. Applying a formula recently derived in XIAO, BRUHNS and MEYERS [30, 32], we infer that the following relation holds:

$$\mathbf{D} = \dot{\mathbf{h}} + \mathbf{h}\boldsymbol{\Omega}^{\log} - \boldsymbol{\Omega}^{\log}\mathbf{h}, \tag{2.2}$$

where $\boldsymbol{\Omega}^{\log}$ is a skewsymmetric tensor, called the logarithmic spin. Since $\boldsymbol{\tau}$ and $\mathbf{h}$ are coaxial, as shown by Eq. (1.5), we have

$$\operatorname{tr}(\boldsymbol{\tau}(\mathbf{h}\boldsymbol{\Omega}^{\log} - \boldsymbol{\Omega}^{\log}\mathbf{h})) = 0.$$

Thus, substituting Eq. (2.2) into Eq. (2.1) and utilizing the equality just given, we derive

$$\operatorname{tr}(\boldsymbol{\tau}\mathbf{D}) = \operatorname{tr}\left(\frac{\partial W}{\partial \mathbf{h}}\dot{\mathbf{h}}\right),$$

[2]We note that the notion of "moderately large" deformations is generally not precisely defined. Here and in what follows we take the definition of ANAND [1, 2]. With reference to the behaviour of most metallic materials these stretches are indeed "moderate", if not "large".

in example

$$\dot{W} = \mathrm{tr}(\boldsymbol{\tau}\mathbf{D})\,. \tag{2.3}$$

The latter relation clearly shows that the material time derivative of the scalar function W given by Eq. (1.4) furnishes the specific stress power of the elastic material defined by Hencky's model (1.5). Thus, Hencky's model is a finite hyperelasticity model and its strain-energy function is exactly the scalar function W given by Eq. (1.4).

Second, we indicate a relation of the model (1.5) with inelastic modeling. In inelastic modeling, especially in modeling of metal plasticity, the hypoelastic equation of grade zero

$$\overset{\circ}{\boldsymbol{\tau}} = 2G\mathbf{D}^e + \Lambda(\mathrm{tr}\mathbf{D}^e)\mathbf{I}\,, \tag{2.4}$$

and its inverse

$$\mathbf{D}^e = \frac{1}{2G}\overset{\circ}{\boldsymbol{\tau}} - \frac{\Lambda}{2G(3\Lambda + 2G)}(\mathrm{tr}\dot{\boldsymbol{\tau}})\mathbf{I}\,, \tag{2.5}$$

are widely used to formulate the linear relation between the elastic rate of deformation, $\mathbf{D}^e$, and an objective stress rate $\overset{\circ}{\boldsymbol{\tau}}$. In the sense of self-consistency, for each process of purely elastic deformation, i.e. for $\mathbf{D}^e = \mathbf{D}$, the above rate equation should be exactly integrable to deliver an elastic relation between a strain measure and the stress $\boldsymbol{\tau}$. Very recently, the present authors (BRUHNS, XIAO and MEYERS [6] and XIAO, BRUHNS and MEYERS [33]) have demonstrated that among the rate type Eqs. (2.4) or (2.5) with all possible corotational stress rates (cf. XIAO, BRUHNS and MEYERS, [32]) and other well-known stress rates, there is one and only one that is exactly integrable to deliver an elastic relation, and that the unique integrable rate-type equation of the form (2.4) or (2.5) exactly results in the Hencky model (1.5).

It turns out that the unique integrable hypoelastic formulation (2.4) or (2.5) is just an equivalent rate form of the Hencky model. Thus, the Hencky model is incorporated as a basic constituent in inelastic modeling.

Finally, it is evident that the potential W given by (1.4) is convex in the logarithmic strain measure $\mathbf{h}$, and hence fulfills Hill's inequality with the logarithmic strain measure (see HILL [17, 18]; see also OGDEN [21] and ŠILHAVÝ [27]).

As mentioned before, it has been confirmed by Anand's impressive work (ANAND [1, 2]) that the model (1.5) with the potential (1.4) and therefore its rate form (2.4) or (2.5) should have wide applicability for elastic behaviour of isotropic materials at moderately large deformations. In fact, it has been incorporated into commercial packets of finite element codes and widely used in numerical computation and simulation, see, e.g., BONET and WOOD [5] for detail.

In the succeeding sections, further study is provided for responses of this model in torsion of cylindrical tubes and solid cylinders.

3. Kinematics for simultaneous extension, inflation and torsion

For elastic materials, the finite deformation mode at issue and the corresponding stress response have been studied by many researchers, in particular including the well-known Poynting effect (cf. POYNTING [22, 23]). The general analyses in this aspect are presented in, e.g. RIVLIN [24, 25], RIVLIN and SAUNDERS [26], GREEN and SHIELD [10], GREEN and ZERNA [12], GREEN and ADKINS [13], TRUESDELL and NOLL [28], and OGDEN [21], *et al.* Investigations of the Poynting effect for elastic materials with particular strain-energy functions, such as neo-Hookean materials, Mooney-Rivlin materials and second order elasticity etc., can be found in, e.g. MURNAGHAN [20], RIVLIN [24, 25], GREEN and SHIELD [10], and GREEN [11], *et al.* Experimental data are available in, e.g. POYNTING [22, 23], RIVLIN and SAUNDERS [26], FOUX [8], FREUDENTHAL and RONAY [9], and BILLINGTON [4], *et al.* Recent development in this respect and related recent literature can be found in the monograph by ANTMAN [3]. Very recently, JIANG and OGDEN [19] have made a comprehensive study of interesting axial shear deformations of compressible elastic circular cylindrical tubes, in which some related references are incorporated.

Consider a fixed rectangular Cartesian coordinate system, $(O; \mathbf{e}_1, \mathbf{e}_2, \mathbf{e}_3)$, with the origin O at the midpoint of the axis of the cylinder under consideration and $\mathbf{e}_3$ in the direction of the just-mentioned axis. Accordingly, let $(O; \mathbf{e}_R, \mathbf{e}_\Theta, \mathbf{e}_3)$ be a fixed cylindrical polar coordinate system. With reference to the two fixed systems, a typical particle P in the cylinder has the coordinates (X_1, X_2, X_3) and (R, Θ, Z), respectively, i.e. the position vector $\overrightarrow{OP}$ of the particle P is given by

$$\mathbf{X} = \overrightarrow{OP} = X_1\mathbf{e}_1 + X_2\mathbf{e}_2 + X_3\mathbf{e}_3 \tag{3.1}$$

with

$$X_1 = R\cos\Theta, \quad X_2 = R\sin\Theta, \quad X_3 = Z\,. \tag{3.2}$$

At a current strained state, the foregoing particle P moves to p. With reference to the afore-mentioned two fixed systems, the point p has the coordinates (x_1, x_2, x_3) and (r, θ, z). For the deformation at issue, we have

$$\mathbf{x} = \overrightarrow{Op} = x_1\mathbf{e}_1 + x_2\mathbf{e}_2 + x_3\mathbf{e}_3 \tag{3.3}$$

with

$$\begin{aligned} x_1 &= r\cos\theta, \quad x_2 = r\sin\theta, \quad x_3 = z\,, \\ r &= r(R), \quad \theta = \Theta + \psi Z, \quad z = \lambda Z\,, \end{aligned} \tag{3.4}$$

where ψ is the angle of twist per unit initial length and λ the axial extension ratio. With Eq. (3.2), Eq. (3.4) may be recast in the form

$$
\begin{aligned}
x_1 &= \frac{r}{R}(X_1 \cos\psi Z - X_2 \sin\psi Z)\,, \\
x_2 &= \frac{r}{R}(X_2 \cos\psi Z + X_1 \sin\psi Z)\,, \\
x_3 &= \lambda Z\,.
\end{aligned} \tag{3.5}
$$

We now introduce a moving system of cylindrical polar coordinates $(O; \mathbf{e}_r, \mathbf{e}_\theta, \mathbf{e}_3)$ by

$$
\begin{aligned}
\mathbf{e}_r &= \mathbf{e}_1 \cos(\Theta + \psi Z) + \mathbf{e}_2 \sin(\Theta + \psi Z)\,, \\
\mathbf{e}_\theta &= -\mathbf{e}_1 \sin(\Theta + \psi Z) + \mathbf{e}_2 \cos(\Theta + \psi Z)\,.
\end{aligned} \tag{3.6}
$$

Utilizing Eqs. (3.5) and (3.2), we obtain the deformation gradient

$$
\mathbf{F} = \frac{\partial \mathbf{x}}{\partial \mathbf{X}} = \frac{\partial x_i}{\partial X_j} \mathbf{e}_i \otimes \mathbf{e}_j,
$$

referred to the fixed system $(O; \mathbf{e}_1, \mathbf{e}_2, \mathbf{e}_3)$. Then, with reference to the moving system given by Eq. (3.6) we arrive at

$$
\begin{aligned}
\mathbf{F} = r' \cos\psi Z \mathbf{e}_r \otimes \mathbf{e}_r + \frac{r}{R} \cos\psi Z \mathbf{e}_\theta \otimes \mathbf{e}_\theta + \lambda \mathbf{e}_3 \otimes \mathbf{e}_3 \\
- r' \sin\psi Z (\mathbf{e}_r \otimes \mathbf{e}_\theta - \mathbf{e}_\theta \otimes \mathbf{e}_r) + \psi r \mathbf{e}_\theta \otimes \mathbf{e}_3\,.
\end{aligned} \tag{3.7}
$$

Throughout the paper we denote $r' = \partial r / \partial R$. Hence, the left Cauchy-Green tensor $\mathbf{B} = \mathbf{F}\mathbf{F}^T$ is given by

$$
\begin{aligned}
\mathbf{B} = r'^2 \mathbf{e}_r \otimes \mathbf{e}_r + r^2 (R^{-2} + \psi^2) \mathbf{e}_\theta \otimes \mathbf{e}_\theta + \lambda^2 \mathbf{e}_3 \otimes \mathbf{e}_3 \\
+ \lambda \psi r (\mathbf{e}_\theta \otimes \mathbf{e}_3 + \mathbf{e}_3 \otimes \mathbf{e}_\theta)\,.
\end{aligned} \tag{3.8}
$$

The three eigenvalues of $\mathbf{B}$ are as follows:

$$
b_1 = r'^2, \quad b_{2,3} = \frac{1}{2}(\lambda^2 + \frac{r^2}{R^2} + \psi^2 r^2 \pm \sqrt{u}) \tag{3.9}
$$

with

$$
u = \left((\lambda + \frac{r}{R})^2 + \psi^2 r^2\right) \left((\lambda - \frac{r}{R})^2 + \psi^2 r^2\right), \tag{3.10}
$$

and their corresponding subordinate eigenprojections are given by

$$
\mathbf{B}_1 = \mathbf{e}_r \otimes \mathbf{e}_r, \quad \mathbf{B}_2 = (\bar{\mathbf{B}} - b_3 \bar{\mathbf{I}})/(b_2 - b_3), \quad \mathbf{B}_3 = (\bar{\mathbf{B}} - b_2 \bar{\mathbf{I}})/(b_3 - b_2)\,, \tag{3.11}
$$

where

$$\bar{\mathbf{I}} = \mathbf{I} - \mathbf{e}_r \otimes \mathbf{e}_r, \quad \bar{\mathbf{B}} = \mathbf{B} - \mathbf{e}_r \otimes \mathbf{e}_r.$$

Then, the Hencky strain tensor $\mathbf{h}$ defined by Eq. (1.3) is given by

$$\mathbf{h} = \frac{1}{2}(\ln b_1 \, \mathbf{B}_1 + \ln b_2 \, \mathbf{B}_2 + \ln b_3 \, \mathbf{B}_3).$$

Hence, we have

$$\mathbf{h} = \lambda\psi r \frac{\ln b_2 - \ln b_3}{2(b_2 - b_3)} (\mathbf{e}_\theta \otimes \mathbf{e}_3 + \mathbf{e}_3 \otimes \mathbf{e}_\theta) + \frac{(b_2 - \lambda^2)\ln b_2 + (\lambda^2 - b_3)\ln b_3}{2(b_2 - b_3)} \mathbf{e}_\theta \otimes \mathbf{e}_\theta + \frac{(\lambda^2 - b_3)\ln b_2 + (b_2 - \lambda^2)\ln b_3}{2(b_2 - b_3)} \mathbf{e}_3 \otimes \mathbf{e}_3 + \ln r' \mathbf{e}_r \otimes \mathbf{e}_r \,. \tag{3.12}$$

4. The governing equations and the boundary conditions

With reference to the moving system (3.6), for the deformation at issue the Cauchy stress tensor $\boldsymbol{\sigma}$ is of the form

$$\boldsymbol{\sigma} = \sigma_{rr}\mathbf{e}_r \otimes \mathbf{e}_r + \sigma_{\theta\theta}\mathbf{e}_\theta \otimes \mathbf{e}_\theta + \sigma_{zz}\mathbf{e}_3 \otimes \mathbf{e}_3 + \sigma_{z\theta}(\mathbf{e}_3 \otimes \mathbf{e}_\theta + \mathbf{e}_\theta \otimes \mathbf{e}_3)\,. \tag{4.1}$$

From the stress-deformation relation (1.5) and Eq. (3.12), we obtain the normal stress components

$$J\sigma_{rr} = \Lambda \ln J + 2G \ln r', \tag{4.2}$$

$$J\sigma_{\theta\theta} = \Lambda \ln J + G \frac{(b_2 - \lambda^2)\ln b_2 + (\lambda^2 - b_3)\ln b_3}{b_2 - b_3}, \tag{4.3}$$

$$J\sigma_{zz} = \Lambda \ln J + G \frac{(\lambda^2 - b_3)\ln b_2 + (b_2 - \lambda^2)\ln b_3}{b_2 - b_3}, \tag{4.4}$$

and the shear stress component

$$J\sigma_{z\theta} = G\lambda\psi r \frac{\ln b_2 - \ln b_3}{b_2 - b_3}, \tag{4.5}$$

where b_2 and b_3 are given by Eqs. (3.9) and (3.10), and

$$J = \det\mathbf{F} = \sqrt{b_1 b_2 b_3} = \frac{\lambda r r'}{R}. \tag{4.6}$$

Noting that each non-vanishing stress component depends merely on r or, equivalently, on R, with reference to the moving system (3.6) the equations of equilibrium are reduced to the single one

$$\frac{\partial \sigma_{rr}}{\partial r} + \frac{\sigma_{rr} - \sigma_{\theta\theta}}{r} = 0 . \tag{4.7}$$

Consider a cylindrical tube with free ends. Assume, further, that there are no tractions exerted on the inner and outer surfaces. Then, the boundary conditions are of the forms:

$$\sigma_{rr}|_{R=R_1} = 0, \quad \sigma_{rr}|_{R=R_0} = 0 , \tag{4.8}$$

$$\int_{R_0}^{R_1} r r' \sigma_{zz} dR = 0 . \tag{4.9}$$

In the above, R_1 and R_0 are used to denote the initial inner and outer radii. When a solid cylinder or a rod with free ends is treated, the conditions (4.8) should be replaced by

$$\sigma_{rr}|_{R=R_1} = 0, \quad r|_{R=0} = r(0) = 0 . \tag{4.10}$$

Finally, the resultant twisting moment at two ends is given by

$$M = 2\pi \int_{R_0}^{R_1} r^2 r' \sigma_{z\theta} dR . \tag{4.11}$$

In Eqs. (4.9) and (4.11), $R_0 = 0$ for solid cylinders and rods.

For the problem at issue, the unknowns are the non-vanishing stress components σ_{rr}, $\sigma_{\theta\theta}$, σ_{zz} and $\sigma_{z\theta}$, as well as the axial extension ratio λ and the current radial coordinate r, each of which is a function of R and ψ. The stress-deformation relations (4.2) – (4.5), the equation of equilibrium (4.7) and the boundary conditions (4.8) and (4.9) (and (4.9) and (4.10), respectively, for a solid cylinder) constitute a coupled system of differential equations for these unknowns. It doesn't seem easy to derive from this system an analytical solution for the general case. In the subsequent sections, we shall provide a small deformation solution for the general case of compressible tubes and rods, and a (moderate) large deformation solution for the case of incompressible tubes and rods.

5. Small deformation solutions for compressible tubes and rods

Suppose that the angle of twist ψ is small, but not necessarily infinitesimal. Both the extension ratio λ and the dimensionless deformation quantity r/R are close to 1, i.e.

$$\tilde{\lambda} = \lambda - 1, \quad \tilde{\alpha} = \frac{r}{R} - 1 \tag{5.1}$$

are small. In fact, the latter two are of the same order of magnitude as ψ^2. Hence we have the asymptotic expressions

$$\begin{aligned}
\tilde{\lambda} &= \mathcal{O}(\psi^2), \quad \tilde{\alpha} = \mathcal{O}(\psi^2), \\
b_2 - b_3 &= \sqrt{u} = 2\psi R + \mathcal{O}(\psi^3), \\
b_2 &= 1 + \psi R + \frac{1}{2}\psi^2 R^2 + \tilde{\lambda} + \tilde{\alpha} + \mathcal{O}(\psi^3), \\
b_3 &= 1 - \psi R + \frac{1}{2}\psi^2 R^2 + \tilde{\lambda} + \tilde{\alpha} + \mathcal{O}(\psi^3), \\
\ln b_2 &= \psi R + \tilde{\lambda} + \tilde{\alpha} + \mathcal{O}(\psi^3), \\
\ln b_3 &= -\psi R + \tilde{\lambda} + \tilde{\alpha} + \mathcal{O}(\psi^3).
\end{aligned}$$

Here and henceforth, the notation $\mathcal{O}(x)$ stands for a small quantity of the same order of magnitude as the small quantity x. Then, utilizing the above asymptotic expressions and neglecting small quantities of higher orders than ψ (for the shear stress component $\sigma_{z\theta}$) or ψ^2 (for the other stress components except $\sigma_{z\theta}$), from Eqs. (3.9), (3.10) and (4.2) – (4.6) we derive

$$\sigma_{rr} = 2G\frac{\partial(R\tilde{\alpha})}{\partial R} + \Lambda\left(\tilde{\lambda} + \tilde{\alpha} + \frac{\partial(R\tilde{\alpha})}{\partial R}\right), \tag{5.2}$$

$$\sigma_{\theta\theta} = 2G(\frac{1}{4}\psi^2 R^2 + \tilde{\alpha}) + \Lambda\left(\tilde{\lambda} + \tilde{\alpha} + \frac{\partial(R\tilde{\alpha})}{\partial R}\right), \tag{5.3}$$

$$\sigma_{zz} = 2G(-\frac{1}{4}\psi^2 R^2 + \tilde{\lambda}) + \Lambda\left(\tilde{\lambda} + \tilde{\alpha} + \frac{\partial(R\tilde{\alpha})}{\partial R}\right), \tag{5.4}$$

$$\sigma_{z\theta} = G\psi R. \tag{5.5}$$

Substituting Eqs. (5.2) and (5.3) into Eq. (4.7) and using $r = R + R\tilde{\alpha}$, we obtain the differential equation

$$(\Lambda + 2G)\left(\frac{\partial^2(R\tilde{\alpha})}{\partial R^2} + \frac{\partial\tilde{\alpha}}{\partial R}\right) = \frac{1}{2}G\psi^2 R. \tag{5.6}$$

The general solution of the above equation is given by

$$\tilde{\alpha} = k_2 R^{-2} + k_1 + \frac{1}{16}\frac{G}{\Lambda + 2G}\psi^2 R^2, \tag{5.7}$$

with the two parameters k_1 and k_2 depending merely on ψ.

Now we consider the boundary conditions. For a tube with the initial outer and inner radii R_1 and R_0, Eqs. (4.8), (4.9), (5.2) and (5.4) yield

$$R = R_1,\ R_0: \quad (\Lambda + 2G)\frac{\partial(R\tilde{\alpha})}{\partial R} + \Lambda(\tilde{\lambda} + \tilde{\alpha}) = 0\,, \tag{5.8}$$

$$\int_{R_0}^{R_1} \left(2G(-\frac{1}{4}\psi^2 R^3 + R\tilde{\lambda}) + \Lambda(R\tilde{\lambda} + R\tilde{\alpha} + R\frac{\partial(R\tilde{\alpha})}{\partial R})\right) dR = 0\,. \tag{5.9}$$

For a rod with the initial radius R_1, Eqs. (4.9), (4.10), (5.2) and (5.4) produce

$$R = R_1: \quad (\Lambda + 2G)\frac{\partial(R\tilde{\alpha})}{\partial R} + \Lambda(\tilde{\lambda} + \tilde{\alpha}) = 0\,, \tag{5.10}$$

$$R = R_0: \quad R\tilde{\alpha} = 0\,, \tag{5.11}$$

$$\int_{0}^{R_1} \left(2G(-\frac{1}{4}\psi^2 R^3 + R\tilde{\lambda}) + \Lambda(R\tilde{\lambda} + R\tilde{\alpha} + R\frac{\partial(R\tilde{\alpha})}{\partial R})\right) dR = 0\,. \tag{5.12}$$

For a tube with the initial outer and inner radii R_1 and R_0, from Eqs. (5.7) – (5.9) we can determine k_1, k_2, $\tilde{\alpha}$ and $\tilde{\lambda}$, and then the stress components. The final results are as follows:

$$\lambda - 1 = \frac{1}{8}\psi^2(R_1^2 + R_0^2)\,, \tag{5.13}$$

$$r = R + \frac{1}{16}\psi^2\left(\frac{G}{\Lambda + 2G}R^3 - \frac{\Lambda + 3G}{\Lambda + 2G}(R_1^2 + R_0^2)R - \frac{2\Lambda + 3G}{\Lambda + 2G}R_1^2 R_0^2 R^{-1}\right), \tag{5.14}$$

$$\sigma_{rr} = \frac{1}{8}\frac{2\Lambda + 3G}{\Lambda + 2G}G\psi^2\left(R^2 - (R_1^2 + R_0^2) + R_1^2 R_0^2 R^{-2}\right), \tag{5.15}$$

$$\sigma_{\theta\theta} = \frac{1}{8}\frac{2\Lambda + 3G}{\Lambda + 2G}G\psi^2\left(3R^2 - (R_1^2 + R_0^2) - R_1^2 R_0^2 R^{-2}\right), \tag{5.16}$$

$$\sigma_{zz} = \frac{1}{8}\frac{\Lambda + 4G}{\Lambda + 2G}G\psi^2(R_1^2 + R_0^2 - 2R^2)\,, \tag{5.17}$$

$$\sigma_{z\theta} = G\psi R\,. \tag{5.18}$$

For a rod with the initial radius R_1, from Eqs. (5.7) and (5.10) – (5.12) we can determine k_1, k_2, $\tilde{\alpha}$ and $\tilde{\lambda}$, and then the stress components. The final results for this case are:

$$\lambda - 1 = \frac{1}{8}\psi^2 R_1^2, \tag{5.19}$$

$$r = R + \frac{1}{16}\psi^2 \left(\frac{G}{\Lambda + 2G} R^3 - \frac{\Lambda + 3G}{\Lambda + 2G} R_1^2 R \right), \tag{5.20}$$

$$\sigma_{rr} = \frac{1}{8} \frac{2\Lambda + 3G}{\Lambda + 2G} G\psi^2 (R^2 - R_1^2), \tag{5.21}$$

$$\sigma_{\theta\theta} = \frac{1}{8} \frac{2\Lambda + 3G}{\Lambda + 2G} G\psi^2 (3R^2 - R_1^2), \tag{5.22}$$

$$\sigma_{zz} = \frac{1}{8} \frac{\Lambda + 4G}{\Lambda + 2G} G\psi^2 (R_1^2 - 2R^2), \tag{5.23}$$

$$\sigma_{z\theta} = G\psi R. \tag{5.24}$$

It is of interest to note that Eqs. (5.19) – (5.23) are also obtainable by setting $R_0 = 0$ in Eqs. (5.13) – (5.17). Thus, Eqs. (5.13) – (5.18) supply the unified solution for both tubes and rods. On the other hand, the solution for incompressible tubes and rods are derivable by evaluating the limits of Eqs. (5.13) – (5.18) when $\Lambda \to \infty$. The results then are:

$$\lambda - 1 = \frac{1}{8}\psi^2 (R_1^2 + R_0^2), \tag{5.25}$$

$$r = R - \frac{1}{16}\psi^2 ((R_1^2 + R_0^2)R + 2R_1^2 R_0^2 R^{-2}), \tag{5.26}$$

$$\sigma_{rr} = \frac{1}{4} G\psi^2 (R^2 - (R_1^2 + R_0^2) + R_1^2 R_0^2 R^{-2}), \tag{5.27}$$

$$\sigma_{\theta\theta} = \frac{1}{4} G\psi^2 (3R^2 - (R_1^2 + R_0^2) - R_1^2 R_0^2 R^{-2}), \tag{5.28}$$

$$\sigma_{zz} = \frac{1}{8} G\psi^2 (R_1^2 + R_0^2 - 2R^2), \tag{5.29}$$

$$\sigma_{z\theta} = G\psi R. \tag{5.30}$$

Now, substituting the results for the rod (Eqs. (5.19) – (5.24)) into Eq. (4.11), and neglecting terms of higher order than ψ^3, we obtain the resultant twisting

moment

$$M = \frac{\pi}{2} G R_1^3 \gamma \left\{ 1 - \frac{1}{48} \gamma^2 \frac{9\Lambda + 17G}{\Lambda + 2G} \right\}. \tag{5.31}$$

In the limit for incompressible materials ($\Lambda \to \infty$), this result turns over to the simple relation

$$\frac{M}{G R_1^3} = \frac{\pi}{2} \gamma \left\{ 1 - \frac{3}{16} \gamma^2 \right\} \tag{5.32}$$

for the dimensionless twisting moment, where here and in what follows the shear strain γ is related to the angle of twist, ψ, through $\gamma = \psi R_1$.

Equation (5.13) indicates that the axial strain $\epsilon_n = \tilde{\lambda}$ is proportional to the square of the angle of twist thus explaining the Poynting effect. According to the experimental data for solid cylindrical specimens of highly filled polyurethane rubber by FREUDENTHAL and RONAY [9], two $\epsilon_n - \gamma$ curves (cf. Fig. 2 therein; the other two curves for creep tests are not included here) for two different strain rates are of the forms:

$$\epsilon_n = 0.095\gamma^2, \quad \epsilon_n = 0.140\gamma^2.$$

The average of the above two curves is

$$\epsilon_n = \tilde{\lambda} = 0.1175\gamma^2.$$

The curve (5.19), i.e. $\epsilon_n = \tilde{\lambda} = 0.125\gamma^2$, predicted by the Hencky model, is in good accord with the above average experimental curve. As a comparison, the prediction from a neo-Hookean model is contrasted with the prediction (5.19) from the Hencky model. By setting $C_2 = 0$ in the classical formula (7.16) given in RIVLIN [25], the $\epsilon_n - \gamma$ relation predicted by the neo-Hookean model assumes the form:

$$\epsilon_n = \frac{1}{12}\gamma^2 = 0.0833\gamma^2.$$

It may be seen that the Hencky model is in better accord with experiments than the neo-Hookean model.

6. Large deformation solution for incompressible tubes and rods

The incompressible Hencky elasticity model assumes the form

$$\boldsymbol{\sigma} = p\mathbf{I} + 2G\mathbf{h}, \tag{6.1}$$

with the hydrostatic pressure $p = p(R)$ and the incompressibility condition

$$J = \det\mathbf{F} = 1. \tag{6.2}$$

For torsion of tubes and rods with free ends under (moderate) large deformations, the two dimensionless deformation quantities $\tilde{\lambda}$ and $\tilde{\alpha}$ defined by Eq. (5.1) are small and of the same order of magnitude. Then, we have the asymptotic expressions

$$b_2 - b_3 = \sqrt{u} = \psi R\sqrt{4+\psi^2R^2} + \frac{2\psi R}{4+\psi^2R^2}\,\tilde{\lambda} + \frac{6\psi R + 2\psi^3R^3}{\sqrt{4+\psi^2R^2}}\,\tilde{\alpha} + \mathcal{O}(\tilde{\lambda}^2),$$

$$b_2 = 1 + \frac{1}{2}\psi^2R^2 + \frac{1}{2}\psi R\sqrt{4+\psi^2R^2} + \left(1 + \frac{\psi R}{\sqrt{4+\psi^2R^2}}\right)\tilde{\lambda} + \left(1 + \psi^2R^2 + \frac{3\psi R + \psi^3R^3}{\sqrt{4+\psi^2R^2}}\right)\tilde{\alpha} + \mathcal{O}(\tilde{\lambda}^2),$$

$$b_3 = 1 + \frac{1}{2}\psi^2R^2 - \frac{1}{2}\psi R\sqrt{4+\psi^2R^2} + \left(1 - \frac{\psi R}{\sqrt{4+\psi^2R^2}}\right)\tilde{\lambda} + \left(1 + \psi^2R^2 - \frac{3\psi R + \psi^3R^3}{\sqrt{4+\psi^2R^2}}\right)\tilde{\alpha} + \mathcal{O}(\tilde{\lambda}^2),$$

$$\ln b_2 = 2\ln\left(\sqrt{1+\frac{1}{4}\psi^2R^2} + \frac{1}{2}\psi R\right) + \left(1 - \frac{\psi R}{\sqrt{4+\psi^2R^2}}\right)\tilde{\lambda} + \left(1 + \frac{\psi R}{\sqrt{4+\psi^2R^2}}\right)\tilde{\alpha} + \mathcal{O}(\tilde{\lambda}^2),$$

$$\ln b_3 = 2\ln\left(\sqrt{1+\frac{1}{4}\psi^2R^2} - \frac{1}{2}\psi R\right) + \left(1 + \frac{\psi R}{\sqrt{4+\psi^2R^2}}\right)\tilde{\lambda} + \left(1 - \frac{\psi R}{\sqrt{4+\psi^2R^2}}\right)\tilde{\alpha} + \mathcal{O}(\tilde{\lambda}^2).$$

Using Eq. (4.6) and neglecting quantities of orders higher than $\tilde{\lambda}$ or $\tilde{\alpha}$, we reduce the condition (6.2) to

$$R\frac{\partial\tilde{\alpha}}{\partial R} + 2\tilde{\alpha} + \tilde{\lambda} = 0. \tag{6.3}$$

Then, we derive

$$\tilde{\alpha} = \frac{1}{R^2}K - \frac{1}{2}\tilde{\lambda}, \tag{6.4}$$

where $K = K(\psi)$ is a quantity of the same order of magnitude as $\tilde{\lambda}$.

On the other hand, replacing $\Lambda \ln J$ in Eqs. (4.2) – (4.4) with p and noting the condition (6.2), we obtain stress-deformation relations. Then, utilizing Eq. (6.4) and the asymptotic expressions given before and neglecting the quantities of higher orders than $\tilde{\lambda}$ or $\tilde{\alpha}$, from the just-mentioned stress-deformation relations we derive the reduced relations

$$\frac{1}{G}\sigma_{rr} = \frac{1}{G}p - \tilde{\lambda} - \frac{1}{2}\omega^{-2}(\psi^2 K)\,, \tag{6.5}$$

$$\frac{1}{G}\sigma_{\theta\theta} = \frac{1}{G}p + \frac{2\omega}{\sqrt{1+\omega^2}}\,\mathrm{sh}^{-1}\omega + \left(\frac{1-2\omega^2}{3(1+\omega^2)} - \frac{1+2\omega^2}{\omega(1+\omega^2)^{3/2}}\,\mathrm{sh}^{-1}\omega\right)\frac{3}{2}\tilde{\lambda} + \frac{1}{4}\omega^{-2}\left(\frac{1+2\omega^2}{1+\omega^2} + \frac{1+2\omega^2}{\omega(1+\omega^2)^{3/2}}\,\mathrm{sh}^{-1}\omega\right)(\psi^2 K)\,, \tag{6.6}$$

$$\frac{1}{G}\sigma_{zz} = \frac{1}{G}p - \frac{2\omega}{\sqrt{1+\omega^2}}\,\mathrm{sh}^{-1}\omega + \left(\frac{1+4\omega^2}{3(1+\omega^2)} + \frac{1+2\omega^2}{\omega(1+\omega^2)^{3/2}}\,\mathrm{sh}^{-1}\omega\right)\frac{3}{2}\tilde{\lambda} + \frac{1}{4}\omega^{-2}\left(\frac{1}{1+\omega^2} - \frac{1+2\omega^2}{\omega(1+\omega^2)^{3/2}}\,\mathrm{sh}^{-1}\omega\right)(\psi^2 K)\,. \tag{6.7}$$

In the above and henceforth, $\mathrm{sh}^{-1}\omega$ is used for the inverse hyperbolic sine function, i.e.

$$\mathrm{sh}^{-1}\omega = \ln(\omega + \sqrt{1+\omega^2})\,, \quad \omega = \frac{1}{2}\psi R\,. \tag{6.8}$$

Moreover, Eq. (4.5) for the shear stress component $\sigma_{z\theta}$ is reduced to

$$\frac{1}{G}\sigma_{z\theta} = \frac{2\mathrm{sh}^{-1}\omega}{\sqrt{1+\omega^2}} - \left(\frac{\omega}{1+\omega^2} - \frac{1+2\omega^2}{(1+\omega^2)^{3/2}}\,\mathrm{sh}^{-1}\omega\right) \cdot \left(\frac{3}{2}\tilde{\lambda} - \frac{1}{4}\omega^{-2}(\psi^2 K)\right)\,. \tag{6.9}$$

Substituting Eqs. (6.5) – (6.6) into Eq. (4.7) and replacing r with R, we derive the differential equation governing the pressure p as follows:

$$\frac{R}{G}\frac{\partial p}{\partial R} = \frac{2\omega}{\sqrt{1+\omega^2}}\,\mathrm{sh}^{-1}\omega + \left(\frac{1}{1+\omega^2} - \frac{1+2\omega^2}{\omega(1+\omega^2)^{3/2}}\,\mathrm{sh}^{-1}\omega\right) \cdot \left(\frac{3}{2}\tilde{\lambda} - \frac{1}{4}\omega^{-2}(\psi^2 K)\right)\,. \tag{6.10}$$

Then, integrating the above equation, we arrive at

$$\frac{1}{G}p = K_0 + (\mathrm{sh}^{-1}\omega)^2 + P(\omega)\tilde{\lambda} + Q(\omega)(\psi^2 K)\,, \tag{6.11}$$

where $K_0 = K_0(\psi)$, and

$$P(\omega) = \frac{3}{2}\frac{\mathrm{sh}^{-1}\omega}{\omega\sqrt{1+\omega^2}}\,, \tag{6.12}$$

$$Q(\omega) = \frac{1}{12}\frac{1}{\omega^2} + \frac{1}{3}\ln\omega - \frac{4\omega^4 + 2\omega^2 + 1}{12\omega^3\sqrt{1+\omega^2}}\,\mathrm{sh}^{-1}\omega\,. \tag{6.13}$$

Then, substituting Eqs. (6.5), (6.7) and (6.10) into the conditions (4.8) and (4.9), we deduce

$$(P_1 - 1)\tilde{\lambda} + (Q_1 - \frac{1}{2\omega_1^2})(\psi^2 K) + K_0 = -(\mathrm{sh}^{-1}\omega_1)^2\,, \tag{6.14}$$

$$(P_0 - 1)\tilde{\lambda} + (Q_0 - \frac{1}{2\omega_0^2})(\psi^2 K) + K_0 = -(\mathrm{sh}^{-1}\omega_0)^2\,, \tag{6.15}$$

$$U_0^1\tilde{\lambda} + V_0^1(\psi^2 K) + 2(\omega_1^2 - \omega_0^2)K_0 = S_0^1\,, \tag{6.16}$$

where $\omega_1 = \frac{1}{2}\psi R_1$, $\omega_0 = \frac{1}{2}\psi R_0$ and the following notations are used

$$Z_0 = Z(\omega_0), \quad Z_1 = Z(\omega_1), \quad Z_0^1 = Z_1 - Z_0,$$

for each function $Z(\omega) \in \{P(\omega), Q(\omega),\ S(\omega), U(\omega), V(\omega)\}$, where $P(\omega)$ and $Q(\omega)$ are given by Eqs. (6.12) – (6.13) and $S(\omega)$, $U(\omega)$ and $V(\omega)$ by

$$S(\omega) = 6\omega\sqrt{1+\omega^2}\mathrm{sh}^{-1}\omega - (3 + 2\omega^2)(\mathrm{sh}^{-1}\omega)^2 - 3\omega^2\,, \tag{6.17}$$

$$U(\omega) = 9(\mathrm{sh}^{-1}\omega)^2 + 4\omega^2 - \frac{6\omega}{\sqrt{1+\omega^2}}\,\mathrm{sh}^{-1}\omega\,, \tag{6.18}$$

$$V(\omega) = \frac{2}{3}\omega^2\ln\omega + \frac{4 - \omega^2 - 2\omega^4}{3\omega\sqrt{1+\omega^2}}\,\mathrm{sh}^{-1}\omega\,. \tag{6.19}$$

From the linear system consisting of Eqs. (6.14) – (6.16), the three functions of the angle of twist ψ, $(\tilde{\lambda}, \psi^2 K, K_0)$, can be determined. The results are as follows:

$$\tilde{\lambda} = \frac{\Delta_1}{\Delta_0}, \quad \psi^2 K = \frac{\Delta_2}{\Delta_0}, \quad K_0 = \frac{\Delta_3}{\Delta_0}\,, \tag{6.20}$$

where Δ_i, $i = 0, 1, 2, 3$, are the four determinants

$$\Delta_0 = \begin{vmatrix} P_1 - 1 & Q_1 - 0.5\omega_1^{-2} & 1 \\ P_0 - 1 & Q_0 - 0.5\omega_0^{-2} & 1 \\ U_0^1 & V_0^1 & 2\omega_1^2 - 2\omega_0^2 \end{vmatrix}, \tag{6.21}$$

$$\Delta_1 = \begin{vmatrix} -(\mathrm{sh}^{-1}\omega_1)^2 & Q_1 - 0.5\omega_1^{-2} & 1 \\ -(\mathrm{sh}^{-1}\omega_0)^2 & Q_0 - 0.5\omega_0^{-2} & 1 \\ S_0^1 & V_0^1 & 2\omega_1^2 - 2\omega_0^2 \end{vmatrix}, \tag{6.22}$$

$$\Delta_2 = \begin{vmatrix} P_1 - 1 & -(\mathrm{sh}^{-1}\omega_1)^2 & 1 \\ P_0 - 1 & -(\mathrm{sh}^{-1}\omega_0)^2 & 1 \\ U_0^1 & S_0^1 & 2\omega_1^2 - 2\omega_0^2 \end{vmatrix}, \tag{6.23}$$

$$\Delta_3 = \begin{vmatrix} P_1 - 1 & Q_1 - 0.5\omega_1^{-2} & -(\mathrm{sh}^{-1}\omega_1)^2 \\ P_0 - 1 & Q_0 - 0.5\omega_0^{-2} & -(\mathrm{sh}^{-1}\omega_0)^2 \\ U_0^1 & V_0^1 & S_0^1 \end{vmatrix}. \tag{6.24}$$

Then, all non-vanishing stress components and the deformation quantity $\tilde{\alpha}$ are obtainable as functions of R and ψ.

For a rod, the second condition in Eq. (4.10) yields Eq. (5.11). From the latter and Eq. (6.4) we infer that $K = 0$, i.e.

$$K = 0, \quad \tilde{\alpha} = -\frac{1}{2}\tilde{\lambda}. \tag{6.25}$$

Thus, Eqs. (6.14) and (6.16) are reduced to

$$(P_1 - 1)\tilde{\lambda} + K_0 = -(\mathrm{sh}^{-1}\omega_1)^2, \tag{6.26}$$

$$U_1\tilde{\lambda} + 2\omega_1^2 K_0 = S_1. \tag{6.27}$$

Then we derive

$$\tilde{\lambda} = \frac{-\omega_1^2\sqrt{1+\omega_1^2} + 2\omega_1(1+\omega_1^2)\mathrm{sh}^{-1}\omega_1 - \sqrt{1+\omega_1^2}(\mathrm{sh}^{-1}\omega_1)^2}{2\omega_1^2\sqrt{1+\omega_1^2} - 3\omega_1\mathrm{sh}^{-1}\omega_1 + 3\sqrt{1+\omega_1^2}(\mathrm{sh}^{-1}\omega_1)^2}, \tag{6.28}$$

$$K_0 = -(\mathrm{sh}^{-1}\omega_1)^2 - \left(\frac{3}{2}\frac{\mathrm{sh}^{-1}\omega_1}{\omega_1\sqrt{1+\omega_1^2}} - 1\right)\tilde{\lambda}. \tag{6.29}$$

Substituting Eqs. (6.25), (6.29), (6.12) and (6.13) into Eqs. (6.11), (6.5) – (6.7) and (6.9), we obtain the stress components

$$\frac{1}{G}\sigma_{rr} = (\mathrm{sh}^{-1}\omega)^2 - (\mathrm{sh}^{-1}\omega_1)^2 + \frac{3}{2}\left(\frac{\mathrm{sh}^{-1}\omega}{\omega\sqrt{1+\omega^2}} - \frac{\mathrm{sh}^{-1}\omega_1}{\omega_1\sqrt{1+\omega_1^2}}\right)\tilde{\lambda}, \tag{6.30}$$

$$\frac{1}{G}\sigma_{\theta\theta} = (\mathrm{sh}^{-1}\omega)^2 - (\mathrm{sh}^{-1}\omega_1)^2 + \frac{2\omega}{\sqrt{1+\omega^2}}\,\mathrm{sh}^{-1}\omega + \frac{3}{2}\left(\frac{1}{1+\omega^2} - \frac{\omega\,\mathrm{sh}^{-1}\omega}{(1+\omega^2)^{3/2}} - \frac{\mathrm{sh}^{-1}\omega_1}{\omega_1\sqrt{1+\omega_1^2}}\right)\tilde{\lambda}, \tag{6.31}$$

$$\frac{1}{G}\sigma_{zz} = (\mathrm{sh}^{-1}\omega)^2 - (\mathrm{sh}^{-1}\omega_1)^2 - \frac{2\omega}{\sqrt{1+\omega^2}}\,\mathrm{sh}^{-1}\omega + \frac{3}{2}\left(\frac{1+2\omega^2}{1+\omega^2} + \frac{2+3\omega^2}{\omega(1+\omega^2)^{3/2}}\,\mathrm{sh}^{-1}\omega - \frac{\mathrm{sh}^{-1}\omega_1}{\omega_1\sqrt{1+\omega_1^2}}\right)\tilde{\lambda}, \tag{6.32}$$

$$\frac{1}{G}\sigma_{z\theta} = \frac{2\mathrm{sh}^{-1}\omega}{\sqrt{1+\omega^2}} + \frac{3}{2}\left(\frac{1+2\omega^2}{(1+\omega^2)^{3/2}}\,\mathrm{sh}^{-1}\omega - \frac{\omega}{1+\omega^2}\right)\tilde{\lambda}. \tag{6.33}$$

Moreover, substituting Eqs. $(5.1)_2$, (6.25) and (6.33) into Eq. (4.11) and neglecting small quantities of higher order than $\tilde{\lambda}$, we obtain the resultant twisting moment

$$M = 2\pi\int_0^{R_1} R^2\left(\frac{2\mathrm{sh}^{-1}\omega}{\sqrt{1+\omega^2}} - \left(\frac{\mathrm{sh}^{-1}\omega}{(1+\omega)^{3/2}} + \frac{\omega}{1+\omega^2}\right)\tilde{\lambda}\right)dR.$$

Hence we have

$$\frac{M}{GR_1^3} = \pi\left\{\frac{2\mathrm{sh}^{-1}\omega_1}{\sqrt{1+\omega_1^2}} - \left(\frac{1}{\omega_1} - \frac{2\mathrm{sh}^{-1}\omega_1}{\omega_1^2\sqrt{1+\omega_1^2}} + \frac{(\mathrm{sh}^{-1}\omega_1)^2}{\omega_1^3}\right)(1+\tilde{\lambda})\right\}, \tag{6.34}$$

the dimensionless twisting moment.

When ψ is small, substituting the asymptotic expressions

$$\sqrt{1+\omega^2} = 1 + \frac{1}{2}\omega^2 + \mathcal{O}(\omega^4), \quad \mathrm{sh}^{-1}\omega = \omega - \frac{1}{6}\omega^3 + \mathcal{O}(\omega^5)$$

into Eq. (6.28), again Eq. (5.19) can be derived. In a similar manner, from Eqs. (6.25) and (6.30) – (6.33) again one can derive Eqs. (5.20) – (5.24). Generally, from Eqs. (6.28) – (6.33) we know that the shear stress component $\sigma_{z\theta}$ is an odd function of ω, while any quantity except $\sigma_{z\theta}$ is an even function of ω. Accordingly, the general expansions with respect to ω are of the forms:

$$\sigma_{z\theta} = \sum_{t=1}^{\infty} A_{2t-1}\,\omega^{2t-1}, \tag{6.35}$$

$$\beta = \sum_{t=1}^{\infty} B_{2t}\,\omega^{2t}, \tag{6.36}$$

where $\beta \in \{\tilde{\lambda}, \tilde{\alpha}, \sigma_{rr}, \sigma_{\theta\theta}, \sigma_{zz}\}$. In the above, the coefficients A_{2t-1} and B_{2t} are independent of ψ and R_1.

7. Results and conclusion

Numerical results have been determined for the axial strain and the resultant twisting moment of a rod at large deformations from Eqs. (6.28) and (6.34), respectively. The corresponding curves of the axial strain $\tilde{\lambda}$ versus ω_1 and the dimensionless resultant twisting moment $M/(GR_1^3)$ versus ω_1 are depicted in Figs. 1 and 2.

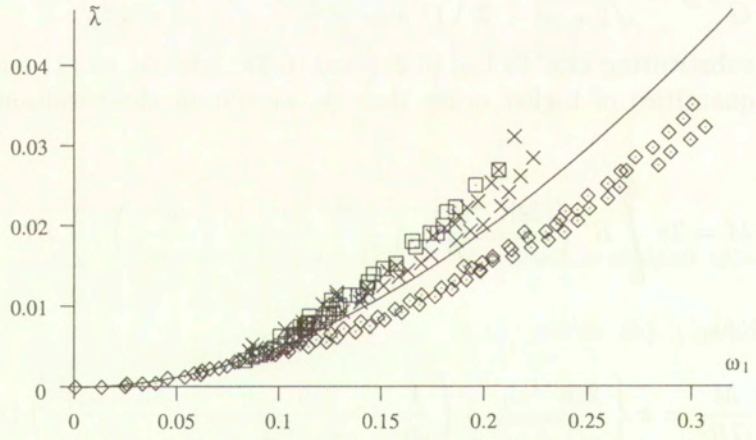

FIG. 1. Axial strain $\tilde{\lambda}$ versus maximum shear strain ω_1.

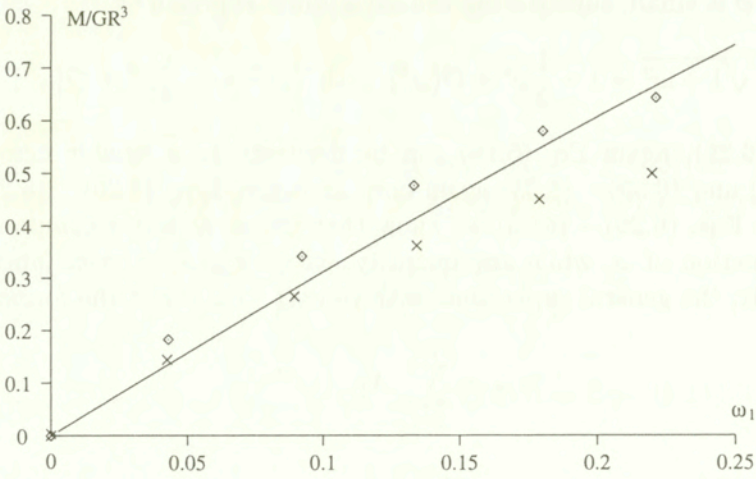

FIG. 2. Dimensionless twisting moment M/GR_1^3 versus maximum shear strain ω_1.

We note that ω_1 herein through (cf. Eq. $(6.8)_2$)

$$\omega_1 = \frac{1}{2}\psi R_1 = \frac{1}{2}\gamma$$

is the normally used maximum shear strain at the outer surface of the rod. In both figures the experimental data of FREUDENTHAL and RONAY [9] for solid cylindrical specimens of highly filled polyurethane rubber at two different strain rates are also incorporated. It can be seen that the $\tilde{\lambda} - \frac{1}{2}\gamma$ relation as well as the twisting moment-$\frac{1}{2}\gamma$ relation predicted by the Hencky model compare favorably with these experiments.

It has to be emphasized further, that even for the moderate large strains under consideration the small deformation solutions for the axial strain (cf. Eq. (5.19)) as well as the twisting moment (cf. Eq. (5.32)) fit fairly well to these data. This finally supports Anand's statement (ANAND [2]) that the Hencky model Eq. (1.5) "*... should be of wide applicability ... for the analysis of general engineering problems involving moderately large elastic strains.*"

Acknowledgement

This work was completed under the financial support of the Deutsche Forschungsgemeinschaft (DFG), contract No.: Br 580/26-1. This support is gratefully acknowledged.

References

1. L. ANAND, *On H. Hencky's approximate strain-energy function for moderate deformations*, ASME J. Appl. Mech., **46**, 78–82, 1979.
2. L. ANAND, *Moderate deformations in extension-torsion of incompressible isotropic elastic materials*, J. Mech. Phys. Solids, **34**, 293–304, 1986.
3. S. S. ANTMAN, *Nonlinear Problems of Elasticity*, Springer Verlag, Berlin 1995.
4. E. W. BILLINGTON, *Non-linear mechanical response of various metals: I. Dynamic and static response to simple compression, tension and torsion in the as-received and annealed states*, J. Phys. D: Appl. Phys., **10**, 519–531, 1977.
5. J. BONET and R. D. WOOD, *Nonlinear Continuum Mechanics for Finite Element Analysis*, Cambridge University Press, Cambridge 1997.
6. O. T. BRUHNS, H. XIAO and A. MEYERS, *Self-consistent Eulerian rate type elastoplasticity models based upon the logarithmic stress rate*, Int. J. Plasticity, **15**, 479–520, 1999.
7. A. CURNIER and L. RAKOTOMANANA, *Generalized strain and stress measures: Critical survey and new results*, Engng. Trans., **39**, 461–538, 1991.
8. A. FOUX, *An experimental investigation of the Poynting effect*, [In:] Second Order Effects in Elasticity, Plasticity and Fluid Dynamics, M. REINER and D. ABIR [Eds.], Pergamon Press, New York etc. 1964.

9. A. M. FREUDENTHAL and M. RONAY, *Second order effects in dissipative media,* Proc. Roy. Soc., **A 292**, 14–50, London 1966.

10. A. E. GREEN and R. T. SHIELD, *Finite extension and torsion of cylinders,* Phil. Trans. Roy. Soc., **A 244**, 47–86, London 1951.

11. A. E. GREEN, *A note on second-order effects in the torsion of incompressible cylinders,* Proc. Cambr. Phil. Soc., **50**, 488–490, 1954.

12. A. E. GREEN and W. ZERNA, *Theoretical Elasticity,* Clarendon Press, Oxford 1954.

13. A. E. GREEN and J. E. ADKINS, *Large elastic deformations,* Clarendon Press, Oxford 1960.

14. H. HENCKY, *Über die Form des Elastizitätsgesetzes bei ideal elastischen Stoffen,* Zeit. Techn. Phys., **9**, 215–220, 457, 1928.

15. H. HENCKY, *The law of elasticity for isotropic and quasi-isotropic substances by finite deformations,* J. Rheology, **2**, 169–176, 1931.

16. H. HENCKY, *The elastic behavior of vulcanized rubber,* Rubber Chem. Techn., **6**, 217–224, 1933.

17. R. HILL, *Constitutive inequalities for simple materials,* J. Mech. Phys. Solids, **16**, 229–242, 1968.

18. R. HILL, *Constitutive inequalities for isotropic elastic solids at finite strain,* Proc. Roy. Soc., **A 314**, 457–472, London 1970.

19. X. JIANG and R. W. OGDEN, *Some new solutions for the axial shear of a circular cylindrical tube of compressible elastic material,* Int. J. Non-linear Mech., **35**, 361–369, 2000.

20. F. MURNAGHAN, *Finite deformation of an elastic solid,* John Wiley and Sons, New York 1951.

21. R. W. OGDEN, *Nonlinear elastic deformations,* Ellis Horwood, Chichester 1984.

22. J. H. POYNTING, *On pressure perpendicular to the shear planes in finite pure shears and on the lengthening of loaded wires when twisted,* Proc. Roy. Soc., **A 82**, 546–559, London 1909.

23. J. H. POYNTING, *On the changes in the dimensions of steel wire when twisted,* Proc. Roy. Soc., **A 86**, 534–561, London 1912.

24. R. S. RIVLIN, *Large elastic deformations of isotropic materials, Part VI. Further results in the theory of torsion, shear, and flexure,* Phil. Trans. Roy. Soc., **A 242**, 173–195, London 1949.

25. R. S. RIVLIN, *The solution of problems in second order elasticity theory,* J. Rat. Mech. Anal., **2**, 53–81, 1953.

26. R. S. RIVLIN and D. W. SAUNDERS, *Large elastic deformations of isotropic materials, Part VII. Experiments on the deformation of rubbers,* Phil. Trans. Roy. Soc., **A 243**, 251–288, London 1951.

27. M. ŠILHAVÝ, *The mechanics and thermodynamics of continuous media,* Springer Verlag, Berlin 1997.

28. C. TRUESDELL and W. NOLL, *The nonlinear field theories of mechanics,* [In:] Handbuch der Physik, S. FLÜGGE [Ed.], Vol. III/3, Springer-Verlag, Berlin etc. 1965.

29. H. XIAO, O. T. BRUHNS and A. MEYERS, *Hypo-elasticity model based upon the logarithmic stress rate,* J. Elasticity, **47**, 51–68, 1997.

30. H. XIAO, O. T. BRUHNS and A. MEYERS, *Logarithmic strain, logarithmic spin and logarithmic rate,* Acta Mechanica, **124**, 89–105, 1997.

31. H. XIAO, O. T. BRUHNS and A. MEYERS, *Strain rates and material spins*, J. Elasticity, **52**, 1–41, 1998.

32. H. XIAO, O. T. BRUHNS and A. MEYERS, *On objective corotational rates and their defining spin tensors*, Int. J. Solids Struct., **35**, 4001–4014, 1998.

33. H. XIAO, O. T. BRUHNS and A. MEYERS, *Existence and uniqueness of the integrable-exactly hypoelastic equation* $\overset{\circ}{\boldsymbol{\tau}}{}^{*} = \lambda(\mathrm{tr}\mathbf{D})\mathbf{I} + 2\mu\mathbf{D}$ *and its significance to finite inelasticity*, Acta Mechanica, **138**, 31–50, 1999.

Received December 3, 2000; revised version June 6, 2000.

Arch. Mech., **52**, 4–5, pp. 511–522, Warszawa 2000

Spatial localization of the error of constitutive law for the identification of defects in elastic bodies

Dedicated to Professor Zenon Mróz on the occasion of his 70th birthday

H. D. BUI ([1-2]), A. CONSTANTINESCU ([2])

([1]) *Electricité de France, Division R& D, Clamart France*

([2]) *Laboratoire de Mécanique des Solides (CNRS UMR 7649) Ecole Polytechnique, 91128 Palaiseau, France bui;constant@lms.polytechnique.fr*

THE ERROR OF CONSTITUTIVE LAW (ECL) is a cost functional currently used in inverse problems for identifying interior distribution of coefficients of partial differential equations from overspecified boundary conditions. In previous works, different authors have shown that the ECL enables a good spatial localization of the perturbations of the coefficients.

The purpose of this paper is to justify this spatial localization property. The result is obtained for the elliptic equations of elasticity using boundary integral representations of the solutions and comparing the linear and the perturbed solution of the problem.

1. Introduction

THE IDENTIFICATION of spatially distributed elastic moduli from overspecified displacement-force boundary measurements is an inverse problem denoted as *generalized elastic tomography* (for an overview see [4]). From a practical point of view this means that an interior distribution of elastic moduli can not be accessed by direct measurements and has to be recovered from boundary information. This can be for example the case, if the initial distribution of elastic moduli is affected by damage.

A series of research papers has been devoted in last years to the solution of different aspects of the problem. The uniqueness and the identifiability results have been obtained in most cases using the observation equation established initially by CALDERON [5] for the linearized electric tomography problem. These

results relate the Dirichlet-to-Neumann data map to integral representations of the distribution of elastic moduli.

Ikehata [9] and Nakamura and Uhlmann [19, 20] solved the linearized isotropic problem (2 Lamé moduli) under different hypothesis of regularity of the moduli. The case of the anisotropic elasticity has been discussed by Constantinescu [7] who constructed a non-uniqueness example based on previous work by Kohn and Vogelius [13] and proposed a reconstruction technique for some cases.

Recently Ikehata [10, 11] gave estimation of the size of inclusion in an integral formulation using the solution of nonperturbed and perturbated linearized direct problem and the Dirichlet-to-Neumann data map.

It is interesting to remark that mathematical results are based on the observation equation and the Dirichlet-to-Neumann data map, whether numerical reconstruction techniques are based on the minimization of error functionals. One of these functionals is the error of constitutive law (ELC), which has the physical dimensions of energy and measures actually the difference between the estimated strain, stress and deformation energy using kinematically and statically admissible fields. Therefore it provides a simple and robust alternating direction minimization algorithm.

This error functional can be first retrieved in the works of Ladevèze and Leguillon [17] as a measure of the error of finite element computations. For the second time it has been utilized as a cost functional for identifying spatially distributed coefficients in partial differential equations. It has been used for electric conductivities by Kohn *et al.* [12, 14], for anisotropic elastic moduli with static measurements by Constantinescu: for two-dimensional problems [6, 7] and for elastic plates [8], or for elastic moduli and modal measurements by Ladèveze *et al.* [18] and Ben Abdallah *et al.* [1, 2].

An intriguing result of the numerical reconstruction using the ELC has been the good spatial localization of the defects or perturbations of the elastic moduli through the error of constitutive law.

The purpose of this paper is to give an formal justification for the spatial localization property of the ELC.

In a first part the solution of the perturbed direct problem is split in a zero order and a first order term. The perturbed, the zero and first order expression of the strains and stresses are represented using a boundary integral formulation. Using these formulations one can estimate the differences between the different solutions as a function of the distance to the boundary or the support of the perturbation. A similar result has been obtained by Isaacson and Isaacson [15] for the inverse electrical problem. Their result is based on the complete solution of an circular domain with a centered inclusion.

As a direct consequence, the estimations for the spatial distribution of the

error of constitutive law as functions of the same distances to the boundary show that the error of constitutive law is negligible outside the defects and far from the boundary.

In the final section some numerical computations of the distribution of the error of constitutive law will illustrate the localization property.

2. The direct and the inverse problem

Let us consider an elastic body under the hypothesis of small strains and rotations. The body occupies a domain Ω in its reference configuration.

The displacement, strain and stress fields respectively, denoted by $\mathbf{u}, \epsilon, \sigma$, are subject, considering the absence of a body force, to the following set of equations:

$$\begin{aligned} \varepsilon &= \frac{1}{2}(\nabla + \nabla^T)\mathbf{u}, \\ \sigma &= \mathbf{L} : \varepsilon, \\ \operatorname{div} \sigma &= \mathbf{0}, \end{aligned} \tag{2.1}$$

where $\mathbf{L}$ represents the fourth order tensor of elastic moduli.

The *direct elasticity problem* consists in computing a solution of the system of partial differential Eq. (2.1) with known elastic moduli $\mathbf{L}$ and given one of the following boundary conditions on $\partial\Omega$: prescribed displacements $\mathbf{u}|_{\partial mit\Omega} = \mathbf{w}$ or prescribed traction $\sigma\mathbf{n}|_{\partial\Omega} = \mathbf{t}$. The pairs of corresponding boundary conditions $(\mathbf{u}, \mathbf{t})$ can generally be described in terms of the Dirichlet-to-Neumann data map:

$$\Lambda_{\mathbf{L}} : \mathbf{w} \longrightarrow \Lambda_{\mathbf{L}}(\mathbf{w}) = \mathbf{t} \tag{2.2}$$

which maps a given boundary displacement at the corresponding boundary traction.

The *inverse elasticity problem* attempts to determine the *unknown* elastic moduli $\mathbf{L}$ from the partial knowledge of the Dirichlet-to-Neumann data map $\Lambda_{\mathbf{L}}$. From a practical point of view; this means that the elastic coefficients have to be determined from a series of overdetermined boundary conditions, i.e. simultaneously known displacements $\mathbf{u}$ and traction $\mathbf{t}$.

Let us suppose that the elastic moduli $\mathbf{L}$ can be expressed as:

$$\mathbf{L} = \mathbf{L}_0 + \eta\mathbf{L}_1, \qquad \forall \mathbf{x} \in \Omega,$$

where $\eta \in \mathbb{R}$ is small parameter. We shall further assume that the support of $\mathbf{L}_1$ is strictly included in the interior of Ω.

In the sequel we shall consider the following series expansion of the displacement field $\mathbf{u}$:

$$\mathbf{u} = \mathbf{u}_0 + \eta \mathbf{u}_1 + o(\eta^2)$$

and of the stress field σ:

$$\sigma = \sigma_0 + \eta \sigma_1 + o(\eta^2),$$

and will inspect the spatial distribution of the various differences of stress terms, remarking that a similar reasoning would hold for the distribution of strains.

The *zero order* displacement $\mathbf{u}_0$ is a solution of the following equation:

$$\text{div } (\mathbf{L}_0 : \nabla \mathbf{u}_0) = \mathbf{0} \tag{2.3}$$

with the boundary conditions:

$$\mathbf{u}_0|_{\partial\Omega} = \mathbf{w} \qquad \text{or} \qquad \sigma_0 \mathbf{n}|_{\partial\Omega} = \mathbf{t}. \tag{2.4}$$

The stress field σ_0 can be expressed using a classical integral representation:

$$\sigma_0(\mathbf{x}) = -\int_{\partial\Omega} \mathbf{P}_{\mathbf{L}_0}(\mathbf{x}, \mathbf{y}) \cdot \mathbf{u}_0(\mathbf{y})\, dS_y + \int_{\partial\Omega} \mathbf{Q}_{\mathbf{L}_0}(\mathbf{x}, \mathbf{y}) \cdot (\sigma_0(\mathbf{y}) \cdot \mathbf{n}(\mathbf{y}))\, dS_y \tag{2.5}$$

with $\mathbf{P}_{\mathbf{L}_0}$ and $\mathbf{Q}_{\mathbf{L}_0}$ vectors fields computed from the Green function of the domain (see Appendix).

If σ_0 has been determined with the imposed displacement $\mathbf{w}$, we can further write:

$$\sigma_0[\mathbf{w}](\mathbf{x}) = -\int_{\partial\Omega} \mathbf{P}_{\mathbf{L}_0}(\mathbf{x}, \mathbf{y}) \cdot \mathbf{w}(\mathbf{y})\, dS_y + \int_{\partial\Omega} \mathbf{Q}_{\mathbf{L}_0}(\mathbf{x}, \mathbf{y}) \cdot \Lambda_{\mathbf{L}_0}(\mathbf{w})(\mathbf{y})\, dS_y. \tag{2.6}$$

The *first order* displacement $\mathbf{u}_1$ is a solution of the following equation:

$$\text{div } (\mathbf{L}_0 : \nabla \mathbf{u}_1) = -\text{ div } (\mathbf{L}_1 : \nabla \mathbf{u}_0) \tag{2.7}$$

with the boundary conditions:

$$\mathbf{u}_1|_{\partial\Omega} = \mathbf{0} \quad \text{or} \quad \sigma_1 \mathbf{n}|_{\partial\Omega} = \mathbf{0}. \tag{2.8}$$

The first order perturbation displacement is therefore generated by the body force term corresponding to stresses created by the zero displacement and the perturbation of the elastic moduli.

The Dirichlet-to-Neuman data map corresponding to this problem will be denoted by $\Lambda_{\mathbf{L}_0, \mathbf{L}_1}$.

The stress field σ_1 can also be expressed using a classical integral representation:

$$\sigma_1(\mathbf{x}) = \int_\Omega \mathbf{L} : \nabla_{\mathbf{x}} \mathbf{G}_{\mathbf{L}_0}(\mathbf{x},\mathbf{y}) \cdot \operatorname{div}_{\mathbf{y}}(\mathbf{L}_1 : \nabla \mathbf{u}_0(\mathbf{y}))\, dV_y \tag{2.9}$$

$$- \int_{\partial\Omega} \mathbf{P}_{\mathbf{L}_0}(\mathbf{x},\mathbf{y}) \cdot \mathbf{u}_1(\mathbf{y})\, dS_y + \int_{\partial\Omega} \mathbf{Q}_{\mathbf{L}_0}(\mathbf{x},\mathbf{y}) \cdot (\sigma_1(\mathbf{y}) \cdot \mathbf{n}(\mathbf{y}))\, dS_y$$

with $\mathbf{P}_{\mathbf{L}_0}$ and $\mathbf{Q}_{\mathbf{L}_0}$ the Green function of the domain (see Appendix).

Similarly, we can rewrite the *perturbed* system of Eq. (2.8) in the form:

$$\operatorname{div}(\mathbf{L}_0 : \nabla \mathbf{u}) = -\operatorname{div}(\eta \mathbf{L}_1 : \nabla \mathbf{u}) \tag{2.10}$$

which yields the following integral representation of the stress field:

$$\sigma(\mathbf{x}) = \int_\Omega \mathbf{L}_0 : \nabla_{\mathbf{x}} \mathbf{G}_{\mathbf{L}_0}(\mathbf{x},\mathbf{y}) \cdot \operatorname{div}_{\mathbf{y}}(\eta \mathbf{L}_1 : \nabla \mathbf{u}(\mathbf{y}))\, dV_y \tag{2.11}$$

$$- \int_{\partial\Omega} \mathbf{P}_{\mathbf{L}_0}(\mathbf{x},\mathbf{y}) \cdot \mathbf{u}(\mathbf{y})\, dS_y + \int_{\partial\Omega} \mathbf{Q}_{\mathbf{L}_0}(\mathbf{x},\mathbf{y}) \cdot (\sigma(\mathbf{y}) \cdot \mathbf{n}(\mathbf{y}))\, dS_y.$$

Let us now compare different stress fields obtained from the same prescribed boundary displacement $\mathbf{w}$.

The difference between the *nonlinear* and the *zero order* solution, $\sigma[\mathbf{w}]$ and $\sigma_0[\mathbf{w}]$, can be written after integration by parts as:

$$\sigma[\mathbf{w}](\mathbf{x}) - \sigma_0[\mathbf{w}](\mathbf{x}) \tag{2.12}$$

$$= (fp) \int_\Omega (\mathbf{L}_0 : \nabla_{\mathbf{x}} \nabla_{\mathbf{y}} \mathbf{G}_{\mathbf{L}_0}(\mathbf{x},\mathbf{y})) \cdot (\mathbf{L}_1 : \nabla \mathbf{u}(\mathbf{y}))\, dV_y$$

$$+ \int_{\partial\Omega} \mathbf{Q}_{\mathbf{L}_0}(\mathbf{x},\mathbf{y}) \cdot (\Lambda_{\mathbf{L}}(\mathbf{w}) - \Lambda_{\mathbf{L}_0}(\mathbf{w}))\, dS_y,$$

where (fp) denotes that the finite part of the integral.

A close inspection of the integrals shows their behavior for $\mathbf{x} \in \Omega \setminus \operatorname{supp}\mathbf{L}_1$. For a three-dimensional problem:

- the first term behaves as $|\mathbf{x} - \mathbf{y}|^{-3}$. As the inclusion lies in the interior of the body, $\operatorname{supp}\mathbf{L}_1 \subset \Omega$, it follows that the integral decreases as r^{-3} where $r = d(\mathbf{x}, \operatorname{supp}\mathbf{L})$,
- the second term behaves as $|\mathbf{x} - \mathbf{y}|^{-2}$, it then follows that the integral decreases as r^{-2} with $r = d(\mathbf{x}, \partial\Omega)$.

For two-dimensional problems, the integral decreases as r^{-2} with the distance from the inclusion ($r = d(\mathbf{x}, \text{supp}\mathbf{L})$) and as r^{-1} with the distance from the boundary ($r = d(\mathbf{x}, \partial\Omega)$).

A direct consequence of this behavior, whether in two or three dimensions, is that the stress difference $\sigma[\mathbf{w}] - \sigma_0[\mathbf{w}]$ is negligible outside the support of the perturbation of the elastic moduli $\mathbf{L}_1$ and far from the boundaries.

The difference between the *nonlinear* stress term and the *first order* solution, $\sigma[\mathbf{w}]$ and $\sigma_0[\mathbf{w}] + \eta\sigma_1[\mathbf{0}]$, can be expressed in a similar way and one obtains:

$$\begin{aligned}(2.13)\qquad &\sigma[\mathbf{w}](\mathbf{x}) - (\sigma_0[\mathbf{w}](\mathbf{x}) + \eta\sigma_1[\mathbf{0}](\mathbf{x})) \\ &= (fp)\int_{\Omega} (\mathbf{L}_0 : \nabla_{\mathbf{x}}\nabla_{\mathbf{y}}\mathbf{G}_{\mathbf{L}_0}(\mathbf{x},\mathbf{y})) \cdot (\eta\mathbf{L}_1(\mathbf{y}) : \nabla(\mathbf{u}(\mathbf{y}) - \mathbf{u}_0)\, dV_y) \\ &\quad + \int_{\partial\Omega} \mathbf{Q}_{\mathbf{L}_0}(\mathbf{x},\mathbf{y}) \cdot (\Lambda_{\mathbf{L}}(\mathbf{w}) - \Lambda_{\mathbf{L}_0}(\mathbf{w}) - \eta\Lambda_{\mathbf{L}_0,\mathbf{L}_1}(\mathbf{0}))\, dS_y.\end{aligned}$$

As before, due to the singular behavior of the Green function and its derivatives, one can remark that this stress difference is also negligible outside the support of the perturbation of the elastic moduli $\mathbf{L}_1$ and far from the boundary, since the behavior of the integrals is similar to the one before.

One can observe that the technique developed before is related to the *multiple reciprocity method* [21, 22] which allows to transform the volume integral corresponding to a body force into an infinite series of boundary integrals using the solutions of a series of auxiliary problems. The developement of the series has been stopped here at its first term in order to obtain the results presented in the sequel.

3. Spatial defect localization of the error of constitutive law

The error of constitutive law is an error functional which can be defined for triplet $(\mathbf{L}, \epsilon, \sigma)$ of a priori independent fields of elastic moduli, strains and stresses respectively, as:

$$\begin{aligned}(3.1)\qquad \mathcal{J}(\mathbf{L},\epsilon,\sigma) &= \int_{\Omega} \left|\mathbf{L}^{-\frac{1}{2}} : \sigma - \mathbf{L}^{\frac{1}{2}} : \epsilon\right|^2 dV \\ &= \int_{\Omega} \left(\sigma : \mathbf{L}^{-1} : \sigma - 2\sigma : \epsilon + \epsilon : \mathbf{L} : \epsilon\right) dV \\ &= \int_{\Omega} \left(\sigma_{ij} L^{-1}_{ijkl} \sigma_{kl} - 2\sigma_{ij}\epsilon_{ij} + \epsilon_{ij} L_{ijkl} \epsilon_{kl}\right) dV.\end{aligned}$$

The symetry and the positive definiteness of $\mathbf{L}$ assure the existence of $\mathbf{L}^{-\frac{1}{2}}$.

The error of constitutive law can also be expressed in one of the following equivalent forms:

$$\mathcal{J}(\mathbf{L},\epsilon,\sigma) = \int_{\Omega} (\sigma - \mathbf{L}:\epsilon) : \mathbf{L}^{-1} : (\sigma - \mathbf{L}:\epsilon)\ dV \tag{3.2}$$

$$= \int_{\Omega} \left(\mathbf{L}^{-1}:\sigma - \epsilon\right) : \mathbf{L} : \left(\mathbf{L}^{-1}:\sigma - \epsilon\right)\ dV.$$

Let us consider the corresponding elastic solutions $(\mathbf{u_L}[\mathbf{w}], \epsilon_{\mathbf{L}}[\mathbf{w}], \sigma_{\mathbf{L}}[\mathbf{w}])$ and $(\mathbf{u_L}[\mathbf{t}], \epsilon_{\mathbf{L}}[\mathbf{t}], \sigma_{\mathbf{L}}[\mathbf{t}])$ determined by the elasticity tensor $\mathbf{L}$ in the absence of body forces and the boundary displacement $\mathbf{w}$ respectively boundary traction $\mathbf{t}$.

For these fields one can write the error of constitutive law from (3.2) as:

$$\mathcal{J}(\mathbf{L}, \epsilon_{\mathbf{L}}[\mathbf{w}], \sigma_{\mathbf{L}}[\mathbf{t}]) \tag{3.3}$$

$$= \int_{\Omega} \left(\mathbf{L}^{-1} : \sigma_{\mathbf{L}}[\mathbf{t}] - \epsilon_{\mathbf{L}}[\mathbf{w}]\right) : \mathbf{L} : \left(\mathbf{L}^{-1} : \sigma_{\mathbf{L}}[\mathbf{t}] - \epsilon_{\mathbf{L}}[\mathbf{w}]\right)\ dV$$

$$= \int_{\Omega} (\epsilon_{\mathbf{L}}[\mathbf{w}] - \epsilon_{\mathbf{L}}[\mathbf{t}]) : \mathbf{L} : (\epsilon_{\mathbf{L}}[\mathbf{w}] - \epsilon_{\mathbf{L}}[\mathbf{t}])\ dV.$$

After integration by parts, using first the equilibrium equations and then the boundary conditions for both solutions, one obtains:

$$\mathcal{J}(\mathbf{L}, \epsilon_{\mathbf{L}}[\mathbf{w}], \sigma_{\mathbf{L}}[\mathbf{t}]) = \int_{\partial\Omega} (\mathbf{u_L}[\mathbf{w}] - \mathbf{u_L}[\mathbf{t}]) : (\sigma_{\mathbf{L}}[\mathbf{w}] \cdot \mathbf{n} - \sigma_{\mathbf{L}}[\mathbf{t}] \cdot \mathbf{n})\ dS \tag{3.4}$$

$$= \int_{\partial\Omega} (\mathbf{w} - \mathbf{u_L}[\mathbf{t}]) \cdot (\sigma_{\mathbf{L}}[\mathbf{w}]\mathbf{n} - \mathbf{t})\ dS.$$

One can see that if $(\mathbf{w}, \mathbf{t})$ is a measurement pair, i.e. $\mathbf{t} = \Lambda_{\mathbf{L}}(\mathbf{w})$, then $\mathbf{u_L}[\mathbf{w}] = \mathbf{u_L}[\mathbf{t}]$, consequently the ECL vanishes as expected: $\mathcal{J}(\mathbf{L}, \epsilon_{\mathbf{L}}[\mathbf{w}], \sigma_{\mathbf{L}}[\mathbf{t}] = \mathbf{0}$.

The last boundary integral provides another physical interpretation for the ELC as the mechnaical work provided by the error in displacements on the error of forces.

Let us now assume that $(\mathbf{w}, \mathbf{t})$ is a measurement pair, i.e. $\mathbf{t} = \Lambda_{\mathbf{L}}(\mathbf{w})$ and compute the zero order approximations $\mathbf{u}_0[\mathbf{w}]$ and $\mathbf{u}_0[\mathbf{t}]$. Using the solution of the unperturbed problem $\mathbf{u}[\mathbf{w}] = \mathbf{u}[\mathbf{t}]$, we obtain the following expressions for the error of constitutive law computed for the zero order fields:

$$\mathcal{J}(\mathbf{L}_0, \epsilon_0[\mathbf{w}], \sigma_0[\mathbf{t}]) = \int_\Omega (\epsilon_0[\mathbf{w}] - \epsilon_0[\mathbf{t}]) : \mathbf{L}_0 : (\epsilon_0[\mathbf{w}] - \epsilon_0[\mathbf{t}])\ dV \tag{3.5}$$

$$= \int_\Omega (\epsilon_0[\mathbf{w}] - \epsilon[\mathbf{w}]) : \mathbf{L}_0 : (\epsilon_0[\mathbf{w}] - \epsilon[\mathbf{w}])\ dV$$

$$+ \int_\Omega (\epsilon[\mathbf{t}] - \epsilon_0[\mathbf{t}]) : \mathbf{L}_0 : (\epsilon[\mathbf{t}] - \epsilon_0[\mathbf{t}])\ dV.$$

It is seen, on the one hand that, this expression is the one minimized in the alternating direction implicit algorithm [7] and, on the other hand, that the ELC is now expressed in terms of the difference between the perturbed and the zero order solution of the direct problem which have been previously computed.

The integrand in the ECL is therefore negligible far from the support of the inclusion and the boundary. More precisely, in the three-dimensional problem they behave as:

- r^{-6} as a function of the distance to the support of the inclusion $r = d(\mathbf{x}, \text{supp}\mathbf{L})$, and as
- r^{-4} as a function of the distance to the boundary $r = d(\mathbf{x}, \partial\Omega)$.

For two-dimensional problems, the decrease is in r^{-4} from the inclusion ($r = d(\mathbf{x}, \text{supp}\mathbf{L})$) and in r^{-2} from the boundary ($r = d(\mathbf{x}, \partial\Omega)$).

4. Numerical examples

The good spatial localization of defects of the error of constitutive law have been reported in a series of papers [1, 2, 6, 7, 8].

We shall present in the next example some localization results of the error of constitutive law. The case treated here has been computed for a square inclusion in an isotropic elastic body. The distribution of the Young modulus is represented in Fig. 1.

First a series of displacement-force measurements $(\mathbf{w}_i, \mathbf{t}_i), i = 1, N$ have been simulated by a direct numerical computation for the perturbed distribution of elastic moduli $\mathbf{L} = \mathbf{L}_0 + \eta\mathbf{L}_1$. These measurements corresspond to the prescribed distributed parabolic pressures at different locations around the body.

Then a series of first order solutions $\mathbf{u}_0[\mathbf{w}_i], i = 1, N$ and $\mathbf{u}_0[\mathbf{t}_i], i = 1, N$ have been computed from the previous measurements $(\mathbf{w}_i, \mathbf{t}_i), i = 1, N$ with the unperturbed moduli $\mathbf{L}_0$.

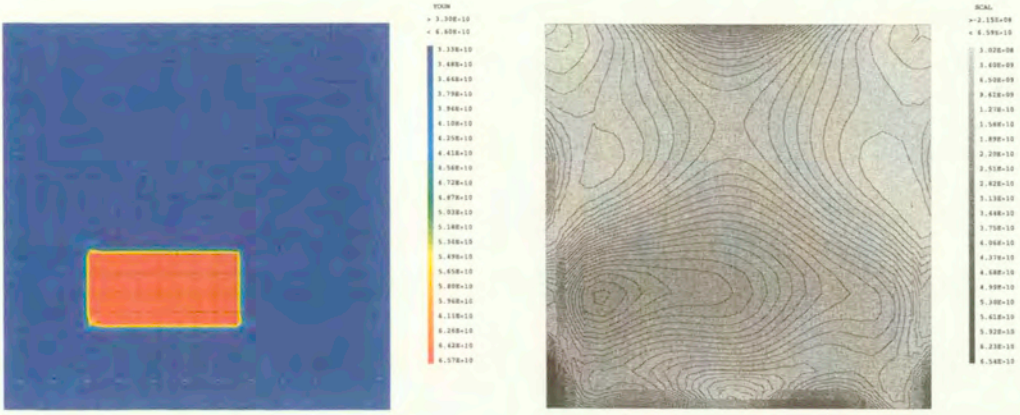

FIG. 1. Spatial distribution of the perturbed moduli $\mathbf{L} = \mathbf{L}_0 + \eta \mathbf{L}_1$ for a square inclusion (left) and the corresponding error of constitutive law given by a parabolic pressure distribution in the middle of the upper surface (right).

For the measurement i, $(\mathbf{w}_i, \mathbf{t}_i)$, the error in the constitutive law is then defined as (see Eq. (3.5)):

$$\mathcal{J}(\mathbf{L}_0, \epsilon_0[\mathbf{w}_i], \sigma_0[\mathbf{t}_i]).$$

In Fig. 2 we have presented the spatial distribution of the inclusion and the distribution of ECL corresponding to only one measurement. It is interesting to see that with only one measurement, a pressure peak appearing in the middle of the upper side of the domain, the inclusion has practically been localized.

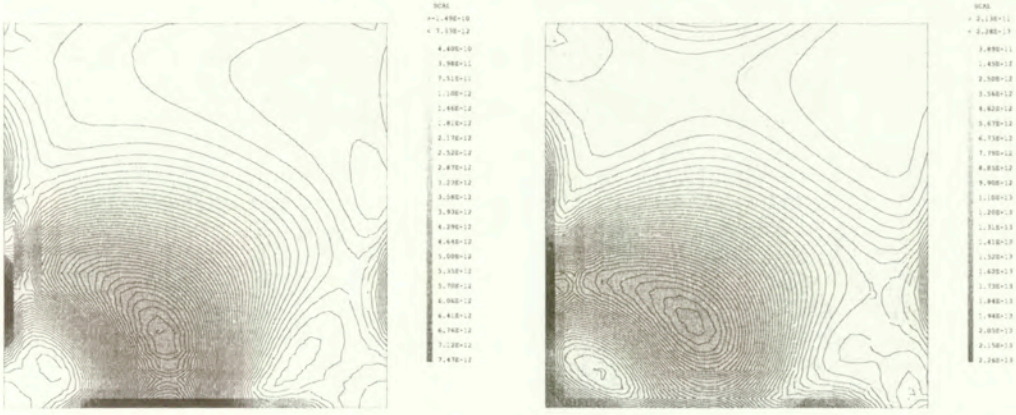

FIG. 2. Spatial distribution of cumulated error of constitutive law for a series of measurements on the lower side (left) and all sides (right) of the square.

If one continues to add the errors corresponding to other measurements, i.e.:

$$\sum_{i=1,N} \mathcal{J}(\mathbf{L}_0, \epsilon_0[\mathbf{w}_i], \sigma_0[\mathbf{t}_i])$$

changing the location of the parabolic pressure distribution along the boundary, one can see that the spatial localization has not been preserved.

A close inspection of the isolines shows that the gradients arround the inclusion are steep, what is in agreement with the theoretical results.

5. Conclusion

In this paper we have shown that the difference between the nonlinear and zero and, respectively, first order approximations of the stresses are negligible far from the perturbation of the elastic moduli and the boundary of the body. As a direct consequence, one can explain the good spatial localization property of the error of constitutive law observed during previous numerical experiments.

It is obvious that, using similar integral equation techniques, localization results could be proved for the inverse electric or the inverse plate problem.

Acknowledgements

This paper was partially supported by EC Contract No. ERBIC15CT970706.

Appendix. Integral representation formulas [3]

The fundamental solution or Green function$\mathbf{G}_{\mathbf{L}_0}$ is defined on an open E compatible with Ω by the equations:

$$\text{(A.1)} \qquad \operatorname{div} \mathbf{L}_0 \nabla_y \mathbf{G}^k_{\mathbf{L}_0}(\mathbf{x}, \mathbf{y}) + \delta(\mathbf{x} - \mathbf{y}) \mathbf{e}_k = \mathbf{0}.$$

For $x \in \Omega$ it can shown that the elastic stress field can be exressed as:

$$\text{(A.2)} \quad \sigma_{ij}(\mathbf{x}) = \int_{\partial\Omega} \mathbf{L}_0 : \nabla_{\mathbf{x}} \mathbf{G}_{\mathbf{L}_0}(\mathbf{x}, \mathbf{y}) \cdot \mathbf{t} dS_y - \int_{\partial\Omega} \mathbf{n} \cdot \mathbf{L}_0 : \nabla_{\mathbf{x}} \mathbf{G}_{\mathbf{L}_0}(\mathbf{x}, \mathbf{y}) \cdot \mathbf{w} dS_{\mathbf{y}} + \int_{\Omega} \mathbf{L}_0 : \nabla_{\mathbf{x}} \mathbf{G}_{\mathbf{L}_0} \cdot \mathbf{b} dV_{\mathbf{y}},$$

where $\mathbf{w}$, $\mathbf{t}$, $\mathbf{b}$ denote respectively the vector of boundary dispacement, boundary traction and body forces. $\mathbf{n}$ represents the unit outward normal the domain. The

following notations will be used for the third order tensor fields:

$$\mathbf{Q}_{\mathbf{L}_0}(\mathbf{x},\mathbf{y}) = \mathbf{L}_0 : \nabla_{\mathbf{x}}\mathbf{G}_{\mathbf{L}_0}(\mathbf{x},\mathbf{y}), \tag{A.3}$$

$$\mathbf{P}_{\mathbf{L}_0}(\mathbf{x},\mathbf{y}) = \mathbf{n}\cdot\mathbf{L}_0 : \nabla_{\mathbf{x}}\mathbf{G}_{\mathbf{L}_0}(\mathbf{x},\mathbf{y}) = \mathbf{n}\cdot\mathbf{L}_0 : \nabla_{\mathbf{x}}\mathbf{Q}_{\mathbf{L}_0}(\mathbf{x},\mathbf{y}). \tag{A.4}$$

References

1. J. BEN ABDALLAH, *Inversion gaussienne appliquée la correction paramétrique de modules structuraux*, PhD Thesis, Ecole Polytechnique, Palaiseau, France 1995.
2. J. BEN ABDALLAH, M. BONNET and M. REYNIER, *Analyse de la localisation par l'erreur en relation de comportement*, Private Communication, 1998.
3. M. BONNET, *Boundary Integral Equations*, CNRS Editions/Eyrolles, Paris 1995.
4. H. D. BUI, *Introduction aux problemes inverses en mecanique des materiaux*, Eyrolles, Paris 1993 (English Version: Inverse Problems in the Mechanics of Materials, An Introduction, CRC Press, Boca Raton, 1994; Japanese Version: Shokabo, Tokyo 1994).
5. A. CALDERON, *On an Inverse Boundary Value Problem*, Seminar on numerical analysis and its application to continuum physics, Soc. Brasiliera de Matematica, 65–73, Rio de Janeiro 1980.
6. A. CONSTANTINESCU, *Sur l'identification des modules elastiques*, PhD Thesis, Ecole Polytechnique, Palaiseau, France 1994.
7. A. CONSTANTINESCU, *On the identification of elastic moduli from displacement-force boundary measurements*, Int. J. of Inverse Problems in Engineering, **1**, 293–315, 1995.
8. A. CONSTANTINESCU, *On the identification of elastic moduli in plates*, [In:] Inverse Problems in Engineering Mechanics, M. TANAKA and G. DULIKRAVICH [Eds.], 205–215, Elsevier 1998.
9. M. IKEHATA, *Inversion for the linearized problem for an inverse boundary value problem in elastic prospection*, SIAM J. Appl. Math., **50**, 6, 1635, 1990.
10. M. IKEHATA, *Identification of the shape of the inclusion having esssentially bounded conductivity*, J. Inv. Ill-Posed Problems, **7**, 6, 533–540, 1999.
11. M. IKEHATA, *Size estimation of an inclusion*, J. Inv. Ill-Posed Problems, **6**, 2, 95–172, 1998.
12. R. KOHN and MCKENNEY, *Numerical implementation of a variational method for electric impedance tomography*, Inverse Problems, **6**, 389–414, 1990.
13. R. V. KOHN and M. VOGELIUS, *Determining conductivity by boundary measurements*, Comm. Pure Appl. Math., **27**, 289–298, 1984.
14. R. V. KOHN and M. VOGELIUS, *Relaxation of a variational method for impedance computed tomography*, Comm. Pure Appl. Math., **15**, 745–777, 1987.
15. D. ISAACSON and E. L. ISAACSON, *Comments on Calderon's Paper "On an Inverse Boundary Value Problem"*, Math. Compt., **52**, 553, 1989.
16. G. NAKAMURA and G. UHLMANN, *Identification of Lamé parameters by boundary measurements*, Invent. Math., **115**, 1161–1188, 1994.

17. P. Ladeveze and D. Leguillon, *Error estimates procedures in the finite element method and applications*, SIAM J. Math. Anal., **26**, 2, 263–279, 1995.

18. P. Ladeveze, M. Reynier and D. Nedjar, *Parametric corrections of finite element models using modal tests*, IUTAM 1992 Symposium, H. D. Bui and M. Tanaka [Eds.], Springer 1993

19. G. Nakamura and G. Uhlmann, *Global uniqueness for an inverse boundary problem arising in elasticity*, Invent. Math., **118**, 457–474, 1994.

20. G. Nakamura and G. Uhlmann, *Inverse problem at the boundary of an elastic medium*, SIAM J. Math. Anal., **26**, 2, 263–279, 1995.

21. A. C. Neves and C. A. Brebbia, *The multiple reciprocity method applied to thermal stress problems*, Int. J. Numer. Methods. Eng., **35**, 443–455, 1992.

22. A. Nowak and C. A. Brebbia, *The multiple-reciprocity method. A new approach for transforming BEM domain integrals to the boundary*, Eng. Anal. Boundary Elements, **26**, 2, 263–279, 1995.

Received February 7, 2000; revised version July 7, 2000.

Arch. Mech., **52**, 4–5, pp. 523–545, Warszawa, 2000

Extremum and saddle-point theorems for elastic solids with dissipative displacement discontinuities

Dedicated to Professor Zenon Mróz on the occasion of his 70th birthday

A. CARINI (1), G. MAIER (2)

(1) *Department of Civil Engineering, University of Brescia, Via Branze 38, 25123 Brescia, Italy*

(2) *Department of Structural Engineering, Technical University (Politecnico), Piazza Leonardo da Vinci 32, 20133 Milano, Italy*

IN A NUMBER OF ENGINEERING SITUATIONS concerning structures made of quasi-brittle, concrete-like materials, all nonlinearities can be reasonably confined to a locus of possible displacement discontinuities. This locus has a lower dimensionality (by one) with respect to the problem domain; it encompasses joints, cracks, fracture process zones (described by cohesive crack models) and their possible propagation paths. Linear elasticity is assumed everywhere else for overall analysis purposes. With reference to a very broad class of interface models, i.e. of (holonomic or nonholonomic, inviscid or time-dependent) relationships between displacement jumps and tractions across that locus, the (possibly multiple, if any) solutions of the initial-boundary-value problem of structural analysis are shown herein to be characterized by duality pairs of extremum and min-max properties.

1. Introduction

1.1. A WIDELY ACCEPTED IDEALIZED INTERPRETATION of fracture processes in quasi-brittle solids and structures (e.g. concrete dams) rests on the "cohesive crack" concept. This model is characterized by the following features: the (two or three-dimensional) open domain Ω where the analysis problem is defined, contains a discontinuity locus (one or two-dimensional, respectively), say Γ_d, across which displacement discontinuities $\mathbf{w}$ may occur; along Γ_d tractions $\mathbf{p}$ are related to relative displacements $\mathbf{w}$ by an "interface constitutive law" which exhibits a softening (unstable) behaviour up to vanishing of the strength; outside of Γ_d the material behaviour is assumed to be linear elastic; deformations are "small" in the sense that equilibrium relations are not influenced by configuration changes, and

kinematic compatibility equations are linear. At a certain stage of the structural response to a given loading history, the locus Γ_d generally encompasses three parts: a portion ("process zone") where the two faces interact by tractions $\mathbf{p}$; a part formed by actual cracks, where there is no interaction; and a portion of virgin material, where no displacement discontinuities has arisen yet.

For the fracture analysis problem based on the above idealizations, the present paper is intended to provide two general variational formulations with the following novel features.

First, a functional of kinematically admissible displacement fields is constructed *by time integrations over the time interval* T of interest, and by space integrations over the domain Ω, over its free and constrained boundary (Γ_p and Γ_u, respectively) and over the locus Γ_d of possible discontinuities. It is proven that the solution (if any) is characterized by the absolute minimum (with a value which can be determined *a priori*) of the above functional and of suitable variants of it.

Second, a functional of statically admissible stress fields is generated over the time interval T and over Ω, Γ_p, Γ_u and Γ_d, and its absolute minimum (at a known value) is proven to characterize the solutions of the boundary-initial value problem.

The two minimum principles are shown to generate two further computationally more attractive saddle-point theorems, and to reduce to the potential and complementary energy principles of elasticity when the discontinuity locus vanishes.

1.2. The present study was motivated by a research project on structural problems in dam engineering. The safety assessment of large concrete dams nowadays often rests on overall three-dimensional analyses in which all nonlinearities can be confined to surfaces where displacement discontinuities may occur (or can be realistically assumed to possibly occur), usually accompanied by energy dissipation. A variety of localised dissipative phenomena need to be allowed for: frictional contact and asperity smoothing on artificial joints and existing cracks; quasi-brittle fracture processes (primarily on concrete-foundation interface). Several nonholonomic path-dependent interface models have been proposed for the computer simulation of the response to loads of dams and many other engineering structures: rigid-plastic, elasto-plastic; plastic damage; viscoplastic; etc., softening and non-associativity being recurrent features together with their possible computationally challenging consequences such as overall instabilities and path branching.

The often reasonable hypothesis of linear behaviour outside the locus of possible dissipative discontinuities makes computationally attractive and competitive

a variety of space discretizations: finite element, boundary element, and meshless methods. Some representative contributions to interface modelling and to limit-state analysis of dams and of similar structures can be found, e.g., in [5, 15, 24, 30, 31], and in [4, 16, 28], respectively. The abundant literature on these topics is surveyed in recent treatises such as [3, 22].

This paper aims at providing a unifying theoretical framework for the above mentioned varieties of interface models and analysis methods, and at contributing to bridge the present gap between structural mechanics and a mathematical research stream on variational principles for initial-boundary-value (i.b.v.) problems.

Such research trend appears so far to be rather separate from the one, fostered by the developments in engineering plasticity, on nonlinear boundary value problems in rates or in finite steps: earlier within the validity range of Drucker's postulate of material stability, (see e.g. [8, 17, 23, 25]), and later outside of it (see e.g. 18, 26]).

The origin of the methodological approach of concern herein can be traced in the adjoint operator method proposed in the fifties for the symmetrization of any non-symmetric linear operator [29], and later extended to classes of nonlinear operators ([20, 37]) and integral operators [36]. This method implies additional unknowns without physical meaning and generally does not lead to extremum characterizations of solutions. Variational formulations of i.b.v. linear problems have been established by this approach, and also by another approach (proposed by Gurtin [21] in 1964) which involves convolution and is deprived of the above disadvantages. The latter approach was further developed for a variety of i.b.v. linear problems in [33, 34, 35, 38] and in [12, 13, 27] for boundary integral formulations of viscoelasticity, dynamics and heat conduction.

A general methodology for variational formulation of any, linear or nonlinear, problem was proposed by E. TONTI [39], and developed for special categories of operators and mechanical situations, such as linear convection-diffusion [32], structural stability [1], nondifferentiable operators [2], quasi-static plasticity [9, 11], elastoplastic dynamics [14].

The present results can be regarded as a further engineering-oriented application of Tonti's approach to variational formulations of i.b.v. problems in the presence of (dissipative, nonholonomic, possibly time-dependent) constitutive models.

2. Problem formulation

The solid or structure referred to herein occupies a region Ω with a boundary Γ. The boundary is supposed to be *smooth*, i.e. the normal direction is

uniquely defined everywhere (a formally convenient restriction, easily removed whenever necessary). Symbols Γ_u and Γ_p will denote the parts of Γ where displacements and surface tractions are imposed, respectively, with $\Gamma = \Gamma_u \cup \Gamma_p$ and $\Gamma_u \cap \Gamma_p = \emptyset$. In an orthogonal Cartesian reference system, $\mathbf{x} = \{x_i, i = 1,2,3\}$ is the position vector of a material point in Ω.

The domain Ω is assumed to contain an *a priori* known discontinuity locus, say Γ_d, across which displacement jumps $\mathbf{w}$ may occur. The locus Γ_d is assumed: (i) to be smooth in the above sense; (ii) to have no intersections with the constrained boundary Γ_u. The latter hypothesis makes simpler some developments in Sec. 4.1 and can be relaxed to the requirement that $\mathbf{w}$ on Γ_d and displacement $\bar{\mathbf{u}}$ on Γ_u are independent over a possible portion of Γ_d which is also part of Γ_u.

The external actions (barred symbols) assigned at any instant t $(0 \leq t \leq \bar{t})$ over a given time interval $T = [0, \bar{t}]$, are: volume forces $\bar{b}_i(\mathbf{x}; t)$ in Ω; imposed (say thermal) strains $\bar{\theta}_{ij}(\mathbf{x}; t)$ in Ω; displacements $\bar{u}_i(\mathbf{x}; t)$ on Γ_u; tractions $\bar{p}_i(\mathbf{x}; t)$ on Γ_p. Inertia forces are regarded as negligible. The material behaviour may be history- and time-dependent (e.g. viscoplastic) or, as a special case, inviscid (then the variable t is to be considered as an event-ordering parameter along the "quasi-static" evolution of the system).

For convenience, but conceptually without any loss of generality, two-dimensional plane-stress situations are referred to wherever it is desirable to make the problem dimensionally explicit (namely: $i, j = 1,2$).

Under the assumption of small strains and displacements (linear kinematics), the equilibrium and compatibility equations, everywhere except on Γ_d, read (the index summation convention is adopted):

$$\sigma_{ij,j} + \bar{b}_i = 0 \quad \text{in} \quad \Omega' \times T \tag{2.1}$$

$$\sigma_{ij} n_j = \bar{p}_i \quad \text{on} \quad \Gamma_p \times T \tag{2.2}$$

$$\epsilon_{ij} = \frac{1}{2}(u_{i,j} + u_{j,i}) \quad \text{in} \quad \Omega' \times T \tag{2.3}$$

$$u_i = \bar{u}_i \quad \text{on} \quad \Gamma_u \times T \tag{2.4}$$

where: $\Omega' = \Omega - \Gamma_d$; σ_{ij} and ϵ_{ij} are components of the stress and the strain tensors, respectively; $(.)_{,j} = \partial(.)/\partial x_j$; n_j are the components of the unit outward normal to the surface Γ.

The material constitutive model in Ω' is assumed to be linear-elastic; namely, in "direct" and "inverse" form, respectively:

$$\sigma_{ij} = D_{ijhk}\left(\epsilon_{hk} - \bar{\theta}_{hk}\right); \qquad \epsilon_{ij} = C_{ijhk}\sigma_{hk} + \bar{\theta}_{ij} \qquad \text{in} \quad \Omega'. \tag{2.5}$$

In Eqs. (2.5) $D_{ijhk} = C^{-1}_{ijhk}$ is the elastic tensor, endowed with the usual symmetry properties and positive definiteness:

$$D_{ijhk} = D_{jihk} = D_{hkij}, \tag{2.6}$$

$$D_{ijhk}(\mathbf{x})\epsilon_{ij}\epsilon_{hk} > 0, \quad \text{for any } \epsilon_{ij} \text{ except for } \epsilon_{ij} = 0. \tag{2.7}$$

The discontinuity line Γ_d is conceived as an interface (smooth) between faces Γ_d^- and Γ_d^+, on which local Cartesian reference are chosen, n_i^- and n_i^+ being the outward unit normal to Γ_d^- and Γ_d^+, respectively (Fig. 1). Let $\mathbf{T}$ be the (orthogonal) matrix which transforms vectors from the local reference $\{\mathbf{n}^-, \mathbf{t}^-\}$ on Γ_d^- to the global reference system. We can write for any $\mathbf{x} \in \Gamma_d$:

$$\begin{Bmatrix} w_1 \\ w_2 \end{Bmatrix} = \begin{Bmatrix} u_1^+ \\ u_2^+ \end{Bmatrix} - \begin{Bmatrix} u_1^- \\ u_2^- \end{Bmatrix} = \mathbf{T} \begin{Bmatrix} w_n \\ w_t \end{Bmatrix} \quad \text{on } \Gamma_d \times T, \tag{2.8}$$

$$\begin{Bmatrix} p_1 \\ p_2 \end{Bmatrix} = \begin{Bmatrix} p_1^- \\ p_2^- \end{Bmatrix} = -\begin{Bmatrix} p_1^+ \\ p_2^+ \end{Bmatrix} = \mathbf{T} \begin{Bmatrix} p_n \\ p_t \end{Bmatrix} \quad \text{on } \Gamma_d \times T. \tag{2.9}$$

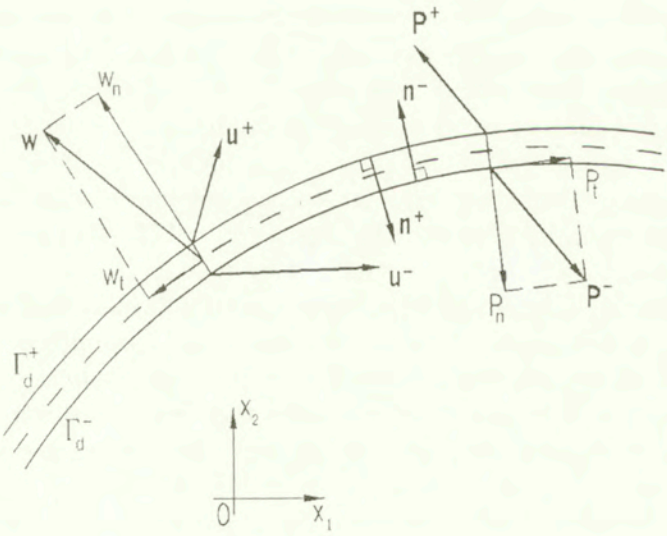

FIG. 1. Illustration of symbols and references for tractions and displacements on the discontinuity locus Γ_d.

Equation (2.8a) defines the kinematic (displacement) discontinuity $\mathbf{w}$ in the global reference; Eq. (2.8b) relates w_i to the normal ("opening", "mode I") relative displacement w_n and to the tangential ("sliding", "mode II") relative displacement w_t, represented in the local reference system on Γ_d^-. Equations (2.9) identify the

interface tractions p_i with those on face 1, express interface equilibrium and relate vector p_i (which describes tractions on Γ_d^-, with components p_1 and p_2 in the global reference) to its normal p_n and tangential p_t components with respect to the locus (line) Γ_d. Tractions and stresses along the discontinuity locus Γ_d are linked by Cauchy equilibrium equations:

$$\sigma_{ij} n_j^- = p_i \quad \text{on} \quad \Gamma_d^- \times T, \qquad \sigma_{ij} n_j^+ = -p_i \quad \text{on} \quad \Gamma_d^+ \times T. \tag{2.10}$$

Static $\{p_n\, p_t\}$ and kinematic $\{w_n\, w_t\}$ variables on the discontinuity line Γ_d are linked to each other by an interface model, see e.g. [5, 15, 24, 30, 31]. The generally nonlinear time- and path-dependent ("nonholonomic", irreversible, dissipative) constitutive models along interface Γ_d will be expressed in the following compact form (direct and inverse, respectively):

$$p_i(t) = f_i[w_j(\tau); 0 \le \tau \le t]; \quad w_i(t) = g_i[p_j(\tau); 0 \le \tau \le t] \quad \text{on } \Gamma_d \times T. \tag{2.11}$$

It is worth noting that in many practical situations under proportional, monotonic loading histories, inviscid interface models may be interpreted as history-independent ("holonomic") to overall analysis purposes, namely: $p_i(t) = f(w_i(t))$, and $w_i(t) = g(p_i(t))$. This short notation will be used in what follows for all interface models, whether holonomic or nonholonomic (or partly so, when detachment occurs). Clearly, both in holonomic and nonholonomic interface models, material instability (softening and/or nonassociativity induced by internal friction and/or damage) is expected, together with consequent multi-value nature of the dependences symbolically expressed by Eqs. (2.11). It is worth noting that these dependences usually can not be described by functionals or functions, but may be mathematically formulated as a problem with multiplicity of solutions (if any exist). Typical formulations of this kind are linear or nonlinear complementarity problems, or sequences of them for nonholonomic models. For applications to the very particular case of hydraulic fracture (an important issue today for oil industries), the interface model can accomodate the crack pressurization, by means of convenient provisions, not dealt with here explicitly.

We assume, for simplicity, that the *initial conditions* are homogeneous (preceded by an undisturbed statical regime):

$$u_i = \epsilon_{ij} = \sigma_{ij} = 0 \qquad \text{on} \quad \Omega' \cup \Gamma, \quad \text{at} \quad t = 0 \tag{2.12}$$

$$w_i = 0 \qquad \text{on} \quad \Gamma_d \quad \text{at} \quad t = 0. \tag{2.13}$$

The b.i.v. problem defined by Eqs. (2.1) – (2.13) will be referred to, in what follows, as *problem P*.

3. Admissible fields

3.1. Consider a stress field history $\sigma^*_{ij}(\mathbf{x}, t)$ which is defined in space over Ω and in time over T, and satisfies the equilibrium equations in Ω' and on Γ_p with the actual statical data $\bar{b}_i(\mathbf{x}, t)$ and $\bar{p}_i(\mathbf{x}, t)$, respectively, and on the discontinuity locus Γ_d between tractions, namely:

$$\sigma^*_{ij,j} + \bar{b}_i = 0 \quad \text{in} \quad \Omega' \times T, \tag{3.1}$$

$$\sigma^*_{ij} n_j = \bar{p}_i \quad \text{on} \quad \Gamma_p \times T, \tag{3.2}$$

$$p^*_i = p^{*-}_i = \sigma^{*-}_{ij} n^-_j = -\sigma^{*+}_{ij} n^+_j = -p^{*+}_i \quad \text{on} \quad \Gamma_d \times T, \tag{3.3}$$

where: $\mathbf{n}^- = \{n^-_i\}$ and $\mathbf{n}^+ = \{n^+_i\}$ denote the unit vectors directed as the outward normals to Γ^-_d and Γ^+_d, respectively; superscripts $-$ and $+$ mark stresses near these two faces of locus Γ_d, like in Eq. (2.10). The corresponding (generally non-compatible) time-histories of strains ϵ^*_{ij} in Ω' and of relative displacement jumps $\mathbf{w}^*$ on Γ_d, can be derived through the Hookean constitutive law $(2.5)_2$ and the interface constitutive law $(2.11)_2$, respectively. They read:

$$\epsilon^*_{ij} = C_{ijhk}\sigma^*_{hk} + \bar{\theta}_{ij} \quad \text{in} \quad \Omega' \times T, \tag{3.4}$$

$$w^*_i = g_i(p^*_j) \quad \text{on} \quad \Gamma_d \times T. \tag{3.5}$$

All fields (in space and time) which satisfy the above conditions will be called henceforth *statically admissible* (and marked by asterisks). It is worth noting that, by this definition, σ^*_{ij} is required not only to balance the given loads and fulfill equilibrium everywhere, but also to comply with the constraints implied by the interface model Eq. (3.5) (e.g. p^*_n cannot exceed the current tensile strength, say $\bar{\sigma}$).

A stress distribution $\sigma^{**}_{ij}(\mathbf{x}, t)$ is defined as *self-equilibrated* when it satisfies the following *homogeneous* equilibrium equations:

$$\sigma^{**}_{ij,j} = 0 \quad \text{in} \quad \Omega' \times T, \tag{3.6}$$

$$\sigma^{**}_{ij} n_j = 0 \quad \text{on} \quad \Gamma_p \times T, \tag{3.7}$$

$$\sigma^{**-}_{ij} n^-_j = -\sigma^{**+}_{ij} n^+_j \quad \text{on} \quad \Gamma_d \times T. \tag{3.8}$$

Note that Eqs. (3.3) and (3.8) enforce traction continuity across Γ_d, an equilibrium requirement which could have been alternatively formulated by Eqs. (3.1) and (3.6), respectively, by substituting in them Ω for $\Omega' = \Omega - \Gamma_d$.

3.2. Now let us consider a time-history of the strain field $\epsilon^o_{ij}(\mathbf{x}, t)$ derived, by means of the geometric compatibility operator, from a displacement field $u^o_i(\mathbf{x}, t)$

which satisfies the assigned kinematic boundary conditions and exhibits a "jump" $\mathbf{w}^o$ on the discontinuity locus Γ_d:

$$\epsilon_{ij}^o = \frac{1}{2}(u_{i,j}^o + u_{j,i}^o) \qquad \text{in} \quad \Omega' \times T, \tag{3.9}$$

$$u_i^o = \bar{u}_i \qquad \text{on} \quad \Gamma_u \times T, \tag{3.10}$$

$$w_i^o = u_i^{o+} - u_i^{o-} \qquad \text{on} \quad \Gamma_d \times T. \tag{3.11}$$

Let stresses σ_{ij}^o in Ω' and interface tractions p_i^o on Γ_d be derived through the constitutive law $(2.5)_1$ from ϵ_{ij}^o and through the interface law $(2.11)_1$ from w_i^o, respectively. They are generally not equilibrated and read:

$$\sigma_{ij}^o = D_{ijhk}(\epsilon_{hk}^o - \bar{\theta}_{hk}) \qquad \text{in} \quad \Omega' \times T, \tag{3.12}$$

$$p_i^o = \sigma_{ij}^{o-} n_j^- = f_i(w_j^o) \qquad \text{on} \quad \Gamma_d \times T. \tag{3.13}$$

Time histories of fields (marked by ^{o}) which satisfy the above definitions will be referred to as *kinematically admissible*. Clearly, besides geometric compatibility, also the constitutive model on Γ_d, Eq. (3.13) is generally expected to set some constraints (e.g. nonegative opening displacement $w_n \geq 0$).

A strain field $\epsilon_{ij}^{oo}(\mathbf{x}, t)$ is here defined as *self-compatible* if it can be derived by means of the compatibility operator from a displacement field $u_i^{oo}(\mathbf{x}, t)$, which is generally discontinuous by w_i^{oo} across Γ_d and vanishes on Γ_u, i.e. satisfies the *homogeneous* compatibility equations:

$$\epsilon_{ij}^{oo} = \frac{1}{2}(u_{i/j}^{oo} + u_{j/i}^{oo}) \qquad \text{in} \quad \Omega' \times T, \tag{3.14}$$

$$u_i^{oo} = 0 \qquad \text{on} \quad \Gamma_u \times T, \tag{3.15}$$

$$w_i^{oo} = u_i^{oo+} - u_i^{oo-} \qquad \text{on} \quad \Gamma_d \times T. \tag{3.16}$$

4. Auxiliary problems

4.1. Elastic responses to imposed displacement jumps on Γ_d

A first auxiliary linear elastic problem will be referred to as *imposed discontinuity* problem and denoted by P^d and superscript d. It is defined by the following set of governing equations, where the input data are represented by displacement discontinuities $w_i^*(\mathbf{x}, t)$, called henceforth *statically admissible* inasmuch they are derived through the interface model on Γ_d, Eq. (3.5), from a *statically admissible* stress field history $\sigma_{ij}^*(\mathbf{x}, t)$ according to the definition of Sec. 3. The formulation of the above problem reads:

$$\sigma^d_{ij,j} = 0 \quad \text{in} \quad \Omega' \times T \tag{4.1}$$

$$\sigma^d_{ij} n_j = 0 \quad \text{on} \quad \Gamma_p \times T \tag{4.2}$$

Problem P^d:

$$\epsilon^d_{ij} = \frac{1}{2}\left(u^d_{i,j} + u^d_{j,i}\right) \quad \text{in} \quad \Omega' \times T \tag{4.3}$$

$$u^d_i = 0 \quad \text{on} \quad \Gamma_u \times T \tag{4.4}$$

$$\epsilon^d_{ij} = C_{ijhk}\sigma^d_{hk} \quad \text{in} \quad \Omega' \times T \tag{4.5}$$

$$w^d_i = -w^*_i \quad \text{on} \quad \Gamma_d \times T \tag{4.6}$$

Another auxiliary linear elastic problem, say $\tilde{P}^d$, is formulated as follows for later use:

$$\tilde{\sigma}^d_{ij,j} = 0 \quad \text{in} \quad \Omega' \times T \tag{4.7}$$

$$\tilde{\sigma}^d_{ij} n_j = 0 \quad \text{on} \quad \Gamma_p \times T \tag{4.8}$$

Problem $\tilde{P}^d$:

$$\tilde{\epsilon}^d_{ij} - \epsilon^*_{ij} = \frac{1}{2}\left(\tilde{u}^d_{i,j} + \tilde{u}^d_{j,i}\right) \quad \text{in} \quad \Omega' \times T \tag{4.9}$$

$$\tilde{u}^d_i = -\bar{u}_i \quad \text{on} \quad \Gamma_u \times T \tag{4.10}$$

$$\tilde{\epsilon}^d_{ij} = C_{ijhk}\tilde{\sigma}^d_{hk} \quad \text{on} \quad \Omega' \times T \tag{4.11}$$

$$\tilde{w}^d_i = -w^*_i \quad \text{on} \quad \Gamma_d \times T \tag{4.12}$$

It is worth noting that in the above problem $\tilde{P}^d$ there are two kinds of (fictitious) input data: (i) the kinematic fields $(-\epsilon^*_{ij})$ and $(-w^*_i)$ which arise, through the inverse constitutive laws Eqs. $(2.5)_2$ and $(2.11)_2$, and through sign inversion, from statically admissible fields σ^*_{ij} and p^*_i, respectively, in the sense of Sec. 3.1; (ii) the actual histories of boundary displacements $\bar{u}_i$, reversed in sign. If u^{ew}_i, ϵ^{ew}_{ij}, σ^{ew}_{ij} represent the fictitious linear elastic response of the solid to the actual time histories of external actions $\bar{b}_i$, $\bar{p}_i$, $\bar{u}_i$ and $\bar{\theta}_{ij}$ in the absence of displacement discontinuities (i.e. with $w_i = 0$ on $\Gamma_d \times T$), the following relationships hold for the solutions of the above two auxiliary linear problems P^d and $\tilde{P}^d$:

$$\tilde{u}^d_i = u^d_i - u^{ew}_i; \qquad \tilde{w}^d_i = w^d_i; \qquad \tilde{\epsilon}^d_{ij} = \epsilon^d_{ij} + \epsilon^*_{ij} - \epsilon^{ew}_{ij}; \tag{4.13}$$

$$\tilde{\sigma}^d_{ij} = \sigma^d_{ij} + \sigma^*_{ij} - \sigma^{ew}_{ij}.$$

These relationships are readily justified by substituting Eqs. (4.13) into Eqs. (4.7) – (4.12) of problem $\tilde{P}^d$ and by applying the effect superposition, account being taken of the definitions of the fields marked by (*).

4.2. Elastic responses to imposed tractions on Γ_d

The following auxiliary problem, referred to henceforth as *imposed interaction* problem P^s, concerns the linear elastic response to only the traction history

$-p_i^o$ on Γ_d generated, through the interface model and sign inversion, by any kinematically admissible strain field ϵ_{ij}^o (in the sense of Sec. 3):

$$\sigma_{ij,j}^s = 0 \quad \text{in} \quad \Omega' \times T \tag{4.14}$$

$$\sigma_{ij}^s n_j = 0 \quad \text{on} \quad \Gamma_p \times T \tag{4.15}$$

$$\textit{Problem} \quad P^s: \quad \epsilon_{ij}^s = \frac{1}{2}\left(u_{i,j}^s + u_{j,i}^s\right) \quad \text{in} \quad \Omega' \times T \tag{4.16}$$

$$u_i^s = 0 \quad \text{on} \quad \Gamma_u \times T \tag{4.17}$$

$$\sigma_{ij}^s = D_{ijhk}\epsilon_{hk}^s \quad \text{in} \quad \Omega' \times T \tag{4.18}$$

$$p_i^s = -p_i^o \quad \text{on} \quad \Gamma_d \times T \tag{4.19}$$

A further auxiliary problem, indicated by $\tilde{P}^s$, is formulated as follows:

$$\tilde{\sigma}_{ij,j}^s - \sigma_{ij,j}^o - \bar{b}_i = 0 \quad \text{in} \quad \Omega' \times T \tag{4.20}$$

$$\tilde{\sigma}_{ij}^s n_j = \sigma_{ij}^o n_j - \bar{p}_i \quad \text{on} \quad \Gamma_p \times T \tag{4.21}$$

$$\textit{Problem} \quad \tilde{P}^s: \quad \tilde{\epsilon}_{ij}^s = \frac{1}{2}\left(\tilde{u}_{i,j}^s + \tilde{u}_{j,i}^s\right) \quad \text{in} \quad \Omega' \times T \tag{4.22}$$

$$\tilde{u}_i^s = 0 \quad \text{on} \quad \Gamma_u \times T \tag{4.23}$$

$$\tilde{\sigma}_{ij}^s = D_{ijhk}\tilde{\epsilon}_{hk}^s \quad \text{in} \quad \Omega' \times T \tag{4.24}$$

$$\tilde{p}_i^s = -p_i^o + \sigma_{ij}^{o-} n_j^- \quad \text{on} \quad \Gamma_d \times T \tag{4.25}$$

In the above problem $\tilde{P}^s$, the input data consist of: (i) fields $(-\sigma_{ij}^o)$ and $(-p_i^o)$ arising, through the direct constitutive laws Eqs. $(2.5)_1$ and $(2.11)_1$ and sign inversion, from any kinematically admissible fields ϵ_{ij}^o and w_i^o, respectively, satisfying the compatibility equations (3.9) – (3.11); (ii) the actual histories of body forces $\bar{b}_i$ and boundary tractions $\bar{p}_i$, reversed in sign. The solutions of the two above linear problems P^s and $\tilde{P}^s$ and the kinematically admissible fields $(u_i^o, w_i^o, \epsilon_{ij}^o, \sigma_{ij}^o)$ generating them, are related to each other. These relationships involve also the solution (marked by superscripts ep) to the linear elastic analysis of the solid supposed to be endowed with a tractionless discontinuity locus Γ_d (i.e. $p_i = 0$ along Γ_d), in the presence of the actual external actions. The above relationships, counterparts of Eqs. (4.13), read:

$$\tilde{u}_i^s = u_i^s + u_i^o - u_i^{ep}; \quad \tilde{p}_i^s = p_i^s + \sigma_{ij}^{o-} n_j^- - p_i^{ep}; \quad \tilde{\epsilon}_{ij}^s = \epsilon_{ij}^s + \epsilon_{ij}^o - \epsilon_{ij}^{ep}; \quad \tilde{\sigma}_{ij}^s = \sigma_{ij}^s + \sigma_{ij}^o - \sigma_{ij}^{ep}. \tag{4.26}$$

It is worth noting that the input quantities in problems $\tilde{P}^d$ and $\tilde{P}^s$ substantially differ: in fact, their geometric compatibility suffices for zero solution to the former problem, they must vanish identically for zero solution to the latter.

5. Extremum theorems

5.1. An extended complementary energy theorem

Consider the following functionals (dimensionally energy×time) of a stress field history $\sigma^*_{ij}(\mathbf{x};t)$, statically admissible in the sense of Sec. 3.1:

$$F_c^I\left[\sigma^*_{ij}\right] = \int_T \left\{ \frac{1}{2}\int_\Omega \sigma^*_{ij} C_{ijhk} \sigma^*_{hk} d\Omega + \int_\Omega \bar{\theta}_{ij}\sigma^*_{ij} d\Omega - \int_{\Gamma_u} \bar{u}_i n_j \sigma^*_{ij} d\Gamma \right. \tag{5.1}$$

$$\left. + \int_{\Gamma_d} g_i\left(p^*_h\right)\left(p^*_i - \sigma^{ew}_{ij} n^-_j\right) d\Gamma + \frac{1}{2}\int_{\Omega'} \sigma^d_{ij}(\sigma^*_{rs}) C_{ijhk} \sigma^d_{hk}(\sigma^*_{rs}) d\Omega \right\} dt$$

$$F_c^{II}\left[\sigma^*_{ij}\right] = \int_T \left\{ \frac{1}{2}\int_{\Omega'} \tilde{\sigma}^d_{ij} C_{ijhk} \tilde{\sigma}^d_{hk} d\Omega \right\} dt + F_c^0 \tag{5.2}$$

where

$$F_c^0 = \int_T \left\{ \frac{1}{2}\int_\Omega \sigma^{ew}_{ij}\epsilon^{ew}_{ij} d\Omega + \int_\Omega \bar{\theta}_{ij}\sigma^{ew}_{ij} d\Omega - \int_{\Gamma_u} \bar{u}_i n_j \sigma^{ew}_{ij} d\Gamma \right\} dt. \tag{5.3}$$

According to definitions given in Sec. 4.1, σ^{ew}_{ij} are the elastic stresses in the solid under the assigned time history of the actual external actions $\bar{b}_i$, $\bar{p}_i$, $\bar{u}_i$ and $\bar{\theta}_{ij}$, with $w_i \equiv 0$ on $\Gamma_d \times T$; σ^d_{ij} and $\tilde{\sigma}^d_{ij}$ denote the stress solutions to the linear auxiliary problems P^d, Eqs. (4.1) – (4.6), and $\tilde{P}^d$, Eqs. (4.7) – (4.12), respectively.

Some meaningful properties of the above functionals are formulated below by three statements proved in what follows: a lemma, a generalized complementary energy theorem and a corollary (propositions 1, 2 and 3, respectively).

PROPOSITION 1. For the same time history of a statically admissible stress field σ^*_{ij}, functionals F_c^I, Eq. (5.1), and F_c^{II}, Eq. (5.2), attain the same value.

P r o o f. The difference functional $F_c^I - F_c^{II}$ can be written as follows by using Eq. $(4.13)_4$:

$$(5.4)\qquad F_c^I - F_c^{II} = \int_T \left\{ \int_\Omega \bar{\theta}_{ij}\sigma_{ij}^* d\Omega - \int_{\Gamma_u} \bar{u}_i n_j \sigma_{ij}^* d\Gamma \right.$$

$$+ \int_{\Gamma_d} g_i(p_h^*)\left(p_i^* - \sigma_{ij}^{ew} n_j^-\right) d\Gamma - \int_{\Omega'} \left(\sigma_{ij}^* - \sigma_{ij}^{ew}\right) C_{ijhk}\sigma_{hk}^d d\Omega$$

$$\left. - \int_\Omega \sigma_{ij}^{ew}\epsilon_{ij}^{ew} d\Omega - \int_\Omega \bar{\theta}_{ij}\sigma_{ij}^{ew} d\Omega + \int_{\Gamma_u} \bar{u}_i n_j \sigma_{ij}^{ew} d\Gamma + \int_\Omega \sigma_{ij}^{ew} C_{ijhk}\sigma_{hk}^* d\Omega \right\} dt.$$

As consequences of the virtual work principle, the third and fourth inner integrals drop out from Eq. (5.4) and the last inner integral can be expressed as:

$$(5.5)\qquad \int_\Omega \sigma_{ij}^{ew} C_{ijhk}\sigma_{hk}^* d\Omega = \int_\Omega u_i^{ew}\bar{b}_i d\Omega + \int_{\Gamma_p} u_i^{ew}\bar{p}_i d\Gamma + \int_{\Gamma_u} \bar{u}_i \sigma_{ij}^* n_j d\Gamma$$

$$- \int_\Omega \bar{\theta}_i \sigma_{ij}^* d\Omega.$$

Thus, the difference functional becomes:

$$(5.6)\qquad F_c^I - F_c^{II} = \int_T \left\{ - \int_\Omega \sigma_{ij}^{ew}\epsilon_{ij}^{ew} d\Omega - \int_\Omega \bar{\theta}_{ij}\sigma_{ij}^{ew} d\Omega + \int_{\Gamma_u} \bar{u}_i n_j \sigma_{ij}^{ew} d\Gamma \right.$$

$$\left. + \int_\Omega u_i^{ew}\bar{b}_i d\Omega + \int_{\Gamma_p} u_i^{ew}\bar{p}_i d\Gamma \right\} dt$$

and is easily seen to vanish because of the virtual work principle again. □

PROPOSITION 2. A statically admissible stress field σ_{ij}^* is a (or the) solution of the original problem P, Eqs. (2.1) – (2.13), if and only if it minimizes (absolute minimum) the functional F_c^I, Eq. (5.1), provided a solution exists. By virtue of Proposition 1, the same stress field σ_{ij}^* minimizes also functional F_c^{II}, Eq. (5.2).

P r o o f. With reference to Eq. (5.2), consider the difference:

$$(5.7)\qquad F_c^{II} - F_c^0 = \frac{1}{2}\int_T \int_\Omega \tilde{\epsilon}_{ij}^d \tilde{\sigma}_{ij}^d d\Omega dt.$$

The inner integral (5.7) represents the elastic strain energy due to: imposed strains $-\bar{\theta}_{ij} - C_{ijhk}\sigma^*_{hk}$; imposed relative displacements $-g_i(p^*_h)$; boundary displacements $\bar{u}_i$ on Γ_u. Therefore, the above difference, Eq. (5.7), cannot be negative. The functional F_c^{II} attains its minimum value F_c^0 if and only if there exists a kinematically admissible strain field ϵ^o_{ij} and a statically admissible stress field σ^*_{ij} such that:

$$\epsilon^o_{ij} = C_{ijhk}\sigma^*_{hk} + \bar{\theta}_{ij} \qquad \text{in} \quad \Omega' \times T, \tag{5.8}$$

$$w^o_i = g_i(p^*_h) \qquad \text{on} \quad \Gamma_d \times T. \tag{5.9}$$

In fact, Eqs. (5.8) and (5.9) mean that the geometrically compatible fields (^{o}) and the statically admissible fields (*) are related to each other through the constitutive models everywhere and, hence, satisfy all the governing relationships of the original problem P, i.e. represent its solution or one of its solutions. □

PROPOSITION 3. The actual problem P has at least one solution if and only if the functional F_c^I (and, hence, F_c^{II} as well) attains, at the global minimum, the value F_c^0, Eq. (5.3).

P r o o f. If at the minimum it turns out that:

$$F_c^{II} > F_c^0 \tag{5.10}$$

then no statically admissible stress field σ^*_{ij} exists such that the constitutive models, Eqs. (5.8) and (5.9), are fulfilled. Then the original problem P has no solution. □

REMARK. The nonlinear (in particular, e.g., softening) nature of the interface models $f_i(w_j)$ may imply nonconvexity of functionals F_c^I and F_c^{II}. However, by virtue of Proposition 3, possible local minima of them do not characterize solutions to the actual nonlinear i.b.v. problem (only absolute minima do).

5.2. An extended potential energy principle

Let us consider now the following generally nonconvex functionals of the kinematically admissible displacement field history $u^o_i(\mathbf{x}; t)$ (cf. Sec. 3.2):

$$(5.11)\qquad F_p^I[u_i^o] = \int_T \left\{ \frac{1}{2}\int_{\Omega'} \left(\epsilon_{ij}^o - \bar{\theta}_{ij}\right) D_{ijhk} \left(\epsilon_{hk}^o - \bar{\theta}_{hk}\right) d\Omega - \int_{\Omega'} \bar{b}_i u_i^o d\Omega \right.$$
$$- \int_{\Gamma_p} \bar{p}_i u_i^o d\Gamma + \int_{\Gamma_d} f_i\left(w_j^o\right)\left(w_i^o - w_i^{ep}\right) d\Gamma$$
$$\left. + \frac{1}{2}\int_{\Omega'} \epsilon_{ij}^s(u_r^o) D_{ijhk} \epsilon_{hk}^s(u_r^o) d\Omega \right\} dt.$$

$$(5.12)\qquad F_{pe}^{II}[u_i^o] = \frac{1}{2}\int_T \int_{\Omega'} \tilde{\epsilon}_{ij}^s D_{ijhk} \tilde{\epsilon}_{hk}^s d\Omega dt + F_p^0$$

having set:

$$(5.13)\qquad F_p^0 = \int_T \left\{ \frac{1}{2}\int_{\Omega'} \left(\epsilon_{ij}^{ep} - \bar{\theta}_{ij}\right) D_{ijhk} \left(\epsilon_{hk}^{ep} - \bar{\theta}_{hk}\right) d\Omega - \int_{\Omega'} \bar{b}_i u_i^{ep} d\Omega \right.$$
$$\left. - \int_{\Gamma_p} \bar{p}_i u_i^{ep} d\Gamma \right\} dt.$$

Here (see Sec. 4.2) w_i^{ep} represent the displacement discontinuities in the elastic solid under the actual external actions $\bar{b}_i, \bar{p}_i, \bar{u}_i$ and $\bar{\theta}_{ij}$, with $p_i = 0$ on $\Gamma_d \times T$; ϵ_{ij}^s and $\tilde{\epsilon}_{ij}^s$ denote the strain solutions to the linear auxiliary problems P^s, Eqs. (4.14) – (4.19), and $\tilde{P}^s$, Eqs. (4.20) – (4.25), respectively. As counterparts to the three theorems established in Sec. 5.1, three further propositions are proven below.

PROPOSITION 4. Functionals F_p^I and F_p^{II}, Eqs. (5.11) and (5.12), attain a common value for the same time history of a kinematically admissible displacement field u_i^o.

P r o o f. In view of Eqs. $(4.26)_3$ we may express the difference $F_p^I - F_p^{II}$ as the following functional:

$$(5.14)\qquad F_p^I - F_p^{II} = \int_T \left\{ -\int_{\Omega'} \bar{b}_i u_i^o d\Omega - \int_{\Gamma_p} \bar{p}_i u_i^o d\Gamma - \int_{\Omega'} \bar{\theta}_{ij} D_{ijhk} \epsilon_{hk}^o d\Omega \right.$$

$$+ \int_{\Gamma_d} f_i(w_h^o)\,(w_i^o - w_i^{ep})\,d\Gamma - \int_{\Omega'} \left(\epsilon_{ij}^o - \epsilon_{ij}^{ep}\right) D_{ijhk} \epsilon_{hk}^s d\Omega - \int_{\Omega'} \sigma_{ij}^{ep} \epsilon_{ij}^{ep} d\Omega$$

$$\left. + \int_{\Omega'} \bar{b}_i u_i^{ep} d\Omega + \int_{\Gamma_p} \bar{p}_i u_i^{ep} d\Gamma + \int_{\Omega'} \epsilon_{ij}^{ep} D_{ijhk} \epsilon_{hk}^o d\Omega \right\} dt.$$

As it can be readily seen by applying once again the virtual work principle, in the above difference functional the sum of the fourth and fifth inner integral vanishes, whereas the last integral becomes:

$$(5.15)\qquad \int_{\Omega'} \epsilon_{ij}^{ep} D_{ijhk} \epsilon_{hk}^o d\Omega = \int_{\Omega'} \bar{b}_i u_i^o d\Omega + \int_{\Gamma_p} \bar{p}_i u_i^o d\Gamma + \int_{\Gamma_u} \sigma_{ij}^{ep} n_j \bar{u}_i d\Gamma$$

$$+ \int_{\Omega'} \bar{\theta}_{ij} D_{ijhk} \epsilon_{hk}^o d\Omega.$$

As a consequence of the above remarks, the difference functional may be given the following expression which turns out to vanish:

$$(5.16)\qquad F_p^I - F_p^{II} = \int_T \left\{ -\int_{\Omega'} \sigma_{ij}^{ep} \epsilon_{ij}^{ep} d\Omega + \int_{\Gamma_u} \bar{u}_i n_j \sigma_{ij}^{ep} d\Gamma + \int_{\Omega'} \bar{b}_i u_i^{ep} d\Omega \right.$$

$$\left. + \int_{\Gamma_p} \bar{p}_i u_i^{ep} d\Gamma \right\} dt.$$

□

PROPOSITION 5. A kinematically admissible displacement field u_i^o is a (or the) solution of the problem P, Eqs. (2.1) – (2.13), if and only if it minimizes (absolute minimum) the functional F_p^I, Eq. (5.11), provided a solution exists. By virtue of Proposition 4, the same displacement field u_i^o minimizes functional F_p^{II}, Eq. (5.12), as well.

P r o o f. Let us consider the difference

$$F_p^{II} - F_p^0 = \frac{1}{2} \int_T \int_{\Omega'} \tilde{\sigma}_{ij}^s \tilde{\epsilon}_{ij}^s d\Omega dt. \tag{5.17}$$

The inner integral of this functional represents the elastic strain energy in the solid if it were subjected to the following (fictitious) external actions: volume forces $\tilde{b}_i = -\left[D_{ijhk}(\epsilon_{hk}^o - \bar{\theta}_{hk})\right]_{,j} - \bar{b}_i$ in Ω', tractions $\tilde{p}_i = D_{ijhk}(\epsilon_{hk}^o - \bar{\theta}_{hk})n_j - \bar{p}_i$ on Γ_p; tractions $-f_i(w_r^o) + D_{ijhk}(\epsilon_{hk}^o - \bar{\theta}_{hk})n_j$ on Γ_d.

The functional F_p^{II} reaches its minimum F_p^0 if and only if the (fictitious, statical) external actions vanish in the auxiliary problem $\tilde{P}^s$ of Sec. 4.2; namely if and only if:

$$\left[D_{ijhk}(\epsilon_{hk}^o - \bar{\theta}_{hk})\right]_{,j} + \bar{b}_i = 0 \qquad \text{in} \quad \Omega' \times T, \tag{5.18}$$

$$D_{ijhk}(\epsilon_{hk}^o - \bar{\theta}_{hk})n_j - \bar{p}_i = 0 \qquad \text{on} \quad \Gamma_p \times T, \tag{5.19}$$

$$D_{ijhk}(\epsilon_{hk}^o - \bar{\theta}_{hk})n_j - f_i(w_r^o) = 0 \qquad \text{on} \quad \Gamma_d \times T. \tag{5.20}$$

When Eqs. (5.18), (5.19) and (5.20) hold, since the very definition of the kinematically admissible fields (^{o}) implies that Eqs. (3.9) – (3.11) are fulfilled, then the whole set of governing equations of the original problem P, Eqs. (2.1) – (2.13), is satisfied by the field u_i^o which, hence, represents a (or the) solution of it. □

PROPOSITION 6. Problem P has at least one solution if and only if functional F_p^I (and, hence, also F_p^{II}), reaches the value F_p^0, Eq. (5.13), as its global minimum.

P r o o f. Like for Proposition 3, suppose that $F_p^{II} > F_p^0$ at the absolute minimum of functional F_p^{II}, then no kinematically admissible displacement field u_i^o (satisfying Eqs. (3.9) – (3.11)) exists such that equilibrium and constitutive laws, Eqs. (5.18) and (5.20), are complied with at the same time. This means that there is no solution to the original problem P. □

REMARK. It is worth noting that functional F_p^I, Eq. (5.11), reduces to total potential energy of linear elasticity when either Γ_d vanishes or there is no interaction along it, i.e. $f_i(w_j) = 0$. Clearly, analogous specification (to complementary energy) can be noticed for F_c^I, Eq. (5.1).

6. Saddle-point theorems

For their applications, a drawback of the preceding theorems (Proposition 2 and 5) lies in the need to evaluate the last term of Eq. (5.1) and Eq. (5.11)

through the solution of the elastic auxiliary problem for every admissible stress field $\boldsymbol{\sigma}^*$ or for every compatible strain field $\boldsymbol{\epsilon}^o$, respectively. In other words, applications of Propositions 2 and 5 would require to find Green functions of the elastic problem. However, the aforementioned last two terms represent elastic energies which can be evaluated, using classical elasticity principles, by maximization of suitable functionals in additional new variables, as shown in what follows.

6.1. A min-max extended complementary energy principle

With reference to Proposition 2, a functional F_c^d to be maximized in order to obtain the last term of (5.1) can be formulated by means of the principle of virtual work as follows (at any instant t):

$$\frac{1}{2}\int_{\Omega'} \sigma_{ij}^d\,(\sigma_{rs}^*)\,C_{ijhk}\sigma_{hk}^d\,(\sigma_{rs}^*)\,d\Omega = -\frac{1}{2}\int_{\Omega'} \sigma_{ij}^d\,(\sigma_{rs}^*)\,C_{ijhk}\sigma_{hk}^d\,(\sigma_{rs}^*)\,d\Omega + \int_{\Gamma_d} g_i\,(p_h^*)\,\sigma_{ij}^{d-} n_j^-\,d\Gamma. \tag{6.1}$$

The right-hand side of (6.1) is readily recognized to be the (changed in sign) value of the complementary energy at the solution of the elastic b.v. problem for imposed relative displacements $-g_i\left(p_j^*\right)$ at instant t. This means that, by virtue of the minimum principle of complementary energy, σ_{ij}^{d**} being any *self-equilibrated* stress field,

$$\frac{1}{2}\int_{\Omega'} \sigma_{ij}^d\,(\sigma_{rs}^*)\,C_{ijhk}\sigma_{hk}^d\,(\sigma_{rs}^*)\;\mathrm{d}\Omega = \max_{\sigma_{ij}^{d**}}\left\{F_c^d\left[\sigma_{ij}^{d**}, \sigma_{ij}^*\right]\right\} \tag{6.2}$$

where

$$F_c^d\left[\sigma_{ij}^{d**}, \sigma_{ij}^*\right] = \int_T \left\{-\frac{1}{2}\int_{\Omega'} \sigma_{ij}^{d**} C_{ijhk}\sigma_{hk}^{d**}\,d\Omega + \int_{\Gamma_d} g_i\,(p_h^*)\,\sigma_{ij}^{d**-} n_j^-\,d\Gamma\right\} dt. \tag{6.3}$$

By substitution of Eq. (6.2), the functional (5.1) is transformed into the following new functional:

$$(6.4)\qquad \mathcal{F}_c\left[\sigma_{ij}^*, \sigma_{ij}^{d**}\right] = \int_T \left\{ \frac{1}{2}\int_\Omega \sigma_{ij}^* C_{ijhk}\sigma_{hk}^* d\Omega + \int_\Omega \bar{\theta}_{ij}\sigma_{ij}^* d\Omega - \int_{\Gamma_u} \bar{u}_i n_j \sigma_{ij}^* d\Gamma \right.$$
$$+ \int_{\Gamma_d} g_i\left(p_h^*\right)\left(p_i^* - \sigma_{ij}^{ew} n_j^-\right) d\Gamma - \frac{1}{2}\int_{\Omega'} \sigma_{ij}^{d**} C_{ijhk}\sigma_{hk}^{d**} d\Omega$$
$$\left. + \int_{\Gamma_d} g_i\left(p_h^*\right)\sigma_{ij}^{d**-} n_j^- d\Gamma \right\} dt.$$

As a consequence of the above remarks the following theorem can now be stated:

PROPOSITION 7. A statically admissible stress field σ_{ij}^* and a self-equilibrated stress field σ_{ij}^{d**} are a (or the) solution of problem P and problem P^d, respectively, if and only if both the following conditions are satisfied:

(i) the two fields make stationary (minimum with respect to σ_{ij}^* and maximum with respect to σ_{ij}^{d**}) the functional F_c, Eq. (6.4)

(ii) the saddle-point value of the functional $\mathcal{F}_c$, Eq. (6.4), is equal to F_c^0, Eq. (5.3).

It is worth noting that: (a) the new functional $\mathcal{F}_c$ does not require the preliminary solution of an elastic auxiliary problem (nor the evaluation of the stress Green function due to distorsions on Γ_d), (b) the new formulation of the original i.b.v. problem P involves with respect to it, a double number of unknown fields.

6.2. A min-max extended total potential energy principle

Following a path of reasoning analogous to the one in the preceding section, a new min-max principle is established below from Proposition 5. A functional F_p^s to be maximized in order to obtain the last term of Eq. (5.11) (at any instant t) may be generated simply by using the principle of virtual work as follows:

$$(6.5)\qquad \frac{1}{2}\int_{\Omega'} \epsilon_{ij}^s\left(\epsilon_{rs}^o\right) D_{ijhk}\epsilon_{hk}^s\left(\epsilon_{rs}^o\right) d\Omega = -\frac{1}{2}\int_{\Omega'} \epsilon_{ij}^s\left(\epsilon_{rs}^o\right) D_{ijhk}\epsilon_{hk}^s\left(\epsilon_{rs}^o\right) d\Omega$$
$$+ \int_{\Gamma_d} f_i\left(w_h^o\right) w_i^s d\Gamma.$$

It is easy to recognize that the right-hand side of Eq. (6.5) represents the (changed in sign) value, at instant t, of the total potential energy at the solution of the

elastic problem (at instant t) with imposed tractions $-f_i\left(w_j^o\right)$ on Γ_d. This means that, by virtue of the minimum principle of total potential energy, we can write:

$$\frac{1}{2}\int_{\Omega'} \epsilon_{ij}^s\left(\epsilon_{rs}^o\right) D_{ijhk}\epsilon_{hk}^s\left(\epsilon_{rs}^o\right) d\Omega = \max_{u_i^{soo}} \left\{F_p^s\left[u_i^{soo}, u_i^o\right]\right\} \tag{6.6}$$

having set:

$$F_p^s\left[u_i^{soo}, u_i^o\right] = \int_T \left\{ -\frac{1}{2}\int_{\Omega'} \epsilon_{ij}^{soo} D_{ijhk}\epsilon_{hk}^{soo} d\Omega + \int_{\Gamma_d} f_i(w_h^o) w_i^{soo}) d\Gamma \right\} dt. \tag{6.7}$$

Here ϵ_{ij}^{soo} denotes any *self-compatible* strain field in Ω', i.e. any strain field which can be derived from a displacement field u_i^{soo} satisfying the homogeneous boundary conditions $u_i^{soo} = 0$ on Γ_u. By substitution of Eq. (6.6), functional F_p^I, Eq. (5.11), can be transformed into the following new functional:

$$\begin{aligned}\mathcal{F}_p\left[u_i^o, u_i^{soo}\right] = \int_T \Bigg\{ & \frac{1}{2}\int_{\Omega'} \left(\epsilon_{ij}^o - \bar{\theta}_{ij}\right) D_{ijhk}\left(\epsilon_{hk}^o - \bar{\theta}_{hk}\right) d\Omega - \int_{\Omega'} \bar{b}_i u_i^o d\Omega \\ & - \int_{\Gamma_p} \bar{p}_i u_i^o d\Gamma + \int_{\Gamma_d} f_i(w_j^o)\left(w_i^o - w_i^{ep}\right) d\Gamma - \frac{1}{2}\int_{\Omega'} \epsilon_{ij}^{soo} D_{ijhk}\epsilon_{hk}^{soo} d\Omega \\ & + \int_{\Gamma_d} f_i(w_j^o) w_i^{soo} d\Gamma \Bigg\} dt\end{aligned} \tag{6.8}$$

and the following statement can be asserted:

PROPOSITION 8. A kinematically admissible displacement field u_i^o and a displacement field u_i^{soo} vanishing on Γ_u are a (or the) solution of problem P and problem P^s, respectively, if and only if both the following conditions are satisfied:

(i) the two fields make stationary (minimum with respect to u_i^o and maximum respect to u_i^{soo}) the functional $\mathcal{F}_p$, Eq. (6.8);

(ii) the saddle-point value of the functional $\mathcal{F}_p$, Eq. (6.8), is equal to F_p^0 Eq. (5.13).

It is worth noting that in the functional (6.8), both fields $\epsilon_{ij}^o = \epsilon_{ij}^o(u_j^o)$ and $\epsilon_{ij}^{soo} = \epsilon_{ij}^{soo}\left(u_h^{soo}\right)$ are geometrically compatible. Remark similar to the one pointed out at the end of Proposition 7 hold here, namely: the new functional does not require the preliminary solution of an elastic auxiliary problem, nor the evaluation

of Green functions for strains due to imposed stresses; on the other hand, the new formulation concerns a double number of unknown fields.

7. Conclusions

The theoretical results achieved in this paper consist of duality pairs of extremum and saddle-point theorems, which characterize the nonlinear response in time to external action histories of linear elastic solids and structures containing loci where displacement discontinuities may occur, according to very general interface laws. These constitutive laws include mathematical models for, e.g.: frictional contacts on interfaces with asperities; fracture process zones in quasi-brittle materials; artificial joints in large concrete and masonry dams; delamination in laminates and debonding in composites.

The computational possibilities and some meaningful applications of the present results are being investigated elsewhere. As an illustrative example and a closing remark, we sketchily outlined below a path-of-reasoning apt to apply the last Proposition 8 (min-max theorem derived from the generalized potential energy principle of Sec. 5.2, Proposition 5).

Consider a four-point-bending or a four-point-shear test on a concrete specimen, as simulated in [16]. The loading history amounts to the monotone increase in time t of the displacement imposed by the testing device. A simulation centered on the above selected present results would encompass the following phases.

(a) A conventional finite element discretization in space is envisaged, account being taken of the conjectured locus Γ_d of possible crack propagation paths, starting from the specimen notches, so that nodal displacements represent degrees of freedom, gathered in vector $\mathbf{U}$.

(b) The duration time T of the test is subdivided into intervals $\Delta t_n = t_n - t_{n-1}$, over which the time-dependent $\mathbf{U}(t)$ can be modelled by interpolations (which may be generalized functions (distributions), so that customary time-integration schemes can be recovered as special cases).

(c) First, the time integral of elastic energy F_p^0, Eq. (5.13), is computed by a single once-for-all linear analysis and turns out to be proportional to t_n^3 at the instants t_n in the preselected sequence.

(d) Over the time step $\Delta t_n = t_n - t_{n-1}$, the nonlinear interface model $f_i(w_j)$ is made explicit so that $\mathcal{F}_p$, Eq. (6.8), becomes a functional of the variable vectors $\mathbf{U}_n^o$ and $\mathbf{U}_n^{soo}$ which govern, in space and in time, the fields u_i^o and u_i^{soo}, respectively, e.g. with stepwise constant modelling in time (the dimensionality of each of these vectors is the same as that of the d.o.f. vector $\mathbf{U}$).

(e) The step solutions, say $\hat{U}_n^o$ and $\hat{U}_n^{soo}$, are characterized by the min-max value $\hat{\mathcal{F}}_p = F_p^0$ of $\mathcal{F}_p$. In the test referred to, here three solutions are expected,

a symmetric and two nonsymmetric ones, if T exceeds a bifurcation threshold, [16]. In the impractical case of force control, no solution would be expected after a time T, a circumstance denoted by $\hat{\mathcal{F}}_p > F_p^0$. The saddle-point stationarity conditions are represented by generally nonlinear systems of algebraic equations and inequalities. The transformation of a min-max into a min problem (see e.g. [7]) might be computationally advantageous.

The solution characterizations by stationarity established in this paper for the continuum nonlinear initial-boundary value problems concerning elastic solids with dissipative interfaces, are seen to provide a theoretical framework for the discretization in space and time, in view of the numerical approximate solution of these problems.

Acknowledgements

A grant from the Italian Ministry of University and Research (MURST) for a research project on integrity assessment of large dams ("Cofinanziamento" 1999-2000) is gratefully acknowledged.

References

1. S. ALLINEY, A. TRALLI, *Extended variational formulations and F.E. methods in the stability analysis of non-conservative mechanics problems*, Comp. Meth. Appl. Mech. Engng., **51**, 209–219, 1986.
2. G. AUCHMUTY, *Variational principles for operator equations and initial value problems*, Nonlinear Analysis, Theory, Methods and Applications, **12**, 531–564, 1988.
3. Z. P. BAZANT, J. PLANAS, *Fracture and size effect in concrete and other quasibrittle materials*, CRC Press, Bocaraton 1998.
4. G. BOLZON, G. COCCHETTI, G. MAIER, G. NOVATI, G. GIUSEPPETTI, *Boundary element and finite element fracture analysis of dams by the cohesive crack model: a comparative study*, International Workshop on Dam and Fracture and Damage, Chambery, France, 16-18 March, 1994, [In:] Dam Fracture and Damage, E. BOURDAROT, J. MAZARS, V. SAOUMA, [Eds.], 69–78, Balkema, Rotterdam, Brookfield.
5. G. BOLZON, A. CORIGLIANO, *A discrete formulation for elastic solids with damaging interfaces*, Comp. Meth. Appl. Mech. Engng., **140**, 329–359.
6. G. BOLZON, G. MAIER, F. TIN-LOI, *Holonomic and non-holonomic simulation of quasi-brittle fracture: a comparative study of mathematical programming approaches*, [In:] Fracture Mechanics of Concrete Structures, F. H. WITTMANN [Ed.], Aedificatio Publishers, Freiburg, 885–898, 1995.
7. J. H. BRAMBLE, J. E. PASCIAK, *A preconditioning technique for indefinite systems resulting from mixed approximation of elliptic problems*, Mathematics of Computation, **50**, 1–17, 1988.
8. M. CAPURSO, G. MAIER, *Incremental elastoplastic analysis and quadratic optimization*, Meccanica, **4**, 107–116, 1970.

9. A. CARINI, *Colonnetti's minimum principle extension to generally nonlinear materials*, Int. J. Solids Structures, **33**, 121–144, 1996.

10. A. CARINI, *Saddle-point principles for general nonlinear material continua*, J. Applied Mechanics (ASME), **64**, 1010–1014, 1997.

11. A. CARINI and O. DE DONATO, *A comprehensive energy formulation for general non-linear material continua*, J. Applied Mechanics (ASME), **64**, 353–360, 1997.

12. A. CARINI, M. DILIGENTI, G. MAIER, *Boundary integral equation analysis in linear viscoelasticity: variational and saddle point formulations*, Computational Mechanics, **8**, 87–98, 1991.

13. A. CARINI, M. DILIGENTI, G. MAIER, *Symmetric boundary integral formulations of transient heat conduction: saddle-point theorems for BE analysis and BE-FE coupling*, Arch. Mech., **49**, 253–283, 1997.

14. A. CARINI, F. GENNA, *Some variational formulations for continuum nonlinear dynamics*, J. Mech. Phys. Solids, **46**, 1253–1277, 1998.

15. I. CAROL, P. C. PRAT and C. M. LOPEZ, *Normal/shear cracking model: application to discrete crack analysis*, J. Engng. Mech., ASCE, **123**, 1–9, 1997.

16. Z. CEN, G. MAIER, *Bifurcation and instability in fracture of cohesive softening structure: a boundary element analysis*, Fatigue and Fracture Engineering of Material and Structures, **15**, 911–928, 1992.

17. G. CERADINI, *A maximum principle for the analysis of elastic-plastic systems*, Meccanica, **1**, 77–82, 1966.

18. C. COMI, A. CORIGLIANO, G. MAIER, *Dynamic analysis of elastoplastic-softening discretized structures*, Proc. ASCE, J. Engng. Mech., **118**, 2352–2375, 1992.

19. C. COMI, G. MAIER, U. PEREGO, *Generalized variable finite element modelling and extremum theorems in stepwise holonomic elastoplasticity with internal variables*, Comp. Meth. Appl. Mech. Engng., **96**, 133–171, 1992.

20. B. A. FINLAYSON, *The method of weighted residual and variational principles with applications in fluid mechanics, heat and mass transfer*, Academic Press, New York 1972.

21. M. E. GURTIN, *Variational principles for linear initial-value problems*, Quart. Appl. Math., **22**, 252–256, 1964.

22. B. L. KARIHALOO, *Fracture Mechanics and Structural Concrete*, Longman Scientific & Technical, Harlow, Great Britain 1998.

23. W. T. KOITER, *General theorems for elastic-plastic solids*, [In:] Progress in Solid Mechanics, I. N. SNEDDON and R. HILL [Eds.], **1**, Ch. IV, 167–221, 1964.

24. H. LOFTI, P. SHING, *Interface model applied to fracture of masonry structures*, J. Struc. Engng., ASCE, **120**, 63–80, 1994.

25. G. MAIER, *Some theorems for plastic strain rates and plastic strains*, Journal de Mécanique, **8**, 5–19, 1969.

26. G. MAIER, *A minimum principle for incremental elastoplasticity with nonassociated flow laws*, J. Mech. Phys. Solids, **18**, 319–330, 1970.

27. G. MAIER, M. DILIGENTI, A. CARINI, *A variational approach to boundary element elastodynamic analysis and extension to multidomain problems*, Comp. Meth. in Appl. Mech. Engng., **92**, 193–212, 1991.

28. G. MAIER, G. NOVATI, Z. CEN, *Symmetric Galerkin boundary element method for quasi-brittle fracture and frictional contact problems*, Computational Mechanics, **13**, 74–89, 1993.

29. P. M. MORSE and H. FESHBACH, *Methods of theoretical physics*, **I**, McGraw-Hill 1953.

30. Z. MRÓZ, SHEN XINPU, *Analysis of progressive interface failure under monotonic loading*, [In:] Microstructure and Mechanical Properties of New Engineering Materials, B. Y. XU, M. TOKUDA, X. C. WANG [Eds.], International Academic Publisher, Beijing, 109–114, 1999.

31. Z. MRÓZ, G. GIAMBANCO, *An interface model for analysis of deformation behaviour of discontinuity*, Int. J. Num. Anal. Meth. Geomech., **20**, 1–33, 1996.

32. M. ORTIZ, *A variational formulation for convection-diffusion problems*, Int. J. Engng. Sci., **23**, 717–731, 1985.

33. P. RAFALSKI, *Orthogonal projection method. I. Heat conduction boundary problem*, Bull. Acad. Polon. Sci., Sér. Sci. Techn., **17**, 63–67, 1969.

34. P. RAFALSKI, *Orthogonal projection method. II. Thermoelastic problem*, Bull. Acad. Polon. Sci., Sér. Sci. Techn., **17**, 69–74, 1969.

35. R. REISS, E. J. HAUG, *Extremum principles for linear initial-value problems of mathematical physics*, Int. J. Engng. Sci., **16**, 231–251, 1978.

36. P. D. ROBINSON, P. K. YUAN, *Bi-variational methods for linear integral equations with non-symmetric kernels*, SIAM, J. Numer. Anal., **23**, 1230–1240, 1986.

37. J. J. TELEGA, *Variational principles for rate boundary-value problems in non-associated plasticity*, ZAMM, **60**, 71–82, 1980.

38. E. TONTI, *On the variational formulation for linear initial value problems*, Annali di Matematica Pura ed Applicata, **45**, 331–359, 1973.

39. E. TONTI, *Variational formulation for every nonlinear problem*, Int. J. Engng. Sci., **22**, 1343–1371, 1984.

Received August 24, 2000.

Arch. Mech., **52**, 4–5, pp. 547–567, 2000

On Prandtl's lifting equation arising in wear mechanics

Dedicated to Professor Zenon Mróz
on the occasion of his 70^{th} birthday

M. DRAGON-LOUISET ([1]), H. D. BUI ([1-2]) and C. STOLZ ([1])

([1]) *Laboratoire de Mécanique des Solides,*
CNRS UMR 7649, École Polytechnique, 91128 Palaiseau Cedex, FRANCE;
e-mail:dragon@lms.polytechnique.fr

([2]) *Électricité de France,*
Division R&D, 92141 Clamart Cedex, FRANCE

A SLIDING WEAR CONTACT between a rigid punch and an elastic halfplane in presence of a thin aggregate film composed of solid debris and a lubricant fluid is studied. The model is based on any wear criterion and constitutive law of the film suggested by micromechanics approximation. The mechanical system is governed by the evolution of the volume fraction of debris, considered as the internal state variable. The key step of iterative computations for solving the nonlinear system of equations is based on the solution of the fundamental linear integro-differential equation for the compressive normal stress (the W-equation). Uniqueness of the solution of the integro-differential equation is then proved. It is shown that there is a profound relationship between the latter equation and Prandtl's lifting equation in aerodynamics: both equations can be solved numerically by Chebyshev's series, and experimentally by similar electrical setups. Mathematically, it is found that both equations are related to real and imaginary components of some complex potential, respectively, and to weakly adjoint integro-differential operators.

1. Introduction

A SLIDING WEAR CONTACT between two elastic solids is typically a nonlinear problem, because of two reasons: on the one hand, the contact problem itself is nonlinear even if there is no wear; on the other hand, the presence of debris or detached particles changes the load transfer conditions at the interface between two contacting solids. Following a terminology introduced in GODET [18, 19], the interface is called "third-body" and should be considered as an aggregate film composed of different particles and a lubricant fluid, having some nonlinear macroscopic rheology, which is not yet known. Different terminologies, interface or third-body, are simply a matter of scales used in describing the macroscopic

or mesoscopic behavior. On a thiner microscopic scale, damage and microcracking at the asperities are wear mechanisms feeding the third-body. Conditions for microscopic wear mechanisms to develop, depend on the macroscopic contact stresses, which are determined by the rheology of the third-body, the internal variable of which is related to the wear rate. This is a fully coupling problem at different levels.

In the literature, formulations of wear contact problems generally ignore this coupling aspect. For instance, by assuming a perfect contact between sound solids (GALIN [14], GALIN and GORIACHEVA [15]), one ignores the debris life in the contact zone or considers that the detached particles are removed instantaneously from the contact interface.

The need of an understanding of third-body processes in order to model and predict wear on a macroscopic scale is expressed by several authors: GODET [18, 19], GEORGES [16], SINGER and WAHL [29], BERTHIER [3, 4], BERTHIER *et al.* [5], MENG and LUDEMA [24]. For a comprehensive review of wear mechanisms on a microscopic scale, see KO [21]. A large amount of models are based on experimental observations and depend on the test conditions. Most of them are derived from ARCHARD's relation [2]. Such models cannot be predictive when the operating conditions cannot be close to the common use conditions of machine components.

Experiments on wear friction contact, as observed in Stribeck's curves, provide a relation between the friction coefficient $\mu = \tau/p$ and the lubricant coefficient $L = \eta V/p$ (where η is the fluid viscosity, V the relative velocity, p the pressure, τ the shear stress). Three regimes are observed in Stribeck's curves (Fig. 1): (I) Coulomb's friction law with constant μ; (II) instable regime occuring probably in earthquakes (SCHOLZ [28]); (III) hydrodynamic regime, for instance $\mu(L) \simeq a + bL$, as proposed in DANG VAN's criterion [8], or $\mu(L) \simeq bL$, as in viscous laminar flow corresponding to mild wear. Stribeck's curves clearly suggest

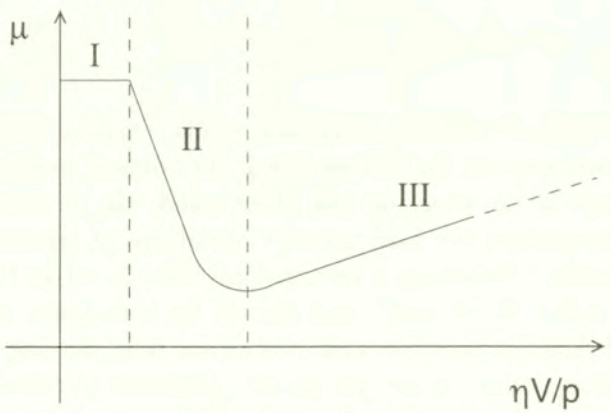

FIG. 1. Stribeck's curve.

an interaction between the debris and the elastic solids, through the evolution of some internal state variables governing the third-body, which is the proportion of solids' debris, defined either by volume fractions or by mass fractions of species. By a simple theory of mixture, one can get an idea on the third-body: constitutive laws, free energy, dissipation, etc... That approach is recently provided in DRAGON-LOUISET [11] for a wear model of regime (III), in the presence of incompressible fluid. A similar approach was given by STUPKIEWICZ and MRÓZ [31] for modeling abrasive wear.

The content of this paper is as follows. In the first part, for the consistency of the paper, we reconsider briefly the general equations of the contact-sliding mild wear model based on micromechanical considerations, given in [11]. The model is applied to the contact-sliding between a circular *rigid* solid and an *elastic* halfplane $\Omega_2 = \{x, y \leqslant -e(x) \simeq 0\}$ in presence of fluid (Fig. 2).

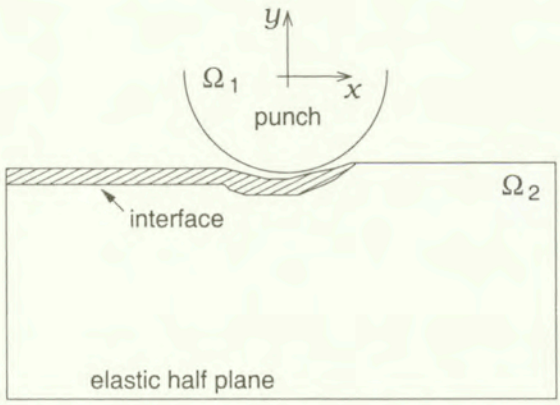

FIG. 2. A punch sliding on an elastic halfplane and their interface.

The coupled nonlinear equations of equilibrium are based on the following ideas:

i. The microscopic wear mechanisms occuring at the asperities level, describing the detachment of particles from sound solids to the third-body, will be modeled on the macroscopic scale. The wear criterion and wear rate will be given in a general form.

ii. The third-body on a mesoscopic scale, in somewhat of a thin film thickness $e(x)$ made of an aggregate of debris and fluid, considered as an *open* thermodynamical system, with mass transfer characterized by the wear rate $v(x)$ feeding the interface, at the surface Γ between sound material and the third-body. Parallel in-flow and out-flow of a two-phase aggregate occur in the third-body which behaves under shear load like a "viscous fluid". In

considering the volume fraction $\varphi(x)$ of debris, as suitable internal variables of the contact zone film, the conservation laws of mass (solid and fluid) provide the relations between the volume fraction, the wear rate and the thickness.

iii. The two-phase aggregate has a specific rheology to determine, depending on the volume fraction.

The coupled nonlinear equilibrium equations of the mechanical system, elastic solid, rigid punch and interface, provided that some reasonable assumptions are made, have the property that, at any step of the iterative computations, only *one* fundamental linear boundary integro-differential equation has to be solved (the W-equation).

In the second part of the paper, we shall focus our analysis on the latter equation. Using methods of complex representations of potentials, we establish a relation between the W-equation and the well-known Prandtl lifting equation in aerodynamics. This relation suggests us similar methods for solving both equations, by Chebyshev's series expansion, using functions of the first kind and the second kind and also an interesting means for solving *experimentally* the W-equation, just as the Prandtl equation has been solved experimentally in the past by Malavard's electrical analogy.

2. The interface model for computational mechanics

Having in mind the plane strain contact-sliding wear model for a rigid punch and an elastic foundation, described later, we consider a thin interface made of a two-phase mixture of solid debris and fluid. The interface extends along Ox, $-a \leqslant x \leqslant a$, with the wake interface $x \leqslant a$ (Fig. 2). For simplicity, to any meso-scale quantity $f(x, y)$ defined in the third-body $-a \leqslant x \leqslant a$, $-e(x) \leqslant y \leqslant 0$, we denote the corresponding average over the thickness $e(x)$ at x, by the same notation $f(x)$. Physically, the third-body is characterized by a proportion of solid debris s and fluid f. It can be characterized either by mass fractions or by volume fractions $\varphi_s(x)$, $\varphi_f(x) = 1 - \varphi_s(x)$. The volume fraction, being a geometrical description of the third-body, allows consideration of *stick* phenomena. For example, the shear flow is impossible for compact hexagonal arrangement of circular debris of equal radius, where $\varphi_s = 62\%$, DRAGON-LOUISET [11]. Hence, geometrical considerations allow the possibility of a threshold value of internal variables based on the volume fractions, beyond which stick phenomenon occurs.

Before analysing the kinematics of the third-body, we first need a macroscopic description of wear condition, i.e. the detachment of particles feeding the interface.

2.1. Macroscopic wear criterion and wear rate

The most general form of wear criterion, was provided by DRAGON-LOUISET and STOLZ [12] who described in a thermodynamical manner the local quantities involved in the wear phenomena and proposed a wear criterion (DRAGON-LOUISET [11]) similar to the well-known *energy release rate* in Fracture Mechanics, applicable to elastic-brittle materials. Let us drop the index 2 for quantities defined in the elastic solid Ω_2, denoted Ω;

$$g = \mathbf{n} \cdot \boldsymbol{\sigma} \cdot \nabla \mathbf{u} \cdot \mathbf{n} - \rho\psi \qquad \text{(elastic solid)}, \tag{2.1}$$

$$g^3 = \mathbf{n} \cdot \boldsymbol{\sigma}^3 \cdot \nabla \mathbf{u}^3 \cdot \mathbf{n} - \rho\psi^3 \qquad \text{(damaged material adjacent to } \Gamma), \tag{2.2}$$

with $\mathbf{n}$ the outward unit vector normal to the boundary Γ of Ω, with $\boldsymbol{\sigma}$ and $\boldsymbol{\sigma}^3$ the stresses, $\mathbf{u}$ and $\mathbf{u}^3$ the displacements vectors, ψ and ψ^3 the free energies of sound and damaged material respectively, ρ (or ρ_s) the density of the solid. The displacements and the stress vectors $\boldsymbol{\sigma}\cdot\mathbf{n}$ are continuous across Γ. Then, assuming the existence of a threshold energy g^s, the wear criterion is $G(\sigma) = g - g^3 - g^s < 0$, when the elastic solid does not lose material, and $G(\sigma) = g - g^3 - g^s \geqslant 0$ when it does. The wear rate is assumed to be given a priori by $v = F(g, g^3) = F(\sigma)$ when the wear criterion is verified. In this analysis wear and frictional energies are dissociated: solids can slide without being affected by wear and the loss of material.

This model is completed by the evaluation of average quantities such like stress and strain on the mesoscopic scale (depending on volume fraction of particles, the presence of a lubricant, chemical reactions, ...). Some models studied in DRAGON-LOUISET [11] provide explicitly the evaluation of g^3 in terms of stress and strain of Ω and the rheology of the third-body.

2.2. Conservation of mass

The volume fraction of solid particles φ_s is simply denoted φ. In the steady-state case, the one-dimensional conservation laws of mass, solid and fluid, can be written respectively as:

$$\frac{\partial}{\partial x}\left[e(x)\varphi(x)\rho_s v_x(x)\right] - \alpha\rho_s v(x) = 0 \quad \text{(solid)}, \tag{2.3}$$

$$\frac{\partial}{\partial x}\left[e(x)(1-\varphi(x))\rho_f v_x(x)\right] = 0 \quad \text{(fluid)}, \tag{2.4}$$

where $v_x(x)$ is the x-coordinate of the mean velocity of solid debris or fluid, equal to $-V/2$; $r_s = \alpha\rho_s v(x)$ is the source term coming from the detachment of debris at rate $v(x)$ feeding the interface through Γ, and α is interpreted as the part of

debris which diffuses toward the third-body. The remaining part $1 - \alpha$ being imprisoned in the asperities is moving out the contact zone, without making any contribution to the third-body rheology, ρ_s and ρ_f are densities of solid and fluid, respectively.

Since up-stream there is no wear, we have $\varphi(a) = 0$. Hence, by assuming α and ρ_s constant, we obtain from (2.3) the relation between the wear rate $v(x)$, the volume fraction $\varphi(x)$ and the thickness $e(x)$

$$\varphi(x) = -\frac{2\alpha}{Ve(x)} \int_a^x v(x)\, dx \quad (x \leqslant a). \tag{2.5}$$

For either incompressible fluid (ρ_f constant) or negligible variation of $\rho_f(x)$ along the interface, Eq. (2.4) can be reduced to $\dfrac{\partial}{\partial x}[e(x)(1 - \varphi(x))v_x(x)] \simeq 0$. Now, by assuming classical *quasi-linear* one-dimensional Stokes flow inside the third-body, between the fixed wall $v_x(x, 0) = 0$ and the sliding one $v_x(x, -e) = -V$, we get the constant mean value $v_x(x) = -V/2$ as mentioned above. This means that two-dimensional fluid flows near the end points of the contact interface are disregarded. We then obtain

$$e(x) = \frac{e_0}{1 - \varphi(x)}. \tag{2.6}$$

Equations (2.5) and (2.6) are equivalent forms of the mass conservation laws of solid particles and fluid, respectively. Provided that $v(x)$ is known, Eqs. (2.5) and (2.6) yields an integral equation for determining $\varphi(x)$ and then $e(x)$. The volume fraction can be written as:

$$\varphi(x) = \frac{B(x)}{1 + B(x)} \quad \text{with} \quad B(x) = -\frac{2\alpha}{Ve_0} \int_a^x v(x)dx. \tag{2.7}$$

$B(x)$ is a monotonic function of x, increasing as x decreases. Down-stream, the volume fraction is constant and equal to its maximum value $\varphi_{\max} = \varphi(-a)$. Generally the latter quantity is very small. A good approximation justified by the smallness of $\dfrac{4a\alpha}{Ve_0} \max|v|$ is simply given by (2.5) with approximate $e(x) \simeq e_0$, or $\varphi(x) = B(x)$.

2.3. Rheology of the third-body

We assume that the compressive contact stress is given by the uniaxial law

$$g[\varphi]\sigma_{yy} = c_1(u_y^+ - u_y^-), \quad \text{with} \quad g(\varphi) > 0 \quad \text{and} \quad c_1 = \frac{E}{2(1 - \nu^2)}, \tag{2.8}$$

where c_1 is introduced for later use, E is the Young modulus, ν is the Poisson's ratio, $(+)$ sign for the punch and $(-)$ for the elastic halfplane. An explicit form can be given for the function $g[\varphi]$ by micromechanical considerations. For example, by making use of Reuss's model of aggregate based on strain additivity or stress homogeneity, on the mesoscopic scale, the first law takes the form

$$\left[\frac{\varphi}{K} + \frac{1-\varphi}{K_f}\right] \frac{e_0}{1-\varphi} \sigma_{yy} = u_y^+ - u_y^-, \tag{2.9}$$

where K is the stiffness of the detached solid particles, K_f is the stiffness of the fluid. For small φ, it follows from (??) and linearization $g[\varphi] = c_1 e_0(\varphi/K + 1/K^f)$. The incompressible case $K_f = \infty$ is considered in [11]. The model (2.9) is rigorous when the fluid viscosity is infinitely small. A different model was given by STUPKIEWICZ and MRÓZ [31] for studying abrasive wear due to asperities. The mesoscopic stresses are considered as microscopic stress averages. As a matter of fact, their model of contact stress additionality corresponds to Voigt's model of aggregate and is therefore the *dual* model to (2.9).

The second law describes the viscous behavior of the thin film under shear load. As suggested by experiments, the shear stress can be assumed in the form $(\sigma_{xy}^- = \sigma_{xy})$

$$\sigma_{xy} = m[\varphi] \left(\frac{du_x^+}{dt} - \frac{du_x^-}{dt} \right) \simeq m[\varphi] V, \tag{2.10}$$

where the relative velocity is approximated by V (the elastic velocity is negligible) and $m[\varphi]$ is a material constant which can be evaluated by micromechanics. As shown later, this approximation justified by in-service conditions of wear allows for the decoupling of equations.

Again, an explicit form of the function $m[\varphi]$ can be provided by classical models of solid dispersion in viscous fluid. The viscosity coefficient of the mixture is given by Einstein's law $\eta[\varphi] = \eta_0(1+2.5\varphi)$ (see LANDAU and LIFCHITZ [22]), so that $\sigma_{xy} = \eta[\varphi] \left(\frac{du_x^+}{dt} - \frac{du_x^-}{dt} \right) / e(x)$ and using (2.6) and linearization, it follows $m[\varphi] = \eta_0(1 + 1.5\varphi)/e_0$.

Finally, the third-body model is a medium having a *hybrid* behavior of an elastic solid in compression and a viscous fluid in shear or a plastic solid with constant threshold (φ and V held fixed). It looks like a ball bearing, capable of transmitting a compressive force, but having some resistance in sliding. The volume fraction φ appears explicitly in the wear equations, making it possible to have a quantitative and predictive analysis of wear, for a given mechanical system. The macroscopic interface between a rigid punch and an elastic solid is characterized by properties summarized in the following box.

INTERFACE MODEL ON THE MACROSCOPIC SCALE

- Wear criterion $G(\sigma) \geqslant 0$ and wear rate $v = H(G(\sigma))F(\sigma)$, with H the Heaviside function

$$\begin{cases} \text{if } G(\sigma) < 0, & \text{no wear and: } v = 0, \\ \text{if } G(\sigma) \geqslant 0, & \text{wear rate: } v = F(\sigma) > 0. \end{cases}$$

- Internal state variable $\varphi(x)$ and mass conservation laws

$$\frac{\partial}{\partial x}[e(x)\varphi(x)v_x(x)] - \alpha v(x) = 0 \qquad \text{(solid)},$$

$$\frac{\partial}{\partial x}[e(x)(1-\varphi(x))v_x(x)] = 0 \qquad \text{(fluid)}.$$

- Constitutive laws

$$\sigma_{xy} = m[\varphi]V, \qquad \text{with } m[\varphi] > 0,$$

$$g[\varphi]\sigma_{yy} = c_1(u_y^+ - u_y^-), \quad \text{with } g[\varphi] > 0 \text{ and } c_1 = \frac{E}{2(1-\nu^2)}.$$

3. Statement of the problem

We consider a rigid circular punch of radius R, defined by the equation $y = f(x) = (x - x_0)^2/(2R)$ sliding on an elastic halfplane, (Fig. 2). In the previous section, we gave the description of the third-body on the mesoscopic scale, $-a \leqslant x \leqslant a$, $-e(x) \leqslant y \leqslant 0$. Here the interface is considered on the macroscopic scale and is defined by $y = 0$. The elastic body Ω is the halfplane $\{x, y \leqslant 0\}$. The vertical displacement of the upper third-body surface (Γ_1, $y = 0$) is

$$u_y^+(x) = \delta + f(x) \quad (\delta < 0), \tag{3.1}$$

where δ is the imposed position of the punch and $f(x)$ its profile. The vertical displacement of the lower surface (Γ_2, $y = -e(x)$) is u_y^- equal to the displacement of the halfplane boundary. The strain ε_{yy} of the interface medium is $\varepsilon_{yy} = (u_y^+ - u_y^-)/e$.

For the present, neither the compressive load nor the contact zone $-a \leqslant x \leqslant a$ have been specified. The punch position x_0 is yet unknown. The following

assumption is only made $-a \leqslant x_0 \leqslant a$. The integral equations for boundary fields in plane strain are given by GALIN [13] (pv means "principal value") ($u_x^- = u_x$, $u_y^- = u_y$)

$$c_1 \, u_x'(x) = c_2 \, \sigma_{yy}(x) + pv \, \frac{1}{\pi} \int_{-a}^{a} \sigma_{xy}(t) \frac{dt}{t-x}, \tag{3.2}$$

$$c_1 \, u_y'(x) = -c_2 \, \sigma_{xy}(x) + pv \, \frac{1}{\pi} \int_{-a}^{a} \sigma_{yy}(t) \frac{dt}{t-x}, \tag{3.3}$$

where $c_1 = E/[2(1-\nu^2)]$, $c_2 = (1-2\nu)/[2(1-\nu)]$ and the prime ($'$) means differentiation. Equations (3.2) and (3.3) establish the relations between tangential gradients of displacement, normal stress σ_{yy} and shear σ_{xy} (cf. also BUI [7] for the reciprocal relations). Setting $\varepsilon_{xx}(x) = u_x'(x)$ in (3.2), i.e. the longitudinal strain parallel to the boundary, substituting (2.8), (2.10), (3.1) in (3.3), we obtain the set of equations:

$$c_1 \, \varepsilon_{xx}(x) = c_2 \, \sigma_{yy}(x) + pv \, \frac{1}{\pi} \int_{-a}^{a} \sigma_{xy}(t) \frac{dt}{t-x}, \tag{3.4}$$

$$c_1 \, f'(x) - \frac{d}{dx} \left[g[\varphi](x) \sigma_{yy}(x) \right] = -c_2 \, m[\varphi](x) V + pv \, \frac{1}{\pi} \int_{-a}^{a} \sigma_{yy}(t) \frac{dt}{t-x}, \tag{3.5}$$

$$\sigma_{yy}(-a) = \sigma_{yy}(a) = 0, \tag{3.6}$$

with additional equations given previously as

$$\sigma_{xy} = m[\varphi] V, \tag{3.7}$$

$$\varphi(x) = -\frac{2\alpha}{V e_0} \int_{a}^{x} v(x) \, dx, \tag{3.8}$$

$$v = H(G) F(\sigma). \tag{3.9}$$

The boundary conditions (3.6) come from the continuity assumption of stresses (no normal load at the fluid interface outside the punch area). In the energy release rate approach, G is expressed in terms of the elastic strain energy densities on both sides of the phase changes line. It depends on σ_{xy}, σ_{yy}, ε_{xx} of the sound

material and on the stresses σ_{xx}, σ_{yy} of the damaged zone adjacent to the interface line. Its expression depends on particular models considered on the mesoscopic scale. Once the expression of $G(\sigma_{xy}, \sigma_{yy}, \varepsilon_{xx}, \varphi)$ in terms of its arguments is explicitly known, it can be evaluated by quantities given by Eq. (3.4) to (3.9).

Let us specify now the data for the whole mechanical system for solving the nonlinear system of Eqs. (3.4) – (3.9). Instead of giving the total compressive force, we *specify the contact zone* $-a \leqslant x \leqslant a$ and then determine the corresponding compression load given by

$$P(a) = -\int_{-a}^{a} \sigma_{yy}(t)\, dt, \tag{3.10}$$

the shear force

$$T(a) = -\int_{-a}^{a} \sigma_{xy}(t)\, dt, \tag{3.11}$$

and the punch position x_0.

It is worth noticing that the key step of the iterative computation is to determine the normal stress σ_{yy} and that for each iteration, until convergence, only one equation, namely (3.5), has to be solved. Other quantities of interest for the wear criterion (3.9) are derived explicitly from φ and σ_{yy} by computations of integrals. For detailed analysis of the nonlinear algorithm, we refer to DRAGON-LOUISET [11].

Here we shall focus on this linear integro-differential equation for the normal stress (3.5), which is referred to as the W-equation.

4. The W-equation

4.1. The step (0) algorithm

For a given volume fraction $\varphi(x)$ and a given contact zone $-a \leqslant x \leqslant a$, we consider the function $\sigma_{yy}^{(0)}$ satisfying the following equations, with $m[\varphi]V = (\eta_0/e_0)V$

$$pv\, \frac{1}{\pi} \int_{-a}^{a} \sigma_{yy}^{(0)}(t) \frac{dt}{t-x} = c_1 f'(x) + c_2 \frac{\eta_0}{e_0} V, \tag{4.1}$$

$$\sigma_{yy}^{(0)}(\pm a) = 0. \tag{4.2}$$

With a Hölderian function in the right-hand side, (4.1) is a classical Hilbert's equation, treated in MUSKHELISHVILI [25]. The corresponding homogeneous

equation possesses a non-zero solution of the type $C(a^2 - x^2)^{-\frac{1}{2}}$. Hence, to obtain a bounded solution (in fact vanishing at $x = \pm a$), there is a consistency condition to be satisfied

$$\int_{-a}^{a} \left[c_1 f'(t) + c_2 \frac{\eta_0}{e_0} V \right] (a^2 - t^2)^{-\frac{1}{2}} \, dt = 0, \tag{4.3}$$

where $f'(x) = (x - x_0)/R$. From the consistency condition (4.3) we obtain $x_0 = c_2 \eta_0 V R/(c_1 e_0)$, which is independent of a, hence a good candidate for starting the step (0) algorithm, provided that $x_0 \leqslant a$. The last condition can be satisfied by choosing appropriately the velocity V. The solution of (4.1) is then given by MUSKHELISHVILI [25],

$$\sigma_{yy}^{(0)}(x) = -(a^2 - x^2)^{\frac{1}{2}} pv \, \frac{1}{\pi} \int_{-a}^{a} \left[c_1 f'(t) + c_2 \eta_0 \frac{V}{e_0} \right] (a^2 - t^2)^{-\frac{1}{2}} \, \frac{dt}{t - x}, \tag{4.4}$$

or $\sigma_{yy}^{(0)}(x) = -(c_1/R)(a^2 - x^2)^{\frac{1}{2}}$. This is a Hertzian distribution of load with the corresponding linear force given by

$$P_0(a) = -\int_{-a}^{a} \sigma_{yy}^{(0)}(t) \, dt = \frac{\pi c_1 a^2}{2R}. \tag{4.5}$$

If the first term of (3.5), $\dfrac{d}{dx}[g[\varphi](x)\sigma_{yy}(x)]$ is small in comparison with the remaining ones, the zero-order solution $\sigma_{yy}^{(0)}(x)$ provides a good approximation of the actual solution, except near the end points $x = \pm a$ where the derivative $\dfrac{d}{dx}\left[\sigma_{yy}^{(0)}(x)\right]$ is singular (this is mathematically a singular perturbation problem not addressed here). In what follows, we outline the method of solving (3.5) using Chebyshev's series expansion suggested by the analogy with Prandtl's equation.

4.2. Chebyshev's series solution

Having determined the approximate center position x_0, it is advantageous to solve the W-equation for the actual stress $\sigma_{yy}(x)$, written in the form

$$\frac{d}{dx}(g[\varphi](x)\sigma_{yy}(x)) + pv \, \frac{1}{\pi} \int_{-a}^{a} \sigma_{yy}(t) \frac{dt}{t - x} = \frac{c_1}{R}(x - x_0) + c_2 m[\varphi](x) V \equiv b(x). \tag{4.6}$$

We set the following change of variables: $t = -a\ \cos(\theta)$, $x = -a\ \cos(\omega)$, with $\theta \in [0, \pi]$. The function $\sigma_{yy}(\omega)$ satisfying (4.6) is expanded in truncated Fourier sine series, ANDERSON [1]:

$$\sigma_{yy}(\theta) = \sum_{n=1}^{N} A_n \sin(n\theta), \quad 0 \leqslant \theta \leqslant \pi. \tag{4.7}$$

Using the Chebyshev identity of the first kind

$$\int_0^{\pi} \frac{\sin(n\theta)\sin(\theta)}{\cos(\theta) - \cos(\omega)}\, d\theta = -\pi \cos(n\omega),$$

and by setting $b(x) = b(x = -\cos(\omega))$, we obtain

$$\sum_{n=1}^{N} aA_n \cos(n\omega)\sin(\omega) + \sum_{n=1}^{N} A_n \frac{d\,[g(\omega)\sin(n\omega)]}{d\omega} - a\sin(\omega)b(\omega) = 0, \quad 0 < \omega < \pi. \tag{4.8}$$

Generally the linear system (4.8) is solved by the collocation method. This method however is unsatisfactory in the choice somewhat arbitrary of the collocation points, $0 < \omega_k < \pi$ $(k = 1, .., N)$. It is of interest to consider instead the Galerkin method. In order to use the Fourier 2π-periodic functions, the functions appearing in the left-hand side of (4.8), defined only in the interval $0 < \omega < \pi$, must be extended to $-\pi < \omega < \pi$ in such a way that the extended functions are *even*. For instance, the first term $\cos(n\omega)\sin(\omega)$ of (4.8) is odd and has to be extended to $-\pi < \omega < \pi$ by the function $sgn(\omega)\cos(n\omega)\sin(\omega)$. Only odd functions have to be extended in this way, by multiplication with the sign-function $sgn(\omega)$. Then, by using the Fourier cosine functions $\cos(k\omega)$, we obtain the set of equations for A_n

$$\sum_{n=1}^{N} \left(A_n \int_0^{\pi} \left\{ a\cos(n\omega)\sin(\omega) + \frac{d}{d\omega}\,[g(\omega)\sin(n\omega)] \right\} \cos(k\omega)\, d\omega \right) - \int_0^{\pi} a\sin(\omega)b(\omega)\cos(k\omega)\, d\omega = 0, \qquad k = 1, .., N. \tag{4.9}$$

Remark that the solution (4.7) contains the factor $\sin(\theta)$, hence the normal stress $\sigma_{yy}(x)$ has the square root behavior $\sigma_{yy}(x) \simeq (a^2 - x^2)^{\frac{1}{2}}$ as $|x| \to a$. It can be shown that the zero-order solution $\sigma_{yy}^{(0)}(x)$ is an approximation of the first term

of the series (4.7). The method outlined here is an adaptation of the one given in DRAGON-LOUISET [11].

4.3. Uniqueness considerations

Having determined a solution satisfying (3.6) and the corresponding total load $P(a)$ by (3.10), we are concerned with the uniqueness of the solution of the W-equation (4.6). It is necessary to specify the space of functions to which the solution belongs. We need the class of Hölderian functions of Muskhelishvili to give a sense to Cauchy integrals, satisfying $\sigma_{yy}(\pm a) = 0$ and regular in $-a \leqslant x \leqslant a$. Suppose that there are two solutions σ^1, σ^2, corresponding to the same total load $P(a)$. Then, $\Sigma = \sigma^1 - \sigma^2$ satisfies the homogeneous W-equation with $b(x) = 0$, $\Sigma(\pm a) = 0$ and $\int_{-a}^{a} \Sigma(t)\, dt = 0$. As shown below, the uniqueness theorem states that $\Sigma(x) \equiv 0$, provided that $g[\varphi] > 0$.

4.4. Proof of uniqueness

Let us prove the theorem by considering the complex function $F(z)$ defined in the upper complex plane $z = x + iy$, $(y \geqslant 0)$:

$$F(z) = \frac{1}{2i\pi} \int_{-a}^{a} i\Sigma(t) \ln(z - t)\, dt = \Phi(x, y) + i\Psi(x, y), \tag{4.10}$$

$$x, y \quad \text{in } \Omega^+ = \{x, y \geqslant 0\},$$

$$F'(z) = -\frac{1}{2i\pi} \int_{-a}^{a} i\Sigma(t) \frac{dt}{t - z} = v_x(x, y) - i\, v_y(x, y), \tag{4.11}$$

$$\Phi(x, 0^+) = \frac{1}{2\pi} \int_{-a}^{a} \Sigma(t) \ln|x - t|\, dt, \tag{4.12}$$

$$v_y(x, 0^+) = \frac{\partial \Phi}{\partial y}(x, 0^+) = \frac{1}{2}\Sigma(x), \quad \text{for } 0 \leqslant |x| \leqslant a, \tag{4.13}$$

$$v_y(x, 0^+) = \frac{\partial \Phi}{\partial y}(x, 0^+) = 0, \quad \text{for } |x| \geqslant a. \tag{4.14}$$

The density $\Sigma(x)$ is assumed to satisfy the following equation with some $H(x)$:

$$g[\varphi](x)\Sigma(x) - \frac{1}{\pi} \int_{-a}^{a} \Sigma(t) \ln|t - x|\, dt = H(x), \quad 0 \leqslant |x| \leqslant a. \tag{4.15}$$

Differentiating (4.15), we find that $\Sigma(x)$ satisfies the W-equation

$$\frac{d}{dx}\,[g[\varphi](x)\Sigma(x)] + pv\,\frac{1}{\pi}\int_{-a}^{a}\Sigma(t)\frac{dt}{t-x} = H'(x). \tag{4.16}$$

Now Eq. (4.15) can be written equivalently as

$$2g[\varphi](x)\frac{\partial\Phi}{\partial y}(x,0^+) - 2\Phi(x,0^+) = H(x), \quad \text{on } 0 \leqslant |x| \leqslant a. \tag{4.17}$$

To investigate the uniqueness, we consider the homogeneous Eq. (4.16) for $\Sigma(x)$, with $H' = 0$, or the homogeneous boundary condition (4.17), with $H = 0$, for the harmonic function $\Phi(x,y)$ in Ω^+

$$g[\varphi](x)\frac{\partial\Phi}{\partial y}(x,0^+) - \Phi(x,0^+) = 0, \quad 0 \leqslant |x| \leqslant a. \tag{4.18}$$

The function $\Phi(x,y)$ is the real part of an holomorphic function $F(z)$, regular at infinity, because in view of $\displaystyle\int_{-a}^{a}\Sigma(t)\,dt = 0$, the logarithmic part of $F(z)$ vanishes at infinity. Hence $|F(z)| \simeq O(1/|z|)$ and $|F'(z)| \simeq O(1/|z^2|)$. Rewriting (4.18) with the outward unit normal to Ω^+, $\partial/\partial y = -\partial/\partial n$, we obtain

$$-\frac{\partial\Phi}{\partial n} - \frac{\Phi}{g[\varphi](x)} = 0, \quad 0 \leqslant |x| \leqslant a, \quad y = 0^+. \tag{4.19}$$

Integrating $\Phi\partial\Phi/\partial n$ on the whole boundary of the upper-half plane $\partial\Omega^+$, noticing that $\Phi\partial\Phi/\partial n = 0$ for $|x| \geqslant a$, $\Phi\partial\Phi/\partial n \simeq O(1/|z^3|)$ at infinity, we obtain on the one hand, since $g > 0$

$$\int_{\partial\Omega^+}\Phi\frac{\partial\Phi}{\partial n}\,ds = \int_{-a}^{a}\Phi\frac{\partial\Phi}{\partial n}\,dx = -\int_{-a}^{a}\frac{\Phi^2}{g}\,dx \leqslant 0,$$

and on the other hand, since Φ is harmonic :

$$\int_{\partial\Omega^+}\Phi\frac{\partial\Phi}{\partial n}\,ds = \int_{\Omega^+}|\nabla\Phi|^2\,d\Omega \geqslant 0.$$

We conclude that $\Phi = 0$ is the unique solution for the homogeneous boundary condition (4.17) and that $\Sigma = 0$.

5. Prandtl's lifting equation in aerodynamics

5.1. Prandtl's equation

Let us recall the well-known Prandtl equation for calculating the circulation distribution of vortex $\Gamma(x)$ along a finite wing $[-a, a]$:

$$\frac{1}{\pi}\frac{\Gamma(x)}{R(x)} - pv\,\frac{1}{\pi}\int_{-a}^{a}\frac{d\Gamma(y)}{y-x} = -4V_\infty J(x) \tag{5.1}$$

where $R(x) > 0$ is the radius of the Kutta-Joukovski circle, corresponding to the section profile of the wing at x, V_∞ is the up-stream velocity and $J(x)$ is the local geometric angle of attack of the wing. Here the derivative of $\Gamma(x)$ appears inside the Cauchy integral. Equation (5.1) is an integro-differential equation, in which the unknown is $\Gamma(x)$; all the other quantities are known, ANDERSON [1], MANDEL [23]. It is well-known that the solution of is (5.1) unique.

It is worth reconsidering the method actually used for solving the Prandtl's equation. Putting $y = -a\,\cos(\theta)$, $x = -a\,\cos(\omega)$, Eq. (5.1) is solved for $\Gamma(y)$ by truncated Fourier sine series

$$\Gamma(\theta) = \sum_{n=1}^{N} B_n \sin(n\theta), \quad 0 \leqslant \theta \leqslant \pi. \tag{5.2}$$

The *pv*-integral at the station ω can be written in a simple form. Using Chebyshev's formula of the second kind

$$\int_0^\pi \frac{\cos(n\theta)}{\cos(\theta)-\cos(\omega)}\,d\theta \equiv \pi\frac{\sin(n\omega)}{\sin(\omega)}, \tag{5.3}$$

we obtain

$$\frac{1}{\pi R(\omega)}\sum_{n=1}^{N} B_n \sin(n\omega) + \sum_{n=1}^{N}\frac{n}{a}B_n\frac{\sin(n\omega)}{\sin(\omega)} = -4V_\infty J(\omega), \quad 0 < \omega < \pi. \tag{5.4}$$

Choosing N different stations $\omega_1, \omega_2, \ldots, \omega_N$ for a collocation method, Eq. (5.4) provides a linear system of N independent algebraic equations with N unknowns, $B_1, B_2, \ldots, B_N$

$$\frac{1}{\pi R(\omega_k)}\sum_{n=1}^{N} B_n \sin(n\omega_k) + \sum_{n=1}^{N}\frac{n}{a}B_n\frac{\sin(n\omega_k)}{\sin(\omega_k)} = -4V_\infty J(\omega_k), \quad (k = 1, .., N). \tag{5.5}$$

In this fashion, the system (5.5) provides the actual solution of Prandtl's equation as used in aerodynamics. Finally, we remark the analogy between both methods used in Secs. 4.2 and 5.1, respectively. As a matter of fact, there is a profound relationship between the W-equation and Prandtl's lifting equation.

5.2. Malavard's analogical method

Let us recall first how Prandtl's Eq. (5.1) can be solved *experimentally* by analogous Malavard's method, MANDEL [23]. An electric conducting medium occupies the halfplane $y \geqslant 0$. The potential $\Phi(x,0)$ is the trace on $y = 0$ of a harmonic function $\Phi(x,y)$, regular in the halfplane $y > 0$. The wing position is divided into N equal segments, centered at x_k, each of them being connected to a resistance $\rho(x_k)$, while the other end of the resistance is subjected to the potential $E(x_k)$. For simplicity, we shall omit the indices k of x_k. In order to choose these quantities, we introduce the complex potential $F(z)$, $z = x + i\,y$ and consider the values of potential and velocity $v_y = \partial\Phi/\partial y$ on $y = 0$, $x \leqslant a$

$$F(z) = \frac{1}{2i\pi}\int_{-a}^{a} \ln(z-t)\, d\Gamma(t),$$

$$\Phi(x,0^+) = -\frac{1}{2}\Gamma(x), \quad \text{for } |x| \leqslant a,$$

$$\Phi(x,0^+) = 0, \quad \text{for } |x| \geqslant a,$$

$$v_y(x) = \frac{1}{2\pi}\, pv \int_{-a}^{a} \frac{d\Gamma(t)}{t-x}.$$

The electric potential $\Phi = 0$ is applied to the segments $|x| \geqslant a$. We set the potential $E(x) = 2\pi R V_\infty J(x)$ to the resistance $\rho(x) = \pi R(x) > 0$. Then we measure the electric current $c = v_y(x)$ provided by Ohm's law $E - \Phi = \rho c$, corresponding to (5.1)

$$2E - 2\Phi = \rho 2c \quad \Leftrightarrow \quad 4V_\infty J(x)\pi R(x) + \Gamma(x) = \pi R(x)\frac{1}{\pi}\,\mathbf{pv}\int_{-a}^{a}\frac{d\Gamma(t)}{t-x}. \tag{5.6}$$

The measurement of the potential Φ at the other end of the resistance provides the distribution of line vortex with density $\Gamma'(x)$.

5.3. Experimental setup for solving the W-equation

By integrating the W-equation for the stress $S(x)$

$$\frac{d}{dx}\left[g(x)S(x)\right] + pv\,\frac{1}{\pi}\int_{-a}^{a} S(t)\frac{dt}{t-x} = h(x), \tag{5.7}$$

with respect to x in the interval $[a, x]$, taking account of $S(a) = 0$, we obtain

$$g(x)S(x) - \frac{1}{\pi}\int_{-a}^{a} S(t)\ln|t-x|\,dt = -\frac{1}{\pi}\int_{-a}^{a} S(t)\ln|t-a|\,dt + H(x), \tag{5.8}$$

where $H(x) = \int_{a}^{x} h(x)\,dx$. We can write

$$g(x)S(x) - \frac{1}{\pi}\int_{-a}^{a} S(t)\ln|t-x|\,dt = H(x) + C \tag{5.9}$$

$$C = -\frac{1}{\pi}\int_{-a}^{a} S(t)\ln|t-a|\,dt. \tag{5.10}$$

The constant C is not known beforehand, since it depends on the solution $S(t)$. Suppose that for a given C, there is a solution $S(x; C)$. Equation (5.10) expresses the implicit condition for determining C

$$C = -\frac{1}{\pi}\int_{-a}^{a} S(t; C)\ln|t-a|\,dt. \tag{5.11}$$

Let us show how (5.11) can be exploited experimentally.

We introduce the complex potential $F(z)$ of a distribution of line source (or sink) with density $S(t)$. The corresponding values of potential and velocity are

$$F(z) = \frac{1}{2i\pi}\int_{-a}^{a} iS(t; C)\ln(z-t)\,dt \equiv \Phi(x,y) + i\,\Psi(x,y),$$

$$F'(z) = \frac{1}{2i\pi}\int_{-a}^{a} iS(t; C)\frac{dt}{z-t} = -\frac{1}{2i\pi}\int_{-a}^{a} iS(t; C)\frac{dt}{t-z} = v_x(x,y) - i\,v_y(x,y),$$

$$\Phi(x,0^+;C) = \frac{1}{2\pi}\int_{-a}^{a} S(t;C)\ln|x-t|\,dt,$$

$$v_y(x,0^+) = \frac{1}{2}S(x), \quad y=0,\ x \leqslant a,$$
$$v_y(x,0^+) = 0, \quad y=0,\ x \geqslant a.$$

Here, the infinite lines $y=0$, $|x| \geqslant a$ are stream lines $v_y = \partial\Phi/\partial y = 0$. On the line $y=0$, $-a \leqslant x \leqslant a$, (5.9) can be rewritten as

$$\Phi(x) - E(x) = \rho(x)c(x) \quad \Leftrightarrow \quad g(x)S(x) - \frac{1}{\pi}\int_{-a}^{a} S(t)\ln|t-x|\,dt = H(x) + C,$$

with the electric potential $E(x) = -(H(x)+C)/2$, applied to the resistance $\rho(x) = g(x) > 0$, the current $c(x) = v_y(x) = S(x)/2$ and the potential $\Phi(x) = \frac{1}{2\pi}\int_{-a}^{a} S(t)\ln|x-t|\,dt$. Far from the resistance, the potential is set to zero. The compatibility condition (5.11) is written as

$$-\frac{C}{2} = \Phi(a,0^+;C).$$

Hence to satisfy the above condition, experimentally, one adjusts the potential $E(x)$ by varying C in such a manner that the measured potential $\Phi(a,0^+;C)$ at $x=a$ is equal to $-C/2$. Since $H(a)=0$, we see that $E = -C/2 = \Phi(a,0^+;C)$ or equivalently $c(a)=0$. Hence the adjustment of C is done in such a way that there is *no current* in the resistance at $x=a$.

5.4. Relation between the Prandtl's equation and the W-equation

As shown in the above sections, the Prandtl's equation and the W-equation are related together through complex potentials of line vortex of density $\Gamma'(x)$ and line source or sink of density $S(t)$, respectively. This does not mean that Eqs. (5.1) and (5.7) are adjoint equations, in the strictly mathematical sense. As a matter of fact, there is only a weak relation of the adjoint type.

Consider the set of functions

$$B = \left\{\sin\left(\frac{\pi x}{2a}\right), \cos\left(\frac{2\pi x}{2a}\right), \sin\left(\frac{3\pi x}{2a}\right), \cos\left(\frac{4\pi x}{2a}\right), \ldots\right\}.$$

If $\Sigma_k(x)$ is the k^{th} element, we get $\Sigma_k''(x) = -(k^2\pi^2/(4a^2))\Sigma_k(x)$ and $\Sigma_k'(\pm a) = 0$. Denote the Prandtl operator by $P_k[\Gamma]$

$$P_k[\Gamma] := \frac{4a^2}{k^2\pi^3}\frac{\Gamma(x)}{R(x)} - \frac{1}{\pi}\, pv \int_{-a}^{a} \frac{d\Gamma(t)}{t-x}$$

where the first term in the left-hand side of (5.1) is divided by $\dfrac{k^2\pi^2}{4a^2}$. Similarly, denote the W-operator by $W[S]$

$$W[S] := \frac{d}{dx}\,(g(x)S(x)) + pv\,\frac{1}{\pi}\int_{-a}^{a} S(t)\frac{dt}{t-x}.$$

The kernels of Cauchy integrals of $P_k[\Gamma]$, $W[S]$ are *adjoint* and there is a permutation of functions and derivatives. Then we obtain an equivalence of the adjoint type

$$\int_{-a}^{a} \Sigma_k(x)W[S](x)\,dx = \int_{-a}^{a} \Sigma_k(x)h(x)\,dx$$

$$\Leftrightarrow \int_{-a}^{a} \Sigma_k'(x)P_k[S](x)\,dx = -\int_{-a}^{a} \Sigma_k'(x)h'(x)\,dx.$$

However, there is an incomplete equivalence in weak forms, because: 1. we make use of only one particular function $\Sigma_k(x)$; 2. the set B is not complete.

6. Conclusion

The mechanics of sliding mild wear contact between a rigid punch and an elastic halfplane considered in this work is characterized by the following features: (1) any wear criterion and wear rate can be used; (2) the constitutive behavior of the thin aggregate film composed of solid debris and a lubricant fluid, on the mesoscopic scale, can have any general form; it is characterized by an elastic law in compression and a fluid viscosity in shear; (3) the interface on the macroscopic scale is characterized by the elastic law in compression and a plastic law in shear; (4) the mechanical system is governed by the volume fraction of solid debris, which satisfies a nonlinear system of equations.

It was shown that the key step of the iterative algorithm for solving the latter nonlinear system is the linear integro-differential equation for the normal contact

stress. There is a profound relation between this equation and Prandtl's lifting equation found in aerodynamics: both equations can be computed using similar Chebyshev's series of the first and the second kind respectively, and can be solved experimentally by similar electrical setups. These equations are related to real and imaginary components of some complex potential respectively, and to weakly adjoint integro-differential operators.

By describing the formation of debris, using for instance the wear energy release rate criterion, and their evolution via the balance equation of mass, by averaging the behavior law of the aggregate film, via a micromechanical model, we were led to a predictive model of mild wear. There are still remaining questions about an effective solution of the nonlinear system of equations. Such questions, particularly mathematical aspects on the *convergence* of the nonlinear algorithm, will be addressed in a forthcoming paper, DRAGON-LOUISET [11].

Acknowledgements

The authors wish to thank Marc Zbinden for his support through an EDF Grant and Professor Mróz for his comments.

References

1. J.D. ANDERSON, *Fundamentals of aerodynamics*, McGraw-Hill, New York 1991.
2. J. F. ARCHARD, *Contact and rubbing of flat surfaces*, J. Appl. Physics, **24**, 8, 981–988, 1953.
3. Y. BERTHIER, *Mécanismes et Tribologie*, Ph.D. Thesis, INSA/UCB Lyon 1989.
4. Y. BERTHIER, *Experimental evidence for friction and wear modeling*, Wear, **139**, 77–92, 1990.
5. Y. BERTHIER, L. VINCENT and M. GODET, *Velocity accommodation in fretting*, Wear, **125**, 25–38, 1988.
6. H. D. BUI, *Mécanique de la Rupture Fragile*, Éditions Masson, Paris 1977.
7. H. D. BUI, *Introduction aux problèmes inverses en mécanique des matériaux*, Éditions Eyrolles, Paris 1993; (English translation: *Inverse problems in the Mechanics of Materials*), CRC Press, Boca Raton 1994.
8. K. DANG VAN and I. V. PAPADOPOULOS, *High-Cycle Metal Fatigue, from theory to applications*, International Centre for Mechanical Sciences, Courses and Lectures No. 392, Springer-Verlag Wien, New York 1999.
9. C. G. DE KRUIF, E. M. F. VAN IERSEL, A. VRIJ and W. B. RUSSEL, *Hard sphere colloidal dispersions: viscosity as a function of shear rate and volume fraction*, J. Chem. Physics, **83**, 9, 4717–4725, 1985.
10. M. DRAGON-LOUISET, *Modélisation micromécanique de l'interface d'un système tribologique dans une approche thermodynamique de l'usure continue*, Mécanique et Industries, **1**, 1, 37–42, 2000.

11. M. DRAGON-LOUISET, *On a predictive macroscopic contact-sliding wear model based on micromechanical considerations*, Int. J. Solids Struct., (to appear).
12. M. DRAGON-LOUISET and C. STOLZ, *Approche thermodynamique des phénomènes d'usure de contact*, C. R. Acad. Sci. Paris, t. 327, Série IIb, 1275–1280, 1999.
13. L. A. GALIN, *Contact Problems of the Theory of Elasticity*, Gostekhizdat, Moscow 1953.
14. L. A. GALIN, *Contact problems of the theory of elasticity in the presence of wear*, J. Appl. Math. Mech., **40**, 6, 981–986, 1976.
15. L. A. GALIN and I. G. GORIACHEVA, *Axisymmetric contact problem of the theory of elasticity in the presence of wear*, J. Appl. Math. Mech., **41**, 5, 826–831, 1977.
16. J. M. GEORGES, *Comment aborder un problème de tribologie. Aspects macroscopiques du frottement et de l'usure*, Écoles CEA-EDF-INRIA "Problèmes non linéaires appliqués": Modélisation mathématique et numérique des problèmes de contact et frottement, Rocquencourt, 15–18 November, 1977.
17. J. M. GEORGES, S. MILLOT, J. L. LOUBET and A. TONCK, *Drainage of thin liquid films between relatively smooth surfaces*, J. Chem. Physics, **98**, 9, 7345–7359, 1993.
18. M. GODET, *Extrapolation in tribology*, Wear, **77**, 1, 29–44, 1982.
19. M. GODET, *Third bodies in tribology*, Wear, **136**, 1, 29–45, 1990.
20. L. HAVET, *Caractérisation tribologique de biolubrifiants*, Ph.D. Thesis, Université de Technologie de Compiègne, 1998.
21. P. L. KO, *Wear of power plant components due to impact and sliding*, Appl. Mech. Review, **50**, 7, 387–411, 1997.
22. L. LANDAU and E. LIFCHITZ, *Mécanique des Fluides*, Éditions Mir, Moscow 1971.
23. J. MANDEL, *Cours de Mécanique des Milieux continus*, Éditions Gauthier-Villars, Paris 1966.
24. H. C. MENG and K. C. LUDEMA, *Wear models and predictive equations; their form and content*, Wear, **181-183**, 443–457, 1995.
25. N. I. MUSKHELISHVILI, *Singular integral equations*, P. Noordhoff N. V., Gröningen 1953.
26. N. I. MUSKHELISHVILI, *Some basic problems of the mathematical theory of elasticity*, Noordhoff Intern. Publ., Leyden 1977.
27. R. M. PRADEILLES-DUVAL and C. STOLZ, *Mechanical transformation and discontinuities along a moving surface*, J. Mech. Phys. of Solids, **43**, 1, 91–121, 1995.
28. C. H. SCHOLZ, *Earthquakes and friction laws*, Nature, **391**, 37–42, 1998.
29. I. L. SINGER and K. J. WAHL, *Role of third bodies in friction and wear*, 1999 MRS Workshop Series: Tribology on the 300th Anniversary of Amonton's Law, San Rose, California, 20–22 June, 1999.
30. T. G. SITHARAM, *Micromechanical modeling of granular materials; effect of confining pressure on mechanical behavior*, Mech. of Materials, **31**, 653–665, 1999.
31. S. STUPKIEWICZ and Z. MRÓZ, *A model of third body abrasive friction and wear in hot metal forming*, Wear, **231**, 124–138, 1999.
32. J. C. VAN DER WERFF and C. G. DE KRUIF, *Hard-sphere colloidal dispersions: the scaling of rheological properties with particle size, volume fraction, and shear rate*, J. Rheology, **33**, 3, 421–454, 1989.

Received February 21, 2000.

Arch. Mech., **52**, 4–5, pp. 569–588, Warszawa 2000

The role of backstress in phase transforming steels

Dedicated to Professor Zenon Mróz
on the occasion of his 70^{th} birthday

F. D. FISCHER (*) [1], T. ANTRETTER (*),
F. AZZOUZ (**), G. CAILLETAUD (**), A. PINEAU (**),
K. TANAKA (***), K. NAGAYAMA (***)

(*) *Institute of Mechanics, Montanuniversität Leoben,*
Franz-Josef-Straße 18, A-8700 Leoben, Austria

(**) *Ecole des Mines, Centre des Matériaux,*
BP 87, F-91003 Evry Cedex, France

(***) *Department of Aerospace Engineering,*
Tokyo Metropolitan Institute of Technology,
Asahigaoka 6-6, J-191 Hino/Tokyo, Japan

TRANSFORMATION INDUCED PLASTICITY (TRIP) is demonstrated by an experimental programme for a Fe-9Ni-12Cr steel for various loading paths with partial or full unloading. The martensitic transformation is considered. A thermodynamical interpretation as well as micromechanical modelling of TRIP are presented. The selection of distinct variants is explained. Finally a modified constitutive equation for the TRIP strain rate is suggested by introducing a transformation surface including a transformation backstress. The backflow after unloading, which cannot be explained by the currently used TRIP strain rate term, can be represented by the proposed formulation. Aspects of future research are discussed.

Key Words: Transformation Induced Plasticity (TRIP), Martensitic Transformation, Transformation Thermodynamics, Transformation Surface, Backstress

1. Introduction

TRANSFORMATION INDUCED PLASTICITY (TRIP) is now a well-known phenomenon that appears when a material like steel or a shape memory alloy (SMA) transforms, e.g. during a cooling process, and the material is subjected to a certain load-stress. In the "classical" definition we are dealing with the *significantly*

[1]) Corresponding author

increased plasticity during a phase change. Plastic deformation occurs for an externally applied load-stress, even for a load-stress level which is small compared to the yield stress of the parent phase. This is a practical, not a rigorous definition of the "TRIP phenomenon". TRIP is now more widely defined as a coupled phenomenon between transformations and deformations which are not only restricted to plasticity. For further details the reader is referred to the book by BERVEILLER and FISCHER [1] and a review paper by FISCHER, SUN and TANAKA [2].

We concentrate here on steels, i.e. materials with the ability to reduce their internal (or free) energy by plastic sliding. Furthermore, we look at the martensitic transformation. Before going into detail, we repeat some aspects of the continuum mechanical representation of the TRIP phenomenon, for details we refer again to [1, 2] and make reference to the papers by LEBLOND *et al.* [3, 4]. Theses papers are most frequently cited in the context of TRIP.

Usually a linear decomposition of the strain rate contributions is assumed as

$$\dot{\varepsilon}_{ij} = \dot{\varepsilon}^e_{ij} + \dot{\varepsilon}^\theta_{ij} + \dot{\varepsilon}^P_{ij} + \dot{\varepsilon}^{TP}_{ij} + \frac{\delta}{3}\dot{\xi}\delta_{ij}. \tag{1.1}$$

$\dot{\varepsilon}^e_{ij}$ is the elastic strain rate tensor, $\dot{\varepsilon}^\theta_{ij}$ is the temperature eigenstrain rate tensor, $\dot{\varepsilon}^P_{ij}$ is the plastic strain rate tensor at a fixed volume fraction ξ, $0 \leq \xi \leq 1$, of the product phase (martensite), $\dot{\varepsilon}^{TP}_{ij}$ is the TRIP strain rate tensor and $\frac{\delta}{3}\dot{\xi}\delta_{ij}$, with the unity tensor δ_{ij}, may be considered as the metallurgical strain rate tensor, where δ stands for the volume change due to the phase transformation. A dot $(\cdot)$ represents the total material derivative. The TRIP strain rate tensor according to Leblond's proposal is given by

$$\dot{\varepsilon}^{TP}_{ij} = \frac{3}{2}K\frac{d\varphi}{d\xi}\dot{\xi}S_{ij}. \tag{1.2}$$

$\varphi(\xi)$ is a – more or less – heuristic function of ξ, e.g.

$$\varphi(\xi) = \xi(2-\xi), \tag{1.3}$$

K is the TRIP constant and S_{ij} is the global stress deviator associated to the stress tensor σ_{ij} which can be assumed as the average over a representative amount of grains (remark: several authors consider to be the stress deviator at the "mesoscopic" level). The TRIP constant K is assumed to be a function of δ being of the order of $5.0{*}10^{-5}$ MPa^{-1}.

The concept as outlined above is implemented in several programs like SYSWELD [5] and applied with more or less success for quenching (heat treatment) applications. However, experiments by the group of CAILLETAUD and

PINEAU, (see e.g. [6, 7]), have shown that the proposal (1.2) does no longer hold true if a non-monotonic loading path (e.g. a full or partial unloading) is followed. Even if a compression test is performed, the constant K must be modified. Therefore, the group of authors of this paper have been performing, for some years now, an extensive experimental programme on the TRIP effect for multiaxial loading and non-monotonic loading paths. This experimental work forms the basis for a better understanding of the TRIP effect as well as for the improved formulation of a TRIP strain rate.

Two crucial phenomena are discussed in the present paper:

- First, the orientation effect (Magee effect) in the martensitic transformations: Martensite variants with different orientations, are formed even during full or partial unloading, resulting in a further TRIP strain growth. The change in the internal stresses around the martensite variants is an important factor to be considered.

- Second, the backstress which, according to the present experiments, must be included in the constitutive equation for the TRIP strain. The evolution of the backstress is also an issue to be investigated.

2. Experimental programme

The test material used was a Cr-Ni-Mo-Al-Ti Maraging steel, provided by Aubert and Duval, first introduced for TRIP testing by CAILLETAUD et PINEAU *et al.* – see [6, 7] – and referred to as Marval X12. The martensite start temperature Ms is found at ca. 150° (423 K), the martensite finish temperature M_f at ca. 80° (353 K). This material is ideally suited for TRIP tests since it transforms to martensite even upon cooling in air. The quenching capability is excellent, leading to no corrosion or oxidation. All these properties allow to use the same specimen several times. For the sake of completeness, the nominal composition is given in Table 1.

Table 1. Nominal composition of the investigated material (weight percent), rest Fe

Cr	Ni	Mo	Al	Ti	C	Si	Mn	P	S	N
12.15	9.05	2.03	0.70	0.35	< 0.01	0.05	0.03	0.009	< 0.002	0.0045

Tubular specimens were machined with a mid-circle radius of 9 mm and a wall thickness of 1.5 mm. The specimens were machined out of rods with an average diameter of 30 mm. Then the specimen is cooled down to the temperature of

200° C (473 K) and the load is applied. Both tension or compression and shear loading are possible. To understand the influence of the microstructure, full or partial unloading is performed at a certain volume fraction ξ of martensite. All the experiments have been performed in the Laboratory of Prof. K. Tanaka. Due to space restrictions, further important information on the material is given without any detail:

Figure 1 demonstrates the stress-strain curve at 205° C (478 K) (full austenite) and at room temperature 30° C (303 K), (full martensite). As can be seen, the material shows a rather soft austenitic and a surprisingly strong martensitic phase.

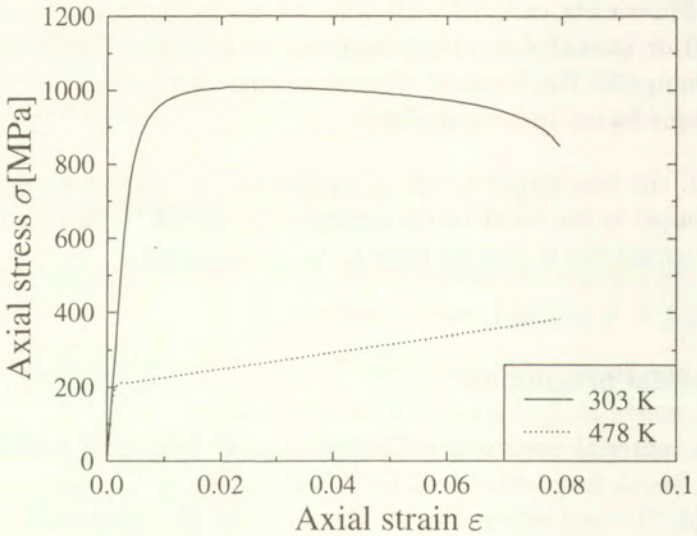

FIG. 1. Stress (σ)-strain (ε)-curve at 30° C (303 K) (full martensite) and at 205° C (478 K) (full austenite).

The following data can be given for the thermoelastic constants:

- Young's modulus E $\sim$ 205.000 MPa at room temperature,
  $\sim$ 179.000 MPa at 180° C (453 K).
- The average value of Poisson's ratio $\nu = 0.33$.
- Average values for the integral thermal expansion coefficients in the temperature range up to 200° C (473 K) are

$$\alpha_\gamma = 19.6 \times 10^{-6\,\circ}\,\mathrm{C}^{-1}, \quad \alpha_\alpha = 11.37 \times 10^{-6\,\circ}\,\mathrm{C}^{-1}.$$

– Application of the crystallographic theory of martensite with the measured lattice constants of both phases yields the transformation volume change δ_c and the transformation shear γ_c. The subscript "c" indicates that these values have been calculated analytically,

$$\delta_c = 0.0178, \quad \gamma_c = 0.227.$$

– A common way to measure δ is to perform a dilatometer test. Those tests were run both for the tubular specimens, called "longitudinal specimens" with respect to the position of the original rod they were machined from, and for very tiny specimens (diameter 2 mm, length 12 mm) in various directions, including radial, relative to the axis of the original rod. Figure 2 shows an "open" loop for the "longitudinal" specimen without any load-stress and an almost perfectly closed dilatation loop for an equal specimen obtained with a hold stress of $\sigma_h = 28$ MPa. Closer inspection of the tiny specimens reveals that the total transformation volume change seems to split in an anisotropic way into $\delta/3 - \delta_a = \tilde{\delta}/3$ in the longitudinal direction, and $\delta/3 + \delta_a/2$ in the radial and circumferential direction. Finally, the dilatometer tests yield $\delta_a = 0.0016$ and $\delta = 0.0192$. Although these values differ somewhat from δ_c, they are used for further investigations since they stem from direct experimental observation and are understood as the result of the internal stresses.

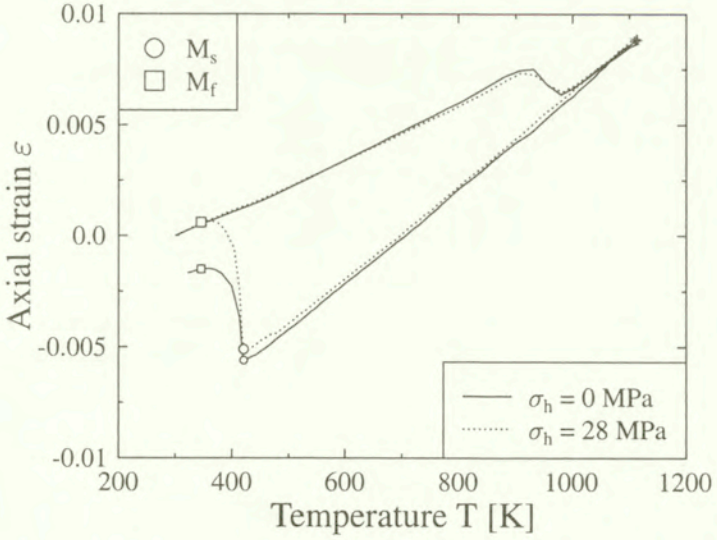

FIG. 2. Dilatometer test for a longitudinal specimen, load-stress-free and with load-stress $\sigma_h = 28$ MPa.

Dilatometer tests are usually applied to determine the transformed volume fraction ξ in accordance with the actual volume change. The following transformation kinetics can be found:

$$(2.1) \qquad \xi = 1 - \exp[-0.0549(M_\sigma - T)], \quad M_\sigma = M_s + 0.046\sigma \text{ in MPa};$$

the label "σ" in this case represents the tension load-stress on the specimen.

As a first result, the M_σ (Martensite start) and M_f (Martensite finish) lines are shown in Fig. 3. They are generated from dilatometer curves performed by the tubular specimens for various hold stresses. One can see clearly that the slope of the start line depends on the kind of loading, as explained in the next section. Obviously a shift of the σ-reference line to $X_z = 28$ MPa leads to the known picture of a M_σ-line. The stress component X_z can, therefore, at first be interpreted as an initial backstress. The former results combined with the yield stress of the material is depicted in Fig. 4. It is vital to mention here that the off-set strain (0.05% or 0.005%) plays a significant role with respect to the definition of the yield stress. The large difference in $\sigma_{0.05}$ and $\sigma_{0.005}$ in the low temperature range can be attributed to the higher work-hardening than in the high temperature range. Actually in this temperature range the specimen is composed of the thermally and stress-induced martensite phase which is much harder than the soft parent phase. The "hook-type" tendency on the left side of the M_σ-line points to this "composite"-effect and would give rise to a rather extensive discussion on its own, and will be published elsewhere. Figure 5 shows

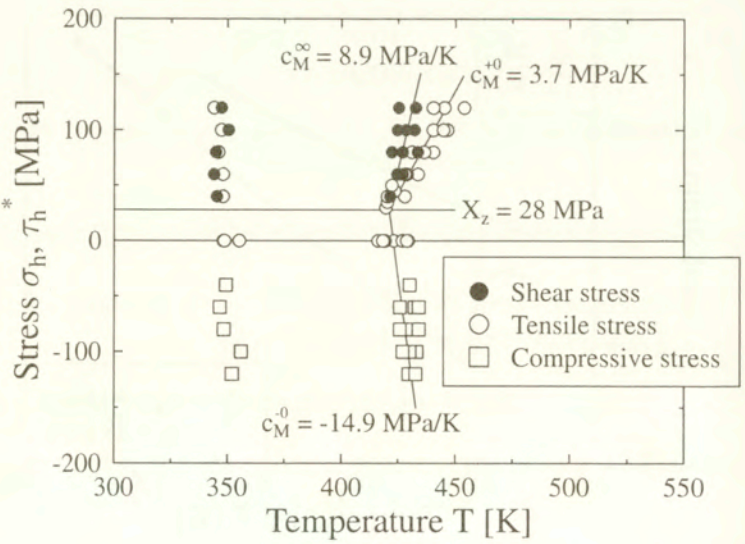

FIG. 3. M_σ-lines (slope c_M^{+0} for tension, c_M^{-0} for compression, c_M^∞ for shear) and M_f lines.

the TRIP strain ε^{TP} for various tensile hold stresses and partial or full unloading, calculated from the relation (2.2).

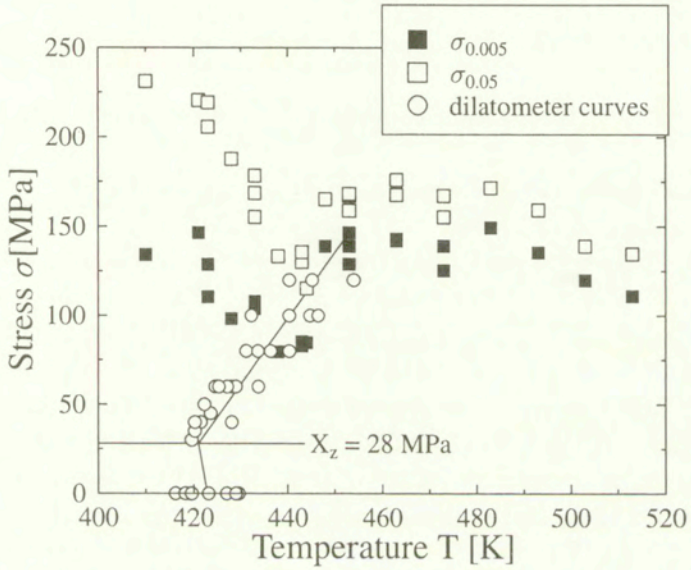

FIG. 4. Combined yield and transformation behaviour characterising the MARVAL X12 steel.

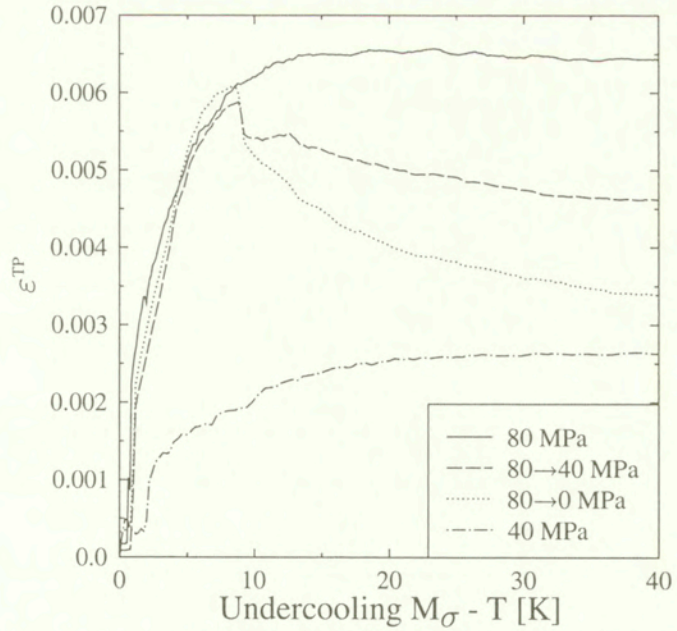

FIG. 5. TRIP-strain ε^{TP} versus the undercooling temperature difference $(M_\sigma - T)$-curves for tension tests; 80 → 0 MPa, 80 → 40 MPa means unloading from 80 MPa to 0 MPa or 40 MPa, respectively.

$$\varepsilon^{\mathrm{TP}}\Big|_{M_\sigma - T} = \varepsilon\Big|_{M_\sigma - T} - \varepsilon\Big|_{M_\sigma} - \frac{\tilde{\delta}}{3}\xi - (M_\sigma - T)[\alpha_\alpha \xi + \alpha_\gamma(1-\xi)]; \tag{2.2}$$

$\varepsilon^{\mathrm{TP}}|_{M_\sigma - T}$ represents the TRIP-strain to a temperature difference $(M_\sigma - T)$, (calculated);
$\varepsilon|_{M_\sigma - T}$ stands for the total strain to a temperature difference $(M_\sigma - T)$, (measured);
$\varepsilon|_{M_\sigma}$ is the total strain at the temperature M_σ, (measured).

The data applied in (2.2) have been provided above.

Tests were carried out as follows: In the process of cooling with a rate of 2 K/s, after annealing and austenitization at 840° C for 30 min, a stress σ_h = 80 MPa is applied at 200° C with the loading rate 80 MPa/s and held constant in the subsequent process. The subscript "h" to σ and later τ^* will refer to the fact that the load is held constant for a certain period of time. The hold stress is then unloaded partially (to 40 MPa) or fully (to 0 MPa) with the unloading rate of 80 MPa/s at a temperature ca. 10° C lower than M_σ. The total strain is measured during the entire thermomechanical loading process. As already mentioned, a TRIP strain of – 0.016 occurs without any load. No TRIP strain appears at a hold stress of 28 MPa as shown in Fig. 2. This induces a certain asymmetry

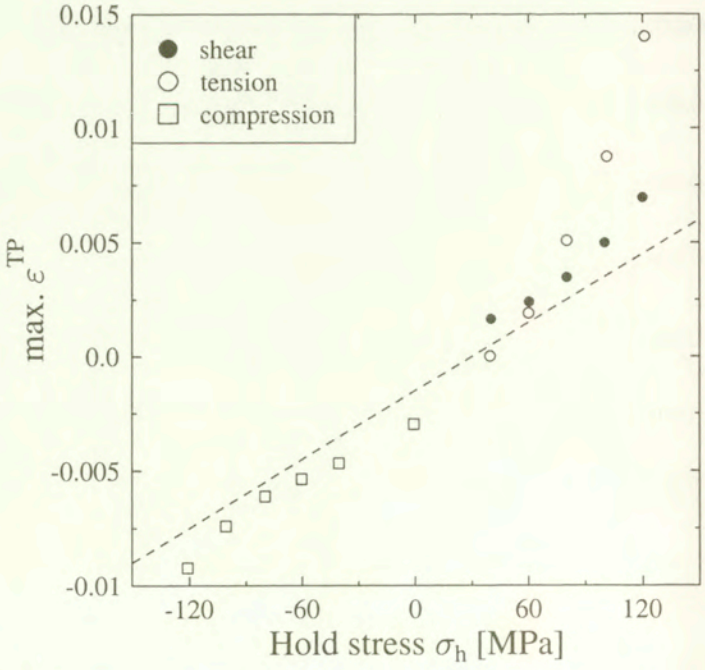

FIG. 6. The "Greenwood-Johnson" line $K = 5 \times 10^{-5}$ MPa^{-1} in relation to the maximum TRIP strain for several hold stress levels.

with respect to tension and compression. Obviously an internal stress X_z state is active, a backstress, which leads to a reduced hardening in the tension regime and, therefore, to higher TRIP strain compared to the compression regime.

As mentioned in the introduction, Greenwood and Johnson proposed a linear relation between the maximum TRIP strain and the hold stress. A line with the slope $K = 5.0 \cdot 10^{-5}$ MPa^{-1} is plotted in Fig. 6 with its origin at $X_z = 28$ MPa. The plots show the results of the tests under constant hold stress. The deviation from this straight line clearly demonstrates the strong sensitivity to σ_h in the tension regime. An interesting fact that will be explained qualitatively in the next section is that the maximum TRIP strain is less sensitive to the hold stress in shear tests. The following two figures demonstrate the TRIP strain for a specimen under compression (Fig. 7) and under shear (Fig. 8), subjected to a hold stress of 80 MPa with constant loading, partial unloading from 80 MPa to 40 MPa and full unloading. To compare the shear tests with the tension tests, an equivalent stress $\tau^* = \tau\sqrt{3}$ and an equivalent strain $\gamma^* = \gamma/\sqrt{3}$ are introduced.

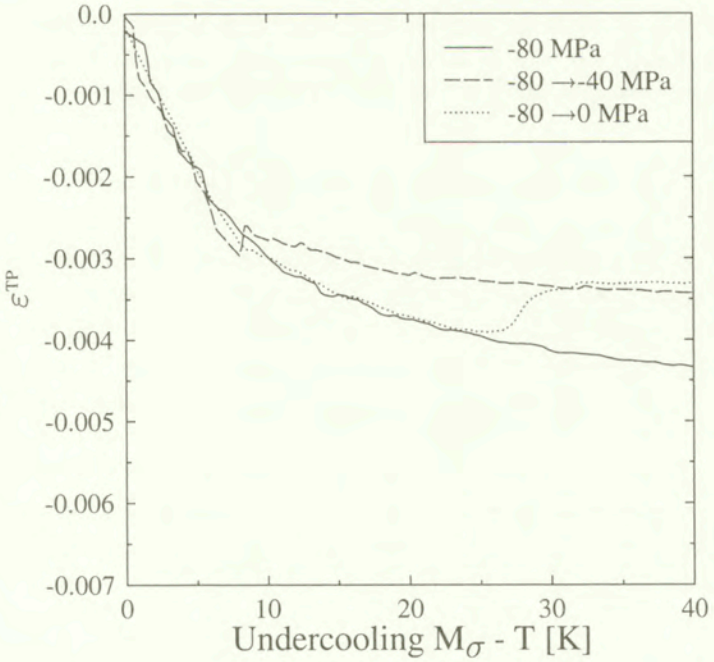

FIG. 7. TRIP-strain ε^{TP} versus the undercooling temperature difference $(M_\sigma - T)$-curves for compression tests; 80 → 0 MPa, 80 → 40 MPa, means unloading from 80 MPa to 0 MPa or 40 MPa, respectively.

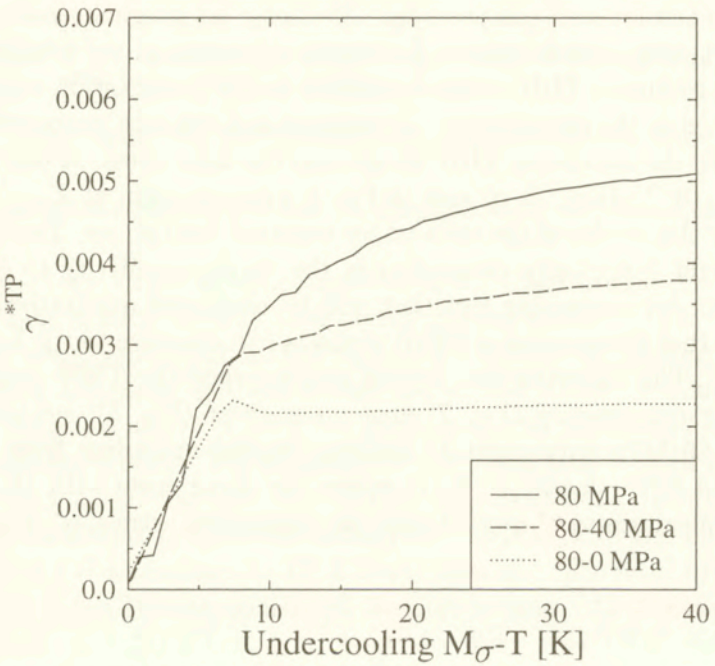

FIG. 8. TRIP-strain $\gamma^{*\mathrm{TP}}$ versus the undercooling temperature difference $(M_\sigma - T)$ -curves for shear tests; $80 \rightarrow 0$ MPa, $80 \rightarrow 40$ MPa means unloading from $\tau^* = 80$ MPa to $\tau^* = 0$ MPa or $\tau^* = 40$ MPa, respectively.

In the case of full unloading (and to a certain degree also with partial unloading) one can observe a significant "backflow" in the tension regime, (see Fig. 5). The "backflow" is smaller but still clearly observable in the compression regime, (see Fig. 7). Since after unloading only the internal stress state influences the formation of martensitic variants, the formation of some new variants obviously reduces the absolute length of the specimen, although the specimen is totally unloaded. The total stress state before unloading (that means the load-stress state plus the internal stress state) obviously leads to an arrangement of martensitic variants that contributes to the "orientation" effect of the TRIP strain. After unloading, some further variants develop which "compensate" the orientation effect to a certain degree. A thermodynamical interpretation is given in the next chapter. The situation is obviously different in the case of shear loading and the TRIP shear strain $\gamma^{*\mathrm{TP}} = \gamma/\sqrt{3}$, (see Fig. 8). In fact, the TRIP shear strain of the specimen remains nearly unchanged after unloading. Obviously the internal stress state after shear unloading is not apt to favour some martensitic variants which contribute to an irreversible shear strain.

The conclusion is that a relation of the type (1.2) cannot be applied to an unloading process in the case of tensile or compressive loading, since $S_{ij} = 0$ would

entail $\dot{\varepsilon}_{ij}^{\mathrm{TP}} = 0$, which contradicts the experimental evidence. However, in the case of shear loading, Eq. (1.2) obviously remains applicable. As a consequence, the authors suggest to reflect both the initial backstress (i.e. X_z in the uniaxial case) and the backstress contribution due to "backflow" by a transformation backstress tensor X_{ij}^{TP} in order to establish a more realistic constitutive law for phase transforming materials.

3. Transformation thermodynamics

3.1. Transformation condition

As mentioned above, the martensitic transformation is accompanied by a transformation volume change δ and a transformation shear γ, finally leading to a transformation tensor ε_{ij}^{*} with the non-zero components $\varepsilon_{13}^{**} = \varepsilon_{31}^{*} = \gamma/2$, $\varepsilon_{33}^{*} = \delta$, described in a local coordinate system with respect to the habit plane of a variant. Both their values as well as the orientation of the martensitic variants (in general 24) can be found by applying the mathematical (crystallographic) theory of martensite. The reader is referred here to the pioneering work by Wechsler, Lieberman and Read (1953), for details see the paper by MARKETZ *et al.* [8]. The orientation of the variants is described by the set of 3 Eulerian angles. The understanding of the effect of a stress state on the formation of a specific martensitic variant goes back to an equally pioneering work by Patel and Cohen (1953). The role of the stress state was intensively studied with respect to the microstructure and the global stress-strain behaviour of shape memory alloys (SMAs). Recently a transformation condition for a microregion V_μ was presented by LEVITAS, (see e.g. [9]) and FISCHER *et al.* [10]. This condition reads

$$\int_{V_\eta} \sigma_{ij} \left|_{t_s} \varepsilon_{ij}^{*} dV + V_\mu [\![\rho\varphi_{\mathrm{chem}}]\!] \geq V_\mu F_c + \Delta\Gamma + W_{p\ell}^{\tau} + W_{e\ell}^{\tau}. \right. \tag{3.1}$$

$\sigma_{ij}|_{t_s}$ represents the stress state just at the onset of transformation. $[\![\rho\varphi_{\mathrm{chem}}]\!]$ is the difference of the chemical free energy of the stress-free parent phase and the product (martensite) phase. F_c is a transformation barrier representing the energy necessary for rearranging the crystallographic lattice (– a given entity which must be measured). $\Delta\Gamma$ represents the surface energy produced during the formation of V_μ and is usually small in the case of plate-type microstructures. $W_{p\ell}^{\tau}$ and $W_{e\ell}^{\tau}$ are the additional plastic and elastic work terms, resp., only due to the stress fluctuation τ_{ij} during the transformation process. REISNER *et al.* give values for these quantities in [11]. As one can easily see, the left-hand side contains a mechanical and a chemical driving force. The transformation condition

is now applied to interpret both the varying slope of the martensite start line and the development of the TRIP strain.

3.2. Slope of the martensite start line

Figure 3 shows clearly that the martensite start line shows a different slope c_M depending on the loading case. Since, to the best knowledge of the authors, such an observation has not been reported for steels yet, an interpretation is presented. A study assuming equal chemical energies for various loading conditions allows to compare the influence of distinct load cases represented by Σ_{ij} on the mechanical driving force (MDF), with

$$\text{MDF} = \Sigma_{ij}\varepsilon^*_{ij}. \tag{3.2}$$

This was done by MARKETZ *et al.* [8] allowing the full space of Eulerian angles to describe a possible martensitic variant (– which is reasonable in a polycrystal). Consideration of a global coordinate system and principal stresses Σ_{11}, Σ_{22}, Σ_{33} the MDF yields

$$\text{MDF} = \Sigma_{33}\frac{1}{2}\left(\delta + \sqrt{\delta^2+\gamma^2}\right) + \Sigma_{11}\frac{1}{2}\left(\delta - \sqrt{\delta^2+\gamma^2}\right) \tag{3.3}$$

$$\text{for} \quad \Sigma_{33} > \Sigma_{22} > \Sigma_{11}.$$

We now compare three loading cases with the same equivalent stress τ_T according to Tresca, $\tau_T = \frac{1}{2}(\Sigma_{33} - \Sigma_{11})$, leading to

$$\text{MDF} = (\Sigma_{33} + \Sigma_{11})\delta/2 + \tau_T\sqrt{\delta^2+\gamma^2}: \tag{3.4}$$

– a tension state $\Sigma_{33} > 0, \Sigma_{11} = 0, \tau_T = \Sigma_{33}/2$,

$$\text{MDF}_T = \tau_T\frac{\delta}{2} + \tau_T\sqrt{\delta^2+\gamma^2}; \tag{3.5}$$

– a compression state $\Sigma_{33} = 0, \Sigma_{11} < 0, \tau_T = -\Sigma_{11}/2$,

$$\text{MDF}_c = -\tau_T\frac{\delta}{2} + \tau_T\sqrt{\delta^2+\gamma^2};$$

– a shear state $\Sigma_{33} = -\Sigma_{11}, \tau_T = \Sigma_{33}$,

$$\text{MDF}_s = \tau_T\sqrt{\delta^2+\gamma^2}. \tag{3.6}$$

Assuming the same value of τ_T tension produces the highest amount of MDF and shows the strongest influence on the martensite start line (see Fig. 3, c_M = 3.7 MPa/K). The shear state produces the intermediate value of MDF. The lowest

value of MDF is found for the compression state. Figure 3 indicates that the slope of the shear martensite start line ($c_M = 8.9$ MPa/K) is more affected by the stress state than the compression martensite start line ($c_M = -14.9$ MPa/K), which exhibits the steepest slope.

This study indicates that the selection of martensitic variants is not only influenced by the magnitude of the stress state (characterised by the equivalent stress) but also by the "orientation relation" between the considered martensitic variant and the stress state.

3.3. Mechanisms for the TRIP strain

The formation of the transformation strain itself and the selection of locally optimal variants are responsible for the irreversible deformation of an iron-based alloy during and after martensitic phase transformation, and lead to the following two mechanisms:

– The accommodation process due to δ and γ enforcing additional elastic and plastic straining in relation to the load-stress state, eventually producing a compatible deformation (and strain) state. This process is often called the "Greenwood-Johnson" effect or "plastification" effect.

– The orientation process due to the formation of preferred variants which may be arranged in some (partially) "self-accommodating" groups. This effect is often referred to as "Magee" or "orientation" effect.

Some further comments may be important:

– There is nowadays a clear evidence that SMAs "thrive" only on the orientation effect, that means through the formation of selected variants. The global deformation state depends on the overall elastic strain and the average transformation tensor

$$\varepsilon_{ij}^{\mathrm{TP}} = \frac{1}{V} \int_V \varepsilon_{ij}^{*} dV. \tag{3.7}$$

SMAs show nearly no volume change and no plastic straining up to a significant stress level. Their original shape can be restored e.g. by heating.

– The orientation effect in steel was recognized only very recently, e.g. in the work of the "Nancy" group, (see e.g. [12, 13]). Most recent experimental observations which have not been published yet, explain the back-transformation in the temperature range of 900 K to 1000 K also, at least partially, as a displacive (martensite-type) transformation. The retained martensite is then transformed at temperatures above this range by a diffusive process. At temperatures lower than ca. 900 K, obviously the martensite variants are pinned by dislocations produced mainly by the accommodation of the volume change. There is a clear

evidence that such high temperatures are necessary to provide the dislocations with enough mobility to release the martensite variants.

3.4. Modelling of the backstress due to "backflow"

Micromechanical modelling has been applied to shed more light on the developing microstructure, both for a loaded and later (partially) unloaded specimen.

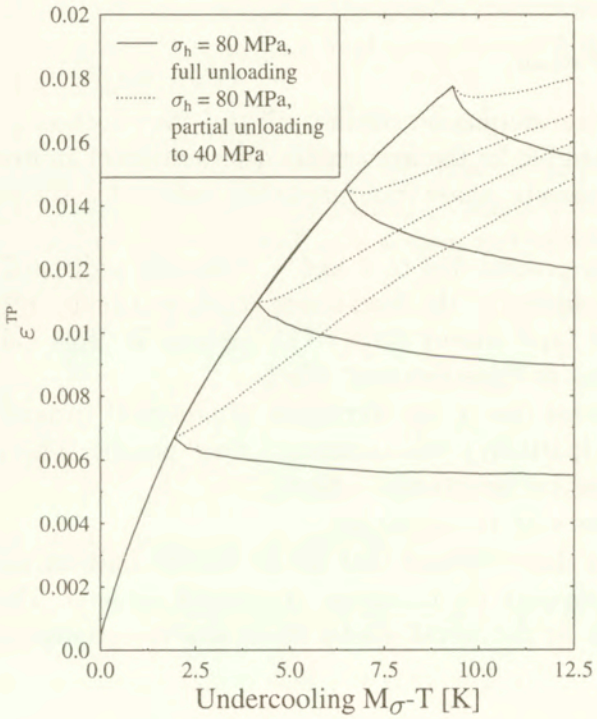

FIG. 9. Simulated TRIP strain ε^{TP} versus to the undercooling temperature difference $(M_\sigma - T)$. The hold stress $\sigma_h = 80$ MPa. Full lines represent unloading to 0 MPa, dotted lines to 40 MPa.

FISCHER *et al.* [14] presented an extensive report on micromechanical modelling of the TRIP effect for specimens subjected to tension or compression, with a full or partial unloading after a certain volume fraction of martensite. They applied the numerical realisation of the transformation condition (3.1) according to a concept by REISNER [15]. Specifically, the backflow due to unloading (see Fig. 5 for tension and unloading and Fig. 7 for compression and unloading) has to be investigated by a numerical method. Only two figures are repeated from this study. Figure 9 shows the TRIP strain depending on the undercooling temperature difference $(M_\sigma - T)$. Note that $(M_\sigma - T)$ is related to ξ by (2.1). Full or

partial unloading from the originally constant stress state of 80 MPa is simulated. Obviously the micromechanical study yields a certain backflow after full unloading. Figure 10 supplies a statistical evaluation of the number of variants which have developed during the progress of transformation. At the initial step of the transformation, the favourite variant in a grain of a polycrystal is created. With the ongoing transformation, an eigenstress state is generated which leads to an increasing number of different variants. Obviously those variants develop which arrange in such a way that a certain "self-accommodation" of the transformation shear can be observed. After the partial unloading, two to three further variants become now favourably oriented due to the residual stress state. This effect is of course more pronounced in the case of full unloading. These new variants enforce a reduction of the length of the specimen by an additional "self-accommodation" to variants developed earlier. The study shows furthermore that after full unloading no further plastification occurs, and that the change in shape is solely due to the "orientation"-effect.

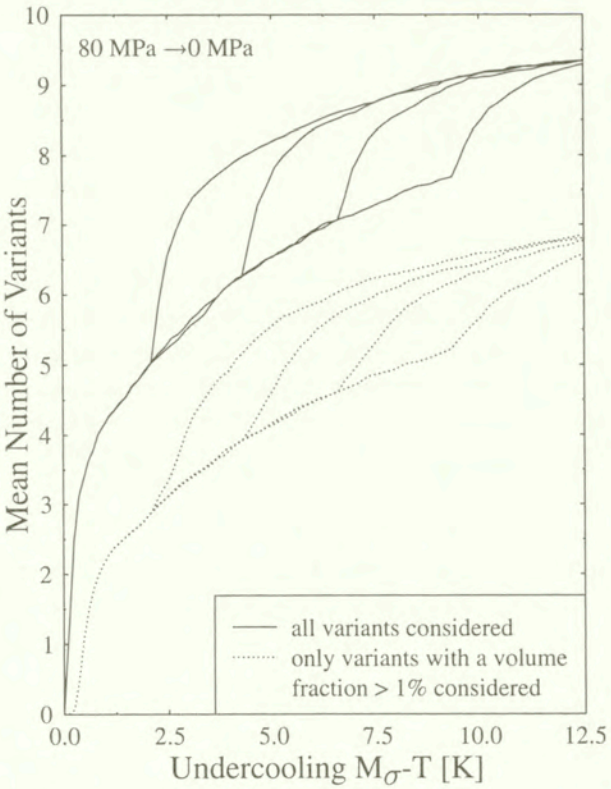

FIG. 10. Number of variants for partial unloading from 80 MPa. The full lines represent all variants, the dotted lines those with a volume contribution of more than 1%.

4. A Hypothetical transformation surface

As explained in the Introduction, we assume a linear decomposition of the strain rate tensor. Furthermore, we introduce a hypothetical transformation surface (assuming the usual summation convention over repeated indices) as

$$f^{\mathrm{TP}} = \left(1-\tilde{\beta}\right) J_2\left(\sigma_{ij} - X_{ij}^{\mathrm{TP}}\right) + \tilde{\beta}\left(J_1\left(\sigma_{ij} - X_{ij}^{\mathrm{TP}}\right)\right)^2 + \tilde{\gamma} J_1\left(\sigma_{ij} - X_{ij}^{\mathrm{TP}}\right) - \left(R^{\mathrm{TP}}\right)^2 \tag{4.1}$$

with $\tilde{\beta}$, $\tilde{\gamma}$ and being the fit parameters and R^{TP} affecting the size of the surface. This surface includes the transformation backstress X_{ij}^{TP}.

J_1, J_2 are the two invariants of the reduced stress tensor $\sigma_{ij} - X_{ij}^{\mathrm{TP}}$,

$$J_1\left(\sigma_{ij} - X_{ij}^{\mathrm{TP}}\right) = \sigma_{ii} - X_{ii}^{\mathrm{TP}}, \tag{4.2}$$

$$J_2\left(\sigma_{ij} - X_{ij}^{\mathrm{TP}}\right) = \left[\frac{3}{2}\left(S_{ij} - \hat{X}_{ij}^{\mathrm{TP}}\right) : \left(S_{ij} - \hat{X}_{ij}^{\mathrm{TP}}\right)\right]. \tag{4.3}$$

S_{ij} is the deviator of σ_{ij}, $\hat{X}_{ij}^{\mathrm{TP}}$ is the deviator of X_{ij}^{TP}. Of course, if we assume X_{ij}^{TP} being a deviator, then

$$J_1 = \sigma_{ii}. \tag{4.4}$$

The above hypothetical surface (4.1) includes the value of J_1 itself to distinguish between the tension and the compression regime or, in other words, to describe the asymmetry of the transformation domain in tension and compression. If f^{TP} reaches 0, then the stress state is sufficient to produce a "macroscopic TRIP flow". If f^{TP} is smaller than 0, then no macroscopic TRIP effect can be observed. The TRIP strain rate will be assumed to be proportional to $\langle f^{\mathrm{TP}}\rangle^{1/2}$, $\langle a\rangle$ is a for $a > 0$ and 0 for $a \leq 0$, defined as

$$\dot{\varepsilon}_{ij}^{\mathrm{TP}} = \frac{1}{2} K \frac{d\varphi}{d\xi} \dot{\xi} \langle \frac{f^{\mathrm{TP}}}{J_2} \rangle^{1/2} \frac{\partial J_2}{\partial \sigma_{ij}}, \tag{4.5}$$

$$\frac{\partial J_2}{\partial \sigma_{ij}} = 3\left(S_{ij} - \hat{X}_{ij}^{\mathrm{TP}}\right). \tag{4.6}$$

Note that $\dot{\varepsilon}_{ij}^{\mathrm{TP}}$ is now parallel to $\left(S_{ij} - \hat{X}_{ij}^{\mathrm{TP}}\right)$ and not only to S_{ij} as reported in the literature, (see e.g. [1 – 5]). This assumption allows a nonzero TRIP strain rate even for $S_{ij} \equiv 0$, (see also [6])!

We adapt now the transformation surface to the experiments explained in Sec. 2. Let us assume a tension or compression stress σ coupled with shear stress τ and consider a plane stress case (like in the tubular specimens investigated). As reported already, we found a backstress component $X_{11}^{\mathrm{TP}} = X_z = 28$ MPa but no backstress component with respect to shear. Direction 1 corresponds to the longitudinal direction. According to the dilatometer test, no backstress is assumed in directions 2 and 3 leading to $\hat{X}_1^{\mathrm{TP}} = \hat{X}_z = \frac{2}{3} X_z$. J_1, J_2, and f^{TP} will now read

$$J_1 = \sigma - X_z, \tag{4.7}$$

$$J_2 = (\sigma - X_z)^2 + 3\tau^2, \tag{4.8}$$

$$f^{\mathrm{TP}} = (\sigma - X_z)^2 + 3(1-\tilde{\beta})\tau^2 + \tilde{\gamma}(\sigma - X_z) - (R^{\mathrm{TP}})^2. \tag{4.9}$$

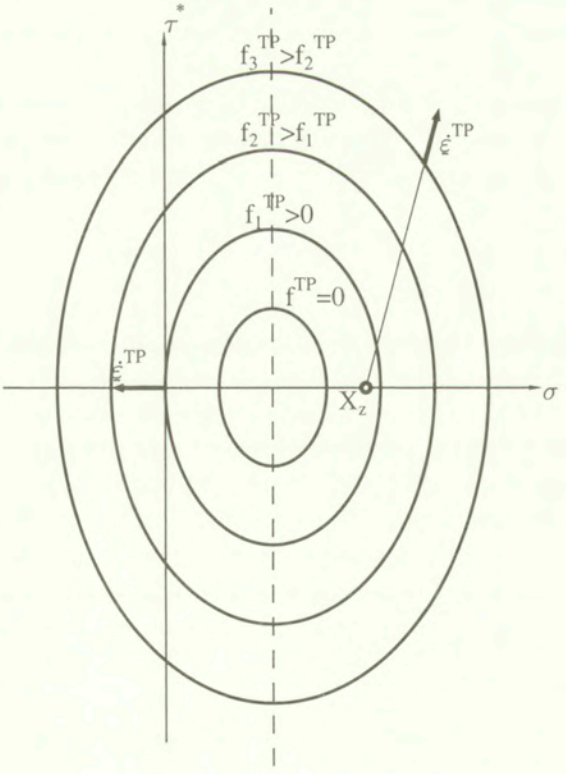

FIG. 11. Isolines for a hypothetical transformation surface for the TRIP strain rate in the modified deviator space S, $\tilde{\tau} = (1-\tilde{\beta})\tau$, $\hat{X}_z = 19$ MPa, $\tilde{\beta} = 0.31$, $\tilde{\gamma} = 44$ MPa; R^{TP} size parameter of the transformation surface.

Working in the $\sigma, \tau^* = \tau\sqrt{3}$ space allows to represent J_2 by a circle with the centre at $\sigma = X_z$, $\tau^* = 0$ and the transformation surface by an ellipse with the centre at $\sigma = X_z - \tilde{\gamma}/2$, $\tau^* = 0$ and the semi-axes e_σ, e_{τ^*}. in the direction, resp.,

$$e_\sigma = \left((R^{\mathrm{TP}})^2 + \tilde{\gamma}/4\right)^{1/2}, \tag{4.10}$$

$$e_{\tau^*} = e_\sigma/(1-\tilde{\beta})^{1/2}. \tag{4.11}$$

The situation is qualitatively depicted in Fig. 11. Both relevant components of the TRIP strain rate can be assembled to a vector with a radial orientation relative to the J_2 surface. The curve $f^{\mathrm{TP}} = 0$ is an ellipse enclosing an area with no further TRIP strain rate. Figure 11 shows schematically the isolines for a transformation surface and some TRIP strain vectors. In the case of $\tau^* = 0$ one can recognize that, firstly, the TRIP strain rates are different for tension and compression for the same load stress intensity and, secondly, that for $\sigma = 0$ (a stress-free specimen, e.g. after unloading) a TRIP strain rate is also possible.

In general, the four parameters describing the transformation surface, X_z, $\tilde{\gamma}$, $\tilde{\beta}$, R^{TP} may evolve with the loading process, since they reflect the microstructure of the material correlating with its transformation behaviour. This requires to develop a proper evolution law. Since a broad experimental basis is a mandatory prerequiste, the proposal for any evolution law can only be the subject of further research. The group of the authors will work in this field in the next years.

5. Conclusion

A broad experimental programme is presented for an Fe-Ni-Cr steel, monitoring the TRIP strain for monotonic and non-monotonic loading paths like partial and full unloading. Even in the case of dilatometer tests without any external load, a backstress can be observed. In the case of unloading, a backflow can be observed depending on the kind of preloading. Transformation thermodynamics is employed to show the influence of the load-stress state and the internal stress state on the formation of an irreversible transformation strain. This TRIP strain consists of two contributions, i.e. one due to the plastic accommodation of the transformation eigenstrain and one due to the selection of distinct martensitic variants. The second effect, named "orientation" effect, can clearly be shown even for a very low load level by means of different martensite start lines. The hypothesis of the existence of a significant orientation effect is supported by means of micromechanical modelling.

The TRIP strain rate proposed in the available literature does not account for the existence of a transformation backstress. Inspired by the work of Prof. Z. Mróz introducing additional surfaces to the yield surface in order to

explain the backstress in the case of classical plasticity, we also define a transformation surface in order to determine the backstress in the case of a phase transformation. The TRIP strain rate can be represented by a vector from the origin of the transformation surface to the corresponding stress point on the transformation surface. The amount of the TRIP strain rate is also related to the actual value of the transformation surface function. Finally this concept is intended to contribute to the development of improved constitutive equations for phase changing materials subjected to arbitrary loading paths.

References

1. M. BERVEILLER and F. D. FISCHER, *Mechanics of solids with phase changes*, Springer Wien, New York 1997.
2. F. D. FISCHER, Q.-P. SUN and K. TANAKA, *Transformation-induced plasticity (TRIP)*, ASME Appl. Mech. Rev. **49**, 317–364, 1996.
3. J. B. LEBLOND, G. MOTTET and J. C. DEVAUX, *A theoretical and numerical approach to the plastic behaviour of steels during phase transformations – I: Derivation of general relations; II: Study of classical plasticity for ideal-plastic phases*, J. Mech. Phys. Solids, **34**, 395–410, 411–432, 1986.
4. J. B. LEBLOND, J. DEVAUX and J. C. DEVAUX, *Mathematical modelling of transformation induced plasticity in steels – I: Case of ideal-plastic phases – II: Coupling with strain hardening phenomena*, Int. J. Plasticity, **5**, 551–572, 573–591, 1989.
5. Sysweld + 2.0: Reference Manual, SYSTUS International, ESI Group: Simulation of Welding and Heat Treatment Processes, Framasoft + CSI, 1997.
6. J.-Chr. VIDEAU, G. CAILLETAUD and A. PINEAU, *Modélisation des effets mécaniques des transformations de phases pour le calcul de structures*, J. de Physique IV, Colloque C3, Supplm. J. de Physique III, **4**, C3-227–C3-232, 1994.
7. J.-Chr. VIDEAU, G. CAILLETAUD and A. PINEAU, *Experimental study of the transformation – induced plasticity in a Cr-Ni-Mo-Al-Ti steel*, J. de Physique IV, Colloque C1, Supplm. J. de Physique III, **6**, C1-465–C1-474, 1996.
8. F. MARKETZ and F. D. FISCHER, *A mesoscale study on the thermodynamic effect of stress on martensitic transformation*, Met. Mater. Trans., **26A**, 267–278, 1995.
9. V. I. LEVITAS, *Thermomechanical theory of martensitic phase transformations in inelastic materials*, Int. J. Solids Structures, **35**, 889–940, 1998.
10. F. D. FISCHER and G. REISNER, *A criterion for the martensitic transformation of a microregion in an elastic-plastic material*, Acta Mater., **46**, 2095–2102, 1998.
11. G. REISNER, F. D. FISCHER, Y. H. WEN and E. A. WERNER, *Interaction energy between martensitic variants*, Met. Mater. Trans., A, **30A**, 2583–2590, 1999.
12. E. GAUTIER and A. SIMON, *Transformation plasticity mechanisms for martensitic transformation of ferrous alloys*, [In:] Int. Conf. on Phase Transformations '87, G. W. LORIMER [Ed.], The Inst. of Metals, 285–287, London 1988.
13. E. GAUTIER, X. M. ZHANG and A. SIMON, *Role of internal stress state on transformation induced plasticity and transformation mechanisms during the progress of stress induced phase transformation*, [In:] Int. Conf. on Residual Stresses – ICRS 2, G. BECK, S. DENIS and A. SIMON [Eds.], Elsevier Applied Sciences, 777–783, London and New York 1989.

14. F. D. FISCHER, G. REISNER, E. WERNER, K. TANAKA, G. CAILLETAUD and T. ANTRETTER, *A new view on transformation induced plasticity*, Int. J. Plasticity, **16**, 723–748, 2000.

15. G. REISNER, E. A. WERNER and F. D. FISCHER, *Micromechanical modelling of martensitic transformation in random microstructures*, Int. J. Solids & Structures, **35**, 2457–2473, 1998.

Received February 9, 2000; revised version June 14, 2000.

Arch. Mech., **52**, 4–5, pp. 589–607, Warszawa 2000

Elastic-plastic stress-strain analysis of notches under non-proportional loading paths

Dedicated to Professor Zenon Mróz on the occasion of his 70th birthday

G. GLINKA ([1]), A. BUCZYŃSKI ([2]), A. RUGGERI ([3])

([1]) *University of Waterloo, Department of Mechanical Engineering, Waterloo, Ontario N2L 3G1, Canada*

([2]) *Warsaw University of Technology, Institute of Heavy Machinery Engineering, ul. Narbutta 85, 02524 Warsaw, Poland*

([3]) *INSA of Toulouse, Department of Mechanical Engineering, 135 Avenue de Rangueil, 31077 Toulouse Cedex 4, France*

AN ANALYTICAL METHOD for calculating notch tip stresses and strains in elastic-plastic bodies subjected to non-proportional loading sequences is discussed in the paper. The method is based on the incremental formulation relating the hypothetical linear elastic and elastic-plastic strain energy densities at the notch tip, and the material stress-strain behavior simulated according to the Mróz-Garud cyclic plasticity model. Two formulations involving the strain energy density and the complementary strain density are discussed in the paper, and they appear to give the lower and the upper bound estimates for the elastic-plastic notch tip strains. Each formulation consists of a set of incremental algebraic equations that can easily be solved for elastic-plastic stress and strain increments, knowing the increments of the hypothetical elastic notch tip stress history and the material stress-strain curve. The validation of the proposed model against finite element data obtained for non-proportional loading is also presented. The method is particularly suitable for fatigue life analysis of notched bodies subjected to multiaxial cyclic loading paths.

Key Words: notches, nonproportional loading, inelastic strains

Notations

$\Delta\varepsilon_{22}$	normal strain increment in the critical plane
$\Delta\varepsilon^p_{ij}$	plastic strain increments
δ_{ij}	Kronecker delta, $\delta_{ij} = 1$ for $i = j$ and $\delta_{ij} = 0$ for $i \neq j$
$\Delta\varepsilon^e_{jk}$	elastic strain increments

$\Delta\varepsilon_{jk}^{E}$	elastic-plastic strain increments according to ESED method
Δ_{jk}^{N}	elastic-plastic strain increments according to Neuber's rule
$\Delta\varepsilon_{eq}^{pE}$	equivalent plastic strain increment according to ESED method
$\Delta\varepsilon_{eq}^{pN}$	equivalent plastic strain increment according to Neuber's rule
$\Delta\sigma_{ik}^{e}$	increments of pseudo-elastic stress components
$\Delta\sigma_{ik}^{E}$	actual elastic-plastic stress increments according to ESED method
$\Delta\sigma_{ik}^{N}$	actual elastic-plastic stress increments according to Neuber's rule
$\Delta\sigma_{eq}^{N}$	equivalent stress increment according to Neuber's rule
ΔS_{ij}^{e}	symmetric tensor of the pseudo-elastic stress state
ΔS_{ij}^{E}	symmetric tensor of elastic-plastic stress state acording to the strain energy density increment
ΔW_{ij}^{e}	tensor of elastic strain energy density increment
ΔW_{ij}^{E}	tensor of elastic-plastic strain energy density increment
$\Delta\Omega_{ij}^{e}$	tensor of elastic total strain energy density increment
$\Delta\Omega_{ij}^{N}$	tensor of elastic-plastic total strain energy density increment
ΔT_{ij}^{e}	symmetric tensor of elastic total strain energy density increment
ΔT_{ij}^{N}	symmetric tensor of elastic-plastic total strain energy density increment
E	modulus of elasticity
ε_{eq}^{p}	equivalent plastic strain
ε_{eq}^{pE}	equivalent plastic strain determined by the ESED method
ε_{ij}^{E}	elasto-plastic notch-tip strains obtained from the ESED method
ε_{ij}^{e}	notch tip strain components obtained from linear elastic analysis
ε_{ij}^{N}	elasto-plastic notch-tip strains obtained by the Neuber method
ε_{ij}^{p}	plastic components of the notch-tip strain tensor
ε_{n}	nominal strain
ESED	equivalent strain energy density
ν	Poisson's ratio
P	axial load
T	torque
R	radius of a cylindrical specimen
S_{ij}	deviatoric stress components
σ_{eq}	equivalent stress
σ_{ij}^{a}	actual stress tensor components in the notch tip
σ_{ij}^{e}	notch tip stress tensor components obtained from linear elastic analysis
σ_{ij}^{E}	notch tip stress tensor components obtained from the ESED model
σ_{ij}^{N}	notch tip stress tensor components obtained from the Neuber solution
σ_{n}	nominal stress
σ_{n}^{P}	nominal (average) stress in the net cross-section due to axial load P
σ_{o}	parameter of the material stress-strain curve (yield limit)
σ_{Y}	yield limit
t	wall thickness
τ_{n}	nominal shear stress in the net cross-section

1. Introduction

FATIGUE ANALYSES of machine and structure components require a detailed elastic-plastic stress-strain analysis at critical locations, such as notches, where the stress concentration occurs. In most cases the stress state in the notch tip region is multiaxial. However, if one of the stress components is the dominant one, it is often assumed that uniaxial stress or plane strain state prevails at the notch tip. Such an approximation might be satisfactory in a wide variety of practical applications but there are cases where all the stress and strain components have to be accounted for. This is particularly true when several loads are applied simultaneously and the stress components at the notch root change non-proportionally. For example, axles and shafts may experience combined out-of-phase torsion and bending loads.

The main focus of this paper is to present a method for calculating multiaxial elastic-plastic stresses and strains in notched bodies subjected to proportional and non-proportional loading histories.

2. Loading histories

Fatigue cracks most often initiate at the notch tip where the highest stress concentration occurs. Therefore, most fatigue analyses are focused on the determination of fatigue life of the material volume adjacent to the notch tip, which is under the effect of the local notch tip stress-strain history. The notch tip stresses and strains are dependent on the notch geometry, the material properties and the loading history applied to the notched body. If the various cyclic stress components are in phase and change proportionally with each other, the loading is called *proportional*. When the applied load causes the directions of the principal stresses and the ratio of the principal stress magnitudes to change after each load increment, the loading is termed *non-proportional*.

If plastic yielding takes place at the notch tip then almost always the stress path in the notch tip region is non-proportional, regardless of whether the remote loading is proportional or not. However, the remote proportional loading does not make the notch tip stress tensor rotate and therefore, it makes the stress analysis easier in spite of the fact that some non-proportionality of the notch tip stress history may occur.

The non-proportional loading/stress paths are usually defined by successive increments of appropriate load/stress parameters and therefore all calculations have to be carried out incrementally.

3. The stress state at the notch tip

If the dimensions and external loads applied to a body are such that the plane stress state dominates in the body, then the stress state at the notch tip is uni-axial (Fig. 1a), providing that the surface at the notch tip is stress-free. If the notched body is in the state of plane strain (Fig. 1b), the notch tip stress-strain state is fully characterized by only two principal non-zero stress components and two non-zero principal strain components.

For the case of general multiaxial loading applied to a notched body, the state of stress near the notch tip is tri-axial. However, the stress state at the notch tip is bi-axial because of the stress-free notch tip surface (Fig. 1c). Since equilibrium of the element at the notch tip must be maintained, i.e. $\sigma_{23} = \sigma_{32}$ and $\varepsilon_{23} = \varepsilon_{32}$, there are in general three non-zero stress components and four non-zero strain components. There are seven unknowns altogether and a set of seven independent equations is required for the determination of all the stress and strain components at the notch tip. The material constitutive relationships provide four equations, leaving three additional relationships to be established.

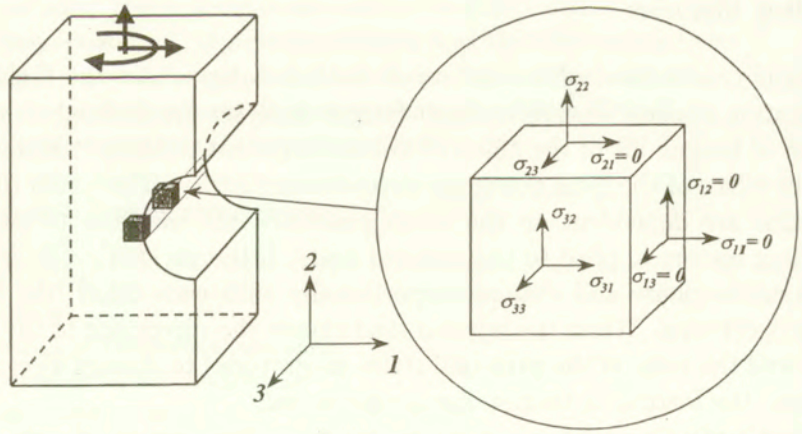

(a) Plane Stress (b) Plane Strain (c) General

$$\sigma_{ij} = \begin{bmatrix} 0 & 0 & 0 \\ 0 & \sigma_{22} & 0 \\ 0 & 0 & 0 \end{bmatrix} \qquad \sigma_{ij} = \begin{bmatrix} 0 & 0 & 0 \\ 0 & \sigma_{22} & 0 \\ 0 & 0 & \sigma_{33} \end{bmatrix} \qquad \sigma_{ij} = \begin{bmatrix} 0 & 0 & 0 \\ 0 & \sigma_{22} & \sigma_{23} \\ 0 & \sigma_{32} & \sigma_{33} \end{bmatrix}$$

$$\varepsilon_{ij} = \begin{bmatrix} \varepsilon_{11} & 0 & 0 \\ 0 & \varepsilon_{22} & 0 \\ 0 & 0 & \varepsilon_{33} \end{bmatrix} \qquad \varepsilon_{ij} = \begin{bmatrix} \varepsilon_{11} & 0 & 0 \\ 0 & \varepsilon_{22} & 0 \\ 0 & 0 & 0 \end{bmatrix} \qquad \varepsilon_{ij} = \begin{bmatrix} \varepsilon_{11} & 0 & 0 \\ 0 & \varepsilon_{22} & \varepsilon_{23} \\ 0 & \varepsilon_{32} & \varepsilon_{33} \end{bmatrix}$$

FIG. 1. Stress state at a notch tip (notation): a) body in plane stress; b) body in plane strain; c) general bi-axial stress state.

4. Material constitutive model

In the case of proportional or nearly proportional notch tip stress path, the Hencky total deformation equations of plasticity can be used in the analysis,

$$\varepsilon_{ij} = \frac{1+\nu}{E}\sigma_{ij} - \frac{\nu}{E}\sigma_{kk}\delta_{ij} + \frac{3}{2}\frac{\varepsilon^p_{eq}}{\sigma_{eq}}S_{ij}. \tag{4.1}$$

The material constitutive model of incremental plasticity, most frequently used in the case of non-proportional loading paths, is the Prandtl-Reuss flow rule associated with the von Mises plastic yielding criterion. For an isotropic body, the Prandtl-Reuss relationship can be expressed as:

$$\Delta\varepsilon_{ij} = \frac{1+\nu}{E}\Delta\sigma_{ij} - \frac{\nu}{E}\Delta\sigma_{kk}\delta_{ij} + \frac{3}{2}\frac{\Delta\varepsilon^p_{eq}}{\sigma_{eq}}S_{ij}. \tag{4.2}$$

The multiaxial incremental stress-strain relation (4.2) is obtained from the uniaxial stress-strain curve by relating the equivalent plastic strain increment to the equivalent stress increment, such that

$$\Delta\varepsilon^p_{eq} = \frac{df(\sigma_{eq})}{d\sigma_{eq}}\Delta\sigma_{eq}. \tag{4.3}$$

The function, $\varepsilon^p_{eq} = f(\sigma_{eq})$, is identical to the plastic strain-stress relationship obtained under uniaxial loading.

5. The load-notch tip stress-strain relations

The load in the case of notched bodies is usually represented by the nominal or reference stress being proportional to the remote applied load or by the pseudo-elastic stresses at the notch tip which would exist there in the absence of plasticity. In the case of notched bodies in plane stress or plane strain state, the relationship between the load and the elastic-plastic notch tip strains and stresses is most often approximated by the Neuber rule [1] or the Equivalent Strain Energy Density (ESED) equation [2]. It was shown later [3, 4] that both methods can be extended to multiaxial proportional and non-proportional modes of loading. However, the multiaxial Neuber and ESED [3, 4] models are not the only methods for determination of multiaxial elastic-plastic strain and stress states at the notch tip. HOFFMAN and SEEGER [5] and BARKEY *et al.* [6] also proposed similar methods. All of the approximate methods consist, in general, of two parts, namely: the constitutive equations and the relationships linking the fictitious linear elastic stress-strain state $(\sigma^e_{ij}, \varepsilon^e_{ij})$ at the notch tip with the actual elastic-plastic stress-strain response $(\sigma^a_{ij}, \varepsilon^a_{ij})$ as shown in Fig. 2.

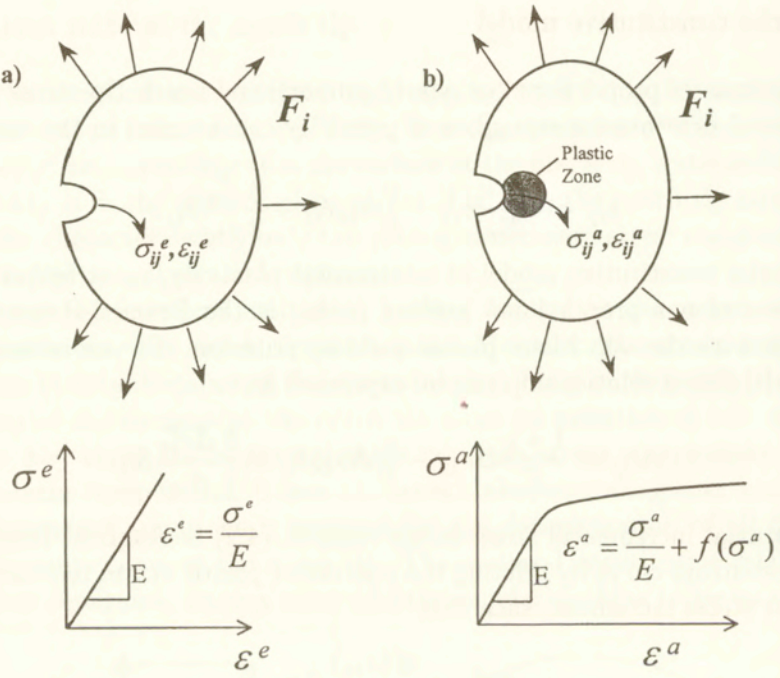

FIG. 2. The linear elastic and elastic-plastic strain and stress states in geometrically identical bodies.

The Neuber and the ESED rule [2, 3] for proportional loading, where the Hencky stress-strain relationships are applicable, can be written in the form of Eqs. (5.1) and (5.2), respectively,

$$\sigma_{ij}^e \varepsilon_{ij}^e = \sigma_{ij}^N \varepsilon_{ij}^N, \tag{5.1}$$

$$\int_0^{\varepsilon_{ij}^e} \sigma_{ij}^e d\varepsilon_{ij}^e = \int_0^{\varepsilon_{ij}^E} \sigma_{ij}^E d\varepsilon_{ij}^E. \tag{5.2}$$

The ESED method is based on the equivalence of the strain energy density as shown in Fig. 3a. The Neuber rule represents the equality of total strain energy shown graphically in Fig. 3b. Detail discussion of the incremental Neuber rule (5.3) and the ESED equation (5.4) and their use for calculating the elastic-plastic notch tip strains and stresses can be found in reference [4]:

– Incremental Neuber's rule

$$\sigma_{ij}^e \Delta\varepsilon_{ij}^e + \varepsilon_{ij}^e \Delta\sigma_{ij}^e = \sigma_{ij}^N \Delta\varepsilon_{ij}^N + \varepsilon_{ij}^N \Delta\sigma_{ij}^N. \tag{5.3}$$

– Incremental ESED equation

$$\sigma_{ij}^e \Delta\varepsilon_{ij}^e = \sigma_{ij}^E \Delta\varepsilon_{ij}^E. \tag{5.4}$$

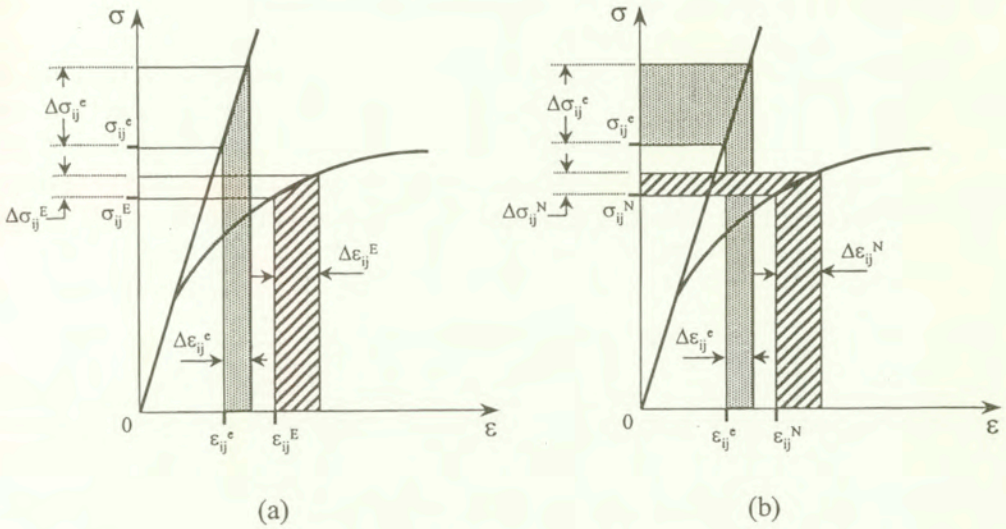

FIG. 3. Graphical representation of: a) Incremental ESED method; b) Incremental Neuber's rule.

The overall energy equivalence in the form of Eq. (5.3) or (5.4), relating the pseudo-elastic and the actual elastic-plastic notch tip strains and stresses, has been accepted in general, but the additional conditions necessary for the complete formulation of the problem are being the subject of controversy. HOFFMAN and SEEGER [5] assumed that the ratio of the actual principal strains at the notch tip is to be equal to the ratio of fictitious elastic principal strain components while BARKEY *et al.* [6] suggested to use the ratio of principal stresses. The data presented by MOFTAKHAR [7] indicate that the accuracy of the analysis based on the principal stress or principal strain ratio at the notch tip depended on the constraint at the notch tip. Unfortunately, it is very difficult to define criteria enabling the proper choice of those additional conditions.

The accuracy of the additional energy equations presented by SINGH *et al.* [4] seems to be less dependent on the geometry and constraint conditions at the notch tip and therefore, the analyst is not forced to make any arbitrary decisions while using them. However, they have a theoretical drawback indicated by CHU [8] because they do not have tensor properties and thus the estimated elastic-plastic notch tip strains and stresses depend on the system of coordinates. The dependence is not very strong and with suitably chosen system of reference, it could be sufficiently accurate for engineering applications. Nevertheless, it is possible to formulate an axis-invariant system of equations similar to those discussed in references [4, 8].

6. Multiaxial equivalent strain energy density equations

The strain energy density equations can be written in terms of equality of components of two tensors ΔW_{ij}^e and ΔW_{ij}^E representing inner products of the stress tensor σ_{ik} and the corresponding strain increment tensor $\Delta\varepsilon_{kj}$. The strain energy density increment, ΔW_{ij}^e, called here the strain energy density tensor induced by the pseudo-elastic stress and strain increments at the notch tip (Fig. 2a) can be determined as:

$$\Delta W_{ij}^e = \sigma_{ik}^e \cdot \Delta\varepsilon_{kj}^e. \tag{6.1}$$

The actual strain energy density tensor, ΔW_{ij}^E, resulting from the actual elastic-plastic stress and strain increments at the notch tip (Fig. 2b) can be also determined as the inner product of the current stress tensor and the strain increment tensor,

$$\Delta W_{ij}^E = \sigma_{ik}^E \cdot \Delta\varepsilon_{kj}^E. \tag{6.2}$$

In the case of the notch tip surface free of stress (Fig. 1c), tensors (6.1) and (6.2) can be presented in the matrix form with all elements in the first column and the first row being equal to zero:

$$\Delta W_{ij}^e = \begin{bmatrix} 0 & 0 & 0 \\ 0 & \sigma_{22}^e\Delta\varepsilon_{22}^e + \sigma_{23}^e\Delta\varepsilon_{32}^e & \sigma_{22}^e\Delta\varepsilon_{23}^e + \sigma_{23}^e\Delta\varepsilon_{33}^e \\ 0 & \sigma_{32}^e\Delta\varepsilon_{22}^e + \sigma_{33}^e\Delta\varepsilon_{32}^e & \sigma_{32}^e\Delta\varepsilon_{23}^e + \sigma_{33}^e\Delta\varepsilon_{33}^e \end{bmatrix} \tag{6.3}$$

and

$$\Delta W_{ij}^E = \begin{bmatrix} 0 & 0 & 0 \\ 0 & \sigma_{22}^E\Delta\varepsilon_{22}^E + \sigma_{23}^E\Delta\varepsilon_{32}^E & \sigma_{22}^E\Delta\varepsilon_{23}^E + \sigma_{23}^E\Delta\varepsilon_{33}^E \\ 0 & \sigma_{32}^E\Delta\varepsilon_{22}^E + \sigma_{33}^E\Delta\varepsilon_{32}^E & \sigma_{32}^E\Delta\varepsilon_{23}^E + \sigma_{33}^E\Delta\varepsilon_{33}^E \end{bmatrix}. \tag{6.4}$$

The physical meaning of the diagonal terms in matrix (6.3) and (6.4) is obvious because the two products in each diagonal term represent the strain energy density increments contributed by individual stress components and the corresponding strain increments. The sum of diagonal terms in both tensors represents the increment of the strain energy density. The meaning of the off-diagonal terms is less clear but they can be interpreted as increments of the virtual strain energy density increments analogously to the term used in the virtual energy method well-known in solid mechanics stress/load analyses. The product, $\sigma_{22}^e\Delta\varepsilon_{23}^e$, in the term W_{23}^e in matrix (6.3), can be interpreted as the virtual strain energy increment contributed by stress, σ_{22}^e, on the strain increment, $\Delta\varepsilon_{23}^e$, induced by the shear stress, σ_{23}^e. The second product, $\sigma_{23}^e\Delta\varepsilon_{33}^e$, being a part of the same

term, W^e_{23}, can be analogously considered as the virtual strain energy density increment contributed by the shear stress component, σ^e_{23}, on the normal strain increment, $\Delta\varepsilon^e_{33}$, induced by normal stress components, σ^e_{22} and σ^e_{33}.

Tensors (6.3) and (6.4) are in general non-symmetric. However, they can easily be made symmetric by taking the average of the sum of both off-diagonal terms.

(6.5) $$\Delta S^e_{ij} =$$

$$= \begin{bmatrix} 0 & 0 & 0 \\ 0 & \sigma^e_{22}\Delta\varepsilon^e_{22} + \sigma^e_{23}\Delta\varepsilon^e_{32} & \dfrac{(\sigma^e_{22}+\sigma^e_{33})\Delta\varepsilon^e_{23} + \sigma^e_{23}(\Delta\varepsilon^e_{22}+\Delta\varepsilon^e_{33})}{2} \\ 0 & \dfrac{(\sigma^e_{22}+\sigma^e_{33})\Delta\varepsilon^e_{23} + \sigma^e_{23}(\Delta\varepsilon^e_{22}+\Delta\varepsilon^e_{33})}{2} & \sigma^e_{32}\Delta\varepsilon^e_{23} + \sigma^e_{33}\Delta\varepsilon^e_{33} \end{bmatrix}$$

and

(6.6) $$\Delta S^E_{ij} =$$

$$= \begin{bmatrix} 0 & 0 & 0 \\ 0 & \sigma^E_{22}\Delta\varepsilon^E_{22} + \sigma^E_{23}\Delta\varepsilon^E_{32} & \dfrac{(\sigma^E_{22}+\sigma^E_{33})\Delta\varepsilon^E_{23} + \sigma^E_{23}(\Delta\varepsilon^E_{22}+\Delta\varepsilon^E_{33})}{2} \\ 0 & \dfrac{(\sigma^E_{22}+\sigma^E_{33})\Delta\varepsilon^E_{23} + \sigma^E_{23}(\Delta\varepsilon^E_{22}+\Delta\varepsilon^E_{33})}{2} & \sigma^E_{32}\Delta\varepsilon^E_{23} + \sigma^E_{33}\Delta\varepsilon^E_{33} \end{bmatrix}$$

Analogously to the hypothesis proposed in references [2, 3, 4], it is assumed that the strain energy increments at the notch tip in the pseudo-elastic and the elastic-plastic body (Fig. 2) of identical geometrical shape and subjected to identical loads, are equal. Such a hypothesis can be written in terms of the equality of tensors (6.5) and (6.6),

$$\Delta S^e_{ij} = \Delta S^E_{ij}. \tag{6.7}$$

The hypothesis written in the form of Eq. (6.7) results in three independent equations relating the pseudo-elastic strain and stress components and the actual elastic-plastic stress-strain response at the notch tip in the elastic-plastic body (Fig. 2).

$$\sigma^e_{22}\Delta\varepsilon^e_{22} + \sigma^e_{23}\Delta\varepsilon^e_{23} = \sigma^E_{22}\Delta\varepsilon^E_{22} + \sigma^E_{23}\Delta\varepsilon^E_{23}, \tag{6.8}$$

$$\sigma^e_{33}\Delta\varepsilon^e_{33} + \sigma^e_{23}\Delta\varepsilon^e_{23} = \sigma^E_{33}\Delta\varepsilon^E_{33} + \sigma^E_{23}\Delta\varepsilon^E_{23}, \tag{6.9}$$

$$(\sigma^e_{22}+\sigma^e_{33})\Delta\varepsilon^e_{23} + \sigma^e_{23}(\Delta\varepsilon^e_{22}+\Delta\varepsilon^e_{33}) = (\sigma^E_{22}+\sigma^E_{33})\Delta\varepsilon^E_{23} + \sigma^E_{23}(\Delta\varepsilon^E_{22}+\Delta\varepsilon^E_{33}). \tag{6.10}$$

Equations (6.8) – (6.10) can be supplemented with four constitutive equations obtained from the general constitutive relationship (4.2).

$$\Delta\varepsilon_{11}^{E} = -\frac{\nu}{E}(\Delta\sigma_{22}^{E} + \Delta\sigma_{33}^{E}) - \frac{1}{2}(\sigma_{22}^{E} + \sigma_{33}^{E})\frac{\Delta\varepsilon_{eq}^{pE}}{\sigma_{eq}^{E}}, \tag{6.11}$$

$$\Delta\varepsilon_{22}^{E} = \frac{1}{2}(\Delta\sigma_{22}^{E} - \nu\Delta\sigma_{33}^{E}) + \frac{1}{2}(2\sigma_{22}^{E} - \sigma_{33}^{E})\frac{\Delta\varepsilon_{eq}^{pE}}{\sigma_{eq}^{E}}, \tag{6.12}$$

$$\Delta\varepsilon_{33}^{E} = \frac{1}{E}(\Delta\sigma_{33}^{E} - \nu\Delta\sigma_{22}^{E}) + \frac{1}{2}(2\sigma_{33}^{E} - \sigma_{22}^{E})\frac{\Delta\varepsilon_{eq}^{pE}}{\sigma_{eq}^{E}}, \tag{6.13}$$

$$\Delta\varepsilon_{23}^{E} = \frac{1+\nu}{E}\Delta\sigma_{23}^{E} + \frac{3}{2}\frac{\Delta\varepsilon_{eq}^{pE}}{\sigma_{eq}^{E}}\sigma_{23}^{E}, \tag{6.14}$$

where:

$$(\sigma_{eq}^{E})^2 = (\sigma_{22}^{E})^2 + (\sigma_{33}^{E})^2 - \sigma_{22}^{E}\sigma_{33}^{E} + 3(\sigma_{23}^{E})^2,$$

$$\Delta\sigma_{eq}^{E} = \frac{(\sigma_{22}^{E} - \sigma_{33}^{E})(\Delta\sigma_{22}^{E} - \Delta\sigma_{33}^{E}) + 3\sigma_{23}^{N}\Delta\sigma_{23}^{N}}{\sigma_{eq}^{N}},$$

$$\Delta\varepsilon_{eq}^{pE} = \frac{df(\sigma_{eq}^{E})}{d\sigma_{eq}^{E}}\Delta\sigma_{eq}^{E}.$$

Equations (6.8) – (6.14) form a set of equations enabling the determination of all the elastic-plastic strains, $(\Delta\varepsilon_{11}^{E}, \Delta\varepsilon_{22}^{E}, \Delta\varepsilon_{33}^{E}, \Delta\varepsilon_{23}^{E})$, and stress increments $(\sigma_{22}^{E}, \sigma_{33}^{E}, \sigma_{23}^{E})$ based on the pseudo-elastic stress history at the notch tip. A graphical representation of the incremental ESED method is shown in Fig. 3a, where the strain energy densities are represented by the vertical bars of the trapezoidal shape whose areas, according to Eqs. (6.8) – (6.9), must be equal.

7. Total strain energy density equations

A set of equations similar to Eqs. (6.8) – (6.10) can also be written in terms of the total strain energy density, i.e. the sum of the strain energy density and the complementary strain energy density, analogously to the well-known Neuber's rule [1]. The tensor representation of the increments of the total strain energy density in the notch tip of linear elastic body (Fig. 2a) can be written as

$$\Omega_{ij}^{e} = \sigma_{ik}^{e} \cdot \Delta\varepsilon_{kj}^{e} + \Delta\sigma_{ik}^{e} \cdot \varepsilon_{kj}^{e}. \tag{7.1}$$

Analogously, the tensor representation of the total strain energy density increments at the notch tip of geometrically identical elastic-plastic body (Fig. 2b) can be written as

$$\Delta\Omega_{ij}^N = \sigma_{ik}^N \cdot \Delta\varepsilon_{kj}^N + \Delta\sigma_{ik}^N \cdot \varepsilon_{kj}^N. \tag{7.2}$$

Tensors (7.1) and (7.2) are non-symmetric but they can be converted into two symmetric tensors T_{ij}^e and T_{ij}^N, respectively. Similarly to the strain energy density tensor (6.1) and (6.2), the sum of the diagonal terms of tensors T_{ij}^e and T_{ij}^N represents the increment of the total strain energy density, i.e., the strain energy density plus the complementary strain energy density. The off-diagonal terms can be interpreted as the virtual strain energy density and the virtual complementary strain energy density, analogously to the formulation discussed above. It is then postulated, similarly to the original Neuber concept, that in the case of localized plastic yielding in the notch tip region the symmetric tensors are equal,

$$\Delta T_{ij}^e = \Delta T_{ij}^N. \tag{7.3}$$

It can be shown that Eq. (7.3) reduces to the well-known Neuber's rule [1, 2] in the case of uni-axial stress state, and to the model proposed by MOFTAKHAR *et al.* [3] for multiaxial proportional loading. Because all the necessary relationships are formulated in terms of tensor equations, it is hoped that the proposed methodology is, contrary to the previous models [4], axis-invariant.

In the case of one surface free of stress, as it often occurs in notches (Fig. 1), the tensorial equation (7.3) leads to three independent equations relating the pseudo-elastic and the elastic-plastic strain and stress increments at the notch tip:

$$\begin{aligned}\sigma_{22}^e\Delta\varepsilon_{22}^e + \Delta\sigma_{22}^e\varepsilon_{22}^e + \sigma_{23}^e\Delta\varepsilon_{23}^e + \Delta\sigma_{23}^e\varepsilon_{23}^e = \sigma_{22}^N\Delta\sigma_{22}^N + \Delta\sigma_{22}^N\varepsilon_{22}^N \\ +\sigma_{23}^N\Delta\varepsilon_{23}^N + \Delta\sigma_{23}^N\varepsilon_{23}^N,\end{aligned} \tag{7.4}$$

$$\begin{aligned}\sigma_{33}^e\Delta\varepsilon_{33}^e + \Delta\sigma_{33}^e\varepsilon_{33}^e + \sigma_{23}^e\Delta\varepsilon_{23}^e + \Delta\sigma_{23}^e\varepsilon_{23}^e = \sigma_{33}^N\Delta\varepsilon_{33}^N + \Delta\sigma_{33}^N\varepsilon_{33}^N \\ +\sigma_{23}^N\Delta\varepsilon_{23}^N + \Delta\sigma_{23}^N\varepsilon_{23}^N,\end{aligned} \tag{7.5}$$

$$\begin{aligned}(\sigma_{22}^e + \sigma_{33}^e)\Delta\varepsilon_{23}^e + (\Delta\sigma_{22}^e + \Delta\sigma_{33}^e)\varepsilon_{23}^e + \sigma_{23}^e(\Delta\varepsilon_{22}^e + \Delta\varepsilon_{33}^e) \\ +\Delta\sigma_{23}^e(\varepsilon_{22}^e + \varepsilon_{33}^e) = (\sigma_{22}^N + \sigma_{33}^N)\Delta\varepsilon_{23}^N + (\Delta\sigma_{22}^N + \Delta\sigma_{33}^N)\varepsilon_{23}^N \\ +\sigma_{23}^N(\Delta\varepsilon_{22}^N + \Delta\varepsilon_{33}^N) + \Delta\sigma_{23}^N(\varepsilon_{22}^N + \varepsilon_{33}^N).\end{aligned} \tag{7.6}$$

Equations (7.4) – (7.6) and the four constitutive equations (7.7) – (7.10) below form a set of seven equations necessary for complete formulation of the notch tip

stress-strain problem.

$$\Delta\varepsilon_{11}^N = -\frac{\nu}{E}(\Delta\sigma_{22}^N + \Delta\sigma_{33}^N) - \frac{1}{2}(\sigma_{22}^N + \sigma_{33}^N)\frac{\Delta\varepsilon_{eq}^{pN}}{\sigma_{eq}^N}, \tag{7.7}$$

$$\Delta\varepsilon_{22}^N = \frac{1}{E}(\Delta\sigma_{22}^N - \nu\Delta\sigma_{33}^N) + \frac{1}{2}(2\sigma_{22}^N - \sigma_{33}^N)\frac{\Delta\varepsilon_{eq}^{pN}}{\sigma_{eq}^N}, \tag{7.8}$$

$$\Delta\varepsilon_{33}^N = \frac{1}{E}(\Delta\sigma_{33}^N - \nu\Delta\sigma_{22}^N) + \frac{1}{2}(2\sigma_{33}^N - \sigma_{22}^N)\frac{\Delta\varepsilon_{eq}^{pN}}{\sigma_{eq}^N}, \tag{7.9}$$

$$\Delta\varepsilon_{23}^N = \frac{1+\nu}{E}\Delta\sigma_{23}^N + \frac{3}{2}\frac{\Delta\varepsilon_{eq}^{pN}}{\sigma_{eq}^N}\sigma_{23}^N, \tag{7.10}$$

where:

$$(\sigma_{eq}^N)^2 = (\sigma_{22}^N)^2 + (\sigma_{33}^N)^2 - \sigma_{22}^N\sigma_{33}^N + 3(\sigma_{23}^N)^2,$$

$$\Delta\sigma_{eq}^N = \frac{(\sigma_{22}^N - \sigma_{33}^N)(\Delta\sigma_{22}^N - \Delta\sigma_{33}^N) + 3\sigma_{23}^N\Delta\sigma_{23}^N}{\sigma_{eq}^N},$$

$$\Delta\varepsilon_{eq}^{pN} = \frac{df(\sigma_{eq}^N)}{d\sigma_{eq}^N}\Delta\sigma_{eq}^N.$$

In the case of uni-axial or plane strain state at the notch tip, the set of seven equations reduces to two equations as proposed originally by NEUBER [1]. The equivalence of the increments of the total strain energy density is graphically shown in Fig. 3b, where the energies are represented by the horizontal and vertical rectangles whose areas are assumed to be equal.

8. Comparison of the calculated elastic-plastic notch tip strains and stresses with finite element data

Comparison of the calculated notch tip stress-strain histories to those obtained by means of the finite element method assessed the accuracy of the proposed incremental Neuber rule. The validation of the ESED method was outside of the scope of this paper. The elastic-plastic results from the finite element analysis of Ref. [4] were obtained using the ABAQUS finite element package. The geometry of the notched element was that of the circumferentially notched bar shown in Fig. 4. The nominal torsional stresses, τ_n, and tensile stresses, σ_{nF}, were determined basing on the net cross-section according to Eq. (8.1).

$$\sigma_{nF} = \frac{F}{\pi(R-t)^2} \quad \text{and} \quad \tau_n = \frac{2T}{\pi(R-t)^3}. \tag{8.1}$$

The basic proportions of the cylindrical component were $\rho/t = 1.0$ and $R/t = 23.333$ resulting in the torsional and tensile stress concentration factor $K_T = \sigma^e_{23}/\tau_n = 1.82$ and $K_P = \sigma^e_{23}/\sigma_{nF} = 2.80$, respectively. The ratio of the notch tip hoop stress to axial stress under tensile loading was $\sigma^e_{33}/\sigma^e_{22} = 0.2179$.

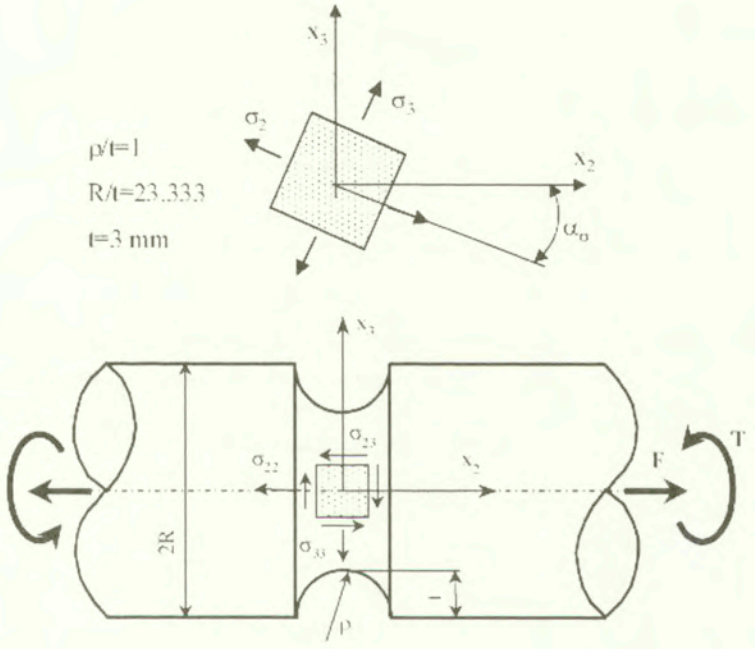

FIG. 4. Geometry and dimensions of the notched bar tested under non-proportional tension and torsion loading.

The linear segments shown in Fig. 5 approximated the material stress-strain curve used in calculations. The curve segments are defined by coordinates $(\varepsilon - \sigma)$ of each transition point, namely: $0-0$, $0.0039-200$ MPa, $0.00317-249$ MPa and $0.029-530$ MPa. The remaining standard elastic constants were $E = 200$ GPa, $\nu = 0.3$, $\sigma_Y = 200$ MPa.

The first set of data was obtained for non-proportional monotonic loading history (no unloading) shown in Fig. 6. The pseudo-elastic axial stress, σ^e_{22}, and the torsional shear stress, σ^e_{23}, at the notch tip represent the loading path. The specimen of Fig. 4 was loaded incrementally from zero to the load level corresponding to $\sigma^e_{22} = 108.89$ MPa and $\sigma^e_{23} = 161.06$ MPa and then the axial stress was further increased to the level of $\sigma^e_{22} = 344.10$ MPa while the shear stress was decreased to $\sigma^e_{23} = 120.78$ MPa, as shown in Fig. 5.

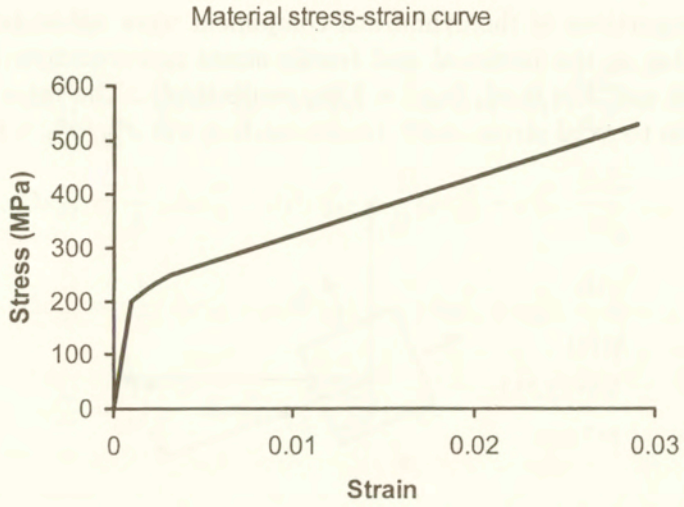

FIG. 5. The three linear segments material stress-strain curve used for the analysis of strain and stresses under the monotonic non-proportional loading path.

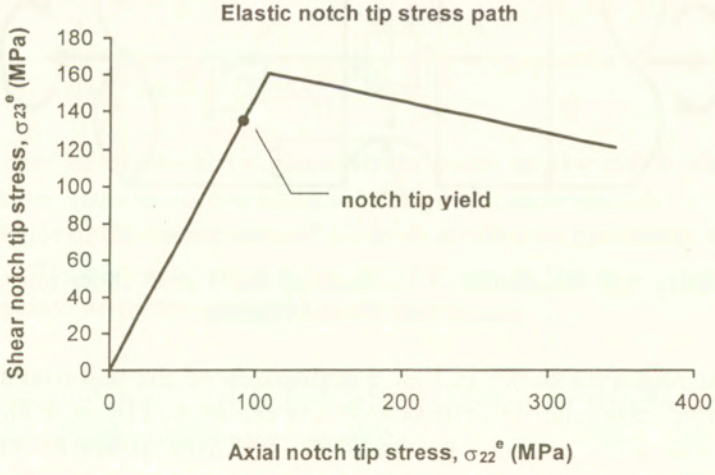

FIG. 6. The monotonic non-proportional torsion-tension load path.

The local pseudo-elastic stress path at the notch tip shown in Fig. 6 was used as the input to calculate the elastic-plastic notch tip stress-strain response. The appropriate 'elastic' stress increments were inputted into Eqs. (7.4) – (7.10) representing the total strain energy density (Neuber) approach. The calculated strains and stresses were subsequently compared with the elastic-plastic finite element data. The strain components, ε_{22} and ε_{23}, and the stress components, σ_{22} and σ_{23}, that were calculated using the method described above, are shown in Figs. 7 and 8. Note that the results from the model and the finite element

analysis are identical in the elastic range. This could be expected since the model converges to the elastic solution in the elastic range. Just beyond the onset of yielding at the notch tip, the strain results that were predicted using the proposed model and the finite element data begin gradually to diverge. However, the method gives reasonably good estimation of the notch tip stress-strain behavior. It can be concluded that the incremental total strain energy density (Neuber) method over-predicts the actual notch tip strains. The investigations up to date have revealed that the actual notch tip strains are always within the band defined by the two methods decribed above, and the average values of the two limits may be used as a good approximation of the actual stress-strain state at the notch tip.

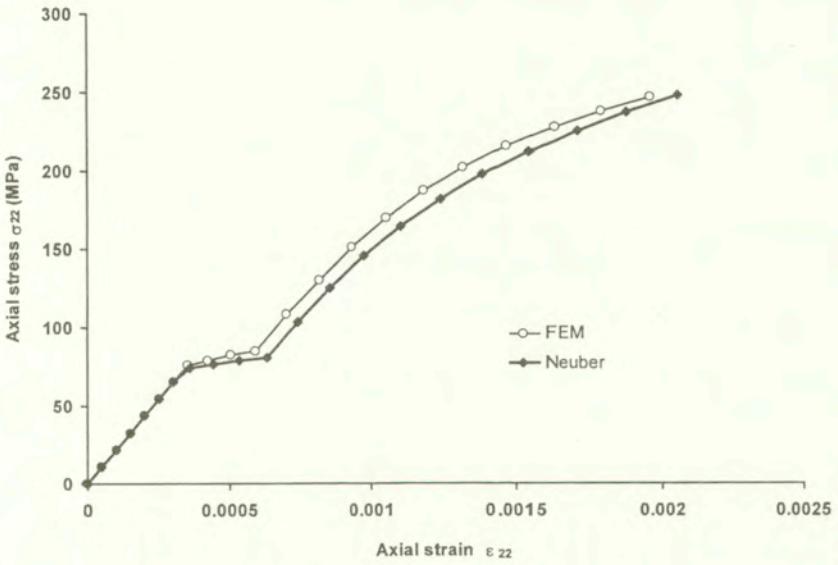

FIG. 7. The axial stress and strain, σ_{22} and ε_{22}, at the notch tip, generated by the monotonic non-proportional loading path.

In order to predict the notch tip stress-strain response of a notched component subjected to multiaxial cyclic loading, the incremental equations discussed above have to be linked with the cyclic plasticity model as described in Ref. [9]. The MRÓZ [10] model modified by GARUD [11] was used with the incremental Neuber model discussed above. The analysis was carried out for a constant amplitude multiaxial proportional cyclic loading history shown in Fig. 9. The loading history is represented by the excursions of three pseudo-elastic stress components. The maximum and minimum stress values were 285.9 and -85.77 MPa for the axial stress σ^e_{22}, 62.30 and -18.69 MPa for the hoop stress σ^e_{33}, and 195.18 and -58.55 MPa for the shear stress σ^e_{23}.

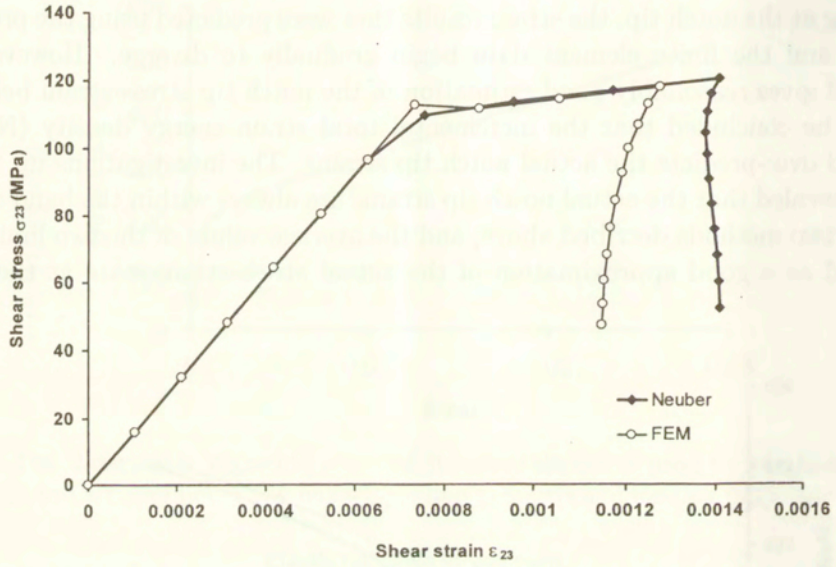

FIG. 8. The shear stress and strain, σ_{23} and ε_{23}, at the notch tip, generated by the monotonic non-proportional loading path.

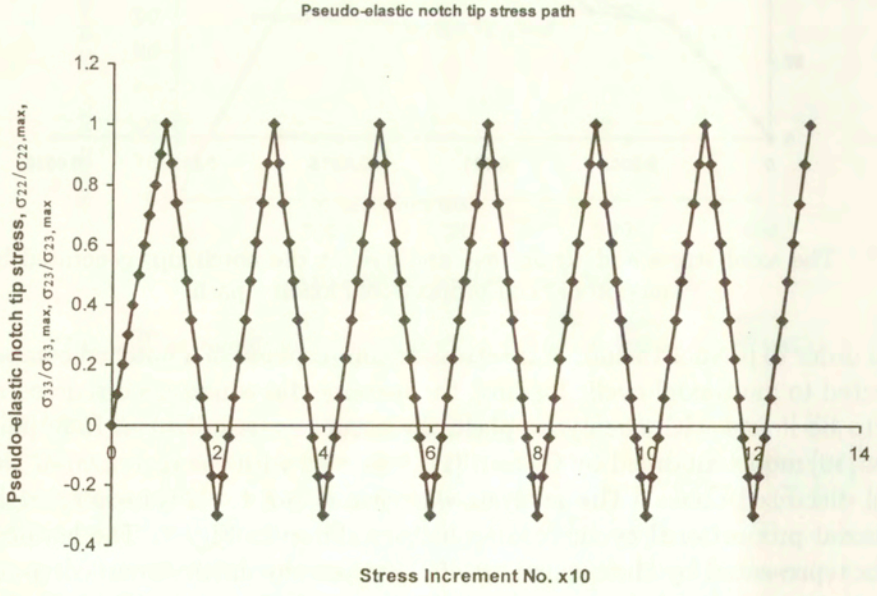

FIG. 9. The multiaxial cyclic loading history.

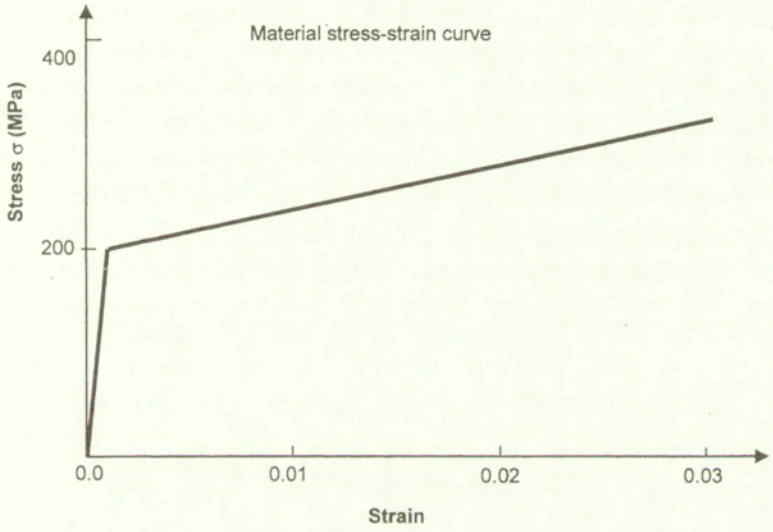

FIG. 10. The two linear segments material stress-strain curve used for the analysis of strain and stresses under the multiaxial cyclic loading path.

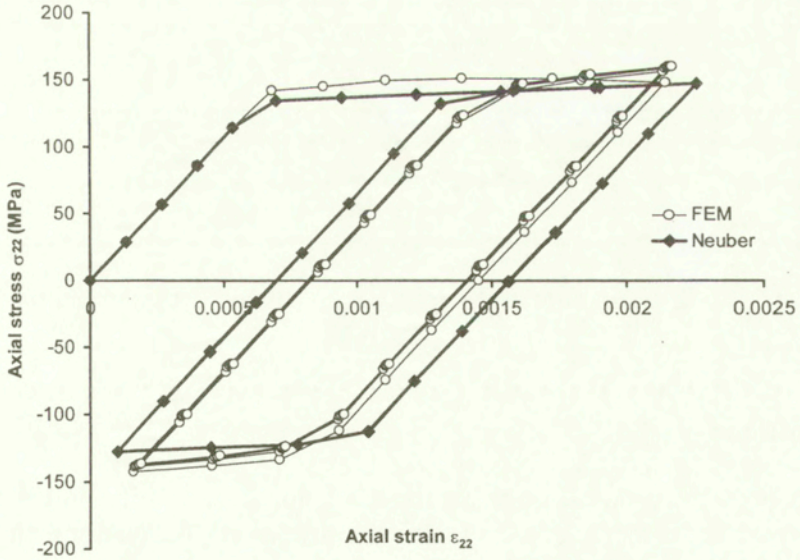

FIG. 11. The axial stress and strain, σ_{22} and ε_{22}, induced by the multiaxial cyclic loading path.

The material stress-strain curve was that one composed of two linear segments (Fig. 10) defined by $\varepsilon - \sigma$ coordinates of the transition points, i.e. $0 - 0$, $0.001 - 200$ MPa and $0.06135 - 450$ MPa. The elastic constants were the same as previously. The elastic-plastic notch tip strain-stress histories are shown in Figs. 11 and 12. It can be noticed that both the axial and the shear strain were over-predicted by the Neuber-based approach, similarly to many previous reports concerning the Neuber rule. However, the over-prediction might be acceptable in many practical applications, where the time available for the analysis is limited. It is worth mentioning that the ABAQUS program required 30 hours CPU time while the total strain energy density-based calculations were completed within a fraction of a second for the same number of load increments run on the same computer.

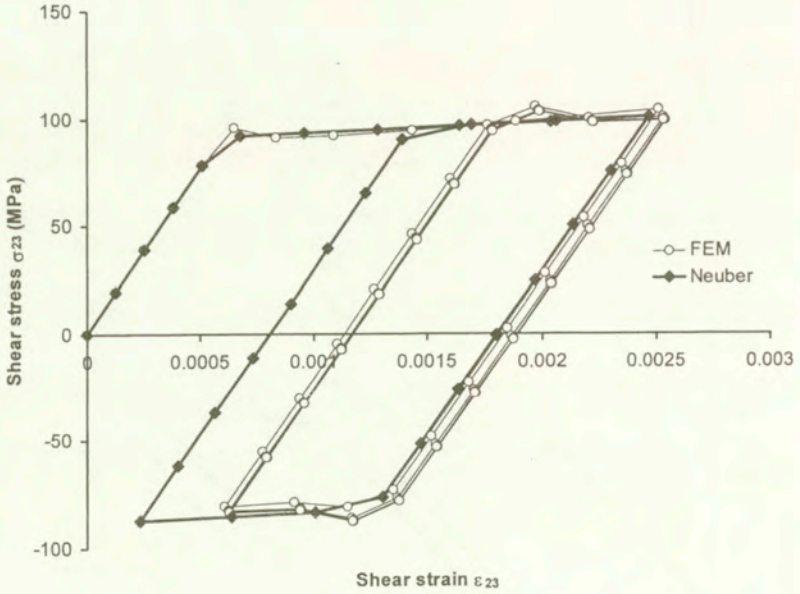

FIG. 12. The shear stress and strain, σ_{23} and ε_{23}, induced by the multiaxial cyclic loading path.

9. Conclusions

Two methods for calculating elastic-plastic notch tip strains and stresses induced by multiaxial loading paths have been proposed. The methods have been formulated using both the total strain energy density and the strain energy density relationships. It has been found that the generalized Neuber's rule, which represents the equality of the total strain energy density at the notch tip, gives an upper bound estimate for the elastic-plastic notch tip strains. The method

has been verified by comparison with the finite element data obtained for non-proportional loading path and nonlinear stress-strain material model. The accuracy of the proposed method was satisfactory, particularly where the notch tip stresses are of primary importance.

The calculated notch tip strains and stresses can be subsequently used for estimating the fatigue damage and life prediction for multiaxial cyclic loading histories.

References

1. H. NEUBER, *Theory of stress concentration shear strained prismatic bodies with arbitrary non-linear stress-strain law*, ASME Journal of Applied Mechanics, **28**, 544–550, 1961.
2. K. MOLSKI and G. GLINKA, *A method of elastic-plastic stress and strain calculation at a notch root*, Material Science and Engineering, **50**, 93–100, 1981.
3. A. MOFTAKHAR, A. BUCZYNSKI and G. GLINKA, *Calculation of elasto-plastic strains and stresses in notches under multiaxial loading*, International Journal of Fracture, **70**, 357–373, 1995.
4. M. N. K. SINGH, G. GLINKA and R. N. DUBEY, *Elastic-plastic stress-strain calculation in notched bodies subjected to non-proportional loading*, International Journal of Fracture, **76**, 1, 39–60, 1996.
5. T. SEEGER and M. HOFFMAN, *The use of Hencky's equations for the estimation of multiaxial elastic-plastic notch stresses and strains*, Report No. FB-3/1986, Technische Hochschule Darmstadt Germany 1986.
6. M. E. BARKEY, D. F. SOCIE and K. J. HSIA, *A yield surface approach to the estimation of notch strains for proportional and non-proportional cyclic loading*, ASME Journal of Engineering Materials and Technology, **116**, 173–180, 1994.
7. A. A. MOFTAKHAR, *Calculation of time-independent and time-dependent strains and stresses in notches*, Doctoral Dissertation, University of Waterloo, Department of Mechanical Engineering, Waterloo, Ontario, Canada 1994.
8. C.-C. CHU, *Incremental multiaxial neuber correction for fatigue analysis*, International Congress and Exposition, SAE Technical Paper No. 950705, Detroit 1995.
9. N. K. SINGH, A. BUCZYNSKI and G. GLINKA, *Notch stress-strain analysis and life prediction in multiaxial fatigue*, Proceedings of the Int. Conference on 'Fatigue Design 95', G. MARQUIS *et al.* [Eds.], Sept. 5-8, Helsinki 1995.
10. Z. MRÓZ, *On the Description of Anisotropic Workhardening*, Journal of Mechanics and Physics of Solids, **15**, 163–175, 1967.
11. Y. S. GARUD, *A new approach to the evaluation of fatigue under multiaxial loading*, Journal of Engineering Materials and Technology, ASME, **103**, 118–125, 1981.

Received February 24, 2000; revised version July 5, 2000.

Arch. Mech., **52**, 4–5, pp. 609–628, Warszawa 2000

Time-dependent elastoplastic constitutive equation

Dedicated to Professor Zenon Mróz on the occasion of his 70^{th} birthday

K. HASHIGUCHI

Dept. Agr. Eng., Kyushu University, Fukuoka, Japan

VARIOUS EXISTING CONSTITUTIVE equations aiming at the description of the time-dependent deformation behavior for a wide range of stress below and over the elastic limit, i.e. the yield stress, are reviewed in detail. It is suggested that the plastic stretching and the creep stretching have to be treated as independent quantities since they have substantially different physical properties, and that a stress goes out from the yield surface at a high rate of deformation since a plastic deformation is suppressed by a high viscous resistance, and then the yield surface is kept unchanged. The *subloading surface model* [1 – 3] would satisfy these requirements since it does not premise that a stress is on the yield surface even in the plastic loading process. In this article, based on the extended subloading surface model [4] which is capable of describing not only monotonic but also cyclic loading behavior, the generalized time-dependent elastoplastic constitutive equation is formulated allowing the stress go out from the yield surface by letting the plastic deformation be suppressed at a high rate of deformation and introducing the creep stretching which proceeds with time in addition to the elastic and the plastic stretching.

1. Introduction

DEFORMATION OF MATERIALS depends on a rate of deformation, i. e. time in general, and thus the description for the time-dependent deformation behavior is of importance for the analysis of practical problems in engineering. The *viscoelastic model* is applicable to the description of deformation behavior of materials at a low stress level but inapplicable to that at a stress level higher than the elastic limit, i.e. the yield stress. Then, various constitutive equations aiming at describing the time-dependent deformation behavior for a wide range of stress from the low stress level below the yield stress to the high stress level over the yield stress have been proposed. In this article they are first reviewed in detail, and then it is revealed that a satisfactory one capable of describing the time-dependent behavior of materials for any stress has not been proposed up to the present.

It should be noted that a plastic deformation based on the mutual slip between microstructures is suppressed under a deformation at a high rate causing the increase of viscous resistance acting between microstructures. Therefore, when a large deformation is induced at a high rate, the stress would go out from the yield surface since the deformation proceeds elastically, the plastic deformation being suppressed by the increase of viscous resistance, and thus the yield surface being kept unchanged. The *subloading surface model* [1 – 4] does not premise that the stress is on the *normal-yield surface* (conventional yield surface) even in the plastic loading process. In this model the subloading surface is introduced, which passes always through the current stress point even if the stress exists inside the normal-yield surface and is similar to the normal-yield surface, and it is assumed that the subloading surface approaches to the normal-yield surface in the plastic loading process. Based on this assumption, the extended consistency condition for the subloading surface is formulated, and applying the associated flow rule to the consistency condition, the plastic stretching induced by the rate of stress on or inside the normal-yield surface is formulated so as to describe the smooth *elastic-plastic transition*. It fulfills the *continuity condition* and the *smoothness condition* which are the mechanical requirements for constitutive equations [5 – 7].

The author [8] extended the initial subloading surface model [1 – 3] with the isotropic hardening so as to describe the time-dependence, while this model is limited to the description of monotonic loading behavior since the similarity-center of the normal-yield and the subloading surfaces is fixed in the origin of the stress space. Besides, based on it, the time-dependent elastoplastic constitutive equation of soils was formulated and its ability to reproduce the time-dependent behavior of real soils was verified. However, the initial subloading surface model is not capable of describing the cyclic loading behavior, in which the similarity-center of the normal-yield and the subloading surfaces are fixed in the origin of stress space. On the other hand, the extended subloading surface model [4] with the translation of the similarity-center due to the plastic deformation would be the only model capable of describing not only monotonic but also cyclic loading behavior pertinently among the existing models as was reviewed in detail in the previous article [6]. In this article, the extended subloading surface model is extended so as to describe the time-dependent deformation behavior by allowing the subloading surface to become larger than the normal-yield surface, and introducing the creep stretching which proceeds with time. That is, the generalized formulation of the time-dependent subloading surface model is given in this article. It falls within the framework of the elastoplastic-creep constitutive equation. Further, based on it, the constitutive equation of metals with the isotropic-kinematic hardening is formulated where the pertinent creep equation is formulated and its adequacy is verified by comparing it with experimental data.

2. Reviews on the existing time-dependent models

Various approaches for describing the time-dependent deformation behavior for a wide range of stress below and over the yield stress have been attempted in the past. They could be classified into the *elasto-viscoplastic model* and the *elastoplastic-creep model*. An inelastic stretching (i.e. the symmetric part of velocity gradient) is treated as a single quantity, called the *viscoplastic stretching*, in the elasto-viscoplastic model. On the other hand, it is decomposed into the *plastic stretching* and the *creep stretching* in the elastoplastic-creep model. Therefore, the elasto-viscoplastic and the elastoplastic-creep models are often called the *unified model* and the *superposition model*, respectively, by the other names. Besides, the elasto-viscoplastic model could be further classified into the *over-stress model* of PERZYNA [9 – 11] and the nonstationary flow surface model of OLSZAK and PERZYNA [12, 13].

2.1. Elasto-viscoplastic model (unified model)

The deformation can be classified into the reversible, i.e. elastic one with the *loading-path independence* and the irreversible, i.e. inelastic one without the *loading path-independence*. The latter can be classified further into the plastic and the creep (viscous) deformation. Here, it should be noted that the plastic stretching does not proceed always, being dependent on the direction of stress rate or stretching, but the creep stretching proceeds always with an elapse of time as illustrated in Fig. 1 for the decrease of stress under the stress control condition. Thus, the switching condition whether or not a stretching is generated, i.e. the *loading criterion* is required for the plastic stretching but is not required for the creep stretching. Therefore, the plastic stretching and the creep stretching have to be formulated as independent quantities different from each other contrary to the unified model, i.e. the elasto-viscoplastic model. Thus, it should be concluded that the unified model has the fundamental importance in the mechanical framework itself. However, let the basic properties of the over-stress and the nonstationary flow surface models in the unified model be further examined in detail below.

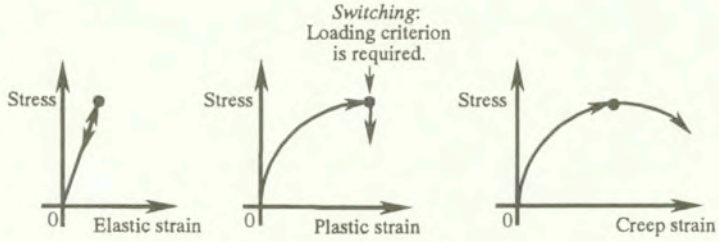

FIG. 1. The responses of the elastic, creep and plastic deformation to the decrease of stress under the stress control conditions.

2.1.1. Over-stress model. HOHENEMSER and PRAGER [14] have extended the BINGHAM'S [15] one-dimensional elasto-viscoplastic model to the three-dimensional stress state by replacing the slider with the J_2-yield condition and incorporating the potential flow rule, while the Bingham model is the modification of the Maxwell's viscoelastic model by replacing the dashpot with the parallel combination of the dashpot and the slider as the threshold for the inception of the movement of the dashpot. The *over-stress model* [9 – 11] can be regarded as the generalization of the HOHENEMSER and PRAGER'S [14] or more explicitly the PRAGER'S [16] elasto-viscoplastic model by replacing the J_2-yield condition with the general yield condition. It has the following basic structure.

i) The viscoplastic stretching is not related to the stress rate but to the stress, while it is related to the stress rate in the elastoplasticity. Thus, both the direction and the magnitude of viscoplastic stretching are independent of the stress rate but dependent of only the state of stress. This is the basic property of the Newtonian (viscous) fluid, while the viscoplastic stretching can be regarded as the viscous stretching with the threshold given by the yield condition. On the other hand, the plastic stretching is related to the stress rate in the elastoplasticity where the direction of the plastic stretching depends on the state of stress but the magnitude depends on the rate of stress.

ii) A loading criterion in terms of stress rate or stretching is not imposed to the viscoplastic stretching.

iii) The viscoplastic stretching is induced only when a stress is outside the yield surface.

Therefore, the Bingham model and the over-stress model are substantially different from the elastoplasticity. Needless to say, the over-stress model cannot reduce to the elastoplastic constitutive equation at any rate of deformation.

Thus, the over-stress model is incapable of describing

1) the plastic stretching which requires the loading criterion, while the creep stretching can be described, and

2) the inelastic deformation when a stress is on or inside the yield surface, contrary to the fact that the time-dependent behavior is generated independently of the yield condition, and thus the stress relaxation and the creep deformation cannot be predicted satisfactorily (for instance, the creep and the relaxation after a stress decreased to the interior of the yield surface by a quick unloading cannot be described).

The Bingham model and the over-stress model may be regarded as the modification of the Maxwell model by limiting the creep (viscous) stretching so as to be not generated in a low stress level below the yield stress (cf. Fig. 2). In order to cover the above defect 2), an unrealistically small yield surface is often used. This treatment results in the fact that the mechanical response reduces to

the viscoelastic behavior of the Maxwell model incapable of describing a plastic deformation, however.

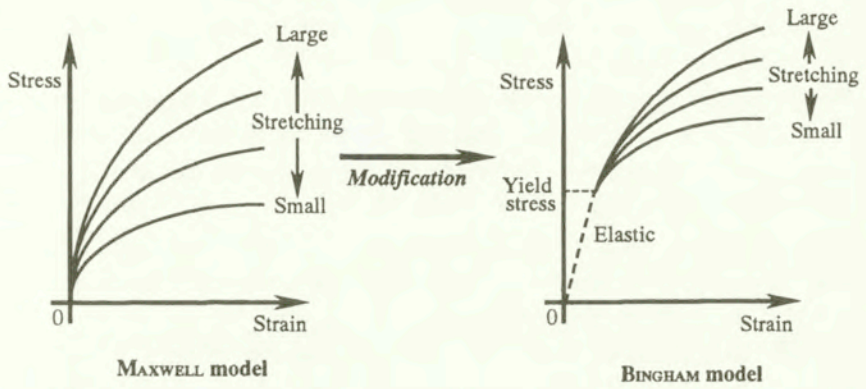

FIG. 2. The deterioration of the Maxwell viscoelastic model by BINGHAM [15].

The over-stress model could be applied to the description of the deformation of metals at high temperature, wet clays, etc. in the state of stress over the yield stress, in which creep deformation is dominant. However, the deformation of metals at room temperature, dry sands [17], etc. in which plastic deformation is dominant, cannot be described satisfactorily by this model.

2.1.2. Nonstationary flow surface model. This model [12, 13] has the following basic structure.

i) The nonstationary flow surface is incorporated, which is extended from the yield surface so as to depend on time by modifying it to include the variable describing a time-dependent alteration of the yielding property of material, in addition to the stress and internal variables, premising that viscoplastic deformation proceeds only when a stress exists on the nonstationary flow surface. Here, it should be noted that any rate tensor of stress or deformation is not incorporated in the equation of the nonstationary flow surface.

ii) The viscoplastic stretching is derived by applying the associated flow rule to the consistency condition obtained by the time-differentiation of the nonstationary flow surface. Therefore, the magnitude of the viscoplastic stretching depends on the stress rate, whilst the magnitude of the creep stretching depends on the state of stress. The stiffness tensor which relates the stretching to the stress rate is dependent of state variables, i.e. the stress, internal variables and time, but independent of any rate variable.

Therefore, this model is incapable of describing

1) the creep stretching the magnitude of which is independent of the stress rate,

2) the inelastic deformation when a stress exists inside the nonstationary flow surface and thus the stress relaxation and the creep deformation cannot be described satisfactorily (for instance, the creep and the relaxation after a stress decreased into the interior of the nonstationary flow surface by a quick unloading cannot be described), and

3) the prompt response in the alteration of stiffness (modulus) due to the abrupt change of the rate of deformation, since the nonstationary flow surface is not influenced by the rate of deformation (for instance, an abrupt increase of stress rate, i.e. an abrupt rising of stress (an almost elastic response) induced by a prompt increase of stretching cannot be described realistically). Thus, the application of this model has to be limited to the monotonic loading without a large variation of the rate of deformation.

Eventually, it should be concluded that the unified model, i.e. the elasto-viscoplastic model, is incapable of describing the time-dependent deformation behavior in the general state of stress.

2.2. Elastoplastic-creep model (superposition model)

The *elastoplastic-creep model* assumes that the stretching is additively decomposed into the elastic, the plastic and further the creep stretchings. That is, the plastic stretching and the creep stretching are formulated as independent quantities different from each other. Therefore, the fundamental defects involved in the elasto-viscoplastic model can be avoided in the elastoplastic-creep model. However, the existing models (cf. e.g. [18 – 20]) in the framework of the elastoplastic-creep model are incapable of describing the deformation behavior at a high rate realistically, since they are not taken account of the fundamental fact that a plastic deformation is suppressed with the increase of rate of deformation.

3. Time-dependent subloading surface model

The subloading surface model will be extended so as to describe time-dependent deformation behavior in the framework of the elastoplastic-creep model in this section.

3.1. Decomposition of stretching

A solid material is the assembly of solid particles, e.g. crystals in metals and soil particles in soils. Thus, the macroscopic deformation of solid materials consists of the deformations of each solid particle itself and the mutual slips between the solid particles. The deformations of each solid particle itself, exhibiting stiff and reversible characteristics, lead macroscopically to the elastic deformation ex-

hibiting the loading path-independence at usual stress level. On the other hand, the mutual slips between the solid particles or irreversible rearrangements within them (e.g. dislocation movement) lead macroscopically to the irreversible deformation exhibiting the loading path-dependence. Then, let the stretching $\mathbf{D}$ be additively decomposed into the elastic stretching $\mathbf{D}^e$ and the inelastic stretching $\mathbf{D}^i$, i.e.

$$\mathbf{D} = \mathbf{D}^e + \mathbf{D}^i, \tag{3.1}$$

where the elastic stretching $\mathbf{D}^e$ is given by

$$\mathbf{D}^e = \mathbf{E}^{-1} \overset{\circ}{\boldsymbol{\sigma}}. \tag{3.2}$$

$\boldsymbol{\sigma}$ is a stress, $(^\circ)$ indicates the proper corotational rate with the objectivity [21, 22] and the fourth-order tensor $\mathbf{E}$ is the elastic modulus given in Hooke's type as

$$E_{ijkl} = \left(K - \frac{2}{3}G\right)\delta_{ij}\delta_{kl} + G(\delta_{ik}\delta_{jl} + \delta_{il}\delta_{jk}), \tag{3.3}$$

where K and G are the bulk and the shear modulus, respectively, which are functions of stress and internal state variables in general and δ_{ij} is the Kronecker's delta, i.e. $\delta_{ij} = 1$ for $i = j$ and $\delta_{ij} = 0$ for $i \neq j$.

The mutual slips are induced by overcoming the frictional resistance and thus the macroscopic deformation due to the mutual slips has been described as the plastic deformation. Now, consider the situation that there exists a viscous medium between solid particles. The mutual slips are induced not only by overcoming the frictional resistance leading macroscopically to the plastic deformation but also with the elapse of time leading macroscopically to the creep deformation. Here, note that the creep deformation proceeds always with the elapse of time but the plastic deformation ceases when the stress becomes lower than the frictional resistance exhibiting the frictional switching, i.e. requiring the loading criterion. Therefore, the plastic and the creep deformation have to be described as independent quantities of each other. Thus, let the inelastic stretching be additively decomposed into the plastic stretching $\mathbf{D}^p$ and the creep stretching $\mathbf{D}^c$, i.e.

$$\mathbf{D}^i = \mathbf{D}^p + \mathbf{D}^c. \tag{3.4}$$

Here, note that the plastic deformation is suppressed with the increase of the deformation rate causing the viscous resistance, and that the stress can go out from the yield surface since at a high rate of deformation the elastic deformation

proceeds, whilst a plastic deformation is hardly induced and the yield surface is kept unchanged.

3.2. Normal-yield and subloading surfaces

Assume the yield condition:

$$f(\hat{\boldsymbol{\sigma}}, \mathbf{H}) = F(H), \tag{3.5}$$

where

$$\hat{\boldsymbol{\sigma}} \equiv \boldsymbol{\sigma} - \boldsymbol{\alpha}. \tag{3.6}$$

The second-order tensor $\boldsymbol{\alpha}$ is the reference point on or inside the yield surface, which plays the role of the kinematic hardening variable as it translates with the plastic deformation. The scalar H and the second-order tensor $\mathbf{H}$ are isotropic and anisotropic hardening variables, respectively. Let it be assumed that the function f is homogeneous of degree one in the tensor $\hat{\boldsymbol{\sigma}}$, satisfying $f(s\hat{\boldsymbol{\sigma}}) = sf(\hat{\boldsymbol{\sigma}})$ for any nonnegative scalar s. Then, if $\mathbf{H} = \text{const}$, the yield surface presents its similarity. An example of $\mathbf{H}$ is the rotational hardening variable for soils [23], while the kinematic hardening is not applicable to soils since the yield surface for soils always involves the origin of stress space.

Hereinafter, the elastoplastic constitutive equation will be formulated in the framework of the *unconventional plasticity* defined by DRUCKER [24] as the *extended plasticity theory* such that the interior of the yield surface is not a purely elastic domain but a plastic deformation is induced by the rate of stress inside the yield surface. Thus, the conventional yield surface is renamed as the *normal-yield surface*, since its interior is not regarded as a purely elastic domain in the present model.

Now, let the *subloading surface* [4] be introduced. This surface always passes through the current stress point $\boldsymbol{\sigma}$ and keeps the similar shape and the positioning of similarity to the normal-yield surface.

The similarity and the positioning of similarity require the followings.

i) All lines connecting the point on or within the subloading surface and the *conjugate point* on the normal-yield surface join at the specified point, i.e. the *similarity-center* s.

ii) The *ratio* of length of an arbitrary line-element connecting two points on or inside the subloading surface and that of an arbitrary conjugate line-element connecting two *conjugate points* on or inside the normal-yield surface has the same value, called the *similarity-ratio*, denoted as R, which is also the same as the ratio of sizes of these surfaces.

Here, note that the similarity-center has to lie inside both the normal-yield and subloading surfaces, since these surfaces are not allowed to intersect to each other, whilst the subloading surface plays the role of loading surface.

The approaching degree to the normal-yield state can be described by the ratio of the size of the subloading surface to that of the normal-yield surface, i.e. the similarity-ratio R of these surfaces. The similarity-ratio will be denoted as R, while $R = 0$ corresponds to the most elastic state in which the stress coincides with the similarity-center, and $R = 1$ to the normal-yield state in which the stress exists on the normal-yield surface. Then, it holds that

$$\boldsymbol{\sigma}_y = \frac{1}{R}\{\boldsymbol{\sigma} - (1-R)\mathbf{s}\} \qquad (\boldsymbol{\sigma} - \mathbf{s} = R(\boldsymbol{\sigma}_y - \mathbf{s})), \tag{3.7}$$

where $\boldsymbol{\sigma}_y$ on the normal-yield surface is the *conjugate stress* of the current stress $\boldsymbol{\sigma}$ on the subloading surface (see Fig. 3).

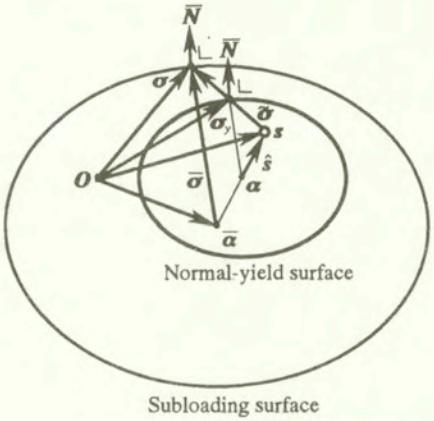

FIG. 3. The normal-yield and the subloading surfaces at a high rate of deformation.

By substituting Eq. (3.7) into Eq. (3.5) with replacing $\boldsymbol{\sigma}$ in Eq. (3.5) with $\boldsymbol{\sigma}_y$, the subloading surface is described as

$$f(\overline{\boldsymbol{\sigma}}, \mathbf{H}) = RF(H), \tag{3.8}$$

where

$$\overline{\boldsymbol{\sigma}} \equiv \boldsymbol{\sigma} - \overline{\boldsymbol{\alpha}}(= R(\boldsymbol{\sigma}_y - \boldsymbol{\alpha})), \tag{3.9}$$

$$\overline{\boldsymbol{\sigma}} \equiv \mathbf{s} - R(\mathbf{s} - \boldsymbol{\alpha}) \quad (\overline{\boldsymbol{\alpha}} - \mathbf{s} = R(\boldsymbol{\alpha} - \mathbf{s})). \tag{3.10}$$

$\overline{\boldsymbol{\alpha}}$ on or inside the subloading surface is the conjugate point of $\boldsymbol{\alpha}$ on or inside the normal-yield surface. In calculation, first R is determined from Eq. (3.8)

with Eqs. (3.9) and (3.10), by substituting values of $\boldsymbol{\sigma}$, H, $\boldsymbol{\alpha}$, $\mathbf{H}$ and s, and thereafter $\overline{\boldsymbol{\alpha}}$ is found from Eq. (3.10). The four internal variables H, $\boldsymbol{\alpha}$, $\mathbf{H}$ and s are introduced in the present model.

The evolution of internal structure of materials is caused by the inelastic stretching $\mathbf{D}^i$, and thus the evolution equations of H, $\mathbf{H}$ and $\boldsymbol{\alpha}$ are homogeneous of degree one in $\mathbf{D}^i$. Here, assume that they are linear functions of $\mathbf{D}^i$, i.e.

$$\begin{aligned} \dot{H} &= \mathrm{tr}\{\mathbf{f}_h(\boldsymbol{\sigma}, H, \mathbf{H}, \boldsymbol{\alpha}, \mathrm{s})\mathbf{D}^i\}, \\ \overset{\circ}{\mathbf{H}} &= \mathbf{f}_H(\boldsymbol{\sigma}, H, \mathbf{H}, \boldsymbol{\alpha}, \mathrm{s})\mathbf{D}^i, \\ \overset{\circ}{\boldsymbol{\alpha}} &= \mathbf{f}_\alpha(\boldsymbol{\sigma}, H, \mathbf{H}, \boldsymbol{\alpha}, \mathrm{s})\mathbf{D}^i, \end{aligned} \tag{3.11}$$

$(\cdot)$ standing for the material time-derivative. Thus they can be additively decomposed into the plastic parts $\dot{H}^p$, $\overset{\circ}{\mathbf{H}}{}^p$, and $\overset{\circ}{\boldsymbol{\alpha}}{}^p$ and the creep parts $\dot{H}^c$, $\overset{\circ}{\mathbf{H}}{}^c$ and $\overset{\circ}{\boldsymbol{\alpha}}{}^c$ by Eq. (3.4) of decomposition of the inelastic stretching.

3.3. Evolution of similarity-ratio

It is observed from experiments that the stress asymptotically approaches the normal-yield surface in the plastic loading process $\mathbf{D}^p \neq \mathbf{0}$, and it has to be postulated as it was described in the foregoing that the plastic deformation is suppressed with the increase of the deformation rate causing the viscous resistance. The stress can go out from the normal-yield surface since at a high rate of deformation, the elastic deformation proceeds without a plastic deformation causing a variation of the normal-yield surface. Therefore, the subloading surface can expand over the normal-yield surface. Thus, let the following evolution equation of the similarity-ratio R be assumed.

$$\dot{R} = U^t \|\mathbf{D}^p\| \quad \text{for} \quad \mathbf{D}^p \neq \mathbf{0}, \tag{3.12}$$

where U^t is additively composed of the monotonically decreasing function U_R of the similarity-ratio R and the monotonically increasing function $U_D(\geq 0)$ of the magnitude $\|\mathbf{D}\|$ of stretching, i.e.

$$U^t = U_R(R) + U_D(\|\mathbf{D}\|), \tag{3.13}$$

satisfying

$$\begin{aligned} U_R &= +\infty \quad \text{for } R = 0, \\ U_R &= 0 \quad \text{for } R = 1, \\ (U_R &< 0 \quad \text{for } R > 1) \end{aligned} \tag{3.14}$$

and

$$U_D = 0 \quad \text{for } \|\mathbf{D}\| = 0. \tag{3.15}$$

$\|\ \|$ stands for the magnitude, i.e. $\|\mathbf{T}\| = \sqrt{\mathrm{tr}(\mathbf{T}\mathbf{T}^T)}$ for arbitrary tensor $\mathbf{T}$, $\mathrm{tr}(\,)$ denoting the trace and $(\ )^T$ the transpose. Note that $\dot{R} = 0$ for $R = 1$ if $\|\mathbf{D}\| = 0$ but $\dot{R} > 0$ even for $R = 1$ if $\|\mathbf{D}\| > 0$. The function U^t is illustrated in Fig. 4.

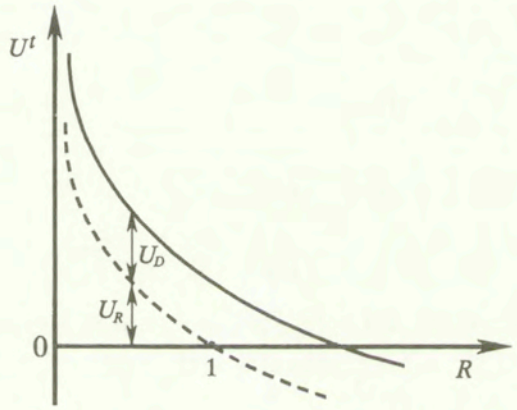

FIG. 4. The function U^t in the evolution rule of the similarity-ratio R.

3.4. The translation rule of similarity-center

The *similarity-center* $\mathbf{s}$ is required to translate with the plastic deformation in order to describe realistically the cyclic loading behavior exhibiting the Masing effect [6, 25, 26]. The translation rule of $\mathbf{s}$ is described below.

The following inequality must hold since the similarity-center $\mathbf{s}$ has to exist inside the normal-yield surface.

$$f(\hat{\mathbf{s}}, \mathbf{H}) \leq F(H), \tag{3.16}$$

where

$$\hat{\mathbf{s}} \equiv \mathbf{s} - \boldsymbol{\alpha}. \tag{3.17}$$

Let the ultimate state $f(\hat{\mathbf{s}}, \mathbf{H}) = F(H)$ be considered, in which the similarity-center just exists on the normal-yield surface, and thus the risk that the similarity-center goes out from the normal-yield surface has to be avoided. The time-differentiation of Eq. (3.16) in the ultimate state gives:

$$\mathrm{tr}\left[\frac{\partial f(\hat{\mathbf{s}}, \mathbf{H})}{\partial \mathbf{s}}\left(\overset{\circ}{\hat{\mathbf{s}}} + \frac{1}{F}\left\{\mathrm{tr}\left(\frac{\partial f(\hat{\mathbf{s}}, \mathbf{H})}{\partial \mathbf{H}}\overset{\circ}{\mathbf{H}}\right) - \dot{F}\right\}\hat{\mathbf{s}}\right)\right] \leq 0 \tag{3.18}$$

$$\text{for} \quad (\hat{\mathbf{s}}, \mathbf{H}) = F(H).$$

The inequality (3.18) or (3.20) is called the *enclosing condition of similarity-center.*

In the ultimate state $f(\hat{\mathbf{s}}, \mathbf{H}) = F(H)$, the vector $\boldsymbol{\sigma}_y - \mathbf{s} (= (\boldsymbol{\sigma} - \mathbf{s})/R)$ makes an obtuse angle with the vector $\partial f(\hat{\mathbf{s}}, \mathbf{H})/\partial \mathbf{s}$ which is the outward normal to the surface, called the *similarity-center surface*, that passes through the similarity-center and is similar to the normal-yield surface, provided that the normal-yield surface is convex. Noting this fact and considering the fact that the similarity-center moves only with the plastic deformation, let the following equation be assumed so as to fulfill the inequality (3.18):

$$\overset{\circ}{\hat{\mathbf{s}}} + \frac{1}{F}\left\{\mathrm{tr}\left(\frac{\partial f(\hat{\mathbf{s}}, \mathbf{H})}{\partial \mathbf{H}}\right) - \dot{F}\right\}\hat{\mathbf{s}} = c\,\mathrm{tr}(\overline{\mathbf{N}}\mathbf{D}^i)\frac{\tilde{\boldsymbol{\sigma}}}{R}, \tag{3.19}$$

provided that the inelastic stretchig $\mathbf{D}^i$ satisfies

$$\mathrm{tr}(\overline{\mathbf{N}}\mathbf{D}^i) \geq 0 \tag{3.20}$$

in the ultimate state $f(\hat{\mathbf{s}}, \mathbf{H}) = F(H)$, where c is a material constant influencing the translating rate of the similarity-center and

$$\tilde{\boldsymbol{\sigma}} \equiv \boldsymbol{\sigma} - \mathbf{s}, \tag{3.21}$$

$$\overline{\mathbf{N}} \equiv \frac{\partial f(\overline{\boldsymbol{\sigma}}, \mathbf{H})}{\partial \boldsymbol{\sigma}} \Big/ \left\| \frac{\partial f(\overline{\boldsymbol{\sigma}}, \mathbf{H})}{\partial \boldsymbol{\sigma}} \right\| \quad (\|\overline{\mathbf{N}}\| = 1) \tag{3.22}$$

which is the outward-normal of the subloading surface. The translation rule of the similarity-center is now derived from Eq. (3.19) as follows:

$$\overset{\circ}{\mathbf{s}} = c\,\mathrm{tr}(\overline{\mathbf{N}}\mathbf{D}^i)\frac{\tilde{\boldsymbol{\sigma}}}{R} + \overset{\circ}{\boldsymbol{\alpha}} + \frac{1}{F}\left\{F'\dot{H} - \mathrm{tr}\left(\frac{\partial f(\hat{\mathbf{s}}, \mathbf{H})}{\partial \mathbf{H}}\overset{\circ}{\mathbf{H}}\right)\right\}\hat{\mathbf{s}}, \tag{3.23}$$

where

$$F' \equiv \frac{dF}{dH}. \tag{3.24}$$

It is conceivable that the similarity-center $\mathbf{s}$ approaches the current stress $\boldsymbol{\sigma}$ as can be seen from the simple case of the nonhardening state ($\overset{\circ}{\boldsymbol{\alpha}} = \overset{\circ}{\mathbf{H}} = \mathbf{0}, \dot{F} = 0$), although the evolution rule (3.23) is assumed to fulfill the requirement (3.18) in the ultimate state $f(\hat{\mathbf{s}}, \mathbf{H}) = F(H)$. Here, note that $\overset{\circ}{\mathbf{s}}$ can be additively decomposed into the plastic part $\overset{\circ}{\mathbf{s}}{}^p$ and the creep part $\overset{\circ}{\mathbf{s}}{}^c$ by the additive decomposition of $\mathbf{D}^i$, $\dot{H}$, $\overset{\circ}{\mathbf{H}}$ and $\overset{\circ}{\boldsymbol{\alpha}}$.

3.5. Plastic stretching

The time-differentiation of Eq. (3.8) is given by

$$\text{(3.25)} \qquad \mathrm{tr}\left(\frac{\partial f(\overline{\sigma},\mathbf{H})}{\partial \boldsymbol{\sigma}} \overset{\circ}{\boldsymbol{\sigma}}\right) - \mathrm{tr}\left(\frac{\partial f(\overline{\sigma},\mathbf{H})}{\partial \boldsymbol{\sigma}} \overset{\circ}{\overline{\boldsymbol{\alpha}}}\right) + \mathrm{tr}\left(\frac{\partial f(\overline{\sigma},\mathbf{H})}{\partial \boldsymbol{\sigma}} \overset{\circ}{\mathbf{H}}\right) = \dot{R}F + RF'\dot{H}.$$

By substituting Eq. (3.12) into Eq. (3.28) one has the *extended consistency condition* for the subloading surface:

$$\text{(3.26)} \qquad \mathrm{tr}\left(\frac{\partial f(\overline{\sigma},\mathbf{H})}{\partial \boldsymbol{\sigma}} \overset{\circ}{\boldsymbol{\sigma}}\right) - \mathrm{tr}\left(\frac{\partial f(\overline{\sigma},\mathbf{H})}{\partial \boldsymbol{\sigma}} \overset{\circ}{\overline{\boldsymbol{\sigma}}}\right) + \mathrm{tr}\left(\frac{\partial f(\overline{\sigma},\mathbf{H})}{\partial \boldsymbol{\sigma}} \overset{\circ}{\mathbf{H}}\right) = U^t\|\mathbf{D}^p\|F + RF'\dot{H},$$

where

$$\text{(3.27)} \qquad \overset{\circ}{\overline{\boldsymbol{\alpha}}} = R\overset{\circ}{\boldsymbol{\alpha}} + (1-R)\overset{\circ}{\mathbf{s}} - U^t\|\mathbf{D}^p\|\hat{\mathbf{s}}$$

from Eqs. (3.10) and (3.12). $\overset{\circ}{\overline{\boldsymbol{\alpha}}}$ can be additively decomposed into the plastic part $\overset{\circ}{\overline{\boldsymbol{\alpha}}}^p$ and the creep part $\overset{\circ}{\overline{\boldsymbol{\alpha}}}^c$ by the additive decomposition of $\overset{\circ}{\boldsymbol{\alpha}}$ and $\overset{\circ}{\mathbf{s}}$.

Now assume the *associated flow rule*

$$\text{(3.28)} \qquad \mathbf{D}^p = \lambda\overline{\mathbf{N}} \quad (\lambda > 0),$$

where λ is the positive proportionality factor. Substitution of Eq. (3.28) into the extended consistency condition (3.26) leads to

$$\text{(3.29)} \qquad \lambda = \frac{\mathrm{tr}(\overline{\mathbf{N}}\overset{\circ}{\boldsymbol{\sigma}}) - \mathrm{tr}(\overline{\mathbf{N}}\overset{\circ}{\overline{\boldsymbol{\alpha}}}^c) - \left\{\frac{F'}{F}\dot{H}^c - \frac{1}{RF}\mathrm{tr}\left(\frac{\partial f(\overline{\sigma},\mathbf{H})}{\partial \boldsymbol{\sigma}}\overset{\circ}{\mathbf{H}}^c\right)\right\}\mathrm{tr}(\overline{\mathbf{N}}\overline{\boldsymbol{\sigma}})}{\overline{M}_p^t},$$

where

$$\text{(3.30)} \qquad \overline{M}_p^t \equiv \mathrm{tr}\left[\overline{\mathbf{N}}\left(\left\{\frac{F'}{F}h^p - \frac{1}{RF}\mathrm{tr}\left(\frac{\partial f(\overline{\sigma},\mathbf{H})}{\partial \mathbf{H}}\mathbf{h}^p\right) + \frac{U^t}{R}\right\}\overline{\boldsymbol{\sigma}} + \overline{\mathbf{a}}^p\right)\right].$$

h^p, $\mathbf{h}^p$ and $\overline{\mathbf{a}}^p$ are functions of the stress, plastic internal state variables and $\overline{\mathbf{N}}$ of homogeneous degree one, while these functions are related to the plastic parts $\dot{H}^p$, $\overset{\circ}{\mathbf{H}}^p$ and $\overset{\circ}{\overline{\boldsymbol{\alpha}}}^p$ of the internal variables $\dot{H}$, $\overset{\circ}{\mathbf{H}}$ and $\overset{\circ}{\overline{\boldsymbol{\alpha}}}$ by

$$\text{(3.31)} \qquad h^p \equiv \frac{\dot{H}^p}{\lambda}, \quad \mathbf{h}^p \equiv \frac{\overset{\circ}{\mathbf{H}}^p}{\lambda},$$

$$\overline{\mathbf{a}}^p \equiv \frac{\overset{\circ}{\overline{\boldsymbol{\alpha}}}^p}{\lambda} = R\mathbf{a}^p + (1-R)\mathbf{z}^p - U^t\hat{\mathbf{s}}, \tag{3.32}$$

$$\mathbf{a}^p \equiv \frac{\overset{\circ}{\boldsymbol{\alpha}}^p}{\lambda}, \tag{3.33}$$

$$\mathbf{z}^p \equiv \frac{\overset{\circ}{\mathbf{s}}^p}{\lambda} = c\tilde{\boldsymbol{\sigma}} + \mathbf{a}^p + \frac{1}{F}\left\{F'h^p - \mathrm{tr}\left(\frac{\partial f(\hat{\mathbf{s}},\mathbf{H})}{\partial \mathbf{H}}\mathbf{h}^p\right)\right\}\hat{\mathbf{s}} \tag{3.34}$$

since these rate variables include λ in homogeneous degree one.

The stretching is given from Eqs. (3.1), (3.2), (3.4), (3.28) and (3.29) as

$$\mathbf{D} = \mathbf{E}^{-1}\overset{\circ}{\boldsymbol{\sigma}} + \frac{\mathrm{tr}(\overline{\mathbf{N}}\overset{\circ}{\boldsymbol{\sigma}}) - \mathrm{tr}(\overline{\mathbf{N}}\overset{\circ}{\overline{\boldsymbol{\alpha}}}^c) - \left\{\frac{F'}{F}\dot{H}^c - \frac{1}{RF}\mathrm{tr}\left(\frac{\partial f(\overline{\boldsymbol{\sigma}},\mathbf{H})}{\partial\boldsymbol{\sigma}}\overset{\circ}{\mathbf{H}}^c\right)\right\}\mathrm{tr}(\overline{\mathbf{N}}\overline{\boldsymbol{\sigma}})}{\overline{\mathbf{M}}_p^t}\mathbf{N} + \mathbf{D}^c. \tag{3.35}$$

The positive proportionality factor in the associated flow rule (3.35) is expressed in terms of the stretching $\mathbf{D}$, replacing λ by Λ, as follows:

$$\Lambda = \frac{\mathrm{tr}(\overline{\mathbf{N}}\mathbf{E}\mathbf{D}) - \mathrm{tr}(\overline{\mathbf{N}}\overset{\circ}{\overline{\boldsymbol{\alpha}}}^c) - \left\{\frac{F'}{F}\dot{H}^c - \frac{1}{RF}\mathrm{tr}\left(\frac{\partial f(\overline{\boldsymbol{\sigma}},\mathbf{H})}{\partial\boldsymbol{\sigma}}\overset{\circ}{\mathbf{H}}^c\right)\right\}\mathrm{tr}(\overline{\mathbf{N}}\overline{\boldsymbol{\sigma}}) - \mathrm{tr}(\overline{\mathbf{N}}\mathbf{E}\mathbf{D}^c)}{\overline{M}_p^t + \mathrm{tr}(\overline{\mathbf{N}}\mathbf{E}\overline{\mathbf{N}})}. \tag{3.36}$$

The inverse expression of Eq. (3.35) is given from Eqs. (3.1), (3.2), (3.4), (3.28) and (3.36) as

$$\overset{\circ}{\boldsymbol{\sigma}} = \mathbf{E}\mathbf{D} - \frac{\mathrm{tr}(\overline{\mathbf{N}}\mathbf{E}\mathbf{D}) - \mathrm{tr}(\overline{\mathbf{N}}\overset{\circ}{\overline{\boldsymbol{\alpha}}}^c) - \left\{\frac{F'}{F}\dot{H}^c - \frac{1}{RF}\mathrm{tr}\left(\frac{\partial f(\overline{\boldsymbol{\sigma}},\mathbf{H})}{\partial\boldsymbol{\sigma}}\overset{\circ}{\mathbf{H}}^c\right)\right\}\mathrm{tr}(\overline{\mathbf{N}}\overline{\boldsymbol{\sigma}}) - \mathrm{tr}(\overline{\mathbf{N}}\mathbf{E}\mathbf{D}^c)}{\overline{M}_p^t + \mathrm{tr}(\overline{\mathbf{N}}\mathbf{E}\overline{\mathbf{N}})} \cdot \mathbf{E}\mathbf{N} - \mathbf{E}\mathbf{D}^c. \tag{3.37}$$

Note that the stretching $\mathbf{D}$ cannot be expressed analytically in terms of the stress rate $\overset{\circ}{\boldsymbol{\sigma}}$ since the right-hand side of Eq. (3.35) includes $\mathbf{D}$ but inversely, the stress rate $\overset{\circ}{\boldsymbol{\sigma}}$ is expressed analytically in terms of the stretching $\mathbf{D}$ as seen in Eq. (3.37). Besides, the constitutive equation (3.35) or (3.37) is of the so-called *rate-nonlinearity* since it includes the magnitude of stretching $\|\mathbf{D}\|$. The

rate-nonlinearity would be the basic property of the constitutive equation for time-dependent deformation for a wide range of stress below and over the yield stress in which the stiffness modulus depends on the rate of deformation.

3.6. Loading criterion

A loading criterion would not be necessary for the creep stretching since it proceeds always with the elapse of time. On the other hand, taking the fact that Λ has to be positive, let the following loading criterion for the plastic stretching be assumed [27].

$$\begin{aligned} &\mathbf{D}^p \neq \mathbf{0} : \Lambda > 0, \\ &\mathbf{D}^p = \mathbf{0} : \Lambda \leq 0. \end{aligned} \tag{3.38}$$

It should be noted that the constitutive equation formulated in the foregoing reduces to the time-independent subloading surface model when $\|\mathbf{D}\| \to 0$ and $\mathbf{D}^c = \mathbf{0}$. Here, note that the time-independent elastoplastic deformation would hold approximately in the case of the moderate rate of deformation for which the function U_D in the plastic modulus and the creep stretching are negligible.

4. Constitutive equation of metals

Based on the equations formulated in the preceding section, the constitutive equation for metals will be formulated in this section.

We adopt the subloading surface of the von Mises type with isotropic kinematic hardening [27], while the hardening variable $\sqrt{2/3}\|\mathbf{D}^p\|$ is extended so as to account for the hardening due to the creep deformation:

$$f(\overline{\boldsymbol{\sigma}}) = \sqrt{\frac{3}{2}}\|\overline{\boldsymbol{\sigma}}^*\| \quad (\mathbf{H} = \mathbf{0}), \tag{4.1}$$

$$\overset{\circ}{\boldsymbol{\alpha}} = \mathbf{a}\,\mathrm{tr}(\mathbf{N}\mathbf{D}^i)(= \mathbf{a}\|\mathbf{D}^i\|), \qquad \mathbf{a} \equiv k_1\frac{\overline{\boldsymbol{\sigma}}}{R} - k_2\boldsymbol{\alpha}, \tag{4.2}$$

$$F = F_0[1 + h_1\{1 - \exp(-h_2 H)\}], \tag{4.3}$$

$$\dot{H} = \sqrt{\frac{2}{3}}\mathrm{tr}(\overline{N}\mathbf{D}^i)\left(\dot{H}^p = \sqrt{\frac{2}{3}}\mathrm{tr}(\overline{\mathbf{N}}\mathbf{D}^p)\left(= \sqrt{\frac{2}{3}}\lambda = \sqrt{\frac{2}{3}}\|\mathbf{D}^p\|\right)\right. \tag{4.4}$$

$$\left.\dot{H}^c = \sqrt{\frac{2}{3}}\mathrm{tr}(\overline{\mathbf{N}}\mathbf{D}^c)\right),$$

where

$$\overline{\boldsymbol{\sigma}}^* \equiv \overline{\boldsymbol{\sigma}} - \overline{\sigma}_m \mathbf{I}, \qquad \overline{\sigma}_m \equiv \frac{1}{3}\mathrm{tr}\overline{\boldsymbol{\sigma}}. \tag{4.5}$$

k_1, k_2, h_1 and h_2 are material constants, and F_0 is the initial value of F.

Let the function U_R satisfying Eq. (3.14) and the function U_D satisfying Eq. (3.15) be given by

$$U_R = -u \ln R, \tag{4.6}$$

and

$$U_D = \xi_1 \ln(1 + \xi_2 \|\mathbf{D}\|), \tag{4.7}$$

where u, ξ_1 and ξ_2 are the material constants.

The following generalization of Norton's creep law to the multi-axial case with the temperature effect by ODQVIST [28, 29] has been often used for the relation of creep stretching and stress.

$$\mathbf{D}^c = \sqrt{\frac{3}{2}}\overline{C}\left(\frac{\|\boldsymbol{\sigma}^*\|}{\sigma_c}\right)^{\overline{n}} \exp\left(-\frac{Q_c}{R_c T}\right)\frac{\boldsymbol{\sigma}^*}{\|\boldsymbol{\sigma}^*\|}, \tag{4.8}$$

where $\overline{C}$ is the material parameter, $\overline{n}$ is the material constant, σ_c is the stress-valued parameter, Q_c is the activation energy, R_c is the gas constant, T is the absolute temperature and $\boldsymbol{\sigma}^*$ is the deviatoric stress. However, $\overline{C}$ cannot be a material constant with an objectivity since it depends on the selection of σ_c. Assuming that the direction of the creep stretching is the outward-normal of the subloading surface, let Eq. (4.8) be modified for the present model as follows:

$$\mathbf{D}^c = \sqrt{\frac{3}{2}} C R^n \exp\left(-\frac{Q_c}{R_c T}\right)\overline{\mathbf{N}}, \tag{4.9}$$

where C and n are material constants, whilst Eq. (4.9) fulfills Eq. (3.20).

The following relations are derived from Eqs. (4.1) – (4.4).

$$\overline{\mathbf{N}} = \frac{\overline{\boldsymbol{\sigma}}^*}{\|\overline{\boldsymbol{\sigma}}^*\|}, \quad \left\|\frac{\partial f(\overline{\boldsymbol{\sigma}})}{\partial \overline{\boldsymbol{\sigma}}}\right\| = \sqrt{\frac{2}{3}}, \quad F' = F_0 h_1 h_2 \exp(-h_2 H), \tag{4.10}$$

$$h^p = \sqrt{\frac{2}{3}}.$$

The measured and predicted uniaxial loading behavior under various axial rates of deformation of $2_{1/4}$Cr-1Mo steel (SA 387, Gr. 22) at 600° C (test data after INOUE *et al.* [30]) are shown in Fig. 5. The material constants and initial values in the prediction are selected as follows:

Isotropic hardening: $h_1 = 0.3$, $h_2 = 20$;

Kinematic hardening: $k_1 = 0,\ k_2 = 0$;
Evolution rate of similarity ratio: $u = 1,500,\ \xi_1 = 30,\ \xi_2 = 5,000$ s;
Evolution of similarity center: $c = 0$;
Elastic moduli: $K = 140,000$ MPa, $G = 100,000$ MPa;
Creep: $C\exp\{-Q_c/(R_cT)\} = 0.00002\ \mathrm{s}^{-1},\ n = 4$;
Initial values: $F_0 = 305$ MPa, $\boldsymbol{\alpha}_0 = \mathbf{0}$ MPa, $\mathbf{s}_0 = \mathbf{0}$ MPa (initial isotropy).

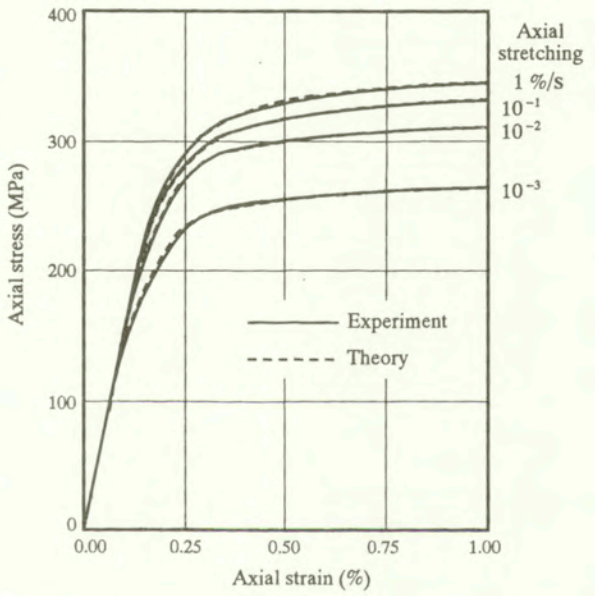

FIG. 5. Uniaxial loading behavior under various rates of deformation (test data after INOUE *et al.* [31]).

The difference of deformation behavior due to the rate of deformation is predicted quite well. The phenomenon that the rise of axial stress is weakened as the axial stretching decreases is predicted well by selecting the high value 4 for the material constant n on the influence of the similarity-ratio R.

5. Concluding remarks

The subloading surface model which would be the only model capable of describing pertinently the cyclic loading behavior among the existing models, is extended so as to describe the time-dependence in this article. The creep stretching is added to the elastic and the plastic ones in the algebraic sum. Thus, it falls within the framework of the elastoplastic-creep constitutive equation, which could be regarded as a natural extension of the traditional elastoplastic constitutive equation.

The novel features of the present constitutive equation are as follows:

1) The subloading surface is extended so as to be able to become larger than the normal-yield surface at a high rate of deformation. Here, it should be noted that there would not generally exist any surface which bounds the state of stress in the stress space. Therefore, the concept of the bounding surface of DAFALIAS [31] must be abandoned in the general deformation process with time-dependence, while in reality a stress goes out from the bounding surface at a high rate of deformation.

2) The plastic stretching is formulated so as to be suppressed by the increase of the rate of deformation through the evolution rule of the similarity-ratio. Thus, a quick response to an abrupt variation of the rate of deformation or stress is described.

3) The novel loading criterion is incorporated, which is defined by the sign of the proportionality factor in terms of stretching in the associated flow rule.

4) The Norton-Odqvist creep equation of metals is modified so as to have the objective material constant.

Acknowledgements

The author wishes to thank Dr. T. Okayasu and Dr. X. Wu, Kyushu University for the support on the calculation in comparison with test data.

References

1. K. HASHIGUCHI and M. UENO, *Elastoplastic constitutive laws of granular materials*, Constitutive Equations of Soils (Proc. 9th ICFSME, Spec. Session 9), Tokyo, JSSMFE, 73–82, 1977.
2. K. HASHIGUCHI, *Plastic constitutive equations of granular materials*, Proc. US-Japan Seminar Continuum Mech. Stast. Appr. Mech. Granular Materials, Sendai, 321–329, 1978.
3. K. HASHIGUCHI, *Constitutive equations of elastoplastic materials with elastic-plastic transition*, J. Appl. Mech. (ASME), **47**, 266–272, 1980.
4. K. HASHIGUCHI, *Subloading surface model in unconventional plasticity*, Int. J. Solids Struct., **25**, 917–945, 1989.
5. K. HASHIGUCHI, *Fundamental requirements and formulation of elastoplastic constitutive equations with tangential plasticity*, Int. J. Plasticity, **9**, 525–549, 1993a.
6. K. HASHIGUCHI, *Mechanical requirements and structures of cyclic plasticity models*, Int. J. Plasticity, **9**, 721–748, 1993b.
7. K. HASHIGUCHI, *The extended flow rule in plasticity*, Int. J. Plasticity, **13**, 37–58, 1997.
8. K. HASHIGUCHI and T. OKAYASU, *Time-dependent elastoplastic constitutive equation based on the subloading surface model and its application to soils*, Soils and Foundations, **40**, 4, 19–36, 2000.
9. P. PERZYNA, *The constitutive equations for rate sensitive plastic materials*, Quart. Appl. Math., **20**, 321–332, 1993.

10. P. PERZYNA, *The constitutive equations for workhardening and rate sensitive plastic materials*, Proc. Vibration Problems, Warsaw, **3**, 281–290, 1993.

11. P. PERZYNA, *Fundamental problems in viscoplasticity*, Advances in Applied Mechanics, **9**, 243–377, 1966.

12. W. OLSZAK and P. PERZYNA, *The constitutive equations of the flow theory for a nonstationary yield condition*, Proc. 11th Int. Congress of Applied Mechanics, 545–553, 1966.

13. W. OLSZAK and P. PERZYNA, *Stationary and nonstationary viscoplasticity*, Inelastic Behavior of Solids, McGraw–Hill, 53–75, 1970.

14. K. HOHENESNER and W. PRAGER, *Über die Ansatze der Mechanik isotroper Kontinua*, Z. Angew. Math. Mech., **12**, 216–226, 1932.

15. E. C. BINGHAM, *Fluidity and plasticity*, McGraw–Hill, New York 1922.

16. W. PAGER, *Linearization in visco-plasticity*, Ingenieur Archiv., **15**, 152–157, 1961.

17. F. TATSUOKA, S. de MAGIATRIS, F. HANANO, Y. MOMOYA and J. KOSEKI, *Some new aspects of time effects on the stress-strain behaviour of stiff geomaterials*, Proc. 2nd Int. Conf. Hard Soils and Soft Rocks, Napoli 1999.

18. J. M. CORUM, W. L. GREENSTREET, K. C. LIU, C. E. PUGH and R. W. SWINDEMAN, *Interim guidelines for detailed inelastic analysis of high-temperature reactor system components*, ORNL-5014.

19. D. KUJAWSKI and Z. MRÓZ, *A viscoplastic material model and its application to cyclic loading*, Acta Mech., **36**, 213–230.

20. C. E. PUGH, *Progress in developing constitutive equations for inelastic design analysis*, J. Pressure Vessel Tech. (ASME), **105**, 273–276, 1983.

21. Y. F. DAFALIAS, *The plastic spin*, J. Appl. Mech. (ASME), **52**, 865–871, 1985.

22. H. M. ZBIB and E. C. AIFANTIS, *On the concept of relative and plastic spins and its implications to large deformation theories. Part I: Hypoelasticity and vertex-type plasticity*, Acta Mech., **75**, 15–33, 1988.

23. K. HASHIGUCHI and Z.-P. CHEN, *Elastoplastic constitutive equations of soils with the subloading surface and the rotational hardening*, Int. J. Numer. Anal. Meth. Geomech., **22**, 197–227, 1998.

24. D. C. DRUCHNER, *Conventional and unconventional plastic response and representation*, Appl. Mech. Rev. (ASME), **41**, 151–167, 1988.

25. G. MASING, *Eigenspannunngen und verfestigung beim massing*, Proc. 2nd Int. Congr. Appl. Mech., 332–335, Zurich.

26. Z. MRÓZ, *On forms of constitutive laws of elastic-plastic solids*, Arch. Mech., **18**, 3–35, 1966.

27. K. HASHIGUCHI, *Fundamentals in constitutive equation: continuity and smoothness conditions and loading criterion*, Soils and Foundations, **40**, 4, 155–162, 2000.

28. K. HASHIGUCHI and T. YOSHIMARU, *A generalized formulation of the concept of nonhardening region*, Int. J. Plasticity, **11**, 347–365, 1995.

29. F. K. G. ODQVIST and J. HULT, *Kriechfestigkeit Metallischer Werkstoffe*, Springer-Verlag, Berlin 1962.

30. F. K. G. ODQVIST, *Mathematical Theory of Creep and Creep Rupture*, Oxford Univ. Press, 1966.

31. T. INOUE, T. IGARI, F. YOSHIDA, A. SUZUKI and S. MURAKAMI, *Inelastic behavior of $2_{1/4}$Cr-1Mo steel under plasticity-creep*, Nuclear Eng. Design, **90**, 287–297.

32. Y. F. DAFALIAS, *Bounding surface plasticity. I: Mathematical formulation and hypoplasticity*, J. Eng. Mech. (ASCE), **112**, 966–987, 1986.

Received January 24, 2000; revised version May 22, 2000.

Arch. Mech., **52**, 4–5, pp. 629–644, Warszawa 2000

On the limit analysis of defective pipelines under complex loadings

Dedicated to Professor Zenon Mróz
on the occasion of his 70^{th} birthday

Y. LIU, B. XU and B. YANG

Department of Engineering Mechanics, Tsinghua University,
Beijing 100084, P.R. China

THE INTEGRITY ASSESSMENT of defective pipelines represents a practically important task of structural analysis and design in various technological areas, such as oil and gas industry, power plant engineering and chemical factories. It is very essential to evaluate the load-carrying capacities of defective pipelines in order to judge safely their working life. In this paper, an iterative algorithm is presented for the kinematic limit analysis of 3-D rigid-perfectly plastic bodies. A numerical path scheme for radial loading is adopted to deal with complex multi-loading systems. The numerical procedure has been applied to carry out the plastic collapse analysis of pipelines with part-through slots under internal pressure, bending moment and axial force. The effects of various shapes and sizes of part-through slots on the collapse loads of pipelines are systematically investigated and evaluated. Some typical failure modes corresponding to different configurations of slots and loading forms are studied.

Key Words: limit analysis, loading path, mathematical programming, pipeline, part-through slot

1. Introduction

PLASTIC LIMIT ANALYSIS plays a significant role in the integrity assessment of defective pipelines. The plastic limit load, which determines the carrying capacity of structures, is an important parameter in performing the two-criteria assessment of structural integrity [1]. In the ASME stress classification framework for pressure vessel design, stresses are classified as the primary, secondary and peak stresses, different admissible values are provided for different stress modes, and the admissible value of primary stress corresponds to the stress state under the limit load. Therefore, the knowledge of limit loads of mechanical components and structures is useful to the designer to address the modes of failure associated with load-controlled effects.

However, the determination of limit loads is by no means an easy task, es-

pecially for complex configurations and loading systems. Therefore, the problem how to determine the limit load efficiently and accurately has attracted the attention of many researchers. With the progress in the finite element technique and mathematical optimization theory, the simplified analysis methods for the computation of plastic limit load have been developed rapidly, such as the GLOSS r-node method of SESHADRI and FERNANDO [2], the elastic compensation method of MACKENZIE and BOYLE [3], the thermoparameter method [4] and mathematical programming methods [5 – 10], etc. The mathematical programming methods can determine the load-carrying capacity of a rigid-perfectly plastic body, which do not concern the loading process and can overcome the difficulties by step-by-step elastic-plastic analysis. The lower and upper bounds of limit load for a perfectly rigid-plastic body can be approached by mathematical programming processes based on the static and kinematic theorems of limit analysis. In comparison with the lower bound analysis, there are more difficulties in the upper bound limit analysis. Because of the nonlinearity and nonsmoothness of the objective function, many existing solution methods for mathematical programming problems cannot be used directly for an upper bound analysis. Although the numerical difficulties have been overcome by some investigators, such as HUH [7], LIU [8], CHEN [9] and ZHANG [10], these methods were mainly presented for single loading or simple 2-D structures. The numerical algorithms for the limit analysis of 3-D structures under multi-loading systems need further study and development.

Pipelines are widely used in various fields such as the petrochemical industry, energy and electric power engineering, etc. During their operation, many local defects such as part-through slots shown in Fig. 4 can be produced by corrosion, mechanical damage or abrasive surface cracks. These defects may jeopardize the integrity (i.e. reduce the load-carrying capacity) of pipelines and sometimes even lead to severe industrial accidents. The integrity assessment of defective pipelines is a very important research subject, with a significant and extensive application background in the pipeline industry. Part-through slots, which can be commonly found on the surfaces of pipelines, are classsified as a type of 3-D volumetric defects. They can result not only in stress concentration, but also in the cracks under fatigue loads. Because of the lack of systematic theoretical analyses as well as satisfactory experimental results, the effects of part-through slots on the strength of pipelines are at present still unclear. The current testing codes and standards for the pipelines in service provide severe limitations to the allowable values of part-through slots. Unnecessary welding treatments of part-through slots required by the codes, are not only resource-consuming processes but also can produce more severe welding defects. Therefore, some serious and systematic attempts should be made to investigate the effects of part-through slots on the load-carrying capacities of pipelines. These attempts are expected

to provide some more scientific and reasonable approaches for defect assessment and treatment, which will significantly reduce the resource consumption in defect treatment but still guarantee the operation safety of the pipelines. Unfortunately, only few research efforts on the plastic collapse analysis of pipelines with various part-through slots have been made up to now.

In the present study, a kinematic approach to the limit analysis of 3-D structures is proposed by means of a direct iterative algorithm. A radial loading path scheme is presented to deal with multi-loading systems. Furthermore, by using the present algorithm, the plastic collapse analysis of defective pipelines is performed under the combinations of two loads of three possible types: internal pressure, bending moment and axial force. The defects considered here include part-through spherical, ellipsoidal and rectangular slots. The limit loads of pipelines are computed for a comprehensive range of geometric parameters.The effects of various shapes and sizes of typical part-through slots on the collapse loads of pipelines are investigated. Some typical failure modes corresponding to different dimensions of slots and loading conditions are analyzed.

2. The radial loading path scheme

To present a loading path scheme used in the numerical limit analysis, we take here as an example a biaxial loading system composed of $\overline{P}_1$ and $\overline{P}_2$. The loading scheme used here is applicable to a more general muti-loading system. As shown in Fig. 1, let the slope of the ray be $\tan\theta = \dfrac{\overline{P}_2}{\overline{P}_1}$, i.e. $\overline{P}_2 = \overline{P}_1 \tan\theta \left(0 \leq \theta \leq \dfrac{\pi}{2}\right)$, where the variation of $\tan\theta$ corresponds to different loading paths which are dependent on the multi-loading systems. At each computation of the limit load multiplier performed by an iterative algorithm (see the next section for the details), take some slope of the loading path $\tan\theta$, namely, fix the relative magnitudes of different loads $\overline{P}_1$ and $\overline{P}_2$. When θ changes from 0 to 90 degrees, the limit state at each last iteration composes the complete limit load interaction curve as shown in Fig. 1. In particular, when θ is equal to 0 or 90 degrees, the iteration solution is the limit load solution corresponding to $\overline{P}_1$ or $\overline{P}_2$. For a rigid-perfectly plastic material, this scheme of loading path can be extended to the limit analysis under the combined action of three loading systems.

For generalized loadings $\langle \overline{P}_1, \overline{P}_2 \rangle$, we have:

$$\langle \overline{P}_1, \overline{P}_2 \rangle = \langle \overline{P}_1, \overline{P}_2 \tan\theta \rangle = \overline{P}_1 \langle 1, \tan\theta \rangle = \mu \overline{P}_{10} \langle 1, \tan\theta \rangle$$

where μ is a weight factor of generalized proportional loadings, $\overline{P}_{10}$ is the base load of $\overline{P}_1$. If the generalized limit load multiplier is denoted by ν, the generalized plastic limit solution is:

$$\langle \overline{P}_1, \overline{P}_2 \rangle_L = \nu \langle \overline{P}_1, \overline{P}_2 \rangle_0 = \nu \overline{P}_{10} \langle 1, \tan\theta \rangle, \tag{2.1}$$

where ν can be computed by a direct iterative algorithm as shown in the next section.

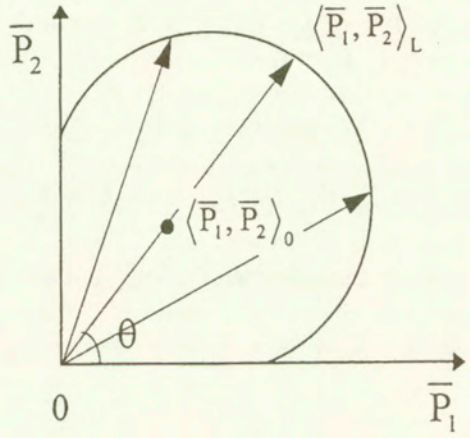

FIG. 1. Radial loading path under two loading systems.

3. Iterative algorithm

Consider a 3-D rigid-perfectly plastic body V with the boundary S. The individually varying multi-loading system $\sum_m \overline{\mathbf{P}}_m$ (m is the number of loadings) is applied on S_σ, and the displacement constraint $u_i = 0$ is imposed on S_u. The plastic incompressibility condition $u_{i,i} = 0$ is satisfied in the body V. On the basis of the kinematic theorem of limit analysis and the finite element discretization technique, we have

$$\left(\sum\nolimits_m \mathbf{P}_m\right)^T \mathbf{U} \le \sum_{e=1}^{N} \int_{V_e} W_P dV \tag{3.1}$$

where W_P is the rate of plastic energy dissipation, $\mathbf{P}_m$ is the m-th equivalent nodal load vector corresponding to $\overline{\mathbf{P}}_m$, $\mathbf{U}$ is the nodal velocity vector, and N is the number of elements.

Adopting the von Mises yield criterion and Gauss integration method, one has

$$V\left(\sum\nolimits_m \mathbf{P}_{mo}\right)^T \mathbf{U} \le \sqrt{\frac{2}{3}}\sigma_y \sum\nolimits_{i\in \mathbf{I}} \rho_i \sqrt{\mathbf{U}^T \mathbf{K}_i \mathbf{U}} |\mathbf{J}|_i \tag{3.2}$$

where I is the set of all Gauss integration points, ρ_i is the integration weight, $|\mathbf{J}|_i$ is the Jacobian determinant $|\mathbf{J}|$ at the Gauss integration point i, ν is the general-

ized limit load multiplier, $\mathbf{P}_{mo}$ is the equivalent nodal load vector corresponding to the m-th base load of $\overline{\mathbf{P}}_{mo}$, $\mathbf{K}_i$ is the stiffness matrix at the Gauss point i, and σ_y is the yield stress of material.

The above inequality leads to the following discretized mathematical programming formulation:

$$\begin{cases} \nu = \min_{\mathbf{U}} : \sqrt{\dfrac{2}{3}}\sigma_y \sum_{i\in I} \rho_i \sqrt{\mathbf{U}^T \mathbf{K}_i \mathbf{U}} |\mathbf{J}|_i, \\ \text{s.t.} \left(\sum_m \mathbf{P}_{mp}\right) \mathbf{U} = \mathbf{1}, \\ \mathbf{U}^T (\mathbf{K}_V)_i \, \mathbf{U} = \mathbf{0} \ \forall i \in \mathbf{I}, \end{cases} \tag{3.3}$$

where the abbreviation "s.t." means "subject to", and the volumetric stiffness matrix $\mathbf{K}_V^e$ for each element can be expressed as

$$\mathbf{K}_V^e = (\mathbf{B}_V^e)^T \mathbf{B}_V^e, \tag{3.4}$$

in which the volumetric strain matrix is $\mathbf{B}_V^e = \operatorname{div} \mathbf{N}^e$ and $\mathbf{N}^e$ is the shape function matrix for each element. For convenience, the constant factor $\sqrt{\dfrac{2}{3}}\sigma_y$ is omitted temporarily in the following discussion.

Obviously, Eq. (3.2) is a non-linear mathematical programming problem, thus it is difficult to find an efficient search direction and the property of upper bound can not be guaranteed. Furthermore, the objective function of Eq. (3.3) is non-smooth. It is difficult to treat the rigid portion because of the singularity of the derivative of objective function over rigid zones. To overcome those difficulties, we perform a series of iterations to solve Eq. (3.3). At each iteration, the rigid and plastic zones are distinguished and the objective function and constraint conditions are suitably modified. Namely, before proceeding with the $(j+1)$-th iteration, we examine the strain value of every integration point and divide the set I of all integration points into the rigid zone subset R_{j+1} and the plastic zone subset P_{j+1}, i.e.:

$$\begin{aligned} I &= R_{j+1} \cup P_{j+1}, \\ R_{j+1} &= \{i \in I, \, \mathbf{U}_j^T \mathbf{K}_i \mathbf{U}_j = 0\}, \\ P_{j+1} &= \{i \in I, \, \mathbf{U}_j^T \mathbf{K}_i \mathbf{U}_j \neq 0\}. \end{aligned} \tag{3.5}$$

The determination of set R_{j+1} and P_{j+1} is essential for removing those points at the rigid state from the sum of integration points of the objective function, so as to ensure that the next iteration can proceed normally. Meanwhile, we can also physically find the distribution of the plastic and rigid zones during the iterative

process by Eq. (3.5). The following iterative formulation is then constructed to solve Eq. (3.3) directly:

$$
\begin{aligned}
&\nu = \min_{U} : \sum\nolimits_{i\in P_j} \frac{\rho_i |\mathbf{J}|_i \mathbf{U}^T \mathbf{K}_i \mathbf{U}}{\sqrt{\mathbf{U}_j^T \mathbf{K}_i \mathbf{U}_j}}, \\
&\text{s.t.} \ \left(\sum\nolimits_m \mathbf{P}_{m0}\right)^T \mathbf{U} = 1, \\
&\mathbf{U}^T (\mathbf{K}_V)_i \mathbf{U} = 0 \qquad \forall i \in P_j, \\
&\mathbf{U}^T \mathbf{K}_i \mathbf{U} = 0 \qquad \forall i \in R_j,
\end{aligned} \tag{3.6}
$$

where $\mathbf{U}_j$ is the nodal velocity array at the j-th iteration.

In the formulation (3.6), the additional constraint condition $(3.6)_4$ imposed on the rigid zone and the incompressibility condition $(3.6)_3$ imposed on the plastic zone can be introduced by the penalty function method. The normalization constraint $(3.6)_2$ can be enforced by the Lagrangian multiplier method. By applying the optimality conditions of the augmented objective function, the problem (3.6) is equivalent to solving the following linear algebraic equations:

$$
\begin{cases}
\sum_{i\in I} \rho_i |\mathbf{J}|_i \tilde{\mathbf{K}}_i \mathbf{U} = \lambda \sum_m \mathbf{P}_{m0}, \\
\left(\sum_m \mathbf{P}_{m0}\right)^T \mathbf{U} = 1,
\end{cases} \tag{3.7}
$$

where λ is the Lagrangian multiplier, and

$$
\tilde{\mathbf{K}}_i = \begin{cases}
\dfrac{\mathbf{K}_i}{\sqrt{\mathbf{U}_j^T \mathbf{K}_i \mathbf{U}_j}} + A_1 (\mathbf{K}_V)_i & \forall i \in P_j, \\
A_2 \mathbf{K}_i & \forall i \in R_j,
\end{cases} \tag{3.8}
$$

in which A_1 and A_2 are the penalty factors. In practice, the typical values of A_1 and A_2 vary from 10^6 to 10^{12}. Solving Eq. (3.7), we get the nodal velocity array $\mathbf{U}_j$ at step j, and then compute the generalized limit load multiplier ν_j by using Eq. $(3.3)_1$.

The iteration is initiated as follows:

$$
\begin{aligned}
&\min_{U} : \sum\nolimits_{i\in I} \rho_i |\mathbf{J}|_i \mathbf{U}^T \mathbf{K}_i \mathbf{U}, \\
&\text{s. t.} \ \left(\sum\nolimits_m \mathbf{P}_{m0}\right)^T \mathbf{U} = 1, \\
&\mathbf{U}^T (\mathbf{K}_V)_i \mathbf{U} = 0 \qquad \forall \mathbf{i} \in \mathbf{I}.
\end{aligned} \tag{3.9}
$$

From Eq. (3.9), we can obtain the initial values of $\mathbf{U}_0$ and ν_0.

The above iterative process is terminated when the following convergence criteria are satisfied:

$$\frac{|\nu_{j+1} - \nu_j|}{\nu_j} \leq \text{VOL1},$$

(3.10)

$$\frac{\|\mathbf{U}_{j+1}\mathbf{U}_j\|}{\|\mathbf{U}_j\|} \leq \text{VOL2},$$

where VOL1 and VOL2 are the desired accuracies of the calculation.

The authors of this paper have shown that the above iterative process leads to the limit load multiplier ν and to a collapse mechanism $\mathbf{U}$ through a convergent sequence with monotonically decreasing ν_j.

4. Applications

4.1. Cylindrical shell joined-both ends to rigid plates subjected to radial pressure and independent axial load

The geometry of a cylindrical shell joined at both ends to rigid plates, subjected to radial pressure and independent axial load and the arrangement of finite element mesh, are shown in Fig. 2.

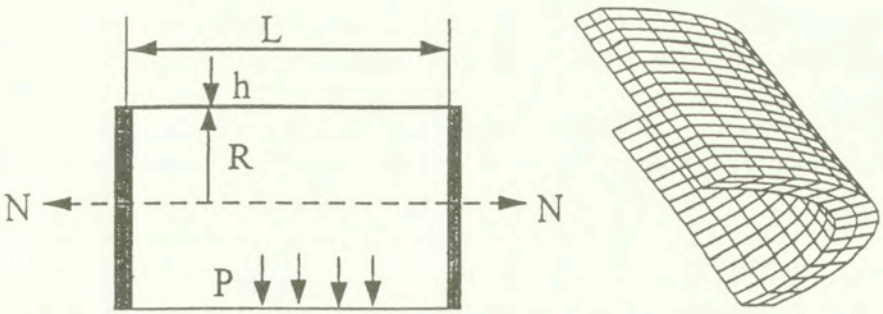

FIG. 2. Cylindrical shell joined at both ends to rigid plates, subjected to a radial pressure and an independent axial load, together with the finite element mesh used in this study.

Let $\omega^2 = \dfrac{L^2}{2hR}$, $p = \dfrac{PR}{\sigma_y h}$, $n = \dfrac{N}{2\pi R\sigma_y h}$, where σ_y is the uniaxial yield stress. HODGE and PANARELLI [11] solved this problem and presented both the lower and upper bound approximations of limit load for a von Mises material. ZHANG [10] also presented the solutions of this problem using the limit analysis and

considering initial constant loadings and proportional loadings. The results of our solution fall between the lower bound and upper bound given by HODGE and PANARELLLI [11], and are in a good agreement with the solutions of Zhang, as shown in Fig. 3. Obviously, this indicates that the proposed radial loading path scheme is reasonable and feasible and the above numerical procedure is effective.

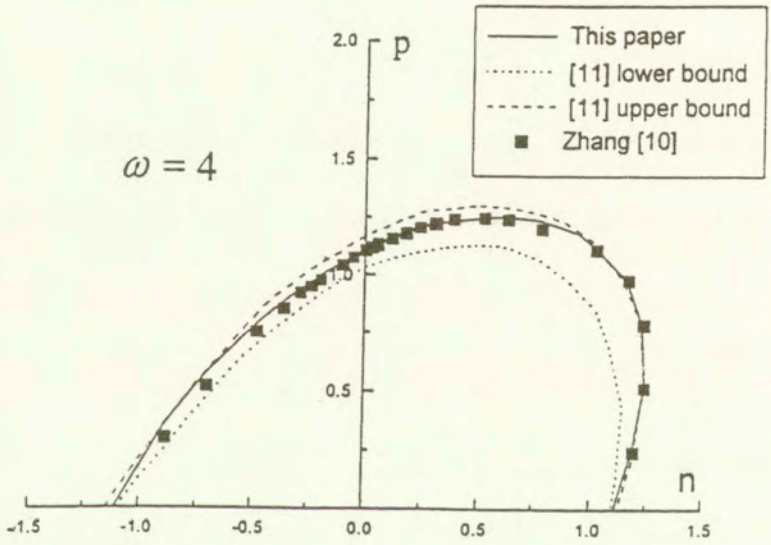

FIG. 3. The limit load interaction curves obtained by different methods.

4.2. Plastic collapse analysis of defective pipelines under internal pressure, axial tension and bending moment

4.2.1. Determination of plastic limit load. The geometry of defective pipeline subjected to internal pressure (P), axial tension (N) and bending moment (M) is shown in Fig. 4. The defects considered here are part-through slots of various geometrical configurations. The engineering situation considered here has a practical important background in the pipeline industry. Here the axial tension (N) includes the independent axial tension N_1 and the additional axial tension N_2 induced by an internal pressure P, i.e. $N_2 = P\pi R_i^2$, where R_i is the inner radius of a pipe. Using the proposed numerical algorithm,we perform the plastic collapse analysis of a cylindrical pipe with different shapes and sizes of part-through slots under internal pressure,bending moment and axial force(more than 1.000 examples have been computed here). The material is assumed to be rigid-perfectly plastic. The radius ratio kk (i.e. the ratio of the external to internal radius) of the pipe is 1.20. The pipe thickness is $T = 20$ mm. The yield stress σ_y of the material is 245 MPa.

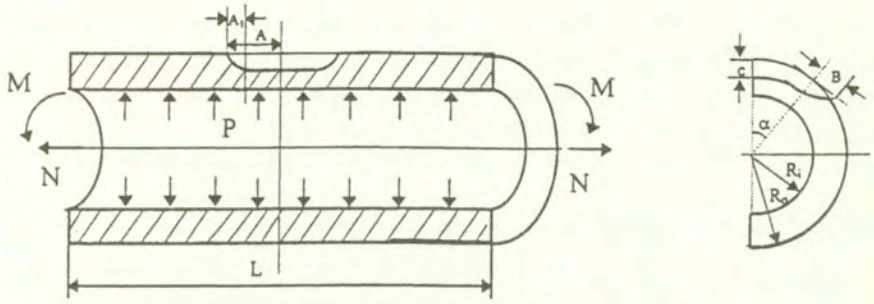

FIG. 4. Geometry of the pipeline with a part-through slot subjected to internal pressure, axial tension and bending moment.

Considering the symmetry of structure, we take a quadrant of the pipeline with four kinds of slots and discretize it by 3-D 20-node isoparametric finite elements. For various sizes of pipes and part-through slots, the finite element analysis meshes are defined by using 500–1000 elements and 600–1500 nodes. The corresponding displacement constraints are imposed on the symmetric boundaries. In order to optimize the numerical efficiency and accuracy, the finite element mesh should be chosen appropriately for a cylinder with a slot so as to make the distribution of the elements around the slot as even and neat as possible, and more dense than those located in other parts of the cylinder.

We define the following non-dimensional parameters:

$$
\begin{aligned}
m &= M/M_0, \quad M_0 = 4R^2T\sigma_y, \\
p &= \frac{P}{P_0}, \quad P_0 = \frac{2}{\sqrt{3}}\sigma_y \quad \ln\frac{R_0}{R_i}, \\
n &= N/N_0, \quad N_0 = \pi(R_0^2 - R_i^2)\sigma_y,
\end{aligned}
\tag{4.1}
$$

with the mean radius of a pipe $R = \dfrac{R_i + R_0}{2}$ and the wall-thickness $T = R_0 - R_i$.

The rectangular slot is analzed first because this kind of slot is relatively dangerous. For the pipeline with a rectangular slot under an internal pressure, we compute the limit loads of pipes for the combinations of the depth of slot $C/T = 0,\ 0.1,\ 0.2,\ 0.3,\ 0.4,\ 0.5,\ 0.6,\ 0.7,\ 0.8,\ 0.9$, the width of slot $\alpha/\pi = 0,\ 0.02,\ 0.04,\ 0.07,\ 0.1,\ 0.2,\ 0.3,\ 0.4,\ 0.5,\ 0.6,\ 0.7,\ 0.8,\ 0.9$ and the length of slot $A/\sqrt{RT} = 0,\ 0.2,\ 0.4,\ 0.6,\ 0.8,\ 1.0$. The calculated results are shown in Fig. 5. We can see that the width of the slot has some effect on the limit loads of pipes. When the depth of the slot is relatively small (e.g. $C/T < 0.2$), variation of the width of the slot has a small effect on the limit loads of pipes; when the depth of the slot is relatively large (e.g. $C/T > 0.5$), the variation of the width of

the slot affects the limit loads of pipes remarkably. With the depth of the slot increasing, the effects of the width of the slot on the limit loads of pipes are more pronounced. We can also see from Fig. 5 that when the width of the slot exceeds a critical value (e.g. $\alpha/\pi > 0.65$) for relatively large axial length of the slot, variation of the width of the slot has a small effect on the limit loads of pipes.

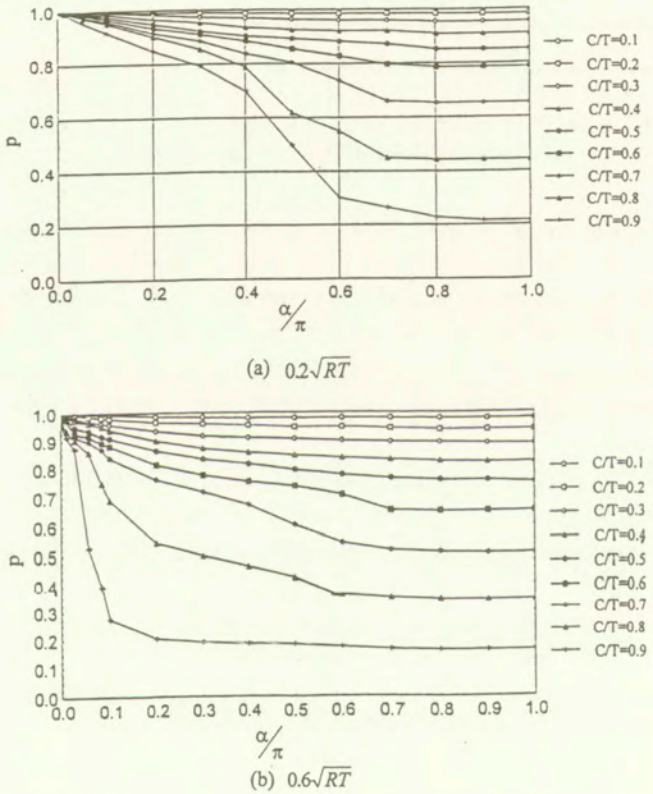

(a) $0.2\sqrt{RT}$

(b) $0.6\sqrt{RT}$

FIG. 5. Effects of the width of a slot on the limit moments of pipeline under a bending moment.

For the pipeline with a rectangular slot under a bending moment, we compute the limit loads of the pipe for the combinations of the circumferential length of the slot $\alpha/\pi = 0.1, 0.2, 0.3, 0.4, 0.5, 0.6, 0.7, 0.8, 0.9, 1.0$, the depth of the slot $C/T = 0.1, 0.2, 0.3, 0.4, 0.5, 0.6, 0.7, 0.8, 0.9$ and the length of the slot $A/\sqrt{RT} = 0, 0.2, 0.5, 0.8, 1.0, 2.0, 3.0, 4.0, 5.0, 6.0, 7.0$. The calculated results are shown in Fig. 6. We can see that when the axial length of the slot exceeds a critical value (e.g. $A/\sqrt{RT} = 1.46$), the variation of the axial length of the slot has no effect on the limit moment of pipes.

The plastic collapse loads of pipelines with four different shapes and sizes of part-through slots under the combined action of an internal pressure, axial

tension and bending moment are computed and analyzed here. The limit load interaction curves of pipeline under the combined actions of internal pressure and bending moment, bending moment and independent axial tension, and internal pressure and independent axial tension, are respectively plotted in Figs. 7 – 9. From these three figures, we can obviously see that the small area slot has a little effect on the limit load curves of the pipelines. The axial slot affects greatly the limit loads of pipelines under an internal pressure, and affects sllghtls the loads under the combined action of bending moment and axial force. On the contrary, for the circumferential slot, the limit loads of pipelines are affected more under the combined action of bending moment and axial force than under the internal pressure. For a large area slot, the corresponding failure mode is not a global collapse but a local collapse, and hence the limit loads of pipelines decrease considerably.

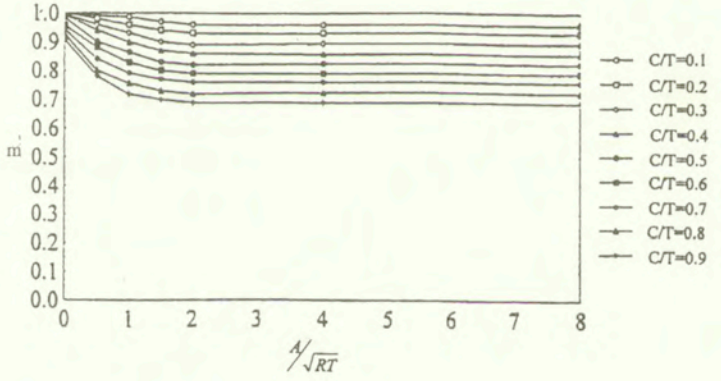

(a) $\frac{\alpha}{\pi} = 0.3$

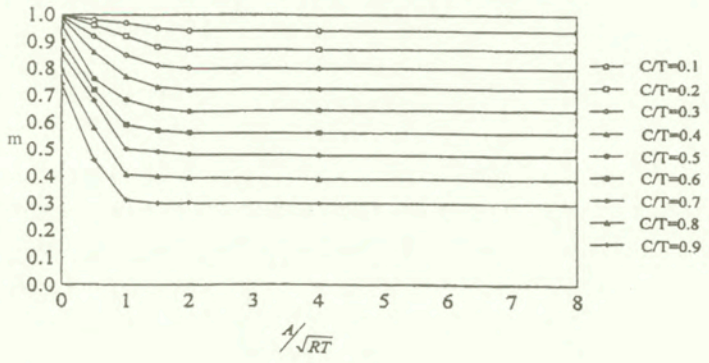

(b) $\frac{\alpha}{\pi} = 0.6$

FIG. 6. Effects of the axial length of a slot on the limit moments of popeline under a bending moment.

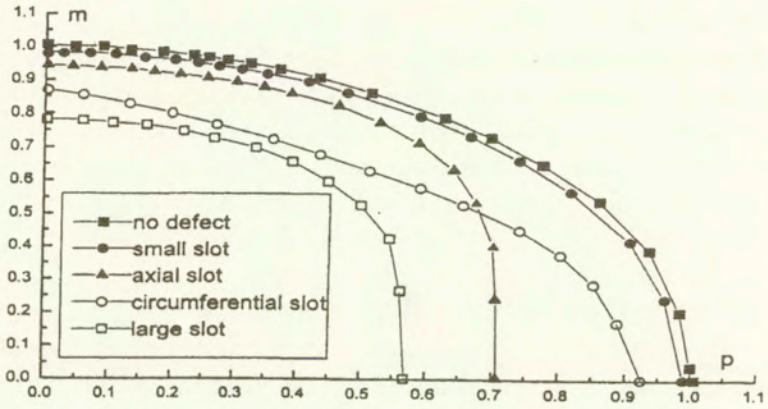

FIG. 7. The limit load interaction curves of pipeline under internal pressure and bending moment.

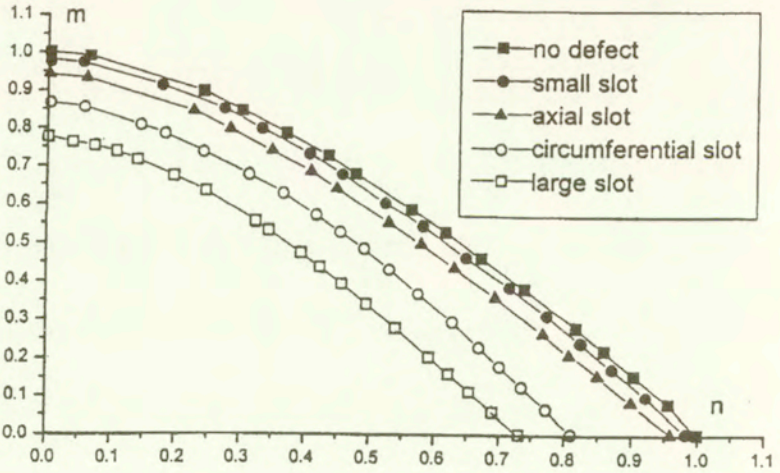

FIG. 8. The limit load interaction curves of a pipeline under axial tension and bending moment.

Some conclusions can also be drawn here. The effects of ellipsoidal and axially rectangular part-through slots on the limit loads of pipelines, which are induced by an internal pressure, are much greater than those induced by a bending moment. Therefore, the pipeline with the above two defects is relatively safe under a bending moment. But under the action of an internal pressure, the load-carrying capacity of a pipeline decreases considerably due to the axial rectangular slot. For the pipeline under the action of a bending moment or an axial force, an axial slot is safer than a circumferential slot. For the pipeline under an internal pressure, an axial slot is more dangerous. Furthermore, on the basis of these solutions of limit load interaction curves, the integrity assessment of pipeline with

various kinds of slots can be performed by the widely used integrity assessment procedures such as Nuclear Electric's (the former CEGB in the UK) R5 and R6 (the standards and codes of assessment of defective structures).

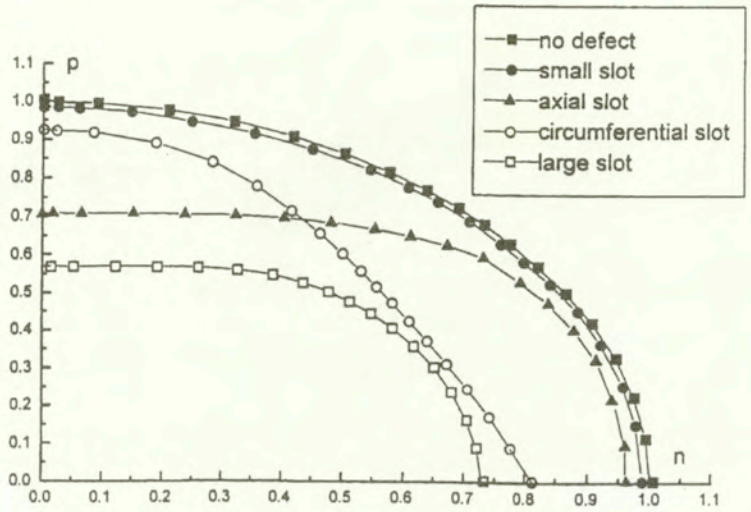

FIG. 9. The limit load interaction curves of a pipeline under internal pressure and independent axial tension.

4.2.2. The failure modes. For the pipeline with a small area slot, when the internal pressure reaches the limit load, most regions of pipe are found to yield except some regions near the outside surface, which are still in rigid states, where the shaded area represents the plastic region. Large areas of plastic deformation develop in the pipe. When the pipeline reaches the limit state under a bending moment, most of the pipe starts to yield except the middle regions. When the limit state is reached under an axial force, almost the entire pipe becomes a plastic region. This failure mode is a global collapse, which is similar to that of a pipe without defects. Therefore, a small area slot has a small effect on the limit loads of a pipe under the above loading systems. For the pipeline with an axial slot, we can see from Fig. 10 that when the limit load is reached by an internal pressure, the part of pipe near the slot starts to yield and the other part of pipe is still rigid. In this case, with the rigid regions near the slot going into yielding, a local plastic hinge is formed around the slot. The ligament of the slot bulges towards the outside, and a local leakage may occur within the slot of the pipe. When the pipe with an axial slot reaches the limit state under the action of a bending moment, the corresponding failure mode is a global collapse and almost the same as that with a small slot. When the pipe with an axial slot reaches the limit state under an axial force, a large region near the slot goes into yielding and

extends in the direction of 45 degrees to the axial direction. These failure modes can also confirm the previously calculated results for the limit loads of the pipe with an axial slot, namely, the axial slot has a great effect on the limit load of pipe under an internal pressure and has a small effect under a bending moment and an axial force.

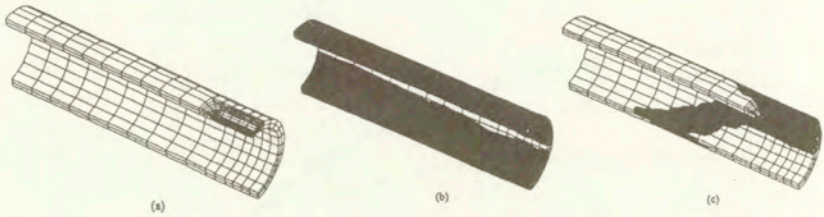

FIG. 10. Failure mode of a pipeline with an axial slot: a) under internal pressure; b) under bending moment; c) under axial tension.

For the pipeline with a circumferential slot, when the pipe reaches the limit state under an internal pressure, bending moment or axial force, the failure mode of the pipe is generally a local collapse. The local character of failure mode is more pronounced in the pipe under a bending moment and an axial force. This demonstrates that the circumferential slot has a greater effect on the limit load of the pipe under a bending moment or an axial force, and has a relatively small effect under an internal pressure.

For the pipeline with a large area slot, we can see from Fig. 11 that the failure mode is again a local collapse around the slot. This demonstrates that a large area slot has a greater effect on the limit loads of pipelines.

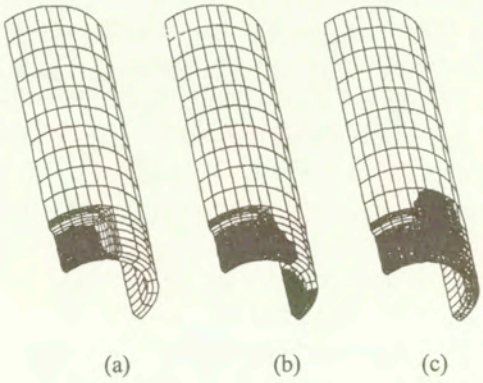

FIG. 11. Failure mode of a pipeline with a large area slot: a) under internal pressure; b) under bending moment; c) under axial tension.

5. Conclusions

By using an iterative algorithm for kinematic limit analysis of 3-D structures, a plastic collapse analysis of pipelines with part-through slots has been performed here under internal pressure, bending moment and axial force (more than 1.000 examples have been computed). The main conclusions can be drawn as follows:

1) The proposed iterative algorithm is efficient and reliable for performing the plastic collapse analysis of 3-D problems with complicated geometric forms and loading conditions.

2) The failure modes for defective pipelines include a global collapse and a local leakage. Corresponding to the former, the plastic load-carrying capacity of a pipeline is less affected. Corresponding to the latter, a plastic hinge is generally formed around the slot and the plastic load-carrying capacity of a pipeline decreases. Which failure mode occurs actually at the limit state for a defective pipeline should be determined by the size, position and orientation of the slot.

3) For the pipeline with a rectangular slot under an internal pressure, the width of slot has some effect on the limit load-carrying capacity of pipes, which is great, especially when the depth of slot is relatively large. The effects of the width of slot on the limit loads of pipes should not be neglected when the assessment of the remaining strength of pipes with slots is performed. For the pipeline with a rectangular slot under a bending moment, when the axial length of the slot exceeds a critical value (e.g. $1.46\sqrt{RT}$), the variation of the axial length of the slot has no effect on the limit moments of the pipes.

4) The small area slot has a small effect on the plastic load-carrying capacity of a pipeline, which collapses globally. For a pipeline with a large area slot, the corresponding load-carrying capacity decreases considerably due to a plastic hinge around the slot at the limit state. A local leakage generally occurs within the slot in this case. It is relatively dangerous to use such a pipeline. The axial slot has a great effect on the limit load of a pipeline under an internal pressure, and has a small effect under a bending moment and an axial force. The conclusion is opposite to the above for the circumferential slot.

Acknowledgements

The present study was supported by the Ministry of Science and Technology of China (96-918-02-03-02). This support is gratefully acknowledged.

References

1. R. SESHADRI and D. L. MARRIOTT, *On relating the reference stress, limit load and the ASME Stress Classification Concepts*, International Journal of Pressure Vessel & Piping, **56**, 387–408, 1993.

2. R. SESHADRI and C. P. D. FERNANDO, *Limit loads of mechanical components and structures using the GLOSS R-NODE method*, Journal of Pressure Vesssel Technology, **114**, 201–208, 1992.

3. D. MACKENZIE, C. NADARAJAH, J. SHI and J. T. BOYLE, *Simple bounds on limit loads by elastic finite element analysis*, Journal of Pressure Vesssel Technology, **115**, 27–31, 1993.

4. L. QIAN and Z. WANG, *Structural limit and shakedown analysis: A thermoparameter method*, Proc. ASME Pressure Vessel and Piping Conf., Nashnille, TN, **87**, 47–53, 1990.

5. T. BELYTSCHKO, *Plane stress shakedown analysis by finite elements*, International Journal of Mechanical Science, **14**, 619–625, 1972.

6. L. CORRADI and A. ZAVELANI, *A linear programming approach to shakedown analysis of structures*, Computer Methods in Applied Mechanics and Engineering, **3**, 37–53, 1974.

7. H. HUH and W. H. YANG, *A general algorithm for limit solutions of plane stress problems*, Int. J. Solids Structures, **28**, 6, 727–738, 1991.

8. Y. H. LIU, Z. Z. CEN and B. Y. XU, *A numerical method for plastic limit analysis of 3-D structures*, Int. J. Solids Structures, **32**, 1645–1658, 1995.

9. H. F. CHEN, Z. Z. CEN, B. Y. XU and S. G. ZHAN, *A numerical method for Reference stress in the evaluation of structure integrity*, International Journal of Pressure Vessel & Piping, **71**, 47–53, 1997.

10. Y. G. ZHANG, P. ZHANG and W. M. XUE, *Limit analysis considering initial constant loadings and proportional loadings*, Computational Mechanics, **14**, 229–234, 1994.

11. M. A. SAVE and C. E. MASSONNET, *Plastic analysis and design of plates, shells and disks*, North-Holland Publish Co., 1972.

Received January 10, 2000; revised version May 15, 2000.

Arch. Mech., **52**, 4–5, pp. 645–661, Warszawa 2000

Brake squeal: a problem of flutter instability of the steady sliding solution?

Dedicated to Professor Zenon Mróz
on the occasion of his 70^{th} birthday

F. MOIROT and Q. S. NGUYEN

Laboratoire de Mécanique des Solides, CNRS-umr7649,
Ecole Polytechnique,
91128-Palaiseau, France
E-mail : son@lms.polytechnique.fr

BRAKE SQUEAL RESULTS FROM friction-induced vibrations. This phenomenon is considered here and interpreted as a flutter instability of the steady sliding solution of an elastic solid in unilateral contact with friction with a moving obstacle. A mechanical analysis of the governing equations is given, in particular to obtain the steady sliding solution. The stability analysis of this solution is discussed. A numerical analysis by the finite element method is performed in order to compute the steady sliding solution and to discuss its stability for an automotive disk brake. The validation of the numerical procedure is examined in relation with some analytical results of the literature.

1. Introduction

THE PROBLEM OF BRAKE NOISES has been intensively discussed in various experimental or theoretical investigations up to the present time. Different kinds of noises and vibrations can be identified in common drum or disk brakes following their frequencies (e.g. [2, 12]). Brake squeals result from high frequency vibrations (greater than 5000 Hz) and have a relatively pure spectrum composed of a few main frequencies accompanied by some harmonics. Although a brake squeal does not affect the mechanical behaviour of the brake, it is less and less accepted by the passengers. The conditions under which a squeal occurs are relatively well known. Most experiments showed that the brake squeal is more excited at low than at high speeds (less than 30 km/h). Squeal occurs only over limited ranges of brake pressure and is most prevalent at low temperature (less than 150° C). The source of noise is attributed to the vibrations of brake components such as drum or pad and disk, and brake noises are generated mainly by the sliding phenomena.

Our objective is to present in this paper a mechanical analysis of brake squeal. The principal interpretation is the fact that brake squeal is a consequence of the flutter instability of the steady sliding solution of the pad on the disk for a disk brake. This analysis leads to the system of governing equations to be considered and enables us to determine the steady sliding solution. The fact that the disk is in rotation can be easily taken into account since the system remains in small strains. The determination of the steady sliding solution is discussed as a function of the coefficient of friction. In particular, the conditions ensuring the existence or the uniqueness of the steady sliding solution are discussed since for high friction, the steady sliding solution may be not unique or does not even exist.

The stability of a steady sliding solution is considered in the second part. Perturbed motions of the mechanical system of pad and disk near the steady sliding solution are introduced. Under the assumption of a slip regime, the dynamic solution can be simplified and the perturbed slip motions can be considered. Stability analysis with respect to these motions can be discussed and leads to the solution of a generalized eigenvalue problem with unsymmetric mass and rigidity matrices. This non-symmetry is due to the presence of friction as well as of the disk rotation. The existence of an eigenvalue with a positive real part and a non-zero imaginary part implies necessarily an instability by flutter of the steady sliding solution.

The numerical aspect of the problem is considered in the third part. The steady sliding solution can be determined by solution of the nonlinear problem in the vehicle reference by iterations. Once this solution is obtained, its stability analysis can be performed. The adopted procedure is based upon a modal basis of free vibrations. The generalized eigenvalue problem is solved in this basis of functions and the eigenvectors are generated by a finite number of the first vibration modes. The numerical procedure is first validated on the problem of contact with friction of infinite elastic layers which has been discussed analytically by ADAMS [1] and by MARTINS *et al.* [10]. Then an example of disk brake is considered.

2. Governing equations

The system of disk and pad is considered in the vehicle axes (Ox), which is a Galilean reference set, since the vehicle motion is assumed to proceed at constant velocity. In this reference, the pad is an elastic solid P in small deformation. For simplicity, it is assumed that this solid is under the action of implied displacements (by the brake action) and contact forces with the disk on a potential contact surface S. If $u^P(x,t)$ and $\sigma^P(x,t)$ denote respectively the displacement and stress at the point x and time t, the dynamic equations for the pad P are

$$\sigma^P = L : \nabla u^P, \quad \text{Div}\, \sigma^P - \rho u^P{}_{,tt} = 0, \quad \forall\ x \in P, \quad \sigma^P \cdot n^P = R, \quad \forall\ x \in S. \tag{2.1}$$

In this expression, R is the reaction of the disk D, which is related to the relative displacement and velocity of the two solids following the unilateral contact and Coulomb's law of dry friction with a constant coefficient of friction, although more elaborated models can be proposed, e.g. [2, 13].

Let ω be the rotation velocity of the disk around the axis Ox_3. It is convenient to consider the rotating axes (OX), where OX_3 coincides with Ox_3. The equations of motion of the solid D in axes (OX) are simply the dynamic equations of an elastic solid at small deformation in a relative reference

$$\Sigma = L : \nabla U, \quad \text{Div}\, \Sigma - \rho\gamma = 0, \quad \forall\ X \in D_o \tag{2.2}$$

with

$$\gamma = \gamma_e + \gamma_r + 2\omega k \wedge V_r = -\omega^2 r + U_{,tt} + 2\omega k \wedge U_{,t}\,, \tag{2.3}$$

where D_o denotes the undeformed volume of the disk in these axes, and $\Sigma = \Sigma(X,t)$, $U = U(X,t)$ are respectively the stress tensor and displacement vector. It is necessary to adopt the vehicle axes (Ox) and a change of variables must be introduced. This change of variables can be expressed in terms of the cylindrical coordinates as shown in Fig. 1:

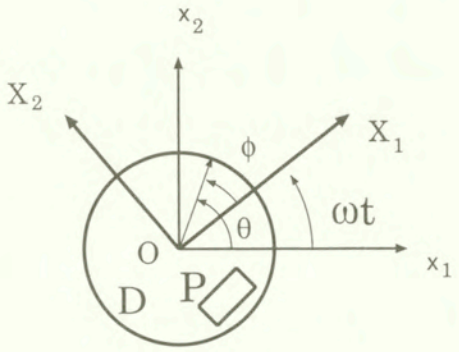

FIG. 1. A model of disk brake.

$$X = (r, \phi, z), \quad x = (r, \theta, z), \quad \theta = \phi + \omega\, t. \tag{2.4}$$

The change of variables

$$u(r,\theta,z,t) = U(r,\theta - \omega t, z, t), \qquad U(r,\phi,z,t) = u(r,\phi + \omega t, z, t) \tag{2.5}$$

$$\sigma(r,\theta,z,t) = \Sigma(r,\theta-\omega t,z,t), \quad \Sigma(r,\phi,z,t) = \sigma(r,\phi+\omega t,z,t) \tag{2.6}$$

gives in the Galilean axes (Ox)

$$\sigma = L : \nabla u, \quad \text{Div}\,\sigma - \rho\gamma = 0, \quad \forall\ x \in D, \tag{2.7}$$

$$\gamma = \omega^2(-r + u_{,\theta\theta} + 2k \wedge u_{,\theta}) + 2\omega(u_{,\theta t} + k \wedge u_{,t}) + u_{,tt} \tag{2.8}$$

with the boundary condition

$$\sigma \cdot n = -R, \quad \forall\ x \in S, \tag{2.9}$$

and implied displacements along the axis of rotation Ox_3. It is also important to give the expression of the material velocity $v(x,t)$ in this reference system. From the expression of the velocity of a material point in the rotating axes

$$v = V_e + V_r = \omega k \wedge r + U_{,t},$$

it follows that

$$v(x,t) = \omega(k \wedge r + u_{,\theta}) + u_{,t}. \tag{2.10}$$

The conditions of unilateral contact and dry friction of the solids P and D can be written now. On the surface S of contact, which is assumed initially without the normal gap, the condition of non-penetration is

$$[u]_N = (u^P - u) \cdot n \geq 0, \quad \forall\ x \in S. \tag{2.11}$$

The unilateral contact condition gives

$$[u]_N \geq 0, \quad R_N \geq 0, \quad [u]_N\, R_N = 0, \quad \forall\ x \in S. \tag{2.12}$$

The relative velocity of material points in contact is

$$w(x,t) = u^P_{,t}(x,t) - v(x,t) = [u]_{,t} - \omega k \wedge r - \omega u_{,\theta}. \tag{2.13}$$

Coulomb's friction law can be written as

$$w = \nu\, R_T, \quad \varphi = \|R_T\| - f R_N \leq 0, \quad \nu \leq 0, \quad \nu\varphi = 0. \tag{2.14}$$

The previous expressions for γ and w show that a possible approximation of the solution is obtained by assuming that the relative velocity is due simply to the rotation of the disk, and one can retain in the dynamic equation of the disk only the centrifugal forces and neglect all other terms of rotation. This approximation $\mathcal{A}$ consists in writing

$$\gamma = -\omega^2 r + u_{,tt}, \quad w(x,t) = [u]_{,t} - \omega k \wedge r. \tag{2.15}$$

3. Steady sliding solution

The steady state solution is obtained when $u(x,t)$ does not depend on t. Thus, the steady state solution is governed by the following equations:

$$\sigma^P = L : \nabla u^P, \quad \text{Div}\, \sigma^P = 0, \quad \forall\ x \in P, \quad \sigma^P \cdot n = -R, \quad \forall\ x \in S, \tag{3.1}$$

$$\sigma = L : \nabla u, \quad \text{Div}\, \sigma - \rho\gamma = 0, \quad \forall\ x \in D, \quad \sigma \cdot n = -R, \quad \forall\ x \in S, \tag{3.2}$$

$$\gamma = \omega^2(-r + u_{,\theta\theta} + 2k \wedge u_{,\theta}) \tag{3.3}$$

together with Eqs. (2.11), (2.12), (2.14) and the following expression of the relative velocity

$$w(x,t) = -\omega(k \wedge r + u_{,\theta}). \tag{3.4}$$

The approximation $\mathcal{A}$ consists in solving the following equations:

$$\sigma^P = L : \nabla u^P, \quad \text{Div}\, \sigma^P = 0, \quad \forall\ x \in P, \quad \sigma^P \cdot n = -R, \quad \forall\ x \in S, \tag{3.5}$$

$$\sigma = L : \nabla u, \quad \text{Div}\, \sigma + \rho\omega^2 r = 0, \quad \forall\ x \in D, \quad \sigma \cdot n = -R, \quad \forall\ x \in S, \tag{3.6}$$

together with Eqs. (2.11), (2.12), (2.14) with $w(x,t) = -\omega k \wedge r$. Within this approximation, since the relative velocity is not zero, the transverse reaction R_T has the direction of $-\tau$ with $\tau = \dfrac{w}{\|w\|}$. Finally, the steady sliding solution is given by Eqs. (2.11), (2.12) and

$$\sigma^P = L : \nabla u^P, \quad \text{Div}\, \sigma^P = 0, \quad \forall\ x \in P, \quad \sigma^P \cdot n = -R_N n + f R_N \tau, \quad \forall\ x \in S. \tag{3.7}$$

$$\sigma = L : \nabla u, \quad \text{Div}\, \sigma + \rho\omega^2 r = 0, \quad \forall\ x \in D, \quad \sigma \cdot n = -R_N n + f R_N \tau, \quad \forall\ x \in S. \tag{3.8}$$

These equations can also be written in the form

$$\int_P \nabla u^P : L : \nabla \delta u \, dV + \int_D \nabla u : L : \nabla \delta u \, dV - \int_D \omega^2 r \cdot \delta u \, dV + \int_S (R_N [\delta u]_N + f R_N \tau \cdot [\delta u]_T) \, dS = 0, \tag{3.9}$$

together with (2.11) and (2.12). To understand the mathematical nature of the problem of steady sliding in the approximation $\mathcal{A}$, let us consider the associated

discrete problem obtained from these equations after discretization by the finite element method, for example. If $U = (U_N, U_T, U_Z)$ denotes for each solid the degrees of freedom representing respectively the normal, tangential displacements of the contact surface and other complementary displacements in the solid, the governing equations are, for each solid,

$$\begin{bmatrix} K_{NN} & K_{NT} & K_{NZ} \\ K_{TN} & K_{TT} & K_{TZ} \\ K_{ZN} & K_{ZT} & K_{ZZ} \end{bmatrix} \begin{bmatrix} U_N \\ U_T \\ U_Z \end{bmatrix} = \begin{bmatrix} R_N \\ f[\Phi]R_N \\ F_Z \end{bmatrix},$$

where Φ denotes the appropriate matrix. The elimination of U_Z leads to a matrix equation in terms of $\Delta = U^P - U$

$$\begin{bmatrix} k_{NN} & k_{NT} \\ k_{TN} & k_{TT} \end{bmatrix} \begin{bmatrix} \Delta_N \\ \Delta_T \end{bmatrix} = \begin{bmatrix} R_N + F_N \\ f[\Phi]R_N + F_T \end{bmatrix}.$$

Finally, the normal displacement Δ_N is related to the normal reaction R_N by

$$[k_{NN} - k_{NT}k_{TT}^{-1}k_{TN}][\Delta_N] = [I - fk_{NT}k_{TT}^{-1}\Phi][R_N] + [g], \tag{3.10}$$

$$\Delta_N^k \geq 0, \quad R_N^k \geq 0, \quad \Delta_N^k \, R_N^k = 0, \quad \forall k = 1, m. \tag{3.11}$$

This is a linear complementary problem, (cf. COTTLE *et al.* [5], ISAC [7] or KLARBRING [9]):

$$[\Delta_N] = [A][R_N] + [F], \quad \Delta_N^k \geq 0, \quad R_N^k \geq 0, \quad \Delta_N^k \, R_N^k = 0, \tag{3.12}$$

with

$$[A] = [k_{NN} - k_{NT}k_{TT}^{-1}k_{TN}]^{-1} - f \;\; [k_{NN} - k_{NT}k_{TT}^{-1}k_{TN}]^{-1}[k_{NT}k_{TT}^{-1}\Phi]. \tag{3.13}$$

It should be recalled that for a given $[F]$, this problem has one and only one solution if the matrix $[A]$ is a P-matrix. This property means that $[A]$ satisfies the condition of P-positivity

$$[A] \text{ is a P-matrix} \;\Leftrightarrow\; \exists \; i \text{ such that } \sum_j X_i A_{ij} X_j > 0 \tag{3.14}$$

$$\forall \; X \neq 0.$$

In fact, the existence of a solution is still ensured if $[A]$ satisfies only a co-P-positivity condition:

$$[A] \text{ is a co-P-matrix} \;\Leftrightarrow\; \exists \; i \text{ such that } \sum_j X_i A_{ij} X_j > 0 \tag{3.15}$$

$$\forall \; X \neq 0, \quad X \geq 0.$$

As usual, for a vector, the compact notation $X \geq 0$ means the component-wise condition $X_i \geq 0$ for all i. This condition is similar to the P-positivity condition but is concerned only with vectors of nonnegative components. It has been established for a matrix not necessarily symmetric that

(3.16) Positive-definiteness $\Rightarrow$ P-positivity $\Rightarrow$ Co-P-positivity,

(3.17) Positive-definiteness $\Rightarrow$ Co-positivity $\Rightarrow$ Co-P-positivity.

For symmetric matrices, it is also true that P-positivity and positive-definiteness are equivalent,

(3.18) Positive-definiteness $\Leftrightarrow$ P-positivity.

When the full expressions (3.3), (3.4) of γ and w are taken into account, the discussion can be done in the same spirit and leads again to a complementary problem.

The significance of the quadratic form $[R_N]^T[A][R_N]$ is very simple. It represents the work done by the normal reactions $R_N \Delta_N$ of the system when subjected to the contact reaction $R = R_N n + f\ R_N \tau$ and to homogeneously implied displacement. The condition of positivity states that for any non-zero distribution of normal reactions, the work done by this distribution is positive. The condition of co-P-positivity is much weaker, it states that for any non-zero and positive distribution of the normal reactions, there exists at least one strictly positive normal displacement associated with a strictly positive normal reaction.

The contribution of the rotation terms to the rigidity matrix of the solid D corresponds to some additional symmetric matrices, since the following expressions hold:

$$\int_D u_{,\theta\theta} \cdot \delta u \ dV = -\int_D u_{,\theta}\, \delta u_{,\theta} \ dV \tag{3.19}$$

$$\int_D (k \wedge u_{,\theta}) \cdot \delta u \ dV = \int_D \det[k, u_{,\theta}, \delta u] \ dV = \int_D -\det[k, u, \delta u_{,\theta}] \ dV \tag{3.20}$$

$$= \int_D \det[k, \delta u_{,\theta}, u] \ dV.$$

After partial integration with respect to θ in the interval $[0, 2\pi]$, these expressions are symmetric with respect to $(u, \delta u)$. Under the assumption of small rotations, ω remains sufficiently small, the contribution of these additional terms to the rigidity of solid D does not change its positivity.

The fact that the co-P-positivity condition is satisfied depends on the considered problem. Even for elastic solids at small strains, it is not difficult to give

simple examples showing that the possibility of steady sliding does not exist for a sufficiently high friction coefficient.

4. Stability analysis of the steady sliding solution

The stability of the steady sliding solution is obtained from the behaviour of the perturbed motions of the system near the considered steady solution. This discussion is a priori difficult since a small perturbed motion near the steady solution is not necessarily governed by linear equations. It is well known that the unilateral contact and Coulomb's laws are non-smooth and cannot be linearized at the steady state, e.g. [3, 8, 10 – 11, 14 – 20]. It is assumed first that the steady sliding solution satisfies on the contact surface S the condition of effective contact

$$R_N(x) > 0 \quad \forall x \in S. \tag{4.1}$$

It is then expected that a small perturbed motion cannot lead to a separation of the contact at any point of S, at least at the early time. This remark enables us to consider only in-contact motions of the solids on the contact surface S, to avoid the difficulties related to the unilateral aspect.

Even in these motions, it is necessary to separate the slip regime $w \neq 0$ from the stick regime $w = 0$. The problem of stick-slip motions has been much discussed in the literature. In particular, for a simple oscillator, the modification of the initial frequency has been considered, (cf. for example POPP and STELTER [18]) for a velocity-dependent coefficient of friction. The stick-slip motion has been computed for a three-dimensional oscillator by CHO and BARBER [4]. The stick-slip motions play an important role in most contact problems (cf. ZHARII [20]), in particular in the study of noise emission. However, the presence of stick-slip motions is a source of difficulty and in this stability analysis, only the slip motions will be explored. Under this restriction, the equations of motion can be effectively linearized near the steady sliding solution. Let u^* and σ^* be the differences

$$u^* = u_p - u_e, \quad \sigma^* = \sigma_p - \sigma_e, \tag{4.2}$$

where u_e, σ_e refer to the steady sliding solution, and u_p, σ_p to the perturbed motion. For small perturbations, u^* and σ^* are governed by the linearized equations at the steady sliding state. Thus, the following equations hold for the slip motions in the vicinity of the steady sliding state:

$$\sigma^{*P} = L : \nabla u^{*P}, \quad \text{Div}\, \sigma^{*P} - \rho u^{*P}{}_{,tt} = 0 \quad \forall \ x \in P, \quad \sigma^{*P} \cdot n = -R^*, \quad \forall \ x \in S, \tag{4.3}$$

$$\sigma^* = L : \nabla u^*, \quad \text{Div}\,\sigma^* - \rho\gamma^* = 0, \quad \forall\ x \in D, \quad \sigma^* \cdot n = -R^*, \quad \forall\ x \in S, \tag{4.4}$$

$$\gamma^* = \omega^2(u^*{}_{,\theta\theta} + 2k \wedge u^*{}_{,\theta}) + 2\omega(u^*{}_{,\theta t} + k \wedge u^*{}_{,t}) + u^*{}_{,tt}, \tag{4.5}$$

$$[u^*]_N = 0. \tag{4.6}$$

In these equations, the tangent reaction R_T^* is related to the normal reaction R_N^* by the linearized expression of the equation

$$R_T = -fR_N \frac{w}{\|w\|},$$

which gives

$$R_T^* = -fR_N^*\tau - fR_N\left(\frac{w^*}{\|w\|} - w\frac{w \cdot w^*}{\|w\|^3}\right) \text{ with} \tag{4.7}$$

$$w^* = [u^*{}_{,t}] - \omega u^*{}_{,\theta}\,. \tag{4.8}$$

These equations can also be conveniently written under the variational form of the virtual work equation. For the solid P, the classical equation

$$\int_P \rho u^{*P}{}_{,tt} \cdot \delta u\ dV + \int_P \nabla u^{*P} : L : \nabla \delta u\ dV = \int_S R^* \cdot \delta u\ dS \tag{4.9}$$

is obtained. For the solid D, the following equation holds:

$$\int_D \rho u^*{}_{,tt} \cdot \delta u\ dV + 2\omega \int_D \rho(u^*{}_{,\theta t} \cdot \delta u + \det[k, u^*{}_{,t}, \delta u])\ dV + \int_D \nabla u^* : L : \nabla \delta u\ dV + \omega^2 \int_D (u^*{}_{,\theta\theta} \cdot \delta u + 2\det[k, u^*{}_{,\theta}, \delta u])\ dV = -\int_S R^* \cdot \delta u\ dS. \tag{4.10}$$

In this equation, it should be noted that the terms involving $u^*{}_{,t}$ are skew-symmetric while the terms involving $u^*{}_{,tt}$ or u are symmetric. If the solution is searched for in the form $(u^*, R^*) = (d(x), r(x))\ \exp st$, the eigenvalues s and eigenvectors d must satisfy the equation:

$$s^2 \int_P \rho d^P \cdot \delta u\ dV + \int_P \nabla d^P : L : \nabla \delta u\ dV = \int_S r \cdot \delta u\ dS \tag{4.11}$$

for the solid P. For the solid D, the following equation holds:

$$(4.12)\quad s^2 \int_D \rho d^D \cdot \delta u \, dV + s\, 2\omega \int_D \rho(d^D{}_{,\theta} \cdot \delta u + \det[k, d^D, \delta u]) \, dV$$
$$+ \int_D \nabla d^D : L : \nabla \delta u \, dV + \omega^2 \int_D (-d^D{}_{,\theta} \cdot \delta u_{,\theta} + 2 \det[k, d^D{}_{,\theta}, \delta u]) \, dV$$
$$= - \int_S r \cdot \delta u \, dS.$$

After discretization by the finite element method with the nodal shape functions $\mathcal{N}_i(x)$

$$(4.13)\quad d(x) = \sum_{i=1}^{n} d_i \mathcal{N}_i(x),$$

the following matrix equations hold:

$$(4.14)\quad (s^2[M^P] + [K^P])[d^P] = [r^P], \quad (s^2[M^D] + s[G^R] + [K^D] + [K^{DR}])[d^D] = -[r^D]$$

with $[d^P] = [d_P, d_{PT}, d_N]^T$, $[d^D] = [d_N, d_{DT}, d_D]^T$, where the notation d_N, d_{DT}, d_D refers to different nodal values of solid D, respectively to the normal and tangent nodal displacements on the contact surface, and to other nodal displacements elsewhere. Note that $[G^R]$ is skew-symmetric and $[K^R]$ is a symmetric matrix. Thus, the effect of rotation of D is finally expressed by a gyroscopic term and by an additional symmetric rigidity. The force matrices $[r^P]$ and $[r^D]$ are related by

$$[r^P] = [0, r_T, r_N]^T, \quad [r^D] = [r_N, r_T, 0]^T.$$

From the expression for R_T^*, the following equation holds:

$$[r_T] = f[\Phi][r_N] + fs[A][d_{PT} - d_{DT}] + f[B_T][d_{DT}] + f[B_N][d_N],$$

where $[A], [B_T], [B_N]$ are some appropriate square matrices. From the expression of $[r_N]$

$$[r_N] = (s^2[M^P_{N.}] + [K^P_{N.}])[d^P] = -(s^2[M^D_{N.}] + s[G^R_{N.}] + [K^D_{N.}] + [K^R_{N.}])[d^D],$$

r_T and r_N can be written in terms of the displacement $[d] = [d_P, d_{PT}, d_N, d_{DT}, d_D]^T$. Finally, the eigenvalues s and eigenvectors $[d]$ must satisfy the condition

$$(4.15)\quad \{s^2([M] - f\,[m]) + s([G] - f\,[\ell]) + [K] + [K^R] - f\,[k]\}\ [d] = [0],$$

with

$$[M] = \begin{bmatrix} M^P_{PP} & M^P_{PN} & M^P_{PT} & 0 & 0 \\ M^P_{TP} & M^P_{TN} & M^P_{TT} & 0 & 0 \\ M^P_{NP} & M^P_{NT} & M^P_{NN} + M^Q_{NN} & M^Q_{NT} & M^Q_{ND} \\ 0 & 0 & M^Q_{TN} & M^Q_{TT} & M^Q_{TD} \\ 0 & 0 & M^Q_{DN} & M^Q_{DT} & M^Q_{DD} \end{bmatrix},$$

$$[K] = \begin{bmatrix} K^P_{PP} & K^P_{PN} & K^P_{PT} & 0 & 0 \\ K^P_{TP} & K^P_{TN} & K^P_{TT} & 0 & 0 \\ K^P_{NP} & K^P_{NT} & K^Q_{NN} + K^P_{NN} & K^Q_{NT} & K^Q_{ND} \\ 0 & 0 & K^Q_{TN} & K^Q_{TT} & K^Q_{TD} \\ 0 & 0 & K^Q_{DN} & K^Q_{DT} & K^Q_{DD} \end{bmatrix}.$$

$$[m] = \begin{bmatrix} 0 & 0 & 0 & 0 & 0 \\ \Phi M^P_{NP} & \Phi M^P_{NT} & \Phi M^P_{NN} & 0 & 0 \\ 0 & 0 & 0 & 0 & 0 \\ 0 & 0 & -\Phi M^D_{NN} & -\Phi M^D_{NT} & -\Phi M^D_{ND} \\ 0 & 0 & 0 & 0 & 0 \end{bmatrix},$$

$$[\ell] = \begin{bmatrix} 0 & 0 & 0 & 0 & 0 \\ 0 & A & 0 & -A & 0 \\ 0 & 0 & 0 & 0 & 0 \\ 0 & -A & -\Phi G^{DR}_{NN} & A - \Phi G^{DR}_{NT} & -\Phi G^{DR}_{ND} \\ 0 & 0 & 0 & 0 & 0 \end{bmatrix},$$

$$[k] = \begin{bmatrix} 0 & 0 & 0 & 0 & 0 \\ \Phi K^P_{NP} & \Phi K^P_{NT} & \Phi K^P_{NN} + B_N & B_T & 0 \\ 0 & 0 & -\Phi(K^D + K^{DR})_{NN} - B_N & -\Phi(K^D + K^{DR})_{NT} - B_T & -\Phi(K^D + K^{DR})_{ND} \\ 0 & 0 & 0 & 0 & 0 \end{bmatrix},$$

$$[G] = \begin{bmatrix} 0 & 0 & 0 & 0 & 0 \\ 0 & 0 & 0 & 0 & 0 \\ 0 & 0 & G^R_{NN} & G^R_{NT} & G^R_{ND} \\ 0 & 0 & G^R_{TN} & G^R_{TT} & G^R_{TD} \\ 0 & 0 & G^R_{DN} & G^R_{DT} & G^R_{DD} \end{bmatrix},$$

$$[K^R] = \begin{bmatrix} 0 & 0 & 0 & 0 & 0 \\ 0 & 0 & 0 & 0 & 0 \\ 0 & 0 & K^{DR}_{NN} & K^{DR}_{NT} & K^{DR}_{ND} \\ 0 & 0 & K^{DR}_{TN} & K^{DR}_{TT} & K^{DR}_{TD} \\ 0 & 0 & K^{DR}_{DN} & K^{DR}_{DT} & K^{DR}_{DD} \end{bmatrix}.$$

This eigenvalue problem can be written as

$$(s^2\,[\bar{M}] + s\,[\bar{Z}] + [\bar{K}])[d] = 0, \tag{4.16}$$

$$[\bar{M}] = [M] - f\,[m],\quad [\bar{Z}] = [G] - f\,[\ell],\quad [\bar{K}] = [K] + [K^R] - f\,[k].$$

Thus the presence of friction breaks the symmetry of the mass and rigidity matrices in the eigenvalue problem to be solved. Since the numerical solution of this non-symmetric problem of dimension n is time-consuming, a reduction of the dimension of the problem is necessary. Thus, it is interesting to consider the basis of vibration modes D_k of the ideal associated system defined by the equations (of dimension n)

$$(s_0^2[M] + [K])[D] = [0]. \tag{4.17}$$

Let $D_k,\ k = 1, m$ denote the first m vibration modes. The reduction of variable consists in searching for $[d]$ in this basis:

$$[d] = [D_1\ \ D_2\ \ \ldots\ \ D_m][q_1\ \ \ldots q_m]^T = [C][q]. \tag{4.18}$$

Finally, the eigenvalue s and eigenvector $[q]$ are defined by an eigenvalue problem of dimension m

$$(s^2[\mathcal{M}] + s[\mathcal{Z}] + [\mathcal{K}])[q] = [0], \tag{4.19}$$

$$[\mathcal{M}] = [C]^T[\bar{M}][C],\quad [\mathcal{Z}] = [C]^T[\bar{Z}][C],\quad [\mathcal{K}] = [C]^T[\bar{K}][C].$$

The solution of (4.19) leads to the complex eigenvalues s_k and complex eigenvectors Q_k. Since $u^*(x,t) = \mathcal{N}_i(x)\ \Re\ (\sum_k\ \ a_k\ C_{ij}Q_{kj}\ \exp s_k t)$, it is concluded

that the steady sliding solution is unstable if there exists an eigenvalue with a positive real part. Although it is not necessary, the choice of this modal basis is interesting since the dynamic behaviour of the system is well generated by a small number of modes, in practice $m \ll n$.

5. Validation of the numerical procedure

The proposed numerical procedure is first validated on a sample problem which is the sliding of a rigid plate on an elastic infinite layer, (cf. Fig. 2). The problem was analytically discussed by MARTINS *et al.* [11] for the case of an elastic half-space, and by ADAMS [1], MOIROT [12] for the case of two elastic layers. The case of an infinite layer is interesting since a closed-form solution can be obtained for any coefficient of friction, in contrast with the case of the half-space.

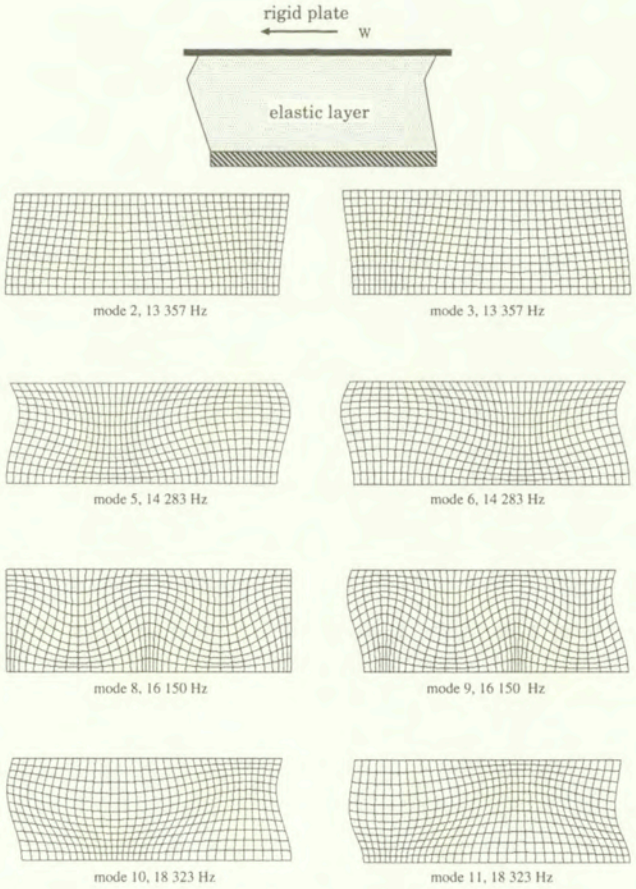

FIG. 2. The sliding problem of a rigid plate on an infinite elastic layer and the vibration basis.

5.1. Sliding of a rigid plate on an elastic layer

The governing equations are

$$(\lambda + 2\mu)u_{,xx} + \mu u_{,yy} + (\lambda + \mu)v_{,xy} = \rho u_{,tt},$$

$$(\lambda + 2\mu)v_{,yy} + \mu v_{,xx} + (\lambda + \mu)u_{,xy} = \rho v_{,tt},$$

with boundary conditions

$$u(x, -h, t) = v(x, -h, t) = 0,$$

and interface conditions on S

$$\delta - v \geq 0, \quad \sigma_{yy} \leq 0, \quad (\delta - v)\sigma_{yy} = 0 \quad \forall \ x, \ y = 0,$$

$$\varphi = |\sigma_{xy}| - f\sigma_{yy} \leq 0, \qquad W - u_{,t} = \nu\sigma_{xy}, \quad \nu \geq 0, \quad \nu\varphi = 0.$$

The steady sliding solution exists for all f,

$$u = \delta f \ (y + h)\frac{\mu}{\lambda + 2\mu} \text{ sign } (W), \quad v = \delta(y + h).$$

The eigenvalue problem (4.16) has been discussed for a solution u^* of the form

$$u^* = \Re \ \exp(st) \exp(kx) U(y), \quad k \in C, \quad s \in C.$$

It has been shown that there exists s with $\Re(s) > 0$ for any $f > 0$, thus the steady sliding solution with friction is always unstable. The mechanism of instability can be understood by the study of the trajectory of the eigenvector $s(f)$ in the complex plane as a function of f. For $f = 0$, all modes are double. When f increases from 0, most eigenvalues remain purely imaginary while some of them are splitting into two complex, simple eigenvalues with a non-zero real part.

5.2. Numerical validation

The modal basis D_k, $k = 1, m$, is first computed by the solution of the Eqs. (4.17). As usual, these frequencies of vibration can be obtained with great precision. The relative error of the computed frequencies as a function of the mesh size is less than 1% for the 30 first frequencies with the mesh 12×36. Figure 2 presents some modes and the associated frequencies of vibration.

The solution of the Eq. (4.19) for a chosen basis D_k, $k = 1, m$ can be done following the standard methods available for example in the Nastran code. Hessenberg's method seems to give good numerical results. It is recalled that Hessenberg's method is obtained in two steps, a reduction to a Hessenberg matrix

and an iteration by a QR algorithm. This method gives all eigenvalues and the associated eigenvectors are obtained by inverse iterations.

The variations of the frequencies as functions of the friction are computed with $m = 200$ and with the 12×36 mesh, and $n = 829$. These frequencies are obtained with error smaller than 3% compared to the exact values. It is found that good results can be obtained with a small number of modes, in practice $m = 200$ is sufficient. These results confirmed numerically the observation that the steady sliding solution is unstable by flutter when friction is introduced.

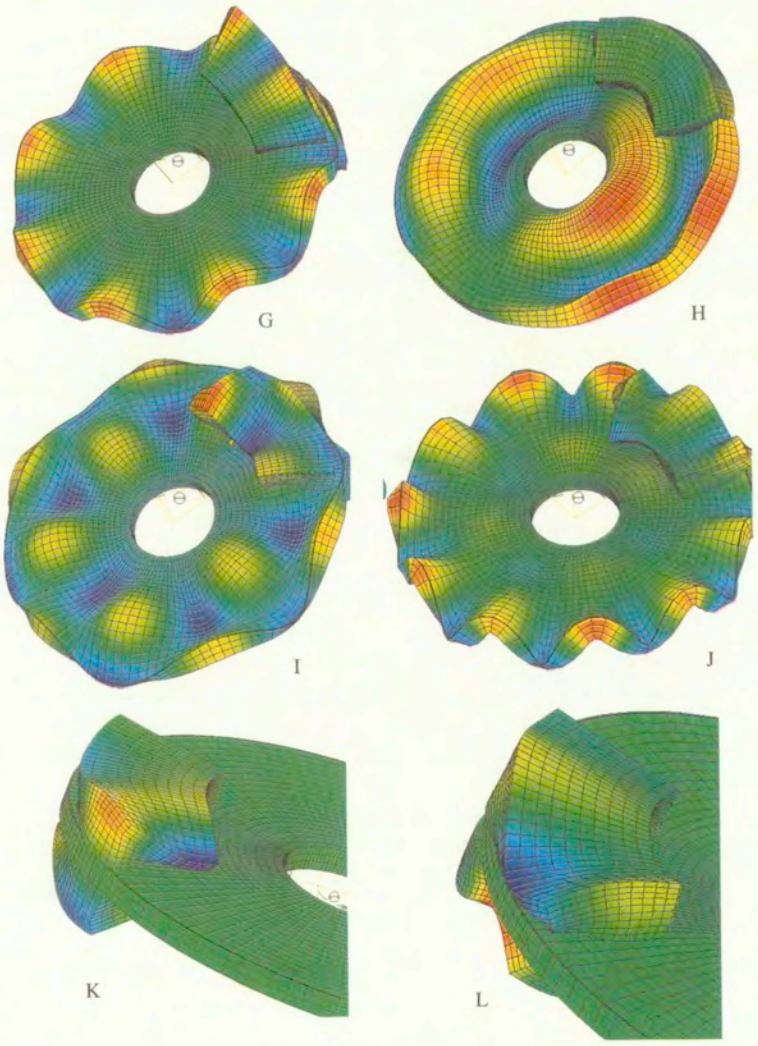

FIG. 3. Flutter instability of the steady sliding solution of the pad-disk system. The real parts of some unstable modes are presented.

6. Numerical results for a disk brake

A disk brake is considered with a finite element mesh using 17860 nodal points, $n = 53580$ is the number of degrees of freedom. The pad is submitted to a uniform pressure on the upper face. Under the approximation $\mathcal{A}$, the steady sliding solution can be obtained within 3 iterations. The associated normal pressure is strictly positive on the whole contact surface, thus the assumption of effective contact is satisfied. The solution of (4.19) is again done using a basis of functions composed of $m = 200$ first vibration modes of the perfect system. For $f = 0.4$, the unstable modes among the first 70 eigenmodes are modes 19, 24, 30, 32, 40, 48, 51, 56, 60, 63, 66, 68 of frequencies 5275, 6483, 8574, 9113, 11418, 11951, 12610, 13721, 14716, 15302, 15534, 15746, respectively. The real parts of the most unstable modes $32, 48, 51, 68, 63, 66$ can be found in Fig. 3.

7. Concluding remarks

It is expected that, in the spirit of Hopf's bifurcation, after a flutter instability the dynamic response of the system will eventually become periodic with different phases of stick, slip and separation regimes, as it can be observed in various examples of the literature, (cf. [12 – 20]). Brake squeal results as a consequence of this periodic regime. The frequencies of the periodic responses, if they exist, are however not directly related to the flutter modes although they may remain close. From the analysis of the mechanism of flutter, our analysis leads already to some suggestions in order to impede such an instability.

References

1. G. G. ADAMS, *Self-excited oscillations of two elastic half-spaces sliding with a constant coefficient of friction*, J. Applied Mechanics, 867-872, 1995.
2. P. CHAMBRETTE, L. JEZEQUEL, *Stability of a beam rubbed against a rotation disk*, Eur. J. Mech. A/Solids, **11**, 107–138, 1992.
3. X. CHATEAU, Q. S. NGUYEN, *Buckling of elastic structures in unilateral contact with or without friction*, Eur. J. Mech, A/Solids, **10**, 71–89, 1991.
4. H. CHO, J. R. BARBER, *Stability of the three-dimensional Coulomb's friction law*, Phil. Trans. Roy Soc., **A 455**, 839–861, London 1999.
5. R. COTTLE, J. S. PANG, R. E. STONE, *The linear complementary problem*, Academic Press, 1992.
6. S. DURAND, *Unilateral contact with bounces*, [In:] Contact Mechanics, Marseille 1995, Plenum Press, 111–118, New York 1996.
7. G. ISAC, *Complementary Problems*, Springer-Verlag, Lecture Note in Mathematics, New York 1992.

8. M. JEAN, J. J. MOREAU, *Dynamics in the presence of unilateral contact and dry friction: a numerical approach*, [In:] Unilateral problems in structural analysis, CISM course, 1–50, Springer-Verlag, Wien 1987.

9. A. KLARBRING, *Contact, friction, discrete mechanical structures and mathematical programming*, CISM Course on Contact Problems, 1997.

10. J. A. C. MARTINS, F. M. F. SIMOES, *On some sources of instable/illposedness in elasticity with Coulomb's friction*, Contact Mechanics, Marseille 1995.

11. J. A. C. MARTINS, S. BARBARIN, M. RAOUS. A. PINTO DA COSTA, *Dynamic stability of finite dimensional linear elastic system with unilateral contact and Coulomb's friction*, Comp. Meth. Appl. Mech. Engng., **177**, 3–4, 298–328, 1999.

12. F. MOIROT, *Etude de la stabilité d'un équilibre en présence de frottement de Coulomb. Application au crissement des freins à disque*, Doctorat thesis, Ecole Polytechnique, Paris 1998.

13. Z MRÓZ, A. JARZĘBOWSKI, *Phemenological models of contact slip*, Acta Mechanica, **102**, 59–72, 1994.

14. Q. S. NGUYEN, *Stabilité et mécanique non linéaire*, Hermès, Paris 1999.

15. V. G. OANCEA, T. A. LAURSEN, *Stability analysis of state-dependent dynamic frictional sliding*, Int. J. Nonlinear Mech., **32**, 5, 837–853, 1997.

16. J. T. ODEN, J. A. C. MARTINS, *Models and computational methods for dynamic friction phenomena*, Comp. Meth. Appl. Mech. Engng., **52**, 527–634, 1985.

17. M. OESTREICH, N. HINRICHS, K. POPP, *Bifurcation and stability analysis for a non-smooth friction oscillator*, Arch. Appl. Mech., **66**, 301–314, 1996.

18. K. POPP, P. STELTER, *Stick-slip vibrations and chaos*, Phil. Trans. Roy Soc., **A 332**, 89–105, London 1990.

19. D. VOLA, M. RAOUS, J. A. C. MARTINS, *Friction and instability of steady sliding squeal of a rubber/glass contact*, Int. J. Num. Meth. Engng., **45**, 1999.

20. O. Y. ZHARII, *Frictional contact between the surface wave and a rigid strip*, J. Applied Mechanics, **63**, 15–20, 1996.

Received February 8, 2000; revised version May 19, 2000.

Arch. Mech., **52**, 4–5, pp. 663–683, Warszawa 2000

3D equilibrium shapes of periodically arranged anisotropic precipitates with elastic misfit

Dedicated to Professor Zenon Mróz
on the occasion of his 70^{th} birthday

R. MUELLER, S. ECKERT and D. GROSS

Institute of Mechanics, Darmstadt University of Technology,
Hochschulstr. 1, D-64289 Darmstadt, Germany

A NUMERICAL PROCEDURE for simulating the equilibrium shapes of precipitates in two-phase materials, such as Ni-base alloys, is presented. Assuming a periodic arrangement of precipitates, a unit cell is analyzed to take particle interaction in 3D into account. Using the concept of generalized driving forces as the source of morphological evolution, a necessary condition for an equilibrium shape is derived. In the derivation of the driving force, elastic strain energy arising from the elastic misfit of the two phases and interface energy is considered. Both phases are assumed to be linear elastic but anisotropic and different from each other. The periodic cell problem is numerically solved by the Boundary Element Method. Numerical simulation for material parameters which mimic Ni-base alloys shows the influence of particle size, stiffness ratio of the two phases, volume fraction and external load on the resulting equilibrium shapes.

Key Words: Micromechanics, Eigenstrains, Anisotropic Boundary Element Method, Periodic Cell, Particle Interaction

1. Introduction

IN HIGH TEMPERATURE applications such as turbine blades, the Ni-base alloys are frequently used. Due to their superior mechanical and thermal properties they are also termed super-alloys. These single crystal materials possess in general a cuboidal microstructure of γ'-precipitates embedded in a Ni-matrix. The morphology on the micro-level strongly influences the mechanical and thermal material properties on the macro-level. Diffusion processes within the crystal lattice change the micromorphology at elevated temperatures and in the presence of stress fields. This phenomenon is called rafting and has been experimentally investigated for many years (see for example [1 – 4]). Due to their industrial importance, there has been a great effort of theoretical investigations of these two-phase materials, see for example [5 – 13]. Many of the theoretical investigations lead to numerical simulations which revealed the influence of certain

material parameters. In general, the modelling efforts of the microstructure can be divided into three groups:

– The first group of researchers treats the two-phase material via a Monte-Carlo simulation [14 – 18]. The different phases are identified by different "atoms" and generating a Boltzmann weighted chain of exchanges, the global energy minimum is found corresponding to an equilibrium configuration. This method is however very time-consuming and only a few 3D results have been published so far [19].

– In the second approach, a concentration or order parameter is introduced to distinguish the two phases. Often the assumption of elastically homogeneous phases is made to apply the method of Fast/Discrete Fourier Transforms (see for example [20 – 24]). The model requires the accurate resolution of very steep gradients. Therefore a very fine numerical grid is required. Due to the numerical effort only very few 3D results are known to the authors [25].

– In the third approach, which is pursued by the authors, the two-phase material is treated with a sharp interface model. The numerical implementation of this model can be done efficiently by using a Boundary Element Method [26 – 32]. In 3D, results were obtained for a fairly general set of material parameters [33, 34], however until now particle interaction has been neglected in 3D. With the periodic cell arrangement, this shortcoming is to be overcome and more realistic simulations are expected.

In the following, the periodic cell arrangement is taken as the first step to take particle interaction into account. From 2D calculations it is known that neighboring particles can disturb the stress field around a precipitate significantly [32] and therefore influence the equilibrium shape. The periodic arrangement is chosen for two reasons. Firstly due to its physical relevance, as many Ni-base alloys display a rather regular periodic microstructure, secondly for its efficient implementation of 3D interaction effects. In this context, it must be mentioned that, with the computational power available to the authors, a complex structure of more than two nonperiodically interacting 3D particles is at the moment not computable. On the other hand, the simulation of a periodic arrangement predicts the effect of the volume fraction of the precipitate phase on the micromorphology. This is generally believed to be an important factor [35 – 37] together with the particle size and the external loading situation.

2. Micromechanical model

2.1. Periodic unit cell model

Considered is a periodic arrangement of unit cells, each consisting of a particle $\mathcal{B}$ (γ'-phase) embedded in a matrix (γ-phase). The normal vector $\mathbf{n}$ points

from the interface $\partial\mathcal{B}$ into the matrix phase (see Fig. 1). The elastic properties of the precipitate and the matrix are assumed to be given by the elasticity tensors $\mathbb{C}^{\text{in/out}}$ respectively, which are allowed to be generally anisotropic. A possible lattice misfit between the γ'-phase and the matrix is taken into account by an inelastic eigenstrain $\boldsymbol{\varepsilon}^0$ in the precipitate phase, which is assumed to be constant in the precipitate. Therefore the stress $\boldsymbol{\sigma}$ can be computed by Hooke's law in the two phases

$$\boldsymbol{\sigma} = \begin{cases} \mathbb{C}^{\text{out}}\boldsymbol{\varepsilon} & \text{in the matrix phase,} \\ \mathbb{C}^{\text{in}}\left(\boldsymbol{\varepsilon} - \boldsymbol{\varepsilon}^0\right) & \text{in the precipitate phase,} \end{cases} \tag{2.1}$$

where $\boldsymbol{\varepsilon}$ is the linearized strain tensor. The interface $\partial\mathcal{B}$ between the precipitate and the matrix is perfectly coherent, thus the jump in the displacements $\mathbf{u}$ vanishes on the surface $\partial\mathcal{B}$:

$$[\![\mathbf{u}]\!] = \mathbf{0}, \quad \text{where} \quad [\![(\cdot)]\!] = (\cdot)^{\text{out}} - (\cdot)^{\text{in}}. \tag{2.2}$$

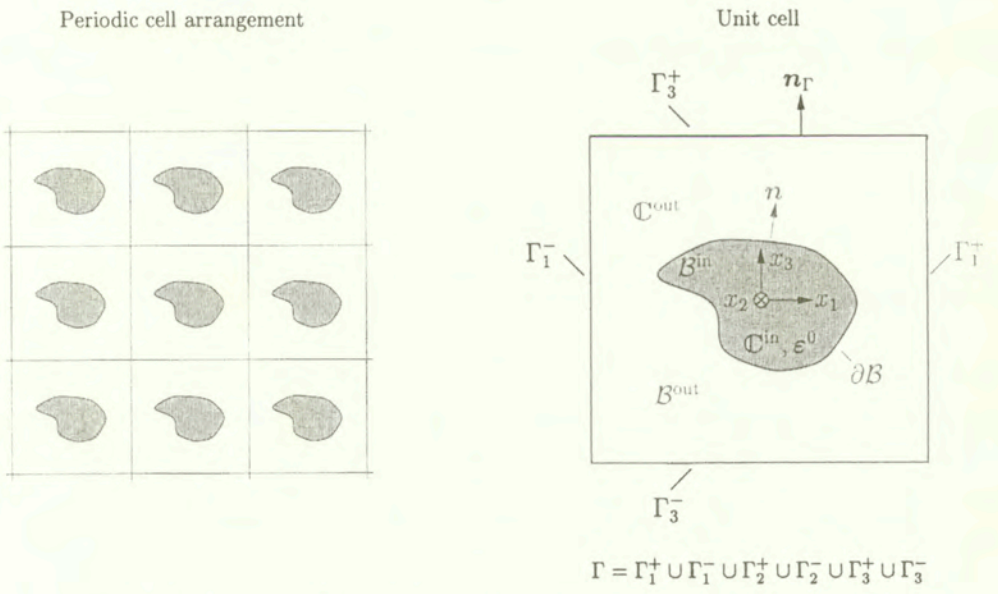

FIG. 1. Periodic arrangement of unit cells with precipitate.

On the exterior boundary of the cubic cell, the displacements $\mathbf{u}$ and tractions $\mathbf{t}$ have to satisfy periodicity conditions in order to ensure periodic filling of the entire material space. The cell boundary is denoted by Γ with its associated outward unit vector given by $\mathbf{n}_\Gamma$. The displacements $\mathbf{u}$ on two opposite cell boundaries $\Gamma_i^\pm$ (see Fig. 1) satisfy

$$\mathbf{u}|_{\Gamma_i^+} - \mathbf{u}|_{\Gamma_i^-} = \mathbf{v}_i \quad \text{for} \quad i = 1, 2, 3, \tag{2.3}$$

where the three vectors $\mathbf{v}_i$ are still undetermined translations. The periodicity conditions for the tractions are given by the following set of equations:

$$\mathbf{t}|_{\Gamma_i^+} + \mathbf{t}|_{\Gamma_i^-} = \mathbf{0} \quad \text{for} \quad i = 1, 2, 3. \tag{2.4}$$

In the absence of external loads, the mechanical equilibrium of the periodic cell arrangement leads to three vector equations

$$\int_{\Gamma_i^+} \mathbf{t}\, dA = \mathbf{0} \quad \text{for} \quad i = 1, 2, 3 \tag{2.5}$$

to determine the unknown translations $\mathbf{v}_i$. Equation (2.5) needs to be modified in the case of an external load $\boldsymbol{\sigma}^\infty$. However with the use of an equivalent eigenstrain

$$\boldsymbol{\varepsilon}^0_{\text{eq}} = \boldsymbol{\varepsilon}^0 - [\![\mathbb{C}^{-1}]\!]\boldsymbol{\sigma}^\infty \tag{2.6}$$

instead of the physical eigenstrains $\boldsymbol{\varepsilon}^0$, Eqs. (2.1) – (2.5) can still be used. A detailed discussion of equivalent eigenstrain is given in [38, 39].

2.2. Variational principle and equilibrium conditions

In the absence of external loads, the total potential of the system is given by the sum of the elastic strain energy

$$E^{\text{el}} = \int_{\mathcal{B}^{\text{in}}} W\, dV + \int_{\mathcal{B}^{\text{out}}} W\, dV, \quad \text{where} \quad W = \frac{1}{2}\boldsymbol{\sigma} : \boldsymbol{\varepsilon}^{\text{el}} \tag{2.7}$$

and the interface energy

$$E^{\text{int}} = \gamma_{\text{s}} \int_{\partial\mathcal{B}} dA. \tag{2.8}$$

Here the interface energy is assumed to be given by a constant interface energy density γ_{s}. For coherent interfaces the assumption of constant interface energy density is a good approximation (see [26, 28, 29], and related works for details and values of γ_{s}). In [27] the authors discuss the possibility of determining γ_{s} inversely by comparing experimental results with the simulated behaviour. Mass conservation dictates that the particle volume

$$V_{\mathcal{B}} = \int_{\mathcal{B}^{\text{in}}} dV = V_0 \tag{2.9}$$

remains constant V_0. Equilibrium is defined by extremizing the total potential for a given particle size V_0. This constraint is expressed by an augmented Lagrange functional

$$\tilde{E}(\mathbf{u}, \partial\mathcal{B}, \lambda) = E^{\text{el}} + E^{\text{int}} + \lambda\,(V_{\mathcal{B}} - V_0)\,, \tag{2.10}$$

with the Lagrange multiplier λ. Applying calculus of variations with respect to the displacement field $\mathbf{u}$, the morphology $\partial\mathcal{B}$ and the Lagrange multiplier λ leads to

$$\delta\tilde{E} = \int_{\mathcal{B}^{\text{in}}} \delta W \, dV + \int_{\mathcal{B}^{\text{out}}} \delta W \, dV - \int_{\partial\mathcal{B}} (\llbracket W \rrbracket + \kappa\gamma_{\text{s}} - \lambda)\, \delta n \, dA + \delta\lambda\,(V_{\mathcal{B}} - V_0) = 0, \tag{2.11}$$

where δn is the morphological variation of the interface $\partial\mathcal{B}$ in the normal direction and κ denotes twice the mean curvature (taken to be negative for a sphere) regarding the change of interface area. Applying the divergence theorem to the precipitate and matrix phase yields

$$\delta\tilde{E} = -\int_{\mathcal{B}^{\text{in}}} \operatorname{div}\boldsymbol{\sigma} \cdot \delta\mathbf{u} \, dV - \int_{\mathcal{B}^{\text{out}}} \operatorname{div}\boldsymbol{\sigma} \cdot \delta\mathbf{u} \, dV + \underbrace{\int_{\Gamma} \boldsymbol{\sigma}\mathbf{n}_{\Gamma} \cdot \delta\mathbf{u} \, dA}_{I} - \int_{\partial\mathcal{B}} \underbrace{\llbracket \boldsymbol{\sigma}\mathbf{n} \cdot \delta\mathbf{u} \rrbracket}_{I\!I} \, dA - \int_{\partial\mathcal{B}} (\llbracket W \rrbracket + \gamma_{\text{s}}\kappa - \lambda)\, \delta n \, dA + \delta\lambda\,(V_{\mathcal{B}} - V_0) = 0, \tag{2.12}$$

where the integral I over Γ vanishes on account of (2.3) and (2.4). The jump term $I\!I$ can further be simplified by the help of

$$\llbracket ab \rrbracket = \langle a \rangle \llbracket b \rrbracket + \llbracket a \rrbracket \langle b \rangle, \quad \text{where} \quad \langle (\cdot) \rangle = \frac{1}{2}\left((\cdot)^{\text{out}} + (\cdot)^{\text{in}} \right), \tag{2.13}$$

therefore leading to

$$I\!I = \llbracket \boldsymbol{\sigma}\mathbf{n} \cdot \delta\mathbf{u} \rrbracket = \langle \boldsymbol{\sigma}\mathbf{n} \rangle \cdot \llbracket \delta\mathbf{u} \rrbracket + \llbracket \boldsymbol{\sigma}\mathbf{n} \rrbracket \cdot \langle \delta\mathbf{u} \rangle. \tag{2.14}$$

As a consequence of the coherency condition (2.2), the jump of the displacement variation is given by

$$\llbracket \delta\mathbf{u} \rrbracket = -\llbracket \nabla\mathbf{u} \rrbracket \mathbf{n}\, \delta n, \tag{2.15}$$

which follows from the Lemma of Hadamard, (see [9] for details). Also note that $\llbracket \boldsymbol{\sigma}\mathbf{n} \rrbracket = \llbracket \boldsymbol{\sigma} \rrbracket \mathbf{n}$, thus Eq. (2.12) can be rewritten as

$$\delta\tilde{E} = -\int_{\mathcal{B}^{\text{in}}} \operatorname{div}\boldsymbol{\sigma} \cdot \delta\mathbf{u} \, dV - \int_{\mathcal{B}^{\text{out}}} \operatorname{div}\boldsymbol{\sigma} \cdot \delta\mathbf{u} \, dV - \int_{\partial\mathcal{B}} \llbracket \boldsymbol{\sigma} \rrbracket \mathbf{n} \cdot \langle \delta\mathbf{u} \rangle \, dA - \int_{\partial\mathcal{B}} (\llbracket W \rrbracket - \llbracket \nabla\mathbf{u} \rrbracket \mathbf{n} \cdot \langle \boldsymbol{\sigma}\mathbf{n} \rangle + \kappa\gamma_{\text{s}} - \lambda)\, \delta n \, dA + \delta\lambda\,(V_{\mathcal{B}} - V_0) = 0. \tag{2.16}$$

For arbitrary and admissible variations $\delta\mathbf{u}$, δn and $\delta\lambda$, the following conclusions can be drawn:

(i) Mechanical equilibrium in the bulk phases:

$$\operatorname{div}\boldsymbol{\sigma} = \mathbf{0} \quad \text{in } \mathcal{B}^{\text{in}} \text{ and } \mathcal{B}^{\text{out}}. \tag{2.17}$$

(ii) Mechanical equilibrium on the interface:

$$[\![\boldsymbol{\sigma}]\!]\mathbf{n} = \mathbf{0} \quad \text{on } \partial\mathcal{B}. \tag{2.18}$$

(iii) Morphological equilibrium condition:
(Note that (2.18) has been used to deduce that $\langle\boldsymbol{\sigma}\mathbf{n}\rangle = \boldsymbol{\sigma}\mathbf{n}$)

$$\tau_{\text{n}} = [\![W]\!] - \mathbf{n}\cdot\left([\![\nabla\mathbf{u}]\!]^{\text{T}}\boldsymbol{\sigma}\right)\mathbf{n} + \kappa\gamma_{\text{s}} = \lambda \quad \text{on } \partial\mathcal{B}. \tag{2.19}$$

(iv) Volume constraint:

$$V_{\mathcal{B}} = V_0. \tag{2.20}$$

In the following, mechanical equilibria (2.17) and (2.18) will be assumed to be satisfied. The remaining morphological variation δ_{m} with respect to the shape and the Lagrange parameter is

$$\delta_{\text{m}}\tilde{E} = -\int_{\partial\mathcal{B}} (\tau_{\text{n}} - \lambda)\,\delta n\,dA + \delta\lambda\,(V_{\mathcal{B}} - V_0) = 0. \tag{2.21}$$

The driving force τ_{n} in the morphological equilibrium (2.21) can be related to Eshelby's concept of a force on an interface [40]. Writing

$$\tau_{\text{n}} = \mathbf{n}\cdot[\![\mathbf{P}]\!]\mathbf{n} + \gamma_{\text{s}}\kappa, \quad \text{where} \quad \mathbf{P} = W\mathbf{1} - (\nabla\mathbf{u})^{\text{T}}\,\boldsymbol{\sigma} \tag{2.22}$$

with $\mathbf{P}$ being the energy-momentum tensor as defined by Eshelby, this identity is obvious. It is mentioned here that τ_{n} can be regarded as a configurational force using the terminology of Gurtin [9]. In the considered inclusion problem, the generalized driving force τ_{n} can be expressed by the strains $\boldsymbol{\varepsilon}$ on the inner side of the interface (see [30])

$$\begin{aligned}\tau_{\text{n}} = -\frac{1}{2}\left[\left(\mathbb{C}^{\text{in}}\boldsymbol{\varepsilon}^0 + [\![\mathbb{C}]\!]\boldsymbol{\varepsilon}\right)\mathbf{n}\right]\cdot\boldsymbol{\Omega}^{-1}\left[\left(\mathbb{C}^{\text{in}}\boldsymbol{\varepsilon}^0 + [\![\mathbb{C}]\!]\boldsymbol{\varepsilon}\right)\mathbf{n}\right] \\ + \frac{1}{2}\boldsymbol{\varepsilon} : \mathbb{C}^{\text{out}}\boldsymbol{\varepsilon} - \frac{1}{2}\left(\boldsymbol{\varepsilon} - \boldsymbol{\varepsilon}^0\right) : \mathbb{C}^{\text{in}}\left(\boldsymbol{\varepsilon} - \boldsymbol{\varepsilon}^0\right) + \gamma_{\text{s}}\kappa,\end{aligned} \tag{2.23}$$

where the components of the acoustic tensor $\boldsymbol{\Omega}$ of the matrix material are given by

$$\Omega_{ik} = \mathbb{C}^{\text{out}}_{ijkl} n_j n_l. \tag{2.24}$$

The computation of τ_{n} requires the solution of the inhomogeneous inclusion problem. In Sec. 3 the solution procedure by a Boundary Element Method is

explained. It should be emphasized, that the computation of the driving force on the interface is independent of the specific arrangement of particles, because only local quantities are involved. The effect of a periodic arrangement enters the calculation of the driving force only through the solution of the elastic field problem, namely through the value of the strains $\boldsymbol{\varepsilon}$.

Equation (2.19) is a necessary condition for a shape to be in morphological equilibrium, however it must be mentioned that this condition is not sufficient. This issue is discussed for example in [41 – 43] on the basis of analytical investigation, and numerical simulations in [27, 31] confirm this result. In order to perform the variation (2.21) in an algorithmic setting, the shape of the inclusion is given by a set of $q_1, \ldots, q_M$ shape parameters. These shape parameters can be a general description of the interface $\partial\mathcal{B}$, but in the calculation they coincide with the distance of the Boundary Element nodes from the origin of the coordinate system. This choice of shape parameters proved to be fairly general, as it covers the range from spheroids to cuboids, which are experimentally observed. Expressing the normal variation δn in (2.21) by variations of the shape parameters $\delta q_1, \ldots, \delta q_M$ leads to a nonlinear system of equations

$$
\begin{aligned}
F_1(q_1, \ldots, q_M, \lambda) &= -\int_{\partial\mathcal{B}} (\tau_n - \lambda) \frac{\partial \mathbf{x}}{\partial q_1} \cdot \mathbf{n}\, dA = 0, \\
&\vdots \qquad\qquad\qquad \vdots \qquad\qquad \vdots \\
F_M(q_1, \ldots, q_M, \lambda) &= -\int_{\partial\mathcal{B}} (\tau_n - \lambda) \frac{\partial \mathbf{x}}{\partial q_M} \cdot \mathbf{n}\, dA = 0, \\
F_{M+1}(q_1, \ldots, q_M, \lambda) &= V_{\mathcal{B}} - V_0 = 0.
\end{aligned}
\tag{2.25}
$$

Here the terms $F_1, \ldots, F_M$ are the work conjugated quantities of the respective shape parameters $q_1, \ldots, q_M$. This system of $M+1$ nonlinear equations for M shape parameters and the Lagrange multiplier λ is solved using a quasi-Newton solver. For details in the solution procedure, the reader is referred to [44]. The general setting is equivalent to that of a shape optimization with a geometrical constraint, i.e. constant particle volume. In the terminology of optimization the total potential of the system is the target function.

3. Boundary Integral Equation Method

The solution of the inhomogeneous inclusion problem can be found by applying the Boundary Integral Equation of elastostatics, which is discretized by Boundary Elements. It is a natural choice for the boundary variations considered here. The advantage of this method is, that the unknowns are shifted from the interior of the considered domain to its boundary, which reduces the problem

dimension and size. The standard integral equation for linear elastic problems follows from [45] to be

$$\mathbf{K}(\mathbf{x})\mathbf{u}(\mathbf{x}) + \int_A \mathbf{T}(\mathbf{x}-\mathbf{y})\mathbf{u}(\mathbf{y})\,dA = \int_A \mathbf{U}(\mathbf{x}-\mathbf{y})\mathbf{t}(\mathbf{y})\,dA, \tag{3.1}$$

with $\mathbf{x}$ representing the source point and $\mathbf{y}$ the observation point, as well as $\mathbf{K} = \frac{1}{2}\mathbf{1}$ for a smooth surface. The fundamental solutions for the tractions and the displacements are expressed through $\mathbf{T}$ and $\mathbf{U}$ respectively.

3.1. Anisotropic fundamental solution

Since the lattice structure of the different phases in general shows anisotropic behaviour, the analytic fundamental solution for the isotropic case, known as the Kelvin problem, cannot be applied. A method to calculate these quantities numerically is proposed by [46] and incorporated to handle anisotropic behaviour. According to [46], the fundamental solution for the displacements can be expressed as follows

$$\mathbf{U} = \frac{1}{8\pi^2|\mathbf{x}-\mathbf{y}|}\mathbf{G}(\theta_1,\theta_2)\,, \tag{3.2}$$

with the kernel

$$\mathbf{G}(\theta_1,\theta_2) = \int_0^{2\pi} \mathbf{M}^{-1}(\mathbf{z}(\varphi))\,d\varphi \tag{3.3}$$

and the argument of the integral

$$M_{ik} = \mathbb{C}_{ijkl} z_j z_l \qquad |\mathbf{z}| = 1\,. \tag{3.4}$$

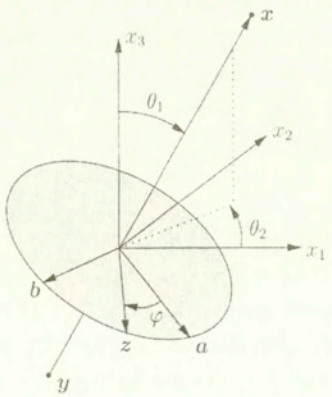

FIG. 2. Anisotropic fundamental solution.

Figure 2 provides a geometric representation of the quantities in Eq. (3.3). The function $\mathbf{G}(\theta_1, \theta_2)$ depends on the orientation of the vector $\mathbf{y} - \mathbf{x}$ but not on its length. Since $\mathbf{G}$ is a smooth function, discrete values for the domain $0 \leq \theta_1 \leq \pi$ and $0 \leq \theta_2 \leq 2\pi$ can be calculated. Instead of performing the integration in Eq. (3.3) for every pair $(\mathbf{x}, \mathbf{y})$ appearing in the problem, quadratic interpolation between the discrete values for the angles θ_1 and θ_2 is utilized. This approach increases the computational speed when integrating the Boundary Integral Equations. A similar procedure can be used to find the fundamental solution for the tractions and is described in [46].

3.2. Boundary Integral Equations

Applying the boundary element method to the problem of periodically arranged precipitates leads to two distinct problems for the matrix- and the particle-phase. Incorporating the jump Eqs. (2.2) and (2.18), the displacement- and the traction-vector are defined as

$$\mathbf{u}^{\text{in}} = \mathbf{u}^{\text{out}} = \mathbf{u} \qquad \text{on} \quad \partial\mathcal{B} \tag{3.5}$$

and

$$-\mathbf{t}^{\text{out}} = \mathbf{t}^{\text{in}} = \mathbf{t} \qquad \text{on} \quad \partial\mathrm{B}\,. \tag{3.6}$$

Following the general procedure, derivation of the boundary integral equations proposed by [45] yields three integral equations, two for the matrix boundaries $\partial\mathcal{B}$ and Γ and one for the particle boundary $\partial\mathcal{B}$:

$$\mathbf{K}^{\text{out}}\,\mathbf{u} - \int_{\partial\mathcal{B}} \mathbf{T}^{\text{out}}\,\mathbf{u}\,dA + \int_{\Gamma} \mathbf{T}^{\text{out}}\,\mathbf{u}^{\Gamma}\,dA + \int_{\partial\mathcal{B}} \mathbf{U}^{\text{out}}\,\mathbf{t}\,dA - \int_{\Gamma} \mathbf{U}^{\text{out}}\,\mathbf{t}^{\Gamma}\,dA = 0 \qquad \text{on} \quad \partial\mathcal{B}, \tag{3.7}$$

$$\mathbf{K}^{\Gamma}\,\mathbf{u}^{\Gamma} - \int_{\partial\mathcal{B}} \mathbf{T}^{\text{out}}\,\mathbf{u}\,dA + \int_{\Gamma} \mathbf{T}^{\text{out}}\,\mathbf{u}^{\Gamma}\,dA + \int_{\partial\mathcal{B}} \mathbf{U}^{\text{out}}\,\mathbf{t}\,dA - \int_{\Gamma} \mathbf{U}^{\text{out}}\,\mathbf{t}^{\Gamma}\,dA = 0 \qquad \text{on} \quad \Gamma, \tag{3.8}$$

$$\mathbf{K}^{\text{in}}\,\mathbf{u} + \int_{\partial\mathcal{B}} \mathbf{T}^{\text{in}}\,\mathbf{u}\,dA - \int_{\partial\mathcal{B}} \mathbf{U}^{\text{in}}\,\mathbf{t}\,dA = \mathbf{K}^{\text{in}}\,\mathbf{u}^{0} + \int_{\partial\mathcal{B}} \mathbf{T}^{\text{in}}\,\mathbf{u}^{0}\,dA \qquad \text{on} \quad \partial\mathcal{B}. \tag{3.9}$$

To achieve a complete system of equations, the periodicity conditions (2.3), (2.4) as well as the traction boundary condition for the unit cell (2.5) have to be considered. The integral equations are then discretized using 4-node elements with a bilinear interpolation of displacements, tractions and geometry. The discretization leads to a non-symmetric linear system of equations for the displacements and tractions on the interface and on the cell boundary. In the calculation of equilibrium shapes, the following discretization has been used:

	Number of nodes	Number of elements
Cell boundary Γ	218	216
Particle boundary $\partial\mathcal{B}$	866	864

This system has to be solved repeatedly with a new particle geometry in the optimization process. About 25 – 50 iterations are needed in the quasi-Newtonian process to obtain the convergence.

4. Results

4.1. Nondimensionalization

For the numerical implementation of the problem it is useful to scale the different quantities in an appropriate way. This increases the numerical efficiency. According to [33], the following positive scalars are defined for the 3D case:

$$l^* = \sqrt[3]{V_{\mathcal{B}}}, \tag{4.1}$$

$$\varepsilon^* = \max_{i=1,2,3} |\varepsilon_i^0|, \tag{4.2}$$

$$\mu^* = \frac{1}{15}\left[c_{11}^{\text{out}} + c_{22}^{\text{out}} + c_{33}^{\text{out}} - c_{12}^{\text{out}} - c_{23}^{\text{out}} - c_{13}^{\text{out}} + 3\left(c_{44}^{\text{out}} + c_{55}^{\text{out}} + c_{66}^{\text{out}}\right)\right]. \tag{4.3}$$

The characteristic length of the particle l^* is defined by the particle volume, and ε^* describes the maximal absolute value of the eigenstrains. The effective shear modulus μ^* characterizes the average stiffness of the anisotropic matrix material, here given by its Voigt constants. Following the procedure used in [31], a dimensionless formulation for all quantities of the system can be derived in conjunction with the dimensionless particle size

$$L = \frac{\mu^* \varepsilon^{*2} l^*}{\gamma_{\text{s}}}. \tag{4.4}$$

Since L can be regarded as the ratio of the systems elastic strain energy E^{el} to the interfacial energy E^{int}, a physical interpretation is possible. If E^{int} approaches zero, L becomes very large and the particle shape is determined by the minimum of the elastic strain energy. In contrast, for a small value of L the influence of E^{int} is dominating, which leads to a sphere as an equilibrium morphology.

4.2. Verification

To check correctness and accuracy of the computations, the numerical results have to be compared with analytic solutions. However, if considering periodic arrangements of anisotropic misfitting particles, no analytic solution exists. To justify the calculations, some tests as well as comparison with 2D results were performed. For the test simulations the elastic behaviour is assumed to be isotropic for both phases with the material parameters

$$\nu^{\text{in}} = \nu^{\text{out}} = 0.25, \quad \frac{\mu^{\text{in}}}{\mu^{\text{out}}} = \frac{1}{2}, \tag{4.5}$$

where $\nu^{\text{in/out}}$ is Poisson's constant and $\mu^{\text{in/out}}$ denotes the corresponding shear modulus. Positive eigenstrains

$$\boldsymbol{\varepsilon}^0 = \varepsilon^* \mathbf{1} \qquad \text{with} \quad \varepsilon^* = 0.001 \tag{4.6}$$

are applied and the volume fraction f of the inclusion compared to the total volume is assumed to be

$$f = \frac{V_{\mathcal{B}^{\text{in}}}}{V_{\mathcal{B}^{\text{tot}}}} = 12.5\%\,. \tag{4.7}$$

In the first calculation, the inclusion is shifted off the matrix center towards one face of Γ to control the assembling of the system matrix for nonsymmetric problems. Such a shift should not alter the stress distribution. For the dimensionless particle size $L = 6$ is chosen. As Fig. 3 shows, the stresses are repeated periodically on the matrix boundary for the symmetric as well as for the nonsymmetric problem.

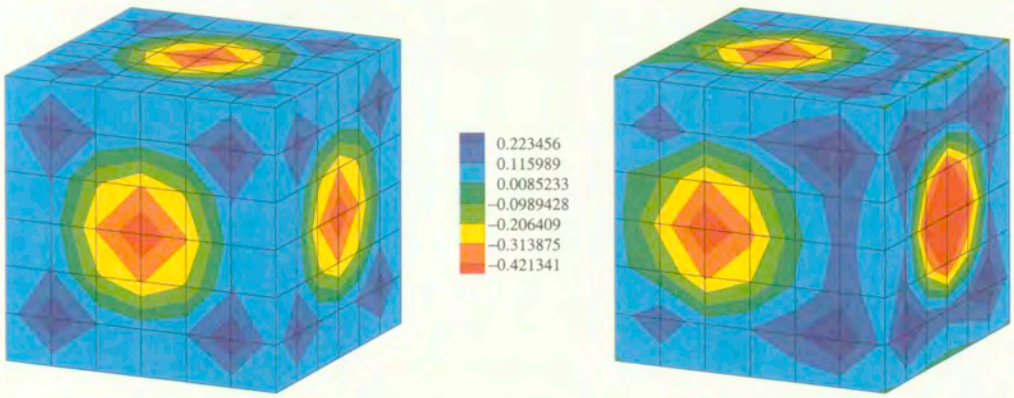

FIG. 3. Resolved normal stresses on the matrix boundary for shifted particle.

For the second test, demonstrating the influence of the matrix boundary to the radial strains on the interface, a value $L = 3$ is assumed. If sufficiently small volume fractions are considered, the periodic arrangement is assumed to have a negligible influence on the inclusion. Thus for $f \to 0$ the strains on the interface are expected to converge to the corresponding values for the single inclusion problem. Assuming isotropic material behaviour, this problem can be treated exactly and is known as Eshelby's solution. The difference in the radial strains is given by

$$\Delta\varepsilon = \frac{\varepsilon - \varepsilon^{\infty}}{\varepsilon^{\infty}}, \tag{4.8}$$

where ε^{∞} denotes the reference strains for the single inclusion problem, and ε are the radial strains for periodic arrangement. Figure 4 shows the position of three different points (P_1, P_2, P_3) on the particle surface, for which the deviation is calculated. On all three points the radial strains show the same qualitative behaviour, for decreasing volume fraction the difference $\Delta\varepsilon$ also decreases and approaches zero for $f \to 0$.

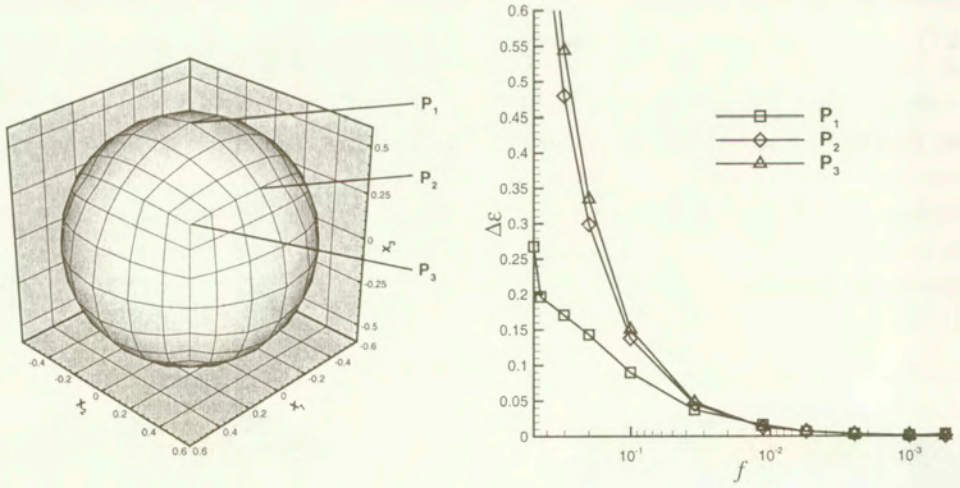

$P_1 - P_3$ on $\partial\mathcal{B}$ $\Delta\varepsilon$ for $P_1 - P_3$

FIG. 4. Difference in radial strains as a function of f.

4.3. Equilibrium shapes

In this section the influence of different parameters on the equilibrium morphology will be discussed. In order to mimic the mechanical behaviour of Ni-base alloys, the elastic constants of Nickel in Voigt notation are used (see [47]):

$$\mathbb{C}^{\text{in}} = \mathbb{C}^{\text{out}} = \begin{pmatrix} 2.465 & 1.473 & 1.473 & 0 & 0 & 0 \\ 1.473 & 2.465 & 1.473 & 0 & 0 & 0 \\ 1.473 & 1.473 & 2.465 & 0 & 0 & 0 \\ 0 & 0 & 0 & 1.247 & 0 & 0 \\ 0 & 0 & 0 & 0 & 1.247 & 0 \\ 0 & 0 & 0 & 0 & 0 & 1.247 \end{pmatrix} \cdot 10^5 \frac{\text{N}}{\text{mm}^2}. \tag{4.9}$$

A dilatational eigenstrain tensor as given in Eq (4.6) is assumed. Due to the fcc-lattice structure, the elastic properties show cubic orthotropy. To visualize the elastic behaviour Fig. 5 shows a 3D representation of the directional Young's modulus. The material possesses a high stiffness along the diagonal direction, whereas along the coordinate axis Young's modulus is lower.

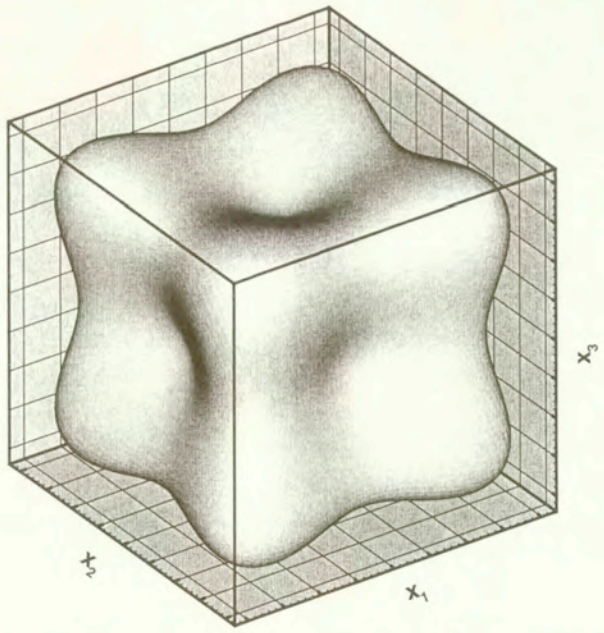

FIG. 5. Directional Young's modulus of material as given in (4.9).

As the computations are quite time-consuming and a lot of parameters influence the equilibrium shape, attention will be restricted to some basic parameters, such as volume fraction, particle size, stiffness ratio of particle to matrix material and loading. Of special interest is the influence of the volume fraction f and the particle interaction in 3D. However, these are only the first results that cannot cover the complete relevant parameter range.

4.3.1. Resolved normal stresses on the cell boundary. Before considering particle morphologies, the importance of the volume fraction f to the normal tractions on the cell boundary is discussed. In Fig. 6 negative normal tractions for $f = 50\%$ can be found at the center of each matrix face, while in the vicinity of the edges positive values appear. This is evident because the matrix material is under compression in the region where the interface of two adjoining particles are close together and leads to a convex cell shape if the assumption of a periodic arrangement is neglected.

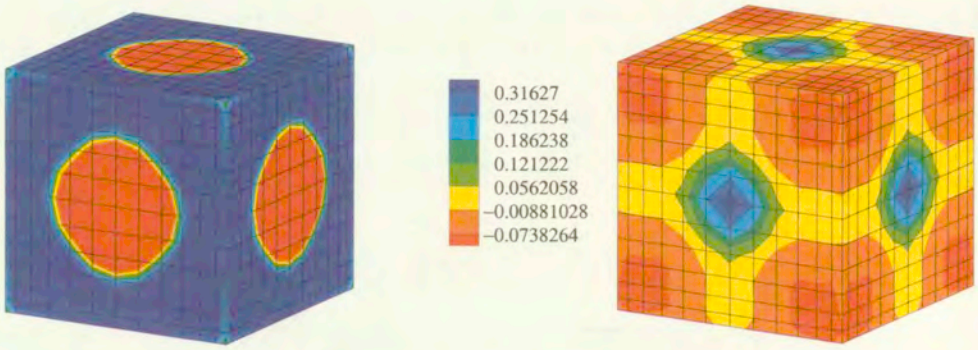

FIG. 6. Resolved normal stresses on the matrix boundary for different volume fractions.

Considering small volume fractions, Fig. 6 shows that the distribution of the normal stresses has changed. For $f = 10\%$ the positive tractions appear in the center, while at the edges negative values can be found. To explain that, the material behaviour due to orthotropy must be recalled. As a consequence of the high stiffness in the diagonal direction, the displacements on the interface along the diagonals are basically translated to the corners of the matrix boundary, leading to a concave deformation of the unit cell. To satisfy the conditions for periodically arranged particles, positive tractions have to be applied in the center of each face of Γ.

4.3.2. Influence of particle size and volume fraction. In the following, the influence of the particle size L as well as the importance of the volume fraction f will be discussed assuming the same elasticity tensor in the matrix and particle. In order to characterize the particle shape,

$$\eta = \frac{d}{l} \tag{4.10}$$

is introduced (see Fig. 7). For $\eta = 1$, the shape is a sphere. A value of $\eta = \sqrt{3}$ characterizes a cube. Figure 7 shows the equilibrium shapes for different

combinations of the two parameters. The particle becomes cuboidal if L increases, independent of f. Recalling that L denotes the ratio of elastic to interface energy, this can be understood. A large particle minimizes the elastic energy by orienting large parts of the interface normal to the soft directions of the material - here normal to the coordinate axis. The interface energy is less dominant at large sizes, thus it rounds off only small regions at the edges and corners to cube-like shapes.

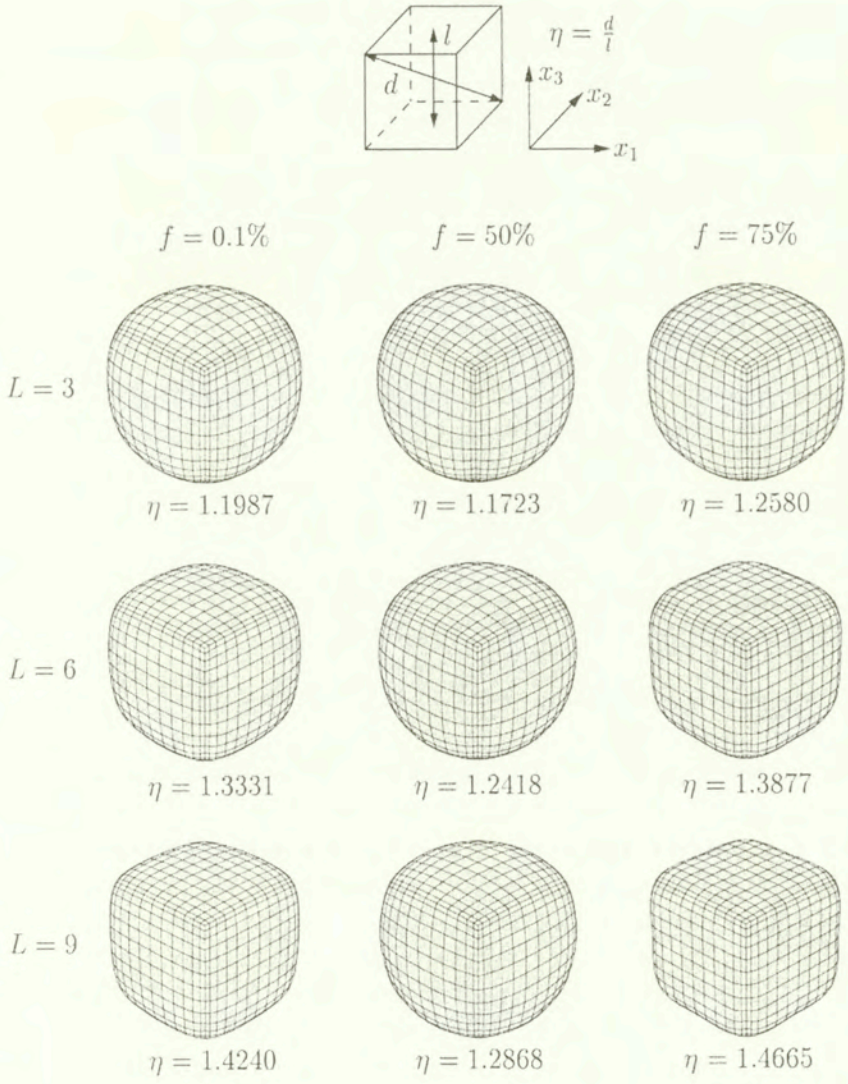

FIG. 7. Equilibrium shapes for different values of L and f.

When keeping the particle size L constant and increasing the volume fraction f, the particle first tends to a more sphere-like morphology but for even higher values of f, the particle looks more cuboidal. To give an explanation, the two components $E^{\mathrm{el,in}}$ and $E^{\mathrm{el,out}}$ contributing to the total elastic strain energy have to be considered. For increasing f, the value of $E^{\mathrm{el,out}}$ decreases, so that the contribution of E^{el} to the total energy also decreases and the particle tends to a more sphere-like shape. This effect is relevant for volume fractions f of about 40 – 50%. Increasing the volume fraction further the particle shape becomes cube-like again, due to the geometrical constraint. A cube-like shape is the only way to place more particle material inside the periodic unit cell. The qualitative behaviour of the equilibrium shapes due to the variation of the parameters L and f agrees with the 2D results of [31].

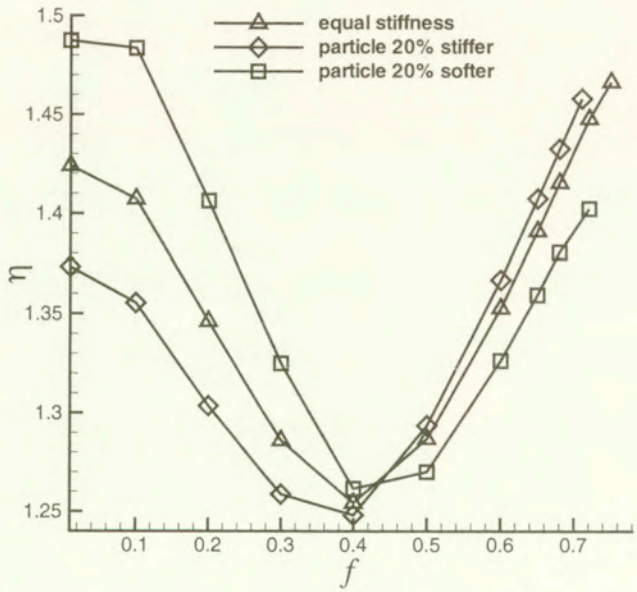

FIG. 8. Shape parameter ν as a function of f for different stiffness ratios.

4.3.3. Influence of particle stiffness. It is known from experimental observations and numerical simulations that the stiffness ratio of particle to matrix material is of great importance. In Fig. 8 the shape parameter η is plotted as a function of the volume fraction f for the stiffness ratio $\mathbb{C}^{\mathrm{in}} = 0.8\,\mathbb{C}^{\mathrm{out}}$, $\mathbb{C}^{\mathrm{in}} = \mathbb{C}^{\mathrm{out}}$ and $\mathbb{C}^{\mathrm{in}} = 1.2\,\mathbb{C}^{\mathrm{out}}$. The particle size is assumed to be $L = 9$. Comparing the three stiffness ratios, the soft particle is more cube-like than the stiff inclusion as long as the volume fraction f is small, whereas for large volume fractions f the stiff particle is more cuboidal than the soft inclusion. This behaviour is also found in [31] for the 2D case. All three stiffness ratios reach a minimal value of

the parameter η for volume fractions of $40 - 50\%$. For large volume fractions f, the particle shape is mostly determined by the material parameters of the inclusion. So a stiff particle leads to higher values of $E^{\mathrm{el,in}}$ from which the cuboidal shape follows. When considering small volume fractions, the matrix material determines the equilibrium morphology. If the particle is assumed to exhibit stiff behaviour, the matrix material is comparatively soft and as a consequence, the inclusion shape looks more sphere-like.

4.3.4. Influence of an applied load. In the last example, the influence of an applied load on the equilibrium shape is considered for increasing volume fractions. The elasticity tensors are chosen to be $\mathbb{C}^{\mathrm{in}} = 0.8\,\mathbb{C}^{\mathrm{out}}$ and $L = 3$, the remote stress field $\sigma_{11}^{\infty} = 50\,\dfrac{\mathrm{N}}{\mathrm{mm}^2}$ is applied. To describe the particle shape, the quantity

$$\rho = \frac{a-b}{a+b} \tag{4.11}$$

is introduced, where a and b define the principal axis of an oblate cuboid (see Fig. 9). If $a = b$, the parameter ρ equals zero, describing the particle shape with cubic symmetry, whereas for values $0 < \rho < 1$ an oblate shape is achieved.

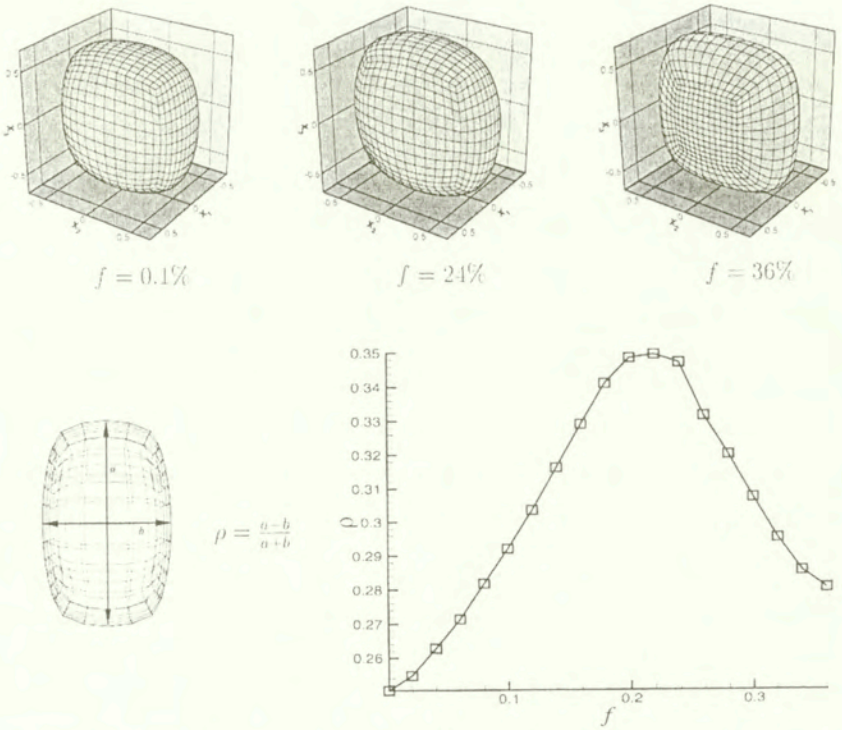

FIG. 9. Equilibrium shapes under external loading for different volume fractions f.

Expressing the external load by equivalent eigenstrains leads to higher values for the eigenstrain tensor in x_1-direction. If the inclusion is assumed to be soft compared to the matrix material, an oblate particle shape minimizes the dominant energy $E^{\mathrm{el,out}}$ with the x_1-axis being normal to the flat face of the particle. An increasing volume fraction supports this effect, therefore ρ increases, until a volume fraction $f = 25\%$ is reached. Even higher values of the volume fraction f lead to large deformations of the matrix material in the regions where $\partial\mathcal{B}$ and Γ are close together, which in turn cause higher values of $E^{\mathrm{el,out}}$. This energy can be reduced if the distance between the matrix and the particle boundary is increased, so smaller values for ρ are the consequence. The occurrence of oblate particle shapes in tensile loading is called rafting. It has a great technical relevance as the rafting process alters the general elastic behaviour of the considered structure.

5. Conclusions

The theory of equilibrium shapes in two-phase materials has been recast for a periodic cell arrangement. A variational principle was used to derive necessary conditions for an equilibrium shape. Material parameters that resemble Ni-base alloys were used in the simulation with Boundary Elements. The influence of some important parameters on the equilibrium shape was discovered by parameter studies. Although not the complete physically relevant parameter range was analyzed, some conclusions can be drawn:

- With increasing particle size the equilibrium shape becomes more cube-like. This is in agreement with results for the isolated particle.
- In the case of no applied loads, increasing the volume fraction makes the equilibrium shape more spheroidal as long as the volume fraction is lower than $40 - 50\%$. Above this critical volume fraction, the particle becomes again more cuboidal. Thus up to volume fractions of about $10 - 15\%$, the particle interaction is not relevant for the equilibrium shape.
- For reasonable stiffness ratios of particle to matrix material, the characteristic behaviour is not altered drastically.
- In the case of applied loads, the rafting tendency increases with increasing particle interaction until a volume fraction of about 25%. Increasing the volume fraction further leads to less oblate shapes. However, in this regime particle coalescence which was neglected in this analysis, might become relevant.

References

1. M. IGNAT, J.-Y. BUFFIERE and J. M. CHAIX, *Microstructures induced by a stress gradient in a nickel-based superalloy*, Acta Metall. Mater., **41**, 3, 855–862, 1993.
2. J. LI, R. WAHI, H. CHEN, W. CHEN and H. WEVER, *Deformation substructure in the nickel-base alloy in 738lc under superimposed creep-fatigue loading*, Z. Metallkd., **84**, 4, 268–272, 1993.
3. T. M. POLLOCK and A. S. ARGON, *Directional coarsening in nickel-base single crystals with high volume fractions of coherent precipitates*, Acta Metall. Mater., **43**, 6, 1859–1874, 1994.
4. M. FAHRMANN, W. HERMANN, E. FAHRMANN, A. BOEGLI, T. M. POLLOCK and H. G. SOCKEL, *Determination of matrix and precipitate elastic constants in $(\gamma-\gamma')$ Ni-base model alloys, and their relevance to rafting*, Materials Science and Engineering, **A 260**, 212–221, 1999.
5. J. W. CAHN, *On spinodal decomposition*, Acta Metall., **9**, 795–801, 1961.
6. J. W. CAHN and J. E. HILLARD, *Spinondal decomposition: A reprise*, Acta Metall., **19**, 151–161, 1971.
7. P. H. LEO and R. F. SEKERKA, *The effect of surface stress on crystal-melt and crystal-crystal equilibrium*, Acta Metall., **37**, 12, 3119–3138, 1989.
8. M. E. GURTIN and P. W. VOORHEES, *The continuum mechanics of coherent two-phase elastic solids with mass transport*, Proc. R. Soc. Lond., A **440**, 323–343, 1993.
9. M. E. GURTIN, *The nature of configurational forces*, Arch. Rational Mech. Anal., **131**, 67–100, 1995.
10. M. E. GURTIN and P. W. VOORHEES, *The thermodynamics of evolving interfaces far from equilibrium*, Acta Mater., **44**, 1, 235–247, 1996.
11. G. A. MAUGIN, *Material Inhomogeneities in Elasticity*, Chapman and Hall, London, Glasgow, New York, Tokyo, Melbourne, Madras 1993.
12. E. FRIED and M. E. GURTIN, *Continnum theory of thermally induced phase transitions based on an order parameter*, Physica D, **68**, 326–343, 1993.
13. E. FRIED and M. E. GURTIN, *Dynamic solid-solid transitions with phase characterized by an order parameter*, Physica D, **72**, 287–308, 1994.
14. J. K. LEE, *Coherency strain analysis via discrete atom method*, Scr. Met. Mat., **32**, 4, 559–564, 1995.
15. J. K. LEE, *Effects of applied stress on coherent precipitates via a disctrete atom method*, Metals and Materials, **2**, 3, 183–193, 1996.
16. J. K. LEE, *A study on coherency strain precipitate morphology via a discrete atom method*, Met. Mat. Trans., **27A**, 1449–1459, 1996.
17. J. K. LEE, *Morphology of coherent precipitates via a discrete atom method*, Mat. Sci., **A238**, 1–12, 1997.
18. S. KOLLING and D. GROSS, *Description of two-phase materials using discrete atom method*, ZAMM, 2000 (to appear).
19. J. K. LEE, *Elastic stress and microstructural evolution*, Materials Transactions, JIM, **39**, 1, 114–132, 1998.
20. A. G. KHACHATURYAN, *Theory of Structural Transformation in Solids*, John Wiley and Sons, 1983.

21. T. KÜPPER and N. MASBAUM, *Simulation of particle growth and Ostwald ripening via the Cahn-Hilliard equation*, Acta Metall. Mater., **42**, 6, 1847–1858, 1994.

22. P. H. LEO, J. S. LOWENGRUB and H. J. JOU, *A diffuse interface model for microstructural evolution in elastically stressed solids*, Acta Mater., **46**, 6, 2113–2130, 1998.

23. Y. WANG, L.-Q. CHEN and A. G. KHACHATURYAN, *Kinetics of strain-induced morphological transformation in cubic alloys with a miscibility gap*, Acta Metall. Mater., **41**, 1, 279–296, 1993.

24. J. D. ZHANG, D. Y. LI and L. Q. CHEN, *Shape evolution and splitting of a single coherent particle*, Mat. Res. Soc. Symp. Proc., **481**, 243–248, 1998.

25. Y. WANG, L.-Q. CHEN and A. G. KHACHATURYAN, *Three-dimensional dynamic calculation of the equilibrium shape of a coherent tetragonal precipitate in mg-partially stabilized cubic ZrO_2*, J. Am. Ceram. Soc., **79**, 4, 967–991, 1996.

26. P. W. VOORHEES, G. B. MCFADDEN and W. C. JOHNSON, *On the morphological development of second-phase particles in elastically-stressed solids*, Acta Metall. Mater., **40**, 11, 2979–2992, 1992.

27. M. E. THOMPSON, C. S. SU and P. W. VOORHEES, *The equilibrium shape of a misfitting precipitate*, Acta Metall. Mater., **42**, 6, 2107–2122, 1993.

28. C. H. SU and P. W. VOORHEES, *The dynamics of precipitate evolution in elastically stressed solids – I, inverse coarsening*, Acta Mater., **44**, 5, 1987–1999, 1996.

29. C. H. SU and P. W. VOORHEES, *The dynamics of precipitate evolution in elastically stressed solids – II, particle alignment*, Acta Mater., **44**, 5, 2001–2016, 1996.

30. I. SCHMIDT and D. GROSS, *A strategy for determining the equilibrium shape of an inclusion*, Arch. Mech., **47**, 2, 379–390, 1995.

31. I. SCHMIDT and D. GROSS, *The equilibrium shape of an elastically inhomogeneous inclusion*, J. Mech. Phys. Solids, **45**, 9, 1521–1549, 1997.

32. I. SCHMIDT, R. MUELLER and D. GROSS, *The effect of elastic inhomogeneity on equilibrium and stability of a two particle morphology*, Mechanics of Materials, **30**, 181–196, 1998.

33. R. MUELLER and D. GROSS, *3D simulation of equilibrium morphologies of precipitates*, Comp. Mat. Sci., **11**, 35–44, 1998.

34. R. MUELLER and D. GROSS, *3D inhomogeneous, misfitting second phase particles – equilibrium shapes and morphological development*, Comp. Mat. Sci., **16**, 53–60, 1999.

35. A. J. ARDELL and P. K. RASTOGI, *The coarsening behaviour of the γ' precipitate in Nickel-Silicon alloys*, Acta Metall., **19**, 321–330, 1971.

36. A. J. ARDELL and A. MAHESHWARI, *Anomalous coarsening behaviour of small volume fractions of Ni_3Al precipitates in binary Ni-Al alloys*, Acta Metall. Mater., **40**, 10, 2661–2667, 1992.

37. A. J. ARDELL and M. MESHKINPOUR, *Role of volume fraction in the coarsening of Ni_3Si precipitates in binary Ni-Si alloys*, Material Science and Engineering, **A 185**, 153–163, 1994.

38. T. MURA, *Micromechanics of Defects in Solids*, Martinus Nijhoff Publishers, 1987.

39. I. SCHMID and D. Gross, *Directional coarsening in Ni-base superalloys: analytical results for an elasticity based model*, Proc. R. Soc. Lond., **455**, 3085–3106, 1999.

40. J. D. ESHELBY, *Energy relations and the energy-momentum tensor in continuum mechanics*, 77–115, McGraw Hill, New York 1970.

41. W. C. JOHNSON and J. W. CAHN, *Elastically induced shape bifurcations of inclusions*, Acta Metall., **32**, 11, 1925–1933, 1984.

42. W. C. JOHNSON, M. B. BERKENPAS and J. W. CAHN, *Precipitate shape transitions during coarsening under uniaxial stress*, Acta Metall., **36**, 2, 3149–3162, 1988.

43. I. M. KAGANOVA and R. L. ROITBURD, *Equilibrium between elastically-interacting phases*, Sov. Phys. JETP, **67**, 4, 1173–1183, 1988.

44. D. G. LUENBERGER, *Linear and nonlinear programming*, Addison-Wesley, 2nd ed. 1984.

45. C. A. BREBBIA and J. F. C. TELLES, *Boundary Element Techniques*, Springer-Verlag, 1985.

46. N. A. SCHCLAR, *Anisotropic Analysis using Boundary Elements*, [In:] Topics in Engineering, **20**, Computational Mechanics Publications, Southampton UK and Boston USA 1994.

47. D. J. BACON, D. M. BARNETT and R. O. SCATTERGOOD, *Anisotropic continuum theory of lattice defects*, Progress in Materials Science, **23**, 55–262, 1979.

Received February 14, 2000.

Arch. Mech., **52**, 4–5, pp. 685–711, Warszawa 2000

Iterative methods for solution of contact optimization problems

Dedicated to Professor Zenon Mróz
on the occasion of his 70^{th} birthday

I. PÁCZELT

University of Miskolc, Miskolc, Hungary

NUMERICAL TREATMENT of frictionless contact optimization problems is presented on the basis of linear elasticity. The minimum of the pressure maximum or other mechanical values (torque, frictional power loss) is sought by controlling the pressure distribution. Smooth contact pressure distribution can be achieved by using an appropriate controlling function on the controlling subdomain. The contact problems are investigated by means of the principle of minimum complementary energy and using the augmented Lagrangian technique. Axially symmetric problems are discretized by p-version finite elements. The optimal shape of a roller bearing is determined by the application of a new controlling function, which takes the rigid body translation and rotation of the roller into consideration. Effectiveness of the proposed algorithms is demonstrated by numerical examples.

1. Introduction

IN ENGINEERING PRACTICE, connections of machine elements are frequently modeled as unilateral contact problems. The contact surfaces should be shaped in such a way that the arising contact stresses remain under a prescribed limit. Consequently, the singularity in the stress field and the danger of fatigue can be eliminated, further only low level wearing can take place on the contacting surfaces.

Contact optimization problems can be divided into two groups. The first group of problems is based on kinematical quantities [1], while the second group of the problems is using dynamical parameters.

In the first case, the following kinematical quantities are minimized in a certain region of one of the bodies (or in several regions of both bodies): the absolute value of the displacement vector, the difference between the largest and the smallest displacement projected on a given direction etc. Let us suppose that the theory of linear elasticity is applicable, and friction is not taking place between the bodies.

The kinematical optimization problem is solved in two steps.

Step 1. We solve the mathematical programming problem, which is linear or quadratic, depending on the objective function. The solution involves the contact pressure.

Step 2. Knowing the contact pressure and using the geometrical condition between the bodies, we determine the shape of that body for which the objective function is not composed [1].

In the second case, when dynamical quantities are minimized during the optimization, we can set up the following problems:

Problem 1. Minimization of the contact pressure maximum.

Problem 2. Optimization of the contact pressure taking also the frictional power loss into account.

Problem 3. Optimization problem for minimization of the maximum equivalent stress.

Problem 4. Maximization of any mechanical value (torque, force...).

The papers by CONRY [2], KLARBRING [3] and PETERSON [4] are concerned with constant contact pressure distribution. The mathematical background is given for these problems by HASLINGER and NEITTAANMAKI [5]. Numerical solutions are given by KLARBRING [3] and ODA *et al.* [6] for contact problems of an elastic or elastic-plastic punch and a rigid target, using displacement based linear and quadratic finite elements. Approximately constant contact pressure distribution is achieved in [6] and [7] by appropriate shape optimization for axially-symmetric bodies assuming that a change in radius has no effect on the stiffness and compliance matrices. A number of papers e.g. OH *et al.* [8], HARNETT [9], CHIU *et al.* [10], de MUL *et al.* [11], PÁCZELT *et al.* [12] are devoted to the issue of the roller's rounding-off. In these papers except the last one the radius of the rounding-off is given, which results in generally non-smooth contact pressure distribution. Works [13, 14] and [12] give solutions for 2D and 3D problems, provided that the contact pressure distribution is influenced by partial controlling of the contact pressure and by minimizing the maximum of the contact pressure.

Discretization of the domain with p-version finite elements is advantageous (SZABÓ *et al.* [15]), since it results in fast convergence, and the high order mapping assures accurate geometry for the shape optimization.

In this paper axially symmetric and 3D contact shape optimization problems, have been investigated. In case of axially symmetric problems the contact pressure is controlled on the whole contact region, and the p-extension of the finite element method is applied for the discretization. For 3D problems, the contact pressure is controlled only partially on the contact surface and the punch performs a rigid body rotation in addition to the rigid body translation.

2. Formulation of the contact problem

Let us consider the contact problem of two elastic bodies ($e = 1, 2$). The surfaces of the bodies will be divided into three regions: S_u^e denotes that part of the body where displacements $\mathbf{u}_o$ are given, in S_t^e the traction $\mathbf{t}_o$ is applied, while S_c^e represents that part of the bodies where contact is expected. The S_c^e part of the body is called the proposed zone of the contact. The bodies are loaded by the body force $\mathbf{b}^e$, initial stress $\mathbf{T}_o^e$ and initial strain $\mathbf{A}_o^e$. We are interested in finding the displacement vector field $\mathbf{u}$, strain $\mathbf{A}$ and stress $\mathbf{T}$ tensor fields. In the domain V^e we have the equilibrium equation

$$\mathbf{T}^e \cdot \nabla + \mathbf{b}^e = \mathbf{0}, \qquad \mathbf{r} \in V^e, \tag{2.1}$$

the strain-displacement relationship

$$\mathbf{A}^e = \frac{1}{2}\left(\mathbf{u}^e \circ \nabla + \nabla \circ \mathbf{u}^e\right), \qquad \mathbf{r} \in V^e, \tag{2.2}$$

and Hooke's constitutive law:

$$\mathbf{T}^e = \mathbf{T}_o^e + \mathbf{D}^e \cdot\cdot \left(\mathbf{A}^e - \mathbf{A}_o^e\right), \qquad \mathbf{r} \in V^e, \tag{2.3}$$

where $\mathbf{D}^e$ is a fourth-order tensor of the material parameters, "$\cdot$", "$\cdot\cdot$", "$\circ$", is the symbol of a scalar, double scalar and tensor product, respectively, and ∇ is the Hamiltonian differential operator.

The boundary conditions are:

$$\mathbf{u}^e = \mathbf{u}_o, \qquad \mathbf{r} \in S_u^e, \tag{2.4}$$

and

$$\mathbf{T}^e \cdot \mathbf{n}^e = \mathbf{t}_o, \qquad \mathbf{r} \in S_t^e. \tag{2.5}$$

For the examination of the contact/separation conditions in the proposed zone of contact, we shall consider the projection of the displacement in a prescribed direction only (e.g., normal to the surface $\mathbf{n}_c$). The contact normal vector $\mathbf{n}_c$ determines the points Q_1, Q_2 on the corresponding surfaces S_c^1 and S_c^2, where the two surfaces may contact each other (see Fig. 1). Therefore the contact surface will be denoted by S_c. We denote the displacement projected in the direction of $\mathbf{n}_c$ by $u_N^e = \mathbf{u}^e \cdot \mathbf{n}_c$, the normal stress by $\sigma_N^e = \mathbf{n}^e \cdot \mathbf{T}^e \cdot \mathbf{n}^e$ and the initial gap between bodies by h. We define the distance (gap) after deformation

$$d = d(\mathbf{u}) = u_N^2 - u_N^1 + h \geq 0, \tag{2.6}$$

and the contact pressure

$$p = -\mathbf{n}^1 \cdot \mathbf{T}^1 \cdot \mathbf{n}_c = \mathbf{n}^2 \cdot \mathbf{T}^2 \cdot \mathbf{n}_c \cong -\mathbf{n}^1 \cdot \mathbf{T}^1 \cdot \mathbf{n}^1 = -\mathbf{n}^2 \cdot \mathbf{T}^2 \cdot \mathbf{n}^2 \geq 0. \tag{2.7}$$

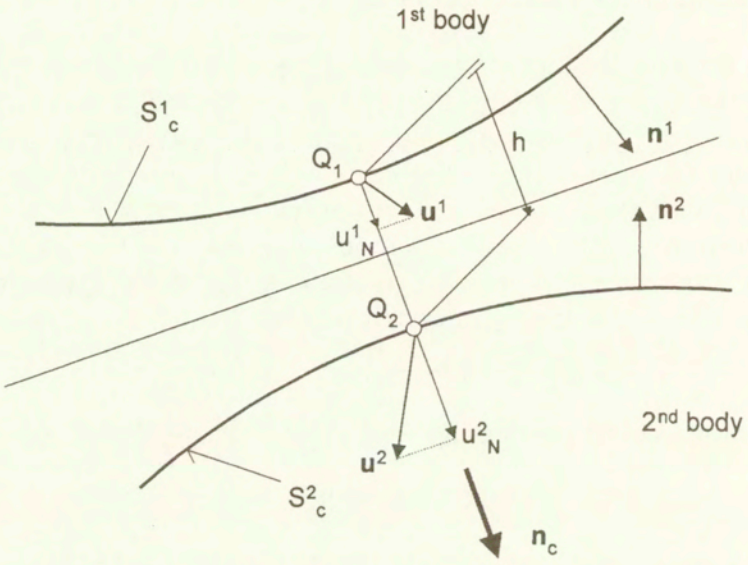

FIG. 1. Normal displacements u_N^e $(e = 1, 2)$.

Denoting the contact zone by C and the separation (gap) zone by G $(S_c = C \cup G)$, we have

$$d = 0, \qquad p \geq 0, \qquad \mathbf{r} \in C, \tag{2.8}$$

$$d > 0, \qquad p = 0, \qquad \mathbf{r} \in G, \tag{2.9}$$

$$pd = 0, \qquad \mathbf{r} \in S_c. \tag{2.10}$$

From the condition of frictionless contact we have zero tangential stress

$$\tau^e = \mathbf{e}_\tau^e \cdot \mathbf{T}^e \cdot \mathbf{n}^e = 0, \qquad \mathbf{r} \in S_c^e, \tag{2.11}$$

where $\mathbf{e}_\tau^e$ is a tangential unit vector.

If one of the bodies – let us suppose it to be the first one – can move as a rigid body, the equilibrium equations for this body must be satisfied

$$\mathbf{F} = \mathbf{F}_o - \int_{S_c^1} p\mathbf{n}_c dS = \mathbf{0}, \qquad \mathbf{M} = \mathbf{M}_o - \int_{S_c^1} \mathbf{r} \times \mathbf{n}_c p dS = \mathbf{0}, \tag{2.12}$$

where $\mathbf{F}_o, \mathbf{M}_o$ are the resultant force and moment at the origin of the coordinate system, and $\mathbf{r}$ is the position vector, "$\times$" is the symbol of a vector product.

3. Weak formulation

3.1. Principles based on the total potential energy

For investigation of the normal contact problem we can use the principle of minimum potential energy $\Pi(\mathbf{u})$ subject to two types of kinematic conditions: $\mathbf{u} = \mathbf{u}_o$ on $\mathbf{r} \in S_u$ and $d \geq 0$ on $\mathbf{r} \in S_c$.

Formally

$$\min\{\Pi(\mathbf{u}) \mid \quad \mathbf{u} = \mathbf{u}_o, \quad \mathbf{r} \in S_u, \quad d \geq 0, \quad \mathbf{r} \in S_c\}, \tag{3.1}$$

which must be solved satisfying the variational inequality $\delta\Pi \geq 0$. The detailed mathematical discussion of this variational inequality and other variational principles can be found in books by HASLINGER *et al.* [5], KIKUCHI *et al.* [16] and in the paper by TELEGA [17].

Here

$$\Pi(\mathbf{u}) = \sum_{e=1}^{2} \left\{ \frac{1}{2} \int_{V^e} (\mathbf{A}(\mathbf{u}) - \mathbf{A}_o) \cdot\cdot \mathbf{D} \cdot\cdot (\mathbf{A}(\mathbf{u}) - \mathbf{A}_o)\, dV \right. \tag{3.2}$$

$$\left. + \int_{V^e} \mathbf{A}(\mathbf{u}) \cdot\cdot \mathbf{T}_o\, dV - \int_{V^e} \mathbf{u} \cdot \mathbf{b}\, dV - \int_{S_t^e} \mathbf{u} \cdot \mathbf{t}_o\, dS \right\}.$$

Practically, instead of the problem (3.1) we can use another method, in which the contact constraints can be introduced via the Lagrangian multipliers or penalty terms. In the Lagrangian multiplier technique we are taking the variation of the following functional

$$\mathcal{L}^{LA} = \mathcal{L}^{LA}(\mathbf{u}, p) = \Pi(\mathbf{u}) - \int_{S_c} p d(\mathbf{u})\, dS \tag{3.3}$$

with respect to $\mathbf{u}$ and p satisfying the conditions $\mathbf{u} = \mathbf{u}_o \quad \mathbf{r} \in S_u, \quad p \geq 0 \quad \mathbf{r} \in S_c$ respectively, that is

$$\delta_u \mathcal{L}^{LA} = 0, \qquad -\delta_p \mathcal{L}^{LA} \geq 0. \tag{3.4}$$

In the penalty method we have the next functional

$$\mathcal{L}^{PE} = \mathcal{L}^{PE}(\mathbf{u}) = \Pi(\mathbf{u}) + \frac{1}{2} \int_{S_c} c_N \left(d^-(\mathbf{u})\right)^2 dS, \tag{3.5}$$

where $c_N >> 0$ is the penalty parameter, and d^- denotes the negative part of d. From the variational equation $\delta_u \mathcal{L}^{PE} = 0$ we have a formula for contact pressure

$$p = -c_N d^- (\mathbf{u}) . \tag{3.6}$$

As $c_N \to \infty$ we have $d^- (\mathbf{u}) \to 0$, that is the $d \geq 0$ condition can be satisfied approximately. The correct choice of the penalty parameter is essential, because the condition number of the coefficient matrix increases as the penalty parameter increases. Using p-version finite elements [15, 18], $c_N \sim 100E - 1000E$ is recommended, where E is the Young modulus.

Combining the Lagrangian method and penalty method we have the augmented Lagrangian functional in the form:

$$\mathcal{L}^{AU} = \mathcal{L}^{AU} (\mathbf{u}) = \Pi (\mathbf{u}) - \int_C p d (\mathbf{u}) \, dS + \frac{1}{2} \int_C c_N (d (\mathbf{u}))^2 \, dS, \tag{3.7}$$

where p is the Lagrangian multiplier, which is kept constant during an iteration loop. From the variational equation $\delta_u \mathcal{L}^{AU} = 0$ we have a formula for the normal contact stress

$$\sigma_N^1 = \sigma_N^2 = - (p - c_N d (\mathbf{u})) . \tag{3.8}$$

During the iteration process, the contact pressure is updated using the formula:

$$p^{(k)} = \left\langle p^{(k-1)} - c_N d \left(\mathbf{u}^{(k)} \right) \right\rangle , \tag{3.9}$$

where the operation $< \cdot >$ is defined by

$$\langle p \rangle = \frac{1}{2} (p + |p|) . \tag{3.10}$$

In the $(k+1)th$ iteration loop the contact surface is subjected to $p^{(k)}$ as an external load in the variational formula:

$$\delta_u \mathcal{L}^{AU} \left(\mathbf{u}^{(k+1)} \right) = \delta \Pi \left(\mathbf{u}^{(k+1)} \right) - \int_C \delta d (\mathbf{u}) \left(p^{(k)} - c_N d \left(\mathbf{u}^{(k+1)} \right) \right) dS = 0. \tag{3.11}$$

3.2. Principle based on the modified complementary energy

Introducing the Green's function $H^e (\mathbf{x}, \mathbf{x}')$ and the normal displacement $u^e_{N,\text{load}}$ due to the given loads, the rigid body displacement of the punch (body 1) projected in normal direction is

$$u_R (\mathbf{x}) = [\lambda_F + \lambda_M \times \mathbf{r} (\mathbf{x})] \cdot \mathbf{n}_c (\mathbf{x}) , \tag{3.12}$$

where $\lambda_F = [\lambda_{F1} \quad \lambda_{F2} \quad \lambda_{F3}]$ is the rigid body translation vector, $\lambda_M = [\lambda_{M1} \quad \lambda_{M2} \quad \lambda_{M3}]$ is the rigid body rotation vector. Then we have the following functional to be minimized:

$$\mathcal{L}^C = \mathcal{L}^C(\mathbf{p}, \lambda_F, \lambda_M) = \frac{1}{2} \int_{S_c} \int_{S_c'} p(\mathbf{x}) \left(H^1(\mathbf{x}, \mathbf{x}') + H^2(\mathbf{x}, \mathbf{x}')\right) p(\mathbf{x}')\, dS' dS + \int_{S_c} p\left(u^2_{N,\text{load}} - u^1_{N,\text{load}} + h\right) dS - \lambda_F \cdot \mathbf{F} - \lambda_M \cdot \mathbf{M}. \tag{3.13}$$

The following variational equations and inequalities can be written:

$$\delta_{\lambda_F, \lambda_M} \mathcal{L}^C = 0, \tag{3.14}$$

which give the equilibrium equations for the punch (body 1) performing rigid-body displacement, and

$$\delta_p \mathcal{L}^C \geq 0, \qquad p \geq 0 \qquad \mathbf{x} \in S_c \tag{3.15}$$

represent here the contact and separation conditions (2.8) – (2.10).

4. Discretization of the functional

4.1. Approximation of the displacement and contact pressure fields

The displacements of the contacting bodies are approximated in the usual form

$$\mathbf{u}^e = \mathbf{u}^e(\mathbf{x}) = \mathbf{N}^e(\mathbf{x})\, \mathbf{q}^e, \tag{4.1}$$

where the shape functions consist of nodal points modes, side modes and internal modes, and $\mathbf{q}^e$ is the vector of displacement parameters [15]. The p-version computation is based on this approximation resulting in high degree of accuracy. The strain vector is given by the following formula:

$$\mathbf{A}^e \to \varepsilon^e = \varepsilon(\mathbf{x}) = \partial \mathbf{u}^e = \mathbf{B}^e(\mathbf{x})\, \mathbf{q}^e, \tag{4.2}$$

where $\mathbf{B}^e(\mathbf{x})$ is the strain-displacement matrix. The stress vector can be expressed as

$$\mathbf{T}^e \to \sigma^e = \sigma^e(\mathbf{x}) = \sigma^e_o(\mathbf{x}) + \mathbf{D}^e(\mathbf{x}) \left(\mathbf{B}^e(\mathbf{x})\, \mathbf{q}^e - \varepsilon^e_o(\mathbf{x})\right), \tag{4.3}$$

where $\mathbf{D}^e(\mathbf{x})$ is the constitutive matrix, $\varepsilon_o^e, \sigma_o^e$ are the initial strain and stress vectors, respectively. Using (4.1) – (4.3), the total potential energy (3.2) can be written in discretized form:

$$\Pi^e(\mathbf{u}) \to \Pi^e(\mathbf{q}^e) = \frac{1}{2}\mathbf{q}^{eT}(\mathbf{K}^e\mathbf{q}^e - 2\mathbf{f}^e), \tag{4.4}$$

where

$$\mathbf{K}^e = \int_{V_e} \mathbf{B}^{eT}\mathbf{D}^e\mathbf{B}^e dV \tag{4.5}$$

is the element stiffness matrix,

$$\mathbf{f}^e = \int_{V_e} \mathbf{N}^{eT}\mathbf{b}^e dV + \int_{S_t^e} \mathbf{N}^{eT}\mathbf{t}_o\, dS + \int_{V^e} \mathbf{B}^{eT}(\mathbf{D}^e\varepsilon_o^e - \sigma_o^e)\, dV \tag{4.6}$$

is the element load vector, and T denotes the transpose of a matrix.

The approximation of the contact pressure by a function of class C^o is recommended

$$p = p(\mathbf{x}) = \mathbf{P}^T(\mathbf{x})\,\mathbf{p} = [P_1 \quad P_2 \quad ...]\,\mathbf{p}, \qquad \mathbf{x} \in S_c, \tag{4.7}$$

where $\mathbf{p}$ is the column matrix of contact pressure at the nodes, P_i is the coordinate function of the *i-th* node.

The gap occuring after deformation is computed by the following projection:

$$d = u_N^2 - u_N^1 + h = -\mathbf{L}^1(\mathbf{x})\mathbf{q}^1 + \mathbf{L}^2(\mathbf{x})\mathbf{q}^2 + h = \mathbf{L}(\mathbf{x})\mathbf{q} + h, \tag{4.8}$$

where the matrix of shape functions $\mathbf{L}^e(\mathbf{x})$ is constructed by the use of $\mathbf{N}^e(\mathbf{x})$ and the definition of the normal displacement u_N^e. The vector of displacement parameters for the whole system is given as $\mathbf{q}^T = [\mathbf{q}^{1T} \quad \mathbf{q}^{2T}]$.

The last integral in the functional (3.3) can be approximated in the following way:

$$\int_{S_c} pd\, dS = \mathbf{p}^T \int_{S_c} \mathbf{PL}\, dS\, \mathbf{q} + \mathbf{p}^T \int_{S_c} \mathbf{P}h\, dS = -\mathbf{p}^T([\mathbf{G}^1\ \mathbf{G}^2]\,\mathbf{q} - \mathbf{h}) \tag{4.9}$$

$$= -\mathbf{p}^T\mathbf{G}\mathbf{q} + \mathbf{p}^T\mathbf{h} = \mathbf{p}^T\mathbf{d},$$

where $\mathbf{d} = -\mathbf{G}\mathbf{q} + \mathbf{h}$ and the penalty term in (3.7) can be written in the discretized form

$$\frac{1}{2}\int_C c_N\,(d\,(\mathbf{u}))^2\,dS = \frac{1}{2}\mathbf{q}^T\left\{\int_C \begin{bmatrix} -\mathbf{L}^{1T} \\ \mathbf{L}^{2T} \end{bmatrix} c_N\,[-\mathbf{L}^1\ \mathbf{L}^2]\ dS\ \mathbf{q} + 2\int_C \begin{bmatrix} -\mathbf{L}^{1T} \\ \mathbf{L}^{2T} \end{bmatrix} h\ dS\right\} + \text{const} = \frac{1}{2}\mathbf{q}^T \begin{bmatrix} \mathbf{C}^{11} & -\mathbf{C}^{12} \\ -\mathbf{C}^{21} & \mathbf{C}^{22} \end{bmatrix} \mathbf{q} + \mathbf{q}^T \begin{bmatrix} -\mathbf{f}_h^1 \\ \mathbf{f}_h^2 \end{bmatrix} + \text{const} = \frac{1}{2}\mathbf{q}^T\mathbf{C}\mathbf{q} + \mathbf{q}^T\mathbf{f}_h + \text{const}, \tag{4.10}$$

where $\mathbf{C}$ is the contact stiffness matrix.

From the integral (3.7), the load vector $\mathbf{f}_p^e$ which corresponds to the contact pressure is

$$\int_C d\,(\mathbf{u})\,p\,dS \to \mathbf{q}^T\int_C \begin{bmatrix} -\mathbf{L}^{1T} \\ \mathbf{L}^{2T} \end{bmatrix} p\,dS = \mathbf{q}^T \begin{bmatrix} -\mathbf{f}_p^1 \\ \mathbf{f}_p^2 \end{bmatrix} = \mathbf{q}^T\mathbf{f}_p. \tag{4.11}$$

Substituting (4.7) into (2.12) we have the equilibrium equation

$$\mathbf{f}_R - \mathbf{G}_R^T\mathbf{p} = \mathbf{0}, \tag{4.12}$$

where $\mathbf{f}_R$ is the external load vector and

$$\mathbf{G}_R = \int_C \begin{bmatrix} \ldots & \mathbf{n}_c\,(\mathbf{x})\,P_i\,(\mathbf{x}) & \ldots \\ \ldots & \mathbf{r}\,(\mathbf{x}) \times \mathbf{n}_c\,(\mathbf{x})\,P_i\,(\mathbf{x}) & \ldots \end{bmatrix} dS \tag{4.13}$$

is the geometrical matrix.

4.2. Discretized functionals

Finally the discretized form of the $\mathcal{L}^{LA}$ and $\mathcal{L}^{AU}$ functionals are written as:

$$\mathcal{L}^{LA} = \mathcal{L}^{LA}\,(\mathbf{q}, \mathbf{p} \geq \mathbf{0}) = \sum\nolimits_e \left\{\frac{1}{2}\mathbf{q}^{eT}\mathbf{K}^e\mathbf{q}^e - \mathbf{q}^{eT}\mathbf{f}^e\right\} + \mathbf{p}^T\,(\mathbf{G}\mathbf{q} - \mathbf{h}), \tag{4.14}$$

$$\mathcal{L}^{AU} = \mathcal{L}^{AU}\,(\mathbf{q}) = \sum\nolimits_e \left\{\frac{1}{2}\mathbf{q}^{eT}\mathbf{K}^e\mathbf{q}^e - \mathbf{q}^{eT}\mathbf{f}^e\right\} + \frac{1}{2}\mathbf{q}^T\mathbf{C}\mathbf{q} + \mathbf{q}^T\,(\mathbf{f}_h - \mathbf{f}_p). \tag{4.15}$$

By substitution of (4.7) into (3.13), the modified complementary energy has the following discretized form:

$$\mathcal{L}^C = \mathcal{L}^C\,(\mathbf{p} \geq \mathbf{0}, \lambda) = \frac{1}{2}\mathbf{p}^T\mathbf{H}\mathbf{p} + \mathbf{p}^T\mathbf{l} - \lambda^T\,(\mathbf{G}_R\mathbf{p} - \mathbf{f}_R), \tag{4.16}$$

where

$$\mathbf{H} = \frac{1}{2} \int_{S_c} \int_{S'_c} \mathbf{P}(\mathbf{x}) \left(H^1(\mathbf{x}, \mathbf{x}') + H^2(\mathbf{x}, \mathbf{x}') \right) \mathbf{P}^T(\mathbf{x}') \, dS' dS = \mathbf{H}^1 + \mathbf{H}^2$$

is the influence matrix, and

$$\mathbf{l} = \int_{S_c} \mathbf{P} \left(u^2_{N,\text{load}} - u^1_{N,\text{load}} + h \right) \, dS$$

is a displacement vector due to the external load and initial gap.

4.3. Systems of algebraic inequalities

Seeking the extremum of the functions (4.14), (4.16) and taking the Kuhn-Tucker conditions into consideration, the following formulae can be written

$$\frac{\partial \mathcal{L}^{LA}}{\partial \mathbf{q}^e} = \mathbf{0}, \qquad \mathbf{d} = -\frac{\partial \mathcal{L}^{LA}}{\partial \mathbf{p}} \geq \mathbf{0}, \qquad \mathbf{p} \geq \mathbf{0}, \qquad \mathbf{p}^T \mathbf{d} = 0, \tag{4.17}$$

$$\frac{\partial \mathcal{L}^{C}}{\partial \lambda} = \mathbf{0}, \qquad \mathbf{d} = \frac{\partial \mathcal{L}^{C}}{\partial \mathbf{p}} \geq \mathbf{0}, \qquad \mathbf{p} \geq \mathbf{0}, \qquad \mathbf{p}^T \mathbf{d} = 0. \tag{4.18}$$

If the determinant of matrix $\mathbf{K}^e$ is not zero, the vector $\mathbf{q}^e$ can be expressed from the following equation

$$\frac{\partial \mathcal{L}^{LA}}{\partial \mathbf{q}^e} = \mathbf{0} = \mathbf{K}^e \mathbf{q}^e + \mathbf{G}^{eT} \mathbf{p} - \mathbf{f}^e, \tag{4.19}$$

and we may substitute it into the inequality (4.17). After some straightforward transformations the compliance matrix is written as

$$\mathbf{H}^e = \mathbf{G}^e \left(\mathbf{K}^e \right)^{-1} \mathbf{G}^{eT}, \tag{4.20}$$

the displacement vector is

$$\mathbf{u}^e_{\text{load}} = -\mathbf{G}^e \left(\mathbf{K}^e \right)^{-1} \mathbf{f}^e, \tag{4.21}$$

and using (4.20) and (4.21), we have the gap in a discretized form

$$\mathbf{d} = \left(\mathbf{H}^1 + \mathbf{H}^2 \right) \mathbf{p} + \mathbf{u}^2_{\text{load}} + \mathbf{u}^1_{\text{load}} + \mathbf{h} \geq \mathbf{0}. \tag{4.22}$$

Let us consider the contact problem when the punch (body 1) has performed a rigid body translation, that is $\det \mathbf{K}^1 = 0$.

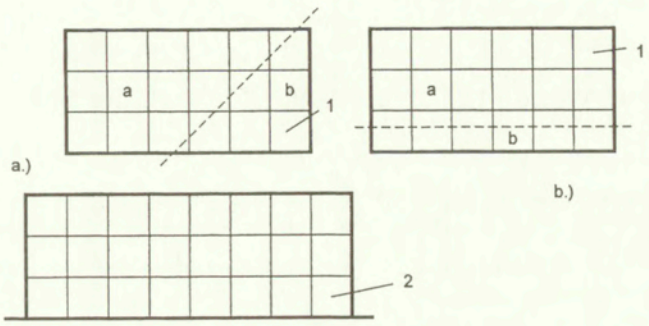

FIG. 2. Two variants for dividing the punch (body 1) into two parts denoted by a and b, (the variant b is recommended).

Let us partition (4.17) of the body 1 in such a way

$$\begin{bmatrix} \mathbf{K}_{aa} & \mathbf{K}_{ab} \\ \mathbf{K}_{ba} & \mathbf{K}_{bb} \end{bmatrix}^1 \begin{bmatrix} \mathbf{q}_a \\ \mathbf{q}_b \end{bmatrix}^1 + \begin{bmatrix} \mathbf{G}_a^T \\ \mathbf{G}_b^T \end{bmatrix}^1 \mathbf{p} = \begin{bmatrix} \mathbf{f}_a \\ \mathbf{f}_b \end{bmatrix}^1, \tag{4.23}$$

that the matrix block $\mathbf{K}_{aa}^1$ is not singular (see Fig. 2). Expressing $\mathbf{q}_a^1$ from the first equation and substituting it into the second one, we have an equation in the reduced form:

$$\mathbf{K}_{\text{red}}^1 \mathbf{q}_b^1 + \mathbf{G}_{\text{red}}^{1T} \mathbf{p} = \mathbf{f}_{\text{red}}^1, \tag{4.24}$$

where

$$\mathbf{K}_{\text{red}}^1 = \left[\mathbf{K}_{bb} - \mathbf{K}_{ba} \left(\mathbf{K}_{aa}\right)^{-1} \mathbf{K}_{ab}\right]^1,$$

$$\mathbf{G}_{\text{red}}^{1T} = \left[\mathbf{G}_b^T - \mathbf{K}_{ba} \left(\mathbf{K}_{aa}\right)^{-1} \mathbf{G}_a^T\right]^1,$$

$$\mathbf{f}_{\text{red}}^1 = \left[\mathbf{f}_b - \mathbf{K}_{ba} \left(\mathbf{K}_{aa}\right)^{-1} \mathbf{f}_a\right]^1.$$

Passing to the target (body 2), three Eqs. (4.19) – (4.21) remain valid in their original forms. Then

$$\mathbf{d} = -\frac{\partial \mathcal{L}^{LA}}{\partial \mathbf{p}} = -\mathbf{G}\mathbf{q} + \mathbf{h} = -\begin{bmatrix} \mathbf{G}_a^1 & \mathbf{G}_b^1 & \mathbf{G}^2 \end{bmatrix} \begin{bmatrix} \mathbf{q}_a^1 \\ \mathbf{q}_b^1 \\ \mathbf{q}^2 \end{bmatrix} + \mathbf{h} \tag{4.25}$$

$$= -\mathbf{G}_{\text{red}}^1 \mathbf{q}_b^1 + \left(\mathbf{H}^1 + \mathbf{H}^2\right) \mathbf{p} + \mathbf{u}_{\text{load}}^2 + \mathbf{u}_{\text{load}}^1 + \mathbf{h} \geq \mathbf{0},$$

where

$$\mathbf{H}^1 = \mathbf{G}_a^1 \left(\mathbf{K}_{aa}^1\right)^{-1} \mathbf{G}_a^{1T}, \qquad \mathbf{u}_{\text{load}}^1 = -\mathbf{G}_a^1 \left(\mathbf{K}_{aa}^1\right)^{-1} \mathbf{f}_a^1.$$

Knowing Eqs. (4.24) and (4.25), the system of inequalities to be solved has the form

$$\begin{bmatrix} \mathbf{H}^1 + \mathbf{H}^2 & -\mathbf{G}_{\text{red}}^1 \\ -\mathbf{G}_{\text{red}}^{1T} & -\mathbf{K}_{\text{red}}^1 \end{bmatrix} \begin{bmatrix} \mathbf{p} \\ \mathbf{q}_b^1 \end{bmatrix} + \begin{bmatrix} \mathbf{u}_{\text{load}}^2 + \mathbf{u}_{\text{load}}^1 + \mathbf{h} \\ \mathbf{f}_{\text{red}}^1 \end{bmatrix} = \begin{bmatrix} \mathbf{d} \\ \mathbf{0} \end{bmatrix}, \tag{4.26}$$

$$\mathbf{p} \geq \mathbf{0}, \qquad \mathbf{d} \geq \mathbf{0}, \qquad \mathbf{p}^T \mathbf{d} = 0.$$

The matrices $\mathbf{H}^e$ $(e = 1, 2)$ are constructed by the solutions of loads P_i $(i = 1, ..., KONT)$ applied to both of the bodies [19]. The rigid body displacements and rotations should be constrained and the P_i load must be equilibrated by appropriately chosen external loads.

There is another approach, when the matrices are blocked as it is shown in Fig. 2b, that is $\mathbf{G}_a^1 = \mathbf{0}$, which involves also $\mathbf{H}^1 = \mathbf{0}$ for the punch (body 1). The size of the vector $\mathbf{q}_b^1$ can be reduced to the degrees of freedom located on the contact surfaces in a similar way as it is applied in the sub-structural technique. From (4.18) we have the following inequality system which is formally similar to (4.26):

$$\begin{bmatrix} \mathbf{H}^1 + \mathbf{H}^2 & -\mathbf{G}_R \\ -\mathbf{G}_R^T & \mathbf{0} \end{bmatrix} \begin{bmatrix} \mathbf{p} \\ \lambda \end{bmatrix} + \begin{bmatrix} \mathbf{l} \\ \mathbf{f}_R \end{bmatrix} = \begin{bmatrix} \mathbf{d} \\ \mathbf{0} \end{bmatrix}, \tag{4.27}$$

$$\mathbf{p} \geq \mathbf{0}, \qquad \mathbf{d} \geq \mathbf{0}, \qquad \mathbf{p}^T \mathbf{d} = 0.$$

The algebraic system of equations associated with (4.15) can be written as follows:

$$\begin{bmatrix} \mathbf{K}^1 + \mathbf{C}^{11} & -\mathbf{C}^{12} \\ -\mathbf{C}^{21} & \mathbf{K}^2 + \mathbf{C}^{22} \end{bmatrix} \begin{bmatrix} \mathbf{q}^1 \\ \mathbf{q}^2 \end{bmatrix} = \begin{bmatrix} \mathbf{f}^1 + \mathbf{f}_h^1 - \mathbf{f}_p^1 \\ \mathbf{f}^2 - \mathbf{f}_h^2 + \mathbf{f}_p^2 \end{bmatrix} \tag{4.28}$$

where the matrix $\mathbf{C}^{ij}$ is modified to fulfill the contact/separation conditions.

The iterational KALKER procedure [11, 20] with the control of the sign of p can be applied for solving (4.26) – (4.28). The contact conditions are checked in the Gauss or Lobatto integration points of the contact elements during the solution of (4.28). Knowing the updated contact pressure $p^{(k+1)}$, the integrals (4.10) and (4.11) can be computed again, that is we have a new penalty (contact) matrix $\mathbf{C}$, and new vectors $\mathbf{f}_h$ and $\mathbf{f}_p$. The $(k+1)th$ displacements are obtained from the solution of (4.28). The procedure is terminated when the following condition is fulfilled:

$$\frac{\int\limits_{S_c} \left| p^{(k+1)} - p^{(k)} \right| dS}{\int\limits_{S_c} p^{(k+1)} dS} \leq 10^{-4}. \tag{4.29}$$

REMARKS

1. Since $d(\mathbf{u})$ is computed in a local coordinate system, the elements which have boundaries on the contact surface, must be transformed from the global coordinate system to the local one. The transformation is performed by the least squares fitting [18].

2. When the p-version is used, then accuracy is typically high enough for singularities to induce oscillations in the numerical solutions. The oscillations are minimized when nodes are located at the boundary of the contact zone. In the contact problems when the ends of contact zone are not situated in nodal points, the derivatives of the shape functions cannot have the appropriate jumps there. By moving the nodal points to the ends of the contact zone C, the jump in the derivatives can be represented in the discretized problem. The positioning technique can be found in [18].

3. The system of inequalities (4.26) and (4.27) is a Linear Complementary Problem, which can be solved by different algorithms as given e.g. in [21, 22] and [23].

4. In the work [24], a two-level algorithm is employed for solution of the contact problem using Lagrangian multipliers.

5. Contact pressure optimization problems

In optimization problems, the design parameters are usually concerned with material parameters, shape, characteristic dimensions (wall thickness, cross-sections), support system, loads, inner links, reinforcement and topology MRÓZ [25]. The sensitivity analysis is related to optimal design problems where design variables are to be determined by requiring minimization/maximization of the objective function subjected to specific design constraints. The references [5, 26, 27, 28] are using the sensitivity analysis for solution of the contact optimization problems.

The contact pressure optimization was investigated for the elastic punch and rigid target problem in case of linear elasticity. It was proved that designing the shape of a rigid body in contact with a fixed linear 2D elastic body by minimizing the potential energy under an isoparametric constraint, results in a uniform contact pressure distribution [3, 29, 30].

At some situations when the shape of an elastic body with a flat rigid foundation is chosen, the displacement gradients must be small [31].

In many earlier works [2, 7, 32], the maximum contact pressure was chosen as the objective function, but it was not differentiable. The articles [5, 29, 30] and [4] are using the total potential energy as a cost function, and the integral of the gap function as the isoparametric constraint. It is interesting that such a cost function is differentiable despite the fact that the mapping from design to state (displacement, stress) is not.

In many practical problems the bodies are in contact, therefore the elimination of the stress singularities is an important engineering task. In order to overcome this problem, application of the contact pressure control is recommended, which assures smooth contact pressure distribution as well as zero value on the border of the contact zone. We note that the constant contact pressure does not satisfy these conditions. This work extends the results of [12, 13, 14] by including rigid-body displacement and rotation of the punch.

5.1. Control of the contact pressure

In our optimization problems we suppose that the bodies are in contact on the whole sub-domain Ω_c of the contact zone $S_c = \Omega$. The contact surface is modified so that the following function is held for the contact pressure

$$p(\mathbf{x}) = v(\mathbf{x})\, p_{\max}, \qquad \mathbf{x} \in \Omega_c, \tag{5.1}$$

where the chosen control function must satisfy the condition $0 \leq v(\mathbf{x}) \leq 1$, and $p_{\max} = \max\ p(\mathbf{x})$, $\mathbf{x} = [s \quad t]$, where s and t are surface coordinates in the region Ω.

In the sub-domain Ω_{nc} ($\Omega = \Omega_c \cup \Omega_{nc}$) the satisfaction of the following inequality is required:

$$\chi(\mathbf{x}) = v(\mathbf{x})\, p_{\max} - p(\mathbf{x}) \geq \mathbf{0}, \qquad \mathbf{x} \in \Omega_{nc}. \tag{5.2}$$

Let us define a function $V(s)$ of class C^1 in the subregion Ω_c:

$$\begin{aligned}
&V(s) = 0, \quad 0 \leq s \leq L_1,\\
&V(s) = 3\left[\frac{(s-L_1)}{(L_2-L_1)}\right]^2 - 2\left[\frac{(s-L_1)}{(L_2-L_1)}\right]^3, \quad L_1 \leq s \leq L_2,\\
&V(s) = 1, \quad L_2 \leq s \leq L_3,\\
&V(s) = 1 - 3\left[\frac{(s-L_3)}{(L_4-L_3)}\right]^2 + 2\left[\frac{(s-L_3)}{(L_4-L_3)}\right]^3, \quad L_3 \leq s \leq L_4,\\
&V(s) = 0, \quad L_4 \leq s \leq L.
\end{aligned} \tag{5.3}$$

In this case $\dfrac{dV}{ds} = 0$ at $s = L_1$ and $s = L_4$ (see Fig. 3).

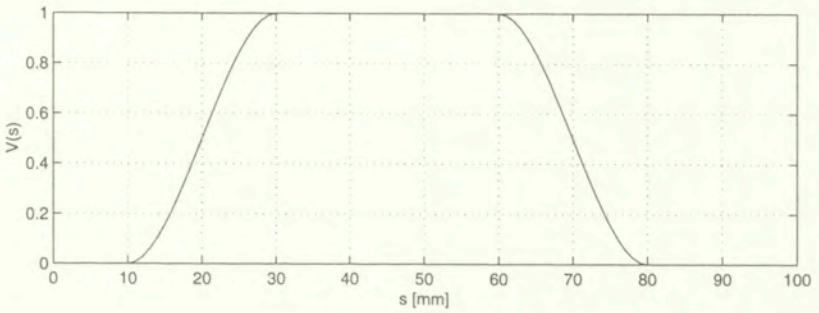

FIG. 3. Function $V(s)$ in Ω_c $L_1 = 10$, $L_2 = 30$, $L_3 = 60$, $L_4 = 80$, $L = 100$.

In 2D contact problems $v(s) = V(s)$ in Ω.

In 3D contact problems it is supposed that the punch (body 1) is subject to rigid body translation and rotation, Ω_c is a line s, and the rotation vector is perpendicular to this line. We define the controlling function along the line s in the following form:

$$v(s) = V(s)\left(1 + B\left(\frac{s}{L}\right)^n\right), \tag{5.4}$$

where B can be determined from equilibrium equations of the punch, n strongly influences the shape of $v(s)$; it is recommended to choose it from the interval $10 \leq n \leq 15$. In the direction t we introduce a simple function $\tilde{v}(t) = 1$, thus the controlling function is defined on Ω as

$$v(\mathbf{x}) = v(s)\,\tilde{v}(t). \tag{5.5}$$

5.2. Formulation of the optimization problem for axisymmetric bodies

The axially symmetric problem shown in Fig. 4 is discretized by p-extension elements. The geometry of the punch is given by inner radius $R_b = 20$ mm and outer radius $R_k = 120$ mm. There are 5 elements in radial direction ($nelr = 5$), and 3 elements in axial direction ($nelz = 3$). The order of approximation is $p = 8$ using the truncated space [15]. The following four problems have been analyzed:

P1. The displacement w_o is prescribed on the top surface of the punch. Using the controlling function with given parameters L_j $(j = 1, ..., 4)$, the shape optimization is performed on the punch, keeping its unloaded original length fixed in axial, direction. Denoting by $\triangle h$ the gap function, the optimization problem is given by variable $s = R - R_b$.

$$\min\{p_{\max} | p \geq 0, \quad d = d(p, \mathbf{u}, \triangle h) = 0, \quad \chi = v(s)\,p_{\max} - p(s) = 0, \quad \min \triangle h = 0\}. \tag{5.6}$$

P2. Applying the displacement and controlling function of problem P1, the shape optimization is performed on the punch yielding a given value of compressive force F_p

$$\min \left\{ p_{\max} | p \geq 0, \quad d = d(p, \mathbf{u}, \triangle h) = 0, \quad \chi = 0 \quad F_p = 2\pi \int_{R_b}^{R_k} Rp \, dR \right\}. \tag{5.7}$$

P3. The punch is loaded by constant pressure $\tilde{p} = 100$ MPa on its top surface. Let us determine the shape of the punch using a controlling function with parameters $L_2 - L_1 = 20$ mm, $L_3 = 80$ mm, $L_4 = 100$ mm, and maximizing the torque M_T

$$\frac{M_T}{\mu} = 2\pi \int_{R_b}^{R_k} R^2 p \, dR, \tag{5.8}$$

where μ is the friction coefficient. It is evident that the maximum of the torque is achieved when only the outer corner of the punch ($R = R_k$) is in contact, and the minimum value occurs when only the inner corner of the punch ($R = R_b$) is in contact.

Since the contact force is $F_o = \pi \left(R_k^2 - R_b^2\right) \tilde{p}$, so

$$M_T^{\max} = \mu\pi \left(R_k^2 - R_b^2\right) \tilde{p} R_k, \qquad M_T^{\min} = \mu\pi \left(R_k^2 - R_b^2\right) \tilde{p} R_b. \tag{5.9}$$

Prescribing the maximum of the contact pressure $p_{\max}$, the optimization problem is formulated as follows:

$$\max \left\{ \frac{M_T}{\mu} | \; p \geq 0, \quad d = d(p, \mathbf{u}, \triangle h) = 0, \quad F = F_o - 2\pi \int_{R_b}^{R_k} Rp \, dR = 0, \right. \tag{5.10}$$

$$\left. \chi = v(s, L_1, L_2(L_1); \; L_3, L_4 \text{ fixed}) \, p_{\max} - p(s) = 0 \right\},$$

where the parameters $\mathbf{u}, L_1, \Delta h, p$ are unknown.

P4. The relative angular velocity ω of the punch is given. The shape of the contact surface is optimized in order to minimize the frictional power loss by applying the controlling function with parameters of $L_1 = 0$, $L = 20$, $L_4 - L_3 = 20$ mm. The power loss is written as

$$D = \int_{R_b}^{R_k} R\omega\mu p 2\pi R \, dR = M_T \omega. \tag{5.11}$$

The closer is the location of the resultant of the contact pressure to radius R_b, the smaller will be the frictional power loss, thus the optimization problem is formulated as

$$\min\left\{\frac{D}{\mu\omega}\,|\; p \geq 0, \quad d = d\,(p, \mathbf{u}, \triangle h) = 0, \quad F = 0,\right. \tag{5.12}$$

$$\left.\chi = v\,(s, L_1, L_2 \text{ fixed};\; L_3\,(L_4)\,, L_4)\, p_{\max} - p\,(s) = 0\right\},$$

where the parameters $\mathbf{u}, L_4, \Delta h$ and p are unknown in the case of given $p_{\max}$.

5.2.1. Iterational algorithm for the solution of P1 - P4. The above problems are discretized when we know the location of the Lobatto integration points, where the contact conditions are checked. The discretized problems are solved with a relatively fast convergent algorithm. The discretized quantities are denoted by $\mathbf{p}^{(k)}$, $p_{\max}^{(k)}$, $\mathbf{d}^{(k)}$, $\Delta\mathbf{h}^{(k)}$, $\mathbf{u}_N^{2(k)}$, $\mathbf{u}_N^{1(k)}$ in the *k-th* iteration loop. The same control function v is used in problems P1, P2, and $p_{\max}$ is given in P3, P4.

The steps of the solution process are as follows:

1. Solution of the original contact problem : $\mathbf{p}^{(0)}$, $p_{\max}^{(0)}$, $k = 0$.
2. $k = k + 1$.
3. Computation of the new $\mathbf{p}^{(k)}$ vector from the following equation

$$\chi = \mathbf{v}\, p_{\max}^{(k-1)} - \mathbf{p}^{(k)} = \mathbf{0}.$$

REMARKS

a) In the problem P2:

$$p_{\max}^{(k-1)} = \frac{F_p}{\int\limits_{R_b}^{R_k} 2\pi R v\, dR} = \frac{F_p}{I_v}.$$

b) In problems P3, P4 the function v defined by new values of L_1 or L_4 to achieve

$$\left|p_{\max}^{(k-1)} - p_{\max}\,(\text{given})\right| \leq 0.01, \qquad p_{\max}^{(k-1)} = \frac{F_o}{I_v}.$$

4. Both the separated bodies are loaded by $p^{(k)}$. In the problem P3, P4, the punch (body 1) is supported by a vertical spring element in order to solve the system of algebraic equations.
5. Evaluation of the vector $\mathbf{m}^{(k)} = \mathbf{u}_N^{1(k)} - \mathbf{u}_N^{2(k)}$.
6. Determination of the minimum value of vector $\mathbf{m}^{(k)} \to m = \min\left(m_j^{(k)}\right)$.

7. In problems P1, P3, P4

$$\Delta \mathbf{h}^{(k)} = \mathbf{m}^{(k)} - m\mathbf{e}, \qquad \mathbf{e}^T = [\ 1 \quad 1 \quad \ldots\ ].$$

In the problem P2 : $\Delta \mathbf{h}^{(k)} = \mathbf{m}^{(k)}$.

8. Solution of (4.28) using the new shape due to $\Delta \mathbf{h}^{(k)}$.
9. Checking of the convergence condition

$$htol = 2\pi \int_{R_b}^{R_k} \left| \frac{R\left(\Delta h^{(k)} - \Delta h^{(k-1)}\right)}{\Delta h^{(k)}} \right| dR \leq 0.0001 = \vartheta.$$

If $htol > \vartheta$, then back to step 2 else stop.

5.2.2. Numerical examples. Material properties of the problem shown in Fig. 4 are Young modulus $E = 2 \cdot 10^5$ MPa, Poisson's ratio $v = 0.3$. The prescribed displacement of the punch on the boundary located at $Z = 80$ mm is $w_0 = -0.15$ mm. The initial gap function is $h = 0.00004 \cdot (R - 20)^2$. The stress distribution computed on the initial shape is shown in Fig. 4b.

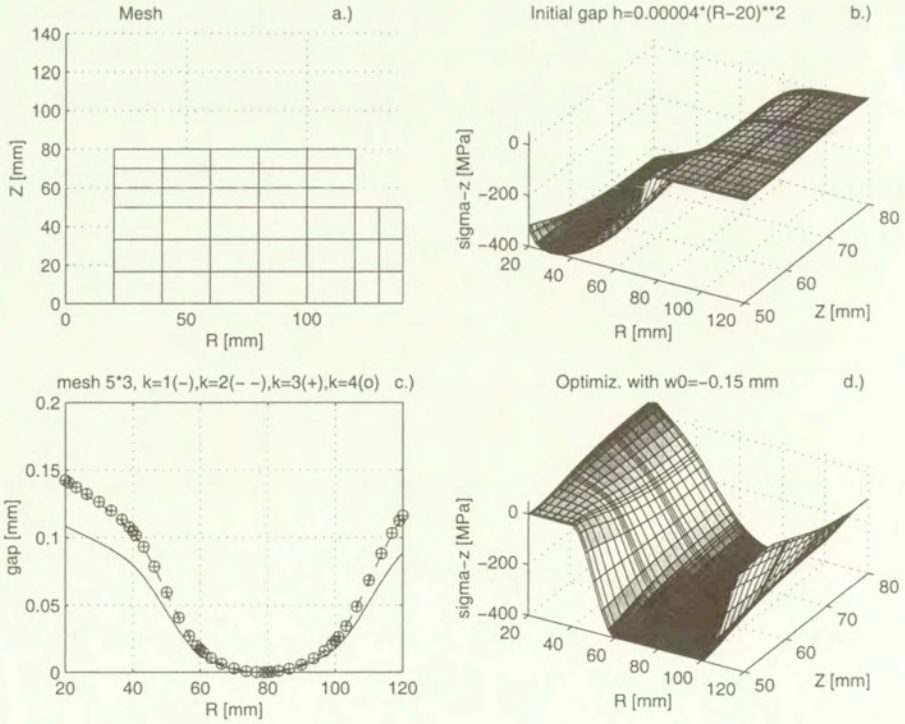

FIG. 4. The mesh of an axially symmetric problem, stress distribution σ_z in the punch, optimal solution of the initial gap and contact pressure distribution of problem P1.

Optimization problem P1. The contact optimization problem was solved by the iteration of Sec. 5.2.1, using the parameters of $L_1 = 20$ mm, $L_2 = 40$ mm, $L_3 = 80$ mm, $L_4 = 100$ mm. The modified shapes $\Delta h^{(k)}$ of the contact surface are shown in Fig. 4c for iteration loops $k = 1, 2, 3, 4$, and the final optimal normal stress is in Fig. 4d. The computed contact pressure maximum is $p_{\max} = 401.39$ MPa and torque $\dfrac{M_T}{\mu} = 6.39 \cdot 10^9$ Nmm for the optimal solution.

Optimization problem P2. The problem P2 was solved for compressive force $F_p = 5000$ kN. The shape of the contact surface is shown in Fig. 5a, the computed stresses $\sigma_R, \sigma_\varphi, \sigma_z$ are in Fig. 5b, 5c and 5d. The computed contact pressure maximum is $p_{\max} = 165.78$ MPa and torque $\dfrac{M_T}{\mu} = 2.64 \cdot 10^9$ Nmm for the optimal solution.

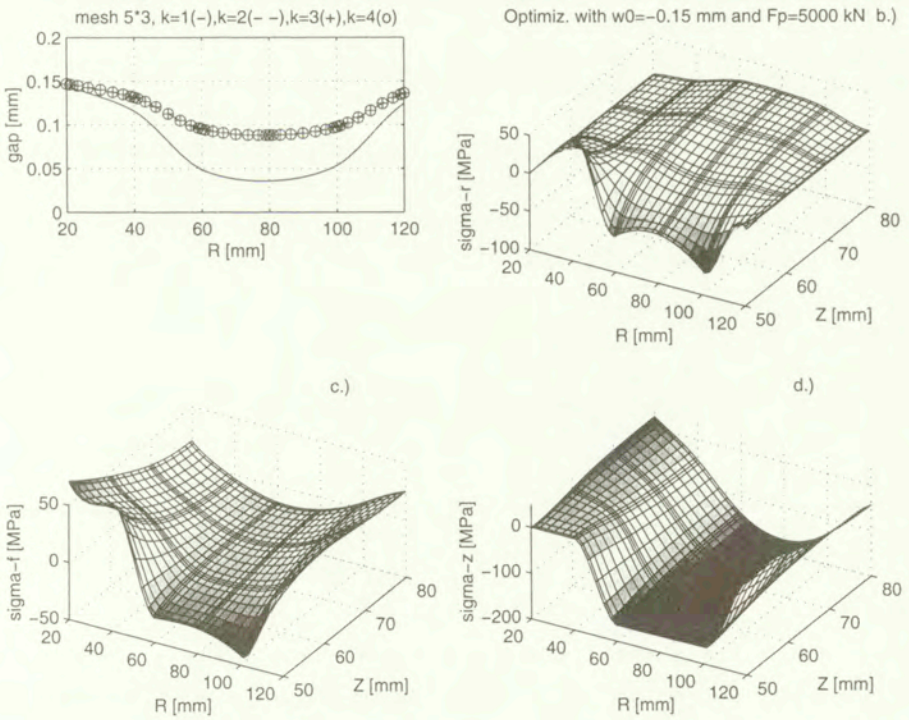

FIG. 5. Results of problem P2.

Optimization problems P3 and P4. Solving the problems P3 and P4 for given $p_{\max}$, the results of $\dfrac{M_T}{\mu}$ denoted by $(-)$ and $\dfrac{D}{\mu\omega}$ denoted by $(--)$ are shown in Fig. 6, as well as the variation of the control parameters L_1 and L_4. The above

optimizations were performed within 5 loops satisfying the tolerance in step 9 of algorithm 5.2.1.

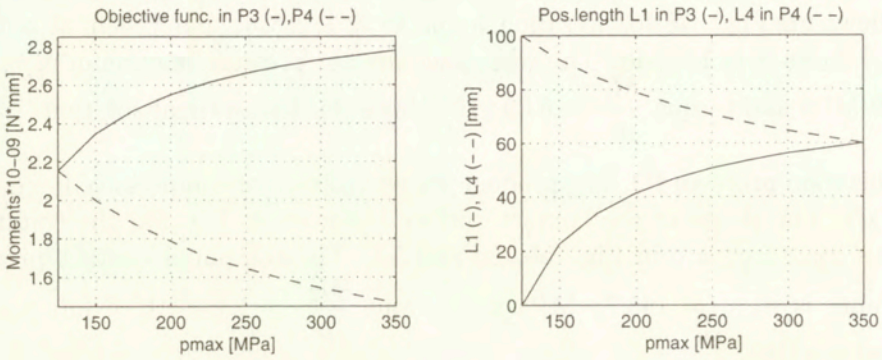

FIG. 6. The results of torque $\frac{M_T}{\mu}$, and parameters L_1, L_4 for problems P3 and P4.

5.3. Optimal shape design of the rollers

In engineering practice the roller is a frequently applied machine element. The meridian curve of the roller strongly influences the maximum of the contact pressure and its distribution, too. Due to the symmetry, a quarter of the model will be investigated, assuming linear elasticity and frictionless contact.

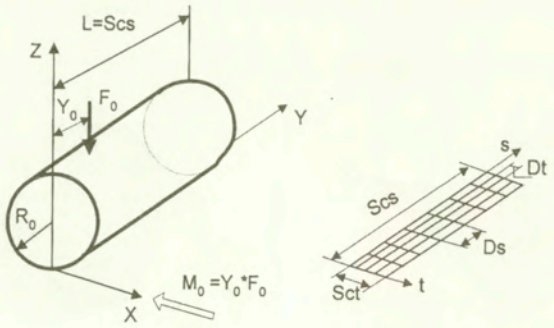

FIG. 7. Geometry and the loads of the roller, and the contact surface $\Omega = Scs \times Sct$ is divided into small elements having dimensions $Ds \times Dt$.

The loads of a roller consist of a resultant force F_o and a couple M_o; furthermore, the roller has a rigid body translation in the direction Z and rigid body rotation around X which is perpendicular to the axis of the roller (see Fig. 7). Since the contact region is sufficiently narrow in comparison to the diameter of the roller R_o, we shall apply the formulation which is valid for the elastic halfspace

to produce the influence function for the roller too, taking the mirror technique [12] into account. On the surface of the halfspace at $Z = 0$, the rectangular region $(Sct \times Scs)$ will be subdivided into small rectangles $(Dt \times Ds)$. Due to the symmetry of the contact problem with respect to the axis Y, we take only one the half of the original construction into consideration.

Elements of the influence matrix $\mathbf{H}$ are computed by applying the unit intensity normal load on six subregions $(Dt \times Ds)$ to the roller (the punch), and on four subregions to the quarter elastic space (the target, with $0 \leq Y \leq \infty$, $-\infty \leq X \leq \infty$, $-\infty \leq Z \leq 0$) in order to eliminate shearing stresses at the bottom and top surfaces of the roller and at the side $Y = 0$ of the quarter space.

Here the controlling region Ω_c is defined as a subregion of $0 \leq t \leq Dt$, $0 \leq s \leq Scs$.

Equilibrium equations for the roller are written as

$$F = F(B, p_{\max}, p \geq 0) = F_o - p_{\max} \int_{\Omega_c} v(s,t)\, dS - \int_{\Omega_{nc}} p\, dS = 0,$$

(5.13)

$$M = M(B, p_{\max}, p \geq 0) = M_o - p_{\max} \int_{\Omega_c} Y(s)\, v(s,t)\, dS - \int_{\Omega_{nc}} Yp\, dS = 0,$$

where the condition $\chi(\mathbf{x}) \geq \mathbf{0}$ must be satisfied. We obtain a formula for B using (5.3) for $V(s) = V(s, L_j)$ $\quad (j = 1, ..., 4)$:

$$B^{(i+1)} = \frac{\left(\dfrac{\displaystyle\int_{\Omega_{nc}} (Y_o - Y)\, p^{(i)} dS}{Dt \cdot p_{\max}^{(i)}} + \displaystyle\int_0^L (Y_o - Y(s))\, V(s, L_j)\, ds \right)}{\displaystyle\int_0^L (Y_o - Y(s))\, V(s, L_j) \left(\frac{s}{L}\right)^n ds}. \tag{5.14}$$

Keeping the parameters L_j, $(j = 1, \ldots, 4)$ fixed, the pressure could be even negative in the region Ω_c $(Y_o \leq L/2)$ depending on the values of F_o and M_o. Therefore keeping the parameters $L_1, L_2, (L_4 - L_3)$ fixed, as in problem P4, the parameter L_4 is modified until the condition $v(s, 0) \geq 0$ is satisfied everywhere. It is supposed that the change of gap in region Ω_{nc} is expressed by the function of gap's change Δh in region Ω_c: $\Delta h_{nc} = f(\Delta h)$.

The optimization problem is

$$(5.15)\qquad \min\{p_{\max}|\ p \geq 0,\quad d = d(p,\lambda,\triangle h) \geq 0,\quad pd = 0\quad \mathbf{x} \in \Omega,$$
$$\chi = 0\quad \mathbf{x} \in \Omega_c,\quad \chi \geq 0\quad \mathbf{x} \in \Omega_{nc},\quad F = 0,\quad M = 0\}.$$

Discretizing (5.15), in view of (4.16), (4.18), (4.27), we have a restricted linear programming problem:

$$(5.16)\qquad \min\{p_{\max}|\ \mathbf{p} \geq \mathbf{0},\quad \mathbf{d} = \mathbf{H}\mathbf{p} - \mathbf{G}_R\lambda + \mathbf{l} + \Delta\mathbf{h} \geq \mathbf{0},\quad \mathbf{p}^T\mathbf{d} = 0\,,$$
$$\chi = \mathbf{v}p_{\max} - \mathbf{p} \geq \mathbf{0}\quad \mathbf{G}_R^T\mathbf{p} - \mathbf{f}_R = \mathbf{0}\}.$$

The following algorithm is proposed to solve it.

5.3.1. Iterational process of solution of the contact optimization problem (5.16).

1. Solution of the original contact problem $\left(\mathbf{p}^{(0)}, \lambda^{(0)}\right)$.
2. Determination of B from (5.14) in which $\Omega_{nc} = 0$, $i = 1$.
3. Computation of the new vector $\mathbf{p}_c$

$$\mathbf{p}^T = [\ \mathbf{p}_c^T\quad \mathbf{p}_{nc}^T\ ],\qquad \mathbf{p}_{\max}^{(0),i} = \frac{\left(p_{\max}^{(0)} + p_{\min}^{(0)}\right)^{(i-1)}}{2},$$

$$\chi_c = \mathbf{v}\left(s, B^{(0)}, L_j\right) p_{\max}^{(0),i} - \mathbf{p}_c^{(0),i} = \mathbf{0}\quad \rightarrow\quad \mathbf{p}_c^{(0),i},\quad i = i+1.$$

If the vector $\mathbf{p}_c^{(0),i}$ has negative terms, the parameters $L_4, L_3(L_4)$ must be modified and go to step 2 else go to step 4.

4. $k = k+1,\qquad i = 1.$
5. If $k > 4$ then $B^{(k)}$ is determined from (5.14).
6. Computation of the new $\mathbf{p}$ vector:

$$6.1\qquad \chi_c = \mathbf{v}\left(s, 0, B^{(k)}\right) p_{\max}^{(k-1),i} - \mathbf{p}_c^{(k),i} = \mathbf{0}\qquad \rightarrow\qquad \mathbf{p}_c^{(k),i},$$

$$6.2\qquad \chi_{nc} = \mathbf{v}\left(s, t, B^{(k)}\right) p_{\max}^{(k-1),i} - \mathbf{p}_{nc}^{(k),i} \geq \mathbf{0}\qquad \rightarrow\qquad \mathbf{p}_{nc}^{(k),i},$$

$$6.3\qquad p_{\max}^{(k-1),i+1} = \frac{\left(F_o - \int\limits_{\Omega_{nc}} p^{(k),i}\,dS\right)}{Dt\int\limits_0^L v\left(s, 0, B^{(k)}\right) ds},$$

6.4

$$\text{If} \quad \frac{\left| p_{\max}^{(k-1),i+1} - p_{\max}^{(k-1),i} \right|}{p_{\max}^{(k-1),i}} > tol = 0.0005 \quad \text{then} \quad i = i + 1 \text{ go to 6.1.}$$

7. Computation of the residual vector in Ω_c

$$\mathbf{m}^{(k)} = -\left(\mathbf{H}\mathbf{p}^{(k)} - \mathbf{G}\lambda^{(k)} + \mathbf{l} \right), \qquad \lambda^{(1)} = \lambda^{(0)}.$$

8. Determination of the maximum value of $m_j^{(k)}$ $(j = 1, \ldots, k_s)$,

$$m = \max_j \left(m_j^{(k)} \right).$$

9. Determination of the change in radius of the roller

$$\Delta \mathbf{r}_{(k_s,1)}^{(k)} = \left(\mathbf{m}_c^{(k)}{}_{(k_s,1)} - m\mathbf{e} \right), \qquad \mathbf{e}^T{}_{(k_s,1)} = \left[\begin{array}{cccc} 1 & 1 & \ldots & 1 \end{array} \right].$$

10. Computation of the gap change due to the radius change

$$\Delta \mathbf{h}^{(k)} = \mathbf{Q} \Delta \mathbf{r}^{(k)},$$

where $\mathbf{Q}$ is a suitable matrix accounting for the geometry of the roller and the elements.

11. Solution of the contact problem by the new shape of the roller

$$\mathbf{d}^{(k+1)} = \mathbf{H}\mathbf{p}^{(k+1)} - \mathbf{G}_R \lambda^{(k+1)} + \mathbf{l} + \Delta \mathbf{h}^{(k)} \geq \mathbf{0}, \qquad -\mathbf{G}_R^T \mathbf{p} = -\mathbf{f}_R,$$

$$\mathbf{p}^{(k+1)} \geq \mathbf{0}, \qquad \mathbf{p}^{(k+1)T} \mathbf{d}^{(k+1)} = 0.$$

12. Checking of the convergence condition:

$$htol = \frac{\sum_{j=1}^{k_s} \left| \Delta h_j^{(k)} - \Delta h_j^{(k-1)} \right|}{\sum_{j=1}^{k_s} \left| \Delta h_j^{(k)} \right|} \leqslant 0.0025 = \vartheta.$$

If $htol \geq \vartheta$ then back to step 4, else stop and the optimization problem is solved.

5.3.2. Numerical example. The quarter of the roller and an elastic halfspace are considered. The radius of the roller is $R_o = 60$ mm. The roller is subjected to loads of $F_o = 2500$ N and $M_o = 33000$ Nmm. The proposed contact region is given by $Sct = 0.6$ mm $\times$ $Scs = 35$ mm, and it is divided into 6×60 rectangular elements, $L_1 = 0$, $L_2 = 4$ mm, $L_4 - L_3 = 4$ mm.

The contact pressure arising in case of the initial geometry is shown in Fig. 8c. The high pressure peaks are at the end of the roller ($Y = 0$).

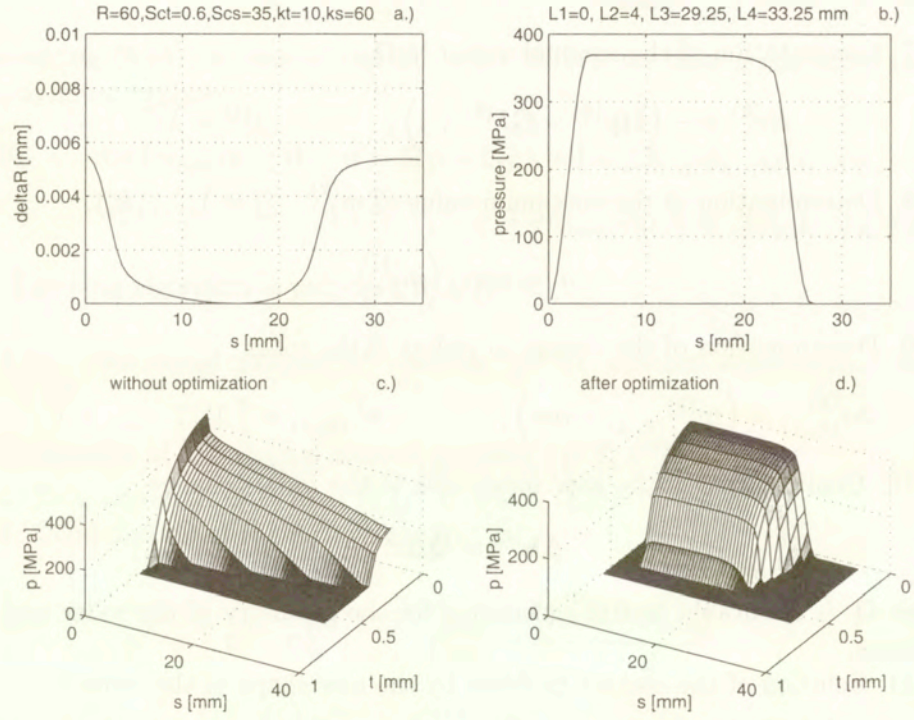

FIG. 8. Investigation of contact for the roller and the quarter space.

The optimization problem is solved for different values of n in the controlling function of $v(s,t)$. The best solution was obtained at $n = 13$, as it gave the smallest pressure value and the smoothest pressure distribution along the line $X = 0$. In case of $n > 13$, the value of the pressure maximum is larger than the value in parenthesis which is dominant around the location of $s = (L_2 + L_3)/2$. The parameters L_3 and L_4 assuring positive contact pressure and the parameter B of the controlling function are also listed in the Table 1. The *kopt* parameter denotes the number of iterations, when the tolerance of 12-*th* step of 5.3.1 is satisfied.

The computation was repeated for a higher density of mesh ($kt = 10$, $ks = 60$). The computed radius change is shown in Fig. 8a, the contact pressure distribution along the line $X = 0$ is in Fig. 8b, and the pressure distribution on the whole contact region is shown in Fig. 8d. The maximum of the contact pressure is $p_{\max}$= 369.11 MPa at $n = 13$.

Table 1.

n	$p_{\max}$ MPa	L_3 mm	L_4 mm	$B^{(0)}$	$B^{(kopt)}$	$kopt$
1	423.63	31	35	-0.9639	0.7092	23
5	372.69	24.583	28.583	−2.419	−1.5996	33
10	368.01	23.416	27.416	−11.349	−8.203	36
11	367.24	22.833	26.833	−9.516	−6.894	35
12	367.17	22.833	26.833	−14.082	−10.483	36
13	367.11	22.833	26.833	−20.734	−15.861	36
14	372.43 (366.45)	22.250	26.250	15.334	11.765	36
15	372.17 (366.47)	22.250	26.250	22.887	17.943	36
20	394.38 (366.06)	21.667	25.667	1328.29	1038.53	36

6. Conclusions

Two types of contact optimization problems have been investigated. In the first type, axially-symmetric problems are discretized by p-version finite elements. The optimizations have been performed by controlling the distribution of the contact pressure:

1. Minimizing the contact pressure maximum,
2. Minimizing the frictional power loss,
3. Maximizing the torque due to friction.

One of the advantages of using the p-version finite elements is that only coarse meshes are needed in our examples. Since high degree of polynomials ($p = 8$) is applied for the approximation of the displacement field and for mapping, the contact optimization problems have been solved with very high accuracy. Optimization problems are solved by means of a special iterative algorithm.

In the second type of the optimization problem, an optimal shape design of the rollers has been investigated. A new control function and a fast algorithm are proposed. In the optimization problem the objective function is not differentiable, the pressure is partially controlled in order to achieve smooth contact pressure. The roller may be subject to rigid body translation and rotation.

Examples are demonstrating the effectiveness of the proposed algorithms.

Acknowledgement

Financial support for this paper was provided by the grants FKFP 0040/1999, OTKA T025172 and AKP 146 2,3/31.

References

1. I. PACZELT, *Some optimization problems of contact bodies within the linear theory of elasticity*, [In:] Variational methods in the mechanics of solids, S. NEMAT-NASSER, Pergamon Press, 349–356, Oxford 1980.
2. T. F. CONRY and A. SEIREG, *A mathematical programming method for design of elastic bodies in contact*, J. Appl. Mech., **38**, 387–392, 1971.
3. A. KLARBRING, *On the problem of optimizing contact force distributions*, J. Optimiz. Theory Appl., **74**, 131–150, 1992.
4. J. PETERSON, *Behaviourally constained contact force optimization*, Structural Optimization, **9**, 189–193, 1995.
5. J. HASLINGER and P. NEITTAANMAKI, *Finite element approximation for optimal shape design*, John Wiley Sons Ltd., London 1988.
6. J. ODA, J. SAKAMOTO and K. SAN, *A method for producing a uniform contact stress distribution in composite with interface*, Structural Optimization, **3**, 23–28, 1991.
7. I. PÁCZELT and B. HERPAL, *Some remarks on the solution of contact problems of elastic shells*, Archives of Machine Structures, XXIV, 197–202, 1977.
8. K. P. OH and E. G. TRACHMANN, *A numerical procedure for designing profiled rolling*, ASME J. Lubrication Technology Series F, **98**, 68–75, 1976.
9. M. J. HARNETT, *The analysis of contact stresses in rolling element bearings*, Trans. ASME, J. Lubrication Technology Series F, **101**, 105–109, 1979.
10. Y. P. CHIU and M. J. HARNETT, *A numerical solution for the contact problem involving bodies with cylindrical surface considering cylinder effect*, ASME J. Tribology, **109**, 479–486, 1987.
11. J. M. de MUL, J. J. KALKER and B. FREDERIKSSON, *The contact between arbitrarily curved bodies of finite dimension*, ASME J. Tribology, **108**, 140–148, 1986.
12. I. PÁCZELT and T. SZABÓ, *Optimal shape design for contact problems*, Structural Optimization, **7**, 66–75, 1994.
13. I. PÁCZELT, *Some contact problems of elastic systems* [in Polish], [In:] Contact Surface Mechanics, Z. Mróz, 7–49, Polish Academy of Sciences, Warsaw 1988.
14. I. PÁCZELT, *Some new developments in contact pressure optimization*, Engng. Trans., **43**, 297–312, 1995.
15. B. A. SZABÓ and I. BABUSKA, *Finite element analysis*, John Wiley and Sons, New York 1991.
16. J. T. ODEN and N. KIKUCHI, *Contact problem in elasticity: a study of variational inequalities and finite element methods*, SIAM, Philadelphia 1988.
17. J. I. TELEGA, *Variational principles for mechanical contact problems* [in Russian], Advances of Mech., **10**, 3–95, 1987.
18. I. PÁCZELT, B. A. SZABÓ and T. SZABÓ, *Solution of contact problem using the hp-version of the finite element method*, Computers and Mathematics with Application, **38**, 4696, 1999.
19. I. PÁCZELT, *Solution of elastic contact problems by the finite displacement method*, Acta Tech. Hung., **82**, 353–375, 1976.
20. J. KALKER, *Three-dimensional elastic bodies in rolling contact*, Academic Publisher, Doordrecht 1990.

21. R. W. CATTLE, S. S. PANG and R. E. STONE, *The linear complementarity problem*, Academic Press, Boston 1992.

22. A. KLARBRING, *Mathematical programming in contact problems*, [In:] Computational Methods in Contact Mechanics, M. H. ALIABADI and C. A. BREBBIA [Eds.], Computational Mechanics Publications, pp. 233–263, Southampton 1993.

23. M. S. KUCZMA, *A viscoelastic-plastic model for skeletal structural systems with clearances*, Cames, **6**, 83–106, 1999.

24. B. NOUR-OMID and P. WRIGGERS, *A two-level iteration method for solution of contact problems*, Comput. Meths. Appl. Mech. Engng., **54**, 131–144, 1986.

25. Z. MRÓZ, *Sensitivity analysis of distributed and discretized systems*, [In:] Advanced TEMPUS Course on Numerical Methods in Computer-Aided Optimal Design, T. Burczyński, pp. 1–60, Silesian Technical University of Gliwice 1992.

26. E. A. FANCELLO and R. A. FEIJÓO, *Shape optimization in frictionless contact problems*, Int. J. Numer. Meth. Engng., **37**, 2311–2335, 1994.

27. E. FANCELLO, J. HASLINGER and R. A. FEIJÓO, *Numerical comparison between two cost functionals in contact shape optimization*, Structural Optimization, **9**, 57–68, 1995.

28. G. SZEFFER, *Shape sensitivity in contact problems of elastic bodies*, [In:] WCSMO-1, N. OLHOFF, G. I. N. ROZVANY, pp. 335–340, Pergamon Press, 1995.

29. R. l. BENEDICT and J. E. TAYLOR, *Optimal design for elastic bodies in contact*, [In:] Optimization of distributed parameter structures, Part II, E. J. HAUG, J. CEA, pp. 1553–1599, Sijthoff and Alphen aan den Rijn 1981.

30. N. KIKUCHI and J. E. TAYLOR, *Shape optimization for unilateral elastic contact problems*, [In:] Num. Meth. Coupl. Probl. University College Swansea, pp. 430–441, Wales 1981.

31. A. KLARBRING and J. HASLINGER, *On almost constant stress distributions by shape optimization*, Structural Optimization, **5**, 213–216, 1993.

32. E. J. HAUG and B. M. KWAK, *Contact stress minimization by contour design*, Int. J. Numer. Meth. Engng., **12**, 917–939, 1978.

Received February 7, 2000; revised version June 27, 2000.

Arch. Mech., **52**, 4–5, pp. 713–735, Warszawa 2000

An approach to elastic shakedown based on the maximum plastic dissipation theorem

Dedicated to Professor Zenon Mróz
on the occasion of his 70th birthday

C. POLIZZOTTO ([1]), G. BORINO ([1]), P. FUSCHI ([2])

([1]) *DISEG Dipartimento di Ingegneria Strutturale & Geotecnica,*
Università di Palermo,
Viale delle Scienze, I-90128, Palermo, Italy.

([2]) *DASTEC Dipartimento Arte Scienza Tecnica del Construire,*
Università di Reggio Calabria,
Via Melissari Feo di Vito, I-89124 Reggio Calabria, Italy.

ELASTIC-PERFECTLY PLASTIC SOLID STRUCTURES are considered subjected to combined loads, superposition of permanent (mechanical) loads and cyclically variable loads, the latter being specified to within a scalar multiplier. The classical maximum dissipation theorem is used to derive known results of the shakedown theory, as well as a few apparently novel concepts: the shakedown limit load associated with a given (noninstantaneous) collapse mode, the mixed upper bound to the shakedown safety factor, and the mixed static-kinematic formulation of the shakedown safety factor problem. The shakedown load boundary surface is also investigated and a number of its notable features are pointed out. A simple illustrative example is presented.

Notation

A compact notation is used throughout the paper, with bold-face symbols for vectors and tensors, with the rules: $\mathbf{u}\cdot\mathbf{v} = u_i v_i$, $\boldsymbol{\sigma} : \boldsymbol{\varepsilon} = \sigma_{ij}\varepsilon_{ij}$, $(\boldsymbol{\sigma}\cdot\mathbf{n})_i = \sigma_{ij}n_j$, $\mathbf{u}\cdot\boldsymbol{\sigma}\cdot\mathbf{n} = u_i\sigma_{ij}n_j$, $(\mathbf{A} : \boldsymbol{\sigma})_{ij} = A_{ijhk}\sigma_{hk}$, $\boldsymbol{\sigma} : \mathbf{A} : \boldsymbol{\sigma} = A_{ijhk}\sigma_{ij}\sigma_{hk}$, where the indicial summation rule applies. The symbol := means equality by definition. Other symbols are defined where they appear for the first time.

1. Introduction

IN THIS PAPER, known notions of (elastic) shakedown theory will be discussed from a non-traditional point of view. The motivation for such an approach to the shakedown theory is suggested by a neighbour theory of plastic limit analysis.

It is known (see e.g. [6, 8, 11, 12]) that, in the latter theory, a central role is played by the maximum plastic work theorem of HILL [7], which in fact enables us to evaluate the limit load corresponding to an arbitrarily assigned collapse mechanism of a given structure, and can thus be utilized as a departure point to develop the static and kinematic approaches to the plastic limit analysis. In particular, within the kinematic approach, the structure's plastic collapse safety factor can be determined as the minimum value, over the entire set of collapse mechanisms, of the so-called kinematic load multiplier, which can be interpreted as the structure's safety factor against a specified collapse mechanism.

In the shakedown theory (see e.g. [4, 5, 9, 10, 12]), a theorem analogous to the above maximum plastic work theorem was provided in [3] for elastic-perfectly plastic structures subjected to combined cyclic/permanent loads. This theorem is capable of providing the combined load at the shakedown limit corresponding to a specified collapse mode. It is the purpose of the present paper to show that, like in the plastic limit analysis, the latter theorem can be utilized as a starting point to develop the static and kinematic approaches to the shakedown theory. Also, the notion of structure's shakedown limit load for an assigned (noninstaneous) collapse mechanism will be introduced to show that its minimum value over the entire set of such mechanisms coincides with the structure's shakedown limit load.

The plan of the paper is as follows. In Sec. 2, the maximum plastic dissipation theorem (written in space integral form) will be recalled and applied to plastic limit analysis for demonstrative purposes. In Sec. 3, the concept of inadaptation collapse mechanism will be briefly discussed and its ingredients, such as the '(noninstantaneous) collapse mechanism' and the 'plastic strain path', pointed out for use in Sec. 4. In the next section, the maximum plastic dissipation theorem (written in time-space integral form) will be employed to derive the concept of 'shakedown limit load for assigned (noninstantaneous) collapse mechanism', for which two alternative formulations are given, static and kinematic respectively, together with the set of equations which govern the related structural problem. Section 5 will be devoted to the shakedown load boundary surface and to its essential features, showing that it plays the role of yield surface for the structure: namely, any load staying within this surface is below the shakedown limit, hence no inadaptation collapse mechanism is produced (i.e. the limit state is elastic), whereas any load on the shakedown boundary surface corresponds to a shakedown limit state, in which it is prone to an impending (noninstantaneous) collapse mechanism represented by a vector normal to the above boundary surface at the load point. In Sec. 6, the maximum dissipation theorem (still written in time-space integral form) is used to derive the classical static and kinematic formulations of the shakedown safety factor for combined cyclic/permanent loads. Alternative formulations are also provided: one is a two-stage kinematic formulation, another is a mixed static-kinematic formulation, the latter being characterized by

the use of free stress variables and compatibility equations. A simple application is presented in Sec. 7. A resumé is presented, together with the conclusions, in Sec. 8.

2. Preliminary considerations

The maximum plastic dissipation theorem [6 – 8, 11, 12] written in space-integral form, reads:

$$\max_{\boldsymbol{\sigma}} \int_V \boldsymbol{\sigma} : \dot{\boldsymbol{\varepsilon}}^p \, dV \quad \text{s.t. } f(\boldsymbol{\sigma}) \leq 0 \ \text{ in } V \tag{2.1}$$

where 's.t.' stands for 'subject to', $\dot{\boldsymbol{\varepsilon}}^p$ is a plastic strain rate field assigned in the structure's domain V, $f(\boldsymbol{\sigma})$ is the (convex, smooth) yield function and $\boldsymbol{\sigma}$ is an unknown stress field. It can be shown that the Euler-Lagrange equations of problem (2.1) coincide with the material plastic flow laws, i.e.

$$\dot{\boldsymbol{\varepsilon}}^p = \dot{\lambda} \frac{\partial f}{\partial \boldsymbol{\sigma}}, \tag{2.2}$$

$$f(\boldsymbol{\sigma}) \leq 0, \quad \dot{\lambda} \geq 0, \quad \dot{\lambda} f(\boldsymbol{\sigma}) = 0, \tag{2.3}$$

where $\dot{\lambda}$ is the consistency coefficient, Eqs. (2.2) and (2.3) being *enforced everywhere* in V. In other words, the optimal stress field $\boldsymbol{\sigma}$ given by problem (2.1) corresponds to $\dot{\boldsymbol{\varepsilon}}^p$ in a point-wise manner through (2.2) and (2.3).

In consideration of the arbitrariness of $\dot{\boldsymbol{\varepsilon}}^p$ in (2.1), let $\dot{\boldsymbol{\varepsilon}}^p$ be chosen to be compatible with the velocity field $\dot{\mathbf{u}}$; that is, the compatibility equations

$$\dot{\boldsymbol{\varepsilon}}^p = \nabla^s \dot{\mathbf{u}} \quad \text{in } V, \qquad \dot{\mathbf{u}} = 0 \quad \text{on } S_D, \tag{2.4}$$

are satisfied. In (2.4), ∇^s is the symmetric part of the gradient operator ∇, S_D is a part of the boundary surface $S = \partial V$, i.e. $S_D \subset S$. The notation $\dot{\boldsymbol{\varepsilon}}^p(\dot{\mathbf{u}})$ will be used in the following to mean that $\dot{\boldsymbol{\varepsilon}}^p$ is related to $\dot{\mathbf{u}}$ by Eq. (2.4). Then, applying the virtual work principle, one can write the equality

$$\int_V \boldsymbol{\sigma} : \dot{\boldsymbol{\varepsilon}}^p \, dV = (\mathbf{p}, \dot{\mathbf{u}}) \tag{2.5}$$

where the internal product $(\mathbf{p}, \dot{\mathbf{u}})$ is given by

$$(\mathbf{p}, \dot{\mathbf{u}}) := \int_V \mathbf{p}_V \cdot \dot{\mathbf{u}} \, dV + \int_{S_T} \mathbf{p}_S \cdot \dot{\mathbf{u}} \, dS. \tag{2.6}$$

Here, the load $\mathbf{p}$ equilibrated by $\boldsymbol{\sigma}$ consists of volume forces $\mathbf{p}_V$ in V and surface forces $\mathbf{p}_S$ on $S_T = S \backslash S_D$, i.e. $\mathbf{p} = \{\mathbf{p}_V \text{ in } V,\ \mathbf{p}_S \text{ on } S_T\}$, and thus

$$\text{(2.7)} \qquad \operatorname{div} \boldsymbol{\sigma} + \mathbf{p}_V = \mathbf{0} \quad \text{in } V, \qquad \boldsymbol{\sigma} \cdot \mathbf{n} = \mathbf{p}_S \quad \text{on } S_D.$$

After the above assumptitions, problem (2.1) can be recast as

$$\text{(2.8)} \qquad \max_{\{\mathbf{p}, \boldsymbol{\sigma}\}} (\mathbf{p}, \dot{\mathbf{u}}) \quad \text{s.t.} \begin{cases} f(\boldsymbol{\sigma}) \leq 0 \text{ in } V \\ \boldsymbol{\sigma} \text{ in equilibrium with } \mathbf{p} \end{cases}$$

where $\dot{\mathbf{u}}$ is an arbitrary fixed field satisfying the boundary condition $\dot{\mathbf{u}} = \mathbf{0}$ on S_D. Problem (2.8) substantially coincides with the aforementioned result of HILL [6] and in fact it provides the *limit load* $\mathbf{p}[\dot{\mathbf{u}}]$ *corresponding to a specified plastic collapse mechanism*, $\dot{\mathbf{u}}$, of the body constrained on S_D. The optional objective value of problem (2.8) equals the overall plastic work developed through the mechanism $\dot{\mathbf{u}}$, i.e.

$$\text{(2.9)} \qquad (\mathbf{p}[\dot{\mathbf{u}}], \dot{\mathbf{u}}) = W[\dot{\mathbf{u}}] := \int_V D(\dot{\boldsymbol{\varepsilon}}^p)\, dV\,,$$

where $\dot{\boldsymbol{\varepsilon}}^p = \dot{\boldsymbol{\varepsilon}}^p(\dot{\mathbf{u}})$. In the load space, the collapse mechanism $\dot{\mathbf{u}}$ is orthogonal to the structure's resistance surface at the corresponding limit load $\mathbf{p}[\dot{\mathbf{u}}]$.

If, additionally, in problem (2.8) some restriction upon the external forces $\mathbf{p}$ is introduced, then $\dot{\mathbf{u}}$ must be suitably relaxed; for instance, if $\mathbf{p} = \alpha \bar{\mathbf{p}}$, where $\bar{\mathbf{p}}$ is a specified external force distribution and the scalar α is arbitrary, one obtains

$$\text{(2.10)} \qquad (\mathbf{p}, \dot{\mathbf{u}}) = \alpha\, (\bar{\mathbf{p}}, \dot{\mathbf{u}})\,.$$

This means that in the maximum plastic work theorem (2.8), the mechanism $\dot{\mathbf{u}}$ needs to be specified only through the scalar parameter a defined as

$$\text{(2.11)} \qquad a := (\bar{\mathbf{p}}, \dot{\mathbf{u}})\,,$$

which represents mechanism's projection in the 'direction' of the specified load $\bar{\mathbf{p}}$. Assuming e.g. $a = 1$, problem (2.8) takes the special form

$$\text{(2.12)} \qquad \alpha_p = \max_{\{\alpha, \boldsymbol{\sigma}\}} \alpha \quad \text{s.t.} \begin{cases} f(\boldsymbol{\sigma}) \leq 0 \text{ in } V \\ \boldsymbol{\sigma} \text{ in equilibrium with } \alpha \bar{\mathbf{p}} \end{cases}$$

and, correspondingly, $W = \alpha_p$. Problem (2.12) is recognized as the well-known static formulation of the plastic collapse safety factor problem. Dualization gives then the related kinematic formulation, i.e.

$$\text{(2.13)} \qquad \alpha_p = \min_{\dot{\mathbf{u}} \in M} W[\dot{\mathbf{u}}] \quad \text{s.t. } (\bar{\mathbf{p}}, \dot{\mathbf{u}}) = 1,$$

where the minimization is performed with respect to the set M of all mechanisms (2.4), and the objective function, given by (2.9), represents the kinematic load multiplier generated by $\dot{\mathbf{u}}$.

The above considerations show that the maximum plastic dissipation theorem can be taken as a starting point to derive the classical results of limit analysis. Following a reasoning similar to that developed above, known results of the shakedown theory will be derived together with a few apparently novel concepts.

3. The inadaptation collapse mechanism

In Sec. 2, the maximum plastic dissipation theorem has been used for the evaluation of the plastic limit load of a structure that undergoes a specified (plastic) collapse mechanism. The key idea consisted in introducing, into the body, a compatible plastic strain rate field, that is, a strain field capable of representing an *instantaneous* collapse mechanism of the structure. In order to apply a similar procedure for evaluating the (shakedown) limit load corresponding to a specified noninstantaneous collapse mechanism, it is necessary to give a precise meaning to the latter sort of mechanisms.

Within the shakedown context, structures are considered to be subjected to (besides, possibly, a permanent (mechanical) load, $\mathbf{p}$) to loads $\mathbf{q}^c$ allowed to vary in a given (closed) domain, say Π^c. Any path within the latter domain represents a potentially active load path, and every load condition is by the hypothesis below the plastic collapse limit value. A closed load path Π^c, repeatedly travelled by the load point, represents a cyclic load, which is potentially dangerous because plastic strain effects may cumulate progressively cycle after cycle until failure. (Among such cyclic loads, most dangerous are the load paths lying on $\partial\Pi^c$. If, as usual, Π^c is a plane, then there is just one most dangerous load path enveloping $\partial\Pi^c$). The failure produced by the cyclic load, referred to as *inadaptation collapse*, exhibits the characteristics that can be specified by explaining the straining process that manifest itself in the course of application of some cyclic load higher than the shakedown limit value. Namely, the structure subjected to a periodic load tends towards (and generally reaches after a few cycles) a steady state in which the response is characterized by stresses $\boldsymbol{\sigma}$ and plastic strain rates, $\dot{\boldsymbol{\varepsilon}}^p$, periodic as the load, such that the ratchet strain, $\Delta\boldsymbol{\varepsilon}^p$, i.e. the net plastic strain accumulated in the steady cycle, is a compatible strain field with zero ratchet displacements, $\Delta\mathbf{u}$, on the constrained boundary of the body (see e.g. [2, 13, 15]).

The above plastic straining process, related to an actual steady cycle, can thus be described by the following equations:

$$\Delta\boldsymbol{\varepsilon}^p(\mathbf{x}) = \nabla^s\Delta\mathbf{u}(\mathbf{x}) \quad \text{in } V, \qquad \Delta\mathbf{u}(\mathbf{x}) = \mathbf{0} \quad \text{on } S_D, \tag{3.1}$$

$$\Delta\boldsymbol{\varepsilon}^p(\mathbf{x}) = \int_0^T \dot{\boldsymbol{\varepsilon}}^p(\mathbf{x}, t)\, dt \tag{3.2}$$

in which (3.1) is like (2.4). Two types of inadaptation collapse modes can be distinguished:

– *Incremental collapse* (or *Ratchetting*), in which the ratchet strain $\Delta\boldsymbol{\varepsilon}^p$ is nonvanishing at least somewhere in the structure, what causes the structure to fail by excessive plastic strain. (It includes, as a special case, the instantaneous plastic collapse by taking $\dot{\boldsymbol{\varepsilon}}^p(\mathbf{x}, t) = \Delta\boldsymbol{\varepsilon}^p(\mathbf{x})\delta_D(t - \bar{t})$, where $\delta_D(t - \bar{t})$ is the Dirac delta centred at time $\bar{t}$.)

– *Alternating plasticity collapse* (or *Plastic shakedown*), in which the ratchet strain $\Delta\boldsymbol{\varepsilon}^p$ is vanishing everywhere in the structure which thus undergoes alternating plasticity with consequent low-cycle fatigue failure.

It is seen that both types of the inadaptation collapse, similarly to the instantaneous plastic collapse, involve a collapse mechanism with its compatible plastic strain field, $\Delta\boldsymbol{\varepsilon}^p$ (though the latter is trivial for alternating plasticity collapse modes). However, in the present case, $\Delta\boldsymbol{\varepsilon}^p$ describes a *noninstantaneous* plastic mechanism because the ratchet strain $\Delta\boldsymbol{\varepsilon}^p$ is the result of cumulating plastic contributions, each occurring at a different time within the strain cycle.

If the applied load is not higher than the (elastic) shakedown limit, no inadaptation collapse mechanism is produced, i.e. the steady-state response is purely elastic and Eqs. (3.1) and (3.2) turn out to be meaningless. However, for load values at the shakedown limit, the structure shakedown limit state can be envisaged, which is characterized by an *impending inadaptation collapse mechanism.* The latter mechanism has the same features as an actual inadaptation collapse mechanism, and thus can be represented as

$$\Delta\mathbf{e}^p(\mathbf{x}) = \nabla^s\mathbf{v}(\mathbf{x}) \quad \text{in } V, \qquad \mathbf{v}(\mathbf{x}) = \mathbf{0} \quad \text{on } S_D, \tag{3.3}$$

$$\Delta\mathbf{e}^p(\mathbf{x}) = \int_0^T \dot{\mathbf{e}}^p(\mathbf{x}, t)\, dt, \tag{3.4}$$

where $\dot{\mathbf{e}}^p(\mathbf{x}, t)$ is some (fictitious) plastic strain rate history. Equations (3.3) and (3.4) can be derived from Eqs. (3.1) and (3.2) by considering the (positive) scalar η measuring the excess value of a load promoting the actual steady cycle (3.1) and (3.2), with respect to the related shakedown limit value. Dividing (3.1) and (3.2) by η and then taking the limit for $\eta \to 0$, one has $\dot{\boldsymbol{\varepsilon}}^p/\eta \to \dot{\mathbf{e}}^p$, $\Delta\boldsymbol{\varepsilon}^p/\eta \to \Delta\mathbf{e}^p$, $\Delta\mathbf{u}/\eta \to \mathbf{v}$, and thus Eqs. (3.3) and (3.4) are generated. In other words, Eqs. (3.3) and (3.4) represent, to within a positive factor, the *incipient* actual inadaptation collapse mechanism produced as soon as the load slightly exceeds the limit value [3, 14, 15].

A (fictitious) plastic strain rate history $\dot{\mathbf{e}}^p$ specified in V for $0 \leq t \leq T$ and satisfying Eqs. (3.3) and (3.4) constitutes a *kinematically admissible plastic strain cycle* after KOITER [9]. It is characterized by two essential ingredients, i.e. the *collapse mechanism* $\{\Delta\mathbf{e}^p, \mathbf{v}\}$ specified by (3.3) and the related *plastic strain path* $\dot{\mathbf{e}}^p$ of (3.4). A field $\mathbf{v}$ satisfying the boundary conditions $\mathbf{v} = \mathbf{0}$ on S_D represents a collapse mechanism in the set M of all possible collapse mechanisms. For a given collapse mechanism $\mathbf{v} \in M$, with related ratchet strain $\Delta\boldsymbol{\varepsilon}^p = \Delta\boldsymbol{\varepsilon}^p(\mathbf{v})$, there is a set, $\Lambda[\Delta\mathbf{e}^p]$ say, of infinite plastic strain paths, $\dot{\mathbf{e}}^p(\mathbf{x}, t)$, all of them satisfying (3.3). For $\Delta\mathbf{e}^p \equiv \mathbf{0}$, the set $\Lambda_0 := \Lambda[\mathbf{0}]$ collects all the cyclic plastic strain paths.

Note that, if the compatible plastic strain cycle of Eqs. (3.3) and (3.4) is applied upon a stress-free strain-free elastic structure as an imposed plastic strain history, the stress and displacement responses, $\boldsymbol{\sigma}^R$ and $\mathbf{u}^R$ say, are such that $\boldsymbol{\sigma}^R(\mathbf{x}, T) = \mathbf{0}$ in V and $\mathbf{u}^R(\mathbf{x}, T) = \mathbf{v}(\mathbf{x})$ in $V \cup S_T$.

4. The shakedown limit load for assigned collapse mechanism

An elastic-perfectly plastic structure is subjected to a combined cyclic/permanent load superposition of a periodic load $\bar{\mathbf{q}}^c(t)$, $0 \leq t \leq T$, and a permanent (mechanical) load $\mathbf{p}$. Let $\mathbf{v} \in M$ be a specified collapse mechanism, and let $\Delta\mathbf{e}^p = \Delta\mathbf{e}^p(\mathbf{v})$ be the related ratchet strain. The following problem is posed: find a cyclic load multiplier, $\beta > 0$, and a permanent (mechanical) load, $\mathbf{p}$, (suitably distributed over $V \cup S_T$) such that the structure subjected to the *combined* load $\mathbf{q}(t) = \mathbf{p} + \beta\,\bar{\mathbf{q}}^c(t)$, $0 \leq t \leq T$, be able to reach a shakedown limit state characterized by an impending inadaptation collapse mechanism complying with the assigned mechanism, $\mathbf{v} \in M$. Later on in this section, the equations governing the above problem will be established and shown to be capable of providing, besides the (shakedown) limit load $\mathbf{q}$ through the unknown pair $\{\mathbf{p}, \beta\}$, also the related plastic strain path $\dot{\mathbf{e}}^p \in \Lambda[\Delta\mathbf{e}^p(\mathbf{v})]$.

In order to solve the above problem, let the maximum plastic dissipation theorem be cast in a time-space integral form as

$$\max_{\boldsymbol{\sigma}} \int_0^T \int_V \boldsymbol{\sigma} : \dot{\boldsymbol{\varepsilon}}^p \, dV \, dt \quad \text{s.t. } f(\boldsymbol{\sigma}) \leq 0 \text{ in } V \times (0, T), \tag{4.1}$$

where $\dot{\boldsymbol{\varepsilon}}^p(\mathbf{x}, t)$, $0 \leq t \leq T$, is a plastic strain-rate history specified in $V \times (0, T)$. In analogy to problem (2.1), it can be stated that problem (4.1) is equivalent to the material plastic flow laws, Eqs. (2.2) and (2.3), enforced everywhere in V and for every t, $0 \leq t \leq T$. Let $\dot{\boldsymbol{\varepsilon}}^p$ be taken as a kinematically admissible plastic strain cycle, say $\dot{\mathbf{e}}^p(\mathbf{x}, t)$, associated with a given collapse mechanism $\mathbf{v} \in M$, that

is $\dot{\mathbf{e}}^p(\mathbf{x}, t)$ satisfies Eq. (3.4) with $\Delta\mathbf{e}^p = \Delta\mathbf{e}^p(\mathbf{v})$, hence $\dot{\mathbf{e}}^p \in \Lambda[\Delta\mathbf{e}^p]$. Also, let the maximization operation of (4.1) be performed within the stress set given by

$$\boldsymbol{\sigma} = \mathbf{s} + \beta\, \bar{\boldsymbol{\sigma}}^c, \tag{4.2}$$

where $\mathbf{s}$ is an unknown time-independent stress field, $\beta > 0$ an unknown scalar, and $\bar{\boldsymbol{\sigma}}^c$ the elastic stress response of the structure to the cyclic load $\bar{\mathbf{q}}^c(t)$. Substituting (4.2) in (4.1) and using Eqs. (3.3) and (3.4), we obtain

$$\int_0^T \int_V \boldsymbol{\sigma} : \dot{\boldsymbol{\varepsilon}}^p \, dV \, dt = \int_V \mathbf{s} : \Delta\mathbf{e}^p \, dV + \beta\, b, \tag{4.3}$$

where $\dot{\boldsymbol{\varepsilon}}^p \equiv \dot{\mathbf{e}}^p$ and b is a scalar parameter defined as

$$b := \int_0^T \int_V \bar{\boldsymbol{\sigma}}^c : \dot{\mathbf{e}}^p \, dV \, dt, \tag{4.4}$$

which represents a measure of the plastic strain path.

It results that, with the above choices for $\dot{\boldsymbol{\varepsilon}}^p$ and $\boldsymbol{\sigma}$, problem (4.1) requires that the kinematically admissible plastic strain cycle, $\dot{\boldsymbol{\varepsilon}}^p = \dot{\mathbf{e}}^p$, should be specified only through the related collapse mechanism $\mathbf{v} \in M$ and (for $\beta > 0$) the scalar parameter b of (4.4); furthermore, ignoring for the moment that β may take zero values for certain $\mathbf{v} \in M$, the maximization operation should be done with respect to the free variables $\mathbf{s}$ and β. In fact, problem (4.1) now reads, with $b = 1$:

$$\psi[\mathbf{v}] := \max_{\{\mathbf{s},\beta\}} \left(\int_V \mathbf{s} : \Delta\mathbf{e}^p(\mathbf{v}) \, dV + \beta \right) \quad \text{s.t. } f(\mathbf{s} + \beta\, \bar{\boldsymbol{\sigma}}^c) \leq 0 \text{ in } V \times (0, T), \tag{4.5}$$

where the condition $b = 1$ amounts to normalizing $\Delta\mathbf{e}^p$ and $\mathbf{v}$. Problem (4.5) is a static formulation of the structure shakedown limit load for a given collapse mechanism, $\mathbf{v} \in M$. The following theorems can be proved.

4.1. Static theorem

For a given structure subjected to combined cyclic/permanent loads, say $\mathbf{q} = \mathbf{p} + \beta\, \bar{\mathbf{q}}^c(t)$, $0 \leq t \leq T$, and for a given mechanism $\mathbf{v} \in M$, the shakedown limit load $\{\hat{\mathbf{p}}, \hat{\beta}\}$ corresponding to the latter mechanism is the load which produces the maximum dissipation through the given mechanism, and thus the stress field $\mathbf{s} = \hat{\mathbf{s}}$, equilibrating $\hat{\mathbf{p}}$ and $\hat{\beta}$, solve problem (4.5); conversely, the solution to

problem (4.5) provides the shakedown limit load, $\{\hat{\mathbf{p}}, \hat{\beta}\}$, corresponding to the given $\mathbf{v} \in M$.

This statement can be proved by investigating the mechanical implications of problem (4.5), which is done by the Lagrange multiplier method. Writing the relevant augmented Lagrangian functional as

$$\chi := -\int_V \mathbf{s} : \Delta\mathbf{e}^p \, dV - \beta + \int_0^T \int_V \dot{l} \, f(\mathbf{s} + \beta \bar{\boldsymbol{\sigma}}^c) \, dV \, dt \tag{4.6}$$

where $\dot{l}(\mathbf{x}, t) \geq 0$ is the Lagrange multiplier, the first variation of χ reads

$$\delta\chi = \delta\beta \left(-1 + \int_0^T \int_V \bar{\boldsymbol{\sigma}}^c : \frac{\partial f}{\partial \boldsymbol{\sigma}} \, \dot{l} \, dV \, dt \right) + \int_V \delta\mathbf{s} : \left(-\mathbf{e}^p + \int_0^T \frac{\partial f}{\partial \boldsymbol{\sigma}} \, \dot{l} \, dt \right) dV + \int_0^T \int_V \delta\dot{l} \, f(\boldsymbol{\sigma}) \, dV \, dt, \tag{4.7}$$

where $\boldsymbol{\sigma} := \mathbf{s} + \beta \, \bar{\boldsymbol{\sigma}}^c$. Since χ must take a minimum with respect to $\mathbf{s}$ and β and a maximum with respect to $\dot{l} \geq 0$, the Euler-Lagrange equations related to (4.5) read as follows:

$$f(\boldsymbol{\sigma}) \leq 0, \quad \dot{l} \geq 0, \quad \dot{l} \, f(\boldsymbol{\sigma}) = 0 \quad \text{in } V \times (0, T), \tag{4.8}$$

$$\boldsymbol{\sigma} := \mathbf{s} + \beta \, \bar{\boldsymbol{\sigma}}^c, \quad \dot{\mathbf{e}}^p := \frac{\partial f}{\partial \boldsymbol{\sigma}} \, \dot{l} \quad \text{in } V \times (0, T), \tag{4.9}$$

$$\int_0^T \dot{\mathbf{e}}^p \, dt = \Delta\mathbf{e}^p(\mathbf{v}) \quad \text{in } V, \qquad \int_0^T \int_V \bar{\boldsymbol{\sigma}}^c : \dot{\mathbf{e}}^p \, dV \, dt = b = 1. \tag{4.10}$$

The following can be remarked in relation to Eqs. (4.8) to (4.10):

a) The Lagrange multiplier $\dot{l}$ takes the meaning of a plastic coefficient for the (fictitious) plastic strain rate $\dot{\mathbf{e}}^p$, Eqs. (4.8) and (4.9).

b) Due to the convexity of problem (4.5), Eqs. (4.8) to (4.10) are not only necessary, but also sufficient conditions, i.e. the/a solution $(\mathbf{s}, \beta, \dot{l})$ to Eqs. (4.8) to (4.10) is such that $\{\mathbf{s}, \beta\}$ solves the problem (4.5).

c) The (fictitious) plastic strain rate history, $\dot{\mathbf{e}}^p(\mathbf{x}, t)$, constitutes a kinematically admissible plastic strain cycle complying with the given collapse mechanism $\mathbf{v} \in M$ and the scalar parameter $b = 1$, Eq. (4.10).

d) Denoting by $\mathbf{s}^E$ the elastic stress response to $\mathbf{p}$ and thus by $\boldsymbol{\sigma}^E = \mathbf{s}^E + \beta\,\bar{\boldsymbol{\sigma}}^c$ the analogous response to the load $\mathbf{q} = \mathbf{p} + \beta\,\bar{\mathbf{q}}^c$, the equality

$$\int_0^T \int_V D(\dot{\mathbf{e}}^p)\,dV\,dt = \int_0^T \int_V \boldsymbol{\sigma}^E : \dot{\mathbf{e}}^p\,dV\,dt \tag{4.11}$$

can be easily shown to hold, which means that the overall plastic work equals the external work and thus, by Koiter's theorem, the load $\mathbf{q}$ cannot be below the shakedown limit. Since, on the other hand, $\mathbf{q}$ cannot exceed this limit by Melan's theorem, it follows that $\mathbf{q}$ is a shakedown limit load and that therefore Eqs. (4.8) to (4.10) describe the related impending inadaptation collapse mechanism.

e) It can be proved that Eqs. (4.8) to (4.10) allow for a unique solution for all except for $\mathbf{s} = \mathbf{s}^E + \boldsymbol{\rho}$, where the selfstress $\boldsymbol{\rho}$ may be indeterminate in the region $V_0 \subset V$ (if any) where the assigned ratchet strain $\Delta\mathbf{e}^p = \mathbf{0}$. The proof rests on Drucker's stability postulate and on the assumption that $f(\boldsymbol{\sigma})$ is smooth, but here it is omitted for brevity.

f) Quite often in practice the load path which Eqs. (4.8) to (4.10) refer to is piecewise linear, i.e. polygonal. In such a case, the load can be regarded as one jumping from a corner to another on the polygonal path, i.e. $\mathbf{q}_{(k)} = \mathbf{p} + \beta\,\mathbf{q}^c_{(k)}$, $(k = 1, 2, ..., m)$, and Eqs. (4.8) to (4.10) can be enforced solely at times $t_{(1)}, t_{(2)}, ..., t_{(m)}$ corresponding to the *basic loads* $\mathbf{q}_{(1)}, \mathbf{q}_{(2)}, ..., \mathbf{q}_{(m)}$, and take a time-discrete form.

g) Considered that for certain $\mathbf{v} \in M$ it may result that $\hat{\beta} = 0$, the constraint $\beta \geq 0$ should be accounted for in problem (4.5), in which case Eqs. (4.8) to (4.10) remain the same as long as $\hat{\beta} > 0$, but the second equation of (4.10) vanishes when $\hat{\beta} = 0$. Since the condition $\hat{\beta} = 0$ occurs when the structure's limit state is (equivalent to) an instantaneous plastic collapse, this condition is as a rule excluded from the discussion.

Following the standard procedures (i.e. maximization of χ of Eq. (4.6) under the constraints (4.8) to (4.10), but the constraint of (4.5) being removed), the following dual problem is obtained:

$$\widetilde{W}[\mathbf{v}] = \min_{\dot{\mathbf{e}}^p} \int_0^T \int_V D(\dot{\mathbf{e}}^p)\,dV\,dt$$

$$\text{s.t.} \int_0^T \dot{\mathbf{e}}^p\,dt = \Delta\mathbf{e}^p(\mathbf{v}) \quad \text{in } V, \qquad \int_0^T \int_V \bar{\boldsymbol{\sigma}}^c : \dot{\mathbf{e}}^p\,dV\,dt = b = 1, \tag{4.12}$$

which contains only kinematic variables and $\mathbf{e}^p(\mathbf{v})$ is still fixed. This problem is the kinematic formulation of the structure's shakedown limit load for the assigned

collapse mechanism, $\mathbf{v} \in M$. It provides the optimal plastic strain path associated with $\Delta\mathbf{e}^p(\mathbf{v})$, as well as the related shakedown limit load $\{\hat{\mathbf{p}}, \hat{\beta}\}$. The following can be stated.

4.2. Kinematic theorem

For a given structure subjected to combined cyclic/permanent loads, say $\mathbf{q} = \mathbf{p} + \beta\,\bar{\mathbf{q}}^c(t)$, $0 \leq t \leq T$, and for a given collapse mechanism, $\mathbf{v} \in M$, the optimal plastic strain path corresponding to the latter mechanism is that one which minimizes the overall plastic dissipation and thus it is the solution to problem (4.12); conversely, the solution to (4.12) provides the optimal plastic strain path related to the given collapse mechanism.

Using again the Lagrangian multiplier method, the relevant augmented functional reads:

$$\chi_1 = \int_0^T \int_V D(\dot{\mathbf{e}}^p)\,dV\,dt + \int_V \mathbf{s} : \left(\Delta\mathbf{e}^p - \int_0^T \dot{\mathbf{e}}^p\,dt\right) dV + \beta\left(1 - \int_0^T \int_V \bar{\boldsymbol{\sigma}}^c : \dot{\mathbf{e}}^p\,dV\,dt\right), \tag{4.13}$$

where $\mathbf{s}$ and β are stress-like and scalar multipliers. With a procedure similar to that used before, it can be easily realized that problem (4.12) is equivalent to problem (4.5) and that the above kinematic theorem holds good, but the proof will be omitted here for brevity.

On comparing problems (4.5) and (4.12) with each other, it is seen that they admit the same *optimal objective functionals*, that is, on considering b as a free parameter,

$$(\hat{\mathbf{p}}, \mathbf{v}) + \hat{\beta}\,b = W[\mathbf{v}, b] := \int_0^T \int_V D(\hat{\dot{\mathbf{e}}}^p)\,dV\,dt \tag{4.14}$$

where $\hat{\mathbf{p}}$ and $\hat{\beta}$ are some functionals of $\mathbf{v}$ and b. For $b = 1$, since $(\hat{\mathbf{p}}, \mathbf{v}) + \hat{\beta} = \psi[\mathbf{v}]$ and $W[\mathbf{v}, 1] = \widetilde{W}[\mathbf{v}]$, it is

$$\psi[\mathbf{v}] = W[\mathbf{v}, 1] = \widetilde{W}[\mathbf{v}]. \tag{4.15}$$

5. The structure's shakedown load boundary

For the purpose of this section, problems (4.5) and (4.12) are considered with the scalar free parameter b such that the pair $\{\mathbf{v}, b\}$ constitutes a collapse

mode, whereas the related shakedown limit load is referred to by the pair $\{\mathbf{p}, \beta\}$, (instead of $\{\hat{\mathbf{p}}, \hat{b}\}$ used in Sec. 4).

Problem (4.5), or (4.12), can be used to generate, for every (noninstantaneous) collapse mode $\{\mathbf{v}, b\}$, the corresponding shakedown limit load $\{\mathbf{p}, \beta\}$. In this way, at least in principle, a surface $F[\mathbf{p}, \beta] = 0$ can be obtained in a suitable load space; if, for instance, $\mathbf{p}$ is a n-parameter load, this surface belongs to an $(n+1)$-dimensional Euclidean space. Solving $F = 0$ with respect to β gives the equation $\beta = \beta_{\text{sh}}[\mathbf{p}]$ which represents the (shakedown) limit value of β (or shakedown safety factor) for the assigned permanent load $\mathbf{p}$.

Let $W[\mathbf{v}, b]$ be the functional resulting as the optimal objective value of problem (4.5) or (4.12), as expressed by (4.14). By assumption this functional exists. The Fréchet derivatives

$$\left.\frac{\partial W}{\partial \mathbf{v}}\right|_{\mathbf{x}} = \begin{cases} \mathbf{p}_V(\mathbf{x}) & \forall\, \mathbf{x} \in V \\ \mathbf{p}_S(\mathbf{x}) & \forall\, \mathbf{x} \in S_T \end{cases}, \qquad \frac{\partial W}{\partial b} = \beta, \tag{5.1}$$

express the sensitivity of $W[\mathbf{v}, b]$ to the changes of $\mathbf{v}$ around $\mathbf{x} \in V \cup S_T$, and with respect to b. Equation (5.1) can be obtained from Eq. (4.6) written at the optimum and by remarking that $-\chi_{\text{opt}} + (\mathbf{p}, \mathbf{v}) = W[\mathbf{v}, b] = [(\mathbf{p}, \mathbf{v}) + \beta\, b]_{\text{opt}}$. Note that $W[\mathbf{v}, b]$ is homogeneous of degree one, i.e. $W[m\mathbf{v}, mb] = mW[\mathbf{v}, b]\ \forall\, m > 0$, as it can be easily proved using Eqs. (4.8) to (4.10).

Let $W^*[\mathbf{p}, \beta]$ be the Legendre transform of $W[\mathbf{v}, b]$, i.e.

$$W^*[\mathbf{p}, \beta] := (\mathbf{p}, \mathbf{v}) + \beta\, b - W[\mathbf{v}, b], \tag{5.2}$$

where $\mathbf{v}$ and b are to be meant as functionals of $\mathbf{p}$ and β obtained from (5.1), such that

$$\left.\frac{\partial W^*}{\partial \mathbf{p}}\right|_{\mathbf{x}} = \mathbf{v}(\mathbf{x}) \quad \forall\, \mathbf{x} \in V \cup S_T, \qquad \frac{\partial W^*}{\partial \beta} = b. \tag{5.3}$$

If $\{\mathbf{p}, \beta\}$ is a shakedown load, by Melan's theorem there exists a stress field $\mathbf{s}$ in equilibrium with $\mathbf{p}$ such that the pair $\{\mathbf{s}, \beta\}$ is a feasible solution to (4.5), which implies that $(\mathbf{p}, \mathbf{v}) + \beta\, b \leq W[\mathbf{v}, b]$, and thus $W^*[\mathbf{p}, \beta] \leq 0$ by (5.2); but $W^*[\mathbf{p}, \beta] = 0$ if $\{\mathbf{s}, \beta\}$ solves (4.5), i.e. if $\{\mathbf{p}, \beta\}$ is a shakedown limit load, provided the collapse mode is not a trivial one. On the other hand, if $\mathbf{v} \equiv \mathbf{0}$ and $b = 0$, it is $W^* = 0$. It follows that the boundary of the shakedown load domain can be represented as a set of points $\{\mathbf{p}, \beta\}$ such that $W^* = \mu\, F[\mathbf{p}, \beta] = 0$, where $\mu \geq 0$ is a scalar. By Eq. (5.3) one then obtains

$$\mathbf{v}(\mathbf{x}) = \mu \left.\frac{\partial F}{\partial \mathbf{p}}\right|_{\mathbf{x}} \quad \forall\, \mathbf{x} \in V \cup S_T, \qquad b = \mu \frac{\partial F}{\partial \beta}, \tag{5.4}$$

where $\mu > 0$ is indeterminate if $F = 0$, but $\mu = 0$ if $F < 0$, i.e. if the load $\{\mathbf{p}, \beta\}$ is below the shakedown limit value.

The above result means that the surface $F[\mathbf{p}, \beta] = 0$ is the boundary of the (convex) shakedown load domain and plays the role of yield surface for the structure, in the sense that for any load $\{\mathbf{p}, \beta\}$ such that $F[\mathbf{p}, \beta] < 0$, hence $\mu = 0$, no inadaptation collapse mechanism is produced and thus the shakedown limit state is elastic (i.e. shakedown occurs), whereas if $F[\mathbf{p}, \beta] = 0$, there is a nonvanishing inadaptation collapse mechanism $\{\mathbf{v}, b\}$, given by (5.4) with $\mu > 0$, which thus lies on the external normal to this surface at point $\{\mathbf{p}, \beta\}$, Fig. 1.

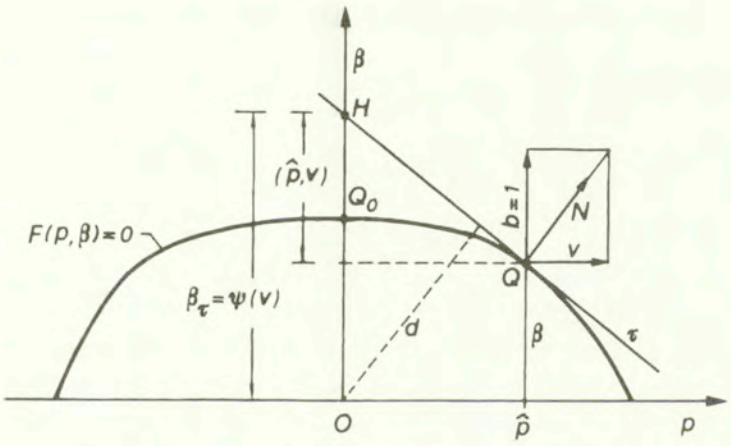

FIG. 1. Geometrical sketch representing the shakedown load boundary $F(p, \beta) = 0$ (or $\beta = \beta_{sh}(p)$ for a one-dimensional permanent load p with an arbitrarily fixed collapse mechanism $\{v, b = 1\}$ and related tangent plane τ.

If $\mathbf{p}$ is a n-parameter load, i.e. $\mathbf{p} = \alpha_1 \bar{\mathbf{p}}_1 + \alpha_2 \bar{\mathbf{p}}_2 + ... + \alpha_n \bar{\mathbf{p}}_n$, the shakedown boundary surface has the form $F(\alpha_1, \alpha_2, ..., \alpha_n, \beta) = 0$ and belongs to an $(n+1)$-dimensional Euclidean space. This case was discussed in [3] with results analogous to those previously expounded. In Fig. 1 the case $n = 1$ is sketched.

It is worth to note that the classical Melan's and Koiter's shakedown theorems play the role of, respectively, static and kinematic criteria in order to assess whether a given combined load $\{\mathbf{p}^*, \beta^*\}$ is within or outside the shakedown load boundary. To show this point, let $\{\mathbf{p}^*, \beta^*\}$ be a shakedown load, i.e. $F(\mathbf{p}^*, \beta^*) \leq 0$. As the pair $\{\mathbf{p}^*, \beta^*\}$ is a feasible solution to (4.5) for any $\mathbf{v}$, one can write the inequality

$$(\mathbf{p} - \mathbf{p}^*, \mathbf{v}) + (\beta - \beta^*)\, b \geq 0 \tag{5.5}$$

where $(\mathbf{p}, \mathbf{v}) + \beta b = W[\mathbf{v}, b]$ is the optimal objective functional of (4.5), as specified by (4.14). Equation (5.5) holds for any load $\{\mathbf{p}^*, \beta^*\}$ such that $F(\mathbf{p}^*, \beta^*) \leq 0$, with $\{\mathbf{v}, b\}$ being any fixed collapse mode, and $\{\mathbf{p}, \beta\}$ the corresponding shakedown limit load. Equation (5.5) is like the Drucker's stability postulate for a (fictitious) material endowed with a yield function $F(\mathbf{p}, \beta) \leq 0$.

By Melan's theorem, a load $\{\mathbf{p}^*, \beta^*\}$ for which there exist some $\mathbf{s}^*$, equilibrating $\mathbf{p}^*$, such that $f(\mathbf{s}^* + \beta^* \bar{\boldsymbol{\sigma}}^c) \leq 0$ in $V \times (0,T)$, either is a safe shakedown load and thus $F(\mathbf{p}^*, \beta^*) < 0$, or makes the structure capable of reaching a shakedown limit state, in which case $F(\mathbf{p}^*, \beta^*) = 0$; otherwise, if such a stress $\mathbf{s}^*$ cannot be found, the load exceeds the shakedown limit, i.e. $F(\mathbf{p}^*, \beta^*) > 0$. By Koiter's theorem, a load $\{\mathbf{p}^*, \beta^*\}$ is a shakedown load, i.e. $F(\mathbf{p}^*, \beta^*) \leq 0$, if inequality (5.5) is satisfied for any $\{\mathbf{v}, b\}$, that is if

$$(\mathbf{p}, \mathbf{v}) + \beta\, b \geq (\mathbf{p}^*, \mathbf{v}) + \beta^* b \tag{5.6}$$

hence, by Eq. (4.14), if

$$\int_0^T \int_V D(\dot{\mathbf{e}}^p)\, dV\, dt \geq \int_V \mathbf{p}^* \cdot \mathbf{v}\, dV + \beta^* \int_0^T \int_V \bar{\boldsymbol{\sigma}}^c : \dot{\mathbf{e}}^p\, dV\, dt; \tag{5.6}'$$

otherwise, if (5.5) is violated for some $\{\mathbf{v}, b\}$, the load $\{\mathbf{p}^*, \beta^*\}$ exceeds the shakedown boundary, i.e. $F(\mathbf{p}^*, \beta^*) > 0$.

Let the collapse mode $\{\mathbf{v}, b\}$ be given and let τ be the plane tangent to the shakedown boundary surface $F[\mathbf{p}, \beta] = 0$ at the point $\{\hat{\mathbf{p}}, \hat{\beta}\}$, ($Q$ in Fig. 1), from where the collapse mechanism $\{\mathbf{v}, b\}$ departs along the (unit) external normal, $\mathbf{N}$. The distance d of τ from the origin O, that is $d = \overrightarrow{OQ} \cdot \mathbf{N}$, using (4.14) can be expressed as

$$d = \frac{1}{K} \left[(\hat{\mathbf{p}}, \mathbf{v}) + \hat{\beta}\, b \right] = \frac{1}{K} W[\mathbf{v}, b] \tag{5.7}$$

where $K := \left((\mathbf{v}, \mathbf{v}) + b^2 \right)^{1/2}$. This means that d is proportional to the common optimal objective value of problems (4.5) and (4.12). Then, the abscissa of the intersection point, H, of τ with the β axis, i.e. $\beta_\tau = \overline{OH}$, is given by

$$\beta_\tau = \frac{d}{b/K} = \frac{1}{b} W[\mathbf{v}, b], \tag{5.8}$$

which for $b = 1$ reads

$$\beta_\tau = W[\mathbf{v}, 1] = \psi[\mathbf{v}]. \tag{5.9}$$

In other words, taking $b = 1$, the common optimal objective value of problems (4.5) and (4.12), $\psi[\mathbf{v}]$, equals the abscissa β_τ of point H on the β axis, Fig. 1. Moreover, $\psi[\mathbf{v}]$ is an upper bound to the shakedown safety factor, β_{sh0}, of the structure for zero permanet load, that is

$$\beta_{sh0} \leq \psi[\mathbf{v}] \quad \forall\, \mathbf{v} \in M \tag{5.10}$$

and thus

$$\beta_{sh0} = \min_{\mathbf{v}\in M} \psi[\mathbf{v}]. \tag{5.11}$$

The latter equation means that, on changing $\mathbf{v}$ in all possible ways, the plane τ changes correspondingly untill H coincides with Q_0, the latter being the intersection point of the surface $F[\mathbf{p}, b] = 0$ with the β-axis, (see Fig. 1).

6. The shakedown safety factor for combined cyclic/permanent loads

Coming back to Eq. (4.1), let the maximization operation be still performed within the stress set (4.2), but $\mathbf{s}$ being in equilibrium with a fixed permanent load, $\mathbf{p}$ say. Such a choice gives

$$\int_0^T \int_V \boldsymbol{\sigma} : \dot{\mathbf{e}}^p \, dV \, dt = \int_V \mathbf{s} : \Delta \mathbf{e}^p \, dV + \beta \, b = (\mathbf{p}, \mathbf{v}) + \beta \, b \tag{6.1}$$

where b is still given by (4.4). Since the internal product $(\mathbf{p}, \mathbf{v})$ is constant with respect to the maximum operation to be performed, Eq. (6.1) shows that the kinematically admissible plastic strain, $\dot{\mathbf{e}}^p$, must now be fixed only through the scalar parameter b. Thus, taking $b = 1$, problem (4.1), and problem (4.5) as well, become:

$$\max_{\{\mathbf{s},\beta\}} \beta \quad \text{s.t.} \quad \begin{cases} f(\mathbf{s} + \beta \, \bar{\boldsymbol{\sigma}}^c) \leq 0 \ \text{ in } \ V \times (0, T) \\ \mathbf{s} \text{ in equilibrium with } \mathbf{p}, \end{cases} \tag{6.2}$$

while its dual reads

$$\begin{aligned} &\min_{\{\dot{\mathbf{e}}^p, \mathbf{v}\}} \left(\int_0^T \int_V D(\dot{\mathbf{e}}^p) \, dV \, dt - (\mathbf{p}, \mathbf{v}) \right) \\ &\text{s.t.} \quad \int_0^T \dot{\mathbf{e}}^p \, dt = \nabla^s \mathbf{v} \text{ in } V, \qquad \mathbf{v} = \mathbf{0} \text{ on } S_D \\ &\int_0^T \int_V \bar{\boldsymbol{\sigma}}^c : \dot{\mathbf{e}}^p \, dV \, dt = b = 1. \end{aligned} \tag{6.3}$$

Problems (6.2) and (6.3) are recognized as the classic continuum static and kinematic formulations of the shakedown safety factor problem for a structure subjected to combined loads $\mathbf{q} = \mathbf{p} + \beta \, \bar{\mathbf{q}}^c(t)$, their common optimal objective value, $\beta_{\mathrm{sh}}[\mathbf{p}]$, being the shakedown safety factor in question. Therefore, it results that the maximum plastic dissipation theorem, suitably applied, enables

the derivation of the static and kinematic approaches to the shakedown limit load.

The shakedown boundary surface, $F(\mathbf{p}, \beta) = 0$, is again considered (Fig. 2), with the tangent plane τ at point $\hat{Q}$ where the given inadaptation mechanism $\{\mathbf{v}, b\}$ departs along the external normal $\mathbf{N}$. Let P be the point representing the permanent load $\mathbf{p}$, R the intersection point of τ with the straight line drawn from P parallel to the β axis, and R_0 the projection of R on the β axis; also, let Q be the intersection point of the shakedown boundary surface with the straight line PR. Obviously, it is $\overline{PQ} = \beta_{\text{sh}}[\mathbf{p}]$ = shakedown safety factor for the assigned permanent load, $\mathbf{p}$. The segment PR, spanned by τ over the axis parallel to the β axis through P, has length $\overline{PR} = \overline{OH} - \overline{R_0 H}$ which is a functional of $\{\mathbf{v}, b\}$ which , for $b = 1$, is found to read:

$$\overline{PR} = \beta_{\text{mix}}[\mathbf{p}, \mathbf{v}] := \psi[\mathbf{v}] - (\mathbf{p}, \mathbf{v}). \tag{6.4}$$

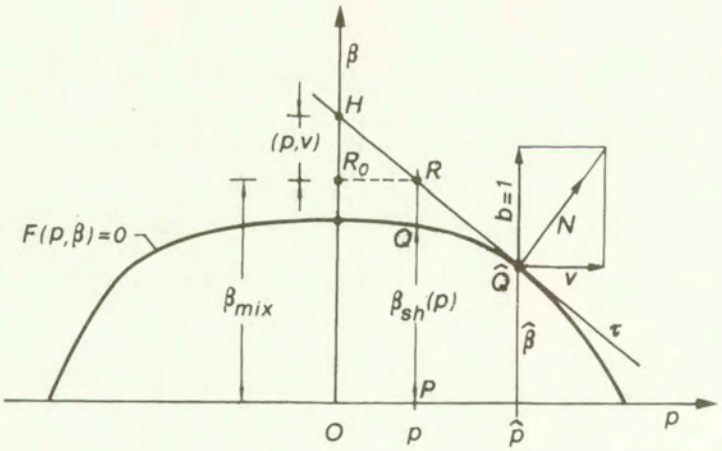

FIG. 2. Geometrical sketch representing the shakedown load boundary: for a given mechanism $\{v, b = 1\}$, the segment $\overline{PR} = \beta_{\text{mix}}$ spanned over a straight, $p = \text{const}$ by the tangent plane τ is an upper bound to $\beta_{sh}(p)$.

In virtue of the convexity of $F = 0$, it is geometrically clear that

$$\beta_{\text{sh}}[\mathbf{p}] \leq \beta_{\text{mix}}[\mathbf{p}, \mathbf{v}] \quad \forall \mathbf{v} \in M. \tag{6.5}$$

This inequality shows that $\beta_{\text{mix}}[\mathbf{p}, \mathbf{v}]$ is an *upper bound* (u.b.) to $\beta_{\text{sh}}[\mathbf{p}]$. This upper bound will be referred to as *mixed* u.b. because $\psi[\mathbf{v}]$ on the right-hand side of (6.4) can be computed either via the static approach (4.5), or via the kinematic approach (4.12). $\beta_{\text{mix}}[\mathbf{p}, \mathbf{v}]$ turns out to be *more stringent* than the classical kinematic u.b., say β_{kin}. In fact, denoting by $\dot{\mathbf{e}}^p(\mathbf{v})$ an arbitrary plastic

strain rate cycle complying with $\mathbf{v} \in M$, one can write:

$$\beta_{\text{kin}}[\mathbf{p}, \dot{\mathbf{e}}^p(\mathbf{v})] = \int_0^T \int_V D\left(\dot{\mathbf{e}}^p(\mathbf{v})\right)\, dV\, dt - (\mathbf{p}, \mathbf{v}) \tag{6.6}$$

and thus, remembering (4.12) and (6.4),

$$\beta_{\text{mix}}[\mathbf{p}, \mathbf{v}] = \min_{\{\dot{\mathbf{e}}^p \in \Lambda(\Delta \mathbf{e}^p(\mathbf{v}))\}} \beta_{\text{kin}}\left[\mathbf{p}, \dot{\mathbf{e}}^p\right]. \tag{6.7}$$

Another formulation of the shakedown safety factor, alternative to (6.2) and (6.3) can be derived as follows. Let the minimization operation of (6.3) be performed by operating first on $\dot{\mathbf{e}}^p$ while taking $\mathbf{v}$ fixed, then by operating on $\mathbf{v}$. In this way, remembering (6.6), problem (6.3) takes the form:

$$\beta_{\text{sh}}[\mathbf{p}] = \min_{\mathbf{v} \in M} \quad \min_{\{\dot{\mathbf{e}}^p \in \Lambda(\Delta \mathbf{e}^p(\mathbf{v}))\}} \beta_{\text{kin}}\left[\mathbf{p}, \dot{\mathbf{e}}^p\right], \tag{6.8}$$

which constitutes a *two-stage kinematic* formulation of the shakedown safety factor. By (6.7), one also can write

$$\beta_{\text{sh}}[\mathbf{p}] = \min_{\mathbf{v} \in M} \beta_{\text{mix}}\left[\mathbf{p}, \mathbf{v}\right], \tag{6.9}$$

which means that structure's shakedown safety factor is the smallest mixed upper bound in the set of all collapse mechanisms, $\mathbf{v} \in M$. The geometric interpretation of (6.9) is quite clear after Fig. 2; namely, changing $\mathbf{v}$ in all possible ways causes τ to change correspondingly until point $R \in \tau$, with fixed abscissa $\mathbf{p}$, coincides with Q on the surface $F = 0$. (Note that, due to the convexity of $F = 0$, point R is external to, or lies on, the surface $F = 0$.)

Another alternative formulation to problems (6.2) and (6.3) is obtained by making use of problem (4.5) to express $\beta_{\text{mix}}[\mathbf{p}, \mathbf{v}]$. According to (4.15) and (6.4), one can write

$$\beta_{\text{sh}}[\mathbf{p}] = \min_{\mathbf{v} \in M} \left\{ \left[\max_{\{\mathbf{s}, \beta\}} \left(\int_V \mathbf{s} : \Delta \mathbf{e}^p(\mathbf{v}) dV + \beta \right) \right.\right. \tag{6.10}$$

$$\left.\left. \text{s.t. } f(\mathbf{s} + \beta \bar{\boldsymbol{\sigma}}^c) \leq 0 \ \text{ in } \ V \times (0, T) \right] - (\mathbf{p}, \mathbf{v}) \right\}$$

what represents a *mixed static-kinematic* formulation of the shakedown safety factor. Such a mixed formulation is rather novel within the shakedown theory. To authors' knowledge, formulations like (6.10) have only recently been proposed in [1, 17, 18].

Note that, if in (6.10) the stress $\mathbf{s}$ is assumed to be in equilibrium with $\mathbf{p}$, problem (6.10) transforms into (6.2).

7. Application

In this section problem (4.5) is solved for a two-bar structure under thermal cyclic load. The aim is to illustrate the way the related shakedown load boundary can be derived starting from collapse modes instead of loading modes.

Two (parallel) bars of equal length L and cross-sections $\Omega_1 = \Omega$, $\Omega_2 = \gamma\Omega$ ($\gamma > 1$) are connected with a rigid block, Fig. 3(a). Bar 2 is maintained at a constant temperature, $T_2 = T_0$, and bar 1 undergoes cyclic temperature variations, i.e. $T_1 = T_0 - \theta\, z(t)$, $0 \leq z(t) \leq 1$, $\theta > 0$, Fig. 3(b).

An external permanent load $p = \alpha\bar{p}$ is applied upon the rigid block, with $\alpha \geq 0$ and $\bar{p} = (1+\gamma)\,\Omega\,\sigma_y$ = plastic limit load, σ_y being the material yield stress. Denoting by s_1 and s_2 the bars' stresses equilibrating p, it is $(s_1 + \gamma s_2)\,\Omega = \alpha\bar{p}$, hence

$$\alpha = (s_1 + \gamma s_2)/(1+\gamma)\sigma_y. \tag{7.1}$$

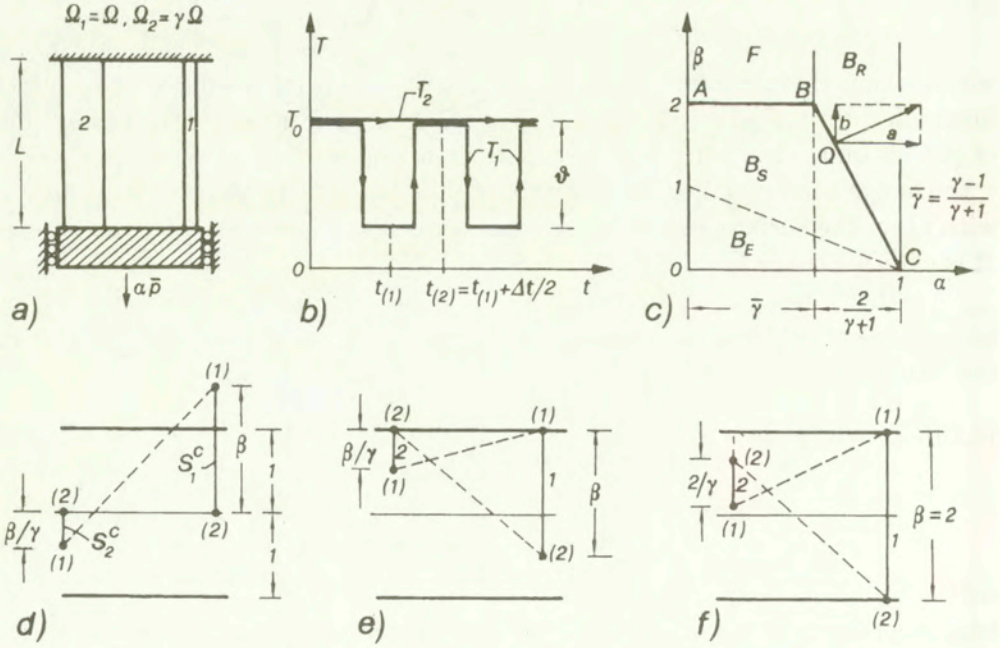

FIG. 3. Two-bar structure subjected to cyclic temperature changes and permament mechanical load: a) Geometrical configuration; b) Bar temperature histories; c) Interaction diagram; d) Elastic stress paths; e) and f) Typical locations of stress paths at the shakedown limit.

The thermo-elastic stresses are: $\sigma_1^c = \sigma_T z(t)$, $\sigma_2^c = -\sigma_1^c/\gamma$, where $\sigma_T := \gamma \alpha_T E \theta(1+\gamma) =$ max thermo-elastic stress, $\alpha_T =$ thermal expansion coefficient and $E =$ Young's modulus. On setting $\beta := \sigma_T/\sigma_y$, the stress paths S_1^c and S_2^c of bars 1 and 2 are located as shown in Fig. 3(d), and the elastic stresses at times $t_{(1)}$ (at which maximum temperature reduction in bar 1 occurs, hence $z(t_{(1)}) = 1$) and $t_{(2)}$ (at which temperature T_0 occurs in bar 1, hence $z(t_{(2)}) = 0$) are: $\sigma_{1(1)}^c = \beta\sigma_y$, $\sigma_{2(1)}^c = -\beta\sigma_y/\gamma$, $\sigma_{1(2)}^c = \sigma_{2(2)}^c = 0$.

The interaction diagram of the system under study is the diagram of the (α, β) plane shown in Fig. 3(c), with the bilateral line ABC being the shakedown load boundary with equations as: $\beta = 2$ for $0 \leq \alpha \leq \bar{\gamma}$, where $\bar{\gamma} := (\gamma-1)/(\gamma+1)$, and $\beta = (1+\gamma)(1-\alpha)$ for $\bar{\gamma} \leq \alpha \leq 1$, (see [3] for more details).

Let v denote the ratchet displacement of the block, and Δe_1^p, Δe_2^p the bars' ratchet strains; obviously, $\Delta e_1^p = \Delta e_2^p = v/L$. Problem (4.5) takes the form ($b = 1$):

$$\max_{\{s_1, s_2, \beta\}} \Phi := (s_1 + \gamma s_2)\, \Omega v + \beta, \tag{7.2}$$

subject to $\beta \geq 0$, as well as to:

$$\begin{aligned} f_1^+ &= s_1 + \beta\sigma_y - \sigma_y \leq 0, \\ f_1^- &= -s_1 - \sigma_y \leq 0, \\ f_2^+ &= s_2 - \sigma_y \leq 0, \\ f_2^- &= -s_2 + \beta\gamma^{-1}\sigma_y - \sigma_y \leq 0. \end{aligned} \tag{7.2$'$}$$

Here, the sign constraint $\beta \geq 0$ has been introduced in order for the analysis to include also the instantaneous plastic collapse mode.

For a fixed $v > 0$ (incremental collapse mode), the maximum is reached when s_1, s_2 and β are such that the elastic stress paths in the bars assume the positions shown in Fig. 3(e), with $f_1^+ = f_2^- = 0$. Thus, by $(7.2)'_{1-4}$ it follows:

$$s_1 = \sigma_y(1-\beta), \quad s_2 = \sigma_y, \tag{7.3}$$

$$\beta \leq 2, \quad \beta \leq 2\gamma. \tag{7.4}$$

Since $\beta \geq 0$ and $\gamma > 1$, the second inequality of (7.4) is certainly satisfied if $\beta \leq 2$, and can thus be disregarded. Using (7.3), problem (7.2) transforms to

$$\psi(a) = \max_{\beta \geq 0} \Phi_1(\beta) = a + \left(1 - \frac{a}{1+\gamma}\right)\beta \quad \text{s.t. } \beta \leq 2, \tag{7.5}$$

where $a := \bar{p}v$. Transforming (7.5) into an unconstrained problem, one can write

$$\min_{\beta \geq 0} \max_{\zeta \geq 0} = \Phi_2(\beta, \zeta) := -a + \left(\frac{a}{1+\gamma} - 1\right)\beta + \zeta(\beta - 2) \tag{7.6}$$

under only sign constraints. The Kuhn-Tucker conditions of (7.6) read

$$\frac{a}{1+\gamma} - 1 + \zeta \geq 0, \quad \beta \geq 0, \quad \beta\left(\frac{a}{1+\gamma} - 1 + \zeta\right) = 0, \tag{7.7}$$

$$\beta - 2 \leq 0, \quad \zeta \geq 0, \quad \zeta(\beta - 2) = 0. \tag{7.8}$$

The following three typical situations can be envisaged:

$$\begin{aligned} &\text{i)} && a > \gamma + 1: \quad \zeta = 0, \quad \beta = 0, \quad \alpha = 1, \quad \psi(a) = a, \\ &\text{ii)} && a = \gamma + 1: \quad \zeta = 0, \quad 0 < \beta < 2, \quad \alpha = 1 - \tfrac{\beta}{\gamma+1}, \quad \psi(a) = a, \\ &\text{iii)} && a < \gamma + 1: \quad \zeta > 0, \quad \beta = 2, \quad \alpha = \bar{\gamma}, \quad \psi(a) = 2 + \bar{\gamma} a. \end{aligned} \tag{7.9}$$

A fourth typical situation is generated for $v = 0$ (alternating plasticity collapse mode), hence $a = 0$ and $\Delta\varepsilon_1^p = \Delta\varepsilon_2^p = 0$. The maximum in (7.2) is then realized when the stress state is as that described in Fig. 3(f) with $f_1^+ = f_1^- = 0$. Thus, by $(7.2)'_{1-4}$, one has $\beta = 2$, hence $\psi(0) = 2$, and

$$s_1 = -\sigma_y, \quad \left(2\gamma^{-1} - 1\right)\sigma_y \leq s_2 \leq \sigma_y. \tag{7.10}$$

As $\alpha \geq 0$, by (7.1) and the first equation of (7.10), one has $s_2 \geq \gamma^{-1}\sigma_y$. Thus, as $2\gamma^{-1} - 1 < \gamma^{-1}$, the continued inequality in (7.10) can be rewritten as

$$\gamma^{-1}\sigma_y \leq s_2 \leq \sigma_y, \tag{7.11}$$

having in this way enforced its lower bound. Then, solving (7.1) for α and substituting in (7.11) gives

$$0 \leq \alpha \leq \bar{\gamma}. \tag{7.12}$$

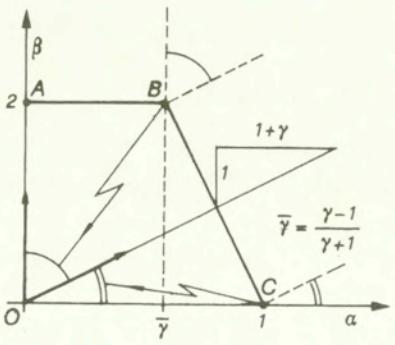

FIG. 4. Geometrical sketch representing the correspondence between collapse mechanism (v, b) and points on the shakedown load boundary curve ABC.

In the preceding considerations, the parameter $a = \bar{p}v$ has been used to generate the collapse mechanisms $v \geq 0$. The correspondence between the a values and the related limit loads is depicted in Fig. 4, where the limit load locus, ABC, is recognized to coincide with the shakedown boundary of Fig. 3(c), as expected.

8. Resumé comments and conclusions

In this paper, the maximum plastic dissipation theorem, suitably written in a time-space integral form, has been used as analytical tool to approach the shakedown theory. This enabled us not only to find the classical results of the shakedown theory, but also to derive some apparently novel concepts within this theory, such as the shakedown limit load associated with an assigned (noninstantaneous) collapse mode, the mixed upper bound to the shakedown safety factor, and the mixed static-kinematic formulation of the shakedown safety factor problem.

The shakedown limit load for the assigned collapse mode is intended as the particular combination of cyclic/permanent load under which the given structure can reach the shakedown limit state characterized by an inadaptation collapse mechanism complying with the assigned collapse mode. Dual static and kinematic problem formulations have been given to evaluate such a load. On changing the given collapse mode in all possible ways, these problem formulations can be used to determine the shakedown load boundary surface in the load space.

As already pointed out in [3], where n-dimensional permanent loads were considered, the shakedown load boundary plays the role of a yield function for the structure, in the sense that the (noninstantaneous) collapse mechanism characterizing the shakedown limit state to which the structure may report itself, obeys a plasticity flow law similar to that obeyed by the plastic strain rate tensor for the material. That is, the shakedown limit load associated with a given (noninstantaneous) collapse mechanism is that load on the shakedown load boundary surface, from where this mechanism departs along the external normal to that surface. The latter geometrical property is a generalization to the shakedown of an analogous property of plastic limit analysis, in which the (instantaneous) collapse mechanism lies on the external normal to the load resistance surface; indeed, in the absence of cyclic load, shakedown degenerates into limit plasticity and the noninstantaneous collapse modes into instantaneous collapse ones.

Another interesting property of the shakedown load boundary surface is that the tangent plane, orthogonal to the assigned collapse mode, intersects the axis drawn from a fixed point on the permanent load hyperplane, parallel to the cyclic load multiplier axis, at a point whose distance from the permanent load hyper-

plane constitutes a mixed upper bound to the shakedown safety factor for the structure under combined loads, i.e. superposition of cyclic loads with that fixed permanent load. This mixed upper bound, which can be computed by static, or kinematic, procedures (and for this reason it is called 'mixed'), is more stringent than the classical kinematic upper bound, since in fact it can be obtained by minimizing the latter kinematic upper bound with respect to the set of plastic strain paths complying with the given collapse mode. The above tangent plane intersects the cyclic load multiplier axis at a point whose distance from the origin equals the common optimal objective value of the two problems, afore-mentioned, dual to each other and related to the shakedown limit load for assigned collpase mode.

The shakedown safety factor can be obtained by minimizing the mixed upper bound with respect to the set of collapse modes. This gives two possible computational procedures, both being alternative to the classical static or kinematic procedures, according to whether the mixed upper bound is obtained via static or kinematic procedure. In the latter case, a two-stage kinematic formulation is obtained for the shakedown safety factor, whereas in the former case a mixed static-kinematic formulation is obtained. A notable feature of the latter formulation is that, contrary to the classical static formulation, it makes use of free stress variables and compatibility equations, and thus the equilibrium equations – which in general cause some computational problems in the shakedown analysis – are not needed. For this reason, a mixed formulation like the one given above, is expected to be suitable for numerical shakedown analysis by the finite element method. Mixed formulations for the shakedown safety factor have started to appear in the literature [1, 17, 18] only recently; they have not been fully exploited yet and deserve further investigation. This is being done in the present research work devoted to a better understanding of the matter, as well as to the application methods with their computer implementation. Methods suggested by MRÓZ and collaborators [16] may be helpful to this purpose.

References

1. G. BORINO, F. PARRINELLO and C. POLIZZOTTO, *Shakedown analysis for incremental collapse*, [In:] Proc. Euromech Colloquium 385 'Inelastic Analysis of Structures under Variable Loads: Theory and Engineering Application', Aachen, Germany, 11–15, Sept. 8–11, 1998.

2. C. O. FREDERICK and P. J. ARMSTRONG, *Convergent internal stresses and steady cyclic state of stress*, J. Strain Analysis, **1**, 154–162, 1966.

3. P. FUSCHI and C. POLIZZOTTO, *The shakedown load boundary of an elastic perfectly plastic structure*, Meccanica, **30**, 155–174, 1995.

4. D. A. GOKHFELD and D. F. CHERNIAVSKY, *Limit Analysis of Structures at Thermal Cycling*, Sijthoff & Noordhoff, Alphen aan der Rijn, The Netherlands 1980.

5. B. HALPHEN, *Accomodation et adaptation des structures élasto-visco-plastiques et plastiques*, [In:] Matériaux et Structures sous Chargement Cyclique, Association Amicale des Ingenieurs Anciens Elèves de E.N.P.C., 203–229, Paris 1979.

6. R. HILL, *A variational principle of maximum plastic work in classical plasticity*, Quat. Jour. Mech. Appl. Math., **1**, 18–28, 1948.

7. R. HILL, *Mathematical Theory of Plasticity*, Oxford University Press, Oxford 1950.

8. L. M. KACHANOV, *Fundamentals of the Theory of Plasticity*, MIR Publishers, Moscow 1974.

9. W. T. KOITER, *General theorems of elastic-plastic solids*, S. SNEDDON, and R. HILL [Eds.], Progress in Solid Mechanics, **1**, 167–221, North Holland, Amsterdam 1960.

10. J. A. KÖNIG, *Shakedown of elastic-plastic structures*, PWN-Polish Scientific Publishers, Warsaw and Elsevier, Amsterdam 1987.

11. J. LUBLINER, *Plasticity Theory*, McMillan Publishing Co, New York 1990.

12. J. B. MARTIN, *Plasticity: Fundamentals and General Results*, The MIT Press, Cambridge, Ma. 1975.

13. Z. MRÓZ, *On the theory of steady plastic cycles in structures*, [In:] Proc. of SMIRT Conf. 1, 6 part L, 489–501, 1972.

14. T. PANZECA and C. POLIZZOTTO, *On shakedown of elastic plastic solids*, Meccanica, **23**, 94–101, 1988.

15. C. POLIZZOTTO, *Steady states and sensitivity analysis in elastic-plastic structures subjected to cyclic loads*, Int. J. Solids Struct., **31**, 953–970, 1994.

16. S. PYCKO and Z. MRÓZ, *Alternative approach to shakedown as a solution of a min-max problem*, Acta Mech., **93**, 205–222, 1992.

17. J. L. L. SILVEIRA and N. ZOUAIN, *On extremum principles and algorithms for shakedown analysis*, Eur. J. Mech. A/Solids, **16**, 753–778, 1997.

18. N. ZOUAIN and J. L. L. SILVEIRA, *Extremum principles for bounds to shakedown loads*, Eur. J. Mech. A/Solids, **18**, 879–901, 1999.

Received February 29, 2000.

Arch. Mech., **52**, 4–5, pp. 737–759, Warszawa 2000

A qualitative approach to Hooke's tensors. Part I

To Zenek Mróz

J. RYCHLEWSKI

Polish Academy of Sciences
Institute of Fundamental Technological Research
Świętokrzyska 21, 00-049 Warszawa, Poland

University of Warmia and Mazury in Olsztyn

THE MAIN QUALITATIVE PROPERTIES of Hooke's tensors can be found in their invariant decompositions, both linear and nonlinear. The invariant nonlinear spectral decompositions are presented in the review [7] and the papers quoted therein. This paper deals with linear invariant decompositions initiated in [12] – [20]. A straightforward and complete description of all such possible decompositions is presented here in Part I. The main results are given in formulae (7.1), (7.3). The next part (to appear), Part II, will contain derivations, conclusions and unexpected applications.

1. Introduction

1.1. In this paper we will call *Hooke's tensor* any Euclidean tensor of the fourth order $\mathbf{H}$ which realises a symmetric linear transfromation of the space of symmetric second order tensors $\mathcal{S}$ into itself, or quite the same, which realises a quadratic form on $\mathcal{S}$,

$$\xi \to \mathbf{H} \cdot \xi \qquad \xi \to \xi \cdot \mathbf{H} \cdot \xi. \tag{1.1}$$

It is convenient to identify *the space of all Hooke's tensors* $\mathcal{H}$ with symetrized tensorial square of space $\mathcal{S}$

$$\mathcal{H} = \operatorname{sym} \mathcal{S} \bigotimes \mathcal{S}. \tag{1.2}$$

1.2. The importance of Hooke's tensors in many applications cannot be overestimated. They are, primarily, the starting point of the linear theory of elasticity, which is still, for many essential areas of science and technology, the most important part of solid state mechanics. This starting point are elasticity tensors: the *stiffness tensor* $\mathbf{S}$ and the *compliance tensor* $\mathbf{C}$ of Hooke's law

$$\sigma = \mathbf{S} \cdot \varepsilon, \quad \varepsilon = \mathbf{C} \cdot \sigma, \quad \mathbf{S} \circ \mathbf{C} = \mathbf{C} \circ \mathbf{S} = \mathbb{I}_{\mathcal{S}} \tag{1.3}$$

Quadratic forms

$$e(\varepsilon) \equiv \varepsilon \cdot \mathbf{S} \cdot \varepsilon, \qquad w(\sigma) \equiv \sigma \cdot \mathbf{C} \cdot \sigma \tag{1.4}$$

are here respectively, doubled *energy of infinitesimal deformation* ε and doubled *work of stress* σ.

The *limit tensor* $\mathbf{M}$ in quadratic limit criterion

$$\sigma \cdot \mathbf{M} \cdot \sigma \leqslant \text{const} \tag{1.5}$$

is also a Hooke's tensor. It was introduced by R. VON MISES [1] and later popularised for the orthotropy case by R. HILL [2] and others. The form $m(\sigma) \equiv \sigma \cdot \mathbf{M} \cdot \sigma$ is sometimes called the Mises stress intensity. Earlier we have demonstrated [3] that the condition (1.5) for *each* anisotropic elastic material defined by compliance tensor $\mathbf{C}$ has a uniquely defined energy meaning.

1.3. The number of theoretical papers on Hooke's tensors is staggering. Yet new ideas, approaches and results appear not very often. For example, although their symmetry with respect to rotations and mirror-reflections of the basic Euclidean space, enjoys great description by A. E. H. LOVE and W. VOIGT, it still remains interesting (see e.g. [4]). Still far from a satisfactory and effective description is the problem of complete systems of invariants of Hooke's tensors (see the key results [5]).

1.4. In the recent years, one of the more promising directions of the qualitative analysis of Hook's tensors are their invariant decompositions. In the last 15 years, particular development can be observed in the direction [6], originated, as it soon turned out, by Lord Kelvin 150 years ago. It consists in **spectral decomposition** of an individual Hooke's tensor. Symmetric operator $\mathbf{H}$ acts in space endowed with scalar product $\alpha \cdot \beta$, hence the unique spectral decomposition is the case (see [6, 7])

$$\mathbf{H} = h_1\mathbf{P}_1 + \ldots + h_r\mathbf{P}_r, \qquad h_1 < \ldots < h_r, \quad r \leqslant 6, \tag{1.6}$$

where invariants $h_1, \ldots, h_r$ are eigenvalues and tensors $\mathbf{P}_1, \ldots, \mathbf{P}_r$ constitute an orthogonal decomposition of unity

$$\mathbb{I}_{\mathcal{S}} = \mathbf{P}_1 + \ldots + \mathbf{P}_r, \qquad \mathbf{P}_k \circ \mathbf{P}_l = \begin{cases} \mathbf{P}_k & k = l, \\ \mathbf{0} & k \neq l. \end{cases} \tag{1.7}$$

The orthogonal projector $\xi \to \mathbf{P}_k \cdot \xi$ projects orthogonally $\mathcal{S}$ onto subspace $\mathcal{P}_k$ composed of proper states ω of tensor $\mathbf{H}$ which correspond to eigenvalue h_k, $\mathbf{H} \cdot \omega = h_k\omega$,

$$\mathcal{S} = \mathcal{P}_1 \dot{+} ... \dot{+} \mathcal{P}_r, \qquad \dim \mathcal{P}_k = \operatorname{Tr} \mathbf{P}_k. \tag{1.8}$$

Sometimes it is more convenient to put the spectral decomposition in a less rigorous form

$$\mathbf{H} = h_1 \boldsymbol{\omega}_1 \otimes \boldsymbol{\omega}_1 + ... + h_6 \boldsymbol{\omega}_6 \otimes \boldsymbol{\omega}_6, \tag{1.9}$$

without demanding the difference between the eigenvalues. Here $\boldsymbol{\omega}_k$ are proper states which constitute the orthonormal basis in $\mathcal{S}$,

$$\mathbf{H} \cdot \boldsymbol{\omega}_1 = h_1 \boldsymbol{\omega}_1, ..., \quad \mathbf{H} \cdot \boldsymbol{\omega}_6 = h_6 \boldsymbol{\omega}_6, \quad \boldsymbol{\omega}_k \cdot \boldsymbol{\omega}_l = \delta_{kl}.$$

For example, for a *cubic crystal*, the stiffness tensor has the spectral decomposition

$$\mathbf{S} = s_1 \mathbf{P}_1 + s_2 \mathbf{P}_2 + s_3 \mathbf{P}_3, \tag{1.10}$$

while the decomposition of the space of deformations into the subspaces of proper states has the form

$$\mathcal{S} = \mathcal{P}_1 \dot{+} \mathcal{P}_2 \dot{+} \mathcal{P}_3, \qquad 6 = 1 + 2 + 3 \tag{1.11}$$

where, using the crystal axis we have

$$\mathcal{P}_1 \sim \begin{pmatrix} x & 0 & 0 \\ 0 & x & 0 \\ 0 & 0 & x \end{pmatrix}, \quad \mathcal{P}_2 \sim \begin{pmatrix} u & 0 & 0 \\ 0 & v & 0 \\ 0 & 0 & -u-v \end{pmatrix}, \quad \mathcal{P}_3 \sim \begin{pmatrix} 0 & p & r \\ p & 0 & q \\ r & q & 0 \end{pmatrix}. \tag{1.12}$$

To this example we will return in Sec. 3, Part II of this paper (to be published in Arch. Mech.).

The invariants h_k and projectors $\mathbf{P}_k$ are isotropic functions on the space $\mathcal{H}$. So the spectral representations (1.6) are *nonlinear* invariant decompositions of Hooke's tensors. As to the history, details and benefits of this approach, see paper [6], the review [7] and the references quoted therein.

1.5. Another, completely different approach to Hooke's tensors consists in their *linear* invariant decompostions. They appeared as a natural adaptation of the classical theory of group representations (see e.g. [8, 9, 10, 11]). Thus the obtained results are given in papers [12, 13, 14, 15, 16, 17, 18, 19, 20], and possibly elsewhere. These papers are useful and have been applied, but they have certain drawbacks. Only some decompositions are described there, while the mathematical tools are unnecessarily complex, and, in any case, uknown

to most of the specialists in solid mechanics. For some historical remarks see paper [4].

1.6. This paper deals with the *very linear invariant decompositions of the space of Hooke's tensors* $\mathcal{H}$. We will try to:

(1) Systematically and completely describe *all such possible* decompositions.

(2) Do this in a straightforward and possibly simple way, referring to the most basic notions of geometry and algebra (on purpose, we do neglect references to the theory of group representations, harmonic functions, etc., being quite unneeded here).

(3) Persuade the Reader that this approach is interesting, and may perhaps lead to applications, worth considering, important and even surprising (see Part II, esp. examples A trough G).

This set of problems dealt with here touches upon the theory of tensor functions and its applications. We do not describe these relations, making references to the exisiting broad reviews [21, 22, 23, 24].

2. A classical decomposition of $\mathcal{H}$ with respect to internal symmetry

2.1. Let us begin with acting on Hooke's tensors of 4! permutations of the symmetric group $\Sigma = \Sigma_4$. These are linear operations $\sigma \times \mathbf{H}$ referred to in Appendix 1. Each linear combination of operators $\sigma\times$ will be called **permuation operator**. Put them as a formal linear combination of elements of the group Σ

$$\mathfrak{p} = (a_1\sigma_1 + ... + a_{24}\sigma_{24}), \quad \mathfrak{p} \times \mathbf{H} \equiv \sum_1^{24} a_i (\sigma_i \times \mathbf{H}) \tag{2.1}$$

(here some of the factors a_i might of course be equal to zero).

Every Hooke's tensor $\mathbf{H}$ has the internal symmetry, usually given in the form of tediously written equations for its components

$$H_{ijkl} = H_{ijlk} = H_{jikl} = H_{klij}. \tag{2.2}$$

Properly speaking, it means that this is a tensor symmetrical to the folbwing subgroup:

$$\Sigma_{\mathcal{H}} \equiv \{(1234), (2134), (1243), (3412), (2143), (4321), (1423), (1324)\}. \tag{2.3}$$

Let us number its elements from 1 to 8. Let us introduce the symmetrization operator with respect to this subgroup

$$\mathfrak{s}_{\mathcal{H}} \equiv \frac{1}{8}(\sigma_1 + \cdots + \sigma_8), \qquad \sigma_i \in \Sigma_{\mathcal{H}}. \tag{2.4}$$

Cleary, repeating this operation does not change the result, i.e. $\mathfrak{s}_{\mathcal{H}} \circ \mathfrak{s}_{\mathcal{H}} = \mathfrak{s}_{\mathcal{H}}$. The operation $\bigotimes^4 \mathcal{E} \ni \mathbf{A} \to \mathfrak{s}_{\mathcal{H}} \times \mathbf{A} \in \bigotimes^4 \mathcal{E}$ is therefore a projector. It projects the entire 81-dimensional space $\bigotimes^4 \mathcal{E}$ onto the 21-dimensional subspace of Hooke's tensors, $\mathcal{H} = \mathfrak{s}_{\mathcal{H}} \times \left(\bigotimes^4 \mathcal{E}\right)$.

The entire group Σ is generated by subgroup $\Sigma_{\mathcal{H}}$ and two appropriately chosen (external to it) permutations, e.g. two transpositions

$$\langle 23\rangle \equiv (1324), \qquad \langle 24\rangle \equiv (1432). \tag{2.5}$$

Let us introduce two convenient permutation operators

$$\mathfrak{l} \equiv id \equiv (1234), \qquad \mathfrak{c} \equiv \frac{1}{2}(\langle 23\rangle + \langle 24\rangle). \tag{2.6}$$

They can be considered to be basic permutation operators acting on Hooke's tensors in the following sense.

LEMMA. Permutation operator $\mathfrak{p}$ transforms each Hooke's tensor into a Hooke's tensor, i.e. $\mathfrak{p} \times \mathcal{H} \subset \mathcal{H}$, iff it can be written in the form

$$\mathfrak{p} = a\mathfrak{l} + b\mathfrak{c}. \tag{2.7}$$

P r o o f. It is evident that the property $\mathfrak{p} \times \mathcal{H} \subset \mathcal{H}$ can be equivalently given as the commutation rule $\mathfrak{p} \circ \mathfrak{s}_{\mathcal{H}} = \mathfrak{s}_{\mathcal{H}} \circ \mathfrak{p}$. Therefore it is necessary to demonstrate that the form (2.7) is sufficient and necessary for the commutation to occur.

Sufficience: Let us divide the group Σ with respect to subgroup $\Sigma_{\mathcal{H}}$ into a sum of three right layers $\Sigma_{\mathcal{H}}$, $\Sigma_{\mathcal{H}} \circ \langle 23\rangle$, $\Sigma_{\mathcal{H}} \circ \langle 24\rangle$ and a sum of left layers $\Sigma_{\mathcal{H}}$, $\langle 23\rangle \circ \Sigma_{\mathcal{H}}$, $\langle 24\rangle \circ \Sigma_{\mathcal{H}}$. The operator $\mathfrak{c}$ commutates with $\mathfrak{s}_{\mathcal{H}}$. Indeed, on both sides of the equation $\mathfrak{c} \circ \mathfrak{s}_{\mathcal{H}} = \mathfrak{s}_{\mathcal{H}} \circ \mathfrak{c}$ there is the same sum of all the 16 elements of the group Σ which do not belong to subgroup $\Sigma_{\mathcal{H}}$. Hence every operator $\mathfrak{p}$ of the form (2.7) commutates with $\mathfrak{s}_{\mathcal{H}}$.

Necessity: Let us take any permutation operator (2.1). Let us denote by $\sigma_9, \cdots, \sigma_{16}$ all the elements of the layer $\langle 23\rangle \circ \Sigma_{\mathcal{H}}$, whereas by $\sigma_{17}, ..., \sigma_{24}$ – the elements of layer $\langle 24\rangle \circ \Sigma_{\mathcal{H}}$. We see that for every Hooke's tensor

$$\mathfrak{p} \times \mathbf{H} = (a_1\sigma_1 + \ldots + a_{24}\sigma_{24}) \times \mathbf{H} = (a\mathfrak{l} + b\langle 23\rangle + c\langle 24\rangle) \times \mathbf{H} \tag{2.8}$$

where $a \equiv (a_1 + \ldots + a_8)$, $b \equiv (a_9 + \ldots + a_{16})$, $c \equiv (a_{17} + \ldots + a_{24})$. In order for the Hooke's tensor $\mathbf{H} = (\mathbf{x} \otimes \mathbf{x} \otimes \mathbf{y} \otimes \mathbf{y} + \mathbf{y} \otimes \mathbf{y} \otimes \mathbf{x} \otimes \mathbf{x})$ to remain after the operation $\mathfrak{p}\times$, a Hooke's tensor, we additionally need $b = c$. Therefore (2.1) must have the form (2.7).

2.2. Let us find the permutation operators acting on Hooke's tensors as projectors, thus fulfilling the condition

$$\mathfrak{p} \times (\mathfrak{p} \times \mathbf{H}) = \mathfrak{p} \times \mathbf{H} \quad \text{for all} \quad \mathbf{H} \in \mathcal{H}. \tag{2.9}$$

This condition is reduced to two equations $2a^2 + b^2 = 2a$, $4ab + b^2 = 2b$ and has only two solutions different from $\mathfrak{l}$, namely

$$\mathfrak{s} = \frac{1}{3}(\mathfrak{l} + 2\mathfrak{c}), \qquad \mathfrak{t} = \frac{2}{3}(\mathfrak{l} - \mathfrak{c}). \tag{2.10}$$

Operator $\mathfrak{s}$ acts upon $\mathcal{H}$ as a total symmetrization of Hooke's tensors, since

$$\mathfrak{s} \times \mathbf{H} = \frac{1}{3}((1234) + \langle 23\rangle + \langle 24\rangle) \times \mathbf{H} = \frac{1}{24}\sum_{1}^{24} \sigma_i \times \mathbf{H}. \tag{2.11}$$

It projects orthogonally Hooke's tensors onto *the subspace of totally symmetric Hooke's tensor* $\mathcal{H}_\mathfrak{s} \equiv \mathfrak{s} \times \mathcal{H}$. Since $\mathfrak{s} + \mathfrak{t} = \mathfrak{l}$ and, as it can be easily verified, for all tensors $(\mathfrak{s} \times \mathbf{H}_1) \cdot (\mathfrak{t} \times \mathbf{H}_2) = 0$, then $\mathcal{H}_\mathfrak{t} \equiv \mathfrak{t} \times \mathcal{H}$ is an orthogonal complement of $\mathcal{H}_\mathfrak{s}$ *in* $\mathcal{H}$.

We have described a classical **basic orthogonal invariant decomposition**.

$$\mathcal{H} = \mathcal{H}_\mathfrak{s} \dot{+} \mathcal{H}_\mathfrak{t}, \qquad 21 = 15 + 6. \tag{2.12}$$

The dimensions follow from the direct calculation: there are 6 binding conditions for 21 components H_{ijkl} if it is to be symmetric to all permutations. The invariance of this decomposition follows from the commutation of operating of the groups $\Sigma, \mathcal{O}$ in $\mathcal{H}$. Further on we shall decompose both parts of (2.12).

Therefore, every Hooke's tensor can be uniquely given in the form of the sum

$$\mathbf{H} = \mathbf{H}_\mathfrak{s} + \mathbf{H}_\mathfrak{t} \tag{2.13}$$

of *the totally symmetric part* $\mathbf{H}_\mathfrak{s}$ and the part $\mathbf{H}_\mathfrak{t}$ orthogonal to it, Fig. 1.

EXAMPLE 1. Totally symmetric stiffness tensors

$$\mathbf{S} = \mathbf{S}_\mathfrak{s}, \quad \mathbf{S}_\mathfrak{t} = \mathbf{0} \tag{2.14}$$

describe Cauchy's elastic materials. The components of the stiffness tensor must satisfy 6 conditions $(\mathfrak{t} \times \mathbf{S})_{ijkl} = 0$, i.e.

$$2S_{ijkl} - S_{iklj} - S_{ilkj} = 0, \tag{2.15}$$

called *Cauchy's conditions*. The discussions on the formal and physical status of these conditions go 170 years back (see e.g. [25, 26, 27, 15]).

$$\mathcal{H} = \mathcal{H}_s + \mathcal{H}_t$$

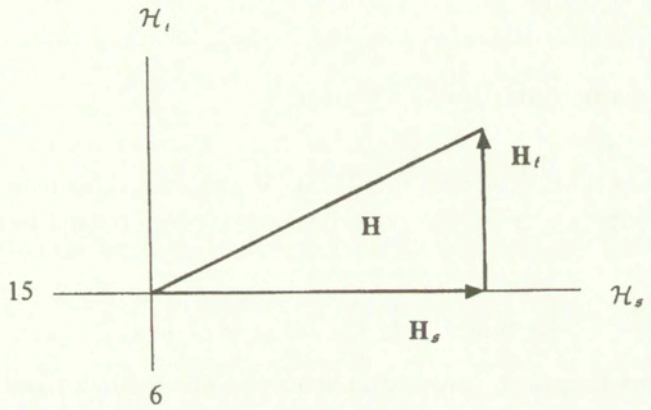

FIG. 1.

3. The decomposition of $\mathcal{H}$ with respect to external symmetry

Isotropic Hooke's tensors constitute a 2-dimensional subspace $\mathcal{H}^{is}$. By denoting its orthogonal complement as $\mathcal{H}^{an}$ we obtain the second **basic orthogonal invariant decomposition**.

(3.1) $$\mathcal{H} = \mathcal{H}^{is} \dot{+} \mathcal{H}^{an}, \qquad 21 = 2 + 19.$$

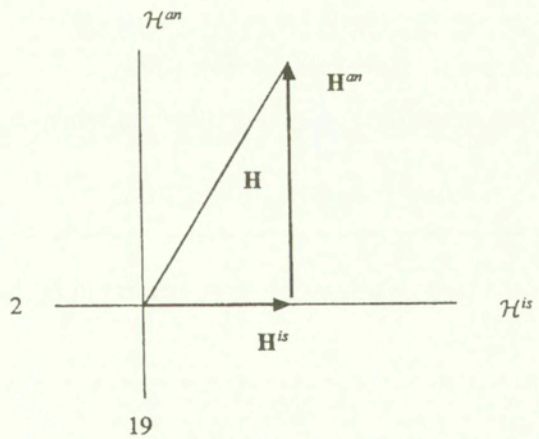

$$\mathcal{H} = \mathcal{H}^{is} + \mathcal{H}^{an}$$

FIG. 2.

Parts of the decomposition

(3.2) $$\mathbf{H} = \mathbf{H}^{is} + \mathbf{H}^{an}$$

will be called, respectively, the *isotropic* and *anisotropic part* of Hooke's tensor **H**, Fig. 2.

4. The plane of isotropic Hooke's tensors[1]

4.1. The building blocks for isotropic Hooke's tensors are, as usual, the unity **1** and the symmmetric group Σ. Every such tensor is proportional to a respectively chosen tensor

$$\mathbb{I}_{\mathfrak{m}} \equiv \mathfrak{m} \times (\mathbf{1} \otimes \mathbf{1}), \qquad \mathfrak{m} = a\mathfrak{l} + b\mathfrak{c}. \tag{4.1}$$

All tensors of this form, proportional to the one with a fixed permutation operator $(a, b) = \text{const}$, constitute an invariant straight line spanned on $\mathbb{I}_{\mathfrak{m}}$ which will be denoted as $\mathcal{J}_{\mathfrak{m}}$. The straight lines $\mathcal{J}_{\mathfrak{m},}$, $\mathcal{J}_{\mathfrak{m}_2}$ are different iff operators $\mathfrak{m}, \mathfrak{m}_2$ are *independent*, i.e. are not proportional, $(a_1, b_1) \neq l(a_2, b_2)$. So we have an **infinite number of invariant decompositions of the plane** $\mathcal{H}^{is}$

$$\mathcal{H}^{is} = \mathcal{J}_{\mathfrak{m}_1} + \mathcal{J}_{\mathfrak{m}_2}, \qquad 2 = (1 + 1). \tag{4.2}$$

Scalar product on this plane is not hard to obtain:

$$\mathbb{I}_{\mathfrak{m}_1} \cdot \mathbb{I}_{\mathfrak{m}_2} = 9a_1a_2 + 6b_1b_2 + 3(a_1b_2 + a_1b_2). \tag{4.3}$$

Hence

$$|\mathbb{I}_{\mathfrak{m}}|^2 = 9a^2 + 6b^2 + 6ab.$$

The invariant decomposition (4.2) is orthogonal when

$$3a_1a_2 + 2b_1b_2 + (a_1b_2 + a_2b_1) = 0. \tag{4.4}$$

4.2. Hooke's isotropic tensors act as linear operators in $\mathcal{S}$ (hence e.g. in Hooke's law) as follows

$$\mathbb{I}_m \cdot \xi = a(\operatorname{tr}\xi)\mathbf{1} + b\xi. \tag{4.5}$$

Their composition has the form

$$\mathbb{I}_{\mathfrak{m}_1} \circ \mathbb{I}_{\mathfrak{m}_2} = \mathbb{I}_{\mathfrak{m}_3}, \quad \mathfrak{m}_3 = (3a_1a_2 + a_1b_2 + a_2b_1)\mathfrak{l} + (b_1b_2)\,\mathfrak{c}. \tag{4.6}$$

[1]It is sensible to gather a few classical formulae of linear isotropic elasticity in a clear geometric form.

Operation $\xi \to \mathbb{I}_{\mathrm{m}} \cdot \xi$ is a projection of $\mathcal{H}^{is}$ on the straight line $\mathbb{I}_{\mathrm{m}}$, i.e.

$$\mathbb{I}_{\mathrm{m}} \circ \mathbb{I}_{\mathrm{m}} = \mathbb{I}_{\mathrm{m}}, \tag{4.7}$$

if equations $3a^2 + 2ab = 2a$, $b^2 = b$ are valid, so for three and only three pairs

$$(0,1), \quad \left(\frac{1}{3}, 0\right), \quad \left(-\frac{1}{3}, 1\right). \tag{4.8}$$

In other words, *only three* isotropic Hooke's tensors act as orthogonal projectors in space $\mathcal{S}$:

the unity (identity operator)

$$\mathbb{I}_{\mathcal{S}} \equiv \mathfrak{c} \times (\mathbf{1} \otimes \mathbf{1}), \qquad \mathbb{I}_{\mathcal{S}} \cdot \xi \equiv \xi, \tag{4.9}$$

the projector onto the straight line of spherical tensors $\mathcal{P}$

$$\mathbb{I}_{\mathcal{P}} \equiv \frac{1}{3}(\mathbf{1} \otimes \mathbf{1}), \qquad \mathbb{I}_{\mathcal{P}} \cdot \xi \equiv \xi_{\mathcal{P}}, \tag{4.10}$$

the projector onto the 5-dimensional subspace of deviators $\mathcal{D}$

$$\mathbb{I}_{\mathcal{D}} \equiv \left(\mathfrak{c} - \frac{1}{3}\mathfrak{l}\right) \times (\mathbf{1} \otimes \mathbf{1}), \quad \mathbb{I}_{\mathcal{D}} \cdot \xi \equiv \xi_{\mathcal{D}}. \tag{4.11}$$

By these definitions we have $\mathbb{I}_{\mathcal{S}} = \mathbb{I}_{\mathcal{P}} + \mathbb{I}_{\mathcal{D}}$. This corresponds to a *classical invariant irreducible decomposition of the space* $\mathcal{S}$,

$$\mathcal{S} = \mathcal{P} \dot{+} \mathcal{D}, \qquad 6 = 1 + 5 \tag{4.12}$$

and, hence, to a unique decomposition of every symmetric tensor ξ into the spherical part $\xi_{\mathcal{P}}$ and deviator $\xi_{\mathcal{D}}$

$$\xi = \xi_{\mathcal{P}} + \xi_{\mathcal{D}}, \quad \xi_{\mathcal{P}} = \frac{\mathrm{tr}\xi}{3}\mathbf{1}. \tag{4.13}$$

Let us consider the formulae

$$\begin{aligned} \mathbb{I}_{\mathcal{S}} \cdot \mathbb{I}_{\mathcal{S}} &= \mathrm{Tr}\,\mathbb{I}_{\mathcal{S}} = \dim \mathcal{S} = 6, \\ \mathbb{I}_{\mathcal{P}} \cdot \mathbb{I}_{\mathcal{P}} &= \mathrm{Tr}\,\mathbb{I}_{\mathcal{P}} = \dim \mathcal{P} = 1, \\ \mathbb{I}_{\mathcal{D}} \cdot \mathbb{I}_{\mathcal{D}} &= \mathrm{Tr}\,\mathbb{I}_{\mathcal{D}} = \dim \mathcal{D} = 5, \end{aligned} \tag{4.14}$$

and a useful identity

$$\mathbf{H} = \mathbb{I}_{\mathcal{S}} \circ \mathbf{H} = \mathbf{H} \circ \mathbb{I}_{\mathcal{S}}. \tag{4.15}$$

4.3. As the most natural basis on the plane $\mathcal{H}^{is}$ we consider the *orthogonal* basis

$$(\mathbb{I}_{\mathcal{P}},\mathbb{I}_{\mathcal{D}}), \quad |\mathbb{I}_{\mathcal{P}}| = 1, \quad |\mathbb{I}_{\mathcal{D}}| = \sqrt{5}, \quad \mathbb{I}_{\mathcal{P}} \cdot \mathbb{I}_{\mathcal{D}} = 0. \tag{4.16}$$

It is reasonable to take the *orthogonal* basis

$$(\mathbb{I}_{\mathfrak{s}},\mathbb{I}_{\mathfrak{t}}), \quad |\mathbb{I}_{\mathfrak{s}}| = \sqrt{5}, \quad |\mathbb{I}_{\mathfrak{t}}| = 2, \quad \mathbb{I}_{\mathfrak{s}} \cdot \mathbb{I}_{\mathfrak{t}} = 0 \tag{4.17}$$

where

$$\mathbb{I}_{\mathfrak{s}} \equiv \mathfrak{s} \times (\mathbf{1} \otimes \mathbf{1}) = \frac{1}{3}(\mathfrak{l} + 2\mathfrak{c}) \times (\mathbf{1} \otimes \mathbf{1}) \tag{4.18}$$

is the isotropic totally symmetric tensor.

In classical elasticity, it was historically assumed to use the *nonorthogonal* basis

$$(\mathbb{I}_{\mathcal{P}},\ \mathbb{I}_{\mathcal{S}}), \qquad \mathbb{I}_{\mathcal{P}} \cdot \mathbb{I}_{\mathcal{S}} = 1. \tag{4.19}$$

We have not seen the non-orthogonal basis $(\mathbb{I}_{\mathcal{D}},\ \mathbb{I}_{\mathcal{S}})$ in use.

All these bases are shown in Fig. 3.

$$\mathcal{H}^{is} = \mathcal{J}_{\mathcal{P}} \dot{+} \mathcal{J}_{\mathcal{D}} = \mathcal{J}_{s} \dot{+} \mathcal{J}_{t} = \mathcal{J}_{\mathcal{P}} + \mathcal{J}_{\mathcal{S}}$$

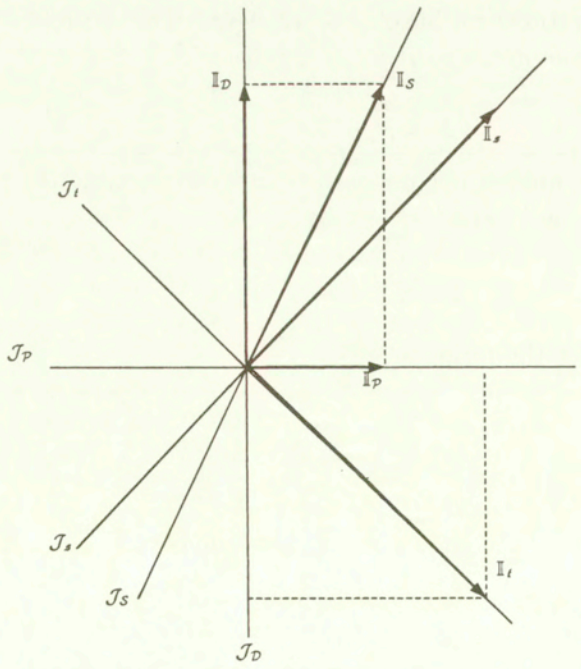

FIG. 3.

The following relations are useful:

$$(4.20)\quad \begin{cases} \mathbb{I}_{\mathcal{P}} = \frac{1}{3}\mathbb{I}_{\mathfrak{s}} + \frac{1}{3}\mathbb{I}_{\mathfrak{t}} = \mathbb{I}_{\mathcal{P}}, \\ \mathbb{I}_{\mathcal{D}} = \frac{2}{3}\mathbb{I}_{\mathfrak{s}} - \frac{5}{6}\mathbb{I}_{\mathfrak{t}} = -\mathbb{I}_{\mathcal{P}} + \mathbb{I}_{\mathcal{S}}, \end{cases} \quad \begin{cases} \mathbb{I}_{\mathfrak{s}} = \frac{5}{3}\mathbb{I}_{\mathcal{P}} + \frac{2}{3}\mathbb{I}_{\mathcal{D}} = \mathbb{I}_{\mathcal{P}} + \frac{2}{3}\mathbb{I}_{\mathcal{S}}, \\ \mathbb{I}_{\mathfrak{t}} = \frac{4}{3}\mathbb{I}_{\mathcal{P}} - \frac{2}{3}\mathbb{I}_{\mathcal{D}} = 2\mathbb{I}_{\mathcal{P}} - \frac{2}{3}\mathbb{I}_{\mathcal{S}}. \end{cases}$$

The relations between the invariant factors of decompositions

$$(4.21)\qquad \mathbf{H}^{is} = h_{\mathcal{P}}\mathbb{I}_{\mathcal{P}} + h_{\mathcal{D}}\mathbb{I}_{\mathcal{D}} = h_{\mathfrak{s}}\mathbb{I}_{\mathfrak{s}} + h_{\mathfrak{t}}\mathbb{I}_{\mathfrak{t}} = k\mathbb{I}_{\mathcal{P}} + l\mathbb{I}_{\mathcal{S}}$$

follow from the previous formulae.

EXAMPLE 2. For the stiffness tensor $\mathbf{S}$ of an elastic isotropic material, when $\mathbf{S} \in \mathcal{H}^{is}$, $\mathbf{S}^{an} = \mathbf{0}$, the invariants $(S_{\mathcal{P}}, S_{\mathcal{D}})$ are examples of Kelvin's moduli (see [6, 7]). We have $k = 3\lambda$, $l = 2\mu$ where λ, μ are *Lamé's constants.*

5. The invariant 10-dimensional subspace of anisotropic Hooke's tensors of the first type

5.1. We are now to examine the possibility of invariant divisions of 19-dimensional space $\mathcal{H}^{an}$, consiting of all anisotropic parts of Hooke's tensors. The orthogonality to $\mathcal{H}^{is}$ can be written in the form of orthogonality conditions to basis $(\mathbb{I}_{\mathcal{P}}, \mathbb{I}_{\mathcal{S}})$

$$(5.1)\qquad 3\mathbb{I}_{\mathcal{P}} \cdot \mathbf{H} = 0, \qquad \mathbb{I}_{\mathcal{S}} \cdot \mathbf{H} = 0.$$

5.2. Let us fix the permutation operator m and consider the set $\mathfrak{D}_{\mathrm{m}}$ of Hooke's tensors of the form

$$(5.2)\qquad \mathrm{m} \times (\mathbf{1} \otimes \boldsymbol{\eta} + \boldsymbol{\eta} \otimes \mathbf{1}), \qquad \mathrm{m} = \mathrm{const},$$

where $\boldsymbol{\eta}$ takes any value from the 5-dimensional space of *deviators* of the second order $\mathcal{D}$. Clearly, the set $\mathfrak{D}_{\mathrm{m}}$:

- is located in $\mathcal{H}^{an}$,
- is a linear subspace,
- dim $\mathfrak{D}_{\mathrm{m}} = 5$,
- this subspace is invariant,
- this subspace is irreducible.

Indeed $\mathfrak{D}_{\mathrm{m}} \subset \mathcal{H}^{an}$, since every tensor (5.2) as a result of the equation $\mathrm{tr}\boldsymbol{\eta} = 0$, is orthogonal to $\mathcal{H}^{is}$. Every linear combination of the tensors of the form (5.2) is

a tensor of this form, hence $\mathfrak{D}_{\mathfrak{m}}$ is a subspace. Every basis $\eta_1, .., \eta_5$ of $\mathcal{D}$ generates a basis in $\mathfrak{D}_{\mathfrak{m}}$, so $\dim\mathfrak{D}_{\mathfrak{m}} = \dim\mathcal{D}$. If we rotate any tensor (5.2) from $\mathfrak{D}_{\mathfrak{m}}$ by any tensor $\mathbf{R} \in \mathcal{O}$

$$\mathbf{R} * [\mathfrak{m} \times (\mathbf{1} \otimes \eta + \eta \otimes \mathbf{1})] = \mathfrak{m} \times [\mathbf{1} \otimes (\mathbf{R} * \eta) + (\mathbf{R} * \eta) \otimes \mathbf{1}], \tag{5.3}$$

it remains in $\mathfrak{D}_{\mathfrak{m}}$ so this is an invariant subspace. Finally, the irreducibility of $\mathfrak{D}_{\mathfrak{m}}$ follows immediately from the irreducibility of the space of deviators $\mathcal{D}$, being a building block for $\mathfrak{D}_{\mathfrak{m}}$.

5.3. Let us take two subspaces $\mathfrak{D}_{\mathfrak{m}_1}$ and $\mathfrak{D}_{\mathfrak{m}_2}$. It is clear that only two situations are possible:

$$\mathfrak{D}_{\mathfrak{m}_1} \cap \mathfrak{D}_{\mathfrak{m}_2} = \{\mathbf{0}\} \qquad \text{when} \quad \mathfrak{m}_1, \mathfrak{m}_2 \text{ are independent,} \tag{5.4}$$

$$\mathfrak{D}_{\mathfrak{m}_1} = \mathfrak{D}_{\mathfrak{m}_2} \qquad \text{when this is not the case.} \tag{5.5}$$

When the pair $(\mathfrak{m}_1, \mathfrak{m}_2)$ is an independent pair, let us take a direct sum (see Appendix 1)

$$\mathfrak{D} \equiv \mathfrak{D}_{\mathfrak{m}_1} + \mathfrak{D}_{\mathfrak{m}_2}, \qquad 10 = (5 + 5). \tag{5.6}$$

Since for all independent $\mathfrak{m}_1$, $\mathfrak{m}_2$

$$\mathfrak{D}_{\mathfrak{m}_1} + \mathfrak{D}_{\mathfrak{m}_2} = \mathfrak{D}_{\mathfrak{l}} + \mathfrak{D}_{\mathfrak{c}}, \tag{5.7}$$

then we have obtained a *10-dimensional invariant subspace of anisotropic* Hooke's *tensors* $\mathfrak{D}$. It contains all 5-dimensional subspaces $\mathfrak{D}_m$ and can be split, in an infinite number of ways, into a sum of two such irreducible subspacess.

Grave warning: It can be easily verified that it is not so that every tensor from the found space $\mathfrak{D}$ has the form $\mathfrak{m} \times (\mathbf{1} \otimes \eta + \eta \otimes \mathbf{1})$ for certain $\mathfrak{m}$, η. To put it more forcefully, an infinite number of tensors from $\mathfrak{D}$ do not belong to any 5-dimensional subspace $\mathfrak{D}_{\mathfrak{m}}$ (some of our geometric intuitions obtained in dimensions 2 and 3 ought to be given a tight rein!).

5.4. Let us calculate the scalar product of the parts of the decomposition

$$\mathbf{H}^{an}_{\mathfrak{D}} \equiv \mathfrak{m}_1 \times (\mathbf{1} \otimes \eta + \eta \otimes \mathbf{1}) + \mathfrak{m}_2 \times (\mathbf{1} \otimes \xi + \xi \otimes \mathbf{1}). \tag{5.8}$$

We have

$$(5.9)\qquad [\mathfrak{m}_1 \times (\mathbf{1}\otimes\eta+\eta\otimes\mathbf{1})]\cdot[\mathfrak{m}_2\times(\mathbf{1}\otimes\xi+\xi\otimes\mathbf{1})] = [6a_1a_2+4(a_1b_2+a_2b_1)+5b_1b_2]\,\eta\cdot\xi.$$

Hence in particular

$$(5.10)\qquad |\mathfrak{m}\times(\mathbf{1}\otimes\eta+\eta\otimes\mathbf{1})|^2=\mu(\mathfrak{m})\,|\eta|^2,$$

where $\mu(\mathfrak{m})=6a^2+8ab+5b^2$.

Two subspaces $\mathfrak{D}_{\mathfrak{m}_1}$ and $\mathfrak{D}_{\mathfrak{m}_2}$ constitute complete invariant *orthogonal* decomposition of space $\mathfrak{D}$ iff

$$(5.11)\qquad 6a_1a_2+4(a_1b_2+a_2b_1)+5b_1b_2=0.$$

There is an infinite number of such decompositions.

5.5. The following particular cases of the decompositions of Hooke's tensors $\mathbf{H}^{an}_{\mathfrak{D}}\in\mathfrak{D}$ will prove to be most interesting:

standard decomposition, non-orthogonal one

$$(5.12)\qquad \mathbf{H}^{an}_{\mathfrak{D}}=(\mathbf{1}\otimes\omega+\omega\otimes\mathbf{1})+\mathfrak{c}\times(\mathbf{1}\otimes\varrho+\varrho\otimes\mathbf{1}),$$

orthogonal decomposition with respect to internal symmetry

$$(5.13)\qquad \mathbf{H}^{an}_{\mathfrak{D}}=\mathfrak{s}\times(\mathbf{1}\otimes\alpha+\alpha\otimes\mathbf{1})+\mathfrak{t}\times(\mathbf{1}\otimes\beta+\beta\otimes\mathbf{1}),$$

orthogonal decomposition

$$(5.14)\qquad \mathbf{H}^{an}_{\mathfrak{D}}=(\mathbf{1}\otimes\varphi+\varphi\otimes\mathbf{1})+\left(\mathfrak{c}-\frac{2}{3}\mathfrak{l}\right)\times(\mathbf{1}\otimes\psi+\psi\otimes\mathbf{1}),$$

seemingly quite artificial, but its role will become evident in Part II of this paper.

The tensor $\mathbf{H}^{an}_{\mathfrak{D}}$ is an orthogonal projection of Hooke's tensor $\mathbf{H}$ onto a 10-dimensional subspace $\mathfrak{D}$. From the definition of permutation operators these relations follow immediately

$$(5.15)\qquad \begin{cases}\alpha=\omega+\varrho,\\ \beta=\dfrac{1}{2}(2\omega-\varrho),\end{cases}\qquad \begin{cases}\omega=\dfrac{1}{3}(\alpha+2\beta),\\ \varrho=\dfrac{2}{3}(\alpha-\beta),\end{cases}$$

$$\begin{cases}\varphi=\dfrac{1}{7}(7\alpha+2\beta)=\dfrac{1}{3}(3\omega+2\varrho),\\ \psi=\dfrac{2}{3}(\alpha-\beta)=\varrho.\end{cases}$$

The norm of tensor $\mathbf{H}^{an}_{\mathfrak{D}}$ from $\mathfrak{D}$ is

$$|\mathbf{H}^{an}_{\mathfrak{D}}|^2 = \frac{14}{3}\alpha\cdot\alpha + \frac{1}{3}\beta\cdot\beta = 5\omega\cdot\omega + 9\omega\cdot\varrho + \frac{19}{4}\varrho\cdot\varrho. \tag{5.16}$$

6. The canonical decomposition of the space of Hooke's tensors

6.1. What is left to describe are the tensors that constitute in $\mathcal{H}^{an}$ the invariant orthogonal complement of the defined invariant space $\mathfrak{D}$.

We denote this complement by D, $\dim \mathsf{D} = 19 - 10 = 9$.

First, it is immediately evident that every tensor $\mathbf{D} \in \mathsf{D}$ is **totally traceless**, i.e.

$$\mathrm{tr}\,\mathbf{D} = 0 \qquad \text{for every operation tr.} \tag{6.1}$$

Indeed, it should be a tensor orthogonal to $\mathcal{H}^{is}$ and to $\mathfrak{D}$. If $\mathbf{D}\cdot(\mathbf{1}\otimes\mathbf{1}) = \mathbf{1}\cdot\mathbf{D}\cdot\mathbf{1} = 0$ and $(\mathbf{1}\otimes\alpha + \alpha\otimes\mathbf{1})\cdot\mathbf{D} = 2\mathbf{1}\cdot\mathbf{D}\cdot\alpha = 0$ for every α, then $D_{ppij} = 0$. Similarly, with the orthogonality conditions of $\mathbf{D}$ to $\mathfrak{c}\times(\mathbf{1}\otimes\mathbf{1})$ and $\mathfrak{c}\times(\mathbf{1}\otimes\alpha + \alpha\otimes\mathbf{1})$, we obtain $D_{ippj} = 0$. From the symmetry with respect to group $\Sigma_{\mathcal{H}}$, it follows that $\mathbf{D}$ is totally traceless.

Secondly, every tensor $\mathbf{D} \in \mathsf{D}$ is **totally symmetric**. This results from orthogonal decompositions: $\mathcal{H} = \mathcal{H}_{\mathfrak{s}} \dot{+} \mathcal{H}_{\mathfrak{t}}$ and

$$\mathcal{H}_{\mathfrak{s}} = \mathcal{J}_{\mathfrak{s}} \dot{+} \mathfrak{D}_{\mathfrak{s}} \dot{+} \mathsf{D}, \qquad 15 = 1 + 5 + 9, \tag{6.2}$$

$$\mathcal{H}_{\mathfrak{t}} = \mathcal{J}_{\mathfrak{t}} \dot{+} \mathfrak{D}_{\mathfrak{t}}, \qquad 6 = 1 + 5, \tag{6.3}$$

evident due to the dimensions of the parts.

6.2. Thus the invariant space D consists of **totally symmetric and traceless** tensors of the fourth order, which we call **fourth-order deviators**[2].

It can be demostrated that space D is irreducible[3].

[2] In [12, 15, 19] and possibly elsewhere, they are called, for certain reasons, *harmonic* tensors, and even the very decompositions to which they led are called *harmonic* decompositions. These names are in our approach neither necessary nor fortunate.

[3] This would be the only proof reaching deeper into the theory of representations of compact groups and that is why it will be neglected here (see e.g. [10] and the classical textbooks quoted therein).

To sum up: we obtained the following **unique canonical decomposition of the space of Hooke's tensors**

$$\boxed{\mathcal{H} = \mathcal{H}^{is} \dot{+} \mathfrak{D} \dot{+} \mathsf{D}\,, \qquad 21 = 2 + 10 + 9\,.} \tag{6.4}$$

The meaning and the gravity of this decomposition and the solemnity of its name will become clear later on (see also J. P. SERRE [11]). Every Hooke's tensor is a unique sum

$$\boxed{\mathbf{H} = \mathbf{H}^{is} + \mathbf{H}^{an}_{\mathfrak{D}} + \mathbf{H}^{an}_{\mathsf{D}}} \tag{6.5}$$

of three mutally orthogonal parts: *the isotropic part* $\mathbf{H}^{is}$, *the first anisotropic part* $\mathbf{H}^{an}_{\mathcal{D}}$ *expressed by two second-order deviators and the second anisotropic part* $\mathbf{H}^{an}_{\mathsf{D}}$ *being a fourth-order deviator*, Fig. 4.

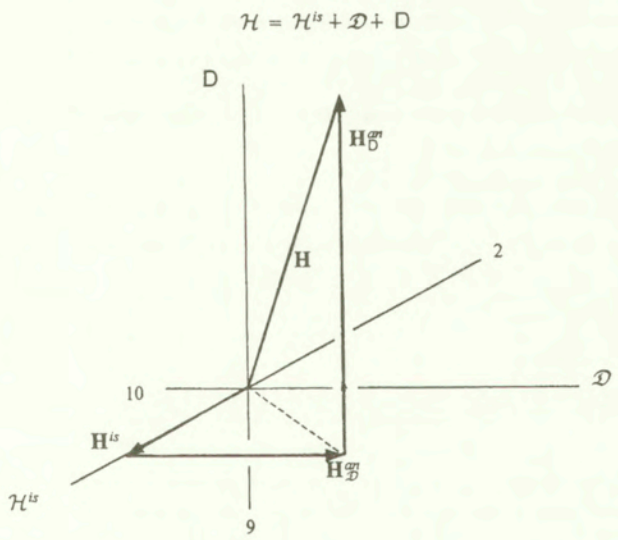

FIG. 4.

7. Summary: all the possible invariant decompositions of the space of Hooke's tensors

7.1. All that has been presented above can be summarised as follows.

Every complete invariant decomposition of the space of Hooke's tensors has the form:

$$\boxed{\mathcal{H} = (\mathcal{J}_{\mathrm{n}_1} + \mathcal{J}_{\mathrm{n}_2}) \dot{+} (\mathfrak{D}_{\mathrm{m}_1} + \mathfrak{D}_{\mathrm{m}_2}) \dot{+} \mathsf{D}, \quad 21 = (1+1) + (5+5) + 9,} \tag{7.1}$$

where $\mathfrak{n}_1, \mathfrak{n}_2$) *and* $(\mathfrak{m}_1, \mathfrak{m}_2)$ *are two pairs of pairwise independent permutation operators. These pairs can be chosen arbitrarily, so there is an infinite number of such decompositions. Each of them is a split of parts* $\mathcal{H}^{is}$ *and* $\mathfrak{D}$ *of the* **unique canonical decomposition** (6.4). *By fixing operators* $\mathfrak{n}_1, \mathfrak{n}_2, \mathfrak{m}_1, \mathfrak{m}_2$ *and grouping arbitrarily the irreducible spaces from* (7.1), *we can obtain every invariant decomposition of space* $\mathcal{H}$.

In particular:

1) the classical decomposition $\mathcal{H} = \mathcal{H}_\mathfrak{s} \dot{+} \mathcal{H}_\mathfrak{t}$ we obtain by taking $\mathfrak{n}_1 = \mathfrak{m}_1 = \mathfrak{s}$, $\mathfrak{n}_2 = \mathfrak{m}_2 = \mathfrak{t}$ and grouping the spaces as in (6.2) and (6.3);

2) the classical decomposition $\mathcal{H} = \mathcal{H}^{is} \dot{+} \mathcal{H}^{an}$ is valid for any choice of permutation operators,

$$\mathcal{H}^{an} = \mathfrak{D} \dot{+} \mathrm{D}, \qquad 19 = 10 + 9. \tag{7.2}$$

7.2. The result obtained (7.1) will be given also in another form, being a handy form for someone primarily interested in applications.

The manual for linear complete invariant decomposition of any Hooke's tensor:

Let $(\mathfrak{n}_1, \mathfrak{n}_2)$ *and* $(\mathfrak{m}_1, \mathfrak{m}_2)$ *be two arbitrary chosen pairs of pairwise independent permutation operators* (2.7). *Then for any Hooke's tensor* $\mathbf{H} \in \mathcal{H}$ *there is a pair of scalars* (h_1, h_2) *a pair of second order deviators* (ξ_1, ξ_2), *a fourth-order deviator* $\mathbf{D}$, *such that*

$$\boxed{\mathbf{H} = h_1 \mathbb{I}_{n_1} + h_2 \mathbb{I}_{n_2} + \mathfrak{m}_1 \times (\mathbf{1} \otimes \xi_1 + \xi_1 \otimes \mathbf{1}) + \mathfrak{m}_2 \times (\mathbf{1} \otimes \xi_2 + \xi_2 \otimes \mathbf{1}) + \mathbf{D}.} \tag{7.3}$$

Having fixed the pairs $(\mathfrak{n}_1, \mathfrak{n}_2)$, $(\mathfrak{m}_1, \mathfrak{m}_2)$, *the correspondence*

$$\mathbf{H} \leftrightarrow (h_1, h_2, \xi_1, \xi_2, \mathbf{D})$$

is isotropic and one-to-one.

The choice of a decomposition, i.e. the choice of operators $(\mathfrak{n}_1, \mathfrak{n}_2)$ and $(\mathfrak{m}_1, \mathfrak{m}_2)$ depends, as we shall see, on the role of Hooke's tensor $\mathbf{H}$ in a given context. The anisotropic part of Hooke's tensor $\mathbf{H}^{an}$ is uniquely determined by pair $(\mathfrak{m}_1, \mathfrak{m}_2)$ and three deviators $(\xi_1, \xi_2, \mathbf{D})$. These deviators will be called *anisotropy deviators.*

For example, we shall demonstrate the complete decomposition choosing $\mathfrak{n}_1 = \frac{1}{3}\mathfrak{l}$, $\mathfrak{n}_2 = \left(\mathfrak{c} - \frac{1}{3}\mathfrak{l}\right)$, $\mathfrak{m}_1 = \mathfrak{s}$, $\mathfrak{m}_2 = \mathfrak{t}$. Then

$$\mathbf{H} = h_\mathcal{P} \mathbb{I}_\mathcal{P} + h_\mathcal{D} \mathbb{I}_\mathcal{D} + \mathfrak{s} \times (\mathbf{1} \otimes \alpha + \alpha \otimes \mathbf{1}) + \mathfrak{t} \times (\mathbf{1} \otimes \beta + \beta \otimes \mathbf{1}) + \mathbf{D}. \tag{7.4}$$

7.3. We shall find explicit isotropic functions defining $(h_1, h_2, \xi_1, \xi_2, \mathbf{D})$ by $\mathbf{H}$. We will do so, for example, for (7.4)

$$\mathbf{H} \to (h_{\mathcal{P}}, h_{\mathcal{D}}, \alpha, \beta, \mathbf{D}). \tag{7.5}$$

It is most simple to obtain the coefficients of the isotropic part $h_{\mathcal{P}}, h_{\mathcal{D}}$. Let us introduce two self-evident *linear invariants* of tensor $\mathbf{H}$

$$\mathbf{H} \cdot (3\mathbb{I}_{\mathcal{P}}) = \mathbf{1} \cdot \mathbf{H} \cdot \mathbf{1} = H_{ppqq}, \tag{7.6}$$

$$\mathbf{H} \cdot \mathbb{I}_{\mathcal{S}} = \operatorname{Tr} \mathbf{H} = H_{pqpq}. \tag{7.7}$$

Every linear invariant of $\mathbf{H}$ has the form $\mathbf{H} \cdot \mathbb{I}_{\mathrm{m}}$, so it is a linear combination of these two. In particular, by scalar multiplication of (7.4) by $\mathbb{I}_{\mathcal{P}}$ and $\mathbb{I}_{\mathcal{D}}$, we have

$$h_{\mathcal{P}} = \frac{1}{3}\mathbf{1} \cdot \mathbf{H} \cdot \mathbf{1}, \quad h_{\mathcal{D}} = \frac{1}{5}(\operatorname{Tr} \mathbf{H} - h_{\mathcal{P}}). \tag{7.8}$$

To obtain the deviators α, β, it is convenient to use *V. V. Novozhilov's tensors*[4]

$$\boldsymbol{\mu} \equiv \mathbf{H} \cdot \mathbf{1}, \quad \mu_{ij} = H_{ijpp}, \tag{7.9}$$

$$\boldsymbol{\nu} \equiv (\langle 23 \rangle \times \mathbf{H}) \cdot \mathbf{1}, \quad \nu_{ij} = H_{ipjp} = H_{ippj}. \tag{7.10}$$

He observed in [27] that these are the only two tensors that can be obtained from Hooke's tensor by direct application of the trace operator.

EXAMPLE 3. If $\mathbf{C}$ is a compliance tensor, then $\varepsilon = \mathbf{C} \cdot \mathbf{1}$ is deformation, to which an elastic material reacts under hydrostatic pressure $\sigma = \mathbf{1}$.

EXAMPLE 4. In the theory of elastic waves, a role is played by the tensor S_{ippj}/ϱ, where ϱ is density and $\mathbf{S}$ is the stiffness tensor, [28] (see also example F in Part II of this paper).

Let us note that

$$h_{\mathcal{P}} = \frac{1}{3}\operatorname{tr}\boldsymbol{\mu}, \qquad h_{\mathcal{D}} = \frac{1}{15}(3\operatorname{tr}\boldsymbol{\nu} - \operatorname{tr}\boldsymbol{\mu}). \tag{7.11}$$

7.4. Let us introduce *Novozhilov's deviators*

$$\boldsymbol{\mu}_{\mathcal{D}} \equiv \boldsymbol{\mu} - \frac{\operatorname{tr}\boldsymbol{\mu}}{3}\mathbf{1}, \qquad \boldsymbol{\nu}_{\mathcal{D}} \equiv \boldsymbol{\nu} - \frac{\operatorname{tr}\boldsymbol{\nu}}{3}\mathbf{1}. \tag{7.12}$$

[4]These tensors are also used in [19]; tensor ν_{ij} is called therein Voigt's tensor (for reasons unknown to me).

By taking $\mathbf{H}$ in the form (7.4) we obtain, by direct calculation, according to definition (7.9), (7.10),

$$\mu_{\mathcal{D}} = \frac{1}{3}(7\alpha + 2\beta), \qquad \nu_{\mathcal{D}} = \frac{1}{3}(7\alpha - \beta). \tag{7.13}$$

Hence

$$\alpha = \frac{1}{7}(\mu_{\mathcal{D}} + 2\nu_{\mathcal{D}}), \qquad \beta = \mu_{\mathcal{D}} - \nu_{\mathcal{D}}. \tag{7.14}$$

Finally, by substituting (7.11), (7.14) in (7.4) we obtain the fourth-order deviator $\mathbf{D}$.

Thus the entire sequence $(h_{\mathcal{P}}, h_{\mathcal{D}}, \alpha, \beta, \mathbf{D})$ *was expressed by Novozhilov's tensors* μ, ν, *as an explicit linear isotropic tensor function of* $\mathbf{H}$.

Similarly we can obtain the sequence $(h_{\mathcal{P}}, h_{\mathcal{D}}, \omega, \varrho, \mathbf{D})$ in a complete decomposition

$$\mathbf{H} = h_{\mathcal{P}}\mathbb{I}_{\mathcal{P}} + h_{\mathcal{D}}\mathbb{I}_{\mathcal{D}} + (\mathbf{1} \otimes \omega + \omega \otimes \mathbf{1}) + \mathfrak{c} \times (\mathbf{1} \otimes \varrho + \varrho \otimes \mathbf{1}) + \mathbf{D}. \tag{7.15}$$

We shall then have

$$\omega = \frac{1}{7}(5\mu_{\mathcal{D}} - 4\nu_{\mathcal{D}}), \qquad \varrho = \frac{2}{7}(3\nu_{\mathcal{D}} - 2\mu_{\mathcal{D}}). \tag{7.16}$$

The identity resulting from these formulae

$$\mathbf{H} = h_{\mathcal{P}}\mathbb{I}_{\mathcal{P}} + h_{\mathcal{D}}\mathbb{I}_{\mathcal{D}} + \mathfrak{m}_1 \times (\mathbf{1} \otimes \mu_{\mathcal{D}} + \mu_{\mathcal{D}} \otimes \mathbf{1}) + \mathfrak{m}_2 \times (\mathbf{1} \otimes \nu_{\mathcal{D}} + \nu_{\mathcal{D}} \otimes \mathbf{1}) + \mathbf{D}, \tag{7.17}$$

where $\mathfrak{m}_1 = \frac{1}{7}(5\mathfrak{l} - 4\mathfrak{c})$, $\mathfrak{m}_2 = \frac{2}{7}(-2\mathfrak{l} + 3\mathfrak{c})$ expresses directly Hooke's tensor by its Novozhylov's tensors μ, ν and $\mathbf{D}$.

Let us also note formulae for the norm of Hooke's tensor

$$|\mathbf{H}|^2 = |\mathbf{H}^{is}|^2 + |\mathbf{H}^{an}_{\mathcal{D}}|^2 + |\mathbf{H}^{an}_{\mathcal{D}}|^2 = h^2_{\mathcal{P}} + 5h^2_{\mathcal{D}} + \frac{14}{3}\alpha \cdot \alpha + \frac{1}{3}\beta \cdot \beta + \mathbf{D} \cdot \mathbf{D}. \tag{7.18}$$

7.5. In most papers on the linear invariant decompositions of Hooke's tensor, the starting point was, what is customary in the theory of group representation, the symmetrization $\mathfrak{s} \times \mathbf{H}$. This leads to decomposition (7.3) with

$$\mathfrak{n}_1 = \mathfrak{m}_1 = \mathfrak{s}, \qquad \mathfrak{n}_2 = \mathfrak{m}_2 = \mathfrak{t}, \tag{7.19}$$

(G. BACKUS [12], YU. I. SIROTIN [13, 14], J. JERPHAGNON, D. CHEMLA, R. BONNEVILLE [15], J. PRATZ [16], R. BAERHAIM [19]). The tools used were

unnecessarily complex. This decomposition is, moreover, often quite unnatural, e.g. for anisotropic parts.

Only E. T. ONAT [17] used one of the infinite number of other decompositions, namely the case

$$\mathfrak{n}_1 = \mathfrak{m}_1 = \mathfrak{l}, \quad \mathfrak{n}_2 = \mathfrak{m}_2 = 2\mathfrak{c}. \tag{7.20}$$

It has been repeated by S. C. COWIN [18], described in [19], and proved to be convenient for S. FORTE and M. VIANELLO [4].

Nowhere is the **unique canonical decomposition** (6.4) noted or underlined, even though it is the true basis for all invariant decompositions of space $\mathcal{H}$.

Appendix 1. Notions

For the readers without everyday touch with multilinear algebra, we remind several introductory notions, necessary and sufficient to understand this paper.

1. Direct sums. Let us take any finite-dimensional *linear space* $\mathcal{L}$ with elements $\mathbf{x}, \ldots$. The subset $\mathcal{P} \subset \mathcal{L}$ is called *linear subspace* in $\mathcal{L}$ when it contains any finite linear combination of its elements. Taking two mutually independent subspaces $\mathcal{P}_1$, $\mathcal{P}_2$, i.e. those that intersect only in $\mathbf{0}$, we will call a *direct sum* of these two, a set of all $\mathbf{x} \in \mathcal{L}$ of the form $\mathbf{x} = \mathbf{x}_1 + \mathbf{x}_2$, $\mathbf{x}_1 \in \mathcal{P}_1$, $\mathbf{x}_2 \in \mathcal{P}_2$. This sum is, of course, a subspace in $\mathcal{L}$. We will use the simplest notation for it: $\mathcal{P}_1 + \mathcal{P}_2$[5]. The decomposition $\mathbf{x} = \mathbf{x}_1 + \mathbf{x}_2$ of every element $\mathbf{x} \in \mathcal{P}_1 + \mathcal{P}_2$ is unique. This uniqueness is best regarded as a generalizing definition: the smallest subspace in $\mathcal{L}$ which contains all the subspaces of the sequence $\mathcal{P}_1, \mathcal{P}_2, \ldots, \mathcal{P}_k$ will be called their *direct sum*, denoted by $\mathcal{P}_1 + \ldots + \mathcal{P}_k$, when the representation of each element $\mathbf{x} \in \mathcal{P}_1 + \ldots + \mathcal{P}_k$ in the form

$$\mathbf{x} = \mathbf{x}_1 + \mathbf{x}_2 + \ldots + \mathbf{x}_k, \qquad \mathbf{x}_1 \in \mathcal{P}_1, \ldots, \ \mathbf{x}_k \in \mathcal{P}_k \tag{A.1}$$

is unique, i.e. when

$$\mathbf{x} = 0 \qquad \text{iff} \qquad \mathbf{x}_1 = \mathbf{x}_2 = \ldots = \mathbf{x}_k = \mathbf{0}. \tag{A.2}$$

A direct sum of the sequence $\mathcal{P}_1, \ldots, \mathcal{P}_k$ such that

$$\mathcal{P}_1 + \ldots + \mathcal{P}_k = \mathcal{L} \tag{A.3}$$

will be called *direct division* of the space $\mathcal{L}$.

If in the space $\mathcal{L}$ a scalar product is defined, and the parts of the direct sum are mutually orthogonal, then the direct sum is called *orthogonal*. In order

[5] There are also other notations instead of $+$ (e.g. $\dot{+}$ or $\oplus$).

to stress this we will write $\dot{+}$ instead of $+$. If $\mathcal{P}_1 \dot{+} \mathcal{P}_2 = \mathcal{L}$ then $\mathcal{P}_2$ is called *orthogonal complement* of $\mathcal{P}_1$ in $\mathcal{L}$ and we write $\mathcal{P}_2 = \mathcal{P}_1^{\perp}$.

2. Spaces of Euclidean tensors. Let $\mathcal{E}$ be our starting Euclidean space with elements $\mathbf{x}, ...$ called vectors with scalar product $\mathbf{xy} \equiv \mathbf{x} \cdot \mathbf{y}$. Every element $\mathbf{A} \in \bigotimes^q \mathcal{E}$ we call, as usual (at least for over fourty years [29]), *q-order Euclidean tensor*. Every tensor is a finite linear combination of *simple tensors* $\mathbf{a}_1 \otimes \mathbf{a}_2 \otimes ..... \otimes \mathbf{a}_q$. In this paper we are only interested in two cases $\dim\mathcal{E} = 3$ and $\dim\mathcal{E} = 2$ (see Sec. 4, Part. II) and $q = 2$ and $q = 4$. Moreover, we examine only symmetric second-order tensors $\boldsymbol{\omega} \in \mathcal{S} \equiv \operatorname{sym} \bigotimes^2 \mathcal{E} \subset \bigotimes^2 \mathcal{E}$ and fourth-order tensors of the type $\mathbf{H} \in \bigotimes^2 \mathcal{S} \subset \bigotimes^4 \mathcal{E}$,

$$\boldsymbol{\omega}^{\mathrm{T}} = \boldsymbol{\omega}, \qquad \mathbf{H}^{\mathrm{T}} = \mathbf{H}. \tag{A.4}$$

It is convenient to view the set of tensors $\bigotimes^q \mathcal{E}$ as a Euclidean space endowed with a natural scalar product $\mathbf{A} \cdot \mathbf{B}$, being a bilinear operation defined on simple tensors by the recipe

$$(\mathbf{a}_1 \otimes ..... \otimes \mathbf{a}_q) \cdot (\mathbf{b}_1 \otimes ..... \otimes \mathbf{b}_q) \equiv (\mathbf{a}_1\mathbf{b}_1).....(\mathbf{a}_q\mathbf{b}_q). \tag{A.5}$$

In every space $\bigotimes^q \mathcal{E}$ acts the group $\mathcal{O}$ of rotations and mirror reflections of the starting space $\mathcal{E}$. This action $\mathbf{A} \longrightarrow \mathbf{R}*\mathbf{A}$, $\mathbf{R} \in \mathcal{O}$ is by definition linear and defined on simple tensors by the recipe

$$\mathbf{R}*(\mathbf{a}_1 \otimes .... \otimes \mathbf{a}_q) \equiv \mathbf{R}\mathbf{a}_1 \otimes .... \otimes \mathbf{R}\mathbf{a}_q, \tag{A.6}$$

where $\mathbf{a} \longrightarrow \mathbf{Ra}$ is action of the group $\mathcal{O}$ on vectors. The subgroup $\mathcal{O}(\mathbf{A})$ consisting of all $\mathbf{R} \in \mathcal{O}$ that preserve $\mathbf{A}$, $\mathbf{R} * \mathbf{A} = \mathbf{A}$, will be called *symmetry group* of tensor $\mathbf{A}$.

The linear subspace of tensors $\mathcal{P} \subset \bigotimes^q \mathcal{E}$ will be called here *isotropic or invariant* subspace[6] when it is stable under group $\mathcal{O}$, $\mathcal{O} * \mathcal{P} = \mathcal{P}$ (i.e. when $\mathbf{R} * \mathbf{A} \in \mathcal{P}$ for all $\mathbf{R} \in \mathcal{O}$, $\mathbf{A} \in \mathcal{P}$). If $\mathcal{P}$ is an invariant subspace, then its orthogonal complement $\mathcal{P}^{\perp}$ is an invariant subspace too. An invariant subspace is called *irreducible* if it does not contain any proper invariant subspace. The decomposition of the examined invariant subspace $\mathcal{L} \subset \bigotimes^q \mathcal{E}$ into a direct sum of invariant subspaces $\mathcal{P}_1, ..., \mathcal{P}_k$

$$\mathcal{P}_1 + ... + \mathcal{P}_k = \mathcal{L} \tag{A.7}$$

will be called a *complete invariant decomposition* if all the subspaces $\mathcal{P}_1, ..., \mathcal{P}_k$ are irreducible. Not always are we interested in complete decompositions.

[6] In multilinear algebra, the name *tensorial subspace* is rather used.

In the space $\bigotimes^q \mathcal{E}$ acts also one more group, namely the *symmetric* group Σ_q consisting of permutations $\sigma, \ldots$ We shall denote permutations in the usual way, e.g. $\sigma = (2413) \in \Sigma_4$ means $\sigma(1) = 2$, $\sigma(2) = 4$, $\sigma(3) = 1$, $\sigma(4) = 3$. The action $\mathbf{A} \to \sigma \times \mathbf{A}$ is linear and defined on simple tensors by the recipe

$$\sigma \times (\mathbf{a}_1 \otimes \ldots\ldots \otimes \mathbf{a}_q) \equiv \mathbf{a}_{\sigma^{-1}(1)} \otimes \ldots\ldots \otimes \mathbf{a}_{\sigma^{-1}(q)}. \tag{A.8}$$

The actions of groups Σ_q and $\mathcal{O}$ are commutative:

$$\sigma \times (\mathbf{R} * \mathbf{A}) = \mathbf{R} * (\sigma \times \mathbf{A}). \tag{A.9}$$

REMARK. We will not really need either a more developed terminology or more profound results of the *theory of group representations*, otherwise truly beautiful.

Appendix 2. Notation

For readers more accustomed to the usual Cartesian index notation, we shall add a convenient rephrasing of the formulae:

$$\begin{aligned}
\mathbf{x}, \mathbf{y} &\leftrightarrow x_i, y_i, & \boldsymbol{\alpha}, \boldsymbol{\xi} &\leftrightarrow \alpha_{ij}, \xi_{ij},\\
\mathbf{x} \otimes \mathbf{y} &\leftrightarrow x_i y_k, & \boldsymbol{\alpha} \otimes \boldsymbol{\xi} &\leftrightarrow \alpha_{ij}\xi_{kl},\\
\mathbf{x}\mathbf{y} &\leftrightarrow x_p y_p, & \boldsymbol{\alpha} \cdot \boldsymbol{\xi} &\leftrightarrow \alpha_{pq}\xi_{pq},\\
\mathbf{1} &\leftrightarrow \delta_{ij} & &\text{(Kronecker's symbol)},\\
\mathbf{A}, \mathbf{H} &\leftrightarrow A_{ijkl}, H_{ijkl}, & \mathbf{H} \cdot \boldsymbol{\omega} &\leftrightarrow H_{ijpq}\omega_{pq},\\
\mathbf{A} \circ \mathbf{H} &\leftrightarrow A_{ijpq}H_{pqkl}, & \boldsymbol{\omega} \cdot \mathbf{H} \cdot \boldsymbol{\omega} &\leftrightarrow H_{pqrs}\omega_{pq}\omega_{rs},\\
\mathbf{A} \cdot \mathbf{H} &\leftrightarrow A_{pqrs}H_{pqrs}, & \boldsymbol{\sigma} = \mathbf{H} \cdot \boldsymbol{\varepsilon} &\leftrightarrow \sigma_{ij} = H_{ijpq}\varepsilon_{pq},\\
(\boldsymbol{\omega}^{\mathrm{T}})_{ij} &\equiv \omega_{ji}, & (\mathbf{H}^{\mathrm{T}})_{ijkl} &\equiv H_{klij},\\
\operatorname{tr} \boldsymbol{\omega} = \mathbf{1} \cdot \boldsymbol{\omega} &= \omega_{pp}, & \operatorname{Tr} \mathbf{A} = \mathbb{I}_{\mathcal{S}} \cdot \mathbf{A} &= A_{pqpq},\\
(\mathfrak{I} \times \mathbf{A})_{ijkl} &= A_{ijkl}, & (\mathfrak{c} \times \mathbf{A})_{ijkl} &= \frac{1}{2}(A_{ikjl} + A_{ilkj}),\\
|\boldsymbol{\omega}| = (\omega_{pq}\omega_{pq})^{\frac{1}{2}}, & & |\mathbf{H}| = (H_{pqrs}H_{pqrs})^{\frac{1}{2}}.
\end{aligned}$$

This dictionary enables one to write any formula in this paper in Cartesian index language. For example,

$$[\mathfrak{t} \times (\mathbf{1} \otimes \boldsymbol{\beta} + \boldsymbol{\beta} \otimes \mathbf{1})]_{ijkl} = \frac{1}{3}(2\delta_{ij}\beta_{kl} + 2\beta_{ij}\delta_{kl} - \delta_{ik}\beta_{jl} - \beta_{ik}\delta_{jl} - \delta_{il}\beta_{kj} - \beta_{il}\delta_{kj})$$

(see (7.4), (2.10), (2.6)).

References

1. R. MISES, *Mechanik der plastichen Formänderung von Kristallen*, ZAMM **8**, 3, 161–185, 1928.
2. R. HILL, *The mathematical theory of plasticity*, Clarendon Press, Oxford 1950.
3. J. RYCHLEWSKI, *Elastic energy decomposition and the limit criteria*, Uspekhy Mekh. (Advances in Mechanics), **7**, 3, 51–80, 1984.
4. S. FORTE, M. VIANELLO, *Symmetry classes for elasticity tensors*, Journal of Elasticity, **43**, 81–108, 1996.
5. J. P. BOEHLER, A. A. KIRILLOV jr., E. T. ONAT, *On the polynomial invariants of elasticity tensor*, J. Elasticity, **34**, 97–110, 1994.
6. J. RYCHLEWSKI, *On Hooke's law*, PMM **48**, 420–433, 1984, (English translation: Prikl. Matem. Mekhan.), **48**, 303–314, 1984.
7. J. RYCHLEWSKI, *Unconventional approach to linear elasticity*, Arch. Mech., **47**, 2, 149–171, 1995.
8. H. WEYL, *The classical groups, their invariants and representations*, Princenton University Press, Princenton 1946.
9. J. A. SCHOUTEN, *Tensor Analysis for Physicists*, Oxford University Press, London 1951.
10. I. M. GELFAND, R. A. MINLOS, Z. JA. SHAPIRO, *Reperesentation of rotation group and Lorentz group*, Fizmatgiz, Moscow 1958.
11. J.-P. SERRE, *Representations linéares des groupes finis*, Hermann, Paris 1967.
12. G. BACKUS, *A geometrical picture of anisotropic elastic tensors*, Reviews of Geophysics and Space Physics, **8**, 633–671, 1970.
13. YU. I. SIROTIN, *Decompositions of material tensors into irreducible parts*, Kristallografiya, **19**, 5, 909–915, 1974.
14. YU. I. SIROTIN, M. P. SHASKOLSKAYA, *Foundations of Cristal Physics*, Nauka, Moscow 1979 (2nd edition).
15. J. JERPHAGNON, D. CHEMLA, R. J. BONNEVILLE, *The description of the physical properties of condensed matter using irreducible tensors*, 1978.
16. J. PRATZ, *Décomposition canonique des tenseurs de rang 4 de l'élasticité*, Journal de Mécanique Théorique et Appliquée, **2**, 6, 893–913, 1983.
17. E. T. ONAT, *Effective properties of elastic materials that contain penny shaped voids*, Int. J. Engng. Sci., **22**, 8–10, 1013–1021, 1984.
18. S. C. COWIN, *Properties of the anisotropic elasticity tensor*, Q. J. Mech. Appl. Math., **42**, 249–266, 1989.
19. R. BAERHEIM, *Harmonic decoposition of the anisotropic elasticity tensor*, Q. J. Mech. Appl. Math., **46**, 3 391–416, 1993.
20. E. MOCHIZUKI, *Spherical harmonic decomposition of an elastic tensor*, Geophysical Journal, **93**, 521–526, 1988.
21. A. J. M. SPENCER, *Theory of invariants*, [In:] Continuum Physics, **1**, A. C. ERINGEN [Ed.], Academic Press, 239–353, New York 1971.
22. J. RYCHLEWSKI, J.-M. ZHANG, *On representations of tensor functions: a review*, Adv. Mech., **14**, 75–94, 1991.

23. A.-S. ZHENG, *Theory of representations for tensor functions: A unified invariant approach to constitutive equations*, Appl. Mech. Rev., **47**, 11, 545–587, 1994.

24. S. JEMIOŁO, J. J. TELEGA, *Representations of tensor functions and applications in continuum mechanics*, IFTR Reports, **3**, 3–112, 1997.

25. A. L. CAUCHY, Mém. Acad. Sci., **9**, 119, Paris 1830.

26. Ch. KITTEL, *Introdution to solid state physics*, John Wiley, New York 1956.

27. V. V. NOVOZHILOV, *Theory of elasticity*, Sudpromgiz, Leningrad 1958.

28. F. I. FEDOROV, *Theory of Elastic Waves in Cristals*, Nauka, Moscow 1965, (English ed. Plenum Press, New York 1968).

29. N. BOURBAKI, *Algébre*, Livre II, Hermann, Paris 1959.

Received May 10, 2000.

Arch. Mech., **52**, 4–5, pp. 761–777, Warszawa 2000

Probabilistic micromechanical description of fatigue crack initiation

Dedicated to Professor Zenon Mróz
on the occasion of his 70th birthday

K. SOBCZYK [1], B. F. SPENCER [2], J. TRĘBICKI [1]

[1] *Institute of Fundamental Technological Research,*
Polish Academy of Sciences,
ul. Świętokrzyska 21, 00–049 Warsaw, Poland

[2] *Department of Civil Engineering and Geological Sciences,*
University of Notre Dame,
Notre Dame, IN 46556-0767, U.S.A.

IN THIS PAPER the Mura-Nakasone model for fatigue crack initiation is extended to the situation where randomness in material microstructure (e.g. in grain size) and in the applied stress are important factors. The analysis and formulae presented provide a quantitative characterization of the effect of statistical scatter in grain size of the metals on the crack initiation time. Also, crack initiation time is analyzed for the situation where the applied stress is a narrow-band stationary stochastic process. The mean value, variance and probability distribution of the time to crack initiation are derived, and the results are illustrated graphically for real empirical data.

1. Introduction

IT IS WELL RECOGNIZED that the nucleation or crack initiation process often comprises a significant portion of the fatigue life in engineering structures. The notion of crack initiation is however, not unique; the definition depends on the scale of observation. For example, in the assessment of fatigue life in engineering design, the crack nucleation time may be associated with the number of cycles necessary to initiate a dominant (long) crack. However, for physicists and material scientists, the initiation time is usually regarded as the time in which the defects in crystals appear and microscopic flaws along the slip bands are generated. It is clear that, in order to gain a proper understanding of the entire fatigue phenomenon in engineering materials, an insight into the microscopic mechanisms of fatigue is of great importance. Development of quantitative microscopic models for crack initiation is also of practical significance, especially at low stress levels

(i.e., high-cycle fatigue) where the crack initiation period usually consumes the predominant part of the fatigue life.

Although the fatigue crack initiation phenomenon is not yet fully understood, a number of proposals have been put forward to explain the origins of fatigue cracks and to estimate the associated initiation time (for a comprehensive analysis of the existing results, see SURESH [1]). In more recent models, various dislocation mechanisms in the metallic structure play a dominant role. The approaches which seem to be especially physically sound are associated with the key role played by persistent slip bands or PSB (i.e., narrow bands with highly localized cyclic strain accumulation) and with modelling the forward and reverse plastic displacement (within PSB) by dislocations motion (cf., MURA, TANAKA [2], TANAKA, MURA [3], LIN, FINE, MURA [4] and MURA, NAKASONE [5]).

In the model of MURA and NAKASONE [5], which has methodical similarities to the Griffith theory of (macroscopic) fracture, the fatigue crack initiation life is predicted as the number of cycles necessary for the Gibbs free energy to reach the maximum value. More specifically, according to Mura and Nakasone, the accumulation of dislocations within PSB (during the load cycles) enhances the internal tensile stress which leads to an energetically unstable state of the material, and therefore, this energy has to be released via the formation of an extremely thin void, i.e., the initiation of a crack. The critical time, in terms of the number of loading cycles, is obtained by considering the balance of the elastic strain energy (enhanced by the accumulated dislocations) and the energy released via the formation of the crack embrion in the PSB. In addition to its convincing physical background and reported applications to crack initiation under contact fatigue (cf., [6]), the model of Mura and Nakasone has features which make it feasible to perform the analysis aimed at quantification of the effects of randomness present in the crack initiation mechanism. The objective of this paper is to extend the Mura and Nakasone predictions of fatigue crack initiation time to the situations when randomness in the microstructure (specifically in the grain size) and in the applied stress occur as important factors. The analysis and formulae presented in the paper provide a quantitative characterization of the crack initiation time in terms of statistical parameters (e.g., variance, higher-order moments) of the grain size and the amplitude of the randomly varying applied stress.

2. Basic features of Mura-Nakasone model

Construction of a quantitative model for crack initiation in metallic polycrystal materials based on the accumulations of dislocation dipoles in PSBs and making use of the change in the Gibbs free energy, is presented in detail by MURA and NAKASONE in Ref. [5] (cf., also the companion paper by VENKATADRYAN,

et al. [7]). Therefore, detailed derivations will not be repeated here. However, for completeness, the general idea has been presented in what follows.

The stress $s(t)$ applied across a slip plane in the material is assumed to be uniformly periodic. This applied stress causes dislocation accumulation which changes the Gibbs free energy of the system. After a certain number of cycles, this energy reaches a maximum value which is allowed to be released by forming a crack. The change in the Gibbs free energy G is (cf. [5])

$$\Delta G = -W_1 - W_2 + 2a_0\gamma_s \tag{2.1}$$

where γ_s is the surface energy of each face of the crack; a_0 is the embryonic micro-crack size; W_1 is the accumulated strain energy of dislocations after N cycles of loading; and W_2 is the elastic energy release anticipated due to the opening of an embryonic initial crack of size a_0. In general, W_2 is defined in terms of the stress intensity factors for Mode I and II, and therefore, it depends on the specific geometrical situation in question, particularly on the location of crack initiation. If the crack initiation site is far from the surface of the body, one may use the intensity factors for a crack in an infinite body. In this case, the energy W_2 can be represented in a simple analytical form (cf. [5]). The embryonic initial crack size a_0 is calculated in terms of the density of dislocations in the slip band.

Appropriate calculations give an explicit result for ΔG in the form of a quadratic function of the number of cycles N, i.e., $\Delta G = -A_1N^2 + A_2N, A_1 > 0$, where $A_1, A_2 > 0$ are constants related to the geometry, material properties, dislocation characteristics, etc. Hence, there exists a critical cycle number N^* for which ΔG takes a maximum and the system becomes unstable, i.e., when

$$\frac{\partial}{\partial N}(\Delta G) = 0. \tag{2.2}$$

Solution of the above algebraic equation yields the following expression for the number N^* of cycles to crack initiation:

$$N^* = C\frac{2-f}{(\Delta s - 2s_f)f}, \qquad C = \frac{\gamma_s}{h\left(\ln\frac{2l}{h} - \frac{3}{2}\right)f}, \tag{2.3}$$

where the following notation is introduced (cf., Fig. 1):

f	– slip irreversibility factor; $0 < f < 1$,
s_f	– frictional stress of the material,
$\Delta s = s_{\max} - s_{\min}$	– the shear stress range acting on slip layer,
h	– width of the slip band,
l	– length of the dislocation pile-up; grain size $d = 2l$.

Formula (2.3) for N^* has been obtained in [5] for an applied shear stress. For a normally applied stress, the shear stress range can be represented as

$$\Delta s = \frac{\Delta s_n}{2} \sin \alpha, \tag{2.4}$$

where $\alpha = \pi/2 - \beta$, and β is the angle between the slip band and the normal stress direction s_n.

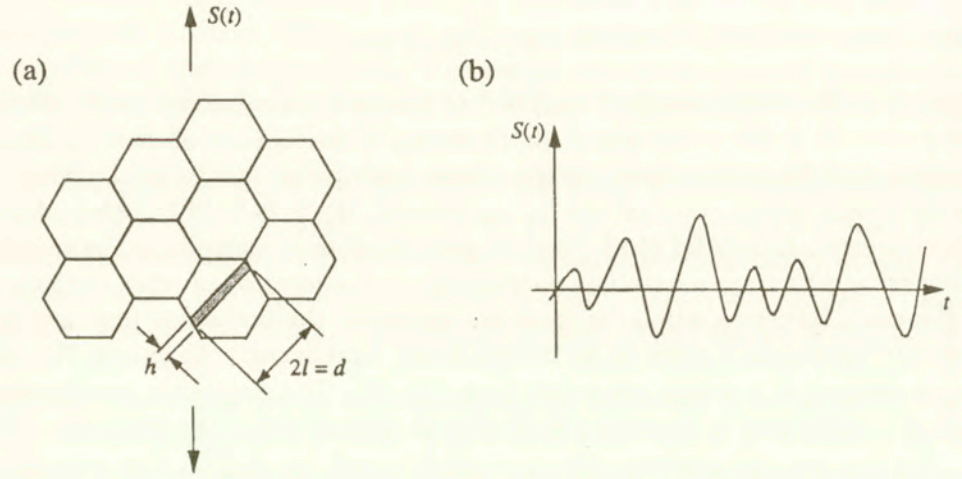

FIG. 1. a) Schematic illustration of the crystalline structure and the PSB in a crystal grain; b) A possible trajectory of a narrowband random stress process acting on the slip plane.

The formula of Mura and Nakasone (2.3) may be regarded as an $S - N$ curve on the microscopic level. It clearly exhibits an inverse relation between the number of cycles for crack nucleation and the applied stress range. The fatigue limit can be regarded as twice the frictional stress s_f of the material, i.e., no crack is initiated at stress ranges lower than s_f. Formula (2.3) also gives an explicit dependence of the crack initiation time on the grain size when the length of the persistent slip band $2l$ is regarded as the grain size. The nucleation time is greater for smaller grain sizes.

The frictional stress s_f is the resistance of material to motion of the dislocations, and its value depends on the structure of the material. For convenience in practical applications, it has been assumed (cf., [6]) that s_f can be replaced by the kinematic shear yield strength s_y. As far as the irreversibility factor f is concerned, the experimental data indicate that values of f are quite small (in the range from 10^{-4} for small plastic strain amplitudes to 10^{-1} for large strain amplitudes). In Ref. [5], the interpretation of the irreversibility factor f is related to the ability to accumulate plastic deformation in the material (e.g., if

the material is purely elastic, it has no plastic deformations, and $f = 0$), and an estimate of f from plastic strain is proposed. Since plastic strain depends on the applied stress amplitude Δs, the value of f is, in general, a function of time. Using the experimental data reported in [8] for the tension-compression tests and the power empirical equation relating f to the plastic strain ε_p, the authors of paper [6] give the following relationship: $f = c(\Delta s - 2s_f)^q$, where q is the exponent in the relation: $f \sim (\varepsilon_p)^q$.

3. Effects of randomness on crack initiation time

3.1. General remarks

As it is seen from the short description of the model of Mura and Nakasone, the crack initiation life N^* (or, $T^* = N^*/\omega_e$, where ω_e is the cyclic frequency of the applied load) depends on the basic material properties (e.g., grain size and frictional stress, which in turn depends on temperature and material hardness), the applied stress and the boundary conditions when a specific crack initiation problem is considered for a finite body. However, what has been widely recognized, an additional factor that plays a significant role is the statistical variability of the mirostructural properties. An important source of this variability is the randomness in the grain size.

In the micromechanical modelling of various phenomena (including the Mura and Nakasone model), a mean (or characteristic) grain size is usually used. However, as we have discussed previously (cf., SOBCZYK, SPENCER [9]), the mean grain diameter is not a number which can be readily derived or estimated from any single kind of metallurgical measurement. It is usually obtained by dividing the total of the mean grain diameters by the number of grains in some "representative volume". But, the mean grain size diameter always provides only a very rough information about the microstructure. Although the basic stereological relationships for the mean grain diameter are viewed as exact, the accuracy of the measurement depends on the number of grid applications and the degree of irregularity of the grains. In addition, the passage from the true spatial dimensions to their counterparts observed on planar sections involves a great loss of information (cf., [9]). Therefore, it seems to be important to incorporate into the model of Sec. 2, a more detailed information on the grain size, e.g., its statistical moments of higher order and probability distribution. Moreover, appropriate modification of the model (2.3) to include randomness in the applied stress seems to be important for wider applicability of the model.

3.2. Randomness in grain size

According to [5], the grain size in formula (2.3) expressing the initiation lifetime, is the mean grain size $d = 2l$. Therefore, the question which arises is: what form should formula (2.3) take if a more detailed information about the grain size is to be taken into account? We mean such an extension of the initiation time formula (2.3) which accounts for a more detailed characterization of the grain size, while at the same time it preserves the information contained in formula (2.3), i.e. regarding the mean grain size. A possible approach is as follows.

Equation (2.3) can be rewritten as

$$N^* = \varphi_{M,N}(d;\alpha), \qquad \varphi_{M,N}(d;\alpha) = \frac{A_0}{\ln d - B_0}, \tag{3.1}$$

where A_0 and B_0 are the following constants:

$$A_0 = \frac{\gamma_s(2-f)}{hf(\Delta s - 2s_f)}, \qquad B_0 = \ln h + \frac{3}{2}, \tag{3.2}$$

and α in (3.1) symbolizes all parameters occurring in A_0 and B_0. Let us consider the relationship

$$N^* = \varphi(X;\alpha) \tag{3.3}$$

where X is a random variable characterizing the grain size. Let us assume that the mean value $\langle X \rangle$ of X is d, the variance of X is σ_X^2, and the third and fourth central moments are denoted by m_3, m_4, respectively. Expansion of $\varphi(X;\alpha)$ in a Taylor series about the point $d = \langle X \rangle$ yields

$$N^* = \varphi(d;\alpha) + (X-d)\frac{d\varphi}{dX}\bigg|_{X=d} + \frac{1}{2}(X-d)^2\frac{d^2\varphi}{dX^2}\bigg|_{X=d} + \dots . \tag{3.4}$$

Formula (3.1) is seen to take into account only the first term in (3.4); in this sense we can say that the Mura, Nakasone formula (2.3) written in the form (3.1) constitutes a zero-order approximation of N^*. In order to account for the variance of the grain size as well as for its higher order moments, the further terms in Eq. (3.4) should be considered. Averaging of both sides of (3.4) yields

$$\hat{N}^* = \varphi(d;\alpha) + \frac{1}{2}\sigma_X^2\frac{d^2\varphi}{dX^2}\bigg|_{X=d} + \frac{1}{6}m_3\frac{d^3\varphi}{dX^3}\bigg|_{X=d} + \dots . \tag{3.5}$$

Therefore, the Mura-Nakasone formula for crack initiation time generalized in this way is

$$\hat{N}^* = \varphi(d;\alpha) + \frac{1}{2}\sigma_X^2 \frac{A_0(\ln d - B_0 + 2)}{d^2(\ln d - B_0)^3} + \frac{1}{6} m_3 \frac{A_0(2B_0 - 2\ln d - 6)}{d^3(\ln d - B_0)^4} + \ldots \tag{3.6}$$

where, according to (3.1), (3.2), the first term on the right-hand side of (3.6) is the right-hand side of the Mura, Nakasone formula (2.3).

Formula (3.6) can be written as:

$$\hat{N}^* = \varphi_{M,N}(d;\alpha)[1 + \eta(d;\alpha,\sigma_X^2, m_3, \ldots)] \tag{3.7}$$

where

$$\eta(d;\alpha,\sigma_X^2, m_3, \ldots) = \frac{1}{2}\sigma_X^2 \frac{\ln d - B_0 + 2}{d^2(\ln d - B_0)^2} + \frac{1}{6} m_3 \frac{2B_0 - 2\ln d - 6}{d^3(\ln d - B_0)^3} + \ldots . \tag{3.8}$$

For the case of uniform distribution of the grain size X in the interval $[d - \Delta, d + \Delta]$, where Δ can be regarded as a scatter parameter, we have

$$\langle X \rangle = d, \quad \sigma_X^2 = \frac{\Delta^3}{3}, \quad m_3 = d(d^2 + \Delta^2) \tag{3.9}$$

and formula (3.8) takes the form

$$\eta(d;\alpha,\sigma_X^2, m_3, \ldots) = \frac{1}{6}\Delta^2 \frac{\ln d - B_0 + 2}{d^2(\ln d - B_0)^2} + \frac{1}{6}(d^2 + \Delta^2)\frac{2B_0 - 2\ln d - 6}{d^3(\ln d - B_0)^3} + \ldots . \tag{3.10}$$

In the case of lognormal distribution of the grain size (which is a common hypothesis) i.e., when the probability density of X is

$$f_X(x) = \frac{1}{\zeta x\sqrt{2\pi}} \exp\left[-\frac{1}{2}\left(\frac{\ln x - \lambda}{\zeta}\right)^2\right], \quad 0 < x < \infty \tag{3.11}$$

where $\zeta > 0$ (λ and ζ^2 are the mean value and variance, respectively, of the normal random variable $\ln X$), formula (3.7) takes the form

$$\hat{N}^* = \varphi_{M,N}(d;\alpha)\left[1 + \frac{1}{2}\left(\exp(\zeta^2) - 1\right)\frac{\ln d - B_0 + 2}{(\ln d - B_0)^2}\right]. \tag{3.12}$$

Figures 2 and 3 visualize the effect of the uniform randomness in the grain size on the number of cycles to crack initiation (along with the Mura-Nakasone predictions).

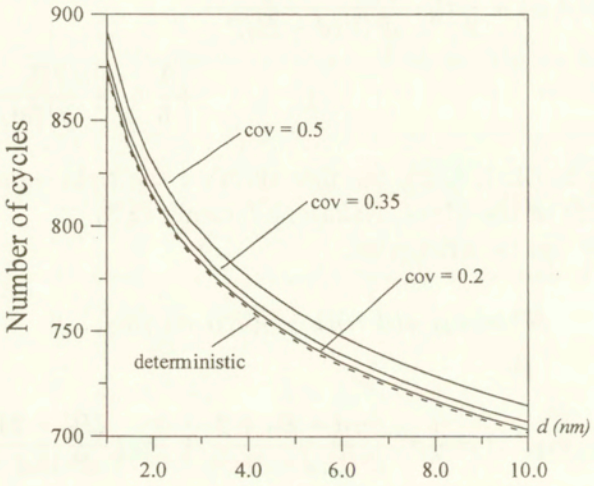

FIG. 2. Mean value of the number of cycles to crack initiation for different values of the coefficient of variation versus mean value of the grain size. Uniform distribution of the grain size is assumed.

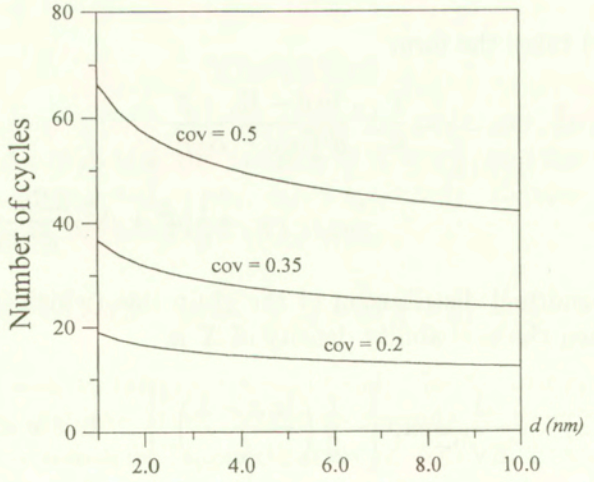

FIG. 3. Standard deviation of the number of cycles to crack initiation.

3.3. Randomness in applied stress

The model of Mura, Nakasone (2.3) has been built under the assumption of constant amplitude cyclic loading. However, most loads which are of interest in engineering practice show significant random variability. Moreover, when the model is used to predict the crack initiation time in such problems as fatigue

under contact stresses (cf., [6]), the stress amplitude Δs occurring in formula (2.3) is determined by the contact pressure p as a function of the horizontal spatial coordinate, the friction force and the residual stresses which depend on the morphology of the surface and properties of the material. These factors provide additional contributions to the random variability of the stress range. Extension of the model to a general randomly varying load which accounts for the interaction effects seem to be premature. However, accounting for a random loading seems to be possible if we restrict our attention to random processes which, in a sense, resemble harmonic oscillations with randomly varying amplitude, i.e., stationary narrow-band random processes. In this case, one can adopt the notions of an equivalent cycle and an equivalent stress range (cf., [10]).

Let us assume that a time-varying stress acting on the structural component and generating fatigue crack initiation is characterized by a narrow-band stationary random process $S(t)$ with the mean $m_S = 0$, standard deviation σ_S and spectral density $g_S(\omega)$. For a narrow-band process, the spectral density $g_S(\omega)$ has significant values over a narrow band of frequencies (around certain central frequency ω_0). The spectral content of such a process is conveniently characterized by the spectral moments λ_k and the regularity factor β (cf., [10])

$$\lambda_k = \int_{-\infty}^{+\infty} \omega^k g_S(\omega) d\omega, \qquad \beta = \frac{\lambda_2}{\sqrt{\lambda_0 \lambda_4}}. \tag{3.13}$$

If the process $S(t)$ is additionally Gaussian, then the regularity factor β is the ratio of the average number of zero-crossings by process $S(t)$ to the average number of peaks. A narrow-band process has (approximately) an equal number of peaks and zero-crossings with positive (or negative) slope, so $\beta \to 1$.

The stress range $\Delta s = H_S$ occurring in formula (2.3) in the case of a random (stationary, Gaussian) $S(t)$ can be characterized in various ways. We propose here two approximations. The first approximation is a mean range:

$$S_{\mathrm{mr}} = \langle \Delta S \rangle = \langle S_{\max} \rangle - \langle S_{\min} \rangle = 2\langle Z \rangle \tag{3.14}$$

where Z is a random height of the peaks of the stress process which has a Rayleigh probability distribution with the density

$$p(z) = \frac{z}{v^2} \exp\left(-\frac{z^2}{2v^2}\right), \qquad z \geq 0 \tag{3.15}$$

with $v = \sigma_S$. After evaluating $\langle Z \rangle$ by integration with respect to the density (3.15), we have

$$S_{\mathrm{mr}} = 2S_{\mathrm{rms}} \sqrt{\frac{\pi}{2}(1 - \varepsilon^2)}, \qquad \varepsilon = \sqrt{1 - v^2}. \tag{3.16}$$

For a narrow band process, $\varepsilon \to 0$ and one obtains

$$S_{\mathrm{mr}} = \sqrt{2\pi} S_{\mathrm{rms}} = \sqrt{2\pi}\sigma_S. \tag{3.17}$$

Therefore, the formula (2.3) of Mura and Nakasone modified in this way is

$$\hat{N}^* = C \frac{2-f}{(\sqrt{2\pi}\sigma_S - 2s_f) f}. \tag{3.18}$$

A second, more satisfactory modification of formula (2.3) is as follows. For a narrow-band random Gaussian stress process, the stress range H_S can be quantified as being equal to $2Z$. Hence, it is a random variable which has a Rayleigh distribution $p(z)$ given by (3.15) with parameter $v = 2\sigma_S$. In this case, the time to crack initiation is a random variable $T^* = N^*/\omega_e$, where ω_e is the equivalent frequency of the stress process $S(t)$. Explicitly,

$$\begin{aligned} \omega_e T^* &= N^* = C \frac{2-f}{(H_S - 2s_f) f} = C_1 \frac{1}{H_S - 2s_f}, \\ C_1 &= \frac{C(2-f)}{f}, \end{aligned} \tag{3.19}$$

where C is given in (2.3). The time to crack initiation is a positive quantity, i.e. $T^* > 0$. This implies that

$$H_S - 2s_f > 0 \tag{3.20}$$

since f occurring in (3.19) is a parameter with its possible numerical values around 0.1 in an air environment. Therefore, to satisfy the condition (3.20) the stress range H_S should have a shifted Rayleigh distribution

$$p_{H_s}(z) = \frac{z - 2s_f}{v^2} \exp\left(-\frac{(z-2s_f)^2}{2v^2}\right), \qquad z > 2s_f \tag{3.21}$$

or a conditional Rayleigh distribution $p_{\tilde{H}_s}(z|H_S > 2s_f) = p(z)/(1 - \int_0^{2s_f} p(x)dx)$ where $p(z)$ is given in (3.15). Our further considerations will be focused on the influence of the shifted Rayleigh distribution on the distribution of the time to crack initiation T^*. Due to (3.19) and (3.21), this distribution has the form

$$p_{T^*}(t) = \frac{C_1}{v^2 t^3} \exp\left(-\frac{C_1^2}{2v^2 t^2}\right), \qquad t > 0 \tag{3.22}$$

where $v = 2\sigma_S$. It is worth noting that the probability density (3.22) has no finite moments of orders higher that two. Distribution (3.22) allows us to calculate

exact values of the mean and the variance of the time to crack initiation. However, in practice, simpler formulae for mean value and variance of N^* may be useful. Using the Taylor expansion of N^* given by (3.19) with respect to the random variable H_S around the mean value $\langle H_S \rangle = h_S$ and averaging, we obtain the following results for $\langle N^* \rangle$

$$\langle N^* \rangle = \frac{C_1}{h_S - 2s_f} + 4\left(2 - \frac{\pi}{2}\right)\frac{C_1}{(h_S - 2s_f)^3}\sigma_S^2 + \ldots \tag{3.23}$$

and the first order estimate of variance $\mathrm{var}(N^*)$

$$\mathrm{var}(N^*) = (4 - \pi)\frac{C_1}{(h_S - 2s_f)^4}\sigma_S^2. \tag{3.24}$$

Since H_S has distribution (3.21) with $v = 2\sigma_S$, hence

$$\langle H_S \rangle = h_S = \sqrt{\pi v/2} + 2s_f = \sigma_S\sqrt{2\pi} + 2s_f. \tag{3.25}$$

It is seen that formula (3.18) accounts only for the first term in (3.23). The equivalent frequency occurring in (3.19) is (cf. [10])

$$\omega_e = 2\pi\langle N^+(0.1)\rangle = \frac{\lambda_2}{\sigma_S} = \frac{\sigma_{\dot{S}}}{\sigma_S}, \tag{3.26}$$

where $\langle N^+(0.1)\rangle$ is the expected number of zero-crossings with positive slope. Therefore,

$$\langle T^* \rangle = \frac{1}{\omega_e}\langle N^* \rangle, \qquad \mathrm{var}(T^*) \approx \frac{1}{\omega_e^2}\mathrm{var}(N^*). \tag{3.27}$$

4. Numerical illustration

In order to determine numerically the effect of randomness on the crack initiation time according to the formulae derived in the previous sections, typical values of the basic parameters of the model have to be specified. The micro-mechanical parameters of the model depend upon the material under consideration, the environment, the temperature etc. For example, the friction stress s_f characterizes the resistance of material to the motion of the dislocations and its value depends on the structure of the material, and usually it is affected by temperature (cf., [12]); as indicated in [6], it can be express in terms of material hardness and some empirical constants.

Here, we adopt the parameters occurring in [5]. They are as follows: $h = 0.016$ mm, $s_f = 25$ MPa $= 25$ N/mm^2, $\gamma_S = 35$ N/m, $f = 0.1$. The values of the parameters γ_S, f are characteristic for air environment. Figures 2 and 3

visualize the effect of randomness in the grain size on the number of cycles N^* to crack initiation. In these figures, the dependence of the mean value and standard deviation of the number of cycles to crack initiation on the coefficient of variation of the grain size are presented versus the mean value of the grain size, respectively. The uniform distribution of the grain size in the interval $[d-\Delta, d+\Delta]$ and the deterministic stress range $\Delta S = 100$ MPa are assumed. The mean values $\hat{N}^*$ presented in the Fig. 2 are calculated on the basis of the formulae (3.7) when only the mean value d and variance $\sigma_X^2 = \Delta^2/3$ of the grain size are taken into account, i.e.

$$\hat{N}^* = \frac{A_0}{\ln d - B_0}\left[1 + \frac{1}{6}\Delta^2 \frac{\ln d - B_0 + 2}{d^2(\ln d - B_0)^2}\right]. \tag{4.1}$$

The dashed curve presents the deterministic number of cycles to crack initiation obtained from the formulae (2.3). Figure 3 shows the standard deviations of the number of cycles $N^* = T^*/\omega_e$ when they are calculated using the following exact probability density:

$$f_{T^*}(t) = \left(\frac{A_0}{\omega_e t^2}\exp(A_0/\omega_e t) + B_0\right) f_d(\exp(A_0/\omega_e t) + B_0), \quad t > 0. \tag{4.2}$$

This density is obtained in the common way (e.g. [10]) when N^* in formula (2.3) is regarded as a function of random variable $d = 2l$ with probability density $f_d(x)$, where $x > h\exp$ (1.5) to satisfy the condition $T^* > 0$. It turns out, that the approximation (4.1) of the mean number of the cycles to crack initiation gives a very satisfactory agreement with the exact mean value $< N^* >_d = \int_0^\infty (t/\omega_e) f_{T^*}(t)dt$ calculated from the exact probability density (4.2). In the case of uniform distribution of the grain size, the relative error $R = |< N^* >_d - \hat{N}^*|/< N^* >_d$ is very small. Namely, for the considered coefficients of variation cov = 0.2, cov = 0.35 and cov = 0.5, the error R satisfies the inequalities $R < 0.01\%$, $R < 0.15\%$ and $R < 0.8\%$, respectively.

To quantify the effect of randomness in applied stress on the basis of the formulae given above, let us assume that process $S(t)$ is Gaussian and stationary with the following correlation function and the corresponding spectral density

$$K_S(t) = \sigma_S^2 \exp(-\alpha^2\tau^2), \quad g_S(\omega) = \frac{\sigma_S^2}{2\alpha\sqrt{\pi}}\exp\left(-\frac{\omega^2}{2\alpha^2}\right), \tag{4.3}$$

where $\tau = t_2 - t_1$, σ_S^2 is the variance of $S(t)$ and α is the correlation parameter characterizing the rate of correlation decay with increase of τ.

According to (3.26), the equivalent frequency is $\omega_e = 2\alpha^2$. The regularity factor, according to (3.13), is $\beta = 1.95\alpha$. To make the considered process narrow-band, we select a value for α for which the regularity factor β tends to one; therefore we take $\alpha \approx 0.5$. In this case

$$\omega_e = \frac{\sigma_{\dot{S}}}{\sigma_S} = \frac{\sqrt{2}\alpha\beta_S}{\sigma_S} = \sqrt{2}\alpha \approx 0.7. \tag{4.4}$$

Figures 4 – 6 show the probability density (3.22) of the random crack nucleation time for various numerical values of the grain size d, standard deviation σ_S

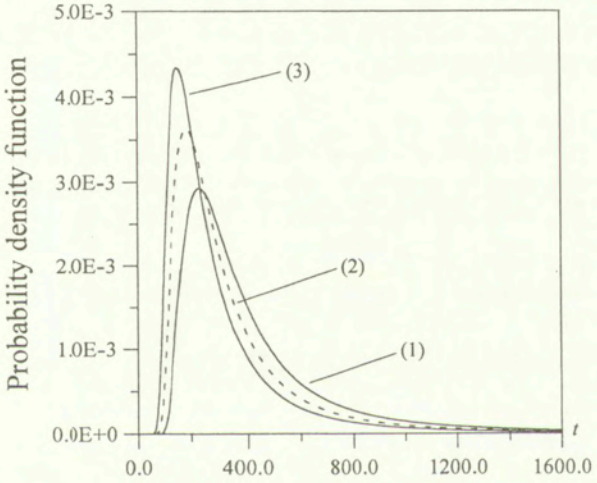

FIG. 4. Probability density of the crack initiation time for different values of grain size: (1) $d = 0.001$; (2) $d = 0.01$; (3) $d = 0.1$ mm; standard deviation of the stress process $\sigma_S = 55$ MPa.

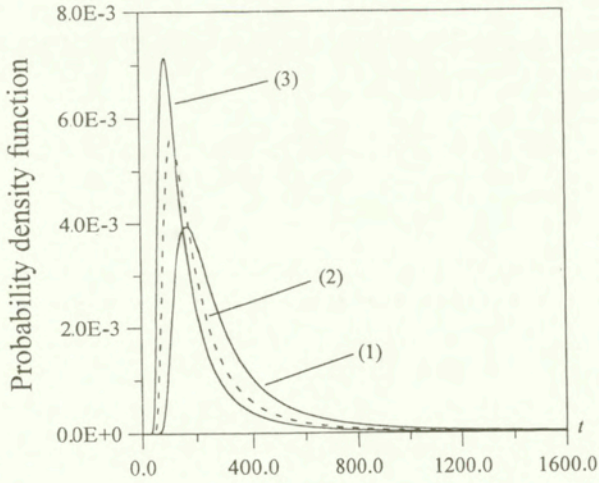

FIG. 5. Probability density of crack initiation time for different values of the standard deviation σ_S of the stress process: (1) 55.0 MPa, (2) 75.0 MPa, (3) 95.0 MPa, grain size $d = 0.05$ mm.

of the random applied stress and width of the slip-band h, respectively. The characteristic behavior of the probability $P(T^* > t) = \int_t^\infty f_{T^*}(x)dx$ of no crack nucleation for fixed time t should be underlined. For each figure given above, growth of the values of the parameters d, σ_S and h causes a decrease in the probability $P(T^* > t)$, which means an increase in the crack nucleation time. It is also interesting to notice that probability densities converge very slowly to zero in their right-hand side tails, especially for the case of the small values of the parameters d, σ_S and h.

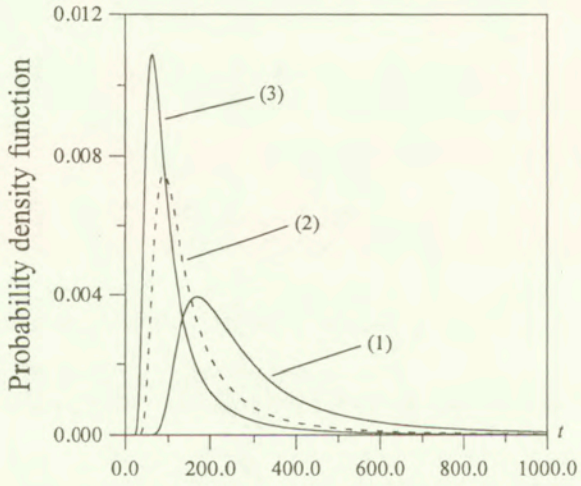

FIG. 6. Probability density of the crack initiation time for different values of the slip band width h: (1) $h = 0.016$; (2) $h = 0.032$; (3) $h = 0.048$ (nm); grain size $d = 0.05$ mm, standard deviation of the stress process $\sigma_S = 75$ MPa.

Figures 7 – 9 illustrate the exact mean value of the crack initiatin time calculated using the exact probability density (3.22), that is

$$\langle N^* \rangle_S = \langle \omega_e T^* \rangle = \omega_e \int_0^\infty t p_{H_s}(t)dt = \frac{C_1\sqrt{2\pi}}{4\sigma_S}, \quad C_1 = \frac{C(2-f)}{f}, \tag{4.5}$$

and its approximations obtained from the formula (3.23). Curve (1) presents the zero-order approximation $\hat{N}^*_{(1)}$ of $\langle N^* \rangle_S$ when only the first term in (3.23) is accounted for. Curve (2) shows the second-order approximation $\hat{N}^*_{(2)}$ of $\langle N^* \rangle_S$ when the first and second terms in (3.23) are included. According to (3.23) and (3.25), the explicit formulae for $\hat{N}^*_{(1)}$ and $\hat{N}^*_{(2)}$ are as follows:

$$\hat{N}^*_{(1)} = \frac{C_1}{\sigma_S \sqrt{2\pi}}, \tag{4.6}$$

$$\hat{N}^*_{(2)} = \frac{4C_1}{\sigma_S \pi \sqrt{2\pi}}. \tag{4.7}$$

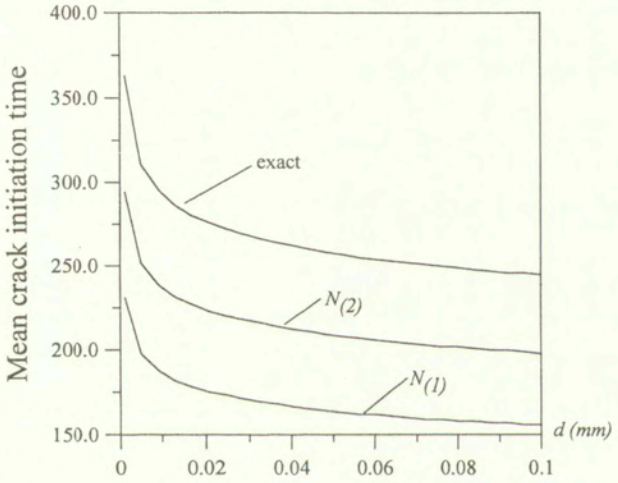

FIG. 7. Exact mean value of the crack initiation and its approximations versus different grain size when random stress process with standard deviation $\sigma_S = 55$ MPa is applied. Width of the slip band $h = 0.016$ nm.

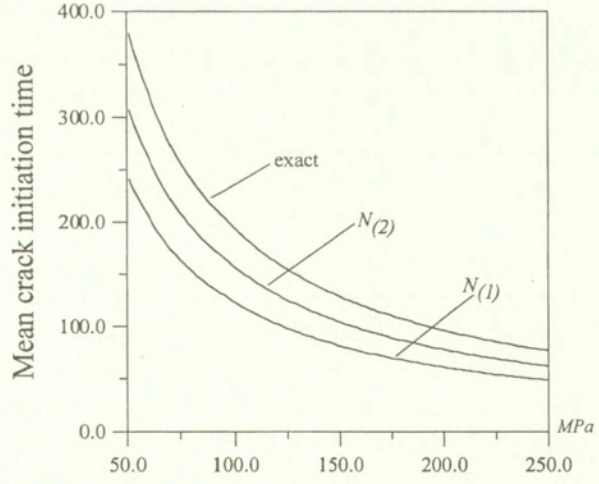

FIG. 8. Exact mean value of the crack initiation time and its approximations versus different standard deviations σ_S of the random stress process. Grain size $d = 0.05$ mm, slip band $h = 0.016$ nm.

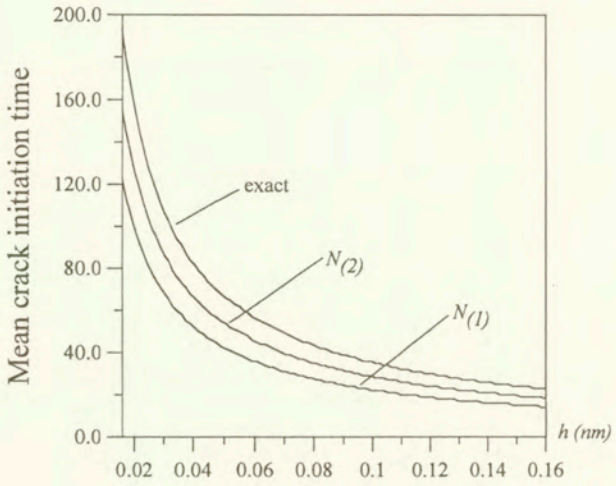

FIG. 9. Exact mean value of the crack initiation time and its approximations versus different width of the slip band h when random stresss process with standard deviation $\sigma_S = 75$ MPa is applied. Grain size $d = 0.05$ mm.

A simple calculation gives the following relationships between the exact mean value $\langle N^* \rangle_S$ and its approximations

$$\langle N^* \rangle_S = \frac{1}{2}\pi \hat{N}^*_{(1)}, \qquad \langle N^* \rangle_S = \frac{1}{8}\pi^2 \hat{N}^*_{(2)}. \tag{4.8}$$

Figures 7 – 9 and relationship (4.8) show that the approximation of the exact mean crack nucleation time, taking into account only the mean value and variance of the loading process, can not be sufficiently satisfactory. In such a case the higher order statistical moments of random loading process should be considered. Nevertheless, the approximation (4.7) seems to be a very effective and simple tool to predict the lower-bound approximation of the exact mean crack initiation time.

5. Conclusions

In the paper the fatigue crack initiation has been studied with a special attention given to the effects of a randomness in the grain size and the applied stress. Making use of the idea proposed for the deterministic case by Mura and Nakasone, we derived simple formulae for the statistical moments and probability distribution of a random crack initiation time. The numerical calculations for real material parameters show the sensivity of the initiation time to the random variations in the grain size or the applied stress.

For example, Fig. 3 shows that the coefficient of variation of grain size affects significantly the standard deviation of the initiation time. This indicates the

importance of the higher-order moments of the grain size in prediction of the initiation time. Figures 4 – 9 illustrate the dependence of various statistics of the initiation time on the basic material constants and characteristics of the applied stress obtained under various approximations. The formulae derived and the figures presented can be easily used for estimation of the crack initiation time for purposes of the reliability assessment.

Acknowledgment

This work was done partially within the research project KBN 7T07A03117 on stochastic modelling of fatigue fracture of micro-heterogeneous materials. The support is greatly acknowledged.

References

1. S. SURESH, *Fatigue of metals*, Cambridge University Press, Cambridge 1991.
2. T. MURA, K. TANAKA, *Dislocation dipole models for fatigue crack initiation*, [In:] Mechanics of Fatigue, T. MUM [Ed.], ASME AMD, **47**, 111–131, 1981.
3. K. TANAKA, T. MURA, *A theory of fatigue crack initiation at inclusions*, Metallurgical Trans., A, **113 A**, 117–123, 1982.
4. M. R. LIU, M. E. FINE, T. MURA, *Fatigue crack initiation on slip bands*, Acta Metallurgica, **34**, 619–628, 1986.
5. T. MURA, Y. NAKASONE, *A theory of fatigue crack initiation in solids*, J. Appl. Mech., ASME Trans., **57**, 1–6, 1990.
6. W. CHENG, H. S. CHENG, T. MURA, L. M. KEER, *Micromechanics modelling of crack initiation under contact fatigue*, Trans. ASME J. Tribology, **116**, 2–8, 1994.
7. C. VENKATARAMAN, Y. N. V. CHUNG, Y. NAKASONE, T. MURA, *Free energy formulation of fatigue crack initiation along persistent slip bands: calculation of S-N curves and crack depth*, Acta Metall. Mater., **38**, 1, 31–40, 1990.
8. G. T. HAHN, V. BHARGAVA, Q. CHEN, *Cyclic stress-strain properties, hysteresis loop shape and kinematic hardening of two high strength bearing steels*, Metallurgical Trans., A, **21**, 653–665, 1990.
9. K. SOBCZYK, B. F. SPENCER, *Random microstructural effects on fatigue accumulation*, Int. J. Fatigue, **17**, 8, 521–530, 1995.
10. K. SOBCZYK, B. F. SPENCER, *Random fatigue: from data to theory*, Academic Press, Boston 1992.
11. A. K-S. ANG, W. H. TANG, *Probability concepts in engineering planning and design*, **I**, John Wiley and Sons, N. York 1975.
12. T. H. COURTNEY, *Mechanical behaviour of materials*, McGraw Hill, N. York 1990.

Received January 12, 2000.

Arch. Mech., **52**, 4–5, pp. 779–798, Warszawa, 2000

On inelastic impact and dynamic hardness

Dedicated to Professor Zenon Mróz
on the occasion of his 70^{th} birthday

B. STORÅKERS and J. LARSSON

Department of Solid Mechanics
Royal Institute of Technology
S-100 44 Stockholm, Sweden

COLINEAR IMPACT AND DYNAMIC HARDNESS is analysed at spherical contact and moderate strains. A consistent three-dimensional contact theory based on viscoplastic material behaviour is laid down involving elements of self-similarity, stationary boundary conditions and cumulative superposition. Universal relations between impact velocity and the resulting contact region, impression depth and duration of impact are derived. Deformed surface shapes are shown to be self-similar for power law material behaviour and their relation to piling-up and sinking-in is explained in detail. The coefficient of restitution at rebound is estimated to first order. The concept of dynamic hardness is not unequivocally defined in general and various definitions in the literature are discussed in relation to true material rate sensitivity. Theoretical and numerical predictions of the present model are compared with pertinent experimental findings for different metals. Particular features such as lip formation, plastic zone size and maximum penetration depth are elucidated.

1. Introduction

TESTING AT HIGH STRAIN RATES has been of considerable and long standing as related to the constitutive behaviour of materials. Since there is a natural limitation in the traditional uniaxial tensile test at rapid straining, several instrumented tests of different degrees of sophistication have been developed, a prominent one being the split Hopkinson pressure bar, (cf. e.g. TIRUPATAIAH and SUNDARARJAN [30]). More conventional testing is usually carried out by forcing a hard body to strike a deformable solid by fall of gravity, a pendulum machine or a gas gun. In particular, the dynamic hardness of metals and alloys at rapid straining has been tested in this more simple way by many investigators, some also with the purpose to quantify the strain-rate sensitivity of plastic material behaviour as this constituent is needed in many applications. The conversion from measurements of an average hardness value to a constitutive equation where a general relation between stress, strain and strain-rate is to be specified is, how-

ever, not a straightforward matter. Instead, the deformation state at impact by a striking spherical ball is inherently inhomogeneous, and an a priori knowledge of material parameters is, in essence, necessary to interpret the test results properly. It is the present purpose to solve the field equations accurately at spherical impact by means of a prototype viscoplastic constitutive equation and draw pertinent conclusions from earlier experimental findings.

To add some perspective and background to the indentation theory, some momentous achievements will first be sketched briefly. BRINELL [5] invented his test by pressing a hardened ball of a given diameter and load into a solid specimen. The residual area of the imprint was then measured in order to determine the mean pressure or hardness number. MEYER [17] found empirically that for a variety of materials, a power law relation exists between the contact pressure and the radius of the spherical imprint. An extensive experimental investigation was subsequently carried out by NORBURY and SAMUEL [20] who, in particular, examined the form of the Brinell impression in the vicinity of the contact region and whether the material would be raised, piling-up, or the converse, sinking-in. Surface profiles after indentation proved to be self-similar and related to the Meyer formula for several annealed and cold-hammered metals. O'NEILL [22] showed that the Meyer exponent could be directly related to the strain-hardening properties determined by simple tensile testing. TABOR [29] made complete a fully quantitative hardness theory by means of an exhaustive output of experimental data. Two universal parameters were incorporated in the Meyer formula and a measure of representative strain was established.

The approach so far was essentially pragmatic though characterized by a thorough insight. A nonempirical theory, starting from first mechanical principles was proposed by BISHOP, HILL and MOTT [2] who assumed similarity of mode shapes at deep indentation with that of a cavity expanded by internal pressure. This point of view was further elaborated upon e.g. by MARSH [15] and JOHNSON [12]. Solutions of higher accuracy became available with the progress of finite element analysis. Perhaps the first attempt was made by AKYUS and MERWIN [1] analysing circular elastic-plastic indentation in plane strain and numerous analyses were then to follow. An analytical and computational investigation was conducted by HILL, STORÅKERS and ZDUNEK [9] of Brinell indentation of power law hardening solids. Many of the issues posed by Meyer, Norbury and Samuel, O'Neill and Tabor were then given a rigorous theoretical background. In this spirit, analyses based also on flow theory were subsequently made by STORÅKERS and LARSSON [24] for creep, BIWA and STORÅKERS [3] for strain-hardening plasticity and STORÅKERS, BIWA and LARSSON [25] for viscoplasticity.

In a section of his classical monograph, TABOR [29] discussed the case of dynamic hardness combined with experiments performed by impact of spheres mainly under the fall of gravity. Effects of a viscous nature were mentioned but

no influence of true strain-rate sensitivity was detailed. The dynamic analysis was carried out in a quasistatic manner with energy absorbed in wave motion being neglected. A measure of dynamic hardness was determined in an average sense as the quotient between the impact energy and the residual volume made by the imprint. At rebound, a coefficient of restitution was established based on Hertz theory of elastic recovery. Phenomenological though significant results were obtained for the indentation depth and duration of impact as functions of projectile velocity. Further progress was summarized by JOHNSON [13] who besides treating dynamic hardness, discussed also the concept of rebound. For one thing it was made perfectly clear that the coefficient of restitution does not only include material parameters but also depends on the indenter shape and size together with the mass and velocity of the impact.

Numerous experimental investigations have been described in the literature where dynamic hardness has been recorded as a function of impact velocity for different materials and indenter shapes, (cf. e.g. SUBHASH, KOEPPEL and CHANDRA [27]), where in particular, the impact of Vicker's pyramids is treated. In these mainly empirically based investigations, the dynamic hardness is usually compared with its static counterpart and the results depending on the indentation depth and its rate. Any attempt to relate hardness measures to the material flow stress and strain-rate dependence in this way is doomed to be empirical as a material particle in the indented solid experiences a complex history of strain and strain-rate. The celebrated constraint factor, relating hardness to flow stress, by TABOR [29] was, however, given a theoretical background by an axisymmetric solution for spherical indentation of power law hardening materials by HILL *et al.* [9], but a corresponding study for strain-rate sensitive materials is lacking and it is the present objective to provide a remedy. First a rigorous analysis is carried out of single impact of solids which exhibit strain-hardening and true strain-rate sensitivity. The theory is based on a contact analysis by STORÅKERS *et al.* [25] where the power law material behaviour was adopted a priori. The consistent impact results per se will be of interest in different applications such as ballistic penetration and particle erosion, HUTCHINGS [10]. The relation between hardness and flow stress is then discussed in some detail and conclusions are drawn regarding the constitutive behaviour due to hardening and strain-rate effects being of interest at e.g. metal forming analyses and car crash simulations. The theoretical results obtained are compared with pertinent experimental findings, but only a few investigators report also field measurements of inelastic deformation under impact load. TIRUPATAIAH and SUNDARARJAN [30] and OKA, MATSUMURA and FUNAKI [21] stand out in this respect.

2. Elements of the theory of viscoplastic contact

In an attractive monograph by MRÓZ [18], a framework was laid down for the constitutive behaviour of viscous, hardening materials. Two viscous potentials ψ, ϕ were introduced generating stresses, σ_{ij}, and strain rates, $\dot{\varepsilon}_{ij}$, as

$$\sigma_{ij} = \frac{\partial \psi}{\partial \dot{\varepsilon}_{ij}}, \qquad \dot{\varepsilon}_{ij} = \frac{\partial \phi}{\partial \sigma_{ij}} \tag{2.1}$$

related through a Legendre transformation, where

$$D = \sigma_{ij}\dot{\varepsilon}_{ij} = \psi + \phi \tag{2.2}$$

is a dissipation function. In particular, if $\psi(\dot{\varepsilon}_{ij})$ is a homogeneous function of degree $(N+1)/N$, then $\phi(\sigma_{ij})$ is by necessity homogeneous of degree $N+1$ due to the duality nature.

A popular and fairly general form of uniaxial material response adopted by MRÓZ [18] reads

$$\sigma = \sigma_0 \varepsilon^M \left(\frac{\dot{\varepsilon}}{\dot{\varepsilon}_0}\right)^N, \tag{2.3}$$

where M, N are positive exponents and σ_0 is a constitutive parameter, $\dot{\varepsilon}_0$ being a reference strain-rate. Although specialized, Eq. (2.3) may represent a wide range of material behaviour. In its complete form it reproduces primary creep, NADAI [19], or strain-rate sensitive plasticity, GHOSH [7]. In degenerated forms when $M = 0$, Eq. (2.3) reduces to Norton's law for stationary creep and when $N = 0$, to strain-hardening plasticity. Equations (2.1) to (2.3) were adopted in a multiaxial form based on von Mises flow by STORÅKERS *et al.* [25] in order to analyse indentation of viscoplastic solids. A general theory was laid down for a family of indenters, their shapes being characterized by smooth homogeneous functions. Here a brief account will be given and confined to axisymmetric indenters having a spherical shape.

In Fig. 1a, a rigid indenter having a spherical, or locally parabolic, shape within Hertzian kinematics is depicted. When formulating an associated boundary value problem, the only nonhomogeneous boundary condition reduces to

$$u_3 = h - r^2/D, \qquad x_3 = 0, \quad r \leq a. \tag{2.4}$$

With the present constitutive equation in mind, a rate formulation is necessary and accordingly by Eq. (2.4)

$$\dot{u}_3 = \dot{h}, \qquad x_3 = 0, \quad r \leq a, \tag{2.5}$$

where a dot denotes differentiation with respect to natural time.

Reduced variables were introduced a priori by

$$x_i = a\tilde{x}_i, \qquad \dot{u}_i = \dot{h}\tilde{u}_i(\tilde{x}_k) \tag{2.6}$$

which has far-reaching consequences as the boundary condition, Eq. (2.5), reduces to

$$\tilde{u}_3 = 1, \qquad \tilde{x}_3 = 0, \quad \tilde{r} \leq 1. \tag{2.7}$$

As seen in Fig. 1, the original problem having a moving boundary and thus incomplete contact is now transformed to an intermediate problem constituting indentation of a circular flat punch (Boussinesq's problem), being well suited for numerical analysis based on finite elements. The solution to the original problem based on a spherical shape may then be accomplished by simple cumulative superposition.

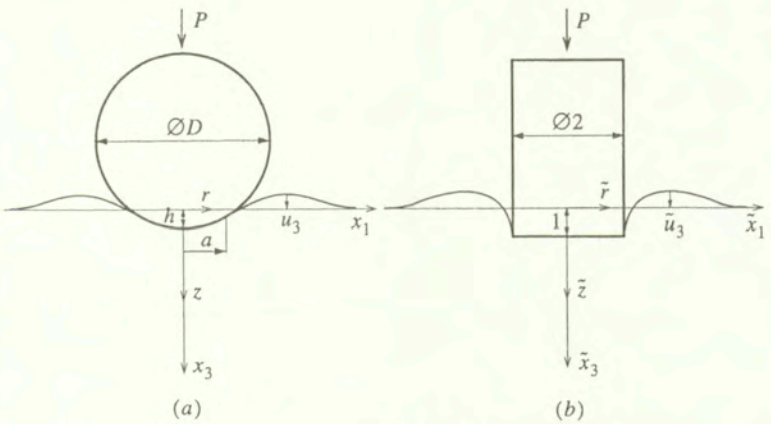

FIG. 1. a) The original contact problem (Brinell); b) The reduced, intermediate problem (Boussinesq).

HILL *et al.* [9] proved that for deformation theory of plasticity, spherical indentation possesses self-similarity for power law hardening materials. In particular it was shown that the expression

$$c_2 = \frac{a^2}{hD} \tag{2.8}$$

is an invariant where c_2 depends solely on the hardening exponent solely. In passing it may be noted that a similar relation for c_p holds true for any homogeneous shape p, STORÅKERS *et al.* [24], where for instance $p = 1$ corresponds to a cone or a pyramid.

The use of an intermediate flat die field to solve problems for a curved indenter was analysed in detail by SPENCE [23] for linear elastic materials. This procedure

was subsequently proved to hold true for normal indentation of nonlinear solids by STORÅKERS *et al.* [3, 24, 25] and more recently by LARSSON and STORÅKERS [14] for oblique indentation.

It may first be observed by introducing Eq. (2.8) into (2.4) that

$$u_3 = h(1 - c_2 r^2/a^2) \tag{2.9}$$

which physically implies that at the contact contour, either the material piles up or sinks in whether c_2 exceeds unity or not.

STORÅKERS *et al.* [25] carried out full finite element solutions to viscoplastic solids for the frictionless flat die problem and subsequently obtained results for spherical dies according to Fig. 2. Ordinarily the invariant c_2 is a general function of the material exponents but as may be seen in Fig. 2, $c_2 = c_2(M + N)$ holds within a very high accuracy. For this finding to be exact, partial proportional straining is required.

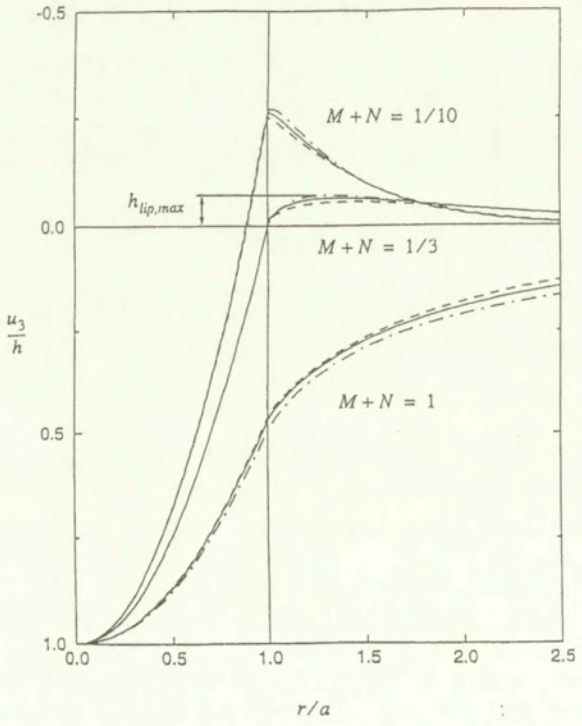

FIG. 2. Deformed surface shapes at spherical indentation of viscoplastic materials for $M + N = 1, 1/3, 1/10$; (—) general viscoplasticity ($M = N$) STORÅKERS, BIWA and LARSSON [25], (- - -) plastic flow theory ($N \to 0$) BIWA and STORÅKERS [3] (— · — · —) creep theory ($M \to 0$) STORÅKERS and LARSSON [24].

For a representative set of M, N values it was found that

$$c_2 = 1.45e^{-(M+N)} \tag{2.10}$$

constitutes a very good approximation for $0 \leq M + N \leq 1$.

Again referring to the notation in Fig. 1a it may readily be shown that the mean pressure at contact may be expressed in the form

$$\frac{P}{\pi a^2} = \sigma_0 \alpha(M,N) \left[\beta_M(M,N)\frac{a}{D}\right]^M \left[\beta_N(M,N)\frac{\dot{a}}{\dot{\varepsilon}_0 D}\right]^N, \tag{2.11}$$

where α, β_M and β_N are universal parameters to be determined. It may be noted that TABOR [29] in his classical empirical investigations of plastic strain-hardening materials correspondingly found $\alpha = 2.8$, $\beta_M = 0.4$.

From a numerical solution of representative M, N values, STORÅKERS *et al.* [25] found for viscoplastic solids that Eq. (2.11) is well reproduced by

$$\frac{P}{\pi a^2} = 3(1+2N)\sigma_0 \left(\frac{a}{3D}\right)^M \left(\frac{\dot{a}}{3\dot{\varepsilon}_0 D}\right)^N. \tag{2.12}$$

So far, the results of the analysis have been given only for a rigid spherical indenter pressed into a viscoplastic half-space. Should normal contact occur between two deforming spheres of different diameters and strength but having the same material exponents, the original results may readily be generalized by replacing the single material constant σ_0 by σ_1 and σ_2, respectively, and the diameter D by D_1 and D_2. Accordingly, STORÅKERS *et al.* [25] showed that by introducing

$$\frac{1}{\sigma_0^{1/q}} = \frac{1}{\sigma_1^{1/q}} + \frac{1}{\sigma_2^{1/q}} \tag{2.13}$$

where $q = M + N$ and

$$\frac{1}{D} = \frac{1}{D_1} + \frac{1}{D_2}, \tag{2.14}$$

then the solution for the half-space problem immediately generates a solution for the two-body problem. The matter was further discussed in more detail by STORÅKERS [26].

3. Analysis of colinear impact

For a start, the equation of motion for the mass centres of two colinearly colliding bodies yields

$$P = -m_1\dot{v}_1 = m_2\dot{v}_2 \tag{3.1}$$

with notation according to Fig. 3 and again, a dot denotes differentiation with respect to natural time.

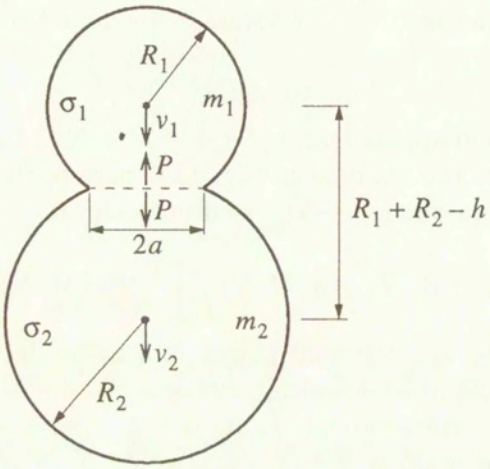

FIG. 3. Colinear collision of two dissimilar spheres.

The local velocities are then related to the approach, h, by

$$\nu_1 - \nu_2 = \dot{h}. \tag{3.2}$$

Introducing a combined mass by

$$\frac{1}{m} = \frac{1}{m_1} + \frac{1}{m_2} \tag{3.3}$$

and using Eqs. (3.1) and (3.2) yields

$$P = -m\ddot{h}. \tag{3.4}$$

At moderate velocities, when the propagation of waves may be neglected, the global constitutive Eq. (2.12) may be adopted in the form

$$P = \gamma\sigma_0 D^2 \left(\frac{h}{D}\right)^{1+(M-N)/2} \left(\frac{\dot{h}}{\dot{\varepsilon}_0 D}\right)^N, \tag{3.5}$$

where σ_0 and D are given by Eqs. (2.13) and (2.14) respectively, and where, on introducing Eq. (2.8),

$$\gamma = 3^{1-M-N} 2^{-N} (1+2N)\pi c_2^{1+(M+N)/2}. \tag{3.6}$$

Combining Eqs. (3.4) and (3.5) then yields

$$\ddot{h} + \frac{\gamma}{m}\sigma_0 D^2 \left(\frac{h}{D}\right)^{1+(M-N)/2} \left(\frac{\dot{h}}{\dot{\varepsilon}_0 D}\right)^N = 0. \tag{3.7}$$

The first integral of Eq. (3.7) gives

$$\dot{h}^{2-N} + \frac{2(2-N)\gamma\sigma_0 D^{1-(M+N)/2}}{(4+M-N)\dot{\varepsilon}_0^N m} h^{2+(M-N)/2} = C, \tag{3.8}$$

where C is a constant.

From the initial conditions $h(0) = 0$, $\dot{h}(0) = \nu_1(0) - \nu_2(0) = \nu_0$, the constant C in Eq. (3.8) becomes

$$C = \nu_0^{2-N}. \tag{3.9}$$

By Eqs. (3.8) and (3.9), the maximum approach depth, h_m, say, at rebound, $\dot{h} = 0$, follows as

$$h_m = D\left[\frac{\left(1+\frac{M+N}{2(2-N)}\right)\dot{\varepsilon}_0^2 m}{\gamma\sigma_0 D}\right]^{\frac{2}{4+M-N}} \left(\frac{\nu_0}{\dot{\varepsilon}_0 D}\right)^{\frac{2(2-N)}{4+M-N}} \tag{3.10}$$

and accordingly, the approach rate

$$\dot{h} = \dot{\varepsilon}_0 D\left[\frac{\gamma\sigma_0 D}{\left(1+\frac{M+N}{2(2-N)}\right)\dot{\varepsilon}_0^2 m}\left(\frac{h_m}{D}\right)^{2+(M-N)/2}\left(1-\left(\frac{h}{h_m}\right)^{2+(M-N)/2}\right)\right]^{\frac{1}{2-N}}. \tag{3.11}$$

By Eqs. (2.8), (3.5) and (3.11), the hardness value becomes

$$\frac{P}{\pi a^2} = \frac{\gamma\sigma_0}{\pi c_2}\left[\frac{\gamma\sigma_0 D}{\left(1+\frac{M+N}{2(2-N)}\right)\dot{\varepsilon}_0^2 m}\right]^{\frac{N}{2-N}} \left(\frac{h_m}{D}\right)^{\frac{M+N}{2-N}} \left(\frac{h}{h_m}\right)^{\frac{M-N}{2}}\left[1-\left(\frac{h}{h_m}\right)^{2+(M-N)/2}\right]^{\frac{N}{2-N}}. \tag{3.12}$$

The impact time as a function of indentation depth is given by simple quadrature of Eqs. (3.8) to (3.10) as

$$t = \dot{\varepsilon}_0^{-1}\left[\frac{\left(1+\frac{M+N}{2(2-N)}\right)\dot{\varepsilon}_0^2 m}{\gamma\sigma_0 D}\right]^{\frac{1}{2-N}} \left(\frac{D}{h_m}\right)^{\frac{M+N}{2(2-N)}} \int_0^{h/h_m} \frac{dx}{\left(1-x^{2+(M-N)/2}\right)^{1/(2-N)}}, \tag{3.13}$$

or by Eq. (3.10)

$$t = \frac{h_m}{\nu_0} \int_0^{h/h_m} \frac{dx}{\left(1 - x^{(4+M-N)/2}\right)^{1/(2-N)}}. \tag{3.14}$$

The impact time, t_m, at maximum approach, $h = h_m$, may be expressed by means of the gamma function, Γ, used in Euler's integral in Eq. (3.14), as

$$t_m = \frac{h_m}{\nu_0} \frac{2}{4+M-N} \frac{\Gamma\left(\dfrac{2}{4+M-N}\right)\Gamma\left(\dfrac{1-N}{2-N}\right)}{\Gamma\left(1 - \dfrac{M+N}{(2-N)(4+M-N)}\right)}, \tag{3.15}$$

(cf. also BORODICH [4]).

The approach time is only weakly dependent on the impact velocity. In particular at perfectly plastic contact, $M = N = 0$, the time as a function of the approach, Eq. (3.13), reduces to

$$t = \frac{2}{\pi} t_m \arcsin\left(\frac{\pi h}{2 t_m \nu_0}\right), \tag{3.16}$$

where

$$t_m = \left(\frac{\pi m}{12 c_2 \sigma_0 D}\right)^{1/2} \tag{3.17}$$

from Eqs. (3.6), (3.10) and (3.15) and accordingly, independent of the initial velocity.

TABOR [29] proposed a frequently used and simple dynamic hardness number, $H_{DT} = W/V$, in an average sense where

$$W = \frac{m\nu_0^2}{2} \tag{3.18}$$

is the energy at initial impact, and

$$V = \pi \int_0^{h_m} a^2 dh \tag{3.19}$$

is the residual imprint volume, (cf. Fig. 1a).

Based on the present theory, Tabor's hardness number may be readily determined by Eqs. (2.8), (3.10), (3.18) and (3.19) to yield

$$H_{DT} = \frac{\gamma\sigma_0}{\pi c_2 \left(1 + \dfrac{M+N}{2(2-N)}\right)} \left[\frac{\gamma\sigma_0 D}{\left(1 + \dfrac{M+N}{2(2-N)}\right)\dot{\varepsilon}_0^2 m}\right]^{\frac{N}{2-N}} \left(\frac{h_m}{D}\right)^{\frac{M+N}{2-N}}. \tag{3.20}$$

When analysing the forward contact collision at fully inelastic behaviour, the influence of elasticity was neglected. At rebound, however, purely elastic response is to be expected and will possibly prevail for the remaining duration of contact. This is not a quite straight-forward matter to analyse but a simple estimate could be made to first order.

It may first be observed that with the constitutive equation presently adopted, the load at maximum approach will vanish, Eq. (3.12), and accordingly, the rebound velocity will reduce to nil. At purely plastic impact, however, the contact force, Eq. (3.12), will attain its maximum value at the rebound event and with the pressure and conjugate elastic surface displacement distributions available, determination of the coefficient of restitution could be made to first order.

The coefficient of restitution, e, is defined as

$$e^2 = \frac{W_e}{W} \tag{3.21}$$

where again W is the impact energy at initial contact and W_e is the released energy at rebound or equivalently

$$e = \frac{\nu_e}{\nu_0}, \tag{3.22}$$

where ν_e is the velocity when the colliding particles separate.

The energy dissipated at forward motion may immediately be determined by means of Eqs. (3.18) and (3.20) to read

$$W = \frac{\gamma \sigma_0 D^3}{2 + M/2} \left(\frac{h_m}{D} \right)^{2+M/2} \tag{3.23}$$

at nonviscous contact, $N = 0$.

As to the determination of the released energy, in Fig. 4 the pressure distributions determined from flow theory by BIWA and STORÅKERS [3] are depicted for a range of values of the strain-hardening exponent M. As may be seen, they deviate considerably from the Hertzian elliptical distribution. In case of perfect plasticity, $M = 0$, the contact pressure, p_m, is approximately uniform and an analytical estimate may then be carried out.

The conjugate elastic surface displacement distribution is well known, (cf. e.g. JOHNSON [13], p. 57), and reads

$$u_z = \frac{4 p_m a}{\pi \overline{E}} E(r/a), \tag{3.24}$$

where $1/\overline{E} = (1 - \nu_1^2)/E_1 + (1 - \nu_2^2)/E_2$ and $E(r/a)$ is the complete elliptical integral of the second kind with modulus r/a. $E(0) = \pi/2$.

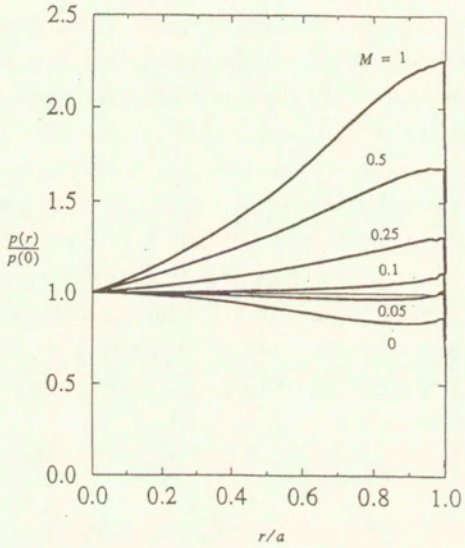

FIG. 4. Normalized contact pressure distribution when $M = 1, 0.5, 0.25, 0.1, 0.05$ and 0 for spherical contact by flow theory.

The energy loss at rebound is then simply $\pi p_m \overline{u} a^2/2$ where $\overline{u}$ is the mean displacement or explicitly

$$\overline{u} = \frac{16 p_m a}{3\pi \overline{E}}, \tag{3.25}$$

and accordingly

$$W_e = \frac{8 p_m^2 a^3}{3\overline{E}}. \tag{3.26}$$

At perfect plasticity, from the above results it may be concluded that $p_m = 3\sigma_0$, Eq. (2.12), and $a^2 = 3Rh_m$, Eqs. (2.8) and (2.10), approximately. The elastic energy loss then reduces to

$$W_e = \frac{72\sqrt{3}\sigma_0^2 (Rh_m)^{3/2}}{\overline{E}} \tag{3.27}$$

and the impact energy, Eq. (3.23), to

$$W = \frac{9}{2}\pi \sigma_0 R h_m^2 \tag{3.28}$$

if c_2 is set to 3/2.

Thus the coefficient of restitution becomes

$$e^2 = \frac{16\sqrt{3}\sigma_0}{\pi \overline{E}} \left(\frac{R}{h_m}\right)^{1/2}. \tag{3.29}$$

Since from Eq. (3.10)

$$h_m = \left(\frac{m}{9\pi\sigma_0 R}\right)^{1/2} \nu_0, \tag{3.30}$$

then by Eq. (3.30)

$$e^2 = \frac{16\sqrt{3}\sigma_0}{\pi \overline{E}} \left(\frac{9\pi\sigma_0 R^3}{m\nu_0^2}\right)^{1/4}. \tag{3.31}$$

As it has been pointed out earlier by JOHNSON [13], the restitution coefficient is not a single material parameter but depends on the geometry of contact and the mass and velocity of initial impact.

A relation similar to Eq. (3.31) was proposed by JOHNSON [13] and the difference, of the order of 20%, reduces only to a constant. This is due to the present account of piling-up and to the fact that the true pressure distribution, in contrast to the Hertzian one, was used at energy release. Some supporting experimental results by GOLDSMITH [8] are seen to be of the relation $e \sim \nu_0^{-1/4}$, Eq. (3.31), as reproduced in Johnson's monograph [13].

4. Experimental aspects and discussion

Some major assumptions and approximations introduced above in the impact analysis will be briefly discussed. The dynamic analysis was carried out with influence of wave motion neglected. This is relevant if the impact velocity is much smaller compared with the elastic wave speed. In the present context and ordinary circumstances in general, it has been estimated by JOHNSON [13] that for shallow imprints, the assumption is tolerable if the impact velocity is less than 500 m/s, approximately. More precisely, TIRUPATAIAH and SUNDARARJAN [30] found in their dynamic tests of copper and iron at recorded impact velocities of 180 m/s by WC balls of 4.67 mm diameter, that the energy loss due to stress waves was within a few per cent. Likewise TIRUPATAIAH and SUNDARARJAN [30] found that the difference between adiabatic and isothermal flow properties was of the same order.

A measure, Λ, in order to quantitatively categorize different regimes of elasto-plastic indentation was proposed by JOHNSON [12] as

$$\Lambda = \frac{Ea}{(1-\nu^2)\sigma_y R} \tag{4.1}$$

in the present notation, where σ_y is the flow stress at a representative strain magnitude

$$\varepsilon = 0.2a/R \tag{4.2}$$

as established by TABOR [29].

From an elastic-plastic finite element analysis, BIWA and STORÅKERS [3] found for a variety of representative materials, that for $\Lambda > 30$ fully plastic flow was reasonably well attained at $a/R > 0.03$. At continued indentation and increasing contact, the accuracy of the present theory based on linear kinematics deteriorates at large strains and the assumptions are less well fulfilled when a/R becomes a decade higher, (cf. MESAROVIC and FLECK [16]). The impact analysis was further carried out at vanishing frictional contact. It is well known, however, that for lumped relations such as between loading, indentation depth and contact region, frictional effects will only slightly affect the results, CARLSSON, LARSSON and BIWA [6].

As a principal finding above, the dynamic hardness value $H_D = P/\pi a^2$ was derived as a function of the indentation depth, h, by Eq. (3.12). It is clear that any effort to derive uniquely a material constraint factor to convert the experimentally determined dynamic hardness values to their static counterparts will not be successful. The mass and the radius of an impacting sphere will be essential parameters as was also the case for the coefficient of restitution, Eq. (3.30) above. A still more striking obstacle remains to relate the dynamic hardness to material flow stress-strain data. It may also be noted from Eq. (3.12) that the influence of piling-up behaviour, as governed by the invariant c_2 in Eq. (2.8), has only a weak influence of hardness when remembering the factor γ from Eq. (3.6).

Before trying to correlate the theoretical findings with experimental results, it should be stressed that by the adopted constitutive Eq. (2.3), both at initial impact and at rebound, the hardness measure vanishes when both the strain-hardening and rate sensitivity are taken into account. Remembering though that this simple prototype model comprises only three parameters to vary and to simulate a wide spectrum including especially low strain-rates, obviously the constitutive equation should include a cut-off stress.

At any instant during the impact process, h/h_m, it may be seen from Eq. (3.13), however, that the dynamic hardness is related to the absolute indentation depth, h, as

$$H_D \sim h^{\frac{M+N}{2-N}}. \tag{4.3}$$

The same dependence also follows if the present analysis is applied to Tabor's estimate, Eq. (3.20).

Using Tabor's measure of representative strain, Eq. (4.2), and the invariant, Eq. (2.8), an apparent measure of dynamic hardness can now be determined by means of Eq. (4.3)

$$H_D \sim \varepsilon^{M+N} \tag{4.4}$$

to the first order as N is ordinarily of the order of 0.1.

An extensive number of experimental investigations of inelastic impact with associated determination of hardness has been presented over the years, for a recent account cf. e.g. TIRUPATAIAH and SUNDARARJAN [31]. However, residual deformation fields are seldom measured and recorded and for this reason only the results of two investigations are examined in some detail. First an admirably careful and thorough investigation was carried out by TIRUPATAIAH and SUNDARARJAN [30] who, by the impact of spherical WC balls of diameter 4.67 mm, determined the dynamic properties of annealed copper and iron over a considerable range of impact velocities of up to 200 m/s. This was achieved by means of a gas gun for high velocities while a gravity drop tower was used for lower velocities, 10 m/s, for accuracy. Dynamic hardness was determined using Tabor's method with elastic effects neglected. Also residual surface profiles outside the contact region, lip formation, were recorded using a digital height measuring equipment with a resolution of 1 μm.

TIRUPATAIAH and SUNDARARJAN [30] observed that the hardness values showed both strain-hardening and rate-sensitivity effects. They found that the dynamic hardness was in excess of 30% compared to static values for copper in the particular circumstances prevailing. At ordinary Brinell testing the hardening exponents, M, were found for copper and iron resulting in 0.41 and 0.31, respectively. At high strain rates, up to 10^4 s^{-1}, the corresponding exponents, $M + N$, for apparent strain-hardening, Eq. (4.4), were 0.56 and 0.18 respectively. It is interesting to notice then, as was also concluded by TIRUPATAIAH and SUNDARARJAN [30], that the tests on iron exhibited strain-rate softening and accordingly, a negative value of the strain-rate exponent, N. As has already been stated, the simple form of the constitutive Eq. (2.3) may not be used for consistency for any strain-rates. In a restricted region, the theoretical predictions of Fig. 2 as regards piling-up or sinking-in and based on the exponents M, N, may be put to trial when comparing experimental recordings of lip formation. More recently, SUNDARARJAN and TIRUPATAIAH [28] determined the exponents for several more metals and alloys by impact experiments. In the data, both significant strain-rate hardening and softening, respectively, were found. However, no corresponding field measurements of deformation profiles were recorded.

In Fig. 5, the experimentally determined residual surface profiles are reproduced from the tests by TIRUPATAIAH and SUNDARARJAN [30] at representative strains of about 7%. It may first be seen that the surface heights of the two materials investigated are of different orders of magnitude and it is difficult to observe any difference between the dynamic and static results. For copper ($M = 0.41, N = 0.15$) as depicted in Fig. 5a, the developed lip profile is not very pronounced but a very modest sinking-in behaviour is perceptible. This is in accordance with the predictions shown in Fig. 2 as the relative profiles depend only on $M + N$ and when the combined exponent is 0.56, a slight sinking-in will

result. More precisely for $M = 0.5$ it was shown by BIWA and STORÅKERS ([3], Fig. 3) that the maximum lip height occurs at $r/a = 2$. In Fig. 5b where results from iron, $M + N = 0.18$, are shown, the lip profiles clearly exhibit piling-up behaviour again in agreement with Fig. 2.

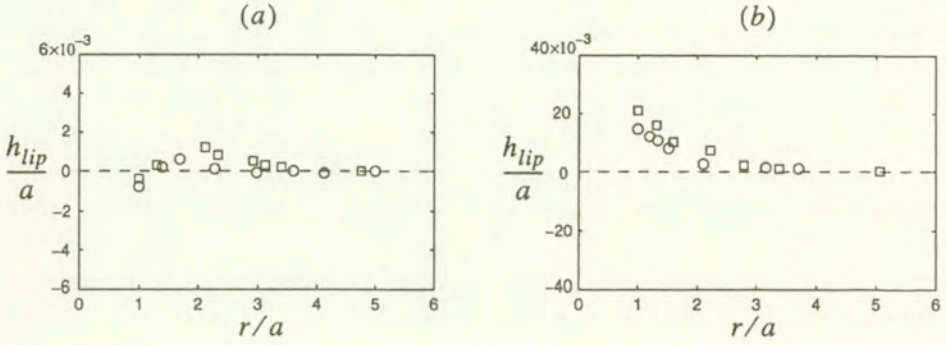

FIG. 5. Dimensionless surface profiles at dynamic impact (□) and static indentation (○); a) Copper; dynamic: $\varepsilon = 7.92\%$ and static: $\varepsilon = 7.79\%$; b) Iron; dynamic: $\varepsilon = 6.88\%$ and static $\varepsilon = 6.3\%$. Experimental data according to TIRUPATAIAH and SUNDARARAJAN [30].

TIRUPATAIAH and SUNDARARJAN [30] concluded from their experimental findings that in the case of copper, static and dynamic profiles coincided which is obvious from the background just given. For iron, however, at straining of 8%, a distinction was observed as shown in Fig. 6 where the maximum lip height is recorded as a function of representative strain by TIRUPATAIAH and SUNDARARJAN [30]. Thus strain-rate softening behaviour, $N < 0$, causes an increase in lip height as is evident in Fig. 2.

OKA, MATSUMURA and FUNAKI [21] investigated dynamic and static indentation of hard steel balls on substrates made of annealed commercially pure aluminium, iron and gray cast iron. Lip heights were recorded by a surface profilometer and strain distributions were measured by a photoengraving method. Most of the experimental observations were made at impact velocities of 200 m/s and the depth of indentations produced was indeed large, $a/R \sim 1$. This is far beyond the assumptions made in the present theory. For moderate imprints, however, dimensionless lip heights are shown in Fig. 7 reproduced from tests on aluminium and iron conducted by OKA *et al.* [21]. No quantitative conclusions may be drawn from the comparison with the present predictions, as no hardening properties were recorded. In Fig. 7a, applicable to aluminium, it may be seen that within the scatter present, the relative lip height is depth-independent, implying self-similar behaviour and that the material is strain-rate hardening. For iron, Fig. 7b, the results are less consistent but there is an indication of strain-rate softening behaviour as was the case also in the investigation made

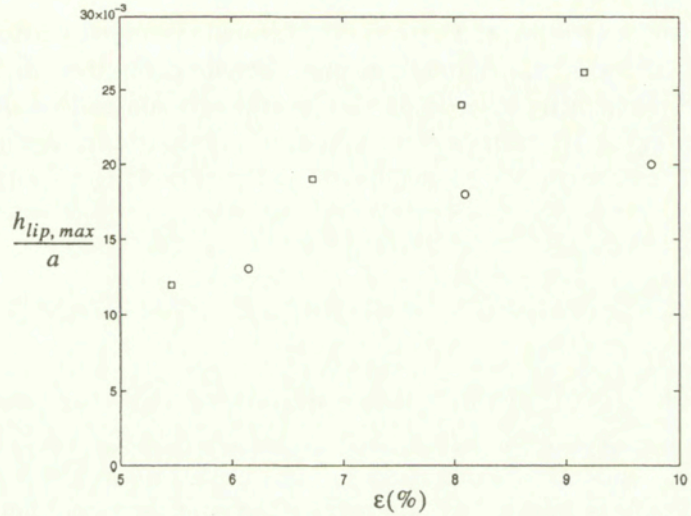

FIG. 6. Dimensionless ratio of maximum lip height to contact radius versus average strain at dynamic impact (□) and static indentation (○). Experimental data for iron according to TIRUPATAIAH and SUNDARARAJAN [30].

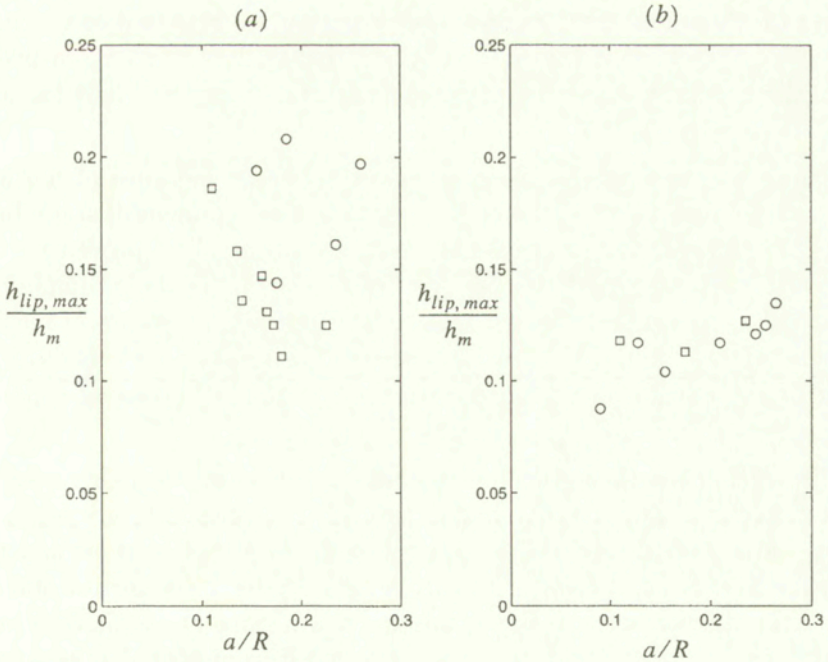

FIG. 7. Dimensionless ratio of maximum lip height to depth of indentation versus average deformation. Experimental data for dynamic impact (□) and static indentation (○) according to OKA *et al.* [21]; (a) Aluminium, (b) Iron.

by TIRUPATAIAH and SUNDARARJAN [30]. In analogy, the relative size of the plastic region increased for aluminium and decreased for iron at high strain-rates. Related phenomena may occur also in other circumstances. For instance, it has been shown by HUTCHINSON and NEALE [11] that for materials whose response is strain-rate sensitive, a considerable delay in necking at uniaxial tension arises.

5. Conclusion

Spherical impact at moderate inelastic strains was studied at quasistatic, frictionless contact by means of a three-dimensional analysis for viscoplastic solids. The constitutive equation was admittedly simple but strain-hardening and strain-rate sensitivity effects were taken into explicit account by power law exponents. A dynamic hardness measure, mean pressure resistance, was derived and it was found that besides the indentation depth, the hardness number necessarily depends on a combination of initial impact velocity, mass and radius of the projectile. Any relation between dynamic hardness and material flow stress must include these variables and also requires a full constitutive equation to be known in advance. Thus essentially, the problem posed has to be solved in an inverse manner and the present theory was intended to fill such a gap in a first tentative way.

At dynamic hardness it was shown that an apparent measure of hardness could be found simply by adding the ordinary power law exponent of static hardening to the presently introduced rate-sensitivity exponent. This proved to be in conformity with experimental findings. A crucial test of the three-dimensional analysis proved to be a correlation with experimental measurements of residual surface profiles. It was found that the presence of the strain-rate sensitivity exponent gave predictions of correct order with the compound hardening exponent introduced.

It is believed that the theoretical results are computationally highly accurate as they are based on self-similarity and a careful finite element procedure. A drawback is that the elastic effects are not taken directly into account and that the viscoplastic material law was based only on one strength parameter and two exponents. With the present purpose in mind, the influence of elasticity is not a primary issue but to improve the model, a greater range of strain-rates is more urgent. This could preferably be done by first introducing a cut-off stress. The price to be paid is that the computational work will be expected to become more cumbersome as self-similarity will be lost.

References

1. F. A. AKYUS and J. E. MERWIN, *Solution of the nonlinear problems of elastoplasticity by finite element methods*, AIAA J., **6**, 1825–1831, 1968.
2. R. F. BISHOP, R. HILL and N. F. MOTT, *The theory of indentation and hardness tests*, Proc. Phys. Soc., **57**, 147–159, 1945.
3. S. BIWA and B. STORÅKERS, *An analysis of fully plastic Brinell indentation*, J. Mech. Phys. Solids, **43**, 1303–1333, 1995.
4. F. M. BORODICH, *The Hertz frictional contact between nonlinear elastic anisotropic bodies (the similarity approach)*, Int. J. Solids Structures, **30**, 1513–1526, 1993.
5. J. A. BRINELL, *Mémoire sur les épreuves à bille en acier*, Congrés International des Méthodes d'Essai des Matériaux de Construction (Paris), tome 2, 83–94, 1901.
6. S. CARLSSON, P.-L. LARSSON and S. BIWA, *On frictional effects at inelastic contact between spherical bodies*, Int. J. Mech. Sci., **42**, 107–128, 2000.
7. A. K. GHOSH, *The influence of strain hardening and strain-rate sensitivity on sheet metal forming*, J. Eng. Mat. Tech., **99**, 264–274, 1977.
8. W. GOLDSMITH, *Impact*, London: Arnold 1960.
9. R. HILL, B. STORÅKERS and A. ZDUNEK, *A theoretical study of the Brinell hardness test*, Proc. R. Soc. Lond., **A423**, 301–330, 1989.
10. I. M HUTCHINGS, *A model for the erosion of metals by spherical particles at normal incidence*, Wear, **70**, 269–281, 1981.
11. J. W. HUTCHINSON and K. W. NEALE, *Influence of strain-rate sensitivity on necking under uniaxial tension*, Acta Metall., **25**, 839–846, 1977.
12. K. L. JOHNSON, *The correlation of indentation experiments*, J. Mech. Phys. Solids, **18**, 115–126, 1970.
13. K. L. JOHNSON, *Contact mechanics*, Cambridge University Press, Cambridge 1985.
14. J. LARSSON and B. STORÅKERS, *Oblique indentation of creeping solids*, Euro. J. Mech. A/Solids, **19**, 565–584, 2000.
15. D. M. MARSH, *Plastic flow in glass*, Proc. Roy. Soc. Lond., **A279**, 420–435, 1964.
16. S. D. MESAROVIC and N. A. FLECK, *Spherical indentation of elastic-plastic solids*, Proc. R. Soc. Lond., **A455**, 2707–2728, 1999.
17. E. MEYER, *Untersuchen über Härteprüfung und Härte*, Z. ver. deutcher Ing., **52**, 645–654, 1908.
18. Z. MRÓZ, *Mathematical models of inelastic material behaviour*, Solid Mechanics Division, University of Waterloo, Waterloo, Ontario 1973.
19. A. NADAI, *The influence of time upon creep: the hyperbolic creep law*, S .Timoshenko Anniversary Volume, McMilan Co, New York 1938.
20. A. L. NORBURY and T. SAMUEL, *The recovery and sinking-in or piling-up of material in the Brinell test, and the effect of these factors on the correlation of the Brinell with certain other hardness tests*, J. Iron Steel Inst., **117**, 673–687, 1928.
21. Y. I. OKA, M. MATSUMURA and H. FUNAKI, *Measurements of plastic strain below an indentation and piling-up between two adjacent indentations*, Wear, **186–187**, 50–55, 1995.
22. H O'NEILL, *The significance of tensile and other mechanical test properties of metals*, Proc. Inst. Mech. Engng., **151**, 116–130, 1944.

23. D. A. SPENCE, *Self similar solutions to adhesive contact problems with incremental loading*, Proc. Roy. Soc. Lond., **A305**, 55–80, 1968.

24. B. STORÅKERS and P.-L. LARSSON, *On Brinell and Boussinesq indentation of creeping solids*, J. Mech. Phys. Solids, **42**, 307–332, 1994.

25. B. STORÅKERS, S. BIWA and P.-L. LARSSON, *Similarity analysis of inelastic contact*, Int. J. Solids Structures, **34**, 3061–3083, 1997.

26. B. STORÅKERS, *Local contact behaviour of viscoplastic particles*, IUTAM Symposium on Mechanics of Granular and Porous Materials, Kluwer Academic Publishers, 173–184, 1997.

27. G. SUBHASH, B. J. KOEPPEL and A. CHANDRA, *Dynamic indentation hardness and rate sensitivity in metals*, J. Eng. Mat. Tech., **121**, 257–263, 1999.

28. G. SUNDARARAJAN and Y. TIRUPATAIAH, *The hardness-flow stress correlation in metallic materials*, Bull. Mat. Sci., **17**, 747–770, 1994.

29. D. TABOR, *Hardness of metals*, Clarendon Press, Oxford 1951.

30. Y. TIRUPATAIAH and G. SUNDARARAJAN, *A dynamic indentation technique for the characterization of the high strain rate plastic flow behaviour of ductile metals and alloys*, J. Mech. Phys. Solids, **39**, 243–271, 1991.

31. Y. TIRUPATAIAH and G. SUNDARARAJAN, *The strain-rate sensitivity of flow stress and strain-hardening rate in metallic materials*, Mat. Sci. Engng., **A189**, 117–127, 1994.

Received March 24, 2000.

Arch. Mech., **52**, 4–5, pp. 799–815, Warszawa 2000

Fatigue crack evolution in a metal reinforced by short fibres

Dedicated to Professor Zenon Mróz
on the occasion of his 70^{th} birthday

V. TVERGAARD and T. Ø. PEDERSEN[1]

Department of Solid Mechanics
Technical University of Denmark
DK-2800 Kgs. Lyngby, Denmark

IN NUMERICAL ANALYSES OF FATIGUE damage evolution in metal matrix composites, the development of final failure and the subsequent crack growth in the material are accounted for. Cell model analyses are used for aluminium reinforced by short SiC fibres, with the matrix material represented by a cyclic plasticity model, in which continuum damage mechanics is incorporated to model fatigue damage. The Bauschinger effect, ratchetting, mean stress relaxation, and cyclic hardening or softening can be accounted for by the material model, as is important in studies of low cycle fatigue. Different fibre aspect ratios and spacings are studied for different loading cases.

1. Introduction

AN INCREASE OF THE TENSILE STRENGTH and the stiffness of a metal can be obtained by a reinforcement using short brittle fibres. However, such reinforcement also leads to poor ductility and low fracture toughness. The failure mechanisms for such metal matrix composites under monotonic loading can be divided in three groups: ductile matrix failure, debonding of the matrix-fibre interface, and brittle failure of the reinforcements, as has been discussed by NEEDLEMAN *et al.* [1]. For these failure mechanisms, numerical cell model studies are well suited to obtain a parametric understanding of the effect of different material parameters, such as the fibre volume fraction, the shape and distribution of fibres, and the matrix parameters (NUTT and NEEDLEMAN [2], TVERGAARD [3, 4, 5, 6], LLORCA *et al.* [7]).

For cyclic loading, where fatigue failure or even ratchetting can develop, ALLISON and JONES [8] have reviewed experimental results on the behaviour of

[1]Present address: MAN B&W Diesel A/S, Research and Development, Teglholmsgade 41, DK-2450 København SV, Denmark

discontinuously reinforced metal matrix composities (MMC), in particular aluminium based composites. Both the matrix fatigue damage, and the effect of particle fracture and debonding at the particle-matrix interface are described in [8]. It is emphasized that the plastic strain range during cycling is the predominant factor influencing fatigue damage, and that it is important to distinguish between average strains and local strains due to the highly nonuniform straining in the two-phase materials. Experiments by LLORCA and POZA [9] for SiC particulate reinforced Al have focussed on effects of reinforcement fracture. Analyses by LLORCA *et al.* [10], using the GURSON model [11] for MMC's under cyclic loading, consider the first 9 cycles and find agreement with some of the damage features observed experimentally. However, the Gurson material model with isotropic hardening does not account for a number of important cyclic plasticity effects.

The present investigation follows the approach used by the authors [12, 13] in studies of the initial damage development for low-cycle fatigue in MMC's. These analyses are here extended to also account for final failure leading to crack formation in the matrix material. Cyclic plasticity in metals can be described by various more complex material models such as the fraction model of BESSELING [14] or the multisurface kinematic hardening model of MRÓZ [15]. The description here is based on a nonlinear kinematic hardening rule (ARMSTRONG and FREDERICK [16], LEMAITRE and CHABOCHE [17]), using a superposition of isotropic hardening and kinematic hardening, for which it has been found that the Bauschinger effect, cyclic hardening or softening, ratchetting, and mean stress relaxation can be described. With continuum damage added to this model (LEMAITRE [18]), fatigue damage evolution can be described, and the particular fatigue model to be used here has been employed by PEDERSEN [19, 20] to study fatigue failure in cold-forging tools. A similar model has been used in [21] to study the creep-fatigue interaction.

Only the matrix fatigue failure is considered in the present study, so that perfect bonding is assumed between the matrix and fibres, and the possibility of fibre fracture is neglected. However, with short fibre reinforcement plastic yielding in the matrix starts early, and there is a wide range of cyclic loads for which fatigue life is mainly controlled by the matrix fatigue characteristics [8].

It should be noted that a damage model directly based on the micromechanics of the failure mechanism would be preferable, but such a model for growing microcrack density during cyclic plasticity has not been developed. Also, the continuum damage model with a single scalar damage parameter cannot describe the orientation effects associated with microcracks. However, a number of studies of low cycle fatigue in structural components have shown that the model has good predictive abilities.

2. Problem formulation and material model

The evolution of fatigue damage and fatigue crack formation in a metal reinforced by short fibres is here studied by analysing a unit cell containing a single fibre. The material with the periodic array of aligned fibres shown in Fig. 1 is modelled approximately by an axisymmetric cell model proposed by TVERGAARD [22]. It was found in [22] that this fibre arrangement gives a better agreement with experimental uniaxial stress-strain curves found by CHRISTMAN *et al.* [23] than that obtained by considering a simpler cell model representing transversely aligned fibres. The square array of fibres shown in Fig. 1b has the fibre spacing $2a_c$, and the initial radius $r_c = (2/\sqrt{\pi})a_c$ of the axisymmetric model is chosen such that the fibre volume fraction f of the cell is equal to that of the material in Fig. 1

$$f = \frac{r_f^2 \ell_f}{r_c^2 \ell_c} \tag{2.1}$$

Here, ℓ_f and r_f are the fibre half-length and radius, respectively, ℓ_c is the cell length, and the aspect ratios of the fibre and cell are

$$\alpha_f = \ell_f / r_f, \qquad \alpha_c = \ell_c / r_c. \tag{2.2}$$

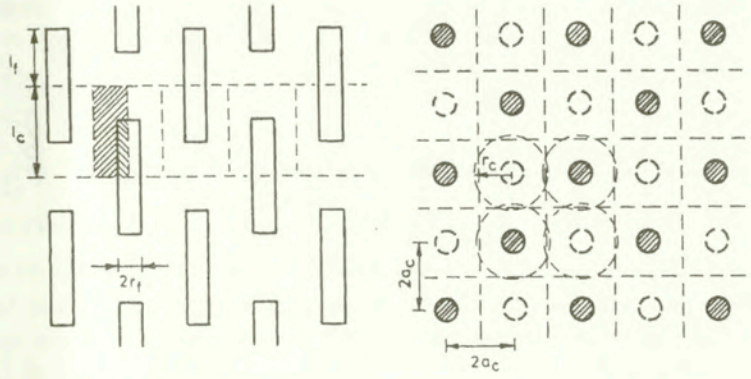

FIG. 1. Periodic array of aligned, transversely staggered fibres. a) cross-section along fibres; b) cross-section normal to fibres.

The major average principal stress σ_1 in the composite is taken to be in the axial direction, and due to the assumed axisymmetry only the cases with a uniform transverse average stress σ_2 can be considered. In the cases to be analysed, a fixed ratio between the axial and transverse average stresses is assumed

$$\sigma_2 = \rho \sigma_1. \tag{2.3}$$

The boundary conditions at the flat ends of the unit cell are straightforward, but on the curved side of the circular cylindrical cell, equilibrium and compatibility with the neighbouring cells has to be represented approximately. As is seen in Fig. 1a, a neighbouring cell is identical to that analysed, but points in the opposite direction. The detailed formulation of these boundary conditions can be found in TVERGAARD [22].

In the following analyses the matrix is modelled by the cyclic plasticity model with fatigue damage, while the fibres are taken to be elastic with Young's modulus E_f and Poisson's ratio ν_f. Furthermore, perfect bonding is assumed between the matrix and fibres, and the possibility of fibre fracture is neglected. Thus, the only type of failure accounted for is the fatigue damage evolution incorporated in the cyclic plasticity law used for the matrix.

The analyses in the present work are based on a small strain formulation of the field equations, since the geometry changes are typically small in fatigue situations, even though the accumulated plastic strain p can grow large. The total strain increment is given by the sum of the elastic and plastic parts, $\dot{\epsilon}_{ij} = \dot{\epsilon}^e_{ij} + \dot{\epsilon}^p_{ij}$. The elastic stress-strain relationship is described by Hooke's law as $\dot{\sigma}_{ij} = L_{ijkl}\dot{\epsilon}^e_{kl}$, where the summation convention is adopted for repeated indices, σ_{ij} is the stress tensor, and the elastic constants for the matrix denoted E and ν.

The plastic strain increment follows the normality rule, $\dot{\epsilon}^p_{ij} = \dfrac{\partial f}{\partial \sigma_{ij}}\dot{\lambda}$, where the plastic multiplier, $\dot{\lambda}$, is obtained from the consistency condition, $\dot{f} = 0$. A Mises yield surface with mixed hardening is used, as specified by

$$f = \tilde{\sigma}_e - (R + k) = 0, \tag{2.4}$$

where the stress state is described by the effective stress tensor, $\tilde{\sigma}_e = (3\tilde{s}_{ij}\tilde{s}_{ij}/2)^{1/2}$, in terms of the effective stress deviator $\tilde{s}_{ij} = \tilde{\sigma}_{ij} - \dfrac{1}{3}\delta_{ij}\tilde{\sigma}_{kk}$. Here, $\tilde{\sigma}_{ij} = \sigma_{ij}/(1 - D) - X_{ij}$, where D is a scalar describing the amount of damage in a material point (LEMAITRE [18]). The kinematic hardening is governed by the back-stress tensor, X_{ij}, representing the centre of the yield surface in the stress space.

The size of the yield surface is described by the scalars R and k. Here, k is a constant and R a variable, which is used for describing the isotropic hardening or softening of the material. The initial conditions of a cyclic hardening material are described by $k = \sigma_y$ and $R = 0$, where σ_y denotes the initial yield stress. The evolution equation for the variable R is described as

$$\dot{R} = b(R_\infty(\Lambda, q) - R)\dot{\lambda}, \tag{2.5}$$

where b is a material parameter and the value $R_\infty(\Lambda, q)$ represents the limit of isotropic hardening or softening, as described in more detail in [24, 25]. The influ-

ence of the nonproportionality of the loading path on the softening or hardening of the material is described as suggested by BENALLAL *et al.* [26].

The kinematic hardening of the material is described by means of the back-stress tensor, X_{ij}, which is taken to be the sum of three contributions, in order to enhance the description of the material stress-strain response

$$X_{ij} = \sum_{n=1}^{3} X_{ij}^{(n)}. \tag{2.6}$$

Each of the back-stress tensors, $X_{ij}^{(n)}$, follow an evolution equation suggested in [16], and modified in [27] to enhance the description of ratchetting. The evolution equation for the back-stress deviator X_{ij}^{D} is of the form

$$\dot{X}_{ij}^{D(n)} = \frac{2}{3}\gamma^{(n)} X_{\infty}^{(n)} \dot{\epsilon}_{ij}^{p} - \left[\frac{X_e^{(n)}}{X_{\infty}^{(n)}}\right]^{m_n} X_{ij}^{D(n)} \gamma^{(n)} \dot{\lambda}, \tag{2.7}$$

where the effective back-stress is $X_e^{(n)} = \left(\frac{3}{2} X_{pq}^{(n)} X_{pq}^{(n)}\right)^{1/2}$. The parameters in (2.7) and the representation of ratchetting are further described in [20, 12].

The scalar, D, which is incorporated in the constitutive equations as outlined by LEMAITRE [18], is used to describe the development of fatigue damage in the material. For an undamaged virgin material, $D = 0$, but when the accumulated plastic strain, p, reaches a threshold value p_d, damage starts developing in the sense of microvoids or microcracks. As it reaches a critical value D_c, the material has a high density of microcracks, which are likely to coalesce into a macrocrack leading to failure of the structural component. The damage development is described by

$$\dot{D} = \frac{Y}{S} \dot{p} \alpha(p), \qquad \alpha = \begin{cases} 1, & \text{if } p \geq p_d \\ 0, & \text{if } p < p_d \end{cases} \tag{2.8}$$

where S, is a material parameter describing the energy strength of damage. The effective plastic strain increment is determined as $\dot{p} = \left(\frac{2}{3}\dot{\epsilon}_{ij}^{p}\dot{\epsilon}_{ij}^{p}\right)^{1/2}$, which gives $\dot{p} = \dot{\lambda}/(1-D)$. The strain energy release rate is given by $Y = \sigma_e^2 R_V/(2E(1-D)^2)$, where the effective stress is denoted by σ_e, and the triaxiality of the stress field is accounted for by the parameter R_V, which is here taken to be specified by

$$R_V = \begin{cases} 1 + C\dfrac{\sigma_{kk}}{\sigma_y}, & \sigma_{kk} \geq 0, \\ \exp\left(C\dfrac{\sigma_{kk}}{\sigma_y}\right), & \sigma_{kk} < 0. \end{cases} \tag{2.9}$$

The material parameter C is adjusted to describe the mean stress sensitivity of fatigue damage development [19], such that fatigue is more pronounced under tensile loading than under compressive loading.

The gradual formation of a crack in the matrix material around fibres, as the damage parameter D reaches the critical value D_c, is described here by using a numerical techinque. In the previous investigations [12, 13] by the authors, only the initial stages of damage development were considered, so that the peak value of D had not exceeded D_c.

The form of the incremental constitutive relations resulting from this material description for cyclic plasticity with fatigue damage has been given in detail in [12]. This material model for the metal matrix has as many as 23 material parameters, which have to be determined by experiments for the matrix material. Among these, E and ν are the elastic constants, while S, p_d, D_c and C characterize the damage evolution, and the remaining 17 parameters are used to describe cyclic plastic deformations, including the Bauchinger effect, cyclic hardening or softening, ratchetting, and mean stress relaxation. Cyclic plasticity is complex and these many parameters are necessary to give an adequate description, as has been explained in a number of the papers cited above.

Numerical solutions are obtained by a finite element approximation, using a linear incremental method based on the principle of virtual work, as explained in [12]. An example of a mesh used for one of the numerical analyses is shown in Fig. 2, with the hatched region representing the fibre. The mesh consists of quadrilaterals, each built up of four crossed triangular elements with linear displacement assumption. A special Rayleigh-Ritz finite element method [28] is used to implement the boundary conditions and to enforce the fixed stress ratio (2.3).

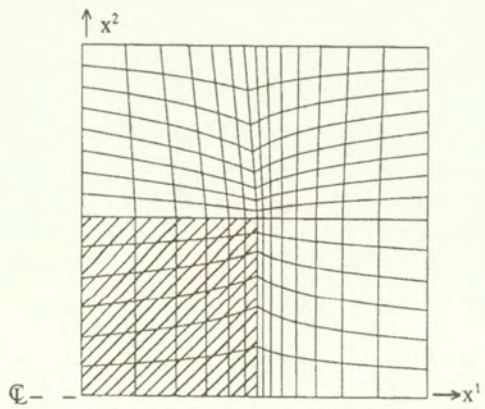

FIG. 2. Mesh used for some of the numerical computations.

The fatigue crack development is incorporated in the computations by using an element vanish technique [29]. Thus, when $D = D_c$ is reached in a triangular element, the stiffnes matrix for this element is set to zero, and the nodal forces corresponding to the remaining stresses in the element are stepped down to zero over a number of subsequent increments.

3. Results

The material values used here to represent the aluminium matrix are $k/E = 0.002$ and $\nu = 0.33$, and $b = 7.0$, $R_{\infty,s}/E = 0.012$, $R_0/E = 0$, $\alpha_R = 0.3$, $\beta_R = 160$, $\gamma_R = 0.5$ and $C_q = 0.5$. Furthermore, in the back-stress evolution equations (2.6) - (2.7), the parameter values used are $\gamma^1 = 400$, $\gamma^2 = 50$, $\gamma^3 = 2000$, $X^1_\infty/E = 0.0008575$, $X^2_\infty/E = 0.00142$, $X^3_\infty/E = 0.000285$, $m_1 = 3$, $m_2 = 3$ and $m_3 = 3$, as in [12]. In the damage evolution equations (2.8) - (2.9), the parameter values are $S/E = 0.000024$, $p_d = 0.03$, $D_c = 0.12$ and $C = 0.04$. Furthermore, the elastic constants of the SiC fibres are specified by $E_f/E = 5.71$ and $\nu_f = 0.21$ (see TEPLY and DVORAK [30]). For a rather soft aluminium most of the parameters needed in the cyclic plasticity model have been specified by HOPPERSTAD [31]. These values are used here, but the values of k and the parameters specifying the kinematic hardening have been modified to better represent the aluminium with higher hardness used by CHRISTMAN *et al.* [23]. Furthermore, while HOPPERSTAD [31] used 2 terms in the sum (26), 3 terms are used here to obtain a more smooth transition from elastic to elastic-plastic deformation. The values of S, p_d and D_c are partly based on data given by LEMAITRE [18], and finally the value of C is chosen to be reasonably representative of the measured mean stress dependence for high cycle fatigue of aluminium.

Figure 3 shows the overall stress-strain loops predicted for a particulate reinforced material with the aspect ratios $\alpha_f = \alpha_c = 1$ and the fibre volume fraction $f = 0.13$. Here a uniaxial cyclic stress is prescribed, $\rho = 0$, using stress-controlled loading with balanced cycling, $\sigma_{\max}/E = -\sigma_{\min}/E = 0.0036$. In this kind of test, strain ratchetting is possible and is in fact often observed [8], as has been discussed in [12]. In Fig. 3, where 27 loops have been reached, the first several loops show a slow movement of the mean strain in the negative direction, i.e. some ratchetting due to the hardening behaviour. But the most significant feature of this figure is the result of final failure development, which gives much larger strain amplitudes in the last loop, and also significantly reduced slopes on the elastic parts of this loop. Towards the end, the stress-strain curve is somewhat jumpy as a result of the gradual failure evolution, which is represented in the solution by using the element vanish technique.

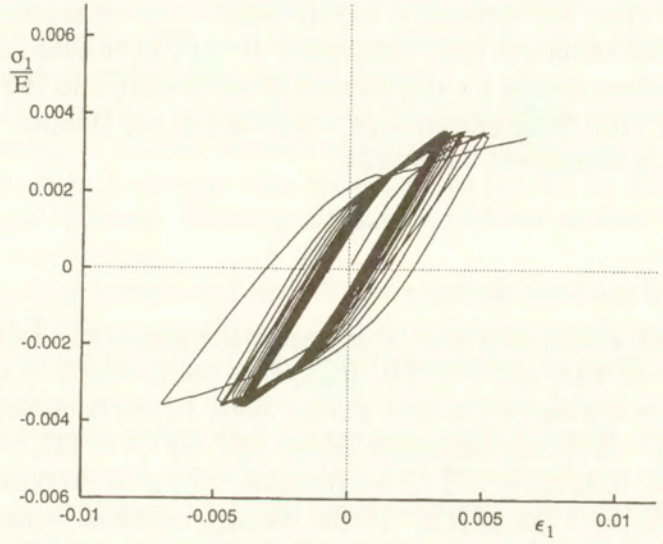

FIG. 3. Overall stress-strain loops for 27 cycles with balanced stress-controlled cycling, $\sigma_{\max}/E = -\sigma_{\min}/E = 0.0036$. Here, $f = 0.13$, $\alpha_f = \alpha_c = 1$ and $\rho = 0$.

Figure 4 shows the distribution of damage at two stages of the solution, i.e. for $\epsilon_1 = -0.0013$, $\sigma_1/E = -0.0019$, during loop No. 22, and for $\epsilon_1 = 0.0060$, $\sigma_1/E = 0.0034$, during loop No. 27, just near the end of the curve shown in Fig. 3.

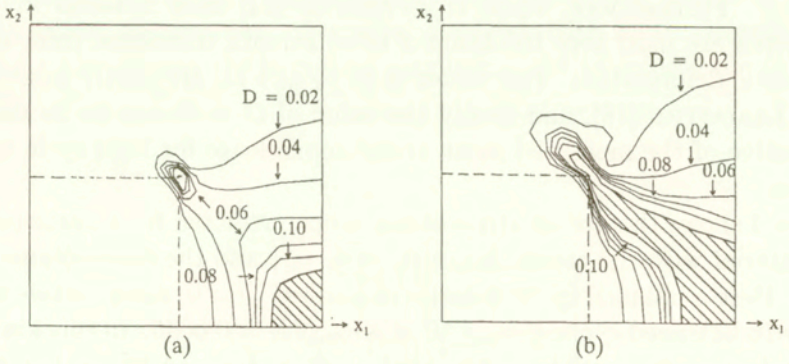

FIG. 4. Contours of constant damage, for balance stress-controlled loading, $\sigma_{\max}/E = -\sigma_{\min}/E = 0.0036$, with $f = 0.13$, $\alpha_f = \alpha_c = 1$ and $\rho = 0$. a) at $\epsilon_1 = -0.0013$, $\sigma_1/E = -0.0019$, during loop No. 22; b) at $\epsilon_1 = 0.0060$, $\sigma_1/E = 0.0034$, during loop No. 27.

The distributions of damage D are shown by the contour curves, and regions where final failure has occured are shown hatched. The location of the particulate is indicated by dashed lines, and it should be noted that the apparent small amount of damage inside the sharp fibre edge is due to a plotting inaccuracy

resulting from averaging in the plotting programme. The distribution of the damage fields is quite similar to the results shown in [12], but the present results are extended to also show the onset of final failure in the matrix material and the subsequent crack growth. Figure 4a shows that failure has first developed at the axis of the cylindrical cell, centrally between two fibre ends, while failure at the sharp fibre edge is just initiating. In Fig. 4b these two failure regions have grown together, forming a crack that significantly reduces the strength of the cell, as is also seen in the last loop of the stress-strain curve in Fig. 3.

Figures 5 and 6 show analogous results for a larger particle volume fraction, $f = 0.35$, with the same values of the material parameters for the matrix and particles. The larger stiffness due to the higher reinforcement volume fraction results in a smaller overall strain range corresponding to the same stress amplitudes. Here, 70 loops have been reached, and the end of the curve shows that final failure is developing under monotonic elongation, without reaching the prescribed tensile stress amplitude in this last loop. The damage distributions in Fig. 6 correspond to two rather late stages, at $\epsilon_1 = 0.00041$, $\sigma_1/E = 0.00067$, during loop No. 67, and at $\epsilon_1 = 0.0052$, $\sigma_1/E = 0.0026$, during loop No. 70. In Fig. 6a only a tiny region of final failure has developed at the sharp particulate edge, but there is a high level of damage in a large material region at the plane of symmetry between two particle ends. Just three loops later Fig. 6b shows that much material has failed completely, and that the two open cracks have nearly linked up.

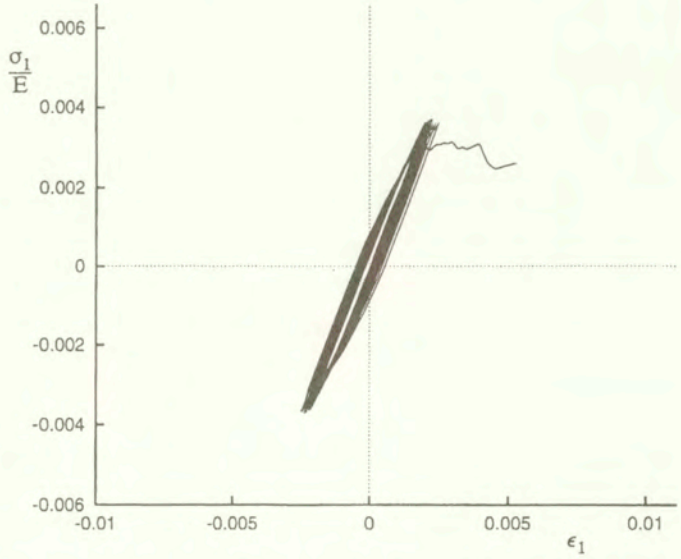

FIG. 5. Overall stress-strain loops for 70 cycles with balanced stress-controlled cycling, $\sigma_{\max}/E = -\sigma_{\min}/E = 0.0036$. Here, $f = 0.35$, $\alpha_f = \alpha_c = 1$ and $\rho = 0$.

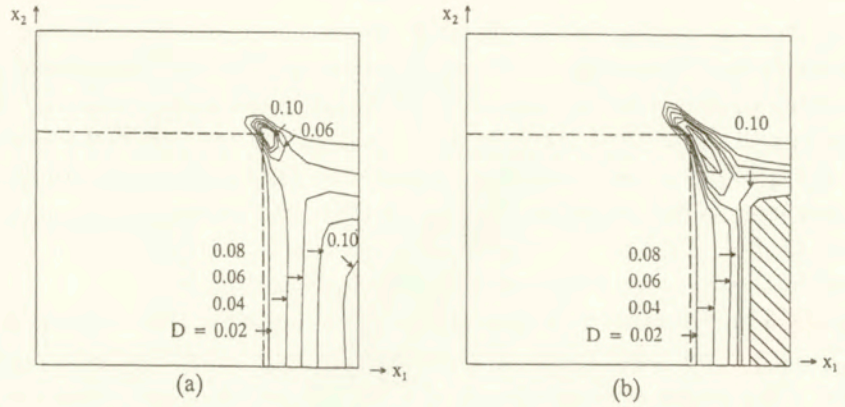

FIG. 6. Contours of constant damage, for balanced stress-controlled loading, $\sigma_{\max}/E = -\sigma_{\min}/E = 0.0036$, with $f = 0.35$, $\alpha_f = \alpha_c = 1$ and $\rho = 0$. a) at $\epsilon_1 = -0.00041$, $\sigma_1/E = 0.00067$, during loop No. 67; b) at $\epsilon_1 = 0.0052$, $\sigma_1/E = 0.0026$, during loop No. 70.

It is noted that the last part of the overall stress-strain curve shown in Fig. 5 would not be stable if a monotonically increasing load was prescribed. In the computations it has been assumed that a low constant strain rate is prescribed (for quasi static behaviour), and that the sign of the strain rate is reversed when the prescribed overall stress amplitude has been reached.

Again for the same values of the material parameters and stress amplitudes, and for $f = 0.13$ as in Figs. 3 and 4, results for higher aspect ratios of the fibre and the unit cell, $\alpha_f = \alpha_c = 2$, are shown in the next two figures. As expected, the longer fibres give higher overall stiffness, which leads to a somewhat smaller overall strain range than that found in Fig. 3, but the stress-strain loops in Fig. 7 still show clearly that the slopes are reduced in the last loop, due to the failure evolution. The damage field at a stage near the end of the solution, at $\epsilon_1 = 0.0039$, $\sigma_1/E = 0.0030$, during loop No. 27 (i.e. the last loop), is illustrated in Fig. 8. Here, the region of final failure has initiated at the sharp fibre, edge, and is currently extended on both sides of this point. It is seen that the maximum damage level along the axis of the cylindrical cell had been reached about one fibre radius ahead of the fibre end, but that the region of final failure is closer to the flat fibre end than indicated by the initial damage distribution.

Also a case of still larger aspect ratios, $\alpha_f = \alpha_c = 4$, has been analysed under the same balanced uniaxial cyclic stress. This gives still more narrow hysteresis loops, more like those shown in Fig. 5. Here, we only show the damage fields and the distribution of final failure in Fig. 9, at $\epsilon_1 = 0,0025$, $\sigma_1/E = 0.0028$, during loop No. 29 (the last loop). This figure shows that the failure distribution near the end of the longer fibre is very similar to that found for $\alpha_f = \alpha_c = 2$.

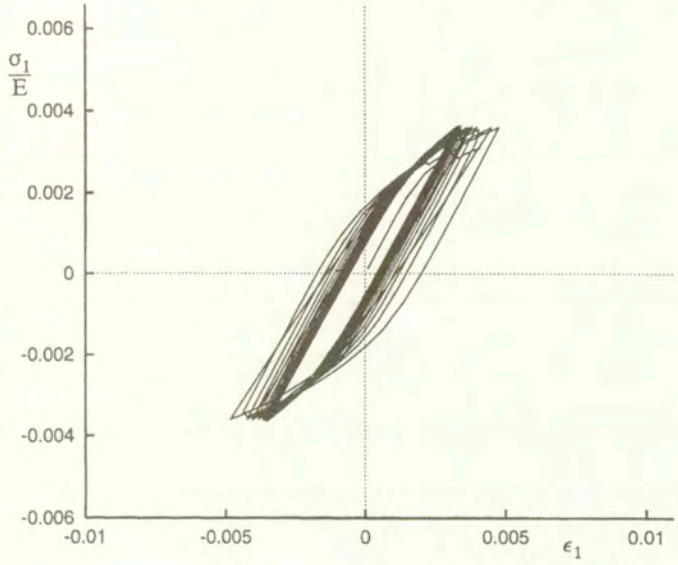

FIG. 7. Overall stress-strain loops for 27 cycles with balanced stress-controlled cycling, $\sigma_{\max}/E = -\sigma_{\min}/E = 0.0036$. Here, $f = 0.13$, $\alpha_f = \alpha_c = 2$ and $\rho = 0$.

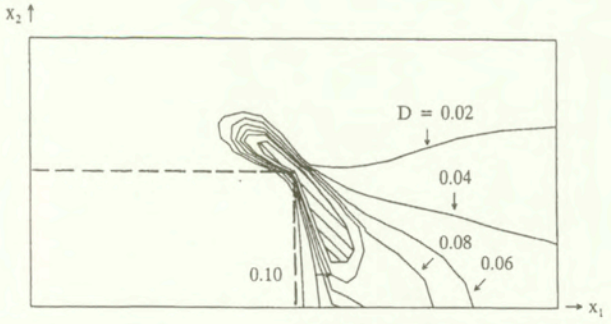

FIG. 8. Contours of constant damage, for balanced stress-controlled loading, $\sigma_{\max}/E = -\sigma_{\min}/E = 0.0036$, with $f = 0.13$, $\alpha_f = \alpha_c = 2$ and $\rho = 0$. At $\epsilon_1 = 0.0039$, $\sigma_1/E = 0.0030$, during loop No. 27.

The effect of stress triaxiality is considered in Figs. 10 and 11, where transverse tension is specified by $\rho = \sigma_2/\sigma_1 = 0.25$ The material is the same as that studied in Figs. 7 and 8, with $\alpha_f = \alpha_c = 2$, but higher stress amplitudes are used here, $\sigma_{\max}/E = -\sigma_{\min}/E = 0.0048$, since an important effect of the increased stress triaxially is that higher stress levels are required to give plastic yielding. The stress-strain loops in Fig. 10 show the same trends at those found in the previous cases, under cyclic uniaxial stress. Thus, the strain range is gradually reduced in the first cycles due to the hardening behaviour, and some ratchetting in the negative direction takes place, while in the last loops the strain range

increases again, due to the evolution of damage and final failure in the matrix material. Figure 11 shows the damage fields and the region of final failure in the last loop (i.e. in loop No. 17), at $\epsilon_1 = 0.0032$, $\sigma_1/E = 0.0039$. It is seen that the failure distribution here is rather similar to that shown in Fig. 8.

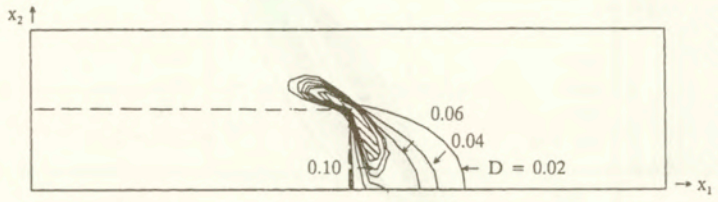

FIG. 9. Contours of constant damage, for balanced stress-controlled, $\sigma_{\max}/E = -\sigma_{\min}/E = 0.0036$, with $f = 0.13$, $\alpha_f = \alpha_c = 4$ and $\rho = 0$. At $\epsilon_1 = 0,0025$, $\sigma_1/E = 0.0028$, during loop No. 29.

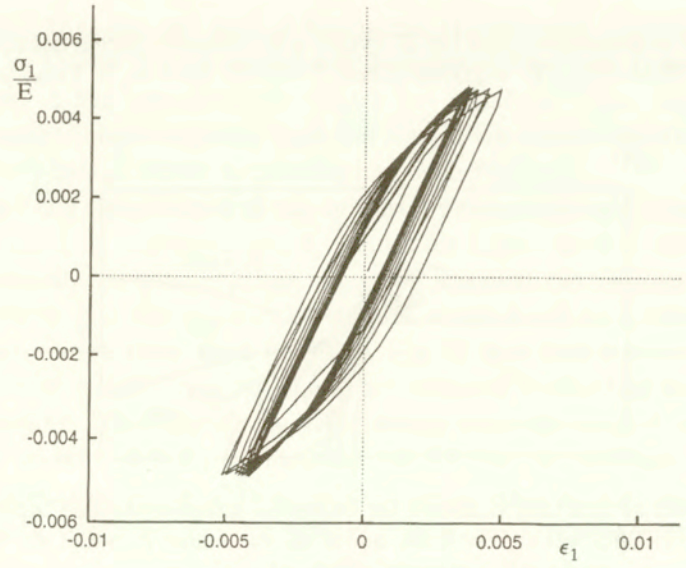

FIG. 10. Overall stress-strain loops for 17 cycles with balanced stress-controlled cycling, $\sigma_{\max}/E = -\sigma_{\min}/E = 0.0048$. Here, $f = 0.13$, $\alpha_f = \alpha_c = 2$ and $\rho = 0.25$.

Also strain-controlled cycling is important in applications and in test situations. A few cases have been analysed here for uniaxial stress conditions, i.e. for $\rho = 0$ in (2.3). For $(\epsilon_1)_{\max} = -(\epsilon_1)_{\min} = 0.004$, stress-strain loops for the material with $f = 0.13$ and $\alpha_f = \alpha_c = 1$ are shown in Fig. 12. The first loops are very similar to those in Fig. 3, but due to the fixed strain amplitude, the cyclic hardening here results in gradually increasing stress amplitudes. Later on, as damage results in the growth of a crack through the matrix, the material

stiffness is reduced, and then the fixed strain amplitude results in significantly reduced stress amplitudes, as is seen for the last loops in Fig. 12. The corresponding development of low-cycle fatigue is illustrated in Fig. 13 for an intermediate stage at $\epsilon_1 = -0.0011$, $\sigma_1/E = -0.00035$, in loop No. 17, and for the last loop analysed (loop No. 64) at $\epsilon_1 \simeq 0$, $\sigma_1/E = -0.00013$. The fields in Fig. 13a are rather similar to those in Fig. 4a, although the situation in Fig. 13a is slightly before the first onset of final failure. Figure 13b shows a very well-developed crack, close to a situation where the fibres are completely separated from parts

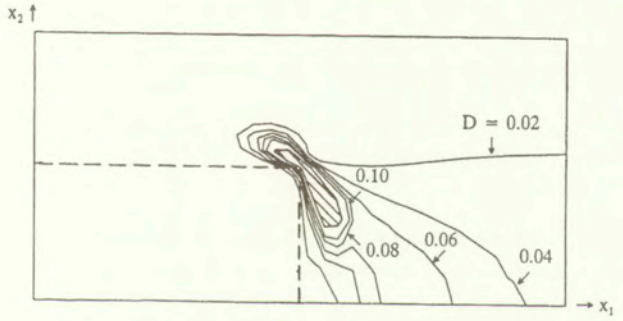

FIG. 11. Contours of constant damage, for balanced stress-controlled loading, $\sigma_{\max}/E = -\sigma_{\min}/E = 0.0036$, with $f = 0.13$, $\alpha_f = \alpha_c = 2$ and $\rho = 0.25$. At $\epsilon 1 = 0.0032$, $\sigma_1/E = 0.0039$, during loop No. 17.

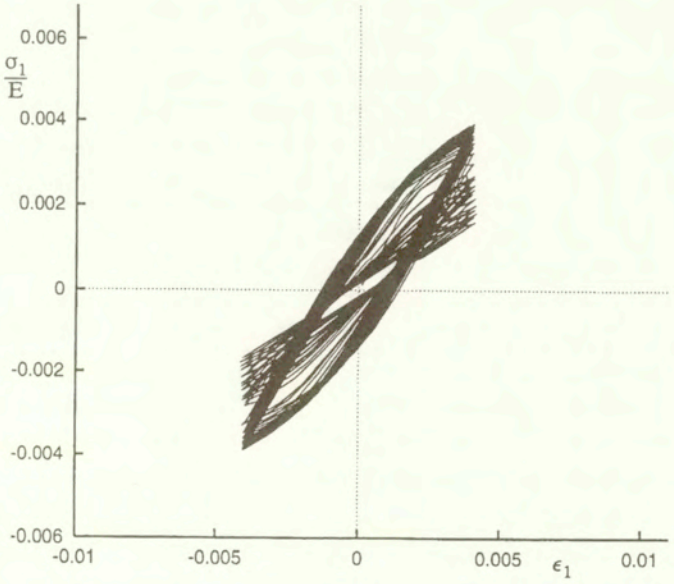

FIG. 12. Overall stress-strain loops for 64 cycles with balanced strain-controlled cycling, $(\epsilon_1)_{\max} = -(\epsilon_1)_{\min} = 0.004$. Here, $f = 0.13$, $\alpha_f = \alpha_c = 1$ and $\rho = 0$.

of the matrix material. Similar analysed for a material with $\alpha_f = \alpha_c = 2$ (as that in Figs. 7 and 8) has shown a behaviour analogous to that found in Fig. 12 and 13.

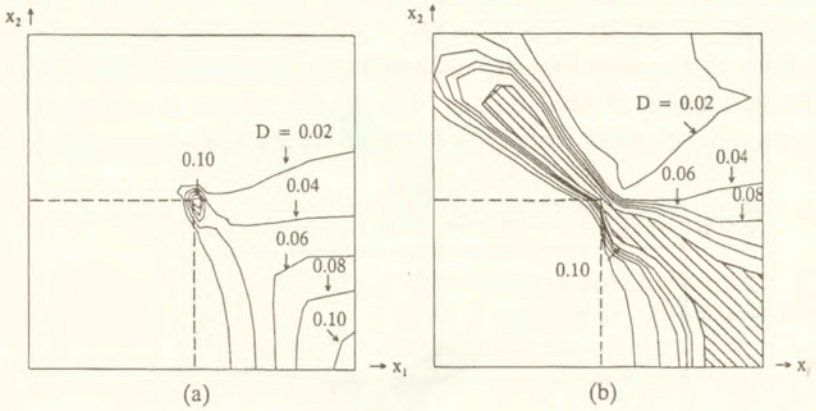

FIG. 13. Contours of constant damage, for balanced strain-controlled loading, $(\epsilon_1)_{\max} = -(\epsilon_1)_{\min} = 0.0036$, with $f = 0.13$, $\alpha_f = \alpha_c = 1$ and $\rho = 0$. a) at $\epsilon_1 = -0.0011$, $\sigma_1/E = -0.0035$, during loop No. 17; b) at $\epsilon_1 \simeq 0$, $\sigma_1/E = -0.00013$, during loop No. 64.

4. Discussion

Previous studies of the damage evolution by fatigue failure in metal matrix composites have been extended here to also account for the final failure of the matrix material and the subsequent growth of a matrix crack. The onset of failure is controlled by the damage model, as the failure criterion relies on reaching a critical value of the damage parameter, and the numerical representation of final failure applied here has made it possible to continue the fatigue analyses far beyond the initial stages of damage evolution.

In should be emphasized that the metal matrix fatigue failure investigated here is only one of the failure mechanisms observed for MMC's (ALLISON and JONES [8]), and that also fibre fracture and debonding of the fibre-matrix interface play a role in practice. But there is a wide range of cyclic loads for which the matrix fatigue characteristics dominate the fatigue life, and for this range of material behaviour the method presented here is expected to be a very useful tool in parametric studies of the effect of the main parameters characterising the metal matrix composite.

The examples used to illustrate the method here are all in the range of low cycle fatigue, since the number of cycles to final failure range from 17 to 70. This choice has been made for convenience, to avoid very large numbers of cycles in the numerical computations. However, since the predicted fatigue damage evolution

is linked to the amount of plastic straining, it is clear that somewhat smaller overall stress amplitudes will give much less plastic strain accumulation in each increment, and therefore a much increased number of cycles before final fatigue failure is predicted.

In comparing the analyses for fixed overall stress amplitudes and for a fixed fibre volume fraction, but with three different values, 1, 2 and 4, of the fibre and cell aspect ratios, it has been noted that increased fibre aspect ratio gives higher axial stiffness, and therefore a smaller overall strain range corresponding to the fixed stress range. But it is also noted that the number of cycles to final fatigue failure in these three cases is practically the same. This emphasizes the fact that the onset of final fatigue failure in the metal matrix is a function of local plastic strains rather than overall plastic strains. While increasing fibre length gives smaller overall strain range, it also results in larger local strain concentrations near the sharp edges at the fibre ends, and the final fatigue life determined in the numerical analyses is a result of competition between these two effects.

References

1. A. NEEDLEMAN, S. R. NUTT, S. SURESH and V. TVERGAARD, *Matrix, reinforcement and interfacial failure*, Fundamentals of Metal Matrix Composites, S. SURESH *et al.* [Eds.], Butterworth-Heinemann, Boston, MA, 233–250, 1993.
2. S. R. NUTT and A. NEEDLEMAN, *Void nucleation at fiber ends in Al-SiC composites*, Scr. Metall., **21**, 705–710, 1987.
3. V. TVERGAARD, *Effect of fibre debonding in a whisker-reinforced metal*, Mater. Sci. Eng., **A 125**, 203–213, 1990.
4. V. TVERGAARD, *Model studies of fibre breakage and debonding in a metal reinforced by short fibres*, J. Mech. Phys. Solids, **41**, 1309–1326, 1993.
5. V. TVERGAARD, *Fibre debonding and breakage in a whisker-reinforced metal*, Mater. Sci. Eng., **A 190**, 215–222, 1995.
6. V. TVERGAARD, *Effects of ductile matrix failure in three dimensional analysis of metal matrix composites*, Acta Mater., **46**, 3637–3648, 1998.
7. J. LLORCA, A. NEEDLEMANN and S. SURESH, *An analysis of the effects of matrix void growth on deformation and ductility in metal-ceramic composites*, Acta Metall. Mater., **39**, 2317–2335, 1991.
8. J. E. ALLISON and J. W. JONES, *Fatigue behaviour of discontinously reinforced metal matrix composites*, Fundamentals of Metal Matrix Composites, S. SURESH *et al.* [Eds.], Butterworth-Heinemann, Boston, MA, 269–294, 1993.
9. J. LLORCA and P. POZA, *Influence of reinforcement fracture on the cyclic stress-strain curve of metal-matrix composites*, Acta Metall. Mater., **43**, 3959–3969, 1995.
10. J. LLORCA, S. SURESI and A. NEEDLEMANN, *An experimental and numerical study of cyclic deformation in metal-matrix composites*, Metall. Trans., **23a**, 919–934, 1992.
11. A. L. GURSON, *Continuum theory of ductile rupture by void nucleation and growth – I. Yield criteria and flow rues for porous ductile media*, J. Engng. Materials Technol., **99**, 2–15, 1977.

12. T. Ø. PEDERSEN and V. TVERGAARD, *On low cycle fatigue in metal matrix composites*, Int. J. Damage Mechanics, **9**, 154–173, 2000.

13. V. TVERGAARD and T. Ø. PEDERSEN, *Fatigue damage development in a steel based MMC*, Proc. 3rd National Congr. Comput. Mech., N. ARAVAS *et al.* [Eds.], University of Thessaly, Greece, 101–108, 1999.

14. J. F. BESSELING, *A theory of elastic, plastic, and creep deformations of an initially isotropic material showing anisotropic strain-hardening, creep recovery, and secondary creep*, J. Appl. Mech., **25**, 529–536, 1958.

15. Z. MRÓZ, *On the description of anisotropic workhardening*, J. Mech. Phys. Solids, **15**, 163–175, 1967.

16. P. J. ARMSTRONG and C. O. FREDERICK, *A mathematical representation of the multiaxial Bauschinger effect*, CEGB Report RD/B/N731, Berkeley Nuclear Laboratories, 1966.

17. J. LEMAITRE and J.-L. CHABOCHE, *Mechanics of Solids Materials*, Cambridge University Press, 1990.

18. J. LEMAITRE, *A Course on Damage Mechanics*, Springer-Verlag, 1992.

19. T. Ø. PEDERSEN, *Numerical modelling of cyclic plasticity and fatigue damage in cold-forging tools*, Int. J. Mechanical Sciences, **42**, 799–818, 2000.

20. T. Ø. PEDERSEN, *Numerical studies of low cycle fatigue in forward extrusion dies*, J. of Materials Processing Technology, 1999 (to appear).

21. H. S. NIELSEN and V. TVERGAARD, *Intergranular fracture under creep-fatigue interaction*, Int. J. Damage Mechanics, **7**, 3–23, 1998.

22. V. TVERGAARD, *Analysis of tensile properties for a whisker-reinforced metal-matrix composite*, Acta Metall. Mater., **38**, 185–194, 1990.

23. T. CHRISTMAN, A. NEEDLEMANN, S. NUTT and S. SURESH, *On microstructural evolution and micromechanical modelling of deformation of a whisker-reinforced metal-matrix composite*, Mat. Sci. Eng., **A107**, 49–61, 1989.

24. O. S. HOPPERSTAD, M. LANGSETH and S. REMSETH, *Cyclic stress-strain behaviour of alloy AA6060, Part I: Uniaxial experiments and modelling*, Int. Journal of Plasticity, **11**, 725–739, 1995.

25. J. L. CHABOCHE, *Time-independent consitutive theories for cyclic plasticity*, Int. Journal of Plasticity, **2**, 149–188, 1986.

26. A. BENALLAL, O. LE GALLO and D. MARQUIS, *Cyclic hardening of metals under complex loadings*, Proc. MECAMAT, Int. seminar on the inelastic behaviour of solids: models and utilisation (Besancon, France), 361–371, 1998.

27. N. OHNO and J.-D. WANG, *Kinematic hardening rules with critical state of dynamic recovery, Part I: Formulation and basic features for ratchetting behaviour*, Int. Journal of Plasticity, **9**, 375–390, 1993.

28. V. TVERGAARD, *Effect of thickness inhomogeneities in internally pressurized elastic-plastic spherical shells*, J. Mech. Phys. Solids, **24**, 291–304, 1976.

29. V. TVERGAARD, *Influence of void nucleation on ductile shear fracture at a free surface*, J. Mech. Phys. Solids, **30**, 399–425, 1982.

30. J. L. TEPLY and G. J. DVORAK, *Bounds on overall instantaneous properties of elastic-plastic composites*, J. Mech. Phys. Solids, **36**, 29–58, 1988.

31. O. S. HOPPERSTAD, *Modelling of cyclic plasticity with application to steel and aluminium structures*, Dr. Ing. Dissertation, Dept. of Structural Engineering, The Norwegian Inst. of Technology, Trondheim, Norway.

Received January 31, 2000.

Arch. Mech., **52**, 4–5, pp. 817–838, Warszawa 2000

Gradient field theory of material instabilities

Dedicated to Professor Zenon Mróz
on the occasion of his 70th birthday

K. C. VALANIS

Endochronics/The University of Portland
Vancouver, WA 98665 USA

PREVIOUSLY, we developed a gradient thermodynamic theory of internal fields (migratory motions). The theory predicts the observed periodic deformation structures, in material domains under uniform tractions. More recently we showed, in a uniform stress field, that the theory has the proper mathematical framework for the prediction of Portevin-Le Chatelier (PLC for short) instabilities.
Here we review our previous work and address the more difficult problem of a non-uniform stress field. Specifically, we predict the points of instability of a solid cylinder under torsion, with the experiments of Dillon as backdrop. Again, we find close agreement between theory and experiment.

1. Introduction

IN A RECENT SERIES of paper, VALANIS [1 – 4], we presented an isothermal, gradient thermodynamic theory of internal fields. The theory provided a theoretical basis for the appearance of *non-uniform strain fields*, in homogeneous material domains, under *uniform surface tractions*, in situations where local theories would predict otherwise. In the most recent paper, VALANIS [4], we demonstrated that imbedded in the theory is a *mathematical framework*, for the theoretical treatment of 'unstable solids'.

Specific attention was given to the Portevin-Le Chatelier effect, whereby a macroscopically uniform domain under uniform, monotonically increasing tractions, suffers *spontaneous* changes in deformation, at specific *discrete* values of the tractions while the resulting strain becomes non-uniform.

It was further shown that this *metastable* behavior is caused by the presence of *particular* internal field ξ_i. These are continuous and twice differentiable and bounded in the material domain D in the sense that $\|\xi_i\| < \infty$ in D, double bars denoting the Euclidean norm. The fields satisfy the partial differential equation:

$$C\nabla^2\boldsymbol{\xi} + \boldsymbol{\Sigma}.\boldsymbol{\xi} = 0 \tag{1.1}$$

in D, where C is a material constant, ∇^2 is the Laplacian and $\boldsymbol{\Sigma}(\boldsymbol{\sigma})$ is a tensor function of the stress $\boldsymbol{\sigma}$, to be discussed in the text. We shall refer to this equation as the *Instability Equation*. In the specific case treated here, ξ_i signify *end-points of diffusion and/or rearrangement processes.* They represent, therefore, *equilibrium states* in the sense that their dual internal forces Ξ_i are zero.

The boundary conditions are:

$$\xi_i = 0 \quad \text{on} \quad S_i,$$

(1.2)

$$\xi_{i',j} n_j = 0 \quad \text{on} \quad S_p,$$

where S_i and S_p denote a permeable and impermeable surface, respectively. Quite clearly the solution of Eq. (1.1) gives rise to an eigenvalue problem. If $\boldsymbol{\Sigma}$ is constant in D, then non-null solutions to Eq. (1.1) will exist only for specific *characteristic* values of $\boldsymbol{\sigma}$.

In our most recent work, cited previously, VALANIS [4], we applied the theory to the experiments by LUBAHN [5], who tested flat steel specimens in tension, DILLON [6] who did experiments on hollow aluminium cylinders under torsion and SHARPE [13] who tested solid aluminium cylinders under tension. All these experiments were done under load control and at a *slow rate* of loading.

All three authors observed metastable behavior of the Portevin-Le Chatelier type in the sense that the deformation was a monotonic continuous function of the tractions, except for specific discrete values of the latter, at which the material body suffered a sudden and spontaneous change in the deformation.

The application of the theory to the above experiments resulted in the demonstration that the Instability Equation (1.1) contains the appropriate physics of metastable behaviour and that its solution, in all three cases, given *precise* predictive values of the tractions at which the instabilities were observed.

Moreover it was shown that the collapse tractions are, within a geometric factor, the *eigenvalues* of the solutions of the Instability Equation (1.1).
We refer the reader to VALANIS [4] for details but treat the flat bar in tension in some detail in Sec. 3.

In this paper we illustrate the ability of the theory to deal with the more complex problem where the tractions are *not uniform.* The work was motivated by the researches of DILLON [6], who carried out experiments in load control, on solid aluminium cylinders in torsion. As in previous cases, material instabilities of the Portevin-Le Chatelier type were observed, in the sense that the cylinders suffered spontaneous changes in twist at discrete values of the applied torque.

As is well known, local theories will predict that the twist is a continuous function of the applied torque. Such theories, therefore, are incapable of describing, let alone predicting, this type of phenomenon.

2. Gradient thermodynamics

The theory is expressed in terms of gradients of internal variables, more appropriately, internal fields. It was given previously, in a Helmoltz and a Gibbs formulation in earlier work by VALANIS [1 – 3]. It is basically the following. The Helmotz (Gibbs) free energy density denoted by ψ (denoted by ϕ) is a function of the strain tensor ϵ_{ij} (stress tensor σ_{ij}) and *three* different types of internal variables:

(i) Second order tensors p_{ij}, which are *dissipative* and obey evolution equations of the local type.

(ii) Vectors q_i and their gradients $q_{i,j}$ which are also *dissipative* and give rise to inhomogeneous strain fields in the presence of uniform surface tractions.

(iii) Vectors ξ_i and their gradients $\xi_{i,j}$. These are a subset of q_i in the sense that their dual internal forces Ξ_i are zero! Thus, either ξ_i are *inviscid* or they represent *terminal equilibrium points* of an irreversible process.

Both q_i and ξ_i are mathematical representations of non-affine migration of subsets of particles, into material subdomains that are exterior to the initial neighborhood of the particles (see VALANIS *[3]). Such motions are brought about by diffusion of dislocations, voids, interstitials and/or other processes such as particle diffusion or microslip.*

2.1. Helmotz formulation

The formulation is based on the global variational inequality (2.1), that pertains to a material domain D of volume V and surface S under prevailing isothermal conditions:

$$\delta\Psi \leq \int_S T_i \delta u_i dS + \int_V f_i \delta u_i dV, \tag{2.1}$$

where Ψ is the total free energy of the domain, T_i – the surface tractions, f_i – the body forces in D, u_i – the displacement field and δ is the variation operator.

The free energy density ψ such that

$$\int_V \psi dV = \Psi \tag{2.2}$$

is then introduced where

$$\psi = \psi(\epsilon_{ij};\ p_{ij};\ q_i;\ q_{i,j}). \tag{2.3}$$

Since ξ_i are a sub-class of q_i they do not appear explicitly in Eq. (2.3).

In variance with local theories, ψ is a function of the strain tensor, m local internal variables p_{ij} and n vectorial internal field variables q_i and their gradients

$q_{i,j}$, subject to the constitutive constraint that for all rigid body displacement variations δu_i^*:

$$\delta\Psi = 0; \quad \delta q_i = 0. \tag{2.4}$$

2.2. Field equations

The following relations then hold in D, VALANIS [1 – 3], for all p_{ij} and q_i:

$$\sigma_{ij} = \partial\psi/\partial\epsilon_{ij}, \tag{2.5}$$

$$Q_{ij} + \partial\psi/\partial p_{ij} = 0. \tag{2.6}$$

$$Q_i = (\partial\psi/q_{i,j})_{,j} - \partial\psi/\partial q_i, \tag{2.7}$$

$$\sigma_{ij,j} + f_i = 0, \tag{2.8}$$

where Q_{ij} is the internal force dual to p_{ij} and Q_i the internal force, dual to q_i. Note that Q_{ij} and q_i must satisfy the dissipation inequalities:

$$Q_{ij}\dot{q}_{ij} > 0 \tag{2.8}$$

$$Q_i\dot{q}_i > 0 \tag{2.9}$$

whenever $\|Q_{ij}\| \neq 0$, $\|Q_i\| \neq 0$, double bars denoting a Euclidean norm. As mentioned previously, the sub-class of q_i such that $Q_i = 0$, is denoted by ξ_i.

The theory is made complete by the addition of "internal constitutive equations". These are relations between Q_{ij} and $\dot{q}_{ij}$ on the one hand and Q_i and $\dot{q}_i$ on the other, whose existence is necessitated by the inequalities (2.8) and (2.9). More will be said about this point in the text to follow.

2.3. Boundary conditions

We shall limit the analysis to the case where the configuration deformation is diffusive in the sense that q_i and ξ_i are migratory motions. The following are then the boundary conditions.

On S_T, the part of the surface where tractions are given:

$$\sigma_{ij}n_j = T_i. \tag{2.10}$$

On S_u, the complement of S_T, where displacements U_i are given:

$$u_i = U_i. \tag{2.11}$$

On S_p, the permeable part of the surface:

$$\partial\psi/\partial q_{i,j}n_j = 0, \tag{2.12}$$

while on S_i, the impermeable complement of S_p:

$$q_i = 0. \tag{2.13}$$

No boundary condition is necessary for p_{ij}.

2.4. Gibbs formulation

The Gibbs free energy density ϕ is given by Eq. (2.16) where:

$$\phi(\sigma_{ij};\ p_{ij} :\ q_i;\ q_{i,j}) = \psi - \sigma_{ij}\epsilon_{ij}. \tag{2.14}$$

Equation (2.16) in conjuction with inequality (2.1) and the equilibrium equation, leads to the following variational inequality that pertrains to the Gibbs formulation:

$$-\int_S u_i \delta T_i - \int_V u_i \delta f_i \geq \int_V \delta\phi dV. \tag{2.15}$$

The pertinent equations that follow, VALANIS [3], are given below. In D:

$$\epsilon_{ij} = -\partial\phi/\partial\sigma_{ij}, \tag{2.16}$$

$$Q_{ij} = -\partial\phi/P_{ij}, \tag{2.17}$$

$$Q_i = (\partial\phi/\partial q_{i,j})_{,j} - \partial\phi/\partial q_i, \tag{2.18}$$

while the constitutive equations for Q_{ij} and Q_i remain the same. The form of the boundary conditions remains unchanged. Thus on S_T:

$$\sigma_{ij}n_j = T_i. \tag{2.19}$$

On S_p:

$$\partial\phi/\partial q_{i,j}n_j = 0. \tag{2.20}$$

On S_u:

$$u_i = U_i. \tag{2.21}$$

On S_i:

$$q_i = 0. \tag{2.22}$$

2.5. A partitioned form of ϕ

In this paper we shall posit that the energies associated with the pertaining deformation mechanisms are additive in the sense that:

$$\phi = \phi_e + \phi_p + \phi_q \tag{2.23}$$

where

$$\phi_e = \phi_e(\sigma_{ij}), \qquad \phi_p = \phi_p(\sigma_{ij}, p_{ij}), \tag{2.24}$$

$$\phi_q = \phi_q(\sigma_{ij};\ q_{i,j};\ q_i). \tag{2.25}$$

Thus, in view of Eq. (2.15):

$$\epsilon_{ij} = \epsilon^e_{ij} + \epsilon^p_{ij} + \epsilon^q_{ij} \tag{2.26}$$

i.e., the strains are also additive.

We shall focus our attention on the variables ξ_i, the dual thermolynamic forces Ξ_i of which are zero. Thus, it suffices to write ϕ in the form:

$$\phi = \phi^*(\sigma_{ij}; p_{ij}; q_i; q_{i,j}) + \phi_\xi(\sigma_{ij}; \xi_i; \xi_{j;j}). \tag{2.27}$$

We shall, however, put mathematical constraints on ϕ^* and ϕ_ξ. We shall require that ϕ^* be continuous in its variables but that ϕ_ξ be continuous n ξ_i and $\xi_{i\cdot j}$. The physical ramifications of these constraints will become evident in what follows.

2.6. The form of ϕ_ξ

The theory proposed here is linear and thus ϕ is quadratic in its arguments. In the full expansion of ϕ, the part attributed to ξ_i and its gradient is given in Eq. (2.30):

$$\phi_\xi = -(1/2)\Sigma_{ij}\xi_i\xi_j + (1/2)C\xi_{i,j}\xi_{i,j} \tag{2.28}$$

where Σ_{ij} is a material function of stress and C is a positive material constant. This form gives rise to material instabilities of the Portevin Le-Chatelier type as shown previously by VALANIS [4].

2.7. Constitutive questions

Inequality (2.1) becomes an equality when $\delta\Psi$ is expressed in terms of the variation δD^* of the dissipation D^*:

$$\delta\Psi = \int_S T_i\delta u_i dS + \int_V f_i\delta u_i dV - \int_V \delta D^* dV \tag{2.29}$$

where

$$\delta D^* = Q_i\delta q_1 > 0 \qquad \text{for all} \quad \|Q_i\| \neq 0. \tag{2.30}$$

Inequality (2.30) is a *Variational Inequality* that ensures that no free energy may be extrated from a material by means of an 'external agency' to which the

variations δq_i are due. Its mathematical significance is that of all the variations δq_i only some, a subset, are admissible, i.e., those that satisfy the inequality $Q_i \delta q_i > 0$, for all $\|Q_i\| \neq 0$.

In the event that $\delta q_i = \dot{q}_i \delta t$, where $\dot{q}_i$ is the actual rate of q_i due to the actual physical process, then the variational inequality becomes the Dissipation Inequality, i.e.,

$$\dot{D}^* = Q_i \dot{q}_i > 0. \tag{2.31}$$

As argued previously, also for local thermodynamics, VALANIS [7], Q_i and $\dot{q}_i$ are thus related. The most obvious such relation is the one where Q_i is linear and homogeneous in $\dot{q}_i$, i.e.,

$$Q_i = b_{ij} \dot{q}_j; \qquad b_{ij} \dot{q}_i \dot{q}_j > 0 \tag{2.32}$$

which may or may not be a good description of the process at hand.

This relation is, however, a member of a broader class of relations for which:

$$Q_i = 0 \quad \text{for all} \quad \dot{q}_i = 0. \tag{2.33}$$

This is the class that we use in this paper. Most probably, the number of relations in this class is infinite and we shall not attempt to enumerate all these in this paper, even if we could.

Since, however, ξ_i are subsets of q_i that represent terminal points in the metastable process, they may be defined by the operational relation:

$$q_i = \xi_i, \quad Q_i = 0. \tag{2.34}$$

3. The Portevin-Le Chatelier effect

Previous theoretical work on this effect appears in the papers by AIFANTIS [8, 9, 10]. There it was demonstrated that the field equations that govern the spatial and temporal evolution of the dislocation densities, have analytical features that give them the capability for describing this effect.

Here, the deformation mechanism of interest results in a series of *contained* collapse events, not associated with a continuous plastic process brought about by coordinated intergranular slip. A collapse process is a spontaneous structural rearranngement that *takes place at constant stress.* We conclude that the internal variables of the collapse process are not those of continuous plastic deformation, but others that obey different internal constitutive laws.

REMARK

It is of historical interest that DILLON [6], observed a small amount of plastic strain between metastable states but LUBAHN [5] did not. Thus in the "Lubahn

solid" the deformation between metastable states is elastic. In this "ideal" solid: $\phi = \phi_e + \phi_\xi$, i.e., ϕ is independent of p_{ij} and q_i. More generally, by virtue of the constraints on ϕ^* and ϕ_ξ, the collapse to a new configuration is brought about through the internal fields ξ_i, which are not present in the continuous plastic process.

In effect: (i) $\phi_\xi = 0$ when $\xi_i = 0$; (ii) the variables ξ_i are constant during (continuous) plastic deformation; (iii) during collapse, $\boldsymbol{\sigma}$, hence $\boldsymbol{\epsilon}^e$, is constant; moreover, p_{ij} and q_i are also constant, since $\boldsymbol{\sigma}$ is *continuous* in these variables, the agents of the plastic process (local and non-local). Hence $\boldsymbol{\epsilon}^p$ and $\boldsymbol{\epsilon}^q$ are also constant. Thus, in Eq. (2.27), ϕ^* is constant during the collapse process.

To proceed with the analysis, we begin with Eq. $(2.6)_2$, which in view of Eq. (2.34), gives rise to the following defining equation for ξ_i:

$$(\partial\phi_\xi/\partial\xi_{i,j})_{,j} - \partial\phi_\xi/\partial\xi_i = 0 \tag{3.1}$$

in D. We further set Σ_{ij} to be linear and homogeneous in σ_{ij}. But since all non-elastic mechanisms are assumed to lead to isochoric deformation, then Σ_{ij} must be linear and homogeneous in the deviatoric stress tensor s_{ij}. Thus, Eq. (2.28) becomes:

$$\phi_\xi = -(B/2)s_{ij}\xi_i\xi_j + (C/2)\xi_{i,j}\xi_{i,j}. \tag{3.1}'$$

Without loss of generality, we set B equal to unity. Then in view of Eq. (3.1), the following second order partial differential equation for ξ_1 is obtained in D:

$$C\xi_{i,jj} + s_{ij}\xi_j = 0. \tag{3.2}$$

3.1. The boundary condition

We shall take the position that the boundary is permeable. This must be true if the material is uniform. In essence, since there is internal diffusion, the boundaries of all internal sub-domains are permeable. Hence the external boundary is also permeable. This conclusion is confirmed by the demonstrated agreement between the theory and the experimental results.

Hence, $S = S_p$ and thus on S:

$$\xi_{i,j}n_j = 0. \tag{3.3}$$

The strain ϵ^ξ_{ij}, which the ξ-field contributes to the total strain is given, in the light of Eq. (2.18), by Eqs. (3.4):

$$\epsilon^\xi_{ij} = \xi_i\xi_j - (1/3)\xi_k\xi_k\delta_{ij}. \tag{3.4}$$

Note that $\epsilon^\xi_{ii} = 0$.

4. Metastable behavior of a flat bar under tension

The problem of the flat bar under tension was solved in a previous work, VALANIS [4]. Because of its relative simplicity and the fact that it illustrates the essential points of metastable behavior, it merits a (brief) review which we give below.

We consider the case of a rectangular domain of length a in direction $x(x_1)$, width b in direction $y(x_2)$ and of small thickness c in direction $z(x_3)$. Thus, $0 < x < a$, $0 \leq y \leq b$ and $0 \leq z \leq c$. Further, we consider solutions such that ξ_i is constant in the thickness direction z. A uniform *tensile* traction T is applied on the boundaries $x = 0, a$, while the boundaries $y = 0, b$ and $z = 0, c$ are traction-free. A uniform stress state prevails throughout the plate by virtue of the equation of equilibrium. The deviatoric stress components s_{ij} are zero for $i \neq j$, while $s_{11} = s = 2T/3$, $s_{22} = s_{33} = -s/2$ where T is a positive scalar. The boundary condition (3.3) now becomes: $\partial\xi_i/\partial x = 0$, $x = 0, a$; $\partial\xi_i/\partial y = 0$, $y = 0, b$.

We seek solutions that lead to repetitive, patterned material structures and thus are *periodic* in the variables x_i. In light of the boundary condition (3.3), the only admissible solution, VALANIS [4] is the following:

$$\xi_i = A_i \cos(n\pi x/a) \cos(m\pi y/b), \tag{4.1}$$

where m and n are integers and A_i are eigenvectors of the characteristic equation:

$$\lambda \begin{pmatrix} A_1 \\ A_2 \\ A_3 \end{pmatrix} = \begin{pmatrix} s_{11} & & \\ & s_{22} & \\ & & s_{33} \end{pmatrix} \begin{pmatrix} A_1 \\ A_2 \\ A_3 \end{pmatrix}, \tag{4.2}$$

where

$$\lambda = C\{(n\pi/a)^2 + (m\pi/b)^2\}. \tag{4.3}$$

Thus it follows that:

$$\lambda = s = (2/3)T, \tag{4.4}$$

$$A_2 = A_3 = 0. \tag{4.5}$$

In view of Eq. (4.4), *a solution exists only for characteristic values of the traction* T. However, A_1 is indeterminate.

The strain field is shown in Eq. (4.6):

$$\epsilon_{ij}^{\xi} = \begin{pmatrix} 2/3 & & \\ & -1/3 & \\ & & -1/3 \end{pmatrix} A_1^2 \cos^2 m\pi(x/a) \cos^2 n\pi(y/b). \tag{4.6}$$

REMARK

The field equation predicts that spontaneous collapse (and self-organization) occurs when the maximum (tensile) principal stress σ reaches an *eigenstate*, at which it attains a characteristic value T_c

$$T_c = (3/2)C(\{(n/a)^2 + (m/b)^2\}\pi^2, \tag{4.7}$$

where m and n are positive integers. The integers m and n are independent, giving rise to denumerably infinite metastable states. Hovewer, given n, the collapse traction T is a maximum for $m = n$. If the material resists collapse as long as possible then it will until $m = n$. This is the maximal traction hypothesis which we adopted previously, VALANIS [4].

Thus setting $m = n$ in Eq. (4.7) we find the following simple relation for the collapse traction T_c:

$$T_c = T_{co}n^2 \tag{4.8}$$

where

$$T_{co} = (3/2)C\pi^2\left[(1/a)^2 + 1/b)^2\right], \tag{4.9}$$

or

$$\boxed{\sqrt{T_c} = \sqrt{T_{co}}n.} \tag{4.10}$$

Hence, the square roots of the collapse tractions are proportional to the ordinal number of their occurrence.

Two things remained to be found: (a) the constant $\sqrt{T_{co}}$ and the ordinal number n_c at which the first collapse takes place. To this end, Eq. (4.10) was written in the form of Eq. (4.11):

$$\sqrt{T_c} = \sqrt{T_{co}}(n_c + r). \tag{4.11}$$

Setting the cross-sectional area of the bar equal to unity (with no loss of generality), a plot of $\sqrt{T_c}$ versus r gave a straight line with a slope 1.972, while setting $r = 0$ determined n_c, found to be equal to 14. Thus:

$$\sqrt{T_c} = 1.972(14 + r), \tag{4.12}$$

$r = 0, 1, 2...m$. The match with individual experimental and calculated values of traction loads and ordinal numbers, shown in Table 1 below, is very close despite reading errors as well as experimental errors.

Table 1. Comparison of observed and calculated tractions and ordinal numbers

$r = 0, 1, 2...m$	0	1	2	3	4	5
Observed P_c	760	860	980	1120	1260	1420
Calculated P_c	764	878	998	1127	1263	1407
Calculated $n_c + r$	14	15	16	17	18	19

5. Metastable states in torsion of a solid cylinder

In this section we apply the theory to predict theoretically the experimental results of DILLON [6], in which solid cylinders made of aluminium 1100 were subjected to pure torsion. Observations were made of the torque at which a cylinder collapsed to a subsequent stable state. A depiction of the experiments is given in Fig. 1.

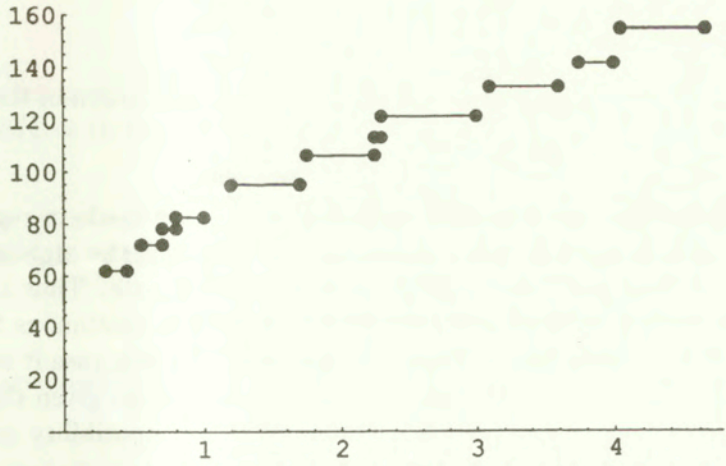

FIG. 1. Experimental values of torque (in 1b) with initial and terminal values of twist (no units) at points of instability.

To this end, we let r, θ and z be the polar coordinates of a cylinder radius a and height h, subjected to pure torsion. We now recall Eq. (3.2), which is the equation of metastable motion:

$$C\nabla^2\xi_i + s_{ij}\xi_j = 0, \tag{5.1}$$

where ∇^2 is the Laplacian operator, given in cylindrical coordinates by Eq. (5.2):

$$\nabla^2\xi_i = \partial^2\xi_i/\partial r^2 + (1/r)\partial\xi_1/\partial r + (1/r^2)\partial^2\xi_i/\partial\theta^2 + \partial\xi_i/\partial z^2. \tag{5.2}$$

We exclude solutions that depend on θ and are thus periodic in θ, because then either ξ_i or $\partial\xi_i/\partial\theta$ will vanish at specific points on the circumference. This is not warranted since all points on the circumference of a continuum have equal status. Equation (5.2) thus becomes:

$$\nabla^2\xi_i = \partial^2\xi_i/\partial r^2 + (1/r)\partial\xi_i/\partial r + \partial^2\xi_i\partial z^2. \tag{5.3}$$

The boundary condition is given by Eq. (3.3), i.e., $\xi_{i,j}n_j = 0$ on S.

It remains to determine the stress tensor s_{ij} in the Cartesian coordinate system x_i. The components of s in the polar coordinate system are zero with the exception of $s_{\theta z} = s_{z\theta} = \tau$. A tensor transformation gives then the following values of s_{ij} in the x_i-system:

$$s_{ij} = \begin{pmatrix} 0 & 0 & -\tau\sin\theta \\ 0 & 0 & \tau\cos\theta \\ -\tau\sin\theta & \tau\cos\theta & 0 \end{pmatrix}. \tag{5.4}$$

DIGRESSION

When the stress field σ_{ij} is not explicity known, the solution of the equation,

$$C\nabla^2\xi_i + s_{ij}\xi_j = 0 \tag{5.5}$$

faces impossible difficulties unless certain hypotheses are made in regard to the mechanism of collapse. The difficulty lies in the fact that the amplitude of the inelastic strain field in all metastable states is indeterminate. Thus the concept of a constitutive equation whereby the stress tensor is a continuous function of the history of the strain tensor, must be abandoned. In this case it is no longer possible to determine, in general, the stress field in a domain given the tractions on the surface. The reason is that the condition of compatibility is no longer applicable since the deformation is not known.

These considerations do not apply in our particular case, because the stress field in a solid cylinder under torsion is statically determinate – what will be discussed shortly.

5.1. Stress field cylinder under torsion

In a cylindrical coordinate system (r, θ, z) the components of the stress tensor are zero with the exception of $\sigma_{\theta z} \equiv \tau$. As a result of the stress feld, the

equilibrium conditions are:

$$\partial\sigma_{\theta z}/\partial z = \partial\sigma_{\theta z}/\partial\theta = 0 \tag{5.6}$$

and therefore $\sigma_{\theta z} = \tau(r)$. It follows that if on the free ends ($z = 0, h$), the tractions $\tau(0, r) = \tau(h, r)$ are prescribed as functions of r, then $\sigma_{\theta z}$ is (statically) determinate.

In the experiments by Dillon, cited previously, a torque T_E (experimental) was applied to one cylinder end, while the other was held fixed. It is not known whether the experimental shear stress distribution $\tau(r)$ was *exactly* linear in r, resulting in a torque $T_L(= T_E)$. If it was not, then the experiment consisted in applying a torque T_L together with a self-equilibrating stress system, very localized at the cylinder end. We will thus proceed on the basis that a torque T_L was applied in the form that $\tau = \tau_0 r/a$, where a is the radius of the cylinder. Our position will be justified by the findings.

Substitution of Eq. (5.1) in (5.4) gives rise to the following set of equations:

$$\begin{aligned} C\nabla^2\xi_1 &= +\tau\sin\theta\,\xi_3, \\ C\nabla^2\xi_2 &= -\tau\cos\theta\,\xi_3, \\ c\nabla^2\xi_3 &= +\tau\sin\theta\,\xi_1 - \tau\cos\theta\,\xi_2. \end{aligned} \tag{5.7}$$

It is shown in the Appendix that this set of simultaneous partial differential equations reduces to the following uncoupled set of equations in ξ_i:

$$C\nabla^2\xi_i + \tau\xi_i = 0 \tag{5.8}$$

which in the light of the linear dependence of τ on r becomes:

$$C\nabla^2\xi_i + \tau_0(r/a)\xi_i = 0. \tag{5.9}$$

The boundary conditions in the cylindrical coordinate system are:

$$\begin{aligned} &\partial\xi_i/\partial r = 0 \quad (r = a); \\ &\partial\xi_i/\partial z = 0 \quad (z = 0, h). \end{aligned} \tag{5.10}$$

5.2. Solution of equation (5.9)

Because the shear stress τ is a function of r only, it is useful to begin with the case where ξ_i are functions of r only, i.e., $\xi_i = \xi_i(r)$. It is pointed out that this is not a maximal field solution. However, it will be shown that the collapse stresses of the maximal field solution are very close to the ones obtained here.

In view of Eq. (5.3), the differential equation for ξ_i is given below:

$$C[d^2\xi_i/dr^2 + (1/r)d\xi_i/dr] + \tau_0(r/a)\xi_i = 0 \tag{5.11}$$

with the boundary conditions $d\xi_i/dr = 0$, $r = a$, and the boundedness condition $\|\xi_i\| < \infty$, $0 \leq r \leq a$.

We introduce the transformation $\rho = r/a$, whereupon Eq. (5.11) becomes:

$$d^2\xi_i/d\rho^2 + (1/\rho)d\xi_i/d\rho + \tau^*\rho\xi_i = 0 \tag{5.12}$$

where $\tau^* = \tau_0 a^2/C$.

To solve this equation we appeal to the "generic" equation:

$$d^2\xi_i/d\rho^2 + (1/\rho)d\xi_i/dr + (bc\rho^{c-1})^2\, xi_i = 0 \tag{5.13}$$

which has the solution, BOAS [11]:

$$\xi_i = A_i J_0(br^c) + B_i Y_0(br^c), \tag{5.14}$$

where J_0 and Y_0 are the Bessel functions of order zero, and A_i and B_i are undetermined constants of the solution. To obtain Eq. (5.11) from Eq. (5.14) we set $c = 3/2$ and thus:

$$2\sqrt{\tau^*/3} = b = (2a/3)\sqrt{(\tau_0/C)}. \tag{5.15}$$

Because ξ_i are bounded in the domain $0 \leq r \leq a$ and in light of the fact that $Y(0) = \infty$, we set $B_i = 0$ and thus:

$$\xi_i = A_i J_0(b\rho^{3/2}). \tag{5.16}$$

The remaining boundary condition, at $\rho = 1$, is $d\xi_i/d\rho = 0$. Hence:

$$J_1(b) = 0 \tag{5.17}$$

where J_1 is the Bessel function of order one.

It follows that a non-null solution for ξ_i exists only for characteristic values of b, these being the zeros of J_1. The amplitudes A_i remain *indeterminate.*

In physical terms, the deformation of the cylinder is continuous in the applied torque, except for specific values of b when the deformation is augmented by the spontaneous appearance of the gradient fields ξ_i. The magnitude of the augmentation, however, is indeterminate. These characteristic values of b are points of instability.

5.3. Values of the toeque at points of instability

The relation between τ_0 and the applied torque is given below:

$$\tau_0 = (2/\pi a^4)T. \tag{5.18}$$

In view of Eq. (5.15),

$$kj_1^{(n)} = \sqrt{T_n}, \tag{5.19}$$

where the constant k is given by Eq. (5.20),

$$k = (3a/2)\sqrt{(C\pi/2)}\,. \tag{5.20}$$

Moreover, $j_1^{(n)}$ is the n-th zero of J_1 and T_n is the value of the applied torque at which the n-th instability occurs. In other words: *the square root of the n-th collapse torque is proportional to the n-th zero of the Bessel function* J_1.

Two issues arise at this juncture: (a) the first measurable collapse torque and (b) the determination of the constant k. In our previous work, in connection with instabilities in a uniform stresses field, as in the case of in tension of a uniform bar and torsion of a hollow cylinder, we found that the first collapse traction was found to occur at a high value of n, generally greater than ten. For such values of n and over substantial intervals Δn, $j_1^{(n)}$ may be approximated by the formula:

$$j_1^{(n)} = j_1^* + \pi n, \qquad n > n_0;\ n_0 > 10 \tag{5.21}$$

where j_1^* is a constant. For these values of n and in view of Eq. (5.21):

$$\sqrt{T_n} = k(j_1^* + \pi n). \tag{5.22}$$

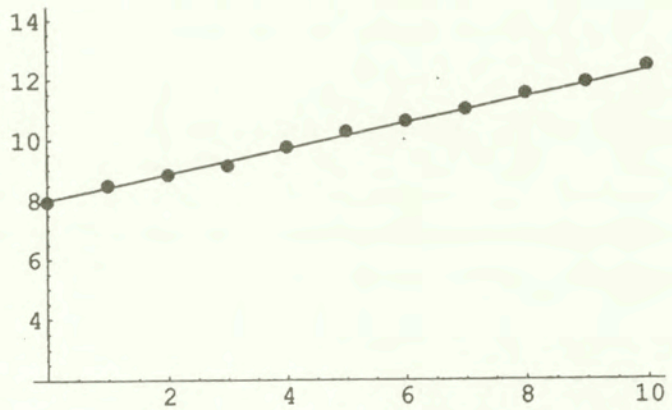

FIG. 2. Square root of experimental values of torque vs. their sequence.

In light of the above considerations, a plot of the experimental values of $\sqrt{T_n}$ versus n, should give a straight line with a slope $k\pi$. Such a plot is shown in Fig. 2, where the experimental points follow closely a straight line with a slope $k\pi$ equal to 0.421 and hence, $k = 0.134$. With this experimentally determined value of k, we have the following theoretical expression for the collapse torque T_n:

(5.23) $$\sqrt{T_n} = 0.134 j_1^{(n)}.$$

This is a remarkable result.

The first observable value of T_n was found by inspection to be T_{19}. The theoretical values of T_n were then calculated and are given together with the experimental values in Table 2. The agreement is quite close.

Table 2. Experimental and theoretical values of collapse torque $(ft - 1b)$.

n	19	20	21	22	23	24	25	26	27	28	29
$(\sqrt{T_n})_{ex}$	7.94	8.50	8.83	9.24	9.75	10.3	10.6	11.0	11.5	11.9	12.4
$(\sqrt{T_n})_{th}$	8.10	8.52	8.94	9.36	9.79	10.2	10.6	11.0	11.5	11.9	12.3
$j_1^{(n)}$	60. 47	63. 61	66. 75	69. 90	73. 04	76. 18	79. 32	82. 46	85. 60	88. 71	91. 89

5.4. Maximal internal fields

We recall that in the case of a flat bar (Sec. 1), the solution for the internal vector field was given by Eq. (4.1), shown here as Eq. (5.24):

(5.24) $$\xi_i = A_i \cos(n\pi x/a) \cos(m\pi y/b).$$

Given n, denumerably infinite set of m may be chosen in the solution. However, it was argued in that section that the *maximal traction* hypothesis requires that $m = n$. The fields that satisfy this conditions were called *maximal fields.*

The solution obtained above is *not* a maximal field solution, yet the agreement between the theoretical collapse torque values and their experimental counterparts was excellent. Is there any inconsistency? We proceed to examine this question.

To this end, we write Eq. (5.11), in cylindrical coordinate system:

(5.25) $$C[\partial^2 \xi_i/\partial r^2 + (1/r)\partial \xi_i/\partial r + \partial^2 \xi_i/\partial z^2] + \tau_0 (r/a)\xi_i = 0.$$

We introduce the transformation, $\rho = (r/a)$, $\zeta = (z/h)$, $0 \leq \rho \leq 1$, $0 \leq \zeta \leq 1$, whereupon Eq. (5.25) becomes:

(5.26) $$\partial^2 \xi_i/\partial \rho^2 + (1/\rho)\partial \xi_i/\partial \rho + (a/h)^2 \partial^2 \xi_i/\partial \zeta^2 + \tau^* \rho \xi_i = 0$$

where $\tau^* = (a^2 \tau_0/C)$. The following set of maximal field solutions satisfy the boundary condition $(5.10)_2$:

(5.27) $$\xi_i^{(n)} = R_n(\rho) \cos(n\pi\zeta),$$

$n = 1, 2, ...\infty$, where $R^{(n)}$ satisfies the differential Eq. (5.28):

$$d^2R^{(n)}/d\rho^2 + (1/\rho)dR^{(n)}/d\rho - (a\pi/h)^2 n^2 R^{(n)} + \tau_n^* \rho R^{(n)} = 0. \tag{5.28}$$

Evidently R_n is not a periodic function and thus it must be interpreted as having n (albeit decreasing) half-oscillations in the domain $0 \leq \rho \leq 1$, just like $\cos n\pi\zeta$ in the domain $0 \leq \zeta \leq 1$.

REMARK

Note that as $h \to \infty$ at constant radius a, Eq. (5.28) tends to (5.12). We can thus say that the solution $\xi_i = \xi_i(r)$ pertains to a cylinder of infinite length. We call the n-th eigenvalue of this solution $(\tau_n^*)_\infty$.

5.5. Solution of equation (5.28)

DILLON [6] tested specimens of diameter of 0.5 inch. ($a = 0.5$) and length of either 9 or 19 inches. He did not specify the specimen length in the test reported. We shall take the conservative position that $h = 9$ – this will become clear shortly – in which event $(h/\pi a) = h^* = 11.46$. The object then is to determine τ_n^* such that the solution $R^{(n)}(\rho)$ has (a) n half-oscillations and (b) a derivative $dR^{(n)}/d\rho$ that vanishes at $\rho = 1$.

REMARK

Because the solution $\xi_i(r)$, independent of z, depicts collapse torque values that were close to their experimental counterparts, we reason that τ_n^* must be close to $(1.5j_1^n)^2$, which are the values of $(\tau_n^*)_\infty$. Furthermore, since:

$$\sqrt{T_n} = 0.134(2/3)\sqrt{\tau_n^*} \tag{5.29}$$

and because the first observable T_n was T_{19}, we also reason that the first τ_n^* is in fact τ_{19}^*.

The solution then consisted in finding the eigenvalue τ_{19}^* such that $R^{(n)}$ had 19 half-oscillations and its derivative $dR^{(n)}/d\rho$ vanished at $\rho = 1$. The solution was found numerically by means of the software NDSolve of MATHEMATICA and the function $R^{(19)}$ is shown in Fig. 3. It has 19 half-oscillations. Its derivative function $dR^{(n)}/d\rho$ shown in Fig. 4, passes through zero at $\rho = 1$ The eigenvalue τ_{19}^* was found to be equal to 8235. This value compares with 8227 which was the value of $(\tau_{19}^*)_\infty$. The difference between the two is of the order of 0.1% which is well within the experimental error. The same was found to be true of all other τ_n^*. For instance τ_{29}^* was found to be 19017. The corresponding value of $(\tau_{29}^*)_\infty$ was 18998. Again the difference between them is about 0.1%.

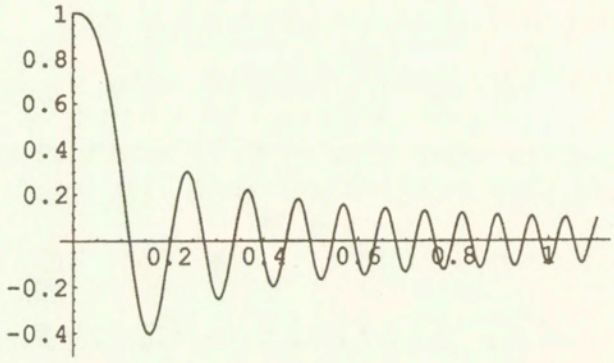

FIG. 3. Eigenfunction $Rn(r); n = 19$.

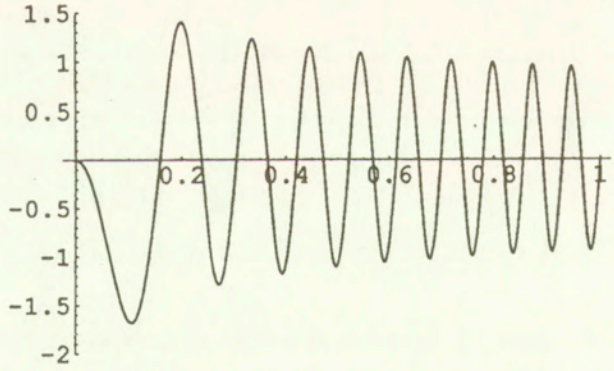

FIG. 4. First derivative of $Rn(r) : n = 19$.

CONCLUSION 1

A parametric study showed that the two values tend to come closer together as $(a\pi/h)^2$ tends to zero, not surprisingly. Thus below a certain value of this parameter, the length of the specimen does not affect the values of the collapse torques. This theoretical finding suggests an interesting experimental program to determine the effect of the cylinder geometry on the values of the collapse torques. The theory predicts that they are proportional to the square of the cylinder radius and become independent of the lenght as the latter becomes asymptotically infinite.

CONCLUSION 2

In the case of the maximal field solutions and for a cylinder geometry such that $(h/\pi a) > 10$, as in the case of the specimens tested, the values of the collapse

torques are given within experimental error, by the relation:

$$\sqrt{T_n} = k j_1^{(n)}, \tag{5.30}$$

where k is a material constant, in this case 0.134. This is an unexpected and remarkable result.

The agreement between the predictions of Eq. (5.30) and the experimental data of DILLON [6], is illustrated in Fig. 5. There, the dots are the experimental points and the lines are the eigenstates, i.e., the "torque states" at points of instability. Use was made of Eq. (5.22).

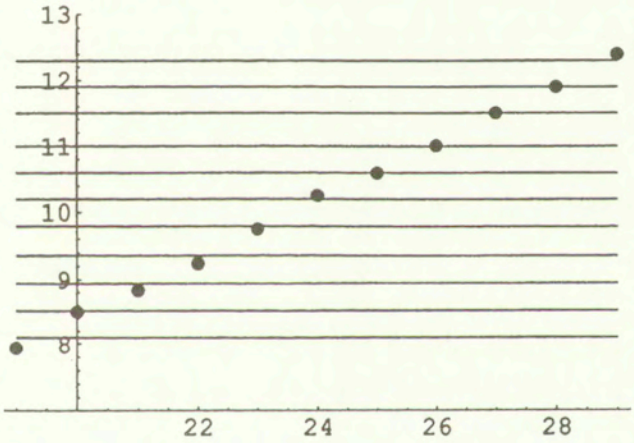

FIG. 5. Experimental points of instability vs. theoretical eigenstates (lines) ordinate: square root of torque; abscissa: ordinal numbers.

Apendix

We begin with Eqs. (5.7) in D, i.e.,

$$\begin{aligned} C\nabla^2\xi_1 &= +\tau \sin\theta\, \xi_3, \\ C\nabla^2\xi_2 &= -\tau \cos\theta\, \xi_3, \\ C\nabla^2\xi_3 &= +\tau \sin\theta\, \xi_1 - \tau \cos\theta\, \xi_2. \end{aligned} \tag{A.1}$$

A vector transformation gives the following relation between (ξ_1, ξ_2) and (ξ_r, ξ_θ):

$$\begin{aligned} \xi_r &= \xi_1 \cos\theta + \xi_2 \sin\theta, \\ \xi_\theta &= -\xi_1 \sin\theta + \xi_2 \cos\theta. \end{aligned} \tag{A.2}$$

Also:

$$\begin{aligned} \xi_1 &= \xi_r \cos\theta - \xi_\theta \sin\theta, \\ \xi_2 &= \xi_r \sin\theta + \xi_\theta \sin\theta. \end{aligned} \tag{A.3}$$

Multiply Eqs. $(A.1)_1$ and $(A.1)_2$ by $\cos\theta$ and $\sin\theta$ respectively, add and use Eqs. $(A.2)_1$ to obtain:

$$\nabla^2 \xi_r = 0. \tag{A.4}$$

A. 1.1. Boundary condition

The boundary condition on S is:

$$\xi_{i,j} n_j = 0. \tag{A.5}$$

In the cylindrical coordinate system Eq. (A.5) on the cylindrical surface $r = a$ becomes:

$$(\partial \xi_i / \partial r) r_{,j} n_j + (\partial \xi_i / \partial \theta) \theta_{,j} n_j = 0. \tag{A.6}$$

However, ξ_i is independent of θ and $r_{,i} = n_i$. Thus Eq. (A.6) reduces to:

$$\partial \xi_i / \partial r = 0. \tag{A.7}$$

Thus and in ligth of Eqs. $(A.2)_1$ and $(A.2)_2$:

$$\partial \xi_r / \partial r = 0; \quad \partial \xi_\theta / \partial r = 0 \tag{A.8}$$

while on the flat surface $z = 0, h$:

$$\partial \xi_i / \partial z = 0 \tag{A.9}$$

in view of which Eqs. (A.4):

$$\partial \xi_r / \partial z = 0, \quad \partial \xi_\theta / \partial z = 0. \tag{A.10}$$

We now use the classical result that, if the Laplacian of a function f vanishes in D while on S: $\partial f / \partial n = 0$, then the function is at most a constant in D. We set this constant equal to zero. Thus in view of Eqs. (A.8) and (A.10) it follows that:

$$\xi_r = 0. \tag{A.11}$$

Hence, in light of Eqs. (A.3) we find that:

$$\xi_1 = -\xi_\theta \sin\theta; \quad \xi_2 = \xi_\theta \cos\theta. \tag{A.12}$$

Hence, from Eq. $(A.1)_3$ on the one hand and Eq. $(A.1)_1$ and $(A.1)_2$ on the other:

$$C\nabla^2 \xi_3 + \tau \xi_\theta = 0; \quad C\nabla^2 \xi_\theta + \tau \xi_3 = 0. \tag{A.13}$$

A solution to the Eq. (A.13) is:

$$\xi_3 = \xi_\theta. \tag{A.14}$$

It is now a short step to show from Eqs. (A.1) and (A.12) that:

$$C\nabla^2\xi_i + \tau\xi_i = 0 \tag{A.15}$$

which is the result that was to be shown.

A. 1.2. Uniqueness of the solution

If another solution exists then $\xi_3 \neq \xi_\theta$. Let $\xi = \xi_3 - \xi_\theta$. Then in view of Eqs. (A.13) and setting $\tau^* = \tau_0/Ca$:

$$\nabla^2\xi = \tau^* r\xi \tag{A.16}$$

or,

$$\partial[r(\partial\xi/\partial r)]/\partial r + r\partial^2\xi/\partial z^2 = \tau^* r^2\xi. \tag{A.17}$$

Thus, if a solution $\xi \neq 0$ exists, it must satisfy Eq. (A.17) with $\tau^* > 0$ and the boundary conditions $\partial\xi/\partial r =$ on $r = a$, and $\partial\xi/\partial z = 0$ on $z = 0, h$ by virtue of Eqs. (A.9) and (A.10).

We multiply both sides of Eq. (A.17) by ξ and integrate over the domain D using integration by parts and the indicated boundary conditions to find the following result:

$$-\int_0^h\int_0^a r(\partial\xi/\partial r)^2 dr dz - \int_0^h\int_0^a r(\partial\xi/\partial z)^2 dr dz = \tau^* \int_0^h\int_0^a r^2\xi^2 dr dz. \tag{A.18}$$

Since the left-hand side of Eq. (A.18) is non-positive (allowing the set of solutions to include $\xi =$ constant) and the integral on the right-hand side is positive, a solution can exist only for non-positive values of τ^*. But τ^* is positive and thus a non-null solution for ξ does not exist.

References

1. K. C. VALANIS, *A gradient theory of internal variables*, Acta Mechanica, **116**, 1–14, 1996.
2. K. C. VALANIS, *A gradient theory of finite viscoelasticity*, Arch. Mech., **49**, 589–609, 1997.
3. K. C. VALAINS, *A gradient thermodynamic theory of self-organization*, Acta Mechanica, **127**, 1–23, 1998.

4. K. C. VALANIS, *The Portevin-Le Chatelier effect. Its prediction and place in gradient thermodynamics*, Acta Mechanica, 2000 [in press].

5. J. D. LUBAHN and R. P. FELGAR, *Plasticity and creep in metals*, John Wiley and Sons, Inc. New York 1965.

6. W. O. DILLON, *Experimental data on aluminum as an unstable solid*, Proc. Fourth International Congress of Rheology, E. H. LEE [Ed.], **2**, 377–394, 1965.

7. K. C. VALANIS, *Fundamental consequences of a new intrinsic time measure. Plasticity as a limit of the endochronic theory*, Arch. Mech., **32**, 171–191, 1980.

8. E. C. AIFANTIS, *Remarks on media with microstructure*, Int. J. Eng. Science, **22**, 961–968, 1980.

9. E. C. AIFANTIS, *The physic of plastic deformation*, International Journal of Plasticity, **3**, 211–247, 1986.

10. E. C. AIFANTIS, *Non-linearity, periodicity and patterning in plasticity and fracture*, Int. J. Non-Linear Mech., **31**, 797–809, 1996.

11. W. N. SHARPE Jr, *The Portevin-LeChatelier effect in aluminium single crystals and polycrystals*, J. Mech. Phys. Sol., **14**, 187–202, 1966.

12. M. L. BOAS, *Mathematical methods in the physical sciences*, John Wiley and Sons, New York 1966.

Received January 17, 2000.

Arch. Mech., **52**, 4–5, pp. 839–855, Warszawa 2000

Material instability in the tensile response of short-fibre-reinforced quasi-brittle composites

Dedicated to Professor Zenon Mróz on the occasion of his 70th birthday

J. WANG ([1]) and B. L. KARIHALOO ([2])

([1]) *Department of Mechanics and Engineering Science Peking University, Beijing 100871, PRC*

([2]) *Cardiff School of Engineering, University of Wales Cardiff Queen's Buildings, P. O. Box 686, Cardiff CF2 3TB, UK*

THIS PAPER GIVES THE CONDITIONS for the onset of instability in the tensile response of short-fibre-reinforced quasi-brittle composites whose deformation is characterised by multiple cracking and localisation. First, the tensile stress-strain relation is established analytically for a body containing multiple bridged microcracks. The material instability is examined using the classical bifurcation criterion, with an emphasis on the role played by fibre bridging in the macroscopic instability. It is found that while the microscopic instability in the bridging traction plays a major role in the macroscopic instability of the composite, it is the level of damage in the matrix that determines when the macroscopic instability is induced by the bridging instability. The satisfaction of the classical bifurcation criterion is identified with several failure modes, depending on the degree of damage in the matrix.

1. Introduction

THE FIRST SIGNS OF TENSILE DAMAGE in short-fibre-reinforced quasi-brittle matrices, such as cements, are the appearance of multiple parallel microcracks. They cause the stress-strain curve to deviate from linearity, i.e. give the composite a strain-hardening response. Bridging of the multiple microcracks by short fibres is an important mechanism for increasing the strength and toughness of these composites and for preventing a sudden loss of their overall stiffness when the microcracks coalesce and localise into large bands. The response of the material after the attainment of ultimate tensile strength is characterised by the localisation of deformation, i.e. by the continuous opening of cracks and stretching of unbroken material ligaments in a narrow localisation band.

On the micromechanical level, a lot of studies have been devoted to the bridging effect of fibres on the crack propagation and the toughening of the

composite in the context of fracture mechanics. On the other hand, there have been relatively few studies on the macroscopic constitutive behaviour of short-fibre-reinforced quasi-brittle composites, such as cementitious composites. The studies at the microlevel benefit the material technologists, whereas those at the macrolevel benefit the structural engineers. The relation between the macroscopic constitutive response and the micomechanical parameters is also vital in the material design. For quasi-brittle monolithic or fibre-reinforced composites, in which the deformation process leading to complete rupture usually involves multiple cracking, the complete constitutive behaviour is important to the analysis of propagation of a macroscopic crack, as was demonstrated by ORTIZ [1]. Multiple cracking also characterises the compressive response of concrete [2].

KARIHALOO *et al.* [3] have previously studied the complete constitutive behaviour of short-fibre-reinforced cementitious composites under unidirectional tension. In their work, the pre-peak strain-hardening is simulated by a doubly periodic array of bridged cracks whose density increases with increasing tensile load. The peak stress, i.e., the ultimate failure stress of the composite material is calculated using the law of mixtures. The post-peak tension-softening response is simulated using a single row of periodic discrete bridged cracks. The model of KARIHALOO *et al.* [3] cannot predict the transition from the strain-hardening to tension-softening. This leads to a discontinuity in the slope of the stress-strain/displacement curve at the peak load. In other words, conditions for localisation are still not clear.

In the present paper, the mechanisms for the material instability which lead to deformation localisation and tension softening will be revealed. The study will be based upon an analytical procedure which allows the conditions for the material instability in short-fibre-reinforced composites to be highlighted. The material instability is examined using the classical bifurcation criterion, with an emphasis on the role played by fibre bridging in the macroscopic instability. It is found that while the microscopic instability in the bridging traction plays a major role in the macroscopic instability of the composite, it is the level of damage in the matrix that determines when the macroscopic instability is induced by the bridging instability. The satisfaction of the classical bifurcation criterion is identified with several failure modes, depending on the degree of damage in the matrix. The phrase 'microscopic instability' is used to define the instant when the bridging stiffness momentarily vanishes.

2. General formulae for multiple cracks

The prediction of the effective elastic and fracture properties of a medium containing multiple cracks has received considerable attention. Among the stud-

ies are the solutions based upon the non-interacting approximation, when the interaction among the cracks is neglected. Under this assumption, the effective elastic properties can be expressed in explicit forms. The interactions among multiple cracks complicate the prediction of the overall material behaviour. The schemes based upon indirect considerations of crack interactions, such as the self-consistent method and the differential scheme may considerably underestimate the overall moduli, as has been pointed by WANG *et al.* [4].

In this section, we shall present an analytical approach for the calculation of the overall tensile modulus of bodies containing multiple parallel bridged cracks. For this, we shall make use of the procedures in the previous work of KARIHALOO *et al.* [3], and those in the recent works of WANG *et al.* [4, 5].

The overall (average) strain and stress of a cracked body are related via (e.g. [6])

$$\varepsilon_{ij} = C^0_{ijkl}\,\sigma_{kl} + \frac{1}{2V}\sum_N \int_{S_N} ([u_i]\,n_j + [u_j]\,n_i)\,dS_N \tag{2.1}$$

where ε_{ij} and σ_{kl} are the average strain and stress components, respectively. u_i and n_i are the total crack opening/sliding displacement (COD/CSD) and the component of the unit vector normal to the crack faces. C^0_{ijkl} is the compliance tensor of the uncracked material. For parallel flat cracks when n_i is a constant, Eq. (2.1) can be rewritten as

$$\varepsilon_{ij} = C^0_{ijkl}\,\sigma_{kl} + \frac{1}{2V}\sum_N (\overline{[u_i]}\,n_j + \overline{[u_j]}\,n_i)\,S_N \tag{2.2}$$

where $\overline{[u_i]}$ is the average COD/CSD for a single crack over its faces, and S_N is its area.

We note that Eq. (2.2) can be written as

$$\varepsilon_{ij} = C^0_{ijkl}\,\sigma_{kl} + \frac{\omega}{L}\,(\overline{[u_i]}\,n_j + \overline{[u_j]}\,n_i) \tag{2.3}$$

where ω is a non-dimensional crack density parameter, and L is an internal length scale, which will be defined later. In the above expression, $\overline{[u_i]}$ is taken to be the COD/CSD for a representative crack.

We consider only infinitesimal deformation and rotation. Taking the time-derivative of the above equation gives

$$\dot{\varepsilon}_{ij} = C^0_{ijkl}\,\dot{\sigma}_{kl} + \frac{1}{L}\,(\overline{[u_i]}\,n_j + \overline{[u_j]}\,n_i)\,\frac{\partial\omega}{\partial\sigma_{kl}}\dot{\sigma}_{kl} + \frac{\omega}{L}\left(\frac{\partial\overline{[u_i]}}{\partial\sigma_{kl}}\,n_j + \frac{\partial\overline{[u_j]}}{\partial\sigma_{kl}}\,n_i\right)\dot{\sigma}_{kl}. \tag{2.4}$$

Here, we have assumed that the crack density is a function of the applied stress.

Strictly speaking, $\overline{[u_i]}$ is also a function of ω, which is in turn a function of σ_{kl}. However, Eq. (2.3) implies that $\overline{[u_i]}$ is a generic crack opening/sliding displacement in a representative element. In analogy with the usual non-interacting solution, we assume at this stage that this generic crack opening/sliding displacement is not related to the crack density, so that the derivative of $\overline{[u_i]}$ with respect to ω vanishes. Equation (2.4) gives the tangent compliance tensor

$$C_{ijkl} = C^0_{ijkl} + \frac{1}{L}\left(\overline{[u_i]}\, n_j + \overline{[u_j]}\, n_i\right)\frac{\partial \omega}{\partial \sigma_{kl}} + \frac{\omega}{L}\left(\frac{\partial \overline{[u_i]}}{\partial \sigma_{kl}}\, n_j + \frac{\partial \overline{[u_j]}}{\partial \sigma_{kl}}\, n_i\right) \tag{2.5}$$

whence the rate form of the constitutive relation (2.4) can be written as

$$\dot{\varepsilon}_{ij} = C_{ijkl}\, \dot{\sigma}_{kl}. \tag{2.6}$$

We now return to the determination of $\overline{[u_i]}$. For bodies containing multiple cracks, the effect of crack interactions and of any bridging tractions must be taken into account in the calculation of the crack opening displacement. Using the pseudo-traction formalism [7], the average crack opening displacement is calculated by applying a pseudo-traction on the faces of a single crack. In order to determine $\overline{[u_i]}$ and thus C_{ijkl} for a body containing randomly distributed multiple parallel bridged cracks, we shall first invoke the analytical procedures in the works of WANG *et al.* [4, 5] for two regular arrays of bridged cracks, namely, a doubly periodic rectangular array and a doubly periodic diamond-shaped array of bridged cracks, shown in Fig. 1. We consider the two-dimensional case, when the parallel cracks are perpendicular to, say, the direction 2. Following the procedures in the above works, the traction consistency condition on each crack in either of the two doubly periodic configurations is expressed as follows:

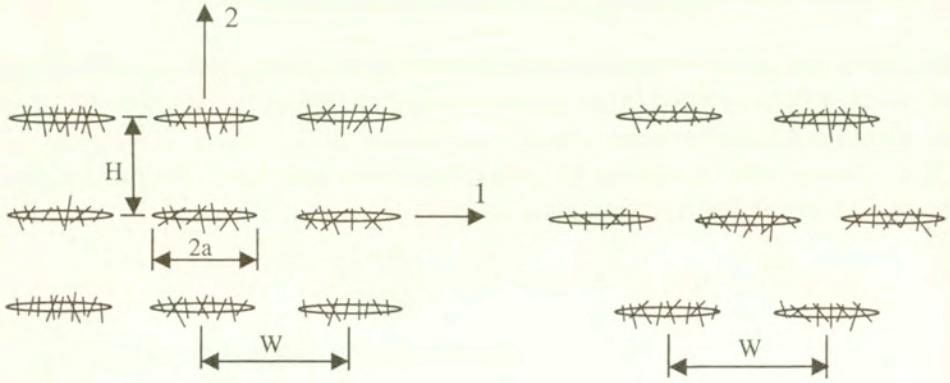

FIG. 1. Doubly periodic rectangular (a) and diamond-shaped array (b) of bridged cracks.

$$\sigma_{ij}^{p}(x) - 2\sum_{j=1}^{+\infty}\int_{0}^{a} K_{ijkl}(x,x^{j})\,\sigma_{kl}^{p}(x^{j})\,dx^{j} + p_{ij}(x) = \sigma_{ij}^{0}, \quad x \in [0,a), \tag{2.7}$$

where σ_{ij}^{p} is the pseudo-traction on the crack faces, σ_{ij}^{0} is the applied stress, p_{ij} is the bridging stress exerted by the fibres, and a is the half-length of a crack. $K_{ijkl}(x,x^{j})$ is the stress influence tensor which has been described in the previous works of the authors (e.g. [4, 8]).

However, in the present paper, in order to trace the nonlinear behaviour of the material, we shall recast the traction consistency condition (2.7) in an incremental form

$$\Delta\sigma_{ij}^{p}(x) - 2\sum_{j=1}^{+\infty}\int_{0}^{a} K_{ijkl}(x,x^{j})\,\Delta\sigma_{kl}^{p}(x^{j})\,dx^{j} + \Delta p_{ij}(x) = \Delta\sigma_{ij}^{0}, \tag{2.8}$$

$$x \in [0,a).$$

For the two-dimensional case under study, the parallel cracks are perpendicular to direction 2, so that we need only the pseudo-tractions σ_{22}^{p} and σ_{12}^{p} for calculating the crack opening/sliding displacements. Following the procedure in the recent work by WANG *et al.* [4], it is found that the incremental pseudo-tractions for the two periodic arrays of cracks shown in Fig. 1 can be written as

$$\begin{Bmatrix} \Delta\sigma_{22}^{pr} \\ \Delta\sigma_{22}^{pd} \end{Bmatrix} = \begin{Bmatrix} \zeta^{r} \\ \zeta^{d} \end{Bmatrix} \Delta\sigma_{22}^{0}, \tag{2.9}$$

$$\begin{Bmatrix} \Delta\sigma_{12}^{pr} \\ \Delta\sigma_{12}^{pd} \end{Bmatrix} = \begin{Bmatrix} \eta^{r} \\ \eta^{d} \end{Bmatrix} \Delta\sigma_{12}^{0}, \tag{2.10}$$

where

$$\zeta^{r} = \left\{1 + 4\sin^{2}\frac{\pi a}{W}\,e^{-2\frac{H}{W}\pi}\left[1 + 2\frac{H}{W}\pi\right] - \frac{2\bar{k}_{22}\,W^{2}}{\pi\,a\,E'}\ln\left(\cos\frac{\pi a}{W}\right)\right\}^{-1}, \tag{2.11}$$

$$\zeta^{d} = \left\{1 - 4\sin^{2}\frac{\pi a}{W}\,e^{-2\frac{H}{W}\pi}\left[1 + 2\frac{H}{W}\pi\right] - \frac{2\bar{k}_{22}\,W^{2}}{\pi\,a\,E'}\ln\left(\cos\frac{\pi a}{W}\right)\right\}^{-1}, \tag{2.12}$$

$$\eta^{r} = \left\{1 + 4\sin^{2}\frac{\pi a}{W}\,e^{-2\frac{H}{W}\pi}\left[1 - 2\frac{H}{W}\pi\right] - \frac{2\bar{k}_{12}\,W^{2}}{\pi\,a\,E'}\ln\left(\cos\frac{\pi a}{W}\right)\right\}^{-1}, \tag{2.13}$$

$$\eta^d = \left\{1 - 4\sin^2\frac{\pi a}{W}\, e^{-2\frac{H}{W}\pi}\left[1 - 2\frac{H}{W}\pi\right] - \frac{2\bar{k}_{12}\, W^2}{\pi\, a\, E'}\ln\left(\cos\frac{\pi a}{W}\right)\right\}^{-1}. \tag{2.14}$$

$E' = E$ for plane-stress, and $E' = E/(1-\nu^2)$ for plane-strain deformation. In deriving Eqs. (2.9) – (2.10), a linear relationship between the incremental bridging stress $\Delta p_{22}(x)$ and incremental COD/CSD has been assumed

$$\Delta p_{22}(x) = \bar{k}_{22}\,\Delta[u_2](x); \qquad \Delta p_{12}(x) = \bar{k}_{12}\,\Delta[u_1](x); \tag{2.15}$$

where $[u_1](x)$ and $[u_2](x)$ are the crack opening/sliding displacements. It is evident that $\bar{k}_{12}$ and $\bar{k}_{22}$ in the above expression should be the tangent bridging stiffnesses.

We presented above the incremental pseudo-tractions on the crack faces following the asymptotic analysis of WANG *et al.* [4, 5]. They are found to be constants (in an average sense only) and dependent upon the geometry of the crack arrays and the instantaneous tangent bridging stiffnesses. $\Delta\sigma_{22}^{pr}$ ($\Delta\sigma_{12}^{pr}$) and $\Delta\sigma_{22}^{pd}$ ($\Delta\sigma_{12}^{pd}$) are the two incremental pseudo-tractions for the doubly periodic rectangular array and diamond-shaped array, respectively. According to the analysis in the work by WANG *et al.* [4], these two regular patterns should represent the two extreme interactions among multiple parallel cracks, namely, the maximum "shielding" and "magnification" effects under unidirectional tension and the maximum "magnification" and "shielding" effects under in-plane shear. Based upon this analysis, WANG *et al.* [4] deduced that the overall modulus of a body containing randomly distributed multiple parallel cracks should be within a pair of bounds corresponding to the moduli for the doubly periodic rectangular and diamond-shaped array, respectively. Moreover, it was found that when the the terms $4\sin^2\frac{\pi a}{W}\, e^{-2\frac{H}{W}\pi}\left[1 + 2\frac{H}{W}\pi\right]$ and $4\sin^2\frac{\pi a}{W}\, e^{-2\frac{H}{W}\pi}\left[1 - 2\frac{H}{W}\pi\right]$ were neglected in the expressions (2.11) – (2.14), i.e., when the expressions (2.11) – (2.14) reduced to

$$\zeta \equiv \left\{1 - \frac{2\bar{k}_{22}\, W^2}{\pi\, a\, E'}\ln\left(\cos\frac{\pi a}{W}\right)\right\}^{-1}, \tag{2.16}$$

$$\eta \equiv \left\{1 - \frac{2\bar{k}_{12}\, W^2}{\pi\, a\, E'}\ln\left(\cos\frac{\pi a}{W}\right)\right\}^{-1}, \tag{2.17}$$

the overall moduli so calculated for low to moderate crack density were always in the middle of the range bounded by those obtained when the terms $4\sin^2\frac{\pi a}{W}\, e^{-2\frac{H}{W}\pi}\left[1 + 2\frac{H}{W}\pi\right]$ and $4\sin^2\frac{\pi a}{W}\, e^{-2\frac{H}{W}\pi}\left[1 - 2\frac{H}{W}\pi\right]$ were retained. Expressions (2.16) – (2.17) are nothing but the so-called non-interacting solution. Numerical computations of KACHANOV [6] for random discrete unbridged

parallel cracks also were found to be close to the non-interacting solution. Thus, it is reasonable to use the expressions (2.16) – (2.17) to calculate the pseudo-tractions

$$\Delta\sigma_{22}^{p} = \zeta\,\Delta\sigma_{22}^{0}, \qquad \Delta\sigma_{12}^{p} = \eta\,\Delta\sigma_{12}^{0}. \tag{2.18}$$

Having obtained the pseudo-tractions, the average crack opening/sliding displacements can be easily found

$$\begin{Bmatrix} \Delta\overline{[u_1]} \\ \Delta\overline{[u_2]} \end{Bmatrix} = \frac{1}{2a}\int_{-a}^{+a} \begin{Bmatrix} \Delta[u_1](x) \\ \Delta[u_2](x) \end{Bmatrix} dx = -\frac{2W^2}{\pi\,aE}\ln\left(\cos\frac{\pi a}{W}\right)\begin{Bmatrix} \Delta\sigma_{12}^{p} \\ \Delta\sigma_{22}^{p} \end{Bmatrix}. \tag{2.19}$$

The subsequent development is for plane-stress deformation condition. Substituting (2.18) into (2.19) gives

$$\begin{Bmatrix} \Delta\overline{[u_1]} \\ \Delta\overline{[u_2]} \end{Bmatrix} = -\frac{2W^2}{\pi\,aE}\ln\left(\cos\frac{\pi a}{W}\right)\begin{Bmatrix} \eta\,\Delta\sigma_{12}^{0} \\ \zeta\,\Delta\sigma_{22}^{0} \end{Bmatrix} \tag{2.20}$$

which can be rewritten as

$$\begin{Bmatrix} \dfrac{\Delta\sigma_{12}^{0}}{E} \\ \dfrac{\Delta\sigma_{22}^{0}}{E} \end{Bmatrix} = \begin{bmatrix} -\dfrac{1}{\dfrac{2W}{\pi a}\eta\ln\left(\cos\dfrac{\pi a}{W}\right)} & 0 \\ 0 & -\dfrac{1}{\dfrac{2W}{\pi a}\zeta\ln\left(\cos\dfrac{\pi a}{w}\right)} \end{bmatrix}\begin{Bmatrix} \dfrac{\Delta\overline{[u_1]}}{W} \\ \dfrac{\Delta\overline{[u_2]}}{W} \end{Bmatrix}. \tag{2.21}$$

Expression (2.21) describes the local behaviour of the cracked material. The global constitutive behaviour of the material can be determined from (2.6), together with (2.5).

3. Analysis of material instability

In this section, we shall study the material instability in the macroscopic tensile response of the composite, especially that induced by the microscopic bridging mechanism. For this, we use the classical bifurcation criterion for discontinuity localisation across parallel planes [9]. As will be seen later, for the case studied in this paper, this criterion is equivalent to other bifurcation criteria identified by NEILSEN and SCHREYER [10] for the study of material instabilities. The classical bifurcation criterion is

$$\det[Q_{ij}] = 0 \tag{3.1}$$

where Q_{ij} is the acoustic tensor defined as

$$Q_{ij} = n_k D_{kijl} n_l. \tag{3.2}$$

D_{kijl} is the tangent stiffness tensor which is the inverse of the tangent compliance tensor C_{kijl} in Eq. (2.5).

In order to obtain the acoustic tensor (3.2), we need to calculate the tangent compliance tensor from Eq. (2.5). For this, we need the total crack opening/sliding displacement $\overline{[u_i]}$, and its partial derivative with respect to σ_k. For fibre-reinforced quasi-brittle composites, it is observed in experiments that the density of the multiple cracks increases with increasing load until it reaches a saturation level ω_s, when the localisation sets in [11]. Moreover, in these materials the damage localisation usually coincides with the pull-out of fibres from the matrix. This implies that at localisation, the partial derivative $\partial\omega/\partial\sigma_{kl}$ in Eq. (2.5) can be equated to zero. Of course, the second term in Eq. (2.5) is essential to the strain hardening description which may be found in the work of KARIHALOO and WANG [12]. The tangent compliance tensor (2.5) at the instant of localisation therefore reduces to

$$C_{ijkl} = C^0_{ijkl} + \frac{\omega_s}{L}\left(\frac{\partial\overline{[u_i]}}{\partial\sigma_{kl}} n_j + \frac{\partial\overline{[u_j]}}{\partial\sigma_{kl}} n_i\right). \tag{3.3}$$

Let us consider the localisation into a planar band under unidirectional tension σ_{22}. For the considered two-dimensional case, the conventional crack density parameter ω is defined as

$$\omega = \frac{a^2}{WH}. \tag{3.4}$$

The rate form of the stress-strain relations (2.6), after making use of Eq.(3.3), are

$$\begin{Bmatrix} \dot{\varepsilon}_{11} \\ \dot{\varepsilon}_{22} \\ \dot{\varepsilon}_{12} \end{Bmatrix} = \begin{bmatrix} \frac{1}{E} & -\frac{\nu}{E} & 0 \\ -\frac{\nu}{E} & \frac{1}{E} + 2\frac{\omega_s}{L}\frac{\partial\overline{[u_2]}}{\partial\sigma_{22}} & 0 \\ 0 & 0 & \frac{2(1+\nu)}{E} + 2\frac{\omega_s}{L}\frac{\partial\overline{[u_1]}}{\partial\sigma_{12}} \end{bmatrix} \begin{Bmatrix} \dot{\sigma}_{11} \\ \dot{\sigma}_{22} \\ \dot{\sigma}_{12} \end{Bmatrix}. \tag{3.5}$$

Calculating $\partial\overline{[u_2]}/\partial\sigma_{22}$ and $\partial\overline{[u_1]}/\partial\sigma_{12}$ from Eq. (2.20), and noting that for the considered case, $L = a$, we get the tangent compliance matrix

(3.6) $$[C_{ij}] =$$

$$= \begin{bmatrix} \frac{1}{E} & -\frac{\nu}{E} & 0 \\ -\frac{\nu}{E} & \frac{1}{E} - 4\left(\frac{W}{a}\right)^2 \frac{\omega_s}{\pi E}\zeta \ln\left(\cos\frac{\pi a}{W}\right) & 0 \\ 0 & 0 & \frac{2(1+\nu)}{E} - 4\left(\frac{W}{a}\right)^2 \frac{\omega_s}{\pi E}\eta \ln\left(\cos\frac{\pi a}{W}\right) \end{bmatrix}$$

and, by inversion, the corresponding tangent stiffness matrix

(3.7) $$[D_{ij}] =$$

$$= \begin{bmatrix} \frac{E\left[1 - 4\left(\frac{W}{a}\right)^2 \frac{\omega_s}{\pi} L_t\right]}{\left[1 - \nu^2 - 4\left(\frac{W}{a}\right)^2 \frac{\omega_s}{\pi} L_t\right]} & \frac{E\nu}{\left[1 - \nu^2 - 4\left(\frac{W}{a}\right)^2 \frac{\omega_s}{\pi} L_t\right]} & 0 \\ \frac{E\nu}{\left[1 - \nu^2 - 4\left(\frac{W}{a}\right)^2 \frac{\omega_s}{\pi} L_t\right]} & \frac{E}{\left[1 - \nu^2 - 4\left(\frac{W}{a}\right)^2 \frac{\omega_s}{\pi} L_t\right]} & 0 \\ 0 & 0! & \frac{E}{2\left[(1+\nu) - 2\left(\frac{W}{a}\right)^2 \frac{\omega_s}{\pi} L_s\right]} \end{bmatrix}$$

Here, we have introduced two non-dimensional parameters

(3.8) $$L_t \equiv \zeta \ln\left(\cos\frac{\pi a}{W}\right),$$

(3.9) $$L_s \equiv \eta \ln\left(\cos\frac{\pi a}{W}\right),$$

where the subscripts t and s denote tension and shear, respectively.

Substituting the tangent stiffness tensor into Eq. (3.2) gives the acoustic tensor whose components in a matrix form are

(3.10) $$[Q_{ij}] = \begin{bmatrix} \frac{E}{2\left[(1+\nu) - 2\left(\frac{W}{a}\right)^2 \frac{\omega_s}{\pi} L_s\right]} & 0 \\ 0 & \frac{E}{\left[1 - \nu^2 - 4\left(\frac{W}{a}\right)^2 \frac{\omega_s}{\pi} L_t\right]} \end{bmatrix}.$$

As we are interested in the unidirectional tensile case, we only discuss L_t in the sequel. We first rewrite L_t (3.8), using Eq. (2.16), and omit the subscript 22 from $\bar{k}_{22}$ for brevity,

$$L_t = \frac{\ln\left(\cos\dfrac{\pi a}{W}\right)}{1 - \dfrac{2\bar{k}\,W^2}{\pi a E}\ln\left(\cos\dfrac{\pi a}{W}\right)}. \tag{3.11}$$

The value $2a/W$ represents the ratio of the cracked area to the nominal area in the direction perpendicular to the loading direction. It therefore represents the conventional damage parameter in the context of damage mechanics. Denoting $\Omega = 2a/W$, L_t can be rewritten as

$$L_t = \frac{\ln\left(\cos\dfrac{\pi}{2}\Omega\right)}{1 - \dfrac{8\bar{k}\,a}{\pi E}\dfrac{1}{\Omega^2}\ln\left(\cos\dfrac{\pi}{2}\Omega\right)}. \tag{3.12}$$

It is seen from Eq. (3.10) that the satisfaction of the localisation criterion (3.1) requires that $L_t \to \infty$. When this condition is met, it is seen from (3.7) that the determinant of the tangent stiffness matrix, $\det[D_{ij}]$, also vanishes. $[D_{ij}]$ is symmetric, as is $[Q_{ij}]$. Therefore, the condition $L_t \to \infty$ leads to the satisfaction of all bifurcation criteria identified by NEILSEN and SCHREYER [10], namely, the classical bifurcation criterion (3.1), the general bifurcation criterion, the limit point bifurcation criterion and the loss of strong ellipticity criterion. In the following, we shall use the phrases "localisation" or "material instability" to refer to the consequences of $\det[Q_{ij}] = 0$, i.e. when $L_t \to \infty$.

4. Conditions for material instability

Several features of the material instability are revealed by the above results. First, for unbridged material ($\bar{k} = 0$), it seen from Eq. (3.12) that the satisfaction of the localisation criterion $\det[Q_{ij}] = 0$ requires that $L_t = \ln\left(\cos\dfrac{\pi}{2}\Omega\right) \to \infty$. This simply means that the damage parameter, or any effective quantity, Ω tends to 1. In this case, L_s also becomes zero. So the material loses instability both under unidirectional tension perpendicular to the crack and under in-plane shear. Thus, the bifurcation criterion is identified with the damage-induced rupture of the material.

When $\bar{k} \neq 0$, it is seen from Eq. (3.12) that L_t is determined by the tangent bridging stiffness $\bar{k}$. For short-fibre-reinforced cementitious composites, a trilinear bridging law, such as OABC shown in Fig. 2, is commonly used (e.g. [3]). This is obviously an idealisation of the actual fibre pull-out test results.

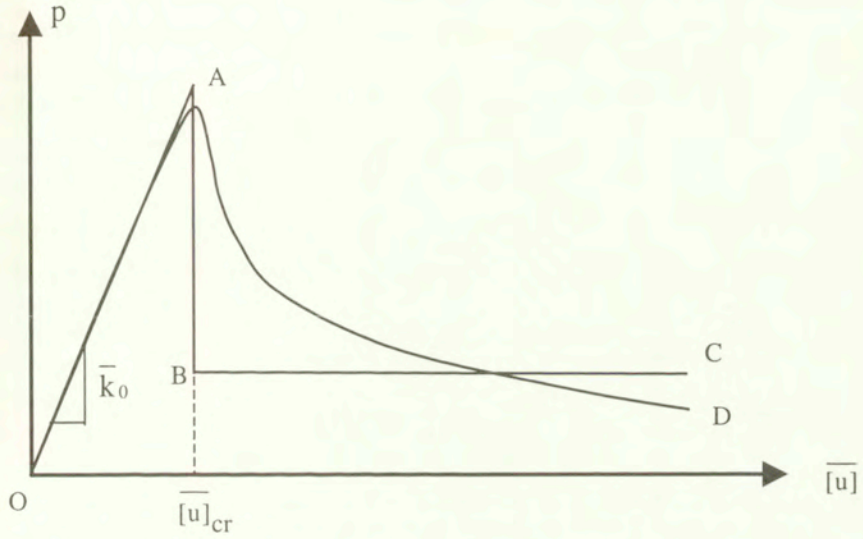

FIG. 2. An idealised trilinear bridging law OABC and a more realistic smooth bridging law OAD with continuous slope.

The problem with the idealised trilinear bridging law is the discontinuity in the tangent bridging stiffness $\bar{k}$. In real materials, especially when the average effect of randomly distributed fibres is considered, the tangent bridging stiffness varies gradually, as shown by OAD in Fig. 2. This continuous bridging traction can, for example, be described by

$$p = \bar{k}\,\overline{[u]}\,e^{-\frac{\overline{[u]}}{\overline{[u]}_{cr}}}. \tag{4.1}$$

The tangent bridging stiffness can thus be written as

$$\bar{k} = \bar{k}_0 \left\{ 1 - \frac{\overline{[u]}}{\overline{[u]}_{cr}} \right\} e^{-\frac{\overline{[u]}}{\overline{[u]}_{cr}}}, \tag{4.2}$$

where $\bar{k}_0$ is the initial tangent bridging stiffness when the fibres are bonded to the matrix (see Fig. 2). It is evident that the tangent bridging stiffness vanishes at $\overline{[u]} = \overline{[u]}_{cr}$ and it becomes negative, when $\overline{[u]} > \overline{[u]}_{cr}$. The expression (4.2) is in line with the simple local constitutive law that JIRÁSEK and BAŽANT [13] used in their study of the localisation phenomenon within the formalism of the non-local theory. The initial tangent bridging stiffness $\bar{k}_0$ can be calculated from the linear bridging model developed by LANGE-KORNBAK and KARIHALOO [14]

$$\bar{k}_0 = V_f \frac{\tau_v}{\tau_g} E_f \frac{h}{L} \tag{4.3}$$

where τ_g and τ_v are the frictional bond strength and the adhesive bond strength, respectively. h is the so-called snubbing factor, L is the length of fibres, and E_f their modulus of elasticity.

When $\bar{k} > 0$, it follows from (3.12) that L_t has the following property:

$$\Omega \to 0: \qquad L_t \to 0. \tag{4.4}$$

In other words, no instability can set in, if there is no damage in the material. Thus, as expected, the case $\Omega \to 0$ can be excluded from the instability analysis.

When $0 < \Omega < 1$, the bifurcation criterion ($L_t \to \infty$) can only be satisfied when the following condition is met (cf. (3.12)):

$$1 - \frac{8\bar{k}a}{\pi E}\frac{1}{\Omega^2}\ln\left(\cos\frac{\pi}{2}\Omega\right) = 0, \tag{4.5}$$

that is

$$\bar{k}^{cr} = \frac{\pi E}{8a}\frac{\Omega^2}{\ln\left(\cos\frac{\pi}{2}\Omega\right)} < 0 \qquad \text{for} \quad 0 < \Omega < 1 \tag{4.6}$$

with

$$\Omega \to 1: \qquad \bar{k}^{cr} \to 0. \tag{4.7}$$

The variation of the normalised $\bar{k}^{cr}$ with Ω given by (4.6) is shown in Fig. 3.

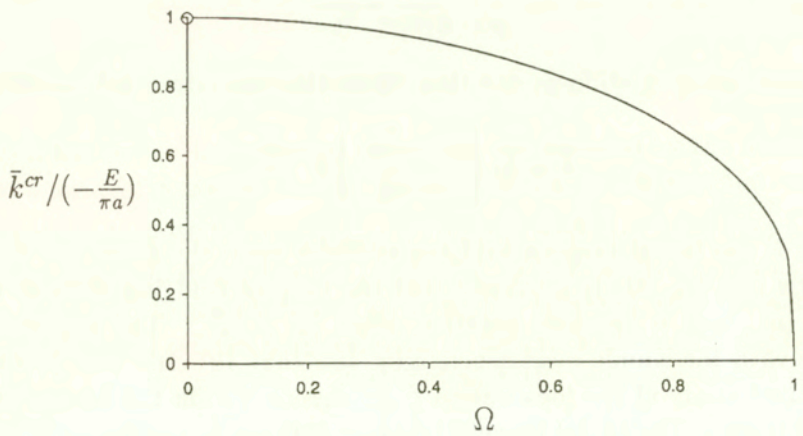

FIG. 3. Variation of normalised tangent bridging stiffness at macroscopic instability with damage parameter. No instability is possible when $\Omega = 0$. Thus the point on the axis of ordinates at 1 is excluded, as highlighted by the open circle.

From the above analysis and Fig. 3, we are able to discern several features of incipient material instability. First, it follows from Eq. (4.6) that for all values of Ω in the range $0 < \Omega < 1$, no instability can set in, if the tangent bridging stiffness $\bar{k}$ is greater than 0. In other words, no matter how much the matrix is damaged, as long as the fibres are still bonded to it ($\bar{k} > 0$) , the composite will not exhibit any instability at the macroscopic level, even when a through crack has formed in the matrix (see Fig. 4(a)). The tangent stiffness of the composite will continue to be positive. This is exactly what happens, for example, in strong continuous fibre-reinforced composites, as is demonstrated by the ACK model [15].

The second feature is that $\bar{k}$ can vanish before or after a through crack has formed, i.e., $\Omega \to 1$. Here, we discuss the formation of a through crack ($\Omega \to 1$) when the fibres are still bonded to the matrix, i.e., $\bar{k} \geq 0$. In this case, L_t (3.12) can be approximated by

$$L_t = -\frac{\pi a E}{4\bar{k}W}. \tag{4.8}$$

Here, W loses its meaning, although its appearance in the above formula simply points to the existence of an internal length scale. The expression (4.8) indicates that the bifurcation condition ($L_t \to \infty$) requires that the fibre bridging stiffness vanishes $\bar{k} = 0$. In other words, after a through crack has formed or is about to form, the macroscopic instability of the composite coincides with the (microscopic) bridging instability (see Fig. 4(b)).

The third feature is that when the localisation band is still not a through crack (i.e. $0 < \Omega < 1$), the localisation criterion can still be satisfied when $\bar{k}^{cr}$ is given by (4.6). We recall that the average crack opening displacement for a row of periodic cracks without the bridging action of fibres can be rewritten as (see, e.g. [16])

$$\Delta\sigma_m = -\frac{\pi E}{8a} \frac{\Omega^2}{\ln\left(\cos\frac{\pi}{2}\Omega\right)} \Delta\overline{[u]}. \tag{4.9}$$

When the cracks are bridged by fibres, the total instantaneous resistance of the composite material to crack opening can be written as the sum of matrix and fibre contributions

$$-\frac{\pi E}{8a} \frac{\Omega^2}{\ln\left(\cos\frac{\pi}{2}\Omega\right)} + \bar{k}. \tag{4.10}$$

Thus the condition (4.6) implies that the resistance of the composite material to crack opening displacement vanishes because the instantaneous resistance of the matrix itself to crack opening is exactly counterbalanced by the loss of the bridging resistance (see Fig. 4(c)).

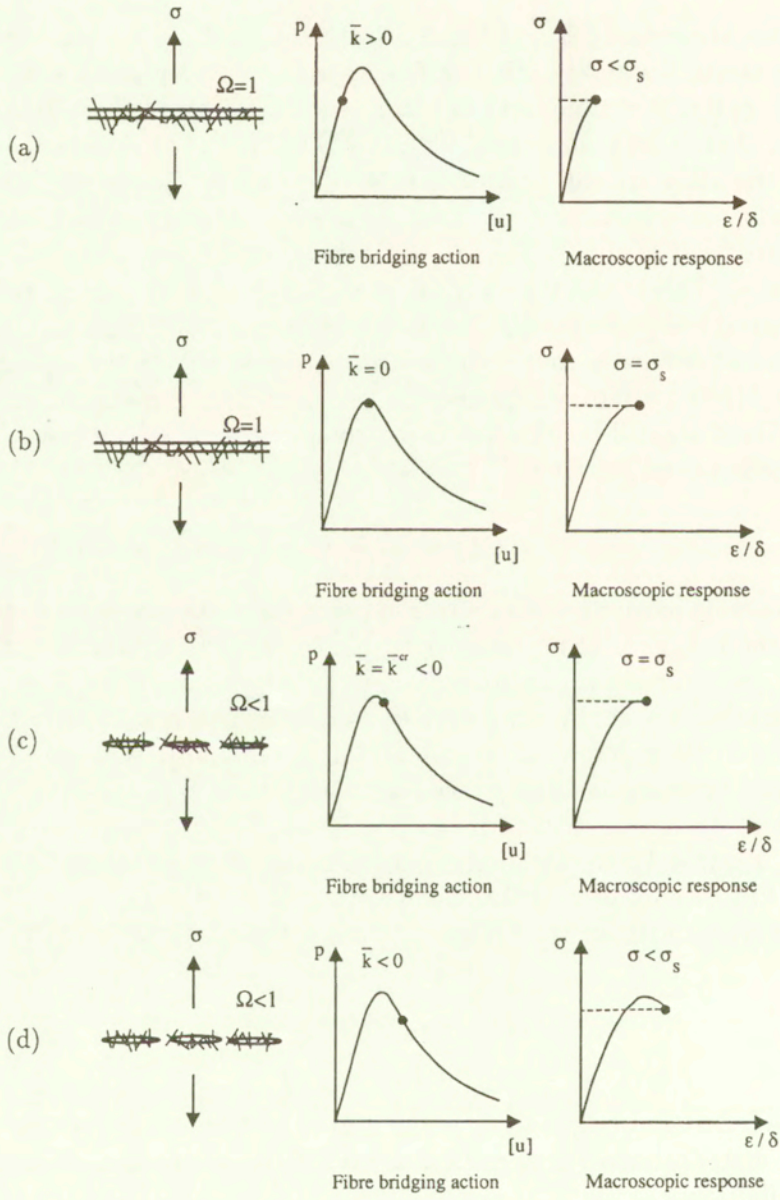

FIG. 4. Relationship between bridging stiffness and macroscopic response of the composite material. (a) no instability, when the fibres are bonded to matrix ($\bar{k} > 0$) even though a through crack has formed in it ($\Omega = 1$); (b) macroscopic instability induced by loss of bridging stiffness ($\bar{k} = 0$) and formation of a through crack ($\Omega = 1$); (c) macroscopic instability induced by a combination of matrix damage ($\Omega < 1$) andinitial softening of bridging stiffness equal to $\bar{k}^{cr} < 0$; (d) macroscopic tension-softening caused by matrix damage ($\Omega < 1$) and considerable softening of bridging stiffness ($\bar{k} < 0$).

The parameter $\bar{k}^{cr}$ in (4.6) includes the physical effect of several factors on the inception of localisation. First, instability of the composite at the macrolevel is possible, when $\bar{k} < 0$, i.e., the fibres are only exerting the residual friction bridging action. The closer Ω is to 1, the smaller the absolute value of $\bar{k}^{cr}$. When $\Omega = 1$, the macroscopic instability occurs at $\bar{k} = 0$, i.e. it coincides with the microscopic (bridging) instability. Second, the dependence of the absolute value of $\bar{k}^{cr}$ on the modulus E of the uncracked matrix indicates that the stiffer the matrix, the less susceptible is the material to microscopic instability. Third, $\bar{k}^{cr}$ contains a length scale, here the half-length a of a crack. As the parameters Ω and E are scale insensitive, $\bar{k}^{cr}$ introduces a scale effect into the loss of macroscopic instability of short-fibre-reinforced materials. The macroscopic response of large specimens made from these composites will be more sensitive to vanishing of bridging stiffness than that of small specimens with the same level of damage ($0 < \Omega < 1$).

It is seen from Fig. 3 that the absolute value of $\bar{k}^{cr}$ increases rapidly when the value of Ω deviates from 1. This means that in order to delay macroscopic instability of the composite, it is very important to prevent or delay the coalescence of the discrete microcracks. In principle, if the microcracks are somehow prevented from coalescing whilst at the same time the tangent bridging stiffness is maintained above the critical value given by (4.6), macroscopic instability of the composite cannot occur. In practice though, the discrete microcracks are likely to propagate and coalesce once the fibres begin to be pulled out, i.e., once $\bar{k}$ reaches zero. Figure 4(d) illustrates such a possibility whereby the composite exhibits tension-softening, while the cracks in the localisation band are still fragmented ($0 < \Omega < 1$) but the tangent bridging stiffness is equal to or less than the critical value (4.6). This provides a softening model which is different from that introduced by LI *et al.* [17] in which the softening is a result of fibre pull-out from a through crack ($\Omega = 1$).

5. Conclusions

In this paper, based upon the pseudo-traction technique and an asymptotic analysis, the tensile stress-strain relation is established analytically for short-fibre-reinforced composites containing multiple parallel bridged microcracks. This allows an analysis to be made of the macroscopic material instability in the tensile deformation process of these composites. The material instability at the macrolevel is examined using the classical bifurcation criterion, with an emphasis on the role of the bridging action of fibres. Conditions for the incipient macroscopic instability are obtained as functions of damage in the matrix, crack length, and the microscopic bridging stiffness. It is found that no macroscopic

instability is possible as along as the tangent bridging stiffness is positive, i.e., as long as the fibres remain bonded to the matrix. However, whilst the bridging instability at the microlevel plays a major role in the macroscopic instability, it is the damage in the matrix that determines when the macroscopic instability is induced by the bridging instability. The microscopic bridging instability does not necessarily induce macroscopic instability. Indeed, macroscopic instability may be delayed until the fibres are only exerting residual frictional action. Likewise, the formation of a through crack is neither a necessary nor a sufficient condition for the onset of tension-softening in the composite. The results also suggest that in order to delay macroscopic instability in the tensile response, it is very important to prevent or to delay the coalescence of the discrete microcracks that form in the strain-hardening stage.

Acknowledgments

This work was completed while J. Wang was visiting The University of Wales Cardiff under financial support from the Royal Society, London, which is gratefully acknowledged.

References

1. M. ORTIZ, *Microcrack coalescence and macroscopic crack growth initiation in brittle solids*, International Journal of Solids and Structures, **24**, 231–250, 1988.
2. Z. MRÓZ, *Modelling slip and damage at concrete or rock interfaces*, Lecture Notes for Summer Course on Mechanics of Concrete, Janowice-Cracow, September 1996.
3. B. L. KARIHALOO, J. WANG and M. GRZYBOWSKI, *Doubly periodic arrays of bridged cracks and short fibre-reinforced cementitious composites*, J. Mech. Phys. Solids, **44**, 1565–1586, 1996.
4. J. WANG, J. FANG and B. L. KARIHALOO, *Asymptotic bounds on overall moduli of cracked bodies*, International Journal of Solids and Structures, **37**, 7055–7069, 2000.
5. J. WANG, J. FANG and B. L. KARIHALOO, *Asymptotics of multiple crack interactions and prediction of effective modulus*, International Journal of Solids and Structures, **37**, 4261–4273, 2000.
6. M. KACHANOV, *Effective elastic properties of cracked solids: critical review of some basic concepts*, Appl. Mech. Rev., **45**, 304–335, 1992.
7. H. HORII and S. NEMAT-NASSER, *Elastic fields of interacting inhomogeneities*, International Journal of Solids and Structures, **21**, 731–745, 1985.
8. B. L. KARIHALOO and J. WANG, *On the solution of doubly periodic array of cracks*, Mech. Mater., **26**, 209–212, 1997.
9. J. W. RUDNICKI and J. R. RICE, *Conditions for the localization of deformation in pressure-sensitive dilatant materials*, J. Mech. Phys. Solids, **23**, 371–394, 1975.
10. M. K. NEILSEN and H. L. SCHREYER, *Bifurcations in elastic-plastic materials*, International Journal of Solids and Structures, **30**, 521–544, 1993.

11. P. TJIPTOBROTO and W. HANSEN, *Tensile strain hardening and multiple cracking in high-performance cement-based composites containing discontinuous fibres*, ACI Mater. J., **90**, 16–25, 1993.

12. B. L. KARIHALOO and J. WANG, *Mechanics of fibre-reinforced cementitious composites*, Computers & Structures, **76**, 19–34, 2000.

13. M. JIRÁSEK and Z. P. BAŽANT, *Localization analysis of nonlocal model based upon crack interactions*, ASCE J. Eng. Mech., **120**, 1521–1542, 1994.

14. D. LANGE-KORNBAK and B. L. KARIHALOO, *Tension softening of fibre-reinforced cementitious composites*, Cement and Concrete Composites, **19**, 315–328, 1997.

15. J. AVESTON, G. A. COOPER and A. KELLY, *Single and multiple fracture*, [In:] The properties of fibre composites, Conference Proceedings of National Physical Laboratory, 15–26, London: IPC, 1971.

16. B. L. KARIHALOO, *Fracture Mechanics and Structural Concrete*, Addison Wesley Longman, UK 1995.

17. V. LI, Y. WANG and S. BAKER, *A micromechanical model of tension-softening and bridging toughening of short random fibre reinforced brittle matrix composites*, J. Mech. Phys. Solids, **39**, 607–625, 1991.

Received November 2, 1999.

Arch. Mech., **52**, 4–5, pp. 857–887, Warszawa 2000

The characteristic-based-split (CBS) algorithm, stability and boundary conditions

Dedicated to Professor Zenon Mróz on the occasion of his 70th birthday

O. C. ZIENKIEWICZ and P. NITHIARASU

Institute for Numerical Methods in Engineering
University of Wales Swansea, Swansea SA2 8PP, UK

RECENTLY SEVERAL PAPERS were published on the subject of the CBS algorithm. This paper presents a brief summary of the theory of the algorithm and some recent findings on stabilization procedures and appropriate boundary conditions. Several solutions are also presented in this paper.

1. Introduction

IN RECENT YEARS, we have published several papers concerning the basis and applications of the CBS algorithm to a large variety of fluid dynamics problems [1 – 9]. The present paper summarises the theory of the algorithm and demonstrates its practical applications. It also contains some other extensions which are important for increasing the accuracy of the CBS procedure.

The algorithm can be used in explicit, semi-implicit, nearly implicit and indeed in fully implicit forms. The algorithm was initially based on a series of preliminary studies conducted between 1990 and 1995 [10 – 12] but the split was correctly introduced only later in Refs. [1, 2].

Before the present algorithm was available, most successes of finite difference and finite element methods in fluid dynamics were based on some variant of the Lax-Wendroff [13] scheme which, by approximating better to the time derivative, also introduced stabilization of the convective terms. The method, when applied to finite elements, became known as the Taylor-Galerkin method [14]. Later it was discovered that for scalar variables, a direct algorithm utilizing the optimal approximation along the characteristics, the characteristic Galerkin method, could be shown to be identical to the Taylor-Galerkin [15, 16] method.

The identity of the two procedures exists only in the scalar case described by the well-known convection-diffusion equation which is often used as a model for fluid dynamics problems. However, for problems involving several variables,

typical of fluid dynamics, the application of characteristic Galerkin method is not possible since only a single characteristic speed must be involved. For this reason, the Taylor-Galerkin procedure has been widely used [17 – 19], though giving a sub-optimal approximation. Motivation of the development of the present algorithm came from the fact that characteristic Galerkin procedures for a scalar variable are optimal in the sense of approximation, and that with suitable splitting, these can be applied for the first stage of the solution of the fluid dynamics equations. The remainder of the split being self-adjoint, can then be solved optimally using the Galerkin procedure.

This split follows the general process initially introduced by CHORIN [20] for incompressible flow problems. Further motivation which originated the new algorithm is based on an additional benefit coming from the fact, already observed, that for incompressible situations, the algorithm permitted equal (and indeed arbitrary) interpolations for all the variables used. This sidesteps the Babuska-Brezzi requirement in finite elements and similarly, all difficulties in standard finite difference schemes. In the present form, the solution turns out to be fully accurate with arbitrary interpolation for velocity and pressure for full incompressibility.

The algorithm involves time integration and in general, the time-step size will be limited by the nature of the time stepping procedure adopted in each part of the split. If a fully explicit procedure is adopted in the first part of the split then the time step is governed by a Courant number defined in terms of the flow velocity $|\mathbf{u}|$ and viscosity ν. If an explicit scheme is also used for the second part of the split then a Courant number depending on the compressible wave celerity c is invoked and may control the time-step size. We shall thus have here several possible categories of problems.

(a) *Transonic and supersonic flows; Fully explicit process.* Here generally fully explicit computation is preferred as the time step limitations for both parts of the split are similar.

(b) *Low Mach number, incompressible flows with low viscosity, Semi-inplicit process.* Here the flow is nearly incompressible and the time step used will be governed by the first part of the split with the Courant number not affected much by viscosity.

(c) *Low Mach number with high viscosity; Nearly implicit process.* In this range of flow, the limiting time step again is governed by the first part of the split but viscosity may pose here very severe limits. In such a regime, a 'nearly' implicit procedure is recommended in which the viscous terms are treated implicitly.

2. The scalar convection-diffusion problem and the characteristic Galerkin explicit approximation

Before proceeding with the description of the full algorithm, we shall recall the application of the Characteristic Galerkin method in the explicit form to a typical convection-diffusion process with a scalar dependent variable ϕ. The governing equations can here be written always in a conservation form as

$$\frac{\partial V}{\partial t} + \frac{\partial F_i}{\partial x_i} + \frac{\partial G_i}{\partial x_i} + Q = 0, \tag{2.1}$$

with x_i being the i-th coordinate (i = 1, 2, 3),

$$F_i = u_i \phi \tag{2.2}$$

– the convected flux,

$$G_i = -k \frac{\partial \phi}{\partial x_i} \tag{2.3}$$

– the diffusion flux; here k is the diffusion coefficient.

$$Q = Q(x, t) \tag{2.4}$$

– the source term, and

$$u_i = u_i(x, t) \tag{2.5}$$

is the velocity field which is assumed to be known.

The full equation can thus be alternatively written as

$$\frac{\partial \phi}{\partial t} = -u_j \frac{\partial \phi}{\partial x_j} + \frac{\partial}{\partial x_i}\left(k \frac{\partial \phi}{\partial x_i}\right) - Q - \phi \frac{\partial u_j}{\partial x_j} = R(\phi) \tag{2.6}$$

in which only the first term on the RHS is not self-adjoint. As that term corresponds precisely to an advection wave moving with a velocity $\mathbf{u}$, a change of coordinates to the characteristic ones given by

$$dx_i' = dx_i - u_i dt \tag{2.7}$$

makes the offending term vanish, leaving a fully self-adjoint system.

For such a self-adjoint system it is known that the standard Galerkin approximation in space is optimal but the inconvenience of a moving coordinate system is introduced. However, this can be overcome with suitable remeshing and the procedure has been used in many early solutions of the above equation. Here the work of ADYE-BREBBIA [21] and Barbara Mróz should be mentioned followed by much later work. For a complete review the reader is directed to Ref. [23]. While

the exact coordinate transformation introduced no error, the simplified procedures using a Taylor approximation within the time step eliminated the costly process of remeshing (or mesh interpolation), introducing however a time-step limitation [23]. This process is fully described in [1, 2] and also in the recent text [23], and an explicit form can be written in fixed coordinates as

$$\Delta\phi = \phi^{n+1} - \phi^n = \Delta t R(\phi)^{n+\theta_3} - \frac{\Delta t^2}{2} u_i \frac{\partial}{\partial x_i} (R(\phi))^n + O(\Delta t^3) \tag{2.8}$$

where $0 \leq \theta_3 \leq 1$ and $\mathrm{R}(\phi)$ is defined by Eq. (2.6).

This, as already mentioned, is of an identical form to that resulting from the Taylor-Galerkin procedures and the second term adds the stabilizing diffusion in the streamline direction. Indeed a similar form can be obtained here in a variety of ways and recently OÑATE [24, 25] introduced an interesting form of stability control by using so-called "finite increment" calculus (FIC). However, only the characteristic form ensures the optimal approximation as Eq. (2.8) is derived from a self-adjoint form in which spatial discretization by the Galerkin method can be optimally used. We can write thus the approximation

$$\phi = \mathbf{N}\overline{\phi}, \tag{2.9}$$

where $\mathbf{N}$ is the shape function and $\overline{\phi}$ is a nodal quantity. We use the weights $\mathbf{N}^{\mathbf{T}}$ in the integrated residual expression. Thus we obtain

$$\mathbf{M}(\overline{\phi}^{\mathbf{n+1}} - \overline{\phi}^{\mathbf{n}}) = -\Delta t[(\mathbf{C}\overline{\phi}^{\mathbf{n}} + \mathbf{K}\overline{\phi}^{\mathbf{n}} + \mathbf{f}^{\mathbf{n}}) - \Delta t(\mathbf{K_u}\overline{\phi}^{\mathbf{n}} + \mathbf{f_s^n})] \tag{2.10}$$

if we assume $\theta_3 = 0$, as is generally done in explicit form and omit higher derivatives and source terms. In the above equation

$$\begin{aligned}
\mathbf{M} &= \int_\Omega \mathbf{N}^{\mathbf{T}}\mathbf{N} d\Omega, \\
\mathbf{C} &= \int_\Omega \mathbf{N}^{\mathbf{T}} \frac{\partial}{\partial x_i}(u_i \mathbf{N}) d\Omega, \\
\mathbf{K} &= \int_\Omega \frac{\partial \mathbf{N}^{\mathbf{T}}}{\partial x_i} k \frac{\partial \mathbf{N}}{\partial x_i} d\Omega, \\
\mathbf{f} &= \int_\Omega \mathbf{N}^{\mathbf{T}}\mathbf{Q} d\Omega + \text{b.t.}
\end{aligned} \tag{2.11}$$

and $\mathbf{K_u}$ and $\mathbf{f_s^n}$ come from the new term introduced by the discretization along the characteristics. b.t. stands for the boundary terms. After integration by parts, the expression of $\mathbf{K_u}$ and $\mathbf{f_s}$ is

$$\mathbf{K_u} = -\frac{1}{2}\int_\Omega \frac{\partial}{\partial x_i}(u_i \mathbf{N}^\mathbf{T})\frac{\partial}{\partial x_i}(u_i \mathbf{N})d\Omega,$$

(2.12)

$$\mathbf{f_s} = -\frac{1}{2}\int_\Omega \frac{\partial}{\partial x_i}(u_i \mathbf{N}^\mathbf{T})\mathbf{Q}d\Omega + \text{b.t.}$$

where b.t stands for integrals extending along the region boundaries [23].
The approximation is valid for any scalar convected quantity even if that is the velocity component u_i itself, as is the case with the momentum conservation equations. For this reason we have presented above all the details of the spatial approximation, since the matrices will be repeatedly used.

It is of interest that the explicit form of the Eq. (2.10) is only conditionally stable. For one-dimensional problems, the stability condition is given as (neglecting the effect of sources)

$$\Delta t \leq \Delta t_{\text{crit}} = \frac{h}{|\mathbf{u}|} \tag{2.13}$$

for linear elements in which h is the size of the element.

In 2D problems, the critical time step may be presented as [26]

$$\Delta t_{\text{crit}} = \frac{\Delta t_u \Delta t_\nu}{\Delta t_u + \Delta t_\nu}, \tag{2.14}$$

where Δt_u is given by Eq. (2.13) and $\Delta t_\nu = h^2/2k$ is the diffusive limit for the critical one-dimensional time step.

Further, with $\Delta t = \Delta t_{\text{crit}}$ the steady-state solution results in a diffusion change (almost) identical to that obtained by using the optimal streamline upwinding procedures [23]. Thus if steady state solutions are the main objective of the computation, such a value of Δt should be used in connection with the $\mathbf{K_u}$ term.

3. The CBS algorithm for the Navier-Stokes equations

3.1. The equations of flow – Navier-Stokes problem

The full conservation form of the Navier-Stokes equations for compressible flow is traditionally written as

$$\frac{\partial \mathbf{V}}{\partial t} + \frac{\partial \mathbf{F_i}}{\partial x_i} + \frac{\partial \mathbf{G_i}}{\partial x_i} + \mathbf{Q} = 0 \tag{3.1}$$

with

$$\mathbf{V}^{\mathbf{T}} = (\rho, \rho u_1, \rho u_2, \rho E) \tag{3.2}$$

being the independent variable vector,

$$\mathbf{F}_{\mathbf{i}}^{\mathbf{T}} = (\rho u_i, \rho u_i u_1 + \delta_{i1} p, \rho u_i u_2 + \delta_{i2} p, u_i(\rho E + p)) \tag{3.3}$$

defining the convective flux vector, and

$$\mathbf{G}_{\mathbf{i}}^{\mathbf{T}} = (0, -\tau_{i1}, -\tau_{i2}, q_i - \tau_{ij} u_j) \tag{3.4}$$

defining the diffusion fluxes. Finally,

$$\mathbf{Q}^{\mathbf{T}} = (0, \rho g_1, \rho g_2, \rho(g_i u_i + q''')) \tag{3.5}$$

gives the source terms.

In the above relations, stress components τ_{ij} are related to velocity gradients by

$$\tau_{ij} = \mu \left(\frac{\partial u_i}{\partial x_j} + \frac{\partial u_j}{\partial x_i} - \frac{2}{3} \frac{\partial u_k}{\partial x_k} \delta_{ij} \right); \tag{3.6}$$

u_i are the velocity components; ρ is the density; E the specific energy; q_i the heat flux, q''' the heat generation per unit mass, p the pressure; g_i the acceleration due to gravity.

The equations are completed by the universal gas law

$$p = \rho R T \tag{3.7}$$

where R is the gas constant and T is the temperature.

The sound velocity is defined, assuming constant entropy, as

$$c^2 = \frac{\partial p}{\partial \rho} = \frac{\gamma p}{\rho}. \tag{3.8}$$

Here γ is the ratio of specific heats.

Further we can write conveniently

$$\frac{\partial \rho}{\partial t} = \frac{\partial \rho}{\partial p} \frac{\partial p}{\partial t} = \frac{1}{c^2} \frac{\partial p}{\partial t} \tag{3.9}$$

though this expression assumes again constant entropy and is therefore only an approximation. In what follows we shall use Eq. (3.9) but elsewhere we discuss the possibility of correcting any errors involved by amendment of the algorithm [4].

While in gas flow all the equations are fully coupled, for incompressible flows in which $c = \infty$ the energy equations can be solved independently after the velocity field has been established. Nevertheless, a single algorithm for the solution of both problems is possible as we shall now show.

Although the form of Eq. (3.1) is identical to that of the convection-diffusion problem of Eq. (2.1), three wave speeds exist and the characteristic Galerkin procedure cannot be directly applied. In the next section we show how this can be done with a fractional step.

3.2. Characteristic-based-split (CBS) algorithm

For convenience we shall rewrite Eq. (3.2) in a more direct form, omitting initially the energy equation. These equations can be solved completely in a time increment Δt as the only coupling which exists is through the speed of sound c for which we shall simply use the value at time t_n due to the explicit nature of the time stepping algorithm. Equation (3.2) can be rewritten in separate equations as (neglecting energy equation):
Continuity

$$\frac{1}{c^2}\frac{\partial p}{\partial t} + \frac{\partial}{\partial x_i}(\rho u_i) = 0. \tag{3.10}$$

Momentum

$$\frac{\partial U_i}{\partial t} + \frac{\partial}{\partial x_j}(u_j U_i) = \frac{\partial \tau_{ij}}{\partial x_j} + \rho g_i + Q, \tag{3.11}$$

where $U_i = \rho u_i$, $Q = -\dfrac{\partial p}{\partial x_i}$. Now the temporal discretization of the above equations is considered.

3.2.1 The split-temporal discretization. We can discretize Eq. (3.11) in time using the Characteristic Galerkin process. Except for the pressure term, this equation is similar to the convection-diffusion Eq. (2.6). This term can however be treated as a known (source type) quantity provided we have an independent way of evaluating the pressure. Before proceeding with the algorithm, we rewrite Eq. (3.11) in the form given below, to which the Characteristic Galerkin process can be applied

$$\frac{\partial U_i}{\partial t} = -\frac{\partial}{\partial x_j}(u_j U_i) + \frac{\partial \tau_{ij}}{\partial x_j} + \rho g_i + Q^{n+\theta_2} \tag{3.12}$$

with $Q^{n+\theta_2}$ being a known quantity evaluated at $t = t^n + \theta_2 \Delta t$ in a time increment Δt. In the above equation

$$Q^{n+\theta_2} = -\frac{\partial p}{\partial x_i}^{n+\theta_2} \tag{3.13}$$

with

$$\left(\frac{\partial p}{\partial x_i}\right)^{n+\theta_2} = \theta_2 \left(\frac{\partial p}{\partial x_i}\right)^{n+1} + (1-\theta_2)\left(\frac{\partial p}{\partial x_i}\right)^{n} \tag{3.14}$$

or

$$\left(\frac{\partial p}{\partial x_i}\right)^{n+\theta_2} = \left(\frac{\partial p}{\partial x_i}\right)^{n} + \theta_2 \frac{\partial \Delta p}{\partial x_i}. \tag{3.15}$$

In this formula

$$\Delta p = p^{n+1} - p^n. \tag{3.16}$$

Using the Eq. (2.8) and replacing ϕ by U_i, we can write

$$U_i^{n+1} - U_i^n = \Delta t \left[-\frac{\partial}{\partial x_j}(u_j U_i)^n + \left(\frac{\partial \tau_{ij}}{\partial x_j}\right)^n + Q^{n+\theta_2} - (\rho g_i)^n + \left(\frac{\Delta t}{2} u_k \frac{\partial}{\partial x_k} \left(\frac{\partial}{\partial x_j}(u_j U_i) - Q + \rho g_i \right) \right)^n \right]. \tag{3.17}$$

At this stage we have to introduce the 'split' in which we substitute a suitable approximation for Q which allows the calculation to proceed before p^{n+1} is evaluated. Two alternative approximations are useful and we shall describe these as *Split A* and *Split B*, respectively. In the first we remove all the pressure gradient terms from Eq. (3.17), in the second we retain in that equation the pressure gradient corresponding to the beginning of the step, i.e. $\left(\frac{\partial p}{\partial x_i}\right)^n$. Though it appears that the second split might be more accurate, there are other reasons for the success of the first split which we shall refer to later. Indeed the 'Split A' is the one which we shall universally recommend.

Split A

Here we introduce an auxiliary variable U_i^* such that

$$\Delta U_i^* = U_i^* - U_i^n = \Delta t \left[-\frac{\partial}{\partial x_j}(u_j U_i) + \frac{\partial \tau_{ij}}{\partial x_j} - \rho g_i + \frac{\Delta t}{2} u_k \frac{\partial}{\partial x_k} \left(\frac{\partial}{\partial x_j}(u_j U_i) + \rho g_i \right) \right]^n. \tag{3.18}$$

This equation will be solved subsequently by an explicit time step applied to the discretized form, and a complete solution is now possible. The "correction" given below is available once the pressure increment is evaluated,

$$\Delta U_i = U_i^{n+1} - U_i^n = \Delta U_i^* - \Delta t \left(\frac{\partial p}{\partial x_i}\right)^{n+\theta_2} - \frac{\Delta t^2}{2} u_k \frac{\partial Q}{\partial x_k}. \tag{3.19}$$

From Eq. (3.10) we have

$$\Delta\rho = \left(\frac{1}{c^2}\right)^n \Delta p = -\Delta t \frac{\partial U_i}{\partial x_i}^{n+\theta_1} . \tag{3.20}$$

Replacing U_i^{n+1} with the known intermediate, auxiliary variable U_i^* and rearranging (after neglecting higher order terms), we have

$$\Delta\rho = \left(\frac{1}{c^2}\right)^n \Delta p = -\Delta t \left[\frac{\partial U_i^n}{\partial x_i} + \theta_1 \frac{\partial \Delta U_i^*}{\partial x_i} - \Delta t \theta_1 \left(\frac{\partial^2 p^n}{\partial x_i \partial x_i} + \theta_2 \frac{\partial^2 \Delta p}{\partial x_i \partial x_i}\right)\right] \tag{3.21}$$

where the U_i^* and pressure terms in the above equation come from Eq. (3.19).

The above equation is fully self-adjoint in the variables Δp (or $\Delta\rho$) which are the unknowns. Now standard Galerkin-type procedure can be optimally used for spatial approximation. It is clear that the governing equations can be solved after spatial discretization in the following order:
Eq. (3.18) to obtain ΔU_i^* ;
Eq. (3.21) to obtain Δp or $\Delta\rho$;
Eq. (3.19) to obtain ΔU_i thus establishing the values at t^{n+1}.

After completing the calculation to establish ΔU_i and Δp (or $\Delta\rho$), the energy equation is dealt with independently, and the value of $(\rho E)^{n+1}$ is obtained by the Characteristic Galerkin process.

It is important to remark that this sequence allows us to solve the governing Eqs. (3.1),in an efficient manner and with adequate numerical damping. *Note that these equations are written in conservation form. Therefore, this algorithm is well suited for dealing with supersonic and hypersonic problems, in which the conservation form ensures that shocks will be placed at right positions and unique solution will be achieved.*

Split B

In this split we also introduce an auxiliary variable U_i^{**} now retaining the known values of $Q^n = -\dfrac{\partial p^n}{\partial x_i}$, i.e.

$$\Delta U_i^{**} = U_i^{**} - U_i^n = \Delta t \left[-\frac{\partial}{\partial x_j}(u_j U_i) + \frac{\partial \tau_{ij}}{\partial x_j} - \frac{\partial p}{\partial x_i} - \rho g_i + \frac{\Delta t}{2} u_k \frac{\partial}{\partial x_k}\left(\frac{\partial}{\partial x_j}(u_j U_i) - Q + \rho g_i\right)\right]^n . \tag{3.22}$$

It may appear that now U_i^{**} is a better approximation of U^{n+1}. We can now write the correction as

$$\Delta U_i = U_i^{n+1} - U_i^n = \Delta U_i^{**} - \theta_2 \Delta t \frac{\partial \Delta p}{\partial x_i}, \tag{3.23}$$

i.e. the correction to be applied is smaller than that assuming 'Split A' (Eq. 3.19). Further if we use the fully explicit form with $\theta_2 = 0$, no mass velocity (U_i) correction is necessary. We proceed to calculate the pressure changes as in 'Split A' as

$$\Delta\rho = \frac{1}{c^2}\Delta p = -\Delta t \left[\frac{\partial U_i}{\partial x_i}^n + \theta_1 \frac{\partial \Delta U_i^{**}}{\partial x_i} - \Delta t \theta_1 \theta_2 \frac{\partial^2 \Delta p}{\partial x_i^2} \right]. \tag{3.24}$$

The solution stages follow the same steps as in 'Split A'. The final matrix form of the above steps and energy step are given as

Split A

Step 1. Intermediate momentum

$$\Delta\tilde{\mathbf{U}}^* = -\mathbf{M_u}^{-1}\Delta t \left[(\mathbf{C_u}\tilde{\mathbf{U}} + \mathbf{K}_\tau\tilde{\mathbf{u}} - \mathbf{f}) - \Delta t(\mathbf{K_u}\tilde{\mathbf{u}} + \mathbf{f_s}) \right]^n. \tag{3.25}$$

Step 2. Pressure

$$(\tilde{\mathbf{M}} + \Delta t^2 \theta_1 \theta_2 \mathbf{H})\Delta\tilde{\mathbf{p}} = \Delta t[\mathbf{G}_{\mathbf{pu}}^{\mathbf{T}}\tilde{\mathbf{U}}^{\mathbf{n}} + \theta_1 \mathbf{G_{pu}}\Delta\tilde{\mathbf{U}}^* - \Delta t\theta_1 \mathbf{H}\tilde{\mathbf{p}} - \mathbf{f_p}]^n. \tag{3.26}$$

Step 3. Momentum correction

$$\Delta\tilde{\mathbf{U}} = \Delta\tilde{\mathbf{U}}^* - \mathbf{M_u^{-1}}\Delta t \left[\mathbf{G}_{\mathbf{up}}^{\mathbf{T}}(\tilde{\mathbf{p}}^{\mathbf{n}} + \theta_2\Delta\tilde{\mathbf{p}}) + \frac{\Delta t}{2}\mathbf{P}\tilde{\mathbf{p}}^{\mathbf{n}} \right]. \tag{3.27}$$

Step 4. Energy

$$\Delta\tilde{\mathbf{E}} = -\mathbf{M_E^{-1}}\Delta t \Big[\mathbf{C_E}\tilde{\mathbf{E}} + \mathbf{C_p}\tilde{\mathbf{p}} + \mathbf{K_T}\tilde{\mathbf{T}} + \mathbf{K}_{\tau\mathbf{E}}\tilde{\mathbf{u}} + \mathbf{f_e} - \Delta t(\mathbf{K_{uE}}\tilde{\mathbf{E}} + \mathbf{K_{up}}\tilde{\mathbf{p}} + \mathbf{f_{es}}) \Big]^n. \tag{3.28}$$

Split B

With the 'Split B', the discretization and solution procedure have to be slightly modified. Leaving the details of the derivation to the Reader and using identical discretization processes, the final steps can be summarised as:

Step 1

$$\Delta\tilde{\mathbf{U}}_\mathbf{i}^{**} = -\mathbf{M_u}^{-1}\Delta t \Big[(\mathbf{C_u}\tilde{\mathbf{U}} + \mathbf{K}_\tau\tilde{\mathbf{U}} + \mathbf{G}_{\mathbf{up}}^{\mathbf{T}}\tilde{\mathbf{p}} - \mathbf{f}) - \Delta t(\mathbf{K_u}\tilde{\mathbf{U}} + \mathbf{f_s} + \tfrac{\Delta t}{2}\mathbf{P}\tilde{\mathbf{p}}^{\mathbf{n}}) \Big]^n; \tag{3.29}$$

here all matrices are the same as in 'Split A' except the forcing term $\mathbf{f}$ which is

$$\mathbf{f} = \int_{\Omega} \mathbf{N}_{\mathbf{u}}^{\mathbf{T}} \rho \mathbf{g} d\Omega + \int_{\Gamma} \mathbf{N}_{\mathbf{u}}^{\mathbf{T}} \mathbf{t} d\Gamma, \tag{3.30}$$

Step 2

$$(\tilde{\mathbf{M}} + \Delta t^2 \theta_1 \theta_2 \mathbf{H}) \Delta \tilde{\mathbf{p}} = \Delta t [\mathbf{G}_{\mathbf{pu}}^{\mathbf{T}} \tilde{\mathbf{U}}^{\mathbf{n}} + \theta_1 \mathbf{G}_{\mathbf{pu}} \Delta \tilde{\mathbf{U}}^{**} - \mathbf{f}_{\mathbf{p}}]^n, \tag{3.31}$$

and

Step 3

$$\Delta \tilde{\mathbf{U}} = \Delta \tilde{\mathbf{U}}^{**} - \mathbf{M}_{\mathbf{u}}^{-\mathbf{1}} \Delta t \left[\theta_2 \mathbf{G}_{\mathbf{up}}^{\mathbf{T}} \Delta \tilde{\mathbf{p}}\right]. \tag{3.32}$$

The 'Step 4' , calculation of energy, is unchanged. The Reader can notice the minor differences in the above equations from those of 'Split A'. For details of the matrices involved, the Reader can consult [1, 2, 7, 23].

4. Explicit, semi-implicit and nearly implicit forms

The algorithm described will always contain an explicit portion in the first Characteristic Galerkin step. However the second step, i.e. that of determination of the pressure increment can be made either explicit or implicit and various possibilities exist here, depending on the choice of θ_2. Now different stability criteria will apply. We refer to schemes being fully explicit or semi-implicit, depending on the choice of the parameter θ_2.

It is also possible to solve the first step in a partially implicit manner to avoid severe time-step restriction due to the viscous term. Now the viscous term is the one for which an implicit solution is sought. We refer to such schemes as quasi (nearly) implicit schemes.

4.1. Fully explicit form

In fully explicit forms, $1/2 \leq \theta_1 \leq 1$ and $\theta_2 = 0$. In general, the time step limitations explained for the convection diffusion equations are applicable, i.e.

$$\Delta t \leq \frac{h}{c + |\mathbf{u}|}, \tag{4.1}$$

since viscosity effects are generally negligible here.

This particular form is very successful in compressible flow computations and has been widely used by the authors for solving many complex problems [6].

4.2. Semi-implicit form

In semi-implicit form the following values apply:

$$\frac{1}{2} \leq \theta_1 \leq 1, \qquad \frac{1}{2} \leq \theta_2 \leq 1. \tag{4.2}$$

Again the algorithm is conditionally stable. The permissible time step is governed by the critical step of the Characteristic Galerkin explicit relation solved in Step 1 of the algorithm. This is the standard convection–diffusion problem and the same stability limits apply Eq. (2.14).

For slightly compressible or incompressible problems in which $\tilde{\mathbf{M}}$ is small or zero, the semi-implicit form is efficient and it should be noted that the matrix $\mathbf{H}$ of Eqs. (3.26) and (3.31) does not vary during the computation process. Therefore $\mathbf{H}$ can be partially inverted leading to an economical procedure.

4.3. Quasi (nearly) implicit form

To overcome the severe time step restriction made by the diffusion terms (viscosity, thermal conductivity etc.), these terms can be treated implicitly This involves solving separately an implicit form connecting the viscous terms with U_i^* or U_i^{**}. Here at each step, simultaneous equations need to be solved and this procedure can be of great advantage in certain cases such as high viscosity flows and low Mach number flows. Now the only time step limitation is $\Delta t \leq h/|\mathbf{u}|$ which appears to be a very reasonable and physically meaningful restriction.

4.4. Evaluation of time-step limit. Local and global time-steps

The time step limits, in spite of being defined in terms of element sizes, are best calculated at nodes of the element. In the calculation we shall specify, if the scheme is conditionally stable, the time step limit at each node by assgning the minimum value for such nodes calculated from all the surrounding elenents. When a problem is being solved in real time, then obviously the smallest of all nodal values has to be adopted for the solution. In many problems transient calculation is adopted to find steady-state solutions, and *local time stepping* is convenient as it allows more rapid convergence and fewer time-steps to be used throughout the problems. Local time stepping can only be applied to problems in which (1) – the mass matrix is lumped, and (2) – the steady-state solution does not depend on the mass matrix. Thus with local time stepping we shall use at every node simply the minimum time-step found at that node. This is, of course, equivalent to assuming identical time steps for the whole problem and simply adjusting the lumped masses. Such a problem with lumped masses adjusted is

still physically and mathematically meaningful and we know that the convergence will be achieved as it invariably is.

Many of the steady-state problems were solved by means of such localized time stepping used in the calculations.

In the context of local and global time stepping it is interesting to note that the stabilizing terms introduced by the Characteristic Galerkin process will not take on the optimal value for any element in which the time-step differs from the critical one. However, on other occasions it may be useful to make sure that (a) in all elements we have introduced optimal damping, (b) the progressive time-step for all elements is identical. The latter of course is absolutely necessary if for instance we deal with transient problems where all time steps are real. For such cases it is possible to consider Δt as being introduced in two stages: (1) as the Δt_{ext} (external) which has of course to preserve stability and that must be left at minimum Δt calculated from any element, and (2): to use inside the calculation of each individual element the Δt_{int} (internal) which is optimal for an element as of course exceeding the stability limit does not matter there and we are simply adding a better damping characteristics.

This internal – external subdivision is of some importance when incompressibility effects are considered. As shown in the next section, the stabilizing diagonal term occurring in steady state depends on the size of the time-step. If the mesh is graded and very small elements dictate the time-step over the whole domain, we might find that the diagonal term introduced overall is not sufficient to preserve incompressibility. For such problems we recommend the use of internal and external time-step which differ and we introduce them in Ref. [9].

5. Circumventing the BB restrictions

In the previous sections we have not restricted the nature of the interpolating shape functions $\mathbf{N_u}$ and $\mathbf{N_p}$, i.e. shape functions for velocity and pressure, respectively. If we chose these interpolations in a manner satisfying the patch test conditions or BB restriction for incompressibility then, of course, completely incompressible problems can be dealt with without any special difficulties by both the 'Split A' and 'Split B' formulations. However, the 'Split A' of the formulation described introduces an important bonus which permits us to avoid any restrictions on the nature of the two shape functions. Let us examine here the structure of equations reached in steady conditions. For simplicity we shall consider here only the Stokes form of governing equations in which the convective terms disappear. Further we shall take the fluid as incompressible and thus uncoupled from the energy equations. Now the three steps of Eqs. (3.18), (3.21) and (3.19) are

written as

$$
\begin{aligned}
\Delta\tilde{\mathbf{U}}^* &= -\Delta t \mathbf{M}^{-1}[\mathbf{K}_\tau \mathbf{u}^{\mathbf{n}} - \mathbf{f}], \\
\Delta\tilde{\mathbf{p}} &= \frac{1}{\Delta t \theta_1 \theta_2}\mathbf{H}^{-1}[\mathbf{G}_{\mathbf{pu}}^{\mathbf{T}}\tilde{\mathbf{U}}^{\mathbf{n}} + \theta_1 \mathbf{G}_{\mathbf{pu}}\Delta\mathbf{U}^* - \Delta t\theta_1 \mathbf{H}\tilde{\mathbf{p}}^{\mathbf{n}} - \mathbf{f}_{\mathbf{p}}], \\
\Delta\tilde{\mathbf{U}} &= \Delta\tilde{\mathbf{U}}^* - \Delta t \mathbf{M}^{-1}\mathbf{G}_{\mathbf{up}}^{\mathbf{T}}(\tilde{\mathbf{p}}^{\mathbf{n}} + \theta_2 \Delta\tilde{\mathbf{p}}).
\end{aligned} \tag{5.1}
$$

In steady state we have $\Delta\tilde{\mathbf{p}} = \Delta\tilde{\mathbf{U}} = 0$ and eliminating $\Delta\tilde{\mathbf{U}}^*$ we can write (dropping now the superscript $\mathbf{n}$)

$$
\mathbf{K}_\tau \tilde{\mathbf{u}} + \mathbf{G}_{\mathbf{up}}^{\mathbf{T}}\tilde{\mathbf{p}} = \mathbf{f} \tag{5.2}
$$

from the first and third of Eqs. (5.1), and

$$
\mathbf{G}_{\mathbf{pu}}^{\mathbf{T}}\tilde{\mathbf{U}} + \theta_1 \Delta t \mathbf{G}_{\mathbf{pu}}\mathbf{M}^{-1}\mathbf{G}_{\mathbf{up}}^{\mathbf{T}}\mathbf{p} - \Delta t\theta_1 \mathbf{H}\mathbf{p} - \mathbf{f}_{\mathbf{p}} = 0 \tag{5.3}
$$

from the second and third of Eqs. (5.1)

We finally have a system which can be written in the form

$$
\begin{bmatrix} \mathbf{K}_\tau/\rho & \mathbf{G}_{\mathbf{up}}^{\mathbf{T}} \\ -\mathbf{G}_{\mathbf{pu}}^{\mathbf{T}} & \Delta t\theta_1 \left[\mathbf{H} - \mathbf{G}_{\mathbf{pu}}\mathbf{M}^{-1}\mathbf{G}_{\mathbf{up}}^{\mathbf{T}}\right] \end{bmatrix} \begin{Bmatrix} \tilde{\mathbf{U}} \\ \tilde{\mathbf{p}} \end{Bmatrix} = \begin{Bmatrix} \mathbf{f}_1 \\ \mathbf{f}_2 \end{Bmatrix}; \tag{5.4}
$$

here $\mathbf{f}_1$ and $\mathbf{f}_2$ follow from the forcing terms.

The system is now always positive definite and therefore leads to non-singular solution for *any interpolation functions* $\mathbf{N}_\mathbf{u}$, $\mathbf{N}_\mathbf{p}$ chosen. In all of the examples discussed in this paper and elsewhere, equal interpolation is chosen for both the U_i and p variables, i.e. $\mathbf{N}_\mathbf{u} = \mathbf{N}_\mathbf{p}$. We must however stress that any other interpolation can be used without violating the stability. This is an important reason for the preferred use of 'Split A' form.

It can be easily verified that if the pressure gradient term is retained as in Eq. (3.22), i.e. if we use 'Split B', the lower diagonal term of Eq. (5.4) is identically zero and the BB conditions in the full scheme cannot be avoided.

6. Boundary conditions

6.1. Fictitious boundaries

In a large number of fluid mechanics problems the flow in open domains is considered. In such problems, the boundaries are simply limits of computation and therefore they are fictitious. With suitable values specified at such boundaries however, accurate solution for the flow inside the isolated domain can be achieved.

1. If the flow is subsonic, the specification of all quantities except the density can be made on both the sides and entry boundaries.

2. For supersonic flows, all the variables can be prescribed at the inlet. At the exit however, no boundary conditions are imposed simply because by definition, the disturbances caused by the boundary conditions cannot travel faster than at the speed of sound.

With subsonic exit conditions the situation is somewhat more complex, and here various possibilities exist.

Condition A : Denoting the most obvious assumptions with regard to the traction and velocities.

Condition B : A more sophisticated condition of zero gradient of traction and stresses existing there. Such conditions will of course apply always to the exit domains for incompressible flow. The condition 'B' was first introduced by ZIENKIEWICZ *et al.* [10].

Of considerable importance especially in view of the new schemes, are the conditions which will be encountered on real boundaries.

6.2. Real boundaries

By real boundaries we mean limits of fluid domains which are physically defined; here three different possibilities exist.

1. *Solid boundaries with no slip conditions*: On such boundaries the fluid is assumed to stick or attach itself to the boundary and thus all velocity components become zero. Obviously, this boundary is only possible for viscous flows.

2. *Solid boundaries in inviscid, flow (slip conditions)*: When the flow is inviscid, we will always encounter slipping boundary conditions where only normal velocity component is specified and is in general equal to zero in steady-state motion. Such boundary conditions will invariably be imposed for problems of Euler flow, whether it is compressible or incompressible.

3. *Prescribed traction boundary conditions*: The last category is that on which tractions are prescribed. This includes zero traction in case of free surfaces of fluid or any prescribed tractions such as those caused by wind being imposed on the surface.

These three basic kinds of boundary conditions have to be imposed on the fluid and special consideration has to be given to these when split operator schemes are used.

7. Some solution of typical examples

In this section we illustrate the applications and show the advantages gained by the use of the CBS algorithm in various classes of problems. In all of the problems discussed, the same computer coding was used and only linear, triangular and quadrilateral elements are used in all examples.

The application of higher order elements and elements of different nature is of course possible under certain circumstances but we shall not make detailed comments on those here.

7.1. Fully explicit procedure, subsonic, transonic and supersonic flows

The use of fully explicit procedure is of course most preferred in aeronautical computations and the present CBS algorithm is well suited for this purpose.

Example 1. NACA 0012 aerofoil with zero angle of attack, $M = 0.5, 1.2$.

In Fig. 1, we show the density distribution along the centerline upto stagnation (see [3] for full details) for Mach number 0.5 with the fully explicit form of the algorithm. Here the performance of the CBS algorithm is compared with the performance of the previously used Taylor-Galerkin scheme.

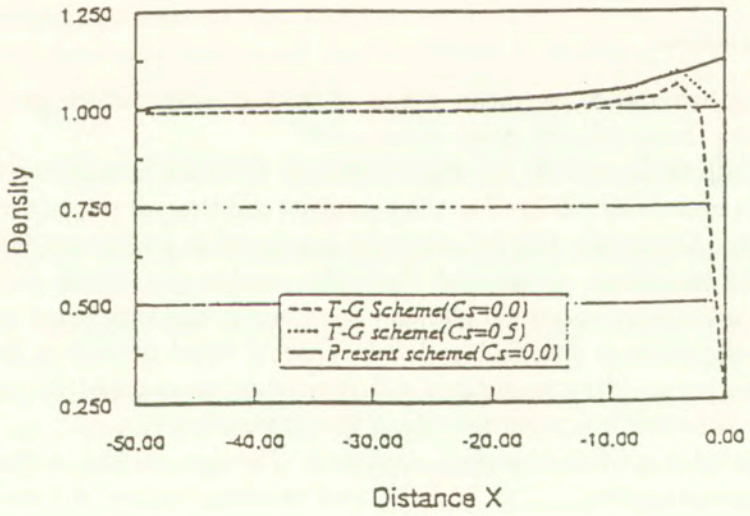

FIG. 1. Subsonic aerofoil inviscid flow past a NACA0012 aerofoil. Comparison of density along mid height. Analytical value at stagnation point 1.13. CBS scheme gives highly accurate solution.

It is interesting that the CBS algorithm improves the results dramatically near the stagnation point without the use of any additional artificial diffusion (which is essential to get any reasonable result using the Taylor-Galerkin scheme).

In Figs. 2, 3 and 4, the domain, mesh and results obtained are given for a supersonic case with Mach number equal to 1.2 of flow around the same aerofoil. The domain size taken is big enough to specify the free-stream conditions at the inlet. As can be seen, the results obtained are very smooth (Fig. 3) and compare excellently with the benchmark AGARD results [27] (Fig. 4).

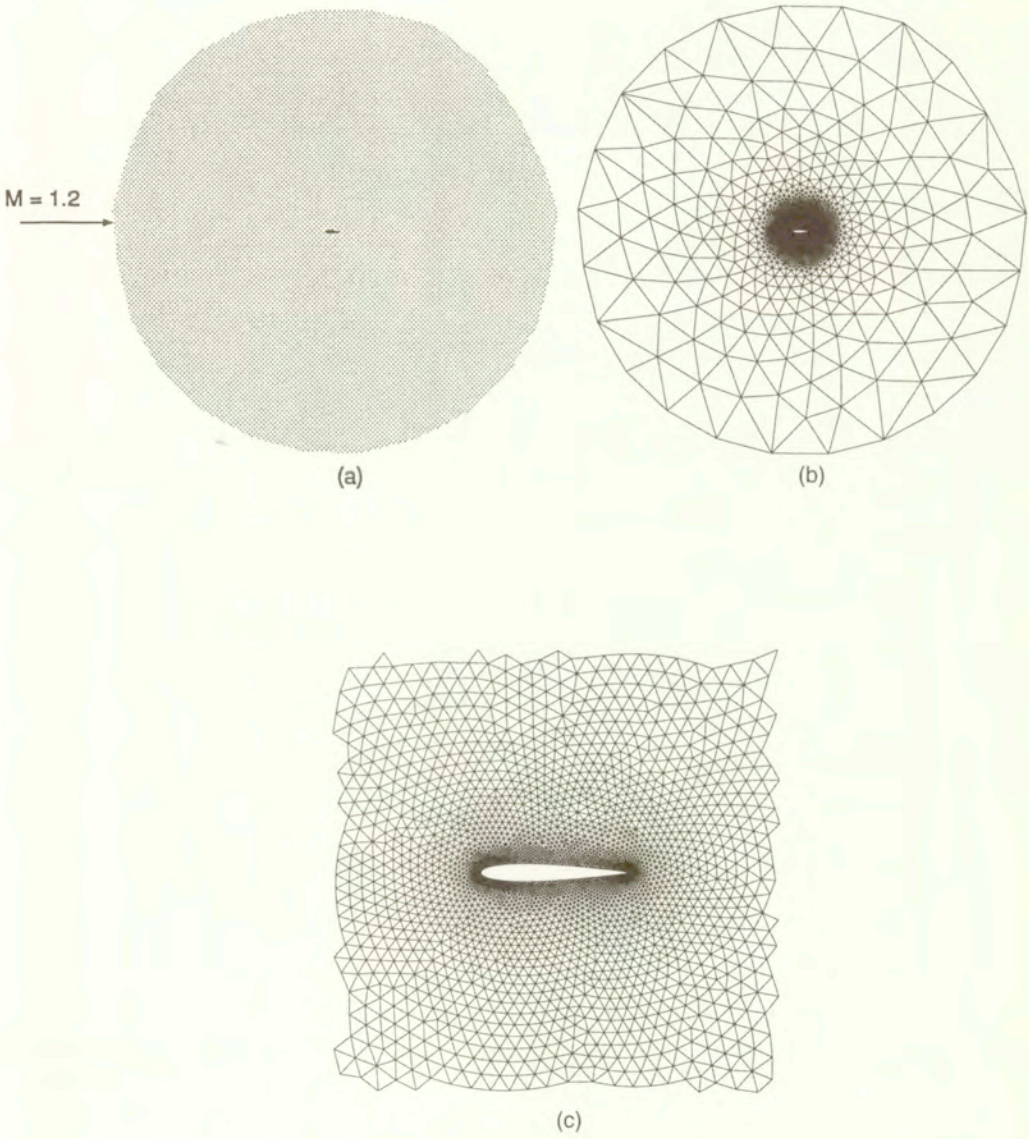

FIG. 2. Supersonic inviscid flow past NACA0012 aerofoil, $M = 1.2$, $\alpha = 0°$. (a) Domain (b) Linear traingular finite element mesh, Nodes: 3753, Elements: 7351 (c) Element distribution near aerofoil surface.

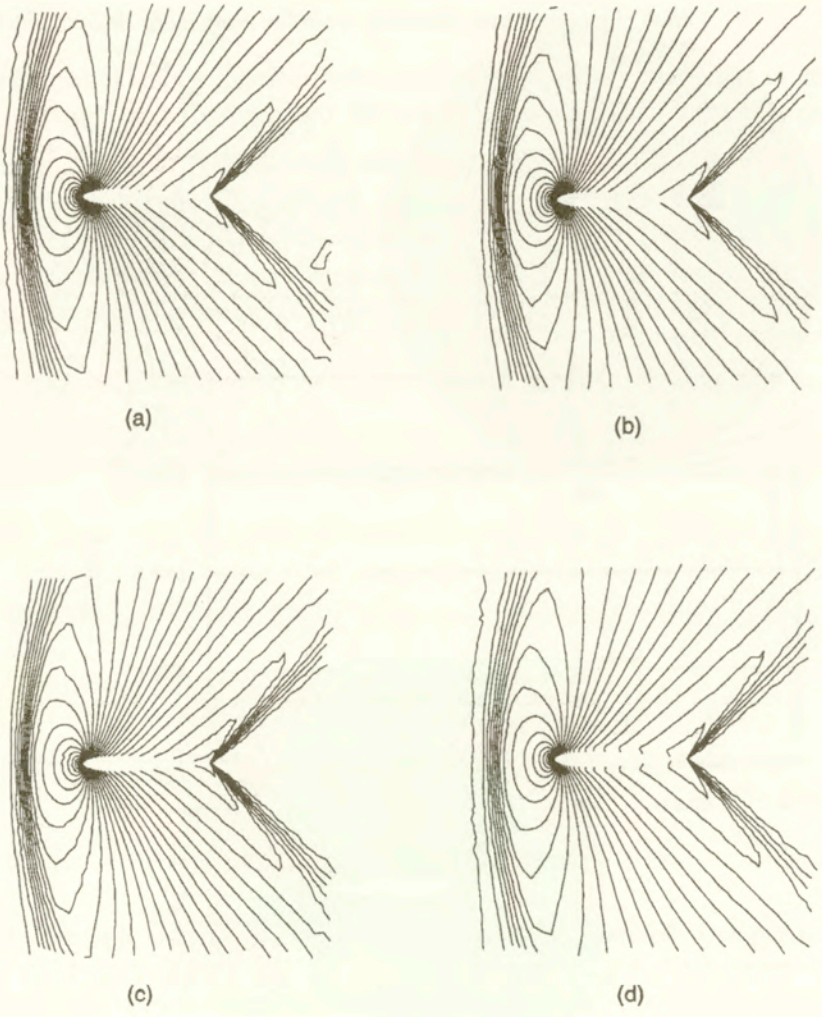

FIG. 3. Supersonic inviscid flow past NACA0012 aerofoil, $M = 1.2$, $\alpha = 0°$, contours of different variables. (a) Density (b) Pressure (c) Temperature (d) Mach number.

Example 2. Hypersonic flow past a cylinder.

Figure 5 shows the domain and quadrilateral mesh generated to study hypersonic flow past a quarter-cylinder. The inlet Mach number is taken as 6. At the inlet, velocity and density are prescribed.

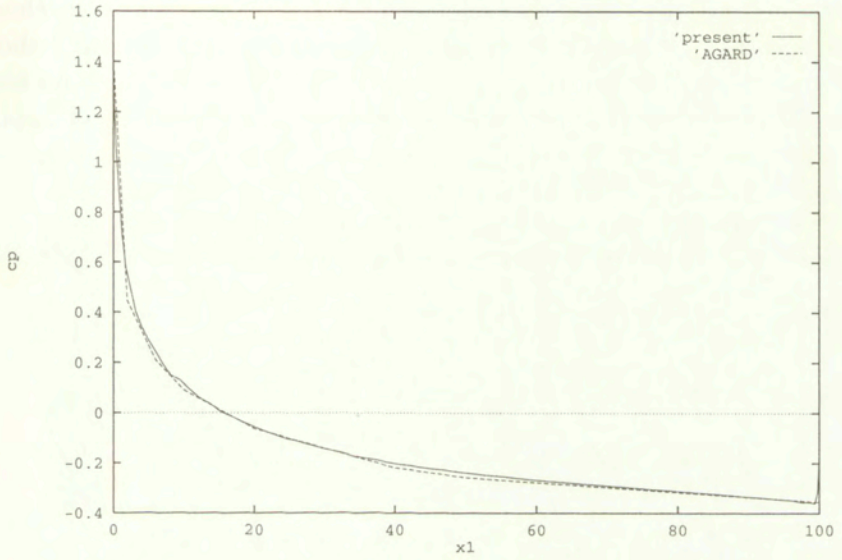

FIG. 4. Supersonic inviscid flow past NACA0012 aerofoil, $M = 1.2$, $\alpha = 0°$. Comparison of coefficient of pressure distribution on the surface of aerofoil.

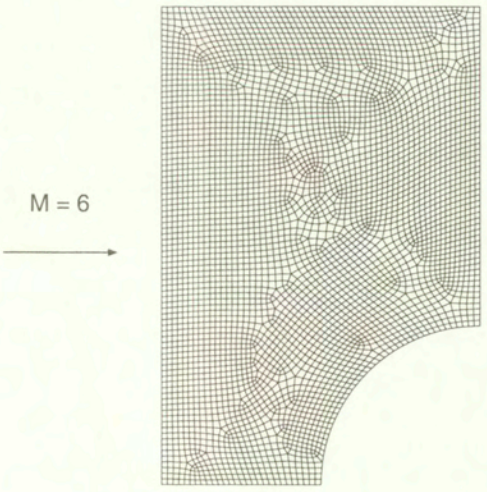

FIG. 5. Hypersonic inviscid flow past a quarter-cylinder, $M = 6$. Linear quadrilateral finite element mesh, Nodes: 4421, Elements: 4286.

In Fig. 6, the contours of all important variables are given. Even at a high Mach number of 6, we have found no oscillations. To smooth out the shocks, we have used some appropriate shock capturing viscosity [28]. Figure 7 shows the Mach number distribution along the bottom line of the domain. As seen, the shock is reasonably sharp even though adaptivity in any form is not applied.

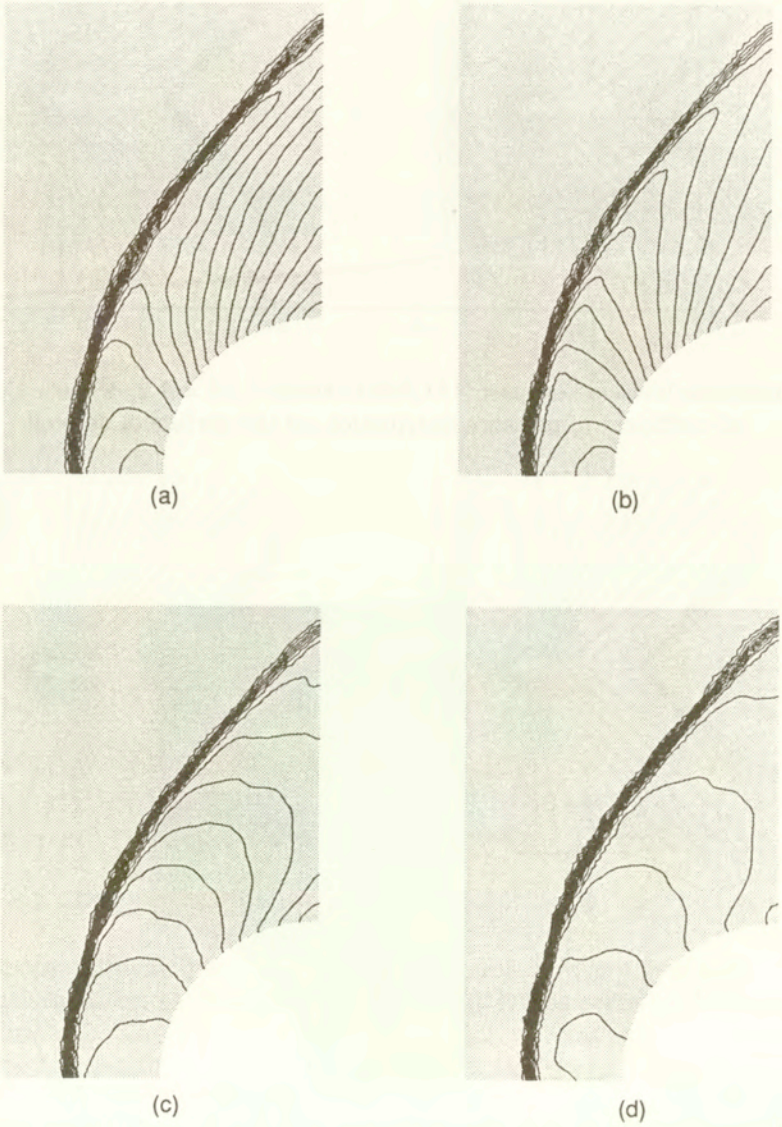

FIG. 6. Hypersonic inviscid flow past a quarter-cylinder, $M = 6$, contours of different variables. (a) Density (b) Pressure (c) Temperature (d) Mach number.

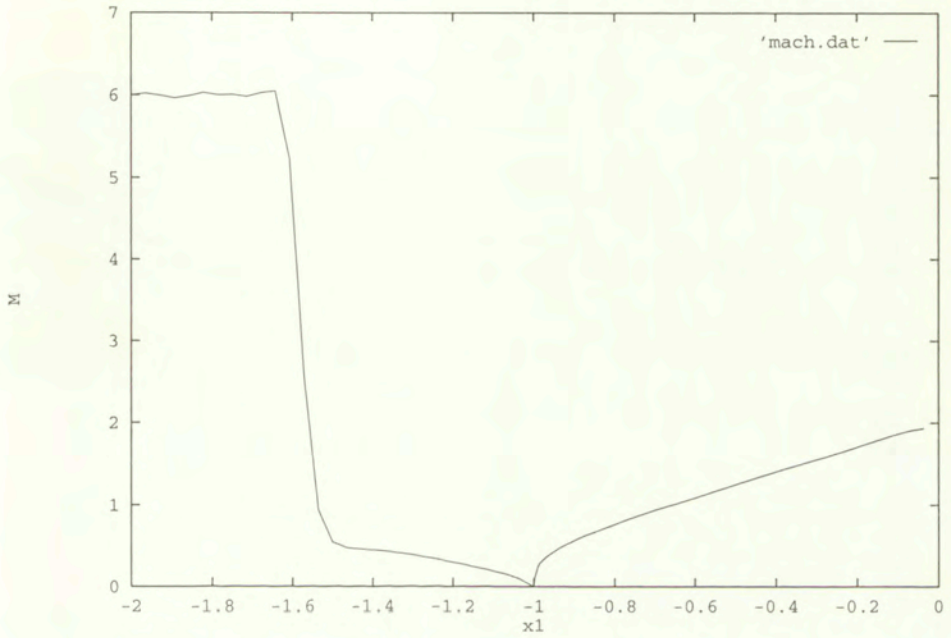

FIG. 7. Hypersonic inviscid flow past a quarter-cylinder, $M = 6$. Mach number distribution along bottom line.

Example 3. Viscous compressible flow past a plate ($M = 3.0$, $Re = 1000$) (Carter).

In this example, a fully explicit scheme is used. Here, the Mach number at the inflow is 3.0 and the inlet Reynolds number based on the length of the plate is 1000. This problem is also known as the Carter problem. The temperature of the plate is assumed to be constant and equal to the stagnation temperature given by

$$T_s = T_\infty \left(1 + \frac{\gamma - 1}{2} M_\infty^2\right). \tag{7.1}$$

The temperature dependence of viscosity is accounted for through the Sutherland's law

$$\frac{\mu}{\mu_r} = \frac{T_r + S_o}{T + S_o} \left(\frac{T}{T_r}\right)^{1.5}, \tag{7.2}$$

where S_o is Sutherland's constant and is equal to 198.6° Rankine.

A uniform rectangular mesh with 8281 nodes and 8100 elements is used in this computation. The results obtained are shown in Figs. 8 and 9. It is seen that the contours are smooth and shocks are in the proper locations. The pressure distribution along the plate and density distribution at the outlet agree excellently

(Fig. 9) with the Carter [29] results (though the latter show some unatural oscillations near the leading edge).

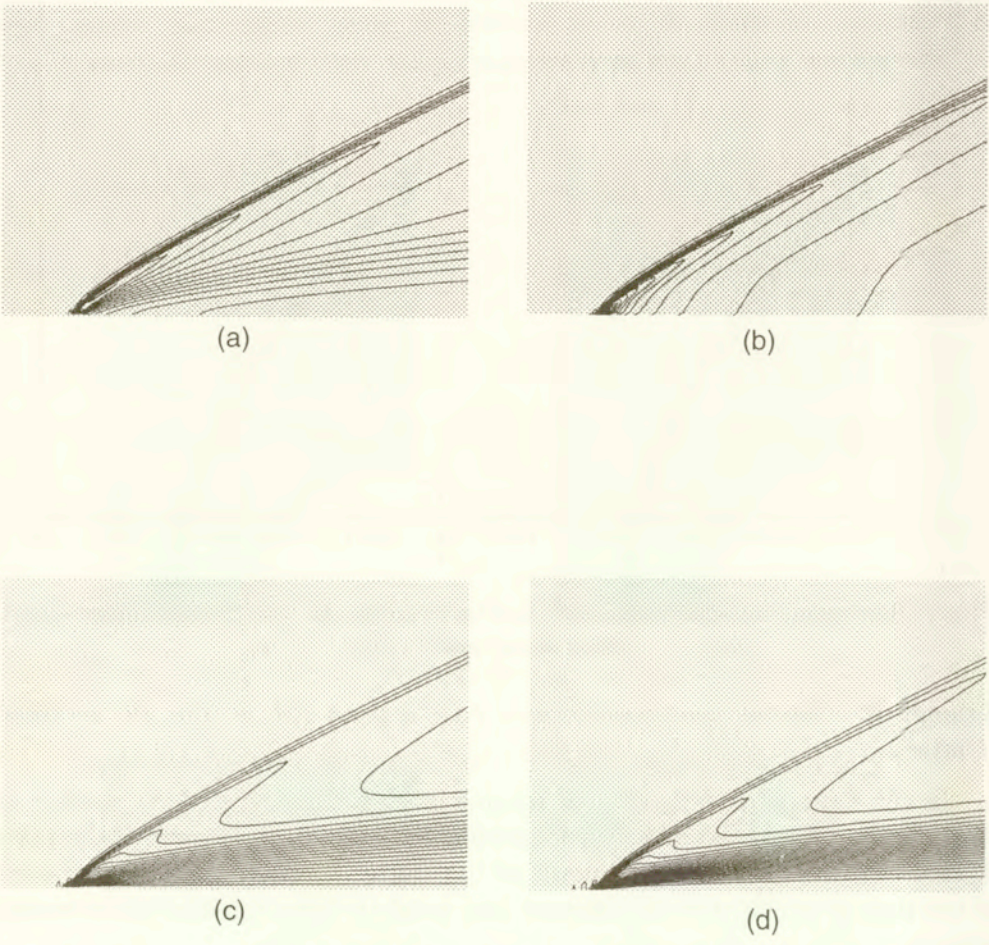

FIG. 8. Supersonic viscous flow past a flat plate, $M = 3$, $Re = 1000$, contours of different variables. (a) Density (b) Pressure (c) Temperature (d) Mach number

7.2. Semi-implicit procedure

Example 1. High Reynolds number flow in a lid-driven cavity, $M = 0$.

The first example is a fully viscous incompressible flow ($M = 0$) in a lid-driven cavity. This is a well known test case used by many authors. A high Reynolds number of 5000 is used in this study. Figure 10 shows the details of rectangular mesh used and comparison with the benchmark solution [30]. The agreement is excellent.

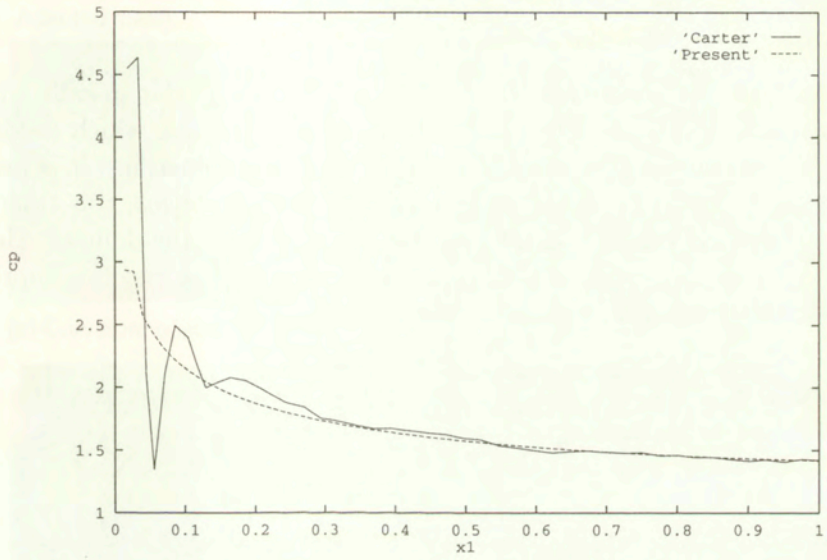

(a)

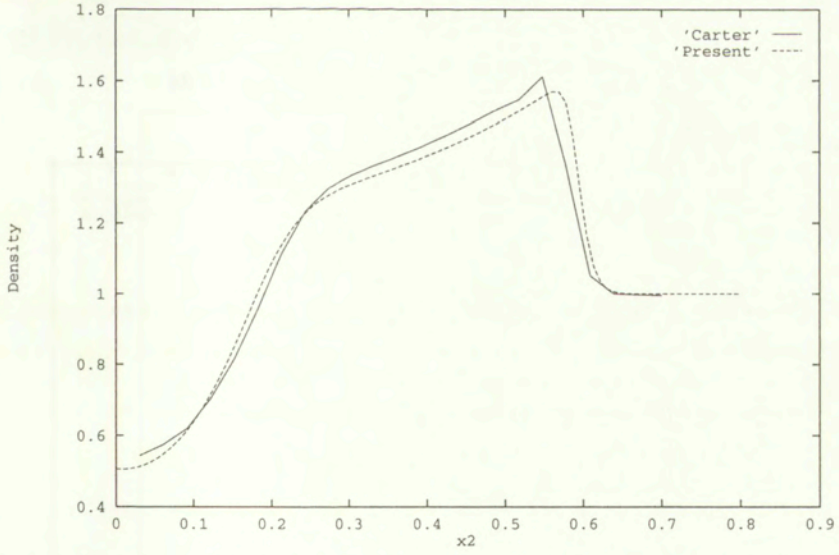

(b)

FIG. 9. Supersonic viscous flow past a flat plate, $M = 3$, $Re = 1000$; (a) Comparison of pressure distribution on the plate surface with CARTER [29]; (b) Comparison density distribution at exit with CARTER [29].

In Fig. 11, we give two adapted meshes using two different forms of adaptive procedure [31, 32] to solve the cavity problem for the same Reynolds number of 5000. It is seen that the results agree excellently with the benchmark.

7.3. Tests on incompressible stabilization

In Sec. 4.4, we mentioned two different time steps, the so-called internal and external time steps. The external time step is the one which needs to be calculated from the explicit step of the algorithm and sometimes it is necessary to use a safety factor to reduce it. In incompressible problems, this time step is taken as the minimum among the values calculated from the domain. However, the internal time step need not be equal to the external one and can improve the incompressible solution.

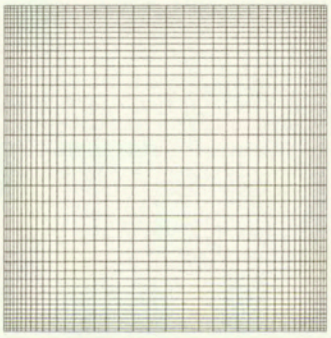

(a)

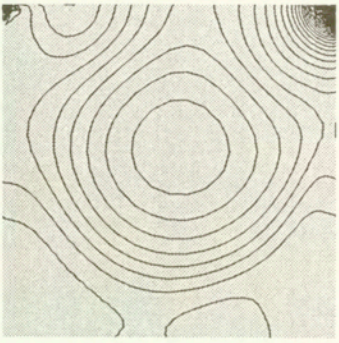

(b)

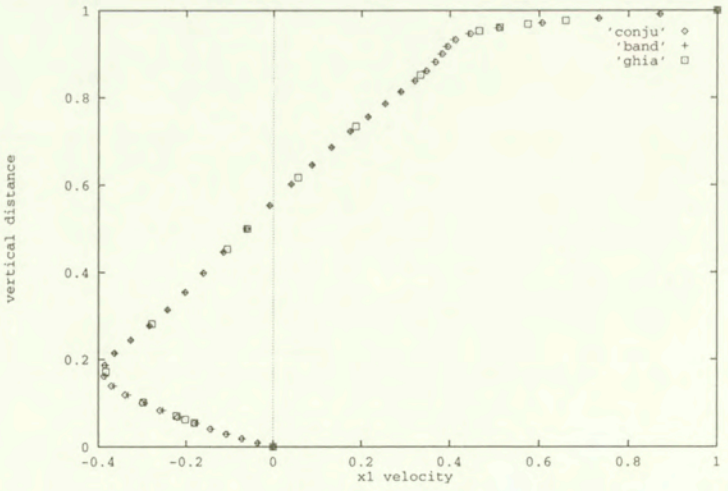

(c)

FIG. 10. Incompressible viscous flow in a lid-driven cavity, $Re = 1000$. (a) Linear quadrilateral mesh, Nodes: 1681, elements: 1600 (b) Pressure contours (c) Comparison of u_1 velocity distribution at mid-height with GHIA *et al.* [30].

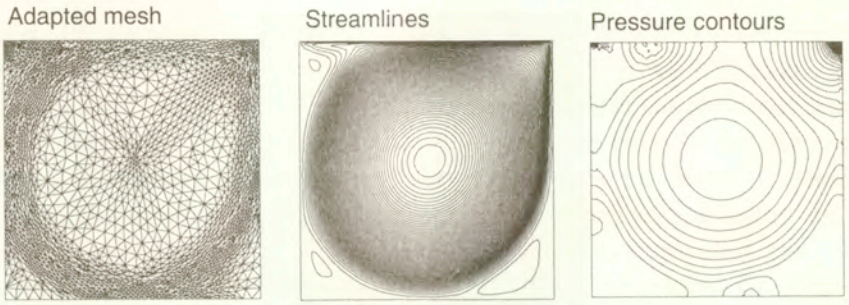

(a) Curvature based procedure, Nodes: 2389, Elements: 4599

(b) Gradient based procedure, Nodes: 1034, Elements: 1962

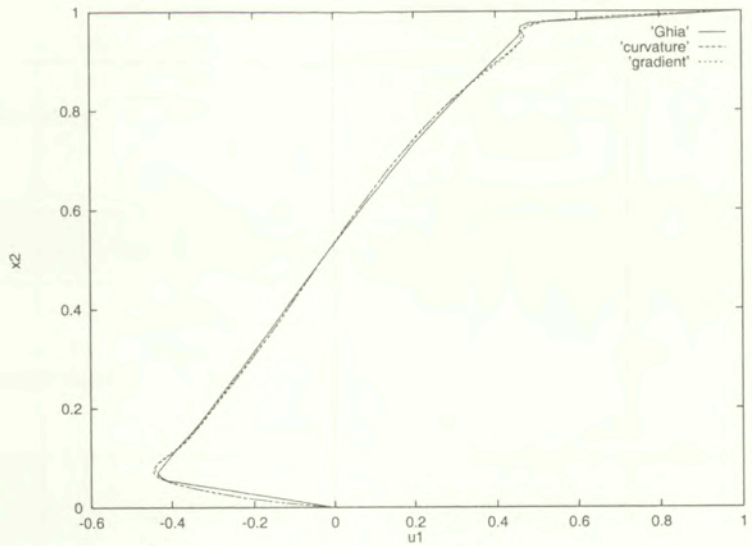

(c) Comparison of velocity at mid-vertical plane

FIG. 11. Incompressible viscous flow in a lid-driven cavity, $Re = 5000$, (a) Curvature based adaptive procedure (b) Gradient based adaptive procedure (c) Comparison of u_1 velocity distribution at mid-height with GHIA *et al.* [30].

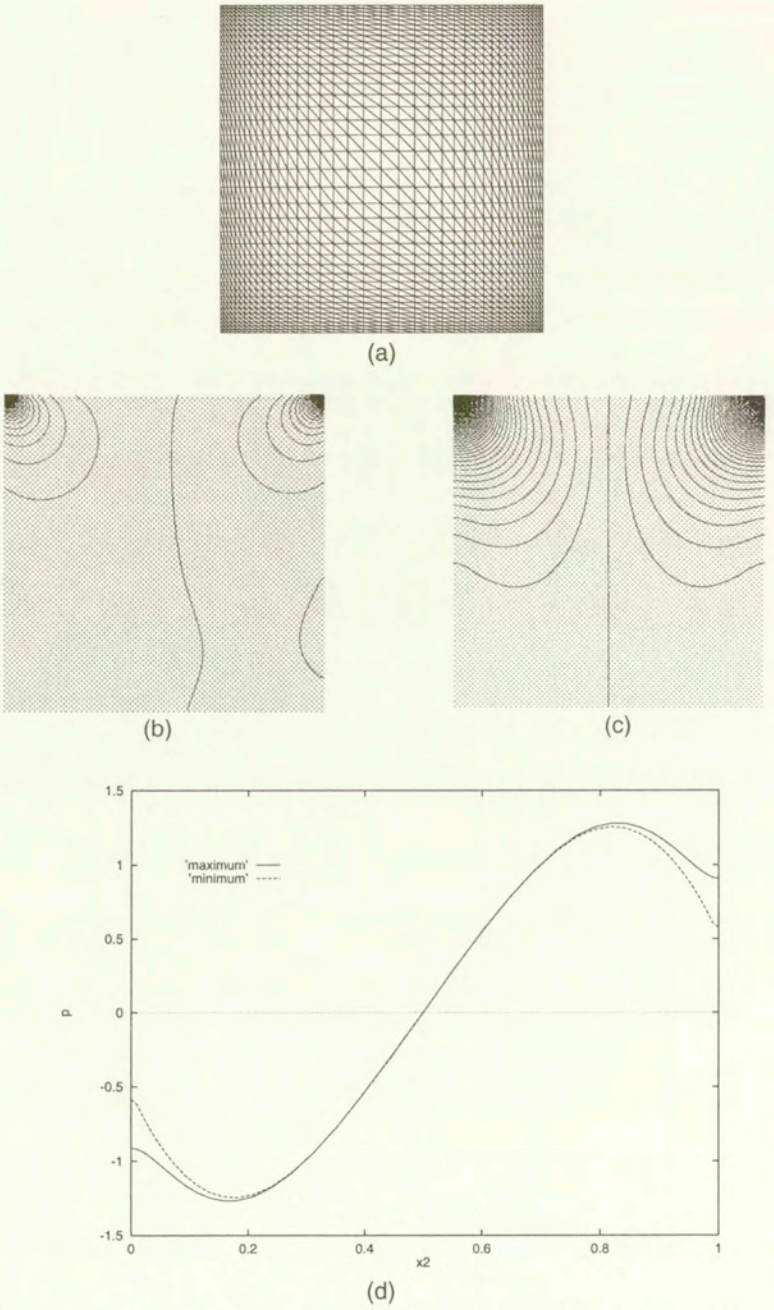

FIG. 12. Exercise on the incompressible stability of the CBS procedure on a Stokes flow problem. (a) Non-uniform triangular mesh (b) Pressure contours, $\Delta t_{\text{ext}} = \Delta t_{\text{crit}} = \Delta t_{\text{int}}$ (c) Pressure contours, $\Delta t_{\text{ext}} = \Delta t_{\text{crit}}$; $\Delta t_{\text{int}} = \Delta t_{\text{max}}$. (d) Comparison of pressure distribution across the cavity at mid-height.

In Fig. 12, we show an example of the Stokes problem in a lid-driven cavity. The mesh used is non-uniform as shown in Fig. 12(a). Figures 12(b) and (c) show two different solutions obtained for the same problem with the same external time step and different internal time steps. In the first case (Fig. 12(b)), the internal time step is identically equal to the external time step, i.e. both the time steps are equal to the minimum value calculated from the problem domain. However, in the second case (Fig. 12(c)), the external time step is same as in case one but the internal time step is the maximum time step value calculated from the whole domain. As it may be seen, the solutions are different and higher internal time steps act as stabilizing factors. Figure 12(d) compares the pressure distribution along the mid-height of the cavity. It is seen that higher internal time step gives an improved solution and here the values are almost equal to the one given by the Galerkin Least Squares approach (GLS) with an optimum GLS factor [23]. A full derivation on the matter of internal and external time steps can be found in Ref. [9].

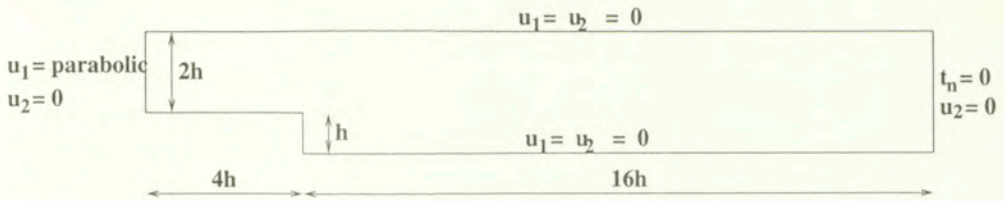

(a) Geometry

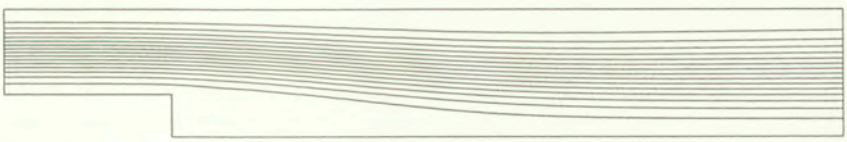

(b) Streamlines

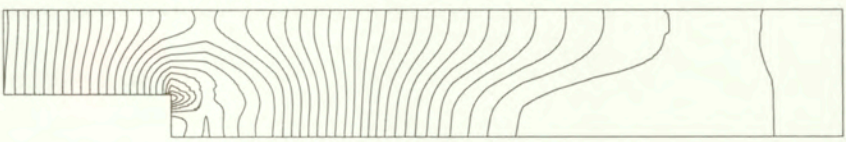

(c) Pressure contours

FIG. 13. Exercise on exit boundary conditions. Incompressible, viscous flow pas a backward facing step, Re = 100 (a) Geometry and boundary conditions (b) Stream lines (c) Pressure contours.

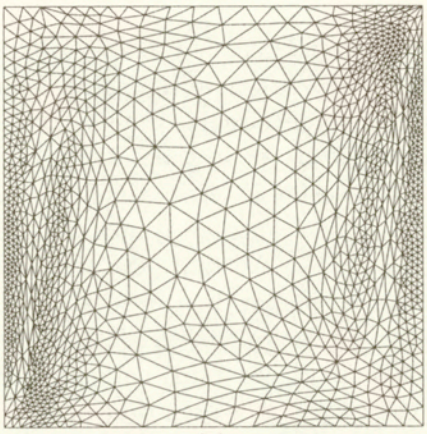

(a)

(b)

(c)

FIG. 14. Buoyancy driven flow in a square cavity, $Ra = 10^5$. (a) Final adapted mesh (b) Stream lines (c) Isotherms.

7.4. Boundary conditions

The problem considered here is the standard backward facing step. The domain and various boundary conditions are shown in Fig. 13(a). The inlet velocity profile is parabolic and the Reynolds number is 100.

Figures 13(b) and 13(c) show the results on exit boundary conditions mentioned earlier. As seen, the results are excellent and agree well with a longer domain results [8].

7.5. Buoyancy driven flows

The domain considered here is a two-dimensional square shape. The buoyancy flow is initiated in the cavity by differentially heating the vertical walls. Both the vertical walls are kept at two different temperatures; the left wall temperature is higher than that on the right one. Bottom and top walls are insulated. Non-slip boundary conditions are assumed on all four sides of the cavity.

An example on buoyancy-driven convection is given in Fig. 14. The adopted meshes are generated by the procedure explained in Ref. [31]. The solution given in this figure are extraordinarily smooth and symmetric for a Rayleigh number of 10^5. The quantitative solutions obtained (Nusselt number = 4.519) agree excellently with the available bench-mark solutions [33]. The difference is less than 0.5%.

8. Concluding remarks

We hope that in the present paper we have fully explained the logical background and the excellent performance of the CBS algorithm. The development of the algorithm has taken some time and the present authors would like to acknowledge the earlier works which pointed the way to the final algorithm. In this paper we addressed several new aspects of the algorithm including the incompressible stabilization procedures. However, further tests are needed to fully understand the nature in which the stabilization introduced affects the compressible and incompressible flow problems.

Acknowledgements

This research has been partially supported by NASA grant NAGW/2127, AMES Control Number 90 – 144.

References

1. O. C. ZIENKIEWICZ and R. CODINA, *Search for a general fluid mechanics algorithm*, Frontiers of Computational Fluid Dynamics, D. A. CAUGHEY and M. M. HAFEZ [Eds.], J. Wiley & Sons, 101–113, 1995.
2. O. C. ZIENKIEWICZ and R. CODINA, *A general algorithm for compressible and incompressible flow, Part I. The split characteristic based scheme*, Int. J. Num. Meth. Fluids, **20**, 869–885, 1995.
3. O. C. ZIENKIEWICZ, B. V. K. SATYA SAI, K. MORGAN, R. CODINA and M. VÁZQUEZ, *A general algorithm for compressible and incompressible flow, Part II. Tests on the explicit form*, Int. J. Num. Meth. Fluids, **20**, 887–913, 1995.
4. R. CODINA, M. VÁZQUEZ and O. C. ZIENKIEWICZ, *General algorithm for compressible and incompressible flows, Part III. A semi-implicit form*, Int. J. Num. Meth. Fluids, **27**, 13–32, 1998.
5. R. CODINA, M. VÁZQUEZ and O. C. ZIENKIEWICZ, *A fractional step method for the solution of compressible Navier-Stokes equations*, Frontiers of computational fluid dynamics, M. HAFEZ and K. OSHIMA [Eds.], **1**, 331–347, World Scientific Pub. co.Ltd, 1998.
6. B. V. K. SATYA SAI, O. C. ZIENKIEWICZ, M. T. MANZARI, P. R. M. LYRA and K. MORGAN, *General purpose Vs Special Algorithms for high speed flows with shocks*, Int. J. Num. Meth. Fluids, **27**, 57–80, 1998.
7. O. C. ZIENKIEWICZ, P. NITHIARASU, R. CODINA, M. VÁZQUEZ and P. ORTIZ, *An Efficient and Accurate Algorithm for Fluid Mechanics Problems. The Characteristic Based Split (CBS) Algorithm*, Int. J. Num. Meth. Fluids, **31**, 1, 359–392, 1999.
8. N. MASSAROATTI, P. NITHIARASU and O. C. ZIENKIEWICZ, *Characteristic-Based-Split (CBS) Algorithm for Incompressible Flow Problems with Heat Transfer*, International Journal of Numerical Methods for Heat and Fluid Flow, **8**, 8, 969–990, 1998.
9. P. NITHIARASU, and O. C. ZIENKIEWICZ, *On Stabilization of the CBS Algorithm. Internal and External Time Steps*, Int. J. Num. Meth. Engng., **48**, 875–880, 2000.
10. O. C. ZIENKIEWICZ, J. SZMELTER and J. PERAIRE, *Compressible and incompressible flow: An algorithm for all seasons*, Comp. Meth. Appl. Mech. Engng., **78**, 105–121, 1990.
11. O. C. ZIENKIEWICZ, *Explicit or semi-explicit general algorithm for compressible and incompressible flows with equal finite element interpolation*, Report 90/5, Chalmers University of Technology, 1990.
12. O. C. ZIENKIEWICZ and J. WU, *A general explicit of semi-explicit algorithm for compressible and incompressible flows*, Int. J. Num. Meth. Engng., **35**, 457–479, 1992.
13. P. D. LAX and B. WENDROFF, *Systems of conservation laws*, Comm. Pure. Appl. Math., **13**, 217–237, 1960.
14. J. DONEA, *A Taylor-Galerkin method for convective transport problems*, Int. J. Num. Meth. Engng., **20**, 101–119, 1984.
15. O. C. ZIENKIEWICZ, R. LÖHNER, K. MORGAN and J. PERAIRE, *High speed compressible flow and other advection dominated problems of fluid mechanics*, Finite elements in fluids, **6**, Ch. 2, 41–88, R. H. GALLAGHER, G. F. CAREY, J. T. ODEN and O. C. ZIENKIEWICZ [Eds.], J. Wiley & Sons, 1985.
16. R. LÖHNER, K. MORGAN and O. C. ZIENKIEWICZ, *The solution of non-linear hyperbolic equation system by the finite element method*, Int. J. Num. Meth. Fluids, **4**, 1043–1063, 1984.

17. H. LAVAL and L. QUARTAPELLE, *A fractional step Taylor-Galerkin method for unsteady incompressible flows*, Int. J. Num. Meth. Fluids, **11**, 501–513, 1990.

18. C. B. JIANG, M. KAWAHARA and K. KASHIYAMA, *A Taylor-Galerkin based finite element method for turbulent flows*, Fluid Dynamic Research, **9**, 165–178, 1992.

19. L. DEMKOWICZ, J. T. ODEN, W. RACHOWICZ and O. HARDY, *An h-p Taylor-Galerkin finite element method for compressible Euler equations*, Comp. Meth. Appl. Mech. Engng., **88**, 363–396, 1991.

20. A. J. CHORIN, *Numerical solution of Navier Stokes equations*, Math. Comp., **22**, 745–762, 1968.

21. R. A. ADEY and C. A. BREBBIA, *Finite element solution of effluent dispersion*, Numerical Methods in Fluid Mechanics, C. A. BREBBIA and J. J. CONNOR [Eds.], 325–354, Pentech Press, 1974.

22. O. PRIONNEAU, *On the transport diffusion algorithm to the Navier-Stokes equation*, Num. Math., **38**, 309–332, 1982.

23. O. C. ZIENKIEWICZ and R. L. TAYLOR, *The finite element method*, **3** Fluid Dynamics, 5^{th} ed., Butterworth, London 2000.

24. E. OÑATE, *Derivation of stabilized equations for numerical solution of advective-diffusive transport and fluid flow problems*, Comp. Meth. App. Mech. Engng., **151**, 233–265, 1998.

25. E. OÑATE and M. MANZÁN, *A general procedure for deriving stabilized space time finite element methods for advective diffusive equations*, Int. J. Num. Meth. Fluids, **31**, 203–221, 1999.

26. R. CODINA, *Stability analysis of forward Euler scheme for the convection diffusion equation using the SUPG formulation in space*, Int. J. Num. Meth. Engng., **36**, 1445–1464, 1993.

27. T. H. PULLIAM and J. T. BARTON, *Euler computations of AGARD working group 07 aerofoil test cases*, AIAA 23rd Aerospace Sciences Meeting, Jan 14 – 17, Reno, Nevada 1985.

28. P. NITHIARASU, O. C. ZIENKIEWICZ, B. V. K. S. SAI, K. MORGAN, R. CODINA, M. VÁZQUEZ, *Shock capturing viscosities for the general fluid mechanics algorithm*, Int. J. Num. Meth. Fluids, **28**, 1325–1353, 1998.

29. J. E. CARTER, *Numerical solutions of the Navier-Stokes equations for the supersonic laminar flow over a two-dimensional compression corner*, NASA TR-R-385, 1972.

30. U. GHIA, K. N. GHIA and C. T. SHIN, *High-Re solution for incompressible flow using the Navier-Stokes equations and multigrid method*, J. Comp. Phys., **48**, 387–411, 1982.

31. P. NITHIARASU and O. C. ZIENKIEWICZ, *Adaptive mesh generation for fluid mechanics problems*, Int. J. Num. Meth. Engng., **47**, 629–662, 2000.

32. J. PERAIRE, M. VAHDATI, K. MORGAN and O. C. ZIENKIEWICZ, *Adaptive remeshing for compressible flow computations*, J. Comp. Phys., **72**, 449–466, 1987.

33. G. de VAHL DAVIS, *Natural convection of air in a square cavity: a bench mark numerical solution*, Int. J. Num. Meth. Fluids, **3**, 249–264, 1983.

Received February 21, 2000; revised version July 4, 2000.

Arch. Mech., **52**, 4–5, pp. 889–910, Warszawa 2000

An attempt to describe heart attacks via continuum damage mechanics

Dedicated to Professor Zenon Mróz
on the occasion of his 70^{th} birthday

M. ŻYCZKOWSKI

Institute of Mechanics and Machine Design,
Politechnika Krakowska (Cracow University of Technology),
ul. Warszawska 24, 31–155 Kraków, Poland

IN AN EARLIER PAPER the author expressed the evolution equations of classical continuum damage mechanics in terms of unit dissipated power and proposed an extension to biological materials *in vivo*, adding a term describing the recovery. In the present paper an analogy with evolution of the coronary artery disease is established. If we denote by S (relative stenosis) one minus the ratio of current luminal area to the initial area, then the condition $S = 1$ at a certain point of the artery means complete blockage at this point resulting in a heart attack (myocardial infarction). This corresponds to the condition of critical state $D = 1$ in damage mechanics, where D denotes a scalar measure of damage. Making use of this analogy, an evolution equation for S is proposed, with unit dissipated power replaced by unit power of flow in individual cross-sections of coronary arteries and, subsequently, by the heart power. Further, another evolution equation describes the required heart power in terms of external loadings acting on the organism as a whole. Numerical integration of the evolution equations proposed makes it possible to distinguish the loadings leading to a myocardial infarction from those subject to recovery. Also, the description of stable and unstable angina pectoris is discussed and illustrated by numerical examples.

Notations

A	current luminal area of an artery
A_0	initial (reference) luminal area of an artery
ΔA	elementary area carrying the stress σ
C_{d}	modulus of resistance of the material to damage
C_{r}	modulus of recovery of the material
D	damage parameter of the material
D_0	initial damage at the moment of loading
G_{d}	modulus of resistance of coronary arteries to heart loading
G_{r}	modulus of recovery of coronary arteries
N	power of heart
N_{f}	power of flow in a current cross-section s of the artery
S	measure of heart damage (relative stenosis)

S_0 initial heart damage (due to atherosclerosis)
X coordinates of a point in the body
Ψ unit dissipated power at a current point X of the body
g dimensionless modulus combining $G_{\rm d}$ and $G_{\rm r}$
h dimensionless power of heart
k_i concentration of ith catecholamine in blood
m_j mass of the drug j taken at $\tau = \tau_o$
n_H heart rate, frequency of heart contractions,
p pressure in coronary arteries
$\bar{p}$ heart pressure as a function of current volume of the ventricle
s coordinate along the arc of axis of an artery
t time
v velocity of flow
z dimensionless power of external loadings
σ uniaxial mechanical stress in a material
τ dimensionless time
φ coefficient of nonlinearity of recovery in a biological material
ψ coefficient of nonlinearity of recovery of coronary arteries

1. Introduction

CARDIOVASCULAR BIOMECHANICS is a well developed discipline, in particular the analysis of blood circulation, heart valve prostheses, strength and deformability of myocardium, CHANDRAN [4]. The present treatment is quite different: the mathematical model of coronary artery disease is based on a phenomenological approach requiring a relatively small number of parameters. Blood circulation itself is not analysed, just the conditions of flow in coronary arteries, in other words – the decrease of current luminal area of these arteries. The paper formulates and applies an analogy between the description of critical state of a structural element by continuum damage mechanics generalized to biological materials, and the description of heart attacks. In what follows, we identify the popularly used term "heart attack" with "acute myocardial infarction" (AMI) and consistently use the latter term throughout the paper. Evolution equations for individual parameters are proposed.

This study of necessity addresses the purely deterministic aspects of myocardial infarction, treating the coronary arteries as tubes with lumina narrowed by atheroma with superposed vasoconstriction. By definition, this is a simplification of the *in vivo* process where events such as plaque fissuring and thrombus formation are responsible for the actual myocardial infarct, and secondary events such as heart failure and arrhythmias may lead to death. This simplification is necessary in order to clarify the initial model, but there is clearly scope for expanding the model by including probabilistic considerations.

Continuum damage mechanics, in its simplest scalar form, is based on the following evolution equation for damage parameter during the creep process in a

structural element, proposed by KACHANOV [18]:

$$\frac{dD}{dt} = \frac{1}{C_1}\left(\frac{\sigma}{1-D}\right)^q . \tag{1.1}$$

The local damage parameter $D = D(X,t)$ is here defined by the formula

$$D = 1 - \frac{\Delta A}{\Delta A_0} . \tag{1.2}$$

X denotes the coordinates of the point under consideration, t – time, ΔA_0 – the elementary initial cross-section transmitting the mechanical stress $\sigma = \sigma(X,t), \Delta A$ – the elementary section decreased in view of microdamage (carrying section), C_1 and q are material constants.

Equation (1.1) formed the basis for a widely developed branch of mechanics, called since late seventies the "continuum damage mechanics". We mention here just the monographs by KACHANOV [19], LEMAITRE [21], KRAJCINOVIC [20], SKRZYPEK and GANCZARSKI [31].

The local condition $D = 1$ reflects the decrease of the elementary carrying cross-section ΔA at the point X under consideration to zero and formation of a certain critical state, namely initiation of a macrocrack. In the case of a homogeneous state of stress, this is equivalent to a total collapse of the structural element, whereas in the case of non-homogeneous states of stress the global condition (reached at a certain time $t = t^*$)

$$\sup_{x \in V} D = 1, \tag{1.3}$$

where the symbol sup denotes upper bound of the function in the domain under consideration; it is also often used as that determining a limit of safe work of the element with the volume V. The location of the point $X = X^*$, where the supremum of D is reached (dangerous point), may be of essential importance. If this is a crucial point, then the structure shows immediate collapse; on the other hand, if X^* is less important, then the condition (1.3) results just in an initiation of a macrocrack leading to total collapse after a certain time. Consider, for example, two simple four-bar trusses shown in Fig. 1, a and b. Thicknesses of the lines correspond here to the cross-sectional area of individual bars. In case (a), first the lower bar will collapse; it carries the whole force P and hence this critical state is equivalent to collapse of the truss as a whole. In case (b), first the vertical upper bar will collapse, but even without that bar the three-bar truss will remain a load-carrying structure. If the upper bound of D is reached simultaneously in several points X_i^*, then the most crucial point is decisive.

Recently, ŻYCZKOWSKI [38] expressed the evolution equations of continuum creep damage mechanics in terms of unit dissipated power Ψ and proposed an

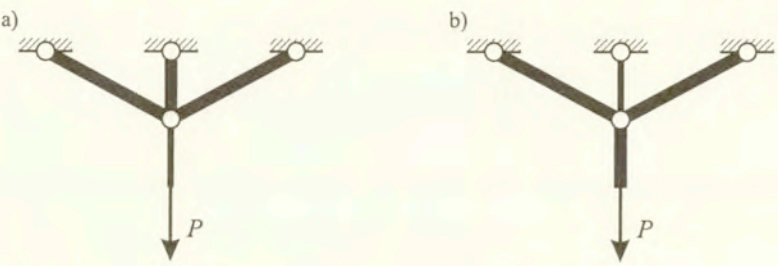

FIG. 1. Basic interpretation: two four-bar truss systems with various cross-sections of individual bars. Secondary interpretation: two schemes of coronary arteries with various luminal area of individual arteries.

extension to biological materials *in vivo*, namely a term describing recovery (or related phenomena, called healing, repair, regeneration, restoration, maintenance) was added. The relevant equation has the form

$$\frac{dD}{dt} = \frac{1}{C_{\mathrm{d}}}\sqrt{\frac{\Psi}{1-D}} - C_{\mathrm{r}}\left[(D-D_0) - \frac{\varphi}{1-D_0}(D-D_0)^2\right], \tag{1.4}$$

where C_{d} denotes the modulus of resistance of the material to damage, C_{r} – the modulus of recovery (with the dimension of reciprocal time), whereas φ – dimensionless coefficient of nonlinearity of recovery; practically $0 \leq \varphi \leq 1$. Moreover, D_0 denotes the initial value of damage, before application of loading; in structural materials it may be due to oxydation (corrosion), in the case of growing tree – to rot, and in the case of a bone – to osteoporosis. Equation (1.4), proposed for biological materials *in vivo*, should be regarded just as an initial step in this direction. First, the variety of such materials may require individual approach in every case, or, at least, for particular classes of biological materials. Second, regeneration or recovery of such materials may consist of several biological processes like growth (mass change), remodelling (property change) and morphogenesis (shape change) in adaptive form, TABER [34], and any of those processes may require a separate description.

The revelant literature was discussed in [38]; here we add just some more recent related references by COWIN [6] (survey on description of internal and surface remodelling), FRANCFORT and MARIGO [10] (damage evolution equations describing osteoporosis), DOLIŃSKI [9] (damage evolution in fatigue processes of bone cement specimens), JEMIOŁO and TELEGA [16] (bone remodelling combined with homogenization). However, most of these approaches, sometimes rather complicated, do not allow for recovery. In the present paper we use the very simple approach (1.4) but with recovery taken into account.

The aim of the present paper is to point out an analogy between the evolution of creep damage in biological materials and the evolution of damage in human

coronary arteries, and to use this analogy to a phenomenological description of coronary artery disease and myocardial infarction.

2. Analogy with the development of coronary artery disease and occurrence of myocardial infarction

Now we show an analogy between creep damage and rupture of biological materials on one side, and heart damage and myocardial infarction on the other. There exist, of course, various forms of heart damage. Here we consider just one, but probably the most important form of heart damage, namely the coronary artery disease being the direct cause of most myocardial infarctions. Coronary artery disease depends, first of all, on narrowing (stenosis) of the luminal cross-section of coronary arteries resulting in reduced supply of blood and oxygen to the heart muscle. Narrowing of the lumen is usually due to atherosclerosis and to coronary vasoconstriction. Atherosclerosis is characterized by slow increase of thickness of walls of coronary arteries up to formation of atheromatous plaques; it depends on many risk factors, specified below, but is almost independent of external loadings. On the other hand, coronary vasoconstriction develops relatively quickly and depends essentially on external loadings of the human organism, also specified below.

The measure of heart damage under consideration will be defined as relative stenosis of coronary arteries S, namely, in full analogy to Eq. (1.2),

$$S = 1 - \frac{A}{A_0}, \tag{2.1}$$

where $A(s,t)$ denotes current effective luminal area of an artery, $A_0(s)$ – reference luminal area (without damage). These quantities are functions of position of the point along the arc of axis of the artery s, moreover A depends on time. As the luminal area A we understand the cross-section after narrowing resulting from all possible reasons, in particular atherosclerosis and vasoconstriction, but also from a thrombosis or fissuring of an atheromatous plaque. The area A may also depend on the blood pressure p, but this dependence will not be taken into account.

The condition (reached at a certain time $t = t^*$)

$$\sup_{s \in CA} S = 1, \tag{2.2}$$

where CA denotes the set of all coronary arteries, results in complete blockage of blood flow in a certain coronary artery and so it may be regarded as the condition of occurrence of acute myocardial infarction, FROELICHER and ATWOOD [11], PASTERNAK *et al.* [27]. The point $s = s^*$ where the supremum of S is reached (dangerous point), is very important here, similarly, as in the case of creep damage

of a structural element. If the point s^* appears at a major coronary artery, in particular in the left circulation, then the myocardial infarction is more likely to result in the death of the patient, whereas if it appears at a marginal artery, after subdividing into smaller branches, then the chances of survival are much greater. Consider now Fig. 1 as the sketch of a system of coronary arteries and suppose that a ventricle is located in the upper side of both figures (a) and (b), blood flows in opposite direction to that shown by the arrows, and thicknesses of lines reflect current luminal area of individual arteries at the instant t_1. This luminal area is subject to decrease. In case (a) we may expect blockage of the major coronary artery probably leading to death of the patient, whereas in case (b) rather the central artery after branching will be blocked, resulting in a less dangerous myocardial infarction. The case of several points $s = s_i^*$ corresponds to that described in Sec. 1.

In view of the analogy between the measure of material damage D and of coronary artery damage S shown above, and the analogy of critical states described by Eqs. (1.3) and (2.2), we postulate for S an evolution equation in a form analogical to Eq. (1.4). Instead of the unit dissipated power Ψ in Eq. (1.4), we substitute here the unit power of blood flow in coronary arteries. Power of a flow, RICHTER [28], is given by

$$N_{\mathrm{f}} = Apv \tag{2.3}$$

where p denotes pressure, and v – velocity of the flow; as the unit power ν_{f} we understand this power divided by the luminal area,

$$\nu_{\mathrm{f}} = \frac{N_{\mathrm{f}}}{A} = pv. \tag{2.4}$$

It is assumed that $\nu_{\mathrm{f}} = \nu_{\mathrm{f}}(s,t)$ at any point s is proportional to the actual heart power (work per minute) $N = N(t)$ and, in analogy with Eq. (1.4), we propose the following hypothesis for the development of heart damage (evolution equation for stenosis S):

$$\frac{dS}{dt} = \frac{1}{G_{\mathrm{d}}}\sqrt{\frac{N}{1-S}} - G_{\mathrm{r}}\left[(S-S_0) - \frac{\psi}{1-S_0}(S-S_0)^2\right] \tag{2.5}$$

where G_{d} denotes the modulus of resistance of coronary arteries to the heart power, G_{r} – the modulus of recovery of coronary arteries, connected here with an increase of luminal area of these arteries (e.g. as a result of decrease of vasoconstriction or thrombus destruction), ψ – coefficient of nonlinearity of this recovery. The moduli G_{d} and G_{r} may depend here on the spatial variable s and on time t; a certain discussion of the latter dependence will be given in Sec. 8, where the effect of drugs will be considered. Moreover, these moduli may depend

on composite structure of the artery wall and on residual strains in it; the problem of residual strains was discussed e.g. by GREENWALD *et al.* [14].

The function $S_0 = S_0(s)$ in Eq. (2.5) denotes the initial damage of coronary arteries, namely damage at the instant of application of a certain, currently considered external loading $t = 0$; the value of S_0 is, first of all, due to atherosclerosis. Atherosclerosis is defined as formation of fatty streak and of fibrous plaques that cause stenosis and in the case of coronary arteries, reduce the blood supply to the myocardium. It may be regarded as the end result of various causes from among the broader group of risk factors, like hypercholesterolaemia, hypertension, clinical diabetes, excessive smoking and obesity, ROSS [29]. It also changes in time and should be described by a separate evolution equation; however, the changes of S_0 are very slow and without going into details, we simply assume that the function $S_0 = S_0(s)$ is known and we assume $S = S_0$ for $t = 0$ as the initial condition for Eq. (2.5).

The evolution equation proposed above, (2.5), will be interpreted as describing the effects of vasoconstriction, essentially dependent on loadings, specified in the next section. Muscular elastic arc of coronary vessel wall provides a mechanism whereby normal (vasoconstriction) or abnormally intense (vasospasm) increases in vasomotor tone may affect the lumen, RUTHERFORD and BRAUNWALD [30]. Vasoconstriction and vasospasm may cause intimal damage that can initiate formation of an atherosclerotic plaque, GERTZ *et al.* [13], PASTERNAK *et al.* [27], they may precipitate coronary thrombosis, VINCENT *et al.* [36], they expose the myocardium to transient ischemia, angina pectoris, or even result in sudden cardiac death, MASERI *et al.* [24], MYERBURG and CASTELLANOS [26]. Description proposed here is deterministic, hence it cannot reflect such phenomena as myocardial infarction resulting from fissuring of an atheromatous plaque and/or thrombus formation. Though the criterion of a myocardial infarction (2.2) is then also satisfied, a proper mathematical description of that phenomenon would require an evolution equation in probabilistic approach.

The power of heart N, as of a pumping system, depends on the heart rate (frequency of heartbeat, pulse) n_H, on the stroke volume V_S equal (for each ventricle) to the difference between end-diastolic volume and end-systolic volume, and on the change of pressure $\bar{p}$ in the course of pumping. It may be described by the formula (in the case of stationary motion)

$$N = -n_H \left[\int_{LV} \bar{p} dV + \int_{RV} \bar{p} dV \right] = \eta n_H \left[(p_{\text{sys}} V_S)_{LV} + (p_{\text{sys}} V_S)_{RV} \right], \tag{2.6}$$

where the line integrals are taken around the pressure-volume loops for the left ventricle (LV) and right ventricle (RV), respectively, p_{sys} denotes the maximal

(end-systolic) pressure in each ventricle, whereas the coefficient $\eta \leq 1$ depends on the variation of pressure $\bar{p}$ during the process and is simply defined by the second part of Eq. (2.6). In the case of non-stationary motions, the derivative of the square bracket with respect to time should be taken.

The term "power", namely the power of external loadings of the human organism and the power of heart, is used in cardiology in parallel with the term "workload": BRAUNWALD *et al.* [3] define stroke power (heart power) as the rate of performance of stroke work, whereas GROSSMAN [15] uses the term "workload" as the power of external loadings. Here we employ consistently the term "power", as used in physics and engineering, but in a slightly extended meaning, since psychological loadings (emotional stresses, defined in Sec. 3) will also be considered.

Many authors, e.g. GROSSMAN [15], and DENNIS [8], join the power of heart directly with the power of external loadings (often the power demanded by external agencies), using in parallel the classical units kgm/min and the units of the metabolic equivalent system (METS). A MET is defined there as a unit of workload that approximates consumption of 3.5 ml 0_2/kg min, the amount of oxygen required under basal conditions. A level of 2 METS corresponds to doubling of the 0_2 consumption and – according to the authors – is equivalent approximately to 75 kgm/min.

However, such an approach is not general enough: it may be used just for stationary states (both powers being constant in a longer period of time), whereas for short-term intensive external loadings, like weight-lifting, it cannot hold: the power of external loadings drops suddenly to zero, but the oxygen consumption remains high for a longer time. Also myocardial infarctions often take place with a considerable delay after external loadings are relieved, PASTERNAK *et al.* [27], hence it should be stated that the heart power depends on the power of external loadings of human organism not directly, but via a differential evolution equation. Now we are going to propose such an equation with at least partial explanation of the mechanism of that evolution.

3. Evolution equations for heart power

The heart should supply blood and oxygen to individual cells to meet the metabolic demand depending in an essential manner on external loadings of the organism.

External loadings may be divided into two groups: physical loadings and psychological loadings, called also emotional stresses (not to be confused with mechanical stresses used in the introduction to the present paper). Coronary vasoconstriction has been observed during exercise, RUTHERFORD and

BRAUNWALD [30], and many recent studies confirmed the importance of physical activity and pointed to emotional stress as another important trigger of myocardial infarction, JENKINS [17], TOFLER *et al.* [35], PASTERNAK *et al.* [27]. The importance of the "rate of work" or "hurrying" (it means of the power, and not of the loading itself) is stressed e.g. by RUTHERFORD and BRAUNWALD [30].

Defining physical loadings is just apparently simple: the relevant power N_p might be defined as a scalar product of force and velocity (e.g. weight of a body times its lifting velocity). As a matter of fact, there exist also many other physical loadings of the organism, not conforming directly to the above definition, for example marching along a horizontal way, in particular with a weight. This problem was considered, for example, by MILLER and VERSTRAETE [25], GARCIA *et al.* [12]. Such types of physical loadings should be suitably estimated and added. So, we assume that N_p reflects the power of all physical external loadings with appropriate overcalculations.

The effect of N_p on heart power is very diverse; to simplify the problem, we consider just one factor transmitting the power and subsequently resulting in heart damage, namely endocrine secrection of catecholamines and their circulation in blood vessels, COUSINEAU *et al.* [5]. Excessive secretion of catecholamines, in particular if alpha adrenoceptors are dominating, produces vasoconstriction and vasospasm, CREA *et al.* [7], BRAUNWALD *et al.* [3], which can lead to myocardial infarction, BERTEL *et al.* [1], PASTERNAK *et al.* [27]. Each of the most important three catecholamines, namely epinephrine (adrenaline), norepinephrine (noradrenaline), and dopamine, may be governed by a separate evolution equation

$$\frac{dk_i}{dt} = f_i(N_p, k_i) \quad i = 1, 2, 3, \tag{3.1}$$

where k_i denotes concentration of ith catecholamine in blood. In view of further simplification we consider just one kind of catecholamines and assume that the rate of concentration of this kind k is proportional to N_p.

Definition of psychological loadings, called also emotional stresses, is much more difficult, and an objective definition seems rather impossible, since the same cause can bring for one organism great stress, and for the other – none. Hence we assume here just a subjective definition of power of external psychological loadings N_s via its effects for the organism under consideration, and namely via the relevant rate of concentration of catecholamines in blood. So, for both loading types, the rate of concentration of catecholamines amounts to

$$\frac{dk}{dt} = \frac{N_p}{c_1} + \frac{N_s}{c_2}, \tag{3.2}$$

where c_1 and c_2 are the relevant coefficients of proportionality. The evolution

equation should also allow for elimination (decomposition and excretion) of catecholamines; finally, we determine the concentration of catecholamines in the cardiovascular system by the evolution equation

$$\frac{dk}{dt} = \bar{N} - c_3(k - k_0)\,, \tag{3.3}$$

where $\bar{N}$ denotes briefly $(N_p/c_1)+(N_s/c_2)$, the second term allows for elimination of the catecholamines, c_3 is the coefficient of the rate of elimination, and k_0 — concentration of the catecholamines corresponding to work of the heart at zero external loadings (it means at rest and without emotional stresses). For the sake of simplicity, the term describing elimination of the catecholamines was assumed here in a linear form; introduction of nonlinearity like in (1.4) and (2.5) is also possible.

The presence of catecholamines results in an increased demand of heart for oxygen and hence it results in an increase of the required heart power N_e. The dependence $N_e = N_e(k)$ may be represented by a Taylor series; leaving in this series for simplicity just two terms, we may write

$$N_e = N_o + \left(\frac{dN_e}{dk}\right)_0 (k - k_0)\,, \tag{3.4}$$

where N_0 is the required heart power corresponding to concentration of catecholamines at rest and without stress, whereas the derivative $(dN_e/dk)_0$ is a certain constant expressing the effect of concentration of catecholamines on the required heart power. This effect is realized mainly by increase of the heart rate n_H, but also of the pressure p_{sys}.

If there are no losses in the cardiac system, then the required power is equal to the real heart power (2.6), and may be substituted into the evolution equation (2.5). If there are losses, e.g. due to leakage of valves (regurgitation), then a suitable coefficient of tightness μ ($\mu \leq 1$), should be introduced, and the real heart power N which ensures the required heart power N_e is given by

$$N = \frac{N_e}{\mu}\,. \tag{3.5}$$

This enlarged value should be substituted into the evolution equation (2.5).

Equations (3.2), (3.3) and (3.4), express the heart power N in terms of powers of the external loadings N_p and N_s via the parameter of concentration of catecholamines k; elimination of k will be given below in dimensionless form.

4. The evolution equations in dimensionless form

Before going to a more detailed analysis of the evolution equations, first we present them in a dimensionless form, thus reducing the number of parameters.

The moduli G_d and G_r in Eq. (2.5) may be functions of time in a double manner. First, they may be subject to a relatively quick change e.g. as a result of application of appropriate drugs; second, they change slowly (usually decrease) with the age of the patient. The latter problem was discussed by WEISFELDT *et al.* [37]; they noticed the age-related diminished catecholamine responsiveness. When considering Eq. (2.5), where the time is measured in hours and minutes, the second change is not particularly important, but the first one should be allowed for. So, we introduce the dimensionless time τ by a differential formula

$$d\tau = G_r(t)dt\,. \tag{4.1}$$

Further, we denote the product of the moduli $G_d G_r$ by G and allow for its dependency on time by the formula $G = G_0 g(\tau)$, where G_0 is a reference value, for example without taking drugs; the dimensionless function $g(\tau)$ will be discussed in detail in Sec. 8. Finally, dividing both sides of Eq. (2.5) by G_r and introducing dimensionless heart power h by the formula $h = N/G_0^2$, we can eliminate all dimensional quantities and write

$$\frac{dS}{d\tau} = \frac{1}{g(\tau)}\sqrt{\frac{h}{1-S}} - \left[(S - S_0) - \frac{\psi}{1-S_0}(S-S_0)^2\right]. \tag{4.2}$$

Since ψ may be regarded as constant for the given organism (it changes slowly in a longer time interval), hence the process of damage evolution is here depending just on one dimensionless parameter h.

In order to estimate the values of the dimensionless time τ, introduced by Eq. (4.1), we integrate Eq. (4.2) in the simplest, rather abstract case of fully unloaded heart and linear recovery $h = \psi = 0$. Then the integral is of the form

$$S - S_0 = [S(0) - S_0]e^{-\tau}\,, \tag{4.3}$$

where $S(0)$ denotes the value of damage at the beginning of the recovery process under consideration. After the passage of time $\tau = 1$, the excess of damage over S_0 would decrease to $1/e$, it means to 0.367 of the initial value. This is a rather large reduction; one may assume that for individual organisms $\tau = 1$ corresponds to t equal to several hours.

Equations (3.3), (3.4) and (3.5) can be reduced to dimensionless form in the same manner. Differentiating equation (3.4) with respect to time we first obtain,

with Eq. (3.5) taken into account,

$$\frac{dk}{dt} = \frac{\mu}{\left(\frac{dN_e}{dk}\right)_0} \frac{dN}{dt}. \tag{4.4}$$

Comparing Eqs. (4.4), (3.3) and (3.4) we arrive at the equation

$$\mu \frac{dN}{dt} = \left(\frac{dN_e}{dk}\right)_0 \bar{N} - c_3(\mu N - N_0). \tag{4.5}$$

Now, introducing dimensionless time τ by Eq. (4.1), dimensionless heart powers h and h_0 as above, finally, defining dimensionless power of external loadings z and dimensionless ratio of the moduli of recovery λ by the formulae

$$z = \frac{1}{G_r G_0^2} \left(\frac{dN_e}{dk}\right)_0 \bar{N}, \qquad \lambda = \frac{c_3}{G_r}, \tag{4.6}$$

we rewrite Eq. (4.5) in the dimensionless form as follows:

$$\frac{dh}{d\tau} = \frac{z}{\mu} - \lambda\left(h - \frac{h_0}{\mu}\right). \tag{4.7}$$

The initial condition for this equation may be assumed in the form

$$h = \frac{h_0}{\mu} \qquad \text{for} \qquad \tau = 0, \tag{4.8}$$

which corresponds to the state of equilibrium before application of the loading with the power $z = z(\tau)$.

The last term in (4.7) may be interpreted as a self-protection mechanism to raise blood flow in the heart when needed. We repeat here once more that derivation of (4.7) via the secretion and excretion of catecholamines should be regarded just as an example; however, it is assumed that other mechanisms of power transmission result in similar evolution equations.

5. Stationary states

In contradistinction to the classical equation of continuum damage mechanics (1.1) which allows for a stationary state $dD/dt = 0$ just at vanishing loadings, $\sigma = 0$, the proposed evolution equations of heart damage (4.2) and of heart power (4.7) describe also the stationary or quasi-stationary states corresponding

to loadings different from zero. Assuming $dS/d\tau = 0$ and $dh/d\tau = 0$, we obtain from Eqs. (4.2) and (4.7) the following algebraic equations:

$$h = (1 - S)\left[(S - S_0) - \frac{\psi}{1 - S_0}(S - S_0)^2\right]^2 g^2(\tau), \tag{5.1}$$

$$\frac{z}{\mu} = \lambda\left(h - \frac{h_0}{\mu}\right). \tag{5.2}$$

The second of these equations determines the heart power in stationary state, corresponding to the constant power of external loadings z, or in quasi-stationary state in the case of slightly changing functions $z = z(\tau)$, $g = g(\tau)$, $\lambda = \lambda(\tau)$. It has always one root h, namely

$$h = \frac{z + \lambda h_0}{\lambda\mu}. \tag{5.3}$$

Just in this stationary case the heart power is linearly related to the power of external loadings and the latter may be expressed in METS with a reasonable level of approximation.

Then, if h is determined, Eq. (5.1) may be regarded as a nonlinear algebraic equation for the unknown S – measure of heart damage in stationary state or in quasi-stationary state in the case of slightly changing function $g = g(\tau)$. Depending on the values h and $g(\tau)$ this equation may have inside the interval $S_0 \leq S \leq 1$ two real roots, or one double root, or no real roots at all. If $h = 0$, then Eq. (5.1) has two roots: $S = S_1^* = S_0$ and $S = S_2^* = 1$; the first corresponds to coronary arteries damaged just as a result of atherosclerosis, whereas the second – to total damage (myocardial infarction). With an increase of heart power h we at first obtain two roots, one of which is located at the branch starting from $S = S_0$, and the other — at the branch starting from $S = 1$. The first root corresponds to a stable process, since an increase of h is connected with the relevant increase of $S = S_1^*$, whereas the second root corresponds to an unstable process, since a further increase of $S = S_2^*$ corresponds here to a decrease of h. The boundary value (double root) $S_1^* = S_2^* = S_{cr}$ corresponds to a maximum of the function $h = h(S)$ determined by Eq. (5.1). Equating the derivative dh/dS to zero we obtain the quadratic equation

$$5\psi S^2 - [3(1 - S_0) + \psi(4 + 6S_0)]S + [(2 - S_0 - S_0^2) + \psi(4S_0 + S_0^2)] = 0. \tag{5.4}$$

It is seen that the coefficient of S is always negative, hence the root of Eq. (5.4) located inside the interval $S_0 \leq S \leq 1$ may be written in the form

$$S = S_{\mathrm{cr}} = \frac{-b - \sqrt{\Delta}}{2a}, \tag{5.5}$$

where $\Delta = b^2 - 4ac$ is the discriminant of the quadratic equation (5.4), and a, b, c are the coefficients in this equation. The relevant maximal value of the heart power h for the stationary state $h = h_{\max}$ is given by Eq. (5.1) with substituted $S = S_{\mathrm{cr}}$ determined by formula (5.5).

The value S_{cr} separating stable and unstable stationary processes may be regarded as the point of critical stenosis, LEVIN and GARDINER [22], hence the notation S_{cr}. Usually it is assumed that the value of S_{cr} is close to 0.7, LILLY [23]. For $S > S_{\mathrm{cr}}$ the coronary blood flow is heavily reduced and individual cells of the heart muscle may be subject to damage. Detailed discussion is given below.

6. On experimental evaluation of parameters in the evolution equations proposed

The evolution equations proposed, even those presented in dimensionless form (4.2) and (4.7), require $1 + 3$ parameters to be determined experimentally, namely ψ, and μ, λ, h_0. In fact, the number of parameters is even larger, since measurements must be carried out in physical time, and not in dimensionless time. Moreover, we have to know the initial relative stenosis $S_0 = S_0(s)$, before vasoconstriction; it may be determined directly by coronary angiography methods.

Hence, two series of experiments are needed. Both series are difficult, but that concerning Eq. (4.7) seems to be easier. It needs several measurements of the heart power under external loading and at rest, for example in the course of weight-lifting and after weight-lifting. In the simplest case we could measure the oxygen consumption per unit of time and suppose that the heart power is proportional to that consumption. The effects of oxygen consumption on various aspects of the heart function were studied in a series of papers by SUGA *et al.* [32, 33], but the proportionality was found to be approximate and essentially depending on hemodynamic conditions. So, rather the integrals in formula (2.6) should be measured and their derivative with respect to time evaluated numerically.

Much greater experimental difficulties brings the evaluation of parameters in Eq. (4.2). One needs to perform subsequent measurements of coronary artery stenosis under external loading and during relaxation time. At present, coronary angiography does not allow for such measurements. Greater chances are given by scintigraphy and positron-emission tomography, but even these need further development.

In view of lack of any experimental verification of the equations proposed, some numerical examples will be given just for representative values of the parameters. Calculations for many sets of parameters were performed; we quote here just the results for the parameters being in agreement with known results

of other investigations (e.g. for critical stenosis point, mentioned above). We assume that the calculations refer to the dangerous point $s = s^*$.

7. Numerical examples, description of angina pectoris

For example, if $\psi = 0.3$, $S_0 = 0.3$, $g(\tau) \equiv 1$, then $S_{cr} = 0.726$, $h_{max} = 0.0332$; if $\psi = 0.7$, $S_0 = 0.5$, $g(\tau) \equiv 1$, then $S_{cr} = 0.745$, $h_{max} = 0.0066$. The first example refers to a heart in better health, with smaller atherosclerosis of coronary arteries ($S_0 = 0.3$) and larger resistance to the effects of damage ($\psi = 0.3$), whereas the second example – to a heart with larger atherosclerosis ($S_0 = 0.5$) and smaller resistance to the effects of damage ($\psi = 0.7$). Hence in the first case h_{max} is much larger than in the second, whereas in both cases the boundary values S_{cr} are almost equal to each other and close to the typical value of the point of critical stenosis given above. Diagrams of the function $h = h(S)$ for both sets of numerical data under discussion are shown in Fig. 2.

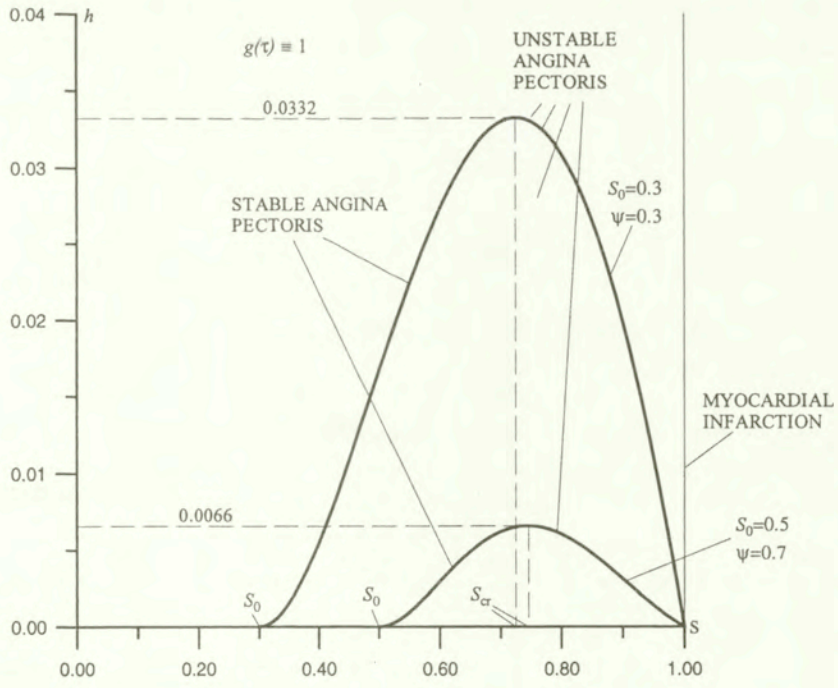

FIG. 2. Real heart power h in terms of heart damage S in quasi-stationary states. Description of stable and unstable angina pectoris.

The following interpretation of the above considerations may be regarded as justified: in the mathematical model proposed, the first, stable branch of the root

$S = S_1^*$ can describe stable angina pectoris (if $S < S_{cr}$ for any s), whereas the second, unstable branch $S = S_2^*$ or any value of heart power h larger than h_{max}, corresponds to unstable angina pectoris. In the latter case any stationary state is not possible at all; such a state may be reached just as a result of decrease of heart power h or as a result of increase of the function $g(\tau)$, for example due to suitable therapy. Without decreased h or increased $g(\tau)$, we have at least for certain values of the coordinate s the derivative $dS/d\tau$, Eq. (4.2), always positive, leading to the critical state $\sup S = 1$, corresponding to a myocardial infarction. Actual history of unstable angina might be described just in probabilistic treatment.

As an example, the evolution equation (4.7) was integrated for the first set of numerical values of parameters ψ, S_0, and for the following program of external loading: $z = z_0$ for $0 < \tau < 0.1$ and $z = 0$ for $\tau > 0.1$ (external loading with constant power z_0 acts just in dimensionless time interval of the length 0.1; this is typical for weight-lifting). Five various values of this constant power were considered: $z_0 = 2, 3, 4, 5$ and 6. Numerical values of z_0 were chosen in such a way, as to evaluate the boundary value of z_0, separating healing from myocardial infarction, without drugs, and then with drugs. The results of integration for the initial condition $h_0 = 0.01$ for $\tau = 0$ are shown in Fig. 3: during the external

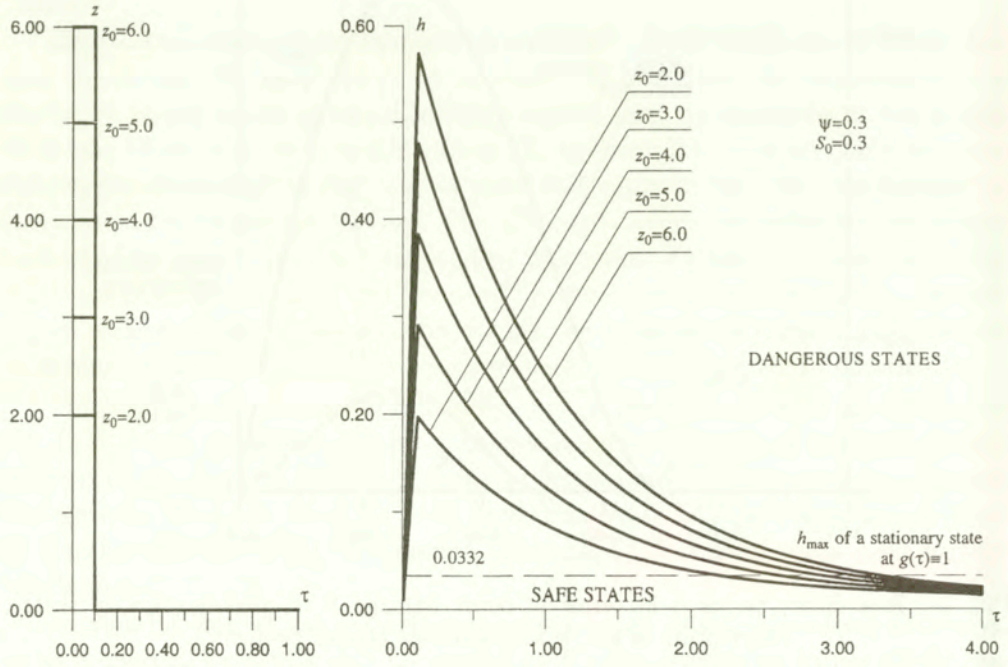

FIG. 3. Five programs of loadings and real heart power h in terms of time τ for these programs.

loading action, the required heart power h increases significantly and exceeds the admissible value of a stationary process, amounting here $h_{\max} = 0.0332$, and then monotonically decreases with time. Since $h_{\max}$ is exceeded, a myocardial infarction is possible. Indeed, the relevant integrals of the damage evolution equation (4.2) determining $S = S(\tau)$ without any therapy, $g(\tau) \equiv 1$, are shown in Fig. 4. Just in the case $z_0 = 2$ the infarction is avoided, whereas for larger values of z_0 we arrive at the value of damage $S = 1$ characterizing a myocardial infarction. The boundary value of z_0 separating AMI from healing without AMI amounts here to 2.39.

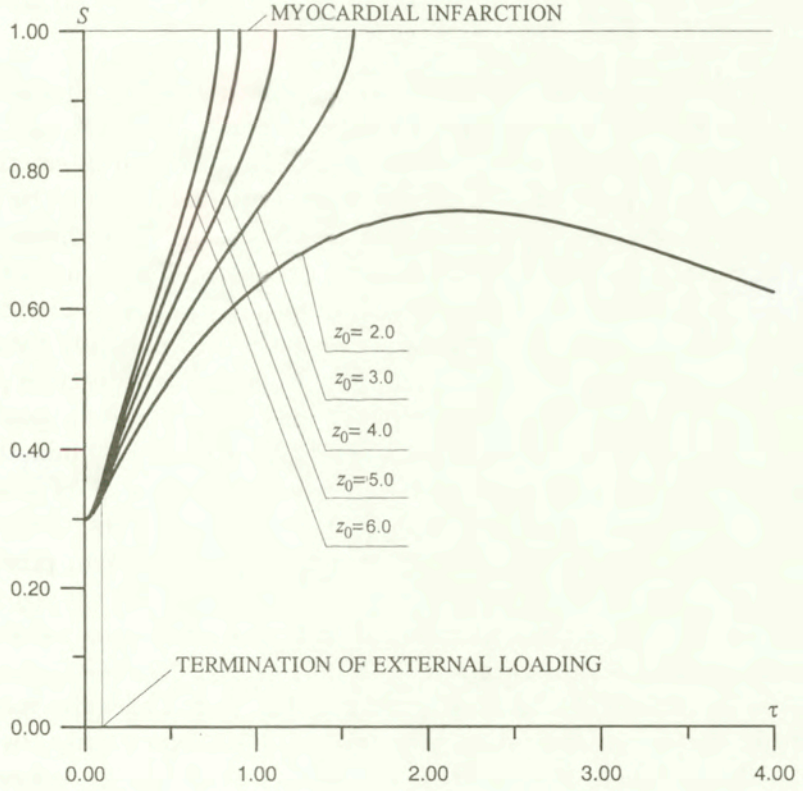

FIG. 4. Heart damage parameter S in terms of time τ without drugs.

8. Estimation of effects of drugs

According to the description given in the last section, the transition from stable to unstable angina and approaching a myocardial infarction depends in an essential manner on the modulus G, it means on the dimensionless function $g(\tau)$. Its value may be raised by taking drugs or by other forms of therapy (e.g. diet or

physical exercises). We propose here a description of the effect of drugs on the value of that function.

A small dosage of a suitably chosen drug (like nitrates which result in an increase of lumen) raises the value of the modulus, whereas excess dosage is, as a rule, harmful. For example, nitroglycerin protects the ischemic myocardium and limits the infarct size, but excessive doses may decrease the cardiac output, PASTERNAK *et al.* [27]. The simplest description of such effect can be obtained by using a quadratic function of masses of individual drugs

$$g(\tau) = 1 + \sum_{j=1}^{M} b_j m_j f_j(\tau - \tau_0) + \sum_{j=1}^{M}\sum_{l=1}^{M} b_{jl} m_j m_l f_j(\tau - \tau_0) f_l(\tau - \tau_0) \tag{8.1}$$

where M denotes the number of simultaneously taken drugs at the instant $\tau = \tau_0$, m_j – their masses, b_j – positive coefficients of the effect of unit mass of individual drugs, b_{jl} – coefficients of abuse of drugs and of their interaction. The quadratic form constituting the third term of the formula (8.1) must be negative definite, since practically always an effect of overdosage of medicines occurs. Hence all diagonal coefficients b_{jj} are negative, whereas off-diagonal coefficients b_{jl}, $j \neq l$, expressing interaction of individual drugs, may be positive in the case of mutually agonistic, and are always negative in the case of mutually antagonistic drugs (like beta-blockers and beta-stimulators). Non-negative functions $f_j(\tau - \tau_0)$ characterize the action in time of individual drugs taken at the instant $\tau = \tau_0$; as a rule, such a function reaches its maximum after some 10–30 minutes in the case of oral application, and after some 1–5 minutes in the case of intravenous or sublingual application, and then monotonically decreases practically to zero after several hours or days. Then a further dose should be taken, provided the heart power does not decrease accordingly.

One might also include into formula (8.1) negative effects, like nicotine; then the relevant coefficients b_j are negative.

An increase of the modulus G according to Eq. (8.1) raises the value $h_{\max}$, and can result in a return from nonstationary to the stationary state. In order to give a numerical example, the evolution equation (4.2) was integrated once more for the same set of parameters as in Sec. 7 and for the same loading program, but under the assumption that at the instant $\tau = 0.2$, in other words after a time twice as long as the period of action of external loading, suitable drugs were taken which resulted in a sudden increase of the value $g(\tau)$ from $g = 1$ to $g = 1.5$. The results of integration are shown in Fig. 5: evidently, for $\tau > 0.2$ the increase of damage S is smaller than in Fig. 4 and just in the case of maximal external loading under consideration, $z_0 = 6$, a myocardial infarction occurs. Now the boundary value of z_0 separating AMI from healing without AMI amounts to 5.34 and is over twice as large as in the case without drugs.

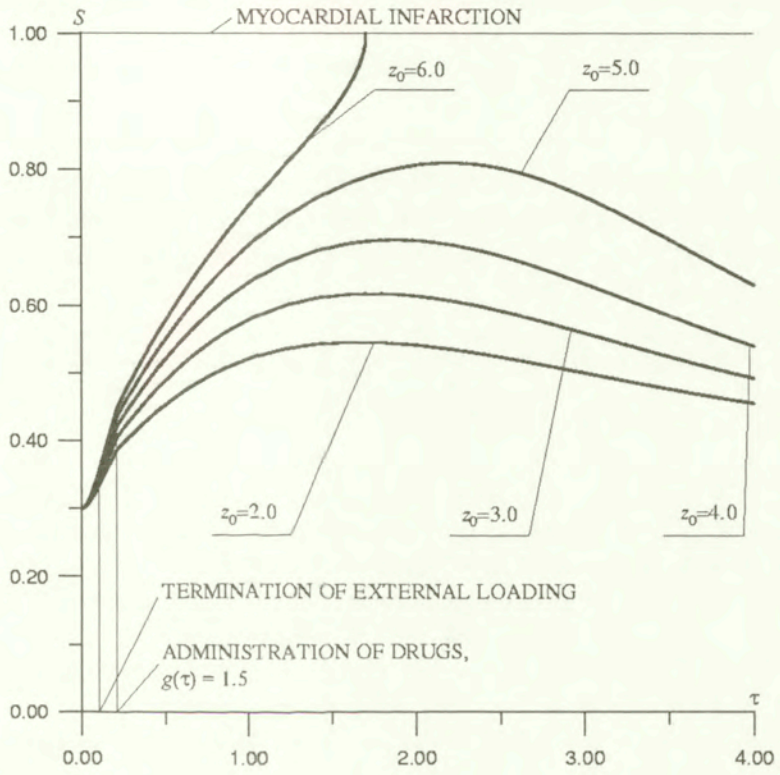

FIG. 5. Heart damage parameter S in terms of time τ with drugs taken at $\tau = 0.2$.

9. Conclusion

The description of coronary artery diseases and myocardial infarction given in the present paper has a phenomenological character and deterministic approach and hence – as it was mentioned above – it cannot reflect such phenomena as myocardial infarction resulting from fissuring of an atheromatous plaque or thrombus formation. It may constitute a first step towards a probabilistic approach describing phenomena of that type. Nevertheless, two basic evolution equations are proposed: that expressing the heart damage in terms of heart power, and that expressing the heart power in terms of power of physical and psychological external loadings. The mathematical model proposed seems to describe rather adequately basic features of development of the coronary artery disease, namely of atherosclerosis, vasoconstriction, stable and unstable angina pectoris, point of critical stenosis and myocardial infarction as a result of superposition of vasoconstriction on atherosclerosis; it considers also the effects of drugs. Evaluation of

necessary coefficients is at present difficult, but some directions of experinental research are also suggested.

Acknowledgments

The author would like to express his thanks to Jolanta Kulczycka-Życzkowska for extensive consulting in cardiology, and also to Jacek Bednarek, Marek Hiesiada, Wojciech Rakowicz, and Bożena Stobierska-Dzierżek for numerous renarks, mostly included in the present paper. Thanks are due to Piotr Trzeciak for numerical integration.

Finally, grant KBN PB 421/T07/96/11 is gratefully acknowledged.

References

1. O. BERTEL, F. R. BUHLER, and G. BAITSCH, *Plasma adrenaline and noradrenaine in patients with acute myocardial infarction*, Chest, **82**, 64–68, 1992.
2. E. BRAUNWALD, [Ed.] *Heart disease, a textbook of cardiovascular medicine*, W. B. Saunders Company, Philadelphia, 4th ed., 1992, (1974+XLIV pp.).
3. E. BRAUNWALD, E. H. SONNENBLICK, and J. ROSS, *Mechanisms of cardiac contraction and relaxation*, In: [2], Chapter 13, 351–392, 1992.
4. K. B. CHANDRAN, *Cardiovascular Biomechanics*, New York Univ. Press, New York1992.
5. D. COUSINEAU, R. J. FERGUSON, and J. DECHAMPLAIN, *Catecholamines in coronary sinus during exercise in man before and after training*, Journal of Applied Physiology, **41**, 801–806, 1977.
6. S. C. COWIN, *Bone stress adaptation model*, Journal of Biomechanical Engineering, **115**, 528–533, 1993.
7. F. CREA, S. CHIERCHIA, and J. C. KASKI, *Provocation of coronary spasm by dopanine in patients with active variant angina pectoris*, Circulation, **74**, 262–269, 1986.
8. C. A. DENNIS, *Rehabilitation of patients with coronary artery disease*, In: [2], Chapter 42, 1382–1393, 1992.
9. K. DOLIŃSKI, *Fatigue damage and reliability assessment of cemented hip prosthesis*, Journal of Theoretical and Applied Mechanics, **37**, 505–518, 1999.
10. G. FRANCFORT and J. J. MARIGO, *Stable damage evolution equations in brittle continuous medium*, European Journal of Mechanics, **12**(A/Solids), 149–189, 1993.
11. V. F. FROELICHER and J. E. ATWOOD, *Cardiac disease*, Year Book Medical Pubishers, Chicago 1986.
12. M. GARCIA, A. CHATTERJEE, A. RUINA, and M. COLEMAN, *The simplest walking model: stability, complexity, and scaling*, Journal of Biomechanical Engineering, **120**, 281–288, 1998.
13. S. D. GERTZ, G. MERIN, and R. C. PASTERNAK, *Endothelial damage and thrombosis following partial coronary artery constriction*, Israel Journal of Medical Sciences, **14**, 384–389, 1978.

14. S. E. GREENWALD, J. E. MOORE, A. RACHEV, T. P. C. KANE, and J. J. MEISTER, *Experimental investigation of the distribution of residual strains in the artery wall*, Journal of Biomechanical Engineering, **119**, 438–444, 1997.

15. W. GROSSMAN, *Cardiac catheterization*, In: [2], Chapter 7, 180–203, 1992.

16. S. JEMIOŁO and J. J. TELEGA, *A contribution to modelling of anisotropic behaviour of bone and bone remodelling*, Journal of Theoretical and Applied Mechanics, **37**, 537–554, 1999.

17. C. D. JENKINS, *Recent evidence supporting psychologic and social risk factors for coronary disease*, New England Journal of Medicine, **294**, 987–990, 1976.

18. L. M. KACHANOV, *On the time to rupture under creep conditions* (in Russian), Izviestia Akademii Nauk SSSR, Otdielenie Tekhnicheskich Nauk, **8**, 26–31, 1958.

19. L. M. KACHANOV, *Introduction to continuum damage mechanics*, Nijhoff, Dordrecht 1986.

20. D. KRAJCINOVIC, *Damage mechanics*, North Holland–Elsevier, Amsterdam 1996.

21. J. LEMAITRE, *A Course in damage mechanics*, Springer, Berlin 1992.

22. D. C. LEVIN and G. A. GARDINER, *Coronary arteriography*, In: [2], Chapter 9, 235–275, 1992.

23. L. S. LILLY, [Ed.] *Pathophysiology of heart disease*, Lea and Febiger, Philadelphia 1993.

24. A. MASERI, A. L'ABBATE, and G. BAROLDI, *Coronary vasospasm as a possible cause of myocardial infarction*, New England Journal of Medicine, **299**, 1271–1274, 1978.

25. C. A. MILLER and M. C. VERSTRAETE, *Determination of the step duration of gait initiation using a mechanical energy analysis*, Journal of Biomechanics, **29**, 1195–1199, 1996.

26. R. J. MYERBURG and A. CASTELLANOS, *Cardiac arrest and sudden cardiac death*, In: [2], Chapter 26, 756–789, 1992.

27. R. C. PASTERNAK, E. BRAUNWALD, and B. F. SOBEL, *Acute myocardial infarction*, In: [2], Chapter 39, 1200–1291, 1992.

28. H. RICHTER, *Rohrhydraulik*, Springer, Berlin 1962.

29. R. ROSS, *The pathogenesis of atherosclerosis*, In: [2], Chapter 36, 1106–1124, 1992.

30. J. D. RUTHERFORD and E. BRAUNWALD, *Chronic ischemic heart disease*, In: [2], Chapter 40, 1292–1364, 1992.

31. J. SKRZYPEK and A. GANCZARSKI, *Modelling of material damage and failure of structures*, Springer, Berlin 1999.

32. H. SUGA, T. HAYASHI, and M. SHIRAHATA, *Ventricular systolic pressure–volume area as predictor of cardiac oxygen-consumption*, American Journal of Physiology, **240**, 39–44, 1981.

33. H. SUGA, T. NOZAWA, and Y. YASUMURA, *Force-time integral does not improve predictability of cardiac O_2 consumption from pressure-volume area in dog left ventricle*, Heart Vessels, **5**, 152–157, 1990.

34. L. A. TABER, *Biomechanics of growth, remodeling and morphogenesis*, Applied Mechanics Reviews, **48**, 487–545, 1995.

35. G. H. TOFLER, P. H. STONE, and M. MACLURE, *Analysis of possible triggers of acute myocardial infarction*, American Journal of Cardiology, **66**, 22–27, 1990.

36. G. M. VINCENT, J. L. ANDERSON, and H. W. MARSHALL, *Coronary spasm producing coronary thrombosis and myocardial infarction*, New England Journal of Medicine, **309**, 220–223, 1983.

37. M. WEISFELDT, E. G. LAKATTA, and G. GERSTENBLITH, *Aging and the heart*, In [2], Chapter 52, 1656–1669, 1992.

38. M. ŻYCZKOWSKI, *Creep damage evolution equations expressed in terms of dissipated pwer*, International Journal of Mechanical Sciences, **42**, 4, 755–769, 2000.

Received December 1, 1999; revised version April 3, 2000.

INSTITUTE OF FUNDAMENTAL TECHNOLOGICAL RESEARCH
is publishing the following periodicals:

ARCHIVES OF MECHANICS – bimontly (in English)
ARCHIVES OF ACOUSTICS – quarterly (in English)
ARCHIVES OF CIVIL ENGINEERING – quarterly (in English)
ENGINEERING TRANSACTIONS – quarterly (in English)
COMPUTER ASSISTED MECHANICS AND ENGINEERING SCIENCES – quarterly (in English)
JOURNAL OF TECHNICAL PHYSICS – quarterly (in English)

Subscription orders for the journals edited by IFTR may be sent directly to the
Editorial Office
Institute of Fundamental Technological Research,
Świętokrzyska 21, p. 508,
00-049 WARSZAWA, Poland.

DIRECTIONS FOR THE AUTHORS

The journal *ARCHIVES OF MECHANICS (ARCHIWUM MECHANIKI STOSOWANEJ)* deals with the printing of original papers which should not appear in other periodicals.

As a rule, the volume of a paper should not exceed 40 000 typographic signs, that is about 20 type-written pages, format: 210×297 mm, leaded. The papers should be submitted in two copies. They must be set in accordance with the norms established by the Editorial Office. Special importance is attached to the following directions:

1. The title of the paper should be as short as possible.

2. The text should be preceded by a brief introduction; it is also desirable that a list of notations used in the paper should be given.

3. The formula number consists of two figures: the first represents the section number and the other the formula number in that section. Thus the division into subsections does not influence the numbering of formulae. Only such formulae should be numbered to which the author refers throughout the paper, and also the resulting formulae. The formula number should be written on the left-hand side of the formula; round brackets are necessary to avoid any misunderstanding. For instance, if the author refers to the third formula of the set (2.1), a subscript should be added to denote the formula, viz. $(2.1)_3$.

4. All the notations should be written very distinctly. Special care must be taken to write small and capital letters as precisely as possible. Semi-bold type should be underlined in black pencil. Explanations should be given on the margin of the manuscript in case of special type face.

5. It has been established to denote vectors by semi-bold type. Trigonometric functions are denoted by sin, cos, tg and ctg, inverse functions – by arc sin, arc cos, arc tg and arc ctg; hyperbolic functions are denoted by sh, ch, th and cth, inverse functions – by Arsh, Arch, Arth and Arcth.

6. Figures in square brackets denote reference titles. Items appearing in the reference list should include the initials of the first name of the author and his surname, also the full title of the paper (in the language of the original paper); moreover;

a) In the case of books, the publisher's name, the place and year of publication should be given, e.g.,

5. S. Ziemba, *Vibration analysis*, PWN, Warszawa 1970;

b) In the case of a periodical, the full title of the periodical, consecutive volume number, current issue number, pp. from ... to ..., year of publication should be mentioned; the annual volume number must be marked in black pencil so as to distinguish it from the current issue number, e.g.,

6. M. Sokołowski, *A thermoelastic problem for a strip with discontinuous boundary conditions*, Arch. Mech., **13**, 3, 337–354, 1961.

7. The authors should enclose a summary of the paper. The volume of the summary is to be about 100 words.

8. The authors are kindly requested to enclose the figures prepared on diskettes (format PCX, BitMap or PostScript).

Upon receipt of the paper, the Editorial Office forwards it to the reviewer. His opinion is the basis for the Editorial Committee to determine whether the paper can be accepted for publication or not.

The printing of the paper completed, the author receives 25 copies of reprints free of charge. The authors wishing to get more copies should advise the Editorial Office accordingly, not later than the date of obtaining the galley proofs.

The papers submitted for publication in the journal should be written in English. No royalty is paid to the authors.

Please send us, in addition to the typescript, the same text prepared on a diskette (flopy disk) 3 1/2″ as an ASCII file, preferably in the TEX or LATEX format in Dos or Unix format.

EDITORIAL COMMITTEE
ARCHIVES OF MECHANICS
(ARCHIWUM MECHANIKI STOSOWANEJ)

Archives of Mechanics

Contents of issue 4–5 vol. 52

(continued on cover III)

Arch. Mech., **52**, nr 4–5, str. 485–912, Warszawa 2000